Structure- and Composition-Performance Relationships of Electrically Conductive Metal-Organic Frameworks, Conjugated Porous Organic Polymers, and Fused Aromatics

by

Tianyang Chen

B. S. Chemistry
Peking University, 2017

SUBMITTED TO THE DEPARTMENT OF CHEMISTRY

IN PARTIAL FULFILLMENT OF THE REQUIREMENTS FOR THE DEGREE OF

DOCTOR OF PHILOSOPHY IN CHEMISTRY

AT THE

MASSACHUSETTS INSTITUTE OF TECHNOLOGY

June 2023

Authored by: Tianyang Chen
Department of Chemistry
May 12, 2023

Certified by: Mircea Dincă
W. M. Keck Professor of Energy
Thesis Supervisor

Accepted by: Adam P. Willard
Associate Professor
Graduate Officer

This doctoral thesis has been examined by a Committee of the Department of Chemistry as follows:

Professor Daniel L.M. Suess...
Chairman, Thesis Committee
Class of '48 Career Development Assistant Professor of Chemistry

Professor Mircea Dincă...
Thesis Supervisor
W. M. Keck Professor of Energy

Professor Yogesh Surendranath...
Member, Thesis Committee
Paul M Cook Career Development Associate Professor of Chemistry

Structure- and Composition-Performance Relationships of Electrically Conductive Metal-Organic Frameworks, Conjugated Porous Organic Polymers, and Fused Aromatics

by

Tianyang Chen

Submitted to the Department of Chemistry
on May 12, 2023, in Partial Fulfillment of the
Requirements for the Degree of
Doctor of Philosophy in Chemistry

ABSTRACT

Combining charge transport with permanent porosity and structural modulability, electrically conductive metal-organic frameworks (MOFs), have drawn increasing attention due to their potential use in a variety of applications including electrochemical energy storage (EES). Although fully conjugated porous organic polymers (POPs) generally exhibit lower electrical conductivities and crystallinity, they are built merely on earth abundant elements, light-weight, and thus offer great potential for EES applications. Fused aromatic materials are one of the most promising electrode materials for EES if not poorly conductive.

In this thesis, the author explores structure- and/or composition-property relationships of electrically conductive MOFs, conjugated POPs, and fused aromatic materials, with the focus on their potential use in energy-related applications. Chapter 1 first introduces recent developments of electrically conductive MOFs and conjugated POPs, with particular attention paid to their structure-property relationships, and their applications as electrode materials for EES. The remaining part of Chapter 1 summarizes the use of organic electrode materials for EES, emphasizing two major obstacles. Focusing on the composition-property relationships, Chapter 2 demonstrates the continuous fine-scale tuning of band gaps over 0.4 eV and of electrical conductivity over four orders of magnitude in a series of highly crystalline binary alloys of two-dimensional electrically conducting MOFs. To probe the structure-property relationships, Chapter 3 reveals the construction of compositionally constant Ni-based MOFs and conjugated coordination polymers with different structural dimensionality, including closely π-stacked one-dimensional chains, aggregated two-dimensional layers, and a three-dimensional framework, based on 2,3,5,6-tetraamino-1,4-hydroquinone and its various oxidized forms. These compositionally constant materials exhibit distinct electronic properties caused by different dimensionality and supramolecular interactions between structural motifs. Chapter 4 presents polymeric tetraoxa[8]circulenes as a new family of porous organic polymers with light-switchable and tunable semiconducting properties. Chapter 5 and 6 focus on the use of conducting fused aromatic materials as electrodes for EES. Chapter 5 describes the design and synthesis of all-organic, fused aromatic materials that store up to 310 mAh g^{-1} and charge in as little as 33 seconds. This performance stems from abundant quinone/imine functionalities that decorate an extended aromatic backbone, act as redox-active sites, engage in hydrogen bonding, and enable a delocalized high-rate energy storage with stability upon cycling. Chapter 6 demonstrates that a small fused aromatic molecule whose high electrical conductivity, high capacity for redox charge storage, and complete lack of solubility in any practical solvent allow it to reversibly intercalate Li$^+$ ions and function as a competitive cathode material for Li-ion batteries, even as a neat material.

Thesis Supervisor: Mircea Dincă
Title: W. M. Keck Professor of Energy

Table of Contents

List of Figures and Schemes

List of Tables

Chapter 1. Electrically Conductive Metal-Organic Frameworks, Fully Conjugated Porous Organic Polymers, and Fused Aromatics for Electrochemical Energy Storage

1.1 Abstract

Combining charge transport with permanent porosity and structural modulability, electrically conductive metal-organic frameworks (MOFs), which are generally composed of metal nodes and redox non-innocent organic linkers, have drawn increasing attention due to both the fundamental interests in their structural, electronic, optical, and magnetic properties, and their potential use in energy conversion and storage, chemiresistive and quantum sensors, electrolysis, thermoelectric devices, and high-density information storage. In comparison, fully conjugated porous organic polymers (POPs) generally exhibit lower electrical conductivities and crystallinity, but they are built merely on earth abundant elements, light-weight, and offer greater chemical tunability. Unlike electrically conductive MOFs and POPs which are emergent classes of materials, fused aromatic molecules/polymers have been known for decades mainly due to their applications as organic (opto)electronics. However, they have rarely been used for electrochemical energy storage (EES) because they are generally functionalized with long side chains to promote charge transport properties through optimizing the intermolecular/interchain van der Waals interactions, which inevitably lower down their gravimetric charge storage capability.

This chapter first reviews the recent developments of electrically conductive MOFs and fully conjugated POPs, with particular attention paid to their structure-property relationships and the applications of conductive MOFs as electrode materials for EES. The remaining part of this chapter is organized around the use of organic electrode materials (OEMs), in particular electrically conducting fused aromatic materials, for EES applications.

1.2 Background and Motivation

Achieving a low-carbon economy is of the utmost importance to tackle climate change and global warming. Decarbonizing the economy requires the development of renewable energies, which inevitably necessitates the concurrent advancement of energy storage technologies because of the great challenge of matching renewables supply and demand.[1] Therefore, electrochemical energy storage (EES) technologies such as lithium-ion batteries (LIBs) and electrochemical capacitors (commonly known as supercapacitors (SCs)) have attracted significant research attention as a versatile way to store energy, which can be easily deployed at a variety of scales, from centralized large-scale grid storage down to the level of distributed residential users.[2-5] In addition to the continued research on LIB and SC electrode materials, several new technologies such as redox-flow, Na-ion, K-ion, Li-S, Li-Air batteries and hybrid capacitors are being explored as potential solutions.[6-13] Nevertheless, the discovery and application of new materials that offer

better charge storage and delivery capabilities remains to be the core challenge. Ideally, these new materials would be synthesized from earth-abundant, renewable precursors in an energy-efficient manner.

Metal-organic frameworks (MOFs) are a class of crystalline materials built from metal nodes (metal ions or clusters) and multitopic organic linkers via coordination interactions, which exhibit permanent porosity with highly tuneable pore sizes.[14,15] This arrangement of various metal nodes and ligands in robust frameworks and their synthetic flexibility and tunability of the chemical and physical properties identifies them as interesting candidates for EES. However, initial research on MOFs was mainly focused on studying MOF-derived materials such as metal-oxides, metal/carbons, and porous carbons due to the poor electrical conductivity of MOFs. Several excellent reviews have provided a comprehensive account of such materials on their applications in various EES devices.[16-23] Over the past few years, transformative advances in the design and synthesis of conductive MOFs have enabled direct applications of pristine MOFs in EES devices and have opened up avenues towards tailoring materials for energy storage.[24-28] The intrinsic electrical conductivity of conductive MOFs not only facilitates the efficient utilization of all accessible redox or ion-sorption sites, but also significantly reduces or even eliminates the use of conducting additives, thus leading to the improved overall charge storage capacity. Moreover, benefitted from the combination of porosity and conductivity, conductive MOFs have demonstrated substantial promise for high-energy, and high-rate charge storage, the Holy Grail of EES.[29] Bearing similar material characteristics, electrically conductive porous organic polymers (POPs) also hold significant promise as electrode materials for EES, especially regarding the potential impact on sustainability. Different from conventional conducting polymers where conjugated organic building blocks are connected in a head-to-tail manner to form one-dimensional (1D) chains, the covalent connection of these building blocks in either two-dimensional (2D) or three-dimensional (3D) manner have produced POPs as 2D layers or 3D frameworks. The continuous 2D or 3D electronic conjugation through π-orbitals generates carrier conduction pathways and facilitates the charge delocalization and stabilization during redox charge storage processes, highlighting their potential for energy storage.[30] As an alternative OEM, although fused aromatic molecules comprising redox active functional groups exhibit outstanding electrochemical performances in terms of high energy capacities that can be twice as high as those of conventional transition-metal-based materials, they have significant drawbacks such as low electrical conductivity and high dissolution properties, which considerably prevent their practical use.[31]

Although significant research efforts have been made to utilize electrically conductive MOFs, fully conjugated POPs, and fused aromatic molecules for EES, systematic and detailed studies of fundamental structure- and composition-performance relationships of these materials have still been their infancy. My research works firstly focused on advancing the understanding of structure- and composition-conductivity relationships of electrically conductive MOFs and POPs, which can provide blueprints for future design

of this class of materials for EES applications. Adapting the obtained design principles to fused aromatic molecules, we developed new OEMs with high electrical conductivity and insolubility for high-energy and high-rate EES in both environmentally friendly aqueous electrolytes and practical-relevant organic electrolytes, and gained insights into tailoring molecular structures for specific EES requirements.

1.3 Batteries and Supercapacitors

Metal-ion batteries (lithium-ion (LIB), sodium-ion (SIB) and potassium-ion (PIB)) store energy through reversible faradaic processes and the amount of charge stored is measured in mAh or C as the standard metrics (Figure 1.1). A SC stores charge through physical adsorption of electrolytic ions on the charged electrode surfaces as electrochemical double layers (EDL) and the capacitance is measured in Farads (F) as the standard metric (Figure 1.1). Owing to these charge storage mechanisms, batteries deliver high-energy and low-power densities whereas SCs deliver high-power and low-energy and have encouraged researchers to develop systems with both high-energy and high-power capabilities. Over the past decade, the emergence of pseudocapacitive materials and high-rate battery materials have together given rise to ambiguity in appropriate metrics and have resulted in major mischaracterizations in scientific reporting.[32,33] Firstly, in terms of reporting the data, materials with clear battery-type redox processes, such as nickel-cobalt oxides/hydroxides, have been reported as materials with high capacitances of ~ 2000 F/g.[32] Capacitance, defined as the charge stored per unit voltage applied, is a constant over the range of voltage studied (Figure 1.2a); hence, calculating capacitance for a battery type curve in Figure 1.2b would be meaningless as the current is clearly not constant over the studied voltage range. Secondly, from a mechanistic point of view, several materials with faradaic processes and high rate capabilities are often misquoted as pseudocapacitive materials.[34] Pseudocapacitance, as first described by Conway, is a surface-based process and involves faradaic reactions that are not limited by the diffusion of ions to the redox sites.[35] Batteries, on the other hand, store charge through diffusion-limited faradaic reactions throughout the bulk of the active material and often undergo phase transformations during ion insertion.[3] Thus, pseudocapacitive materials differ from traditional battery-type materials with their fast reaction kinetics and are a unique class of materials studied in SCs.[36,37]

In the past few years, several excellent tutorial reviews and perspectives have summarized the basic differences between batteries and SCs and the way to distinguish pseudocapacitance from a typical battery-type performance using cyclic voltammograms (CVs), electrochemical impedance spectroscopy (EIS) and from galvanostatic charge-discharge voltage profiles (GCD).[29,34,38-41] In addition to identifying the obvious differences from above curves, kinetic analysis of charge storage has been established as a standard way to distinguish different types of charge storage. Since MOFs are an emerging class of materials that are

studied increasingly as electrodes for energy storage applications, here we reiterate the established reporting and analysis guidelines in the energy community.
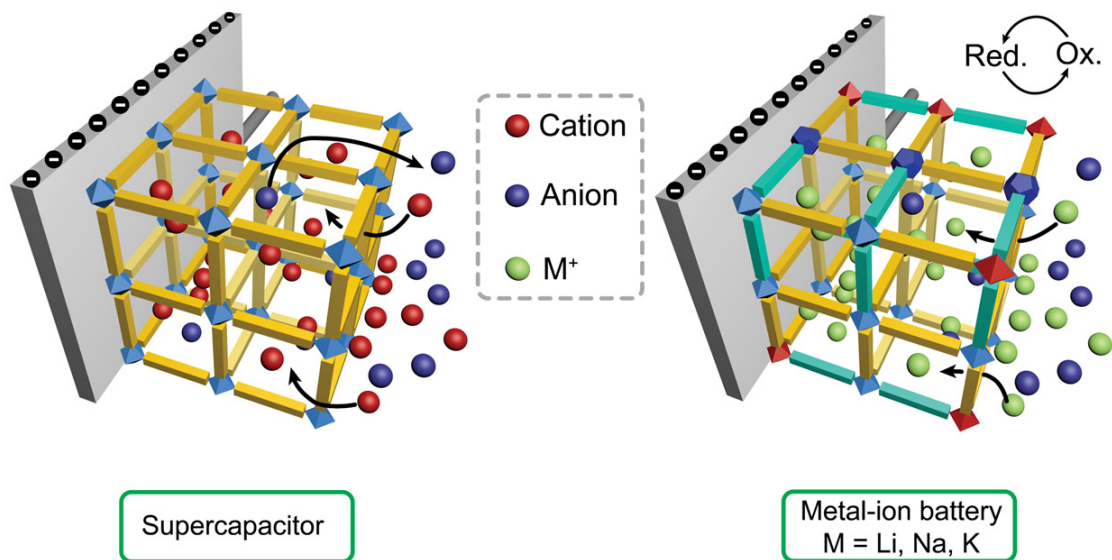
Figure 1.1. Schematic representation of electrode processes in a typical supercapacitor and a metal-ion battery. An ideal supercapacitor electrode displays physical sorption of electrolytic ions whereas a metal-ion battery electrode undergoes reversible redox transformations.
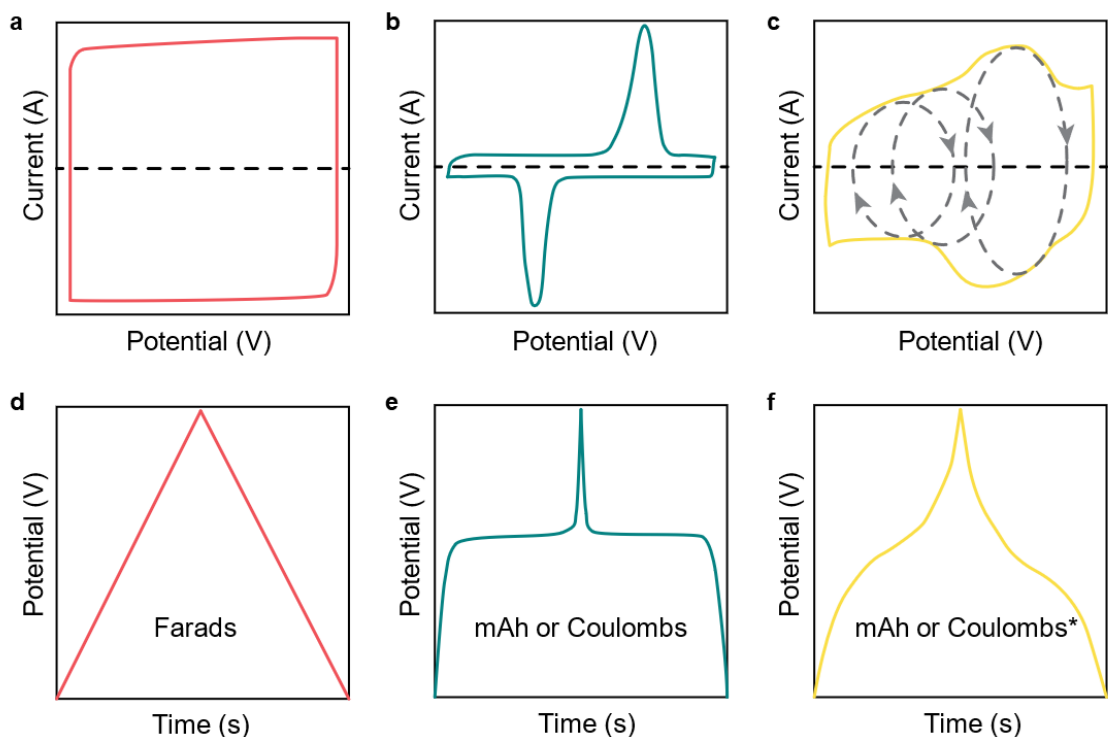
Figure 1.2. Representative electrochemical signatures of the three types of charge storage. (a, d) electrical double layer, (b, e) battery, and (c, f) pseudocapacitive. (a–c) Cyclic voltammetry (CV) curves and corresponding (d-f) galvanostatic charge-discharge (GCD) profiles with standard metrics shown for each type of storage. *Farad is also a rightful metric if CV curves and GCD are rectangular and linear, respectively, resembling a capacitor like-curve (e.g., RuO_2).

A material with a double layer capacitor-like response shows a rectangular curve in the CVs and a linear voltage vs. time response in the GCD profiles (Figure 1.2a, 1.2c). Specific capacitance of a material could then be reported as Farads per unit weight (F/g), volume (F/L) or the surface area of the electrode (F/cm^2). An electrode with a battery-type mechanism displays intense and clearly separated oxidation and redox peaks in CVs and has distinct plateaus in the GCD curves (Figure 1.2b, 1.2d). Specific charge could be calculated either as coulombs (C) or mAh per unit weight, volume, or electrode surface area. Pseudocapacitive materials demonstrate characteristics that appear intermediate to batteries and SCs, which can be easy to spot in some cases but could require further analysis in others. Typically, pseudocapacitive CVs show visible oxidative and reductive features that have minimal peak separation and are superposed over a significant and continuous capacitive current over the voltage window (Figure 1.2c). Similarly, GCD curve of such an electrode shows gradually broad and sloping plateaus (Figure 1.2e). In this case, total charge stored should ideally be reported as C or mAh as capacitance has no relevance in this case. However, pseudocapacitive materials such as $RuO_2 \cdot xH_2O$ and MoS_2 are known to exhibit rectangular CVs and linear GCD profiles as a result of multiple closely placed redox couples.[36] In such a case, it is perfectly rightful to report performances using specific capacitance as the metric.

Kinetic analysis of charge storage is a straightforward way to identify and classify an electrochemical process. In a CV experiment, the current response (i) upon varying the scan rate (v) is dependent on the charge-storage process in the electrode. Specifically, a power law relationship can be used to correlate this dependence (1):[37]

$$i(v) = av^b \text{ (1)}$$

where a is a constant and b is the exponent. b value can be obtained from the slope of a $\log(i)$ vs. $\log(v)$ plot and can be used to qualitatively distinguish the charge-storage mechanism. As described earlier, a battery-type electrode shows diffusion-controlled behaviour and the relationship between peak current (i_p) and v follows Randles-Sevick equation (2):

$$i_p(v) = 0.4463nFAcD^{1/2}v^{1/2} (\alpha nF/RT)^{1/2} \text{ (2)}$$

where c is the surface concentration of the electrode material, α is the transfer coefficient, D is the chemical diffusion coefficient, A is the electrode surface area, R is the molar gas constant and T is the absolute temperature. The i_p scales with square root of v, hence b = 0.5 whereas, pseudo-capacitors and SCs display surface-controlled behaviour and i_p has a linear relationship with v as given in (3) and hence, b = 1.

$$i_p = vCA \text{ (3)}$$

While several battery and capacitive materials are reported with strict b values of 0.5 or 1, respectively, many others are known to exhibit values in between 0.5 and 1 and are suggestive of a mixture of diffusion-controlled and capacitor-like responses.[29] A related approach is also proposed to evaluate these

contributions in a material by treating the total current as a sum of intensities from surface-controlled and diffusion-controlled processes (4).

$$i(v) = k_1 v + k_2 v^{1/2} \ (4)$$

where k_1 and k_2 are the proportionally constants that describe the surface-controlled and diffusion-controlled processes. In order to allow for better classification and rapid development of electrode materials in batteries and SCs, we encourage researchers to report appropriate metrics and perform kinetic analyses for their studies on new electrode materials.

1.4 Electrically Conductive MOFs

1.4.1 Recent Development of Electrically Conductive MOFs

Many reviews covering the electrical conductivity in MOFs, contributed by us[42-44] and others,[45-57] have appeared in recent years. Sun et al. described general methods for measuring the electrical conductivity of MOFs and the guidance of reporting conductivity values.[58] Therefore, this section will primarily focus on the advances in the field since the publication of the most recent review article by us.[44]

1.4.1.1 New Ligand Designs
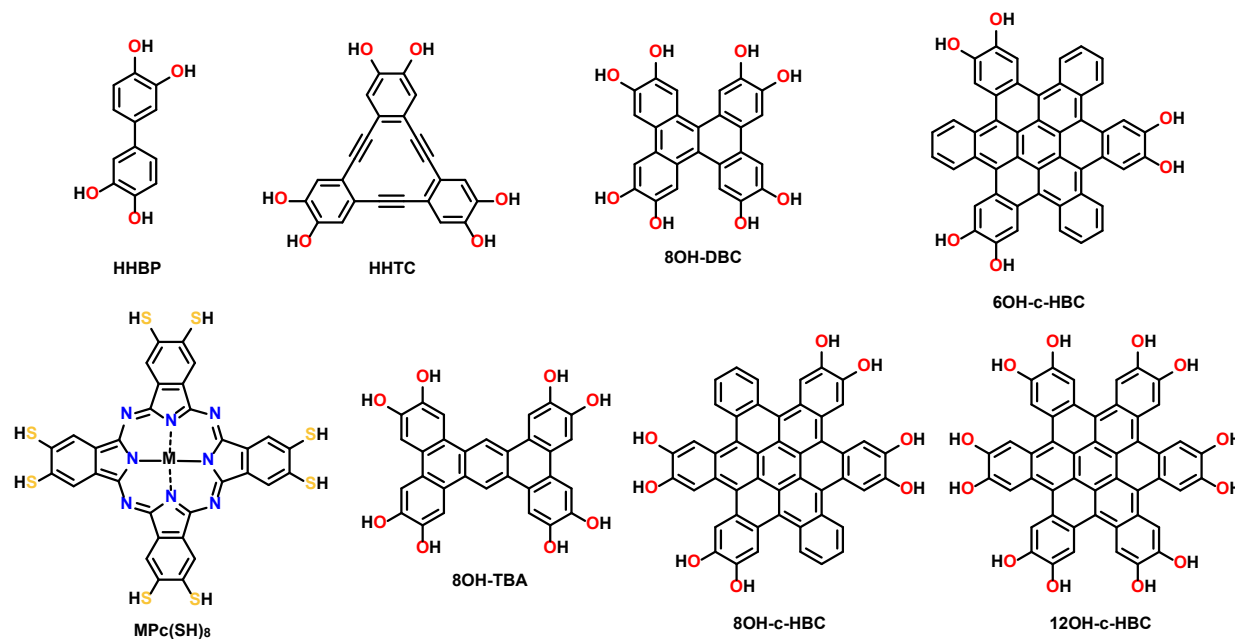
Scheme 1.1. Molecular structures of representative newly designed linkers for electrically conductive MOFs.

A vast majority of highly conductive MOFs are built on simple single metal nodes. Although using different metal nodes can easily change the properties of corresponding conductive MOFs, designing new linkers with various chemical characteristics can lead to a significantly expanded material space for new conductive MOFs and facilitate the systematic investigations of structure-property relationships.

We recently reported a MOF, named FeHOBP, with a rare two-dimensional (2D) secondary building unit (SBU). The SBU comprises mixed-valent Fe^{2+} and Fe^{3+} metal ions bridged by oxygen atoms pertaining to the polytopic ligand 3,3',4,4',5,5'- hexahydroxybiphenyl (HHBP) (Scheme 1.1), which also define the iron-oxide 2D layers.[59] FeHOBP crystallizes in the monoclinic space group $P2_1/c$ (Figure 1.3), comprising an infinite 2D SBU situated in the (*bc*) plane supported by pyrogallate moieties. Within the SBU there are two crystallographically independent, octahedral iron atoms. One (Fe_{oct}, oct: octahedral) is bound to four distinct HOBP ligands (two being κ_2 and two being κ_1), and the second (Fe_{sp}, sp: square planar) is bound to two distinct κ_2 ligands, in addition to two axially-bound, heavily disordered solvent molecules (Figure 1.3B). Perpendicular to the SBU are one-dimensional (1D) channels that run parallel to the *a*-axis of the unit cell. The contents of these channels are heavily disordered, but likely contain charge balancing dimethylammonium (DMA) cations that could not be resolved crystallographically but detected by X-ray photoelectron spectroscopy (XPS) and elemental analysis. FeHOBP belongs to a **4,6-c** net with 4,6T5 topology (Figure 1.4). The presence of Fe^{3+}/Fe^{2+} mixed valency was confirmed and quantified by high resolution Fe2p XPS and Mössbauer spectroscopy, and accounted for the electrical conductivity of ~10^{-6} S/cm. A complicated co-existence of ferromagnetic interactions and antiferromagnetic interactions was observed in FeHOBP, similar to magnetite, which probably stemmed from the high dimensionality of the SBU, and multiple metal-ligand coordination modes present in the material. These results highlight the importance of dimensionality control of MOF SBUs for discovering new topologies in reticular chemistry, and especially for improving electronic communication within the MOF skeleton.[a]
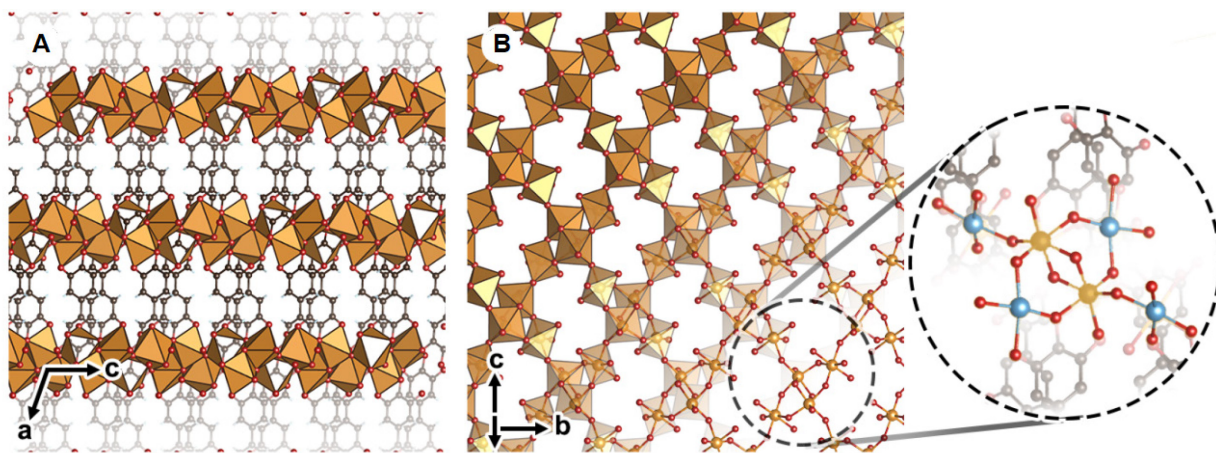
Figure 1.3. Structure of FeHOBP. View of the crystal structure along (**A**) the (ac) plane, showing the connection of the 2D SBUs through the HOBP linkers, and (**B**) along the (bc) plane, showing the 2D SBUs. Atoms corresponding to hydrogen and solvent molecules are omitted for clarity. The gray, red, and yellow spheres correspond to carbon, oxygen, and iron atoms, respectively. In the selected area of the structure (B), the two crystallographically unique iron sites, Fe_{sp} and Fe_{oct} are represented by blue and yellow spheres, respectively.

---

[a] This paragraph and Figure 1.3 and 1.4 are adapted with permission from S. Kampouri, M. Zhang, T. Chen, J. J. Oppenheim, A. C. Brown, M. Payne, J. L. Andrews, J. Sun, and M. Dincă, *Angew. Chem. Int. Ed.*, 2022, **61**, e202213960. Copyright © 2022 WILEY-VCH.
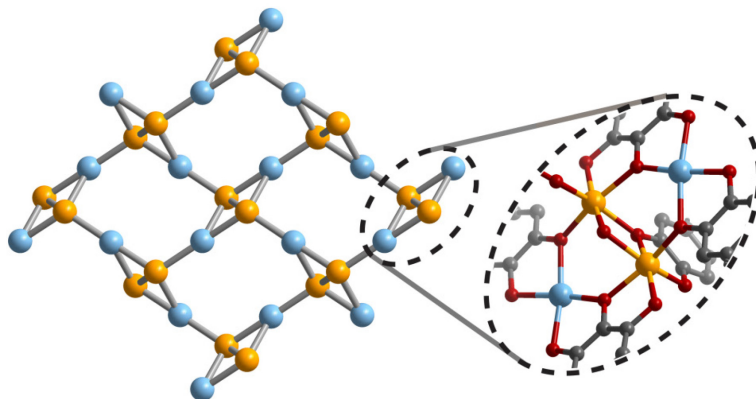
Figure 1.4. Schematic illustration of the FeHOBP topology through the cluster simplification approach, whereby the structure is broken down into parts with high connectivity. The two crystallographically independent iron sites, Fesp and Feoct are represented by blue and yellow spheres, respectively.

Park and co-workers employed a trigonal planar macrocyclic linker 2,3,8,9,14,15-hexahydroxyltribenzocyclyne (HHTC) (Scheme 1.1) to generate a hexagonal 2D MOF $Cu_3(HHTC)_2$, featuring a large surface area up to 1196 m^2/g.[60] $Cu_3(HHTC)_2$ exhibited electrical conductivity of ~2×10^{-3} S/cm and a thermally activated temperature-dependent charge transport with an activation energy of 0.26 eV. Interestingly, $Cu_3(HHTC)_2$ can undergo post-synthetic metalation through the macrocyclic linker, where Ni^{2+} and Co^{2+} can be captured by the electron-donating alkyne moieties through coordination. Although lacking strong experimental evidence, Ni^{2+} ions are calculated to prefer the intrinsic pocket of HHTC linker (in-plane), whereas Co^{2+} ions prefer to be sandwiched by two pockets (in between layers). The surface areas of Ni- and Co-metalated $Cu_3(HHTC)_2$ both dropped significantly, but the electrical conductivity of both materials increased slightly relative to the pristine state. We envision that HHTC-based 2D MOFs would generate a versatile platform to host single-atom catalysts for electrocatalysis.

Although phthalocyanine (Pc)-based 2D electrically conductive MOFs have demonstrated their use in energy storage and chemiresistive sensing, most of them are based on catechol and phenylene-diamine chemistries. Feng and co-workers reported very recently the synthesis of a Pc-based nickel-bis(dithiolene) (NiS_4)-linked 2D conductive MOF $Ni_2[CuPcS_8]$ (Scheme 1.2) and its use in pseudocapacitive electrochemical energy storage.[61] Similar to its analogs based on O and N donors, $Ni_2[CuPcS_8]$ has a square lattice with a surface area of ~220 m^2/g. The two-electron reduction of the NiS_4 linkage within $Ni_2[CuPcS_8]$ led to a remarkable specific capacitance of 312 F g^{-1} in 1 M TEABF$_4$/acetonitrile at a current density of 0.5 A/g 1 in a potential window of −0.2 to −1.3 V vs. Ag. The specific capacitance of the $Ni_2[CuPcS_8]$ electrode retained 155 F/g and 87 F/g at 10 A/g and 50 A/g, respectively, indicating its good rate capability. However, the $Ni_2[CuPcS_8]$ electrode only contains 60 wt.% of the active material $Ni_2[CuPcS_8]$, likely because $Ni_2[CuPcS_8]$ has a room-temperature electrical conductivity of ~10^{-6} S/cm which is not sufficient for high rate EES devices such as supercapacitors. Therefore, 30 wt.% of conducting carbon is required to make the $Ni_2[CuPcS_8]$ electrode, while 10 wt.% or less conducting carbon is commonly used for

supercapacitor electrodes. To this end, it is also questionable if the high-rate performance is the intrinsic properties of $Ni_2[CuPcS_8]$ or just the result of the large amount of conducting carbon.
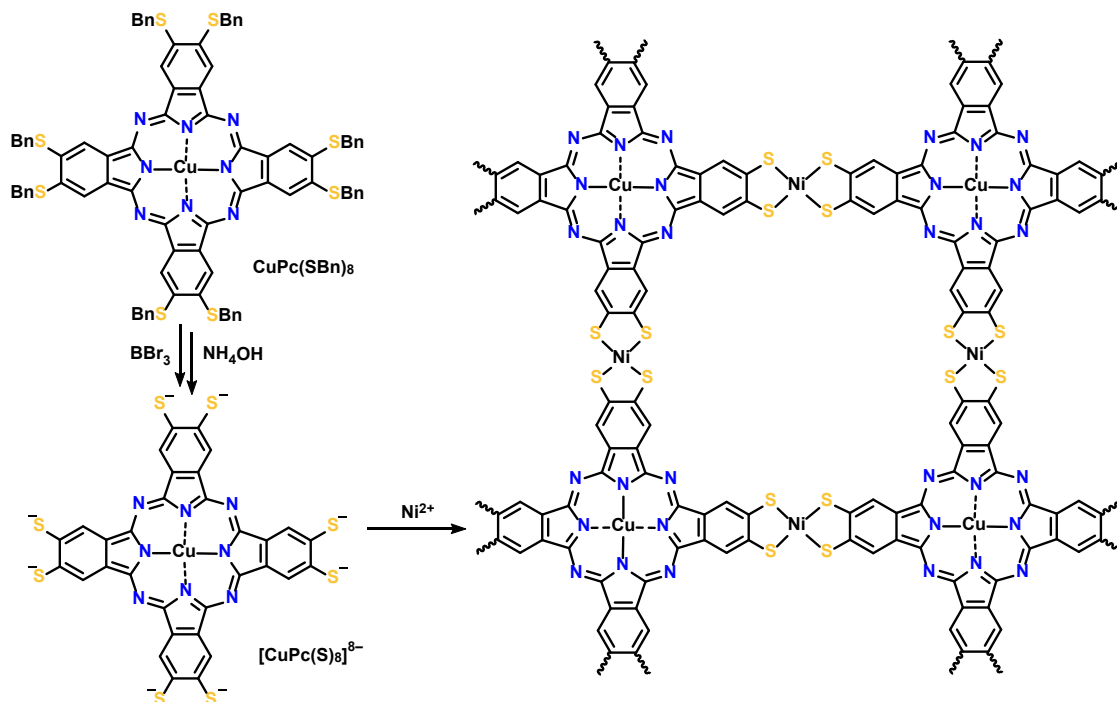
Scheme 1.2. The synthetic scheme of $Ni_2[CuPcS_8]$.
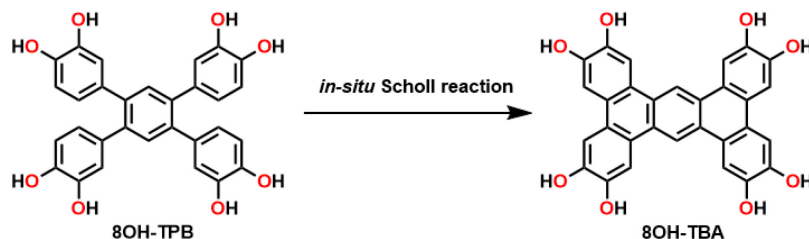
Scheme 1.3. The in-situ Scholl reaction happened during the synthesis of both *sql*-TBA-MOF and *kgm*-TBA-MOF that converted 8OH-TPB to 8OH-TBA.

Chen and co-workers developed a one-pot synthesis of 2D conductive MOFs starting from a non-planar precursor 8OH-TPB (octahydroxyl tetraphenylbenzene) with a D_2 symmetry, where 8OH-TPB underwent the *in-situ* Scholl reaction (Scheme 1.3) to form a planar linker 8OH-TBA (octahydroxyl tetrabenzoanthracene) during the MOF synthesis.[62] Two copper-based 2D conductive MOF polymorphs with either a rhombus structure (*sql*-TBA-MOF) or kagome structure (*kgm*-TBA-MOF) can be obtained accordingly through the control of pH during the synthesis. Only *kgm*-TBA-MOF can be obtained when ammonia is added to the synthesis, whereas *sql*-TBA-MOF can only be obtained without the addition of base. Interestingly, *kgm*-TBA-MOF with a room-temperature conductivity value as high as 1.65×10^{-3} S/cm is more conductive than *sql*-TBA-MOF with a room-temperature conductivity value of 4.48×10^{-4} S/cm, confirmed by two-probe conductivity measurements of the corresponding pressed pellets. Although

the authors rationalized such small difference to the hexagonal nanoflake morphology of *kgm*-TBA-MOF that facilitates the in-plane charge transport, we suggest that more thorough characterizations of electrical conductivities are required to draw any meaningful conclusions.

Fully conjugated non-planar electrically conductive MOFs have attracted significant attention recently not only because such MOFs are rare but also they could potentially exhibit more isotropic charge transport behaviors with similar electrical conductivity values relative to their 2D counterparts. One of the well-known examples is the 3D Cu-DBC MOF built from dibenzo[g,p]chrysene-2,3,6,7,10,11,14,15-octaol (8OH-DBC), which is a fully conjugated (containing only sp^2 carbons) but non-planar due to the steric hindrance of hydrogen atoms.[63] Cu-DBC formed a 4-fold interpenetrated distorted diamond network (**dia**) with 1D channels, leading to a specific surface area of 271 m^2/g. The room-temperature electrical conductivity of Cu-DBC is as high as 0.07 S/cm with a thermally activated semiconducting charge transport behavior.

Chen and co-workers recently reported the construction of three fully conjugated non-planar electrically conductive MOFs using non-planar fully conjugated organic linkers C_3-symmetrical 6OH-*c*-HBC, C_{2h}-symmetrical 8OH-*c*-HBC, and D_{2d}-symmetrical 12OH-*c*-HBC (*c*-HBC = contorted hexabenzocoronene).[64] Cu_3(6O-*c*-HBC)$_2$ is composed of wavy 2D layers formed by the coordination between Cu ions and 6OH-*c*-HBC, which then stack in a ABC manner to form the bulk material. Similarly, Cu_2(8O-*c*-HBC) is also composed of wavy 2D layers but in a different AA stacking manner. Instead of forming 2D structures, 12OH-*c*-HBC connected Cu ions to form a 4-fold interpenetrated network, leading to an overall 3D structure. Different structures led to obviously different electrical conductivities. Cu_3(6O-*c*-HBC)$_2$, Cu_2(8O-*c*-HBC), and Cu_3(12O-*c*-HBC) exhibited electrical conductivity values of 1.95×10^{-4}, 1.14×10^{-3}, and 0.0331 S/cm at room temperature, respectively. Ultrafast optical-pump THz-probe (OPTP) spectroscopy revealed the estimated Drude-Smith charge carrier mobilities of 48, 38, and 64 cm^2 V^{-1} s^{-1} for Cu_3(6O-*c*-HBC)$_2$, Cu_2(8O-*c*-HBC), and Cu_3(12O-*c*-HBC), respectively.

We note that most of the ligands for electrically conductive MOFs are highly symmetrical. However, we propose that linkers with lower symmetry, such as the examples shown in Scheme 1.4, might have the opportunity to produce conductive MOFs with unprecedented electrical/optical/magnetic properties.
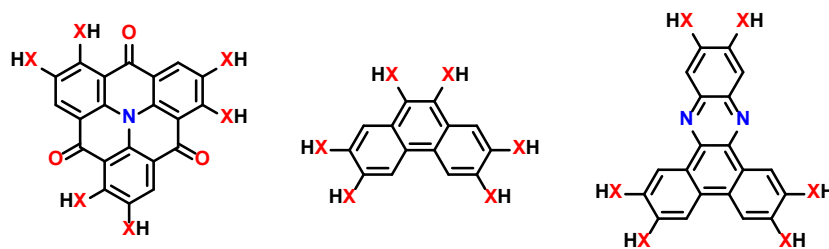
Scheme 1.4. Proposed linkers for electrically conductive MOFs with low symmetry. X = O, NH, and S.

1.4.1.2 Size and Morphological Control

The sizes and shapes of MOF crystals have been shown to exhibit significant impacts on their physical properties and applications. For example, nanosizing MOF particles have revealed enhanced properties compared to their bulk counterparts, such as improved mass transport and gas permeability, higher ratio of surface active sites for catalytic processes, and greater processability since nano-sized crystals can easily form stable suspensions in appropriate solvents.[65-68] However, size control of electrically conductive MOFs has been a long-standing challenge. Through precise size control of conductive MOF particles, the systematic study of the influence of grain boundaries on bulk electrical conductivity can be realized. Apart from the fundamental importance, decreasing the size of conductive MOFs would significantly increase the surface exposed sites for chemiresistive sensing, thus improving the sensitivity of MOF sensors.
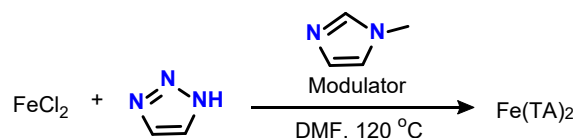
Scheme 1.5. General synthetic route to $Fe(TA)_2$ nanoparticles using 1-methylimidazole as the modulator.
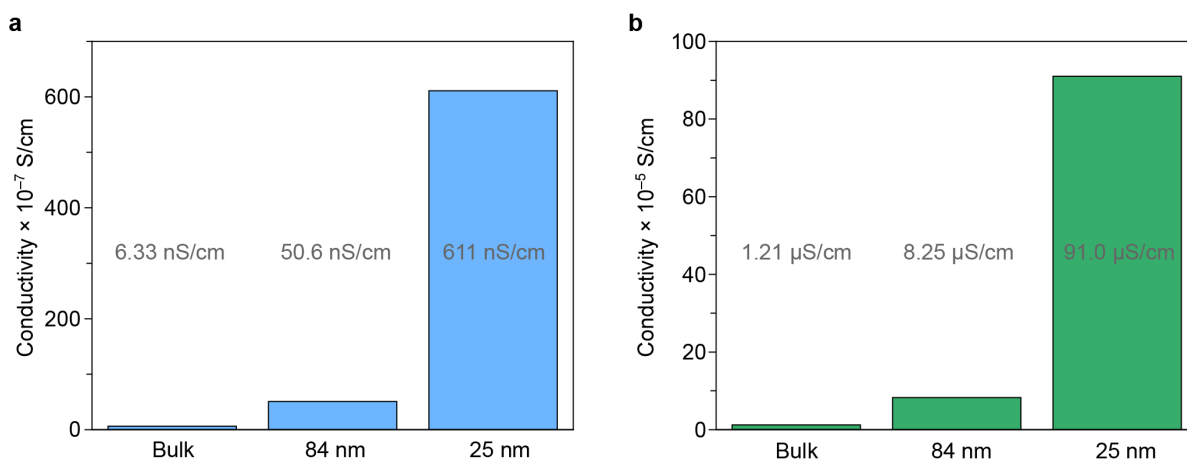
Figure 1.5. van der Pauw DC conductivity values of three $Fe(TA)_2$ thin films under N_2 (**a**) and after three days of air exposure (**b**).

Brozek and co-workers employed 1-methylimidazole (1-mIm) as a modulator for the synthesis of $Fe(TA)_2$ (TA = 1,2,3-triazolate), an electrically conductive 3D MOF, to produce nanoparticles with controllable sizes (Scheme 1.5).[69] By using different amount of the 1-mIm modulator, $Fe(TA)_2$ nano-crystals with average sizes ranging from 130 nm to 5.5 nm can be readily synthesized. Remarkably, these nano-sized $Fe(TA)_2$ crystals exhibited unprecedented solution processability due to the formation of colloidal suspension in solvents. Strong size dependent optical absorptions were observed where the major absorptions can be shifted as high as about 0.2 eV. Similarly, thin films made from these nanoparticles also exhibited size dependent electrical conductivity, where $Fe(TA)_2$ with smaller particle sizes is more

conductive (Figure 1.5). The increase of the electrical conductivity upon air exposure is caused by the oxidation of Fe^{2+} to Fe^{3+} which enables inter-valence charge transfer. Speaking from the larger amount of grain boundaries present in the smaller particles, it might be unexpected to see increasing of conductivity as the particles size decreases. However, the denser packing enabled by the smaller particles significantly reduced the contact resistance between particles, and won over the impact of increased grain boundaries.

Morphological control has been an important subject in the research of MOFs. Complementary to the tunability through the change of the fundamental chemical structures, morphological tunability enables the control of properties of the solid at the microscopic scales. Although tuning the morphology of conventional MOF particles has been successful, realizing rational morphological tunability in electrically conductive MOFs has yet been achieved. We previously reported the synthesis of both flake-like and rod-like crystals of a prototypical 2D conductive MOF $Cu_3(HHTP)_2$ (HHTP = 2,3,6,7,10,11-hexahydroxytriphenylene), but have not systematically investigated this phenomenon.[70] Recently, Xiao and co-workers revealed that partial oxidation by benzoquinone derivatives dictated the morphology of $Cu_3(HHTP)_2$ (Scheme 1.6).[71] They first replaced air, the oxidant used in the common synthetic procedures of $Cu_3(HHTP)_2$, with quinones during the synthesis, which successfully produced $Cu_3(HHTP)_2$ rod crystals. Furthermore, employing an additional 0.3 eq. and 0.5 eq. of 2,5-dichloro-1,4-benzoquinone as a pre-oxidant for the HHTP ligand, hexagonal block-like crystals and thin flake-like crystals can be obtained, respectively. Despite the different morphologies, these three $Cu_3(HHTP)_2$ samples (rods, blocks, and flakes) have indistinguishable PXRD patterns, identical infrared spectra, and similar surface areas. Interestingly, all three samples exhibited similar electrical conductivities between $10^{-2}\sim10^{-3}$ S/cm, which is quite unexpected since it is known that morphology would have a significant impact on both the amount of grain boundaries and the packing density of particles. Therefore, we believe a more thorough analysis of these samples using four-probe conductivity measurements is necessary to address this issue.
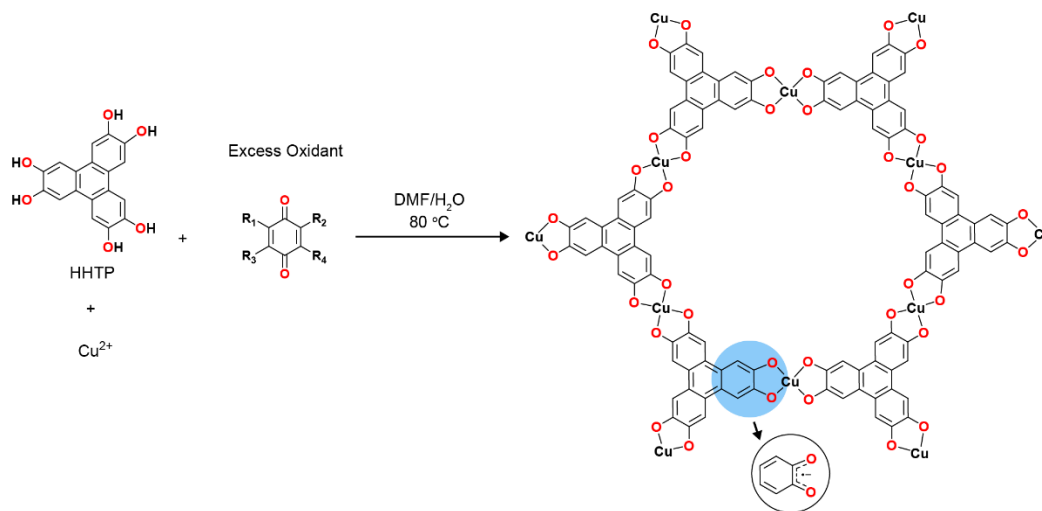
Scheme 1.6. Synthetic scheme and the oxidative control over the morphology of $Cu_3(HHTP)_2$.

1.4.1.3 Electrically Conductive Metal-Organic Macrocycles as the Bridge Between Tri-Nuclear Model Complexes and Conductive MOFs

Dimensional reduction has demonstrated its power in understanding the complicated physical properties of extended solid materials, where smaller building blocks of a larger system are isolated in the form of molecular complexes.[72] This strategy has also proved useful for studying the structure-property relationships of triphenylene-based 2D conductive MOFs, where we showed the constructions of tri-metallic HOTP and HITP model complexes and studied the electronic and magnetic communication between ligand and metal centers.[73-75]
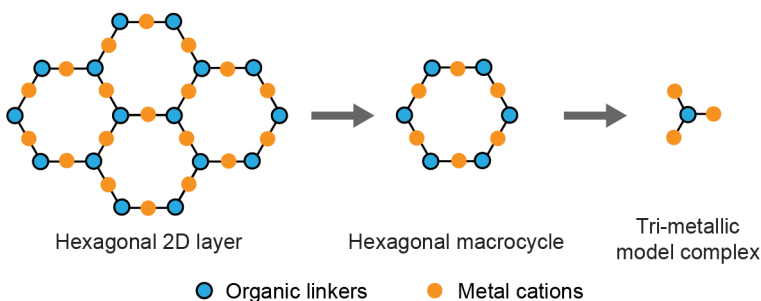
Figure 1.6. The dimensional reduction strategy.

Despite all the efforts we have made on the trimetallic model complexes of triphenylene-based 2D MOFs, there is still an important element missing in between the zero-dimensional (0D) complexes and the 2D layers of MOFs, which is the hexagonal macrocycles consisting of six organic linkers connected by six metal cations. Xiao and co-workers recently reported a family of hexagonal macrocycles consisting of Cu cations and HHTP linkers which resemble truncated fragments of $Cu_3(HHTP)_2$ and serve as the perfect bridge between 0D complexes and 2D layers.[76] These planar macrocycles, termed as CuTOTP-OR (Scheme. 1.7), stacked through interlayer π–π interaction to produce columnar 1D nanotubes, which then formed a hexagonal lattice through self-assembly, leading to a much more dynamic structure than its 2D MOF counterparts. Interestingly, the columnar stacks of CuTOTP-OC18 can be separated individually and suspended into appropriate solvents to form stable colloidal dispersions, whereas CuTOTP-OR with shorter chains only resulted in unstable dispersion. Remarkably, CuTOTP-OR exhibited similar spectroscopic characteristics to $Cu_3(HHTP)_2$, indicating that even the macrocycle contains the majority of the chemical identity of the whole 2D layer. CuTOTP-OR revealed side-chain-length dependent electrical conductivities, where CuTOTP-OC2 is the most conductive with an electrical conductivity of 2×10^{-3} S/cm, and the conductivity decreases with side chain length increases. CuTOTP-OC18 has a conductivity of 1×10^{-7} S/cm, four orders of magnitude drop. FET devices made from CuTOTP-OR macrocycles revealed ambipolar transport properties with the average saturation hole mobility ($\mu_{h,sat}$) of $(6.17 \pm 0.51) \times 10^{-3}$ cm^2 V^{-1} s^{-1}, and the average saturation electron mobility ($\mu_{e,sat}$) of $(2.16 \pm 0.61) \times 10^{-3}$ cm^2 V^{-1} s^{-1}.

R = C₂H₅ (**C2**), C₄H₉ (**C4**), C₆H₁₃ (**C6**), C₁₈H₃₇ (**C18**)
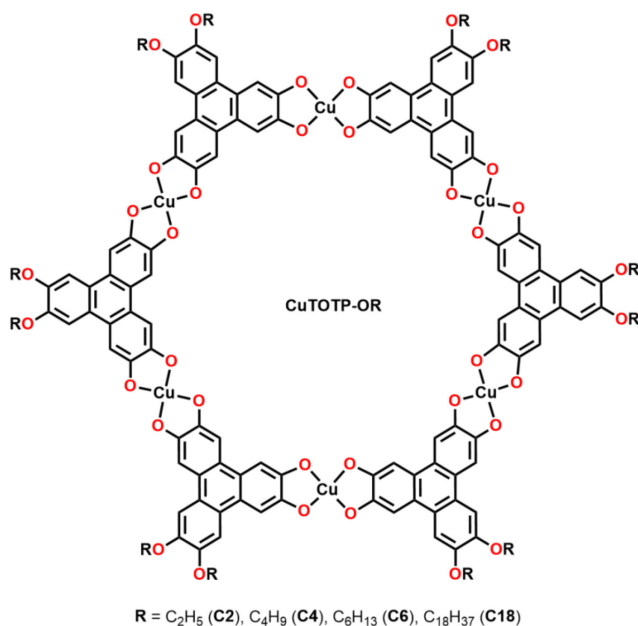
Scheme 1.7. Chemical structures of Cu-HHTP based metal-organic macrocycles CuTOTP-OR.

1.4.2 Electrically Conductive MOFs as Electrode Materials for Metal-Ion Batteries

The above-mentioned tremendous efforts on the development of 2D MOFs with excellent electrical conductivities that are on par with graphite have paved the way for their use in EES applications. As one of the pioneering examples of using electrically conductive MOFs as the active materials (AM) of MIBs, Wada and co-workers studied the 2D hexagonal layered MOF Ni_3HIB_2 (Scheme 1.8; HIB = hexaiminobenzne) as an electrode (Ni_3HIB_2: multi-wall carbon nanotube: polyvinylidene difluoride (PVDF) = 7: 2: 1) for LIBs and found a specific capacity of 155 mAh/g[b] at a very low current density of 10 mA/g. Although increasing current density to 250 mA/g led to a drop of specific capacity to ~70 mAh/g_{AM}, stable cycling over 300 cycles was achieved.[77] However, the measured voltage window of Ni_3HIB_2 was set to be 4.5 to 2.0 V vs. Li^+/Li to allow both p-type (anion insertion) and n-type (cation insertion) redox processes, leading to sloping voltage profiles. Interestingly, the authors proposed a metal and ligand-based dual-redox activity in Ni_3HIB_2 according to the *ex-situ* XPS and FT-IR analyses of the polarized electrodes, likely due to the electronic delocalization within Ni_3HIB_2. Park and co-workers applied the Co-variant (Co_3HIB_2) with high electrical conductivity of 50 S/m and N-based redox activity in SIBs (Scheme 1.8).[78] The synthesized MOF is classified with uniform pore size of 8.3 Å and a surface area of 240 m^2/g. Considering the MOF as a dense assembly of six imine groups, authors proposed Co_3HIB_2 as an ideal candidate for energy-dense electrodes. Specific discharge capacities of 228 and 151 mAh/g were observed at very high current densities of 1 and 12 A/g, respectively, for Co_3HIB_2 electrodes

---

[b] This specific capacity value and all the remaining capacity values in this chapter, except other notice, is based on the mass of active material, not the mass of the whole electrode.

(Co_3HIB_2: carbon black: PVDF = 9: 0.5: 0.5), indicating an excellent power capability, which probably originates from the high electrical and ionic conductivities in the studied MOF. The observed high capacities and power capability in a SIB are among the best reported values. Detailed XPS analysis of the polarized electrodes identify a ligand based redox activity during charge storage (Scheme 1.9). However, similar to Ni_3HIB_2, the observed sloping discharge voltage profiles from 3.0 – 0.5 V vs. Na^+/Na leads to a nominal voltage of around 1 V vs. Na^+/Na, hindering their application as either a cathode or anode material. Further detailed investigation is necessary to clearly identify the redox activity in MOF synthesized with HIB ligands.
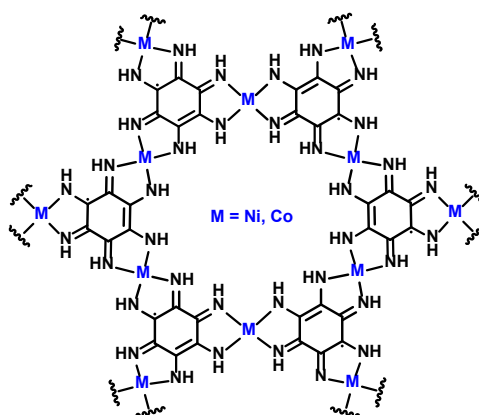
Scheme 1.8. Chemical structure of M_3HIB_2 MOFs.
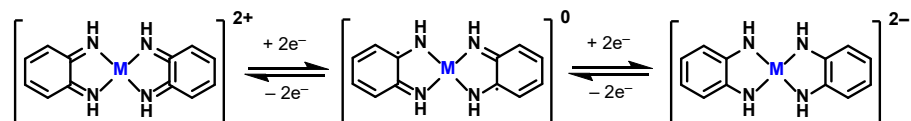
Scheme 1.9. Proposed ligand-based redox processes of M_3HIB_2 MOFs.

First synthesized by Yaghi and co-workers,[15] $Cu_3(HHTP)_2$ has a 2D hexagonal lattice and an excellent electrical conductivity reaching 150 S/m (single crystal) or 20 S/m (pressed pellet).[70] Moreover, the crystalline structure of $Cu_3(HHTP)_2$ offers high surface area of 506 m^2/g with a uniform pore size of 1.9 nm. Recently, Gu and co-workers explored the redox capability of $Cu_3(HHTP)_2$ in LIB, presenting the first report of $Cu_3(HHTP)_2$ for batteries (Figure 1.7).[79] With a working voltage of 1.7 – 3.5 V vs. Li^+/Li, $Cu_3(HHTP)_2$ cathode ($Cu_3(HHTP)_2$: PVDF = 8: 2) showed a reversible charge-discharge capacity of 95 mAh/g at 1 C after a gradual increase of capacity from 81 mAh/g at the second cycle, corresponding to an activation process of $Cu_3(HHTP)_2$. The stabilized specific capacity matches well with the theoretical value of 96 mAh/g calculated from a one-electron reduction. XPS analysis of the pristine and polarized $Cu_3(HHTP)_2$ identifies a clear reduction of Cu^{2+} to Cu^+. Detailed analysis of the reduction peak through slow scan cyclic voltammograms identified a multi-step gradual reduction (or oxidation) of the Cu^{2+} sites to Cu^+. Notably, high-rate cycling of $Cu_3(HHTP)_2$ from 1 C (charge or discharge in 1 h) to 20 C (charge or discharge in 3 min) showed excellent retention of capacity from 95 mAh/g to 85 mAh/g, respectively.

This high-rate performance in MOF-based batteries is unprecedented and is attributed to the excellent electrical conductivity and the ordered 1D channels presented in the porous structure that allow rapid electron transfer and ion diffusion to the redox sites. In addition, cycling over 500 cycles at 20 C rate has resulted in good capacity retention of 85%. First-principle DFT calculations of the fully lithiated $Cu_3(HHTP)_2$ show that the lithium atom adheres to one copper atom between 2D layers with minor changes in the lattice parameters, explaining this stability over 500 cycles. However, the charge storage capacity of $Cu_3(HHTP)_2$ is still significantly lower than conventional transition-metal-oxide-based cathodes such as LiFePO4 (~160 mAh/g) and $LiNi_{1-x-y}Mn_xCo_yO_2$ (160~200 mAh/g).
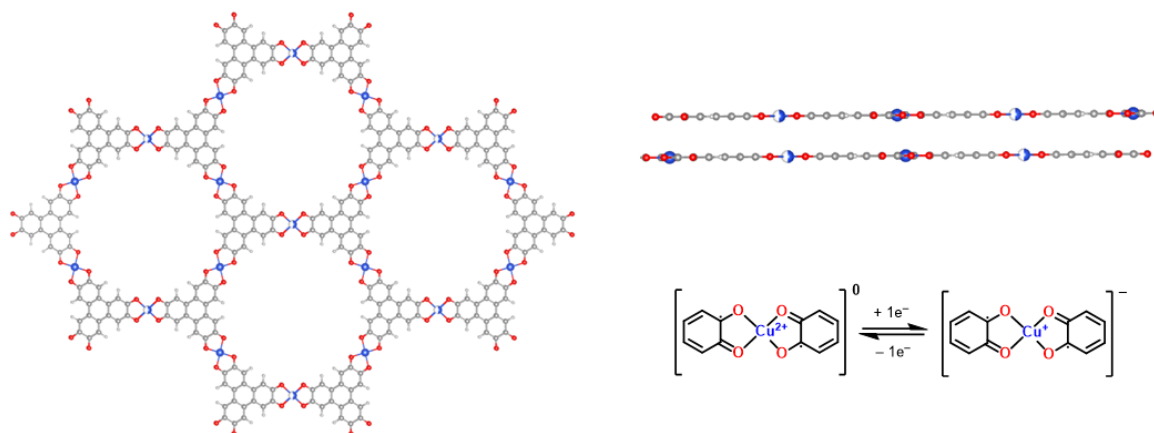
Figure 1.7. 2D layered structure of $Cu_3(HHTP)_2$ and Cu-based redox process reported by Gu and co-workers.

Nam, Park, and co-workers employed $Cu_3(HHTP)_2$ ($Cu_3(HHTP)_2$: acetylene black: PVDF = 6: 2: 2) as the cathode for aqueous zinc-ion battery (ZIB).[80] In a voltage window from 0.5 V to1.3 V vs. Zn^{2+}/Zn, $Cu_3(HHTP)_2$ delivered an initial discharge capacity of 228 mAh/g at a current density of 50 mA/g, followed by the gradual decrease of capacity to ~190 mAh/g after 30 cycles, which demonstrated a significant improvement compared to the $Cu_3(HHTP)_2$-based LIB (vide supra). Increasing current densities to 4000 mA/g (~18 C) led to a drop of capacity to 124.5 mAh/g, corresponding to 57.9% retention relative to 50 mA/g, which indicates a remarkable rate capability. Such high rate performance of $Cu_3(HHTP)_2$ originated from the intercalation of hydrous Zn^{2+} ions into the porous framework during discharge, which resulted in decent diffusion coefficients of Zn^{2+} within the electrode, and low interfacial resistance of Zn^{2+}. *Ex-situ* XPS analysis of $Cu_3(HHTP)_2$ electrodes at different charge states revealed that both copper and the quinoid structure have been utilized as redox sites (Scheme 1.10). However, the cycling stability of $Cu_3(HHTP)_2$-based ZIB — 75% of the initial capacity (152.5 mAh/g) after 100 cycles at 500 mA/g (~2 C) — is still far away from the average performance of well-known metal-oxide-based cathodes, such as $Zn_xV_2O_5$,[81] thus requiring further optimization.
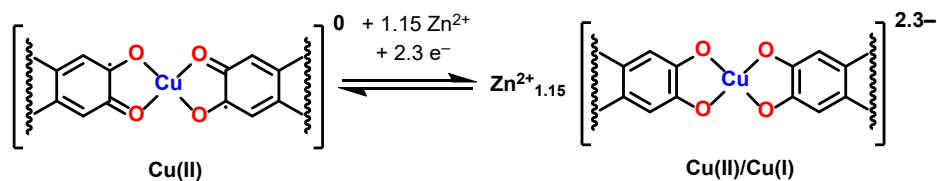
Scheme 1.10. Proposed redox process of the coordination unit of $Cu_3(HHTP)_2$ in ZIB. Both metal and linker are involved in the redox process.

Despite the prior attempts of 2D conductive MOF-based MIBs generally gave less satisfying charge storage capacity, Chen and co-workers reported the use of a 2D copper-benzoquinoid MOF Cu_3THQ_2 (Figure 1.8) as the cathode (Cu_3THQ_2: graphene: sodium alga acid binder = 7: 2: 1) for LIB which showed an unprecedentedly high reversible capacity of 387 mAh/g at a current density of 50 mA/g.[82] Similar to the LIB studies using $Ni_3(HIB)_2$,[77] the voltage window of Cu_3THQ_2 was set to be from 1.2 V to 4.0 V vs. Li^+/Li to accommodate both p-type (PF_6^- insertion) and n-type (Li^+ insertion) redox processes during discharge. The sloping discharge voltage profile led to a discharge nominal voltage of ~2 V, while a significant polarization during the charging process was observed, resulting in a charging nominal voltage of ~2.8 V. The drastic difference between discharging and charging voltage profiles indicated a poor energy efficiency. Due to its poor intrinsic electrical conductivity (2.15×10^{-3} µS/cm at 30 °C), Cu_3THQ_2 delivered less than half of the capacity at 500 mA/g (159 mAh/g) relative to 50 mA/g, followed by a further drop to 93 mAh/g at 1000 mA/g. Therefore, only the combination of high density of redox sites and high intrinsic electrical conductivity can lead to high-energy and high-power EES performances. A variety of *ex-situ* techniques have identified both copper and linker as redox sites, where Cu(II)/Cu(I) redox process takes place at the p-type region while the quinoid linker accounts for the n-type redox process.
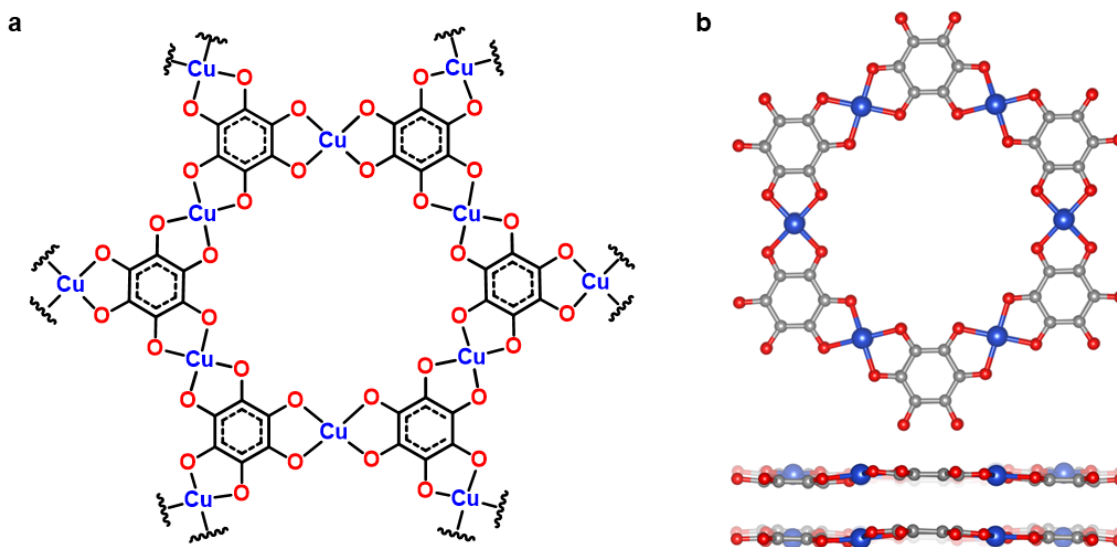
Figure 1.8. (a) Chemical structure of Cu_3THQ_2. (b) Crystal structure of Cu_3THQ_2.

As one of the most conductive coordination polymers, Cu_3(benzenehexathiolate) (Cu_3BHT), with an electrical conductivity reaching 1500 S/cm,[83] has been reported by Wu and co-workers as the cathode

(Cu$_3$BHT: multiwall CNT: PVDF = 7: 2: 1) for LIBs.[84] Operating in the voltage window from 1.5 V to 3.0 V vs. Li$^+$/Li, Cu$_3$BHT electrodes delivered reversible specific capacity as high as 232 mAh/g at 50 mA/g through a four-electron redox process. Remarkably, Cu$_3$BHT electrodes with relatively high mass loadings up to ~3.1 mg/cm^2 can still exhibit 189 mAh/g at 50 mA/g, likely due to its high electrical conductivity which allows the maximized utilization of redox sites regardless of mass loadings. Although stable cycling was confirmed for Cu$_3$BHT electrodes, the charge storage performances under high current densities (> 1000 mA/g) deteriorated significantly, possibly due to the increased ion transport/diffusion barriers at high rates.

We envision that further developments of electrically conductive MOFs as electrode materials for batteries could lead to the discovery of materials that can offer both high energy and high power, and last long.

1.4.3 Electrically Conductive MOFs as Electrode Materials for Supercapacitors

Distinct from batteries, SCs store energy through ion sorption at the electrode-electrolyte interface in electrochemical double-layer capacitors (EDLCs) or through rapid and reversible interfacial Faraday processes in pseudocapacitors. Free from the limitations of redox kinetics and ion diffusion, SCs exhibit high power density, fast charge-discharge capability, and superior long cycling life. Electrode materials with high surface areas, high electrical and ionic conductivities are usually favoured for SCs. Owing to their permanent and tuneable porosity, MOFs have been extensively studied as electrodes for SCs. In the following sections, we specifically review reports on electrically conductive MOFs as electrodes in EDLCs and pseudo-capacitors in their pristine forms (albeit with added binder and conducting carbon) and as composites prepared with carbon scaffolds.

1.4.3.1 Electrochemical double-layer capacitors (EDLCs)

A Co-Zn bimetallic MOF named Co8-MOF-5 was first reported by Díaz and co-workers in 2011 as the electrode material (Co8-MOF-5: carbon black: polytetrafluoroethylene (PTFE) =7.5: 1.5: 1) for SCs.[85] The nearly rectangular shapes of cyclic voltammograms and triangular shapes of charge/discharge voltage profiles demonstrated the interfacial ion sorption process, which is a typical EDLC behaviour. However, the specific capacitances are dominated by the carbon black additive due to the neglectable intrinsic electrical conductivity of Co8-MOF-5, therefore resulting in very low specific capacitance values (0.49 F·g^{-1} at 25 mV·s^{-1} from CVs). Therefore, improved electrical conductivities of MOFs are strongly desired to obtain better capacitances, and the recent emergence of electrically conductive MOFs promises a great potential to overcome the bottleneck of using traditional insulating MOFs as electrode materials for EDLCs. Nevertheless, to the best of our knowledge, this is the first time that MOF is used as the active electrode material for a SC.

Top view

Side view

Ni$_3$(HITP)$_2$

N
H
C
Ni

Ion adsorption

Ion adsorption

Ion desorption

Electrolyte (1 M TEABF$_4$ in acetonitrile)
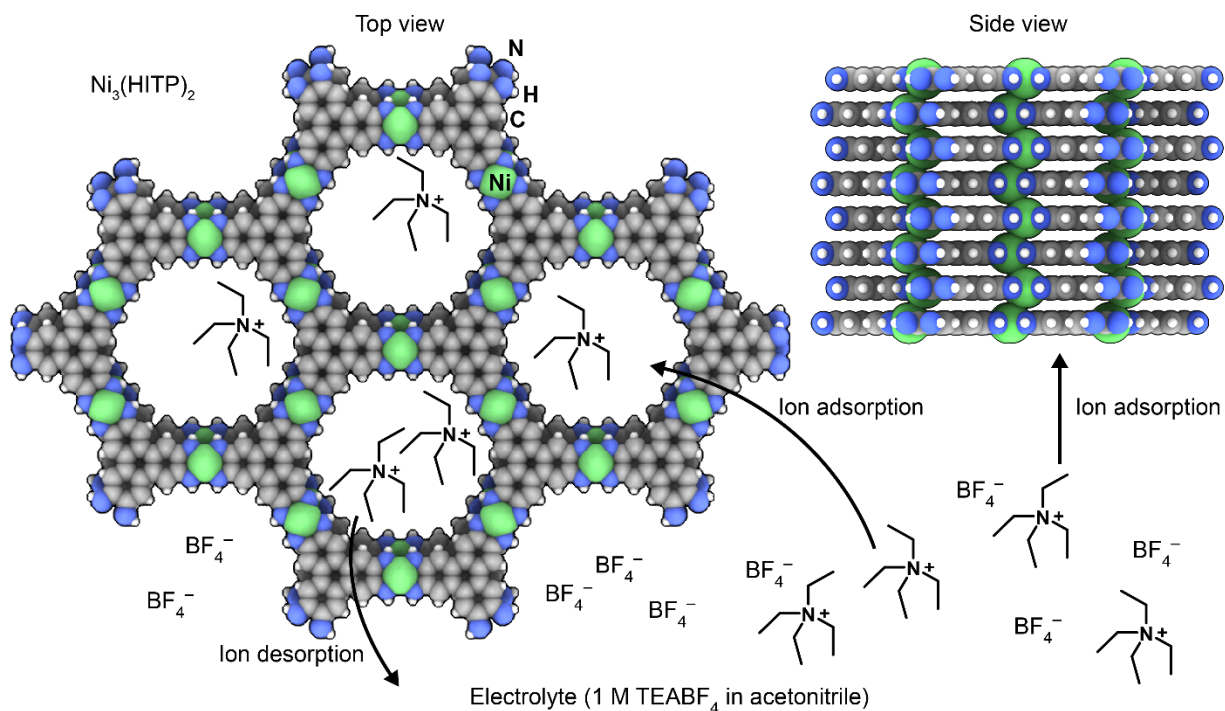
Figure 1.9. Structure and EDL charge storage mechanism of Ni$_3$(HITP)$_2$ as the electrode for supercapacitors. TEABF$_4$: tetraethyl ammonium tetrafluoroborate.

Recent work by us has demonstrated that a 2D MOF with 1D hexagonal channels (~1.5 nm) and a bulk conductivity exceeding 50 S/cm, namely Ni$_3$(2,3,6,7,10,11-hexaiminotriphenylene)$_2$ (Ni$_3$(HITP)$_2$), could be used as a pristine electrode in its neat form for EDLCs (Figure 1.9). We reported rectangular cyclic voltammograms with a specific capacitance of 110 F/g and a high surface area-normalized capacitance (areal capacitance) of ∼18 µF/cm^2 with excellent cycling ability of 90% capacitance retention after 10000 cycles.[86] Noticeably, the areal capacitance of Ni$_3$(HITP)$_2$ is comparable and even higher than common carbon-based materials, including activated carbons, carbide-derived carbons, and carbon nanotubes. The symmetric cell with Ni$_3$(HITP)$_2$ exhibits very low equivalent series resistance due to the high electrical conductivity of Ni$_3$(HITP)$_2$, and thus solves the challenge of electron transport in the electrode, leading to a sorely ion transport-controlled process. Therefore, electrically conductive MOFs are good candidates for electrodes in EDLCs but are much less studied than conventional MOFs and could be a promising future research direction. Advanced electrode fabrication methods such as electrophoretic deposition (EPD) of Ni$_3$(HITP)$_2$ onto Ni foam gives densely packed films, resulting in fast electron and ion transport and an 84.14% retention of capacitance after 100000 cycles.[87] Nevertheless, improved capacitances, high rate capability and cell operation in larger voltage windows are required to outperform porous carbon-based SCs.

Although electrically conductive MOFs gained enormous research interest in the recent years, the development of new conductive MOFs are limited by the lack of understanding of the structure-property

relationships and the rational designs of organic linkers, which renders the choice of active electrode materials also limited. Instead, a variety of composites which consist of MOFs and conductive matrices such as graphene and conductive polymers have been developed to be used as active electrode materials for EDLCs.[88-91] Rational strategies of choosing MOFs and conductive additives, reasonable design for their interactions, and appropriate synthetic approaches are required to achieve a good synergy effect for optimized electrode performances. One of the biggest challenges of synthesizing high-performance MOF-composites is the realization of effective electron transport between MOFs via conductive matrices. Several strategies have been applied to overcome this difficulty, including utilizing specially designed MOF-conductive matrix interactions and confined growth of MOFs within nano-porous carbon matrices.

Direct growth of MOFs onto conductive matrices have demonstrated to be one of the most powerful methods to produce good composites, which could provide superior contact between these two components and result in better performance than simple blending. Li and co-workers reported in 2017 the growth of $Cu_3(HHTP)_2$ onto carbon fibre to form crystalline nano-wire arrays (NWAs) with semi-controlled growth directions.[89] The $Cu_3(HHTP)_2$ NWAs electrode shows a typical double-layer capacitive behaviour with a specific capacitance of 202 F/g at 0.5 A/g, which is more than two times higher than that of neat $Cu_3(HHTP)_2$ electrode. The authors attributed this improvement to better electron transport at the $Cu_3(HHTP)_2$-carbon fibre paper interface as a result of the direct growth method. In addition, the aligned manner of $Cu_3(HHTP)_2$ NWAs might also favour the ion transport which is thought to be the bottleneck of the performance of electrically conductive MOF-based SCs. A symmetrical solid-state SC fabricated by $Cu_3(HHTP)_2$ NWAs exhibits a gravimetric specific capacitance of 120 F/g at 0.5 A/g and a superior surface area normalized capacitance of around 22 $\mu F/cm^2$ with a good cycling ability.
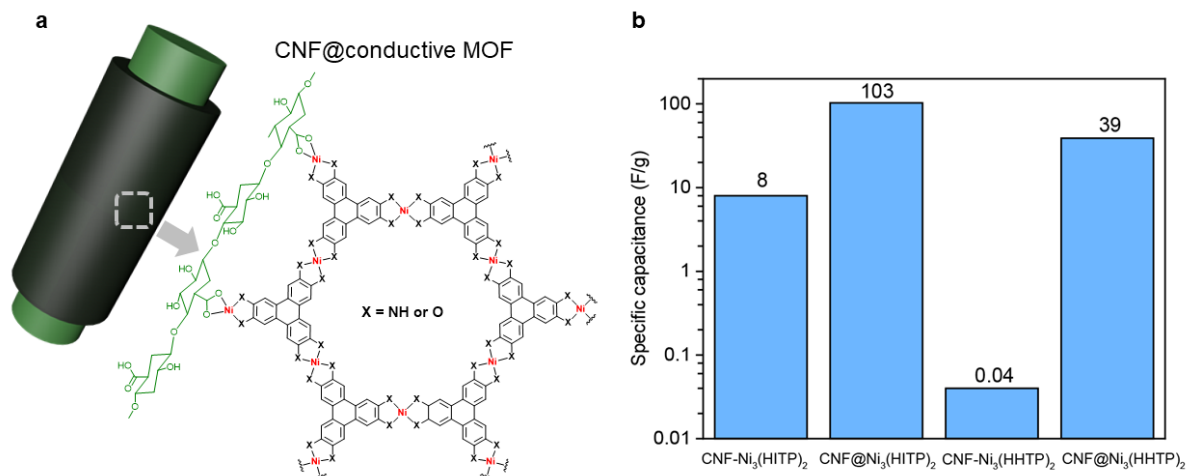
Figure 1.10. Electrochemical performances of CNF@conductive MOF composites. (a) Schematic representation of a free-standing, flexible carbon nanofiber (CNF) bound MOF paper electrodes. (b) A comparison of the specific capacitances of CNF@Ni₃(HITP)₂ and CNF@Ni₃(HHTP)₂ composites with physically mixtures of CNF-Ni₃(HITP)₂ and CNF-Ni₃(HHTP)₂, respectively in SCs.

Similarly, the interfacial growth of nanostructured $Ni_3(HITP)_2$ and $Ni_3(2,3,6,7,10,11$-hexahydroxyltriphenylene)$_2$ ($Ni_3(HHTP)_2$) on surface-modified cellulose nanofibers (CNFs) into free-standing, flexible nano-papers CNF@$Ni_3(HITP)_2$ and CNF@$Ni_3(HHTP)_2$ resulting in better charge transport characteristics (Figure 1.10).[91] Indeed, the capacitances of CNF@$Ni_3(HITP)_2$ and CNF@$Ni_3(HHTP)_2$ electrodes (103 F/g and 39 F/g at 50 mV/s) are about 10 times higher than those of CNF-$Ni_3(HITP)_2$ and CNF-$Ni_3(HHTP)_2$ electrodes (8 F/g and 0.04 F/g at 50 mV/s), which are made by dispersing $Ni_3(HITP)_2$ and $Ni_3(HHTP)_2$ particles in the CNF matrices. Additionally, this improvement might also be due to fast ion sorption processes assisted by the reduced sizes and aligned packing of $Ni_3(HITP)_2$ and $Ni_3(HHTP)_2$ at the CNF surfaces. Homogeneous dispersion of MOFs in a conductive matrix is desired for superior SC performances but is hard to achieve by the simple blending method. In this regard, we envision that the confined growth of MOFs inside the micropores or nanopores of pre-defined carbonaceous materials may be a promising solution.

1.4.3.2 Pseudocapacitors

Pseudocapacitors utilize the fast and reversible redox processes with partial electron transfer that occur only at the electrode-electrolyte interfaces. The energy density associated with Faradaic reactions is usually substantially larger than that of pure double-layer capacitive processes, resulting in both high energy density and excellent power density. However, pseudocapacitive materials should be distinguished from battery-type materials based on their distinct characteristics of CVs and output electrical response during charge and discharge, where the former tends to resemble capacitive behaviour while the latter shows clear redox peaks with large peak separation in CVs and plateaus in GCD profiles (as discussed in section 1.3). In this section, we focused only on electrically conductive MOFs and corresponding composites that show clear pseudocapacitive behaviours rather than the materials with battery-type behaviours that were misinterpreted as capacitive materials.

Feng and co-workers demonstrated in 2018 that a sub-millimeter-thick pellet made from $M_3(HIB)_2$ (M = Cu, Ni) achieved high gravimetric capacitance of volumetric capacitance up to 760 F/cm^3 for $Ni_3(HIB)_2$ at 0.2 mV/s and a high areal capacitance of 20 F/cm^2.[92] The high intrinsic conductivity of ~70 S/m provides efficient pathways for electron conduction, and the inherent nano-sized morphology with periodically distributed sub-nanometer pores (~8 Å) facilitates rapid ion sorption. Interestingly, compared with $Ni_3(HITP)_2$ which shows double-layer capacitive behaviours, $M_3(HIB)_2$ exhibits clear pseudocapacitive behaviour with less than 10% double-layer contribution to the overall capacitance for $Ni_3(HIB)_2$. A following study conducted by Lukatskaya and co-workers demonstrated that the Ni^{2+} ions in $Ni_3(HIB)_2$ are not involved in redox processes during discharge/charge in aqueous electrolytes, whereas all of the redox processes are HIB-centered, and the charge is stored through reversible redox reactions involving HIB moieties at the particle external surface, i.e., surface-confined pseudocapacitance.[93]

We recently reported a non-porous coordination polymer, Ni_3BHT (BHT = benzenehexathiolate), is an excellent electrode material that stores charge through an intercalation-based pseudocapacitive mechanism.[94] Ni_3BHT composes of Kagome-type 2D layers made up of square-planar Ni^{2+} ions bonded to four S atoms in a square planar coordination and BHT ligands surrounded by 6 Ni atoms (Figure 1.11A,B) A high electrical conductivity of 500 S/m (Figure 1.12) and the layered structure allow efficient intercalation of Li^+ ions in a non-aqueous $LiPF_6$/acetonitrile electrolyte to deliver a high gravimetric capacitance of 245 F/g and a volumetric capacitance of 426 F/cm^3 at a scan rate of 3 mV/s. Structural and electrochemical studies relate the favorable performance to pseudocapacitive intercalation of Li^+ ions between the 2D layers of Ni_3BHT (Figure 1.13), a charge-storage mechanism that has thus far been documented only in inorganic materials such as TiO_2, Nb_2O_5, and MXenes. This first demonstration of pseudocapacitive ion intercalation in non-porous CPs, a class of materials comprising thousands of members with distinct structures and compositions, provides important motivation for exploring this vast family of materials for non-traditional, high-energy pseudocapacitors. Furthermore, we have also shown that Ni_3BHT reversibly intercalates not just cations, but also anions in aqueous electrolytes, thereby qualifying as a rare dual-ion intercalation electrode material.[95] Whereas cation intercalation is pseudocapacitive, anions intercalate in a purely capacitive fashion. This excellent EC performance of Ni_3BHT provides a general basis for investigating similar dual-ion intercalation mechanisms in the large family of non-porous 2D CPs.[c]
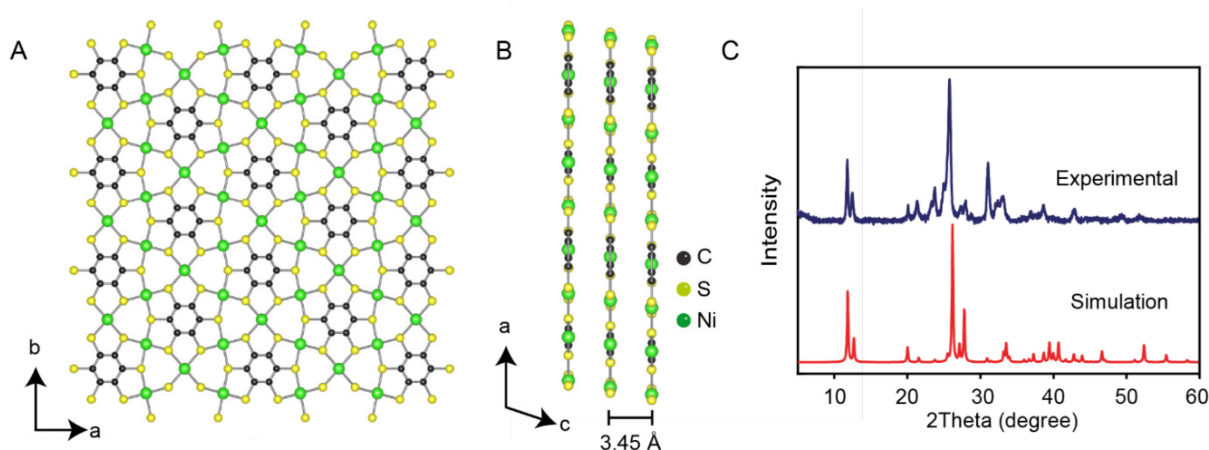
Figure 1.11. The simulated structure of Ni_3BHT shown normal to the (A) *c* axis and (B) *b* axes. (C) Experimental and simulated X-ray diffraction patterns of Ni_3BHT.
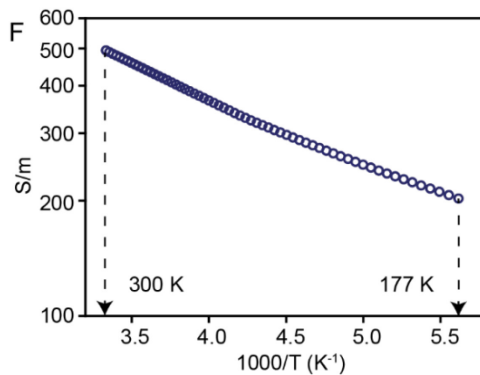
Figure 1.12. Variable-temperature electrical conductivity of a pressed Ni$_3$BHT pellet.

Intercalation-Pseudocapacitance in 2D Coordination Polymers

Figure 1.13. Cation intercalation pseudocapacitance in Ni$_3$BHT.

1.5 Electrically Conductive Conjugated Porous Organic Polymers

Since the discovery of organic synthetic metals[96-98] and conjugated polymers[99] in 1970s, the electrical conductivities of organic materials can vary from traditionally less than 10^{-9} S/cm, which is essentially insulating, to as high as 10^4 S/cm, such as the zwitterionic radical based on tetrathiafulvalene-extended dicarboxylate (TED),[100,101] iodine-doped polyacetylene, and poly(3,4-ethylenedioxythiophene) polystyrene sulfonate (PEDOT:PSS). However, most of these highly conducting organic materials are lower dimensional materials including charge-transfer complexes (molecular or zero dimensional), single component organic conductors (molecular or zero dimensional), and one-dimensional (1D) conjugated polymer chains. Inspired by the emergence of graphene, which is a two-dimensional (2D) layer of sp^2 carbon and has generated numerous exotic physical properties, extending the π–conjugation of organic building blocks into 2D or three-dimensional (3D) space through covalent bonding have attracted significant attention. Furthermore, the increased dimensionality can generate potential voids inside the materials, leading to the construction of porous organic conductors.[102]

Porous organic polymers (POPs) are a class of organic solids with intrinsic porosity formed by multi-dimensional covalent linkages of organic building blocks.[103] POPs can be either amorphous or crystalline, where the former mainly include hyper-crosslinked polymers (HCPs),[104] polymers of intrinsic microporosity (PIMs),[105] conjugated microporous polymers (CMPs),[106-108] and porous aromatic

frameworks (PAFs),[109,110] while the latter are generally termed as covalent organic frameworks (COFs).[111-114] Among them, HCPs, PIMs, and most of the 3D PAFs and COFs intrinsically do not exhibit continuous π–conjugation (i.e., not fully conjugated) due to the presence of structural sp^3 carbon linkages. In comparison, a large number of CMPs, 2D PAFs, and 2D COFs exhibit in-plane conjugated structures.[d] However, only a very small number of conjugated POPs exhibit non-negligible electrical conductivity (e.g., $> 10^{-9}$ S/cm). Therefore, we present in the following part of section 1.5 a brief overview and summary of POPs exhibiting intrinsic electrical conductivities, with specific attention paid to fully conjugated POPs. Note that composites containing POPs with other electrically conductive components are out of the scope of this section.[115-120]

1.5.1 Conjugated 2D POPs

The electrical conductivity of 2D POPs depends on the in-plane electronic delocalization through extended π–conjugation of electroactive organic building blocks and the out-of-plane through-space π–π stacking of 2D layers. Although the choices of electroactive organic building blocks with π–conjugation are plentiful,[121] the layer-forming covalent linkages between different building blocks can be sorted as a handful of classes (Scheme 1.11), and play a crucial role in determining the electrical conductivity. Although boronic esters and boroxine linkages are the earliest and one of the most studied linkages of 2D POPs, they provide minimal to no electronic conjugation between two adjacent organic building blocks due to the ionic nature of the B–O bonding. Therefore, boronic esters and boroxine linkages act as carrier traps and block any degree of in-plane charge transportation, leading to inferior electrical conductivity. Although several boronic ester-based POPs have been reported to exhibit electrical conductivities between 10^{-10} and 10^{-7} S/cm,[122] and TRMC (time resolved microwave conductivity) carrier mobility $\sim10^{-4}$ cm^2 V^{-1} s^{-1},[123] the conduction pathways are most likely through π–π stacking of 2D layers or hopping of localized charges.

Due to the excellent chemical reversibility of imine formation reaction (e.g., Schiff base forming reactions), imine linkage (C=N) has also been extensively employed in the construction of 2D POPs, usually with remarkable crystallinity. Although moderate electronic delocalization through the polar C=N connection can be realized in imine-based 2D POPs, which in principle should lead to higher electrical conductivities compared with boronic ester-based analogues, the contribution of in-plane conduction pathways to the total electrical conductivity is still marginal. Instead, the ordered interlayer stacking could significantly promote the through-space carrier conduction. For example, a porous, crystalline 2D π–conjugated COF formed by connecting triamino-trioxaazatriangulene (TANG) with 2,5-dihydroxyterephthaldehyde through imine linkage (TANG-COF, Scheme 1.12) exhibits an in-plane and

---

[d] CMPs, 2D PAFs, and 2D COFs have a significant degree of material overlap.

out-of-plane room-temperature electrical conductivity of 5×10^{-12} S/cm and 1.6×10^{-5} S/cm, respectively (measured as a thin film). Interestingly, I_2 doping of TANG-COF led to a dramatic increase in both in-plane and out-of-plane electrical conductivities to 2×10^{-3} S/cm and 1.5×10^{-3} S/cm, respectively, likely through the generation of N-centered radicals.[124] As a variant of imine linkage, keto-enamine linkage could lead to some degree of tautomerization and provide potential hydrogen bonding sites, which are beneficial for enhancing the electronic delocalization. More detailed studies of the chemical doping (I_2, $SbCl_5$, F_4TCNQ) of imine-based 2D COFs have been reported in Wurster-type COFs both experimentally and theoretically.[125,126]
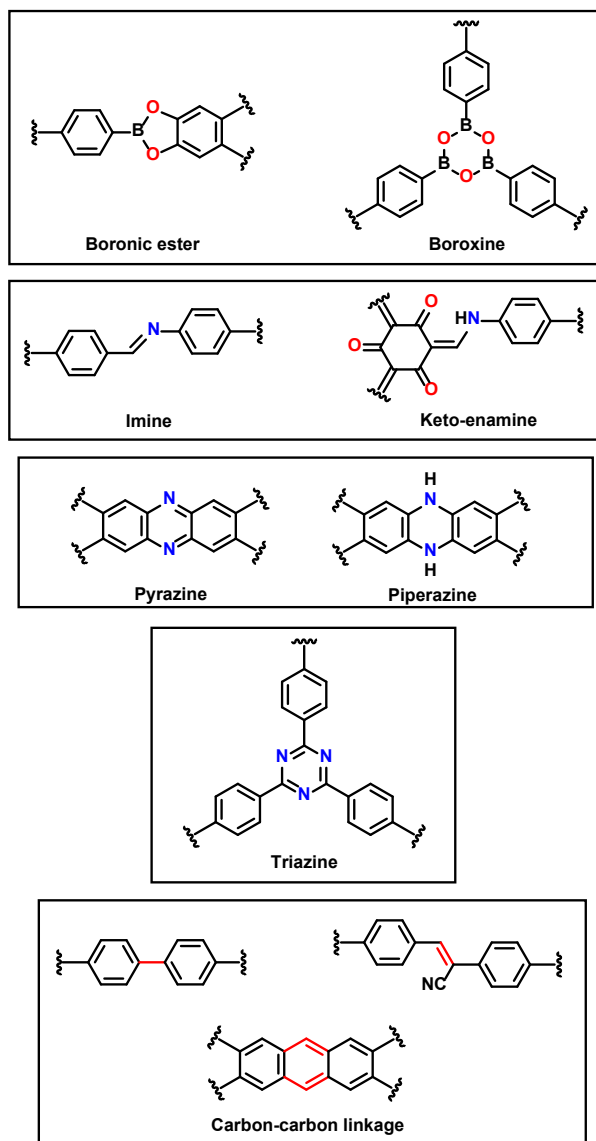
Scheme 1.11. Typical linkages employed for the construction of conductive COFs and POPs.
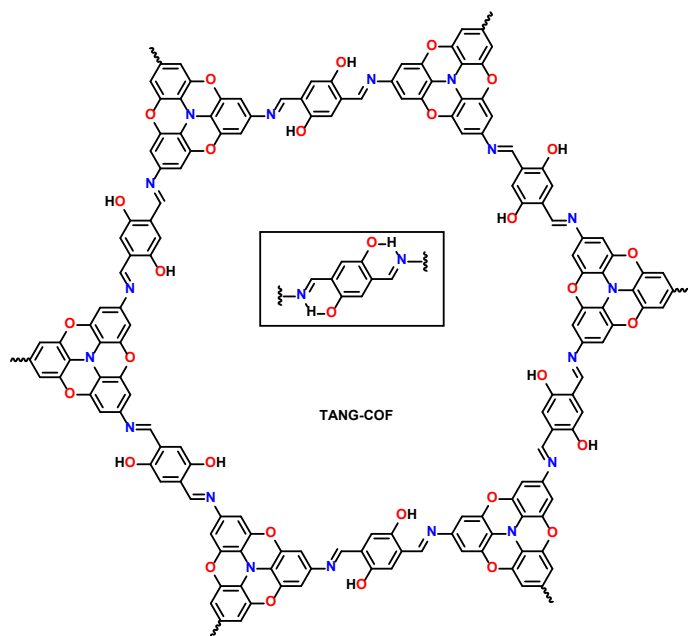
TANG-COF

Scheme 1.12. Chemical structure of TANG-COF.

Carbon-carbon linkages through sp^2 carbon atoms can lead to significantly improved electronic delocalization and can be considered as truly full conjugation. However, $C(sp^2)$–$C(sp^2)$ (olefin) formation reactions are usually irreversible, leading to the formation of poorly crystalline or even amorphous materials, such as JUC-Z2 formed by Yamamoto-type Ullmann reaction (Scheme 1.13).[127] One exception is crystalline 2D COFs formed by Knoevenagel polycondensations such as sp^2-c-COF (Scheme 1.13). This cyanovinylene-linked pyrene-based COF exhibited intrinsic electrical conductivity of ~10^{-16} S/cm, which increased to ~10^{-4} S/cm after I_2 doping.[128] In comparison, predominantly amorphous JUC-Z2 exhibited electrical conductivity of around 1×10^{-2} S/cm after I_2 doping,[127] suggesting higher degree of electronic delocalization compared with more crystalline sp^2-c-COF. Recently, olefin-linked 2D COFs were reported to be synthesized through Brønsted acid-catalyzed Aldol condensation between the activated methyl groups of 1,3,5-triazine and aryl aldehydes.[129,130] Although electrical conductivity of corresponding COFs have not been studied yet, they might enrich the library for electrically conductive olefin-linked 2D COFs, especially beneficial for structure-conductivity relationship studies, which to our knowledge have been done for olefin-linked 2D COFs.
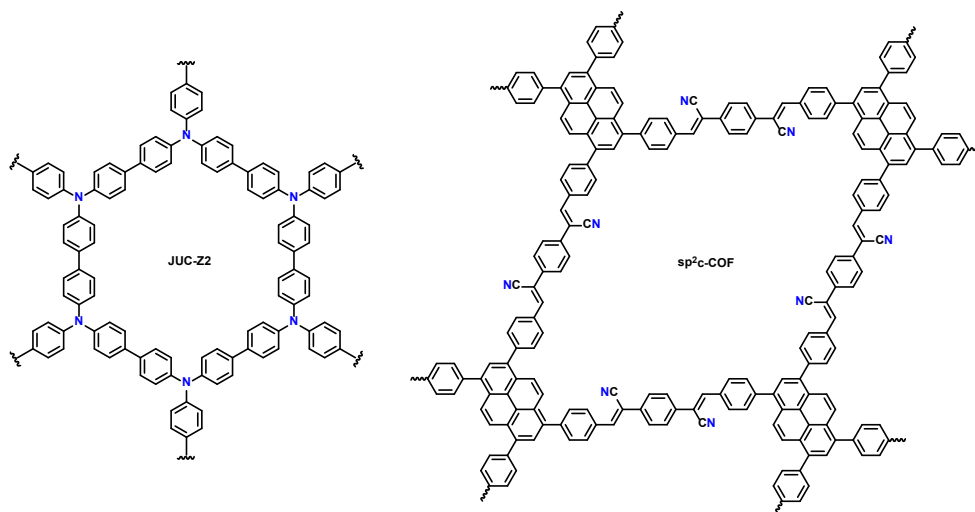
Scheme 1.13. Chemical structures of JUC-Z2 (left) and sp^2-c-COF (right).

The use of pyrazine linkages has generated a number of semiconducting POPs due to the ladder-type linkage (Figure 1.14) which ensures the in-plane full conjugation and great electronic delocalization. One of the earliest examples of pyrazine-linked 2D POPs was reported by Jiang and co-workers, which exhibited a hole mobility of 4.2 cm^2 V^{-1} s^{-1} by the time-resolved microwave conductivity method (Scheme 1.14, CS-COF).[131] However, its electrical conductivity was not reported. Interestingly, an ambipolar 2D POP C$_2$N-h2D (Scheme 1.14), constructed from the polycondensation between hexaaminobenzene and hexaketocyclohexane, exhibited an electron mobility of 13.5 cm^2 V^{-1} s^{-1} and a hole mobility of 20.6 cm^2 V^{-1} s^{-1}, respectively, when fabricated as a thin-film field-effect transistor (FET).[132] C2P-5 COF, a reticular expansion of C$_2$N-h2D (Scheme 1.14) synthesized by HHTP and HATP, showed a hole mobility of 4 cm^2 V^{-1} s^{-1} and an electrical conductivity of 1.75 S/cm when measured as a thin film.[133] To our knowledge, C2P-5 COF represents the most electrically conductive POPs to date.

Pyrazine-linked metal-Pc (MPc)-based 2D COFs (MPc-pz COFs) built from 2,3,9,10,16,17,23,24-octaaminophthalocyaninato metal[II] (MPc[NH$_2$]$_8$) and a variety of tetra-ones represents a family of square-shaped electrically conductive POPs (Scheme 1.14). MPc-pz COFs exhibited electrical conductivities of 7.0×10^{-7} S/cm, 3.3×10^{-7} S/cm, and 2.51×10^{-5} S/cm when M is Zn (R = ^{t}Bu),[134] Cu (R = ^{t}Bu),[134] and Ni (R = H),[135] respectively. Recently, Huang and co-workers reported a piperazine-linked MPc-based 2D POP M$_1$Pc-NH-M$_2$PcF$_8$ (Scheme 1.15) synthesized by the solvothermal nucleophilic aromatic substitution reaction between NiPc[NH$_2$]$_8$ and 1,2,3,4,8,9,10,11,15,16,17,18,22,23,24,25-hexadecafluoro-9H,31H-phthalocyaninato metal[II] (MPcF$_{16}$, M = Co or Cu).[136] NiPc-NH-CoPcF$_8$ and NiPc-NH-CuPcF$_8$ exhibited electrical conductivities of 0.0272 S/cm and 0.0241 S/cm when measured as pressed pellets, respectively. Higher values were observed when NiPc-NH-CoPcF$_8$ and NiPc-NH-CuPcF$_8$ thin films were measured, leading to 0.127 S/cm and 0.115 S/cm, respectively. The carrier mobility of both NiPc-NH-CoPcF$_8$ and NiPc-NH-CuPcF$_8$ were also measured by two methods, including Hall

measurements and FET measurements. Interestingly, the Hall mobility of NiPc-NH-CoPcF$_8$ and NiPc-NH-CuPcF$_8$ films were determined as 35.4 cm^2 V^{-1} s^{-1} and 35.1 cm^2 V^{-1} s^{-1}, while the values obtained from FET measurements were only 0.13~0.34 cm^2 V^{-1} s^{-1}.
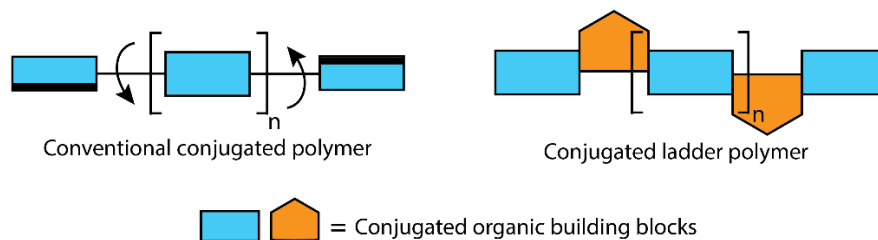
Figure 1.14. Comparison between conventional conjugated polymers linked by rotatable C–C single bonds and conjugated ladder polymers linked by two bonds to form full conjugation.
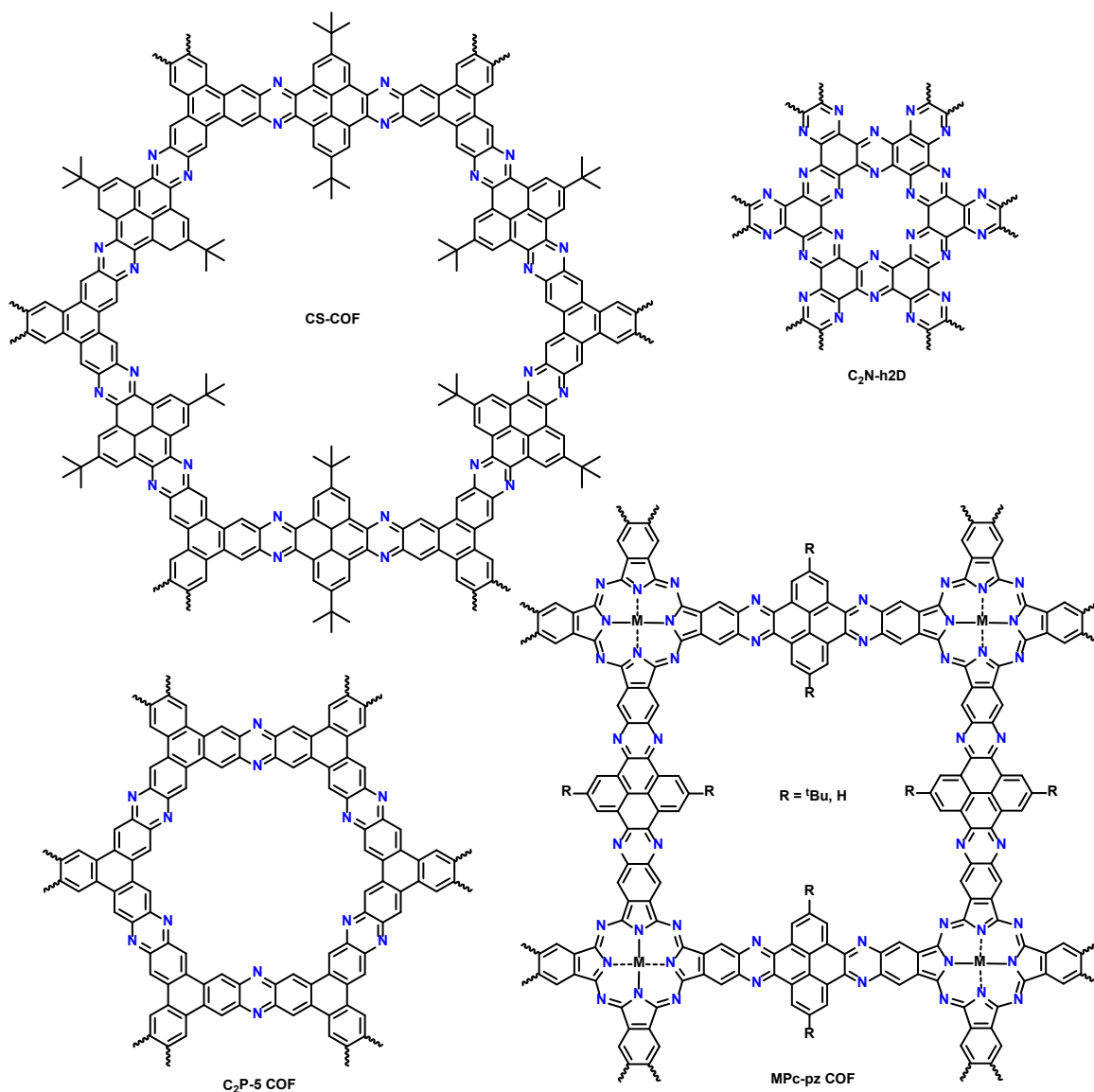
Scheme 1.14. Chemical structures of representative pyrazine-linked 2D POPs.

43

M₁Pc-NH-M₂PcF₈
M₁ = Ni; M₂ = Co, Cu
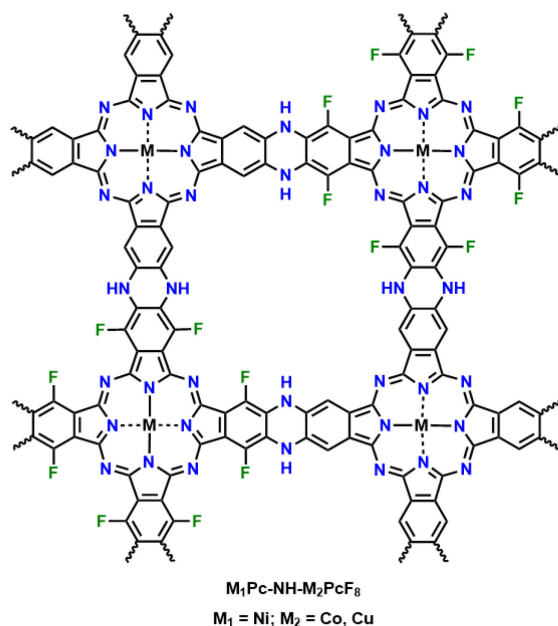
Scheme 1.15. Chemical structure of M_1Pc-NH-M_2PcF_8 COFs.

1.5.2 Expanding Conjugation into Three Dimension

3D POPs are usually constructed by tetra-topic linkers such as tetraphenylmethane and adamantane derivatives, which inherently prohibit the extended conjugation throughout the framework backbone. However, by carefully choosing the other building blocks such as tetrathiafulvalene and thiophene derivatives, electrically conductive POPs can also be synthesized where the through-space π–π interactions between these conjugated building blocks likely account for the charge transport. For example, 3D-TTF-COFs, termed as JUC-518 (JUC = Jilin University China) and JUC-519, were built from tetrathiafulvalene-tetrabenzaldehyde (TTF-TBA) and 1,3,5,7-tetraaminoadamantane (TAA) or tetra(4-aminophenyl)methane (TAPM) (Scheme 1.16), and exhibited electrical conductivity of $\sim 10^{-7}$ S/cm and $\sim 10^{-4}$ S/cm before and after I_2 doping.[137] Remarkably, replacing the conjugated organic building blocks from TTF-TBA to linear bithiophene or tetrathiophene revealed a significant increase of electrical conductivity to 2.1×10^{-3} S/cm and 6.7×10^{-3} S/cm, respectively.[138]

To construct a fully conjugated 3D POP, an organic building block that has a non-planar geometrical structure and continuous conjugation of π–orbitals is required. Consisting of all sp^2 carbon atoms, cyclooctatetraene (COT) has a non-planar molecular structure, revealing a great potential as the building block for fully conjugated 3D POPs. Cao and co-workers reported in 2021 the construction of such an example from saddle-shaped aldehyde-substituted α,α,α,α-tetraphenyl-cyclooctatetrathiophene (COThP-CHO) and 1,4-phenylenediamine.[139] Although this 3D COF, termed as BUCT-COF-1 (Scheme 1.16), is poorly crystalline, it exhibited a Hall electron mobility of 2.75 ± 0.22 cm^2 V^{-1} s^{-1} and an electrical conductivity of 1.51×10^{-8} S/cm.
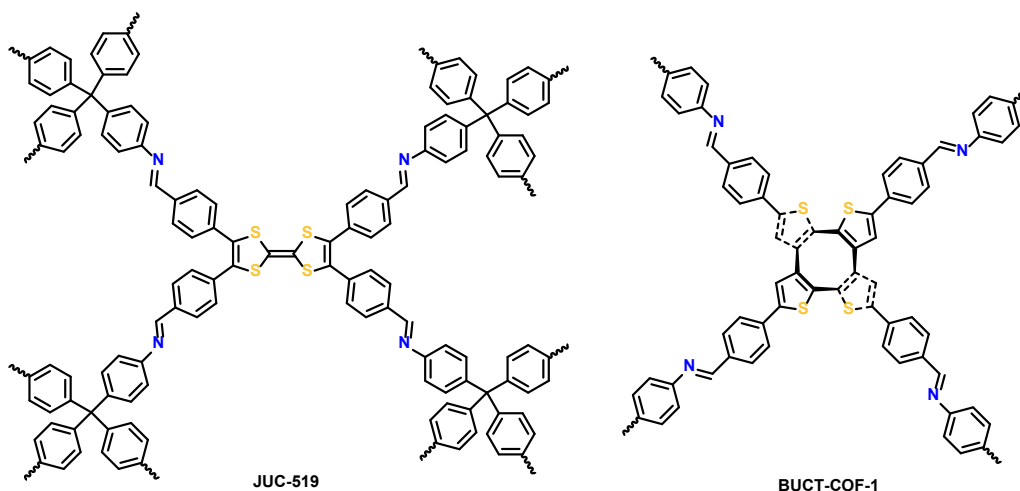
Scheme 1.16. Chemical structures of two 3D POPs.

To achieve ladder-type fully conjugated 3D POPs, Coskun and co-workers, together with us, demonstrated the synthesis of epoxide-bearing 3D POPs (3D ep-POP) via the Diels–Alder cycloaddition polymerization, which was subsequently aromatized to form a 3D graphitic porous polymer (3D p-POP) consisting of only sp^2 carbons. Upon aromatization, an immediate increase of two orders of magnitude in the electrical conductivity from 8×10^{-10} S/cm to 5×10^{-8} S/cm was observed, which could be further improved by I_2 doping to 6×10^{-4} S/cm (Scheme 1.17).[140]
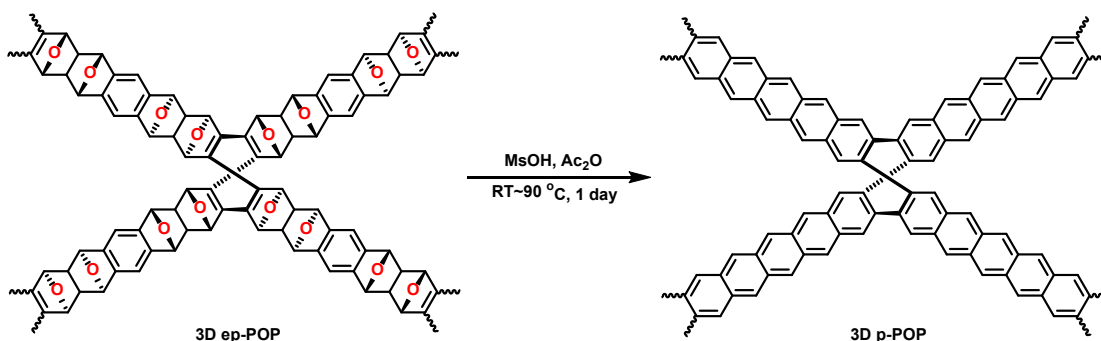
Scheme 1.17. The conversion from 3D ep-POP to fully conjugated 3D p-POP.

Although the number of electrically conductive 3D POPs are still relatively small compared with their 2D counterparts, there is no intrinsic chemical limitation of the construction of 3D POPs. With generally higher porosity relative to 2D POPs, 3D conductive POPs would be a better candidate for supercapacitors or chemiresistive sensors if they can exhibit similar electrical conductivity as 2D conductive POPs.

1.6 Fused Aromatic Materials for Electrochemical Energy Storage

Recent years have witnessed rapid market growth of EES devices, especially lithium-ion batteries (LIBs), mainly due to the prevalence of portable electronics and electric vehicles (EV). The global EV stock increased to over 16.5 million in 2021 from about 10 million in 2020 (Figure 1.15), and is expected to keep expanding in the foreseeable future. Such extraordinary growth speed leads to significant pressure on the raw material supply, especially transition metals such as cobalt and nickel, since conventional LIBs rely on transition-metal-oxide based cathodes. However, the resources and the production of transition-metal are both limited, inevitably leading to high costs, and their large-scale use is neither environmentally benign nor sustainable. The mining, refining, and manufacturing of transition-metal-based electrode materials currently account for 30~50% of the global warming impact of battery-manufacturing industries.[141,142] Therefore, eliminating the use of transition metals in battery-manufacturing industries would substantially alleviate their environmental impact. Moreover, producing battery electrodes from earth-abundant elements, such as carbon, oxygen, nitrogen, sulfur, etc., would also potentially make the price of batteries lower and less sensitive to swings in the raw-material price.
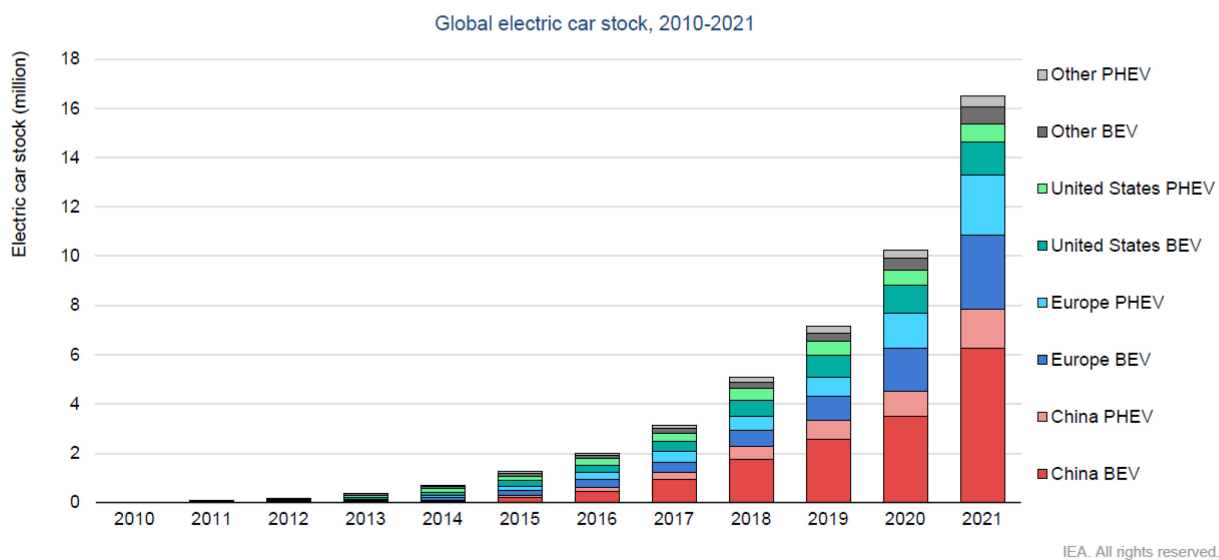
Notes: BEV = battery electric vehicle; PHEV = plug-in hybrid electric vehicle. Electric car stock in this figure refers to passenger light-duty vehicles. "Other" includes Australia, Brazil, Canada, Chile, India, Japan, Korea, Malaysia, Mexico, New Zealand, South Africa and Thailand. Europe in this figure includes the EU27, Norway, Iceland, Switzerland and United Kingdom.

Figure 1.15. Over 16.5 million electric cars were on the road in 2021, tripling in just three years. Figure source: Global Electric Vehicle Outlook 2022, IEA.

Redox-active organic electrode materials (OEMs), which mostly comprising earth-abundant carbon, oxygen, nitrogen, sulfur, and hydrogen, have thus emerged as alternative electrode materials for metal-ion batteries (MIBs) relative to the conventional transition-metal-based inorganic electrodes. Due to their light weights, OEMs are able to accommodate a considerable number of redox-active sites per electrode mass, leading to a significantly higher energy density at the active-material level compared with their inorganic counterparts. Furthermore, unlike transition-metal-oxide-based electrode materials which are formed by

densely packed transition metal cations and O^{2-} anions through strong ionic or covalent bonding, OEMs are composed of molecules or polymer chains which are held by much weaker van der Waals interactions. Therefore, OEMs are "more flexible" and can generally store electrochemical energies regardless of the choice of counter ions that undergo insertion/desertion into/out of the electrode during charge storage, a phenomenon that has very rarely observed for inorganic electrode materials. From a more practical perspective, OEMs are predicted to have prices in the range of 5 to 20 US dollars per kilogram, which is only about one third of the unit price of cobalt metal and $LiCoO_2$ and can lead up to ~30% price drop of the total cell costs.[31]

Although OEMs exhibit such huge advantages over traditional inorganic electrode materials, they have still been far away from commercialization and their use as electrode materials for MIBs is still at the stage of academic research in laboratories because they have several significant drawbacks, including the tendency of dissolution during charging/discharging, and their poor electrical conductivity, which we will discuss in detail in the following parts. We will not cover all of the aspects of OEMs in this section because there have been several phenomenal reviews articles pertaining to this topic.[31,143-146]

To solve both the dissolution and conductivity problems, we propose that strong intermolecular interactions can 1) increase the energy penalty of dissolution and thus decrease the solubility of OEMs in electrolytes, and 2) promote charge conduction and transfer. Therefore, we hypothesize that fused aromatic materials, formed by fusion of multiple aromatic rings, have the potential to exhibit good performance as electrode materials due to their ability to form strong intermolecular interactions through π–π interaction. A few well-known examples are naphthalene (bicyclic), anthracene (tricyclic), chrysene (quadro-cyclic), and pentacene (penta-cyclic). However, these hydrocarbons lack redox activity and can only be potentially used as anode materials where the reduction of aromatic rings takes place. To enable their applications as cathode materials, additional redox-active motifs have to be installed onto the molecular backbones. We will discuss common redox-active functional groups in section 1.6.1 below.

1.6.1 Common Classes of Organic Electrode Materials

Adapting the concepts from organic electronics where n-type means the injection of electrons and p-type means the injection of holes (i.e., positive charges), OEMs can also be classified as n-type (Scheme 1.18), p-type (Scheme 1.19), or bipolar-type (Scheme 1.20) based on their capabilities of accepting electrons (reduction, n-type) or donating electrons (oxidation, p-type) in their neutral state during the electrochemical reaction. n-Type OEMs undergo reduction with the insertion of cations from the electrolyte, while p-type OEMs undergo oxidation with the insertion of anions from the electrolyte.

Earliest studies employing OEMs for LIBs can be tracked back to 1970s, when carbonyl compounds were used to construct the battery systems.[147,148] However, the rapid dissolution of these carbonyl

compounds into electrolyte led to fast decay in capacity. Conducting polymers such as polyacetylene, poly-(*p*-phenylene), polyaniline, polypyrrole, and polythiophene have been utilized as electrode materials for batteries since 1980s due to their intrinsic electrical conductivity and less soluble nature compared with carbonyl compounds.[149-152] However, conducting polymers suffered from several significant drawbacks, including low energy capacities (usually < 150 mAh/g) due to the low density of redox-active sites and low doping density, and sloping voltage profiles which usually lead to low nominal discharge voltage. Although the cycling stability of conducting polymers improved a lot relative to carbonyl compounds, they still suffered from gradual material degradation during cycling due to unfavorable side reactions of polymer backbones. Another kind of polymeric electrode materials is stable-organic-radical-containing polymers such as TEMPO-bearing ((2,2,6,6-tetramethylpiperidin-1-yl)oxyl) polymers, which are capable of store and release charge in exceptionally high rates because the presence of minimal bond rearrangements during charging and discharging, and the electron-transfer rate of TEMPO groups are high.[153,154] However, these polymers commonly exhibit low specific capacity (<100 mAh/g) due to the presence of redox-innocent polymer backbones and linkage between the backbone and organic radicals.

Although the research of OEMs has been continuously expanding since 1970s, the renaissance started in 2008 after the seminal article published by Armand and Tarascon predicting a bright future for organic batteries.[155] To pursuit a more sustainable world, alternative electrode materials made from earth-abundant elements must be developed to lower down the carbon emissions of battery industries which is currently still based on conventional inorganic electrode materials. Therefore, numerous new OEMs have been designed, synthesized, and applied in batteries, which are mostly based on the redox motifs presented in Scheme 1.18 to 1.20. However, the major problems of OEMs that have been known since the early days of OEM research, such as the dissolution-induced poor cycling stability and sluggish charge transport properties, have not been solved yet. We provide discussions in detail about these two major problems in the following two sections and propose several strategies to overcome them in the last section, 1.6.4.
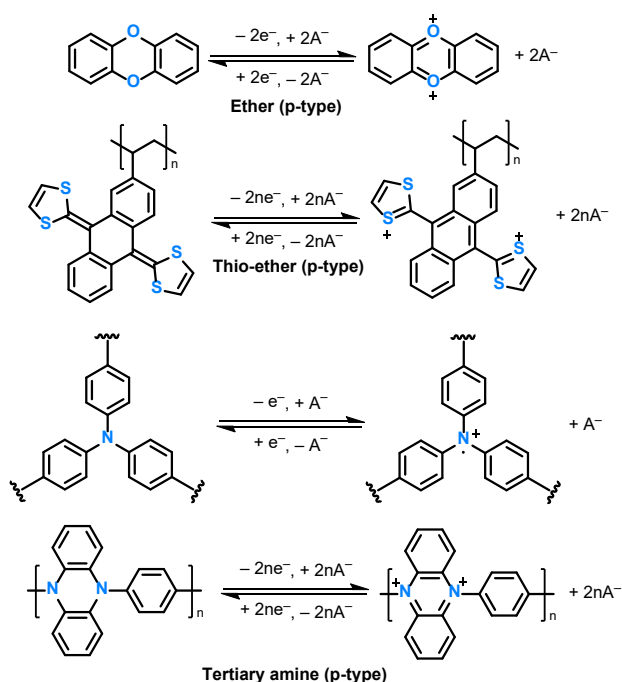
Scheme 1.18. Common p-type redox motifs. $A^- = ClO_4^-$, PF_6^-, BF_4^-, FSI^-, $TFSI^-$, etc.
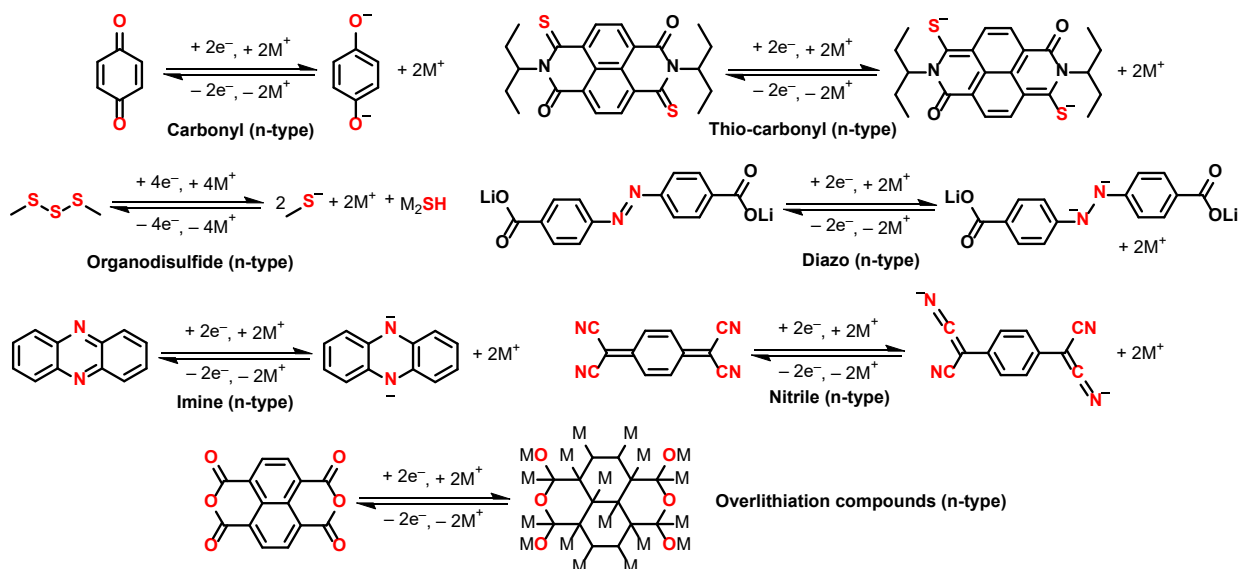
Scheme 1.19. Common n-type redox motifs. M^+ = metal cations. The use of "M^+" here is for simplification and does not mean that these redox reactions are only restricted to monovalent cations.
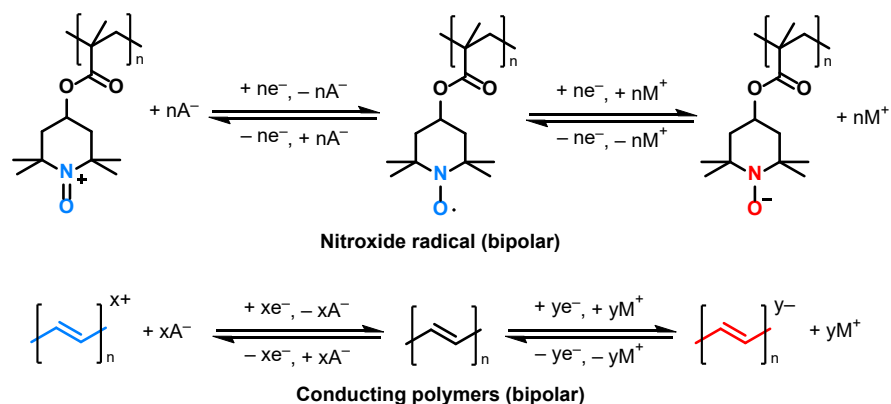
Scheme 1.20. Common bipolar-type redox motifs. $A^- = ClO_4^-$, PF_6^-, BF_4^-, FSI^-, $TFSI^-$, etc. M^+ = metal cations. The use of "M^+" here is for simplification and does not mean that these redox reactions are only restricted to monovalent cations.

1.6.2 The Dissolution Problem

As one of the most important performance metrics of batteries (and also other EES devices), cycling stability depends on both active materials and electrode compositions. Most relevant properties of active materials include the stability (upon electrochemical polarization) and solubility (in electrolytes), whereas the binder, conducting additives, and even the electrode architectures can also play important roles in determining the cycling stability.

A vast majority of OEMs have intrinsically high solubility in electrolytes at their pristine state. The problem usually gets worse when they are electrochemically polarized (i.e., reduced or oxidized). The continuous dissolution of active materials from the electrode results in a gradual decrease of capacity upon cycling, which is a key obstacle limiting the practical use of OEMs. For example, p-benzoquinone based cathode lost two thirds of initial capacity after only 20 cycles even with the mixing of 60 wt.% of carbon and 10 wt.% of PTFE binder.[156] In comparison, transition-metal-oxide-based inorganic cathodes can generally retain 80% of the initial capacity after 1000 cycles. Through molecular design and engineering, OEMs with more complicated chemical structures have been realized (Scheme 1.21). Some of them exhibit significantly lower solubility, however, at the expense of specific capacity because of the presence of redox-innocent parts. Although compositing OEMs with advanced carbon materials (e.g., graphene, carbon nanotubes, mesoporous carbon, etc.) can lead to a more robust integration of OEMs into electrode due to π–π interactions, the resulting active material loadings are generally low, which inevitably reduces the electrode-level capacity. Therefore, there are continuously growing interests in strategies that can either decrease the solubility of OEMs or prevent OEMs from dissolution without significant sacrifice of other key performance metrics.

50
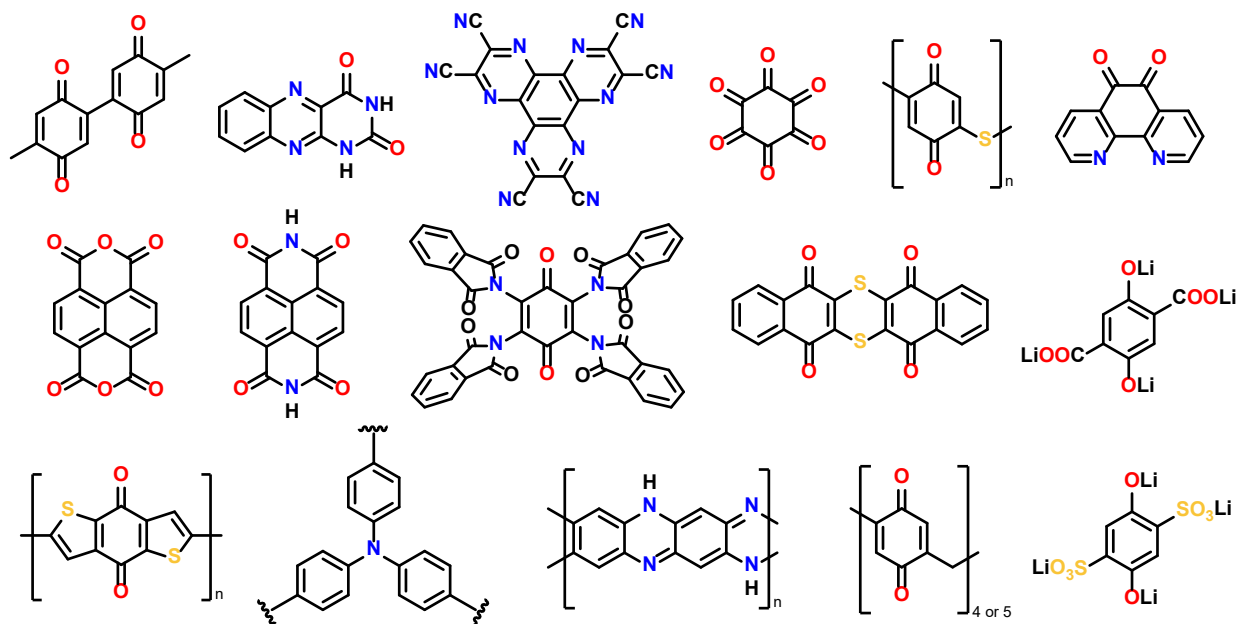
Scheme 1.21. Representatives of OEMs.

1.6.3 The Poor-Conductivity Problem

The electrical conductivities of electrode active materials have huge influences on the rate capability of batteries. Electrodes made from more conductive active materials generally exhibit better power density at similar electrode compositions. Simply mixing electrically conducting additives with electrode active materials can increase the conductivity of the whole electrode, but has no influence on the electron conduction within active materials. Therefore, more advanced treatments are required to make electrodes out of poorly conducting or even insulating active materials. For example, although $LiFePO_4$-based batteries are known to exhibit high rate performances, $LiFePO_4$ particles have to be coated with a thin layer of carbon before being mixed with carbon black and binders to make electrodes because it has a low electrical conductivity value of around 10^{-9} S/cm.

Apart from conducting polymers, common OEMs generally possess electrical conductivities on par or lower than that of $LiFePO_4$.[31,155] Some rare examples exhibit conductivity values between 10^{-9} and 10^{-6} S/cm. Therefore, large amounts of conducting additives, such as 50 wt.% of carbon black, are commonly required to make electrodes from OEMs. Although doped conducting polymers can have conductivities as high as 10 S/cm, they have other major disadvantages as electrode materials, as we have discussed above in section 1.6.1. Therefore, there is an urgent need of new OEMs with high intrinsic electrical conductivity (> 10^{-5} S/cm) and high energy density.
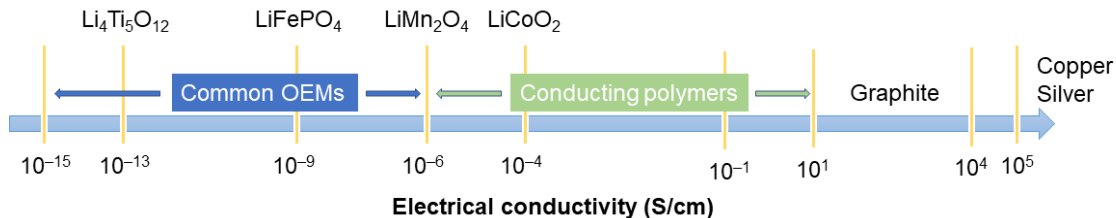
Figure 1.16. Common electrical conductivities of OEMs and representative inorganic electrode materials.

1.6.4 Perspective

We believe that the practical use of OEM-based batteries will not be a fantasy but a reality in the foreseeable future if the two majors obstacles, the dissolution, and poor-conductivity problems, can be solved by new material designs. These two problems are not completely isolated from each other because they are both closely related to the intermolecular interactions within OEMs. Therefore, we propose that common strategies of increasing the strength of intermolecular interactions, such as π–π stacking, donor-acceptor interactions, and hydrogen bonding interactions, shall also apply to OEMs and could potentially lead to low solubility and high electrical conductivity simultaneously.

1.7 References

(1) *The Future of Energy Storage*, MIT Energy Initiative

(2) J.-M. Tarascon, *Nat. Chem.*, 2010, **2**, 510–510.

(3) J.-M. Tarascon, and M. Armand, *Nature*, 2001, **414**, 359–367.

(4) B. Dunn, H. Kamath, and J.-M. Tarascon, *Science*, 2011, **334**, 928–935.

(5) M. Salanne, B. Rotenberg, K. Naoi, K. Kaneko, P.-L. Taberna, C. P. Grey, B. Dunn, and P. Simon, *Nat Energy*, 2016, **1**, 1–10.

(6) L. Chen, and L. L. Shaw, *J. Power Sources*, 2014, **267**, 770–783.

(7) A. Manthiram, Y. Fu, S.-H. Chung, C. Zu, and Y.-S. Su, *Chem. Rev.*, 2014, **114**, 11751–11787.

(8) Y.-X. Yin, S. Xin, Y.-G. Guo, and L.-J. Wan, *Angew. Chem. Int. Ed.*, 2013, **52**, 13186–13200.

(9) Y. Zheng, S. Zheng, H. Xue, and H. Pang, *J. Mater. Chem. A*, 2019, **7**, 3469–3491.

(10) C. Vaalma, D. Buchholz, M. Weil, and S. Passerini, *Nat. Rev. Mater.*, 2018, **3**, 1–11.

(11) C. Wang, Z. Xie and Z. Zhou, *APL Mater.*, 2019, **7**, 040701.

(12) M. Li, J. Lu, Z. Chen, and K. Amine, *Adv. Mater.*, 2018, **30**, 1800561.

(13) A. Manthiram, *ACS Cent. Sci.*, 2017, **3**, 1063–1069.

(14) H. Furukawa, K. E. Cordova, M. O'Keeffe, and O. M. Yaghi, *Science*, 2013, **341**, 123044.

(15) M. Hmadeh, Z. Lu, Z. Liu, F. Gándara, H. Furukawa, S. Wan, V. Augustyn, R. Chang, L. Liao, F. Zhou, E. Perre, V. Ozolins, K. Suenaga, X. Duan, B. Dunn, Y. Yamamto, O. Terasaki, and O. M. Yaghi, *Chem. Mater.*, 2012, **24**, 3511–3513.

(16) R. R. Salunkhe, Y. V. Kaneti, and Y. Yamauchi, *ACS Nano*, 2017, **11**, 5293–5308.

(17) W. Xia, A. Mahmood, R. Zou, and Q. Xu, *Energy Environ. Sci.*, 2015, **8**, 1837–1866.

(18) S. Sundriyal, H. Kaur, S. K. Bhardwaj, S. Mishra, K.-H. Kim, and A. Deep, *Coord. Chem. Rev.*, 2018, **369**, 15–38.

(19) W. Yang, X. Li, Y. Li, R. Zhu, and H. Pang, *Adv. Mater.*, 2019, **31**, 1804740.

(20) Z. Liang, R. Zhao, T. Qiu, R. Zou, and Q. Xu, *EnergyChem*, 2019, **1**, 100001.

(21) Z. Wang, H. Tao, and Y. Yue, *ChemElectroChem*, 2019, **6**, 5358–5374.

(22) X. Zhang, P. Dong, and M.-K. Song, *Batteries Supercaps*, 2019, **2**, 591–626.

(23) I. Stassen, N. Burtch, A. Talin, P. Falcaro, M. Allendorf, and R. Ameloot, *Chem. Soc. Rev.*, 2017, **46**, 3185–3241.

(24) A. Morozan, and F. Jaouen, *Energy Environ. Sci.*, 2012, **5**, 9269–9290.

(25) Y. Xu, Q. Li, H. Xue, and H. Pang, *Coord. Chem. Rev.*, 2018, **376**, 292–318.

(26) Z. Wu, J. Xie, Z. J. Xu, S. Zhang, and Q. Zhang, *J. Mater. Chem. A*, 2019, **7**, 4259–4290.

(27) A. E. Baumann, D. A. Burns, B. Liu, and V. S. Thoi, *Commun. Chem.*, 2019, **2**, 1–14.

(28) Z. Liang, C. Qu, W. Guo, R. Zou, and Q. Xu, *Adv. Mater.*, 2018, **30**, 1702891.

(29) C. Choi, D. S. Ashby, D. M. Butts, R. H. DeBlock, Q. Wei, J. Lau, and B. Dunn, *Nat. Rev. Mater.* 2020, **5**, 5–19.

(30) M. Souto, and D. F. Perepichka, *J. Mater. Chem. C*, 2021, **9**, 10668-10676.

(31) J. Kim, Y. Kim, J. Yoo, G. Kwon, Y. Ko, and K. Kang, *Nat. Rev. Mater.* 2023, **8**, 54–70.

(32) T. Brousse, D. Bélanger, and J. W. Long, *J. Electrochem. Soc.*, 2015, **162**, A5185–A5189.

(33) P. Simon, Y. Gogotsi, and B. Dunn, *Science*, 2014, **343**, 1210–1211.

(34) T. S. Mathis, N. Kurra, X. Wang, D. Pinto, P. Simon, and Y. Gogotsi, *Adv. Energy Mater.*, 2019, **9**, 1902007.

(35) B. E. Conway, *J. Electrochem. Soc.*, 1991, **138**, 1539–1548.

(36) V. Augustyn, P. Simon, and B. Dunn, *Energy Environ. Sci.*, 2014, **7**, 1597–1614.

(37) V. Augustyn, J. Come, M. A. Lowe, J. W. Kim, P.-L. Taberna, S. H. Tolbert, H. D. Abruña, P. Simon, and B. Dunn, *Nat. Mater.*, 2013, **12**, 518–522.

(38) M. D. Stoller, and R. S. Ruoff, *Energy Environ. Sci.*, 2010, **3**, 1294–1301.

(39) Y. Shao, M. F. El-Kady, J. Sun, Y. Li, Q. Zhang, M. Zhu, H. Wang, B. Dunn, and R. B. Kaner, *Chem. Rev.*, 2018, **118**, 9233–9280.

(40) Y. Gogotsi, and R. M. Penner, *ACS Nano*, 2018, **12**, 2081–2083.

(41) M. R. Lukatskaya, B. Dunn, and Y. Gogotsi, *Nat. Commun.*, 2016, **7**, 1–13.

(42) L. Sun, M. G. Campbell, and M. Dincă, *Angew. Chem. Int. Ed.* 2016, **55**, 3566−3579.

(43) M. G. Campbell, and M. Dincă, *Sensors* 2017, **17**, 1108.

(44) L. S. Xie, G. Skorupskii, and M. Dincă, *Chem. Rev.*, 2020, **120**, 8536–8580.

(45) D. D. Medina, A. Maehringer, and T. Bein, *Isr. J. Chem.*, 2018, **58**, 1089−1101.

(46) D. M. D'Alessandro, J. R. R. Kanga, and J. S. Caddy, *Aust. J. Chem.*, 2011, **64**, 718−722.

(47) C. H. Hendon, D. Tiana, and A. Walsh, *Phys. Chem. Chem. Phys.*, 2012, **14**, 13120−13132.

(48) C. F. Leong, P. M. Usov, and D. M. D'Alessandro, *MRS Bull.*, 2016, **41**, 858−864.

(49) A. Walsh, K. T. Butler, and C. H. Hendon, *MRS Bull.*, 2016, **41**, 870−876.

(50) M. Ko, L. Mendecki, and K. A. Mirica, *Chem. Commun.*, 2018, **54**, 7873−7891.

(51) W. Zheng, C.-S. Tsang, L. Y. S. Lee, and K.-Y. Wong, *Mater. Today Chem.*, 2019, **12**, 34−60.

(52) M. A. Solomos, F. J. Claire, and T. J. Kempa, *J. Mater. Chem. A*, 2019, **7**, 23537−23562.

(53) R. Murase, C. F. Leong, and D. M. D'Alessandro, *Inorg. Chem.*, 2017, **56**, 14373−14382.

(54) C. A. Downes, and S. C. Marinescu, *ChemSusChem*, 2017, **10**, 4374−4392.

(55) W.-T. Koo, J.-S. Jang, and I.-D. Kim, *Chem*, 2019, **5**, 1938−1963.

(56) Z. Meng, R. M. Stolz, L. Mendecki, and K. A. Mirica, *Chem. Rev.*, 2019, **119**, 478−598.

(57) I. Stassen, N. Burtch, A. Talin, P. Falcaro, M. Allendorf, and R. Ameloot, *Chem. Soc. Rev.*, 2017, **46**, 3185−3241.

(58) L. Sun, S. S. Park, D. Sheberla, and M. Dincă, *J. Am. Chem. Soc.*, 2016, **138**, 14772−14782.

(59) S. Kampouri, M. Zhang, T. Chen, J. J. Oppenheim, A. C. Brown, M. Payne, J. L. Andrews, J. Sun, and M. Dincă, *Angew. Chem. Int. Ed.*, 2022, **61**, e202213960.

(60) H. T. B. Pham, J. Y. Choi, S. Huang, X. Wang, A. Claman, M. Stodolka, S. Yazdi, S. Sharma, W. Zhang, and J. Park, *J. Am. Chem. Soc.*, 2022, **144**, 10615−10621.

(61) P. Zhang, M. Wang, Y. Liu, Y. Fu, M. Gao, G. Wang, F. Wang, Z. Wang, G. Chen, S. Yang, Y. Liu, R. Dong, M. Yu, X. Lu, and X. Feng, *J. Am. Chem. Soc.*, 2023, **145**, 6247−6256.

(62) M. Qi, Y. Zhou, Y. Lv, W. Chen, X. Su, T. Zhang, G. Xing, G. Xu, O. Terasaki, and L. Chen, *J. Am. Chem. Soc.*, 2023, **145**, 2739−2744.

(63) J. Liu, Y. Zhou, Z. Xie, Y. Li, Y. Liu, J. Sun, Y. Ma, O. Terasaki, and L. Chen, *Angew. Chem. Int. Ed.*, 2020, **59**, 1081–1086.

(64) G. Xing, J. Liu, Y. Zhou, S. Fu, J-J. Zheng, X. Su, X. Gao, O. Terasaki, M. Bonn, H. Wang, and L. Chen, *J. Am. Chem. Soc.*, 2023, **145**, 8979−8987.

(65) S. Wuttke, M. Lismont, A. Escudero, B. Rungtaweevoranit, and W. J. Parak, *Biomaterials* 2017, **123**, 172−183.

(66) R. Gao, G. Zhang, X. Ru, C. Xu, M. Li, R. Lin, and Z. Wang, *J. Solid State Chem.*, 2021, **297**, 122031.

(67) B. L. Bonnett, E. D. Smith, M. De La Garza, M. Cai, J. V. Haag, J. M. Serrano, H. D. Cornell, B. Gibbons, S. M. Martin, and A. J. Morris, *ACS Appl. Mater. Interfaces*, 2020, **12**, 15765−15773.

(68) Q. Qian, P. A. Asinger, M. J. Lee, G. Han, K. M. Rodriguez, S. Lin, F. M. Benedetti, A. X. Wu, W. S. Chi, and Z. P. Smith, *Chem. Rev.*, 2020, **120**, 8161−8266.

(69) C. R. Marshall, J. P. Dvorak, L. P. Twight, L. Chen, K. Kadota, A. B. Andreeva, A. E. Overland, T. Ericson, A. F. Cozzolino, and C. K. Brozek, *J. Am. Chem. Soc.*, 2022, **144**, 5784–5794.

(70) R. W. Day, D. K. Bediako, M. Rezaee, L. R. Parent, G. Skorupskii, M. Q. Arguilla, C. H. Hendon, I. Stassen, N. C. Gianneschi, P. Kim, and M. Dincă, *ACS Cent. Sci.*, 2019, **5**, 1959–1964.

(71) K. M. Snook, L. B. Zasada, D. Chehada, D. J. Xiao, *Chem. Sci.*, 2022, **13**, 10472–10478.

(72) E. G. Tulsky, and J. R. Long, *Chem. Mater.*, 2001, **13**, 1149–1166.

(73) L. Yang, J. J. Oppenheim, and M. Dincă, *Dalton Trans.*, 2022, **51**, 8583–8587.

(74) L. Yang, and M. Dincă, *Angew. Chem. Int. Ed.*, 2021, **60**, 23784–23789.

(75) L. Yang, X. He, and M. Dincă, *J. Am. Chem. Soc.*, 2019, **141**, 10475–10480.

(76) L. B. Zasada, L. Guio, A. A. Kamin, D. Dhakal, M. Monahan, G. T. Seidler, C. K. Luscombe, and D. J. Xiao, *J. Am. Chem. Soc.*, 2022, **144**, 4515−4521.

(77) K. Wada, K. Sakaushi, S. Sasaki, and H. Nishihara, *Angew. Chem. Int. Ed.*, 2018, **57**, 8886–8890.

(78) J. Park, M. Lee, D. Feng, Z. Huang, A. C. Hinckley, A. Yakovenko, X. Zou, Y. Cui, and Z. Bao, *J. Am. Chem. Soc.*, 2018, **140**, 10315–10323.

(79) S. Gu, Z. Bai, S. Majumder, B. Huang, and G. Chen, *J. Power Sources*, 2019, **429**, 22–29.

(80) K. W. Nam, S. S. Park, R. Dos Reis, V. P. Dravid, H. Kim, C. A. Mirkin, and J. F. Stoddart, *Nat. Commun.*, 2019, **10**, 4948.

(81) D. Kundu, B. D. Adams, V. Duffort, S. H. Vajargah, and L. F. Nazar, *Nat. Energy*, 2016, **1**, 16119.

(82) Q. Jiang, P. Xiong, J. Liu, Z. Xie, Q. Wang, X.–Q. Yang, E. Hu, Y. Cao, J. Sun, Y. Xu, and L. Chen, *Angew. Chem. Int. Ed.*, 2020, **59**, 5273–5277.

(83) Huang, X.; Sheng, P.; Tu, Z.; Zhang, F.; Wang, J.; Geng, H.; Zou, Y.; Di, C.-A.; Yi, Y.; Sun, Y.; W, Xu., and Zhu, D., *Nat. Commun.* 2015, **6**, 7408.

(84) Z. Wu, D. Adekoya, X. Huang, M. J. Kiefel, J. Xie, W. Xu, Q. Zhang, D. Zhu, and S. Zhang, *ACS Nano*, 2020, **14**, 12016−12026.

(85) R. Díaz, M. G. Orcajo, J. A. Botas, G. Calleja, and J. Palma, *Mater. Lett.*, 2012, **68**, 126–128.

(86) D. Sheberla, J. C. Bachman, J. S. Elias, C.-J. Sun, Y. Shao-Horn, and M. Dincă, *Nat. Mater.*, 2017, **16**, 220–224.

(87) D. K. Nguyen, I. M. Schepisi, and F. Z. Amir, *Chem. Eng. J.*, 2019, **378**, 122150.

(88) A. K. Gupta, M. Saraf, P. K. Bharadwaj, and S. M. Mobin, *Inorg. Chem.*, 2019, **58**, 9844–9854.

(89) W.-H. Li, K. Ding, H.-R. Tian, M.-S. Yao, B. Nath, W.-H. Deng, Y. Wang, and G. Xu, *Adv. Funct. Mater.*, 2017, **27**, 1702067.

(90) H. S. Kim, M. S. Kang, and W. C. Yoo, *J. Mater. Chem. A*, 2019, **7**, 5561–5574.

(91) S. Zhou, X. Kong, B. Zheng, F. Huo, M. Strømme, and C. Xu, *ACS Nano*, 2019, **13**, 9578–9586.

(92) D. Feng, T. Lei, M. R. Lukatskaya, J. Park, Z. Huang, M. Lee, L. Shaw, S. Chen, A. A. Yakovenko, A. Kulkarni, J. Xiao, K. Fredrickson, J. B. Tok, X. Zou, Y. Cui, and Z. Bao, *Nat. Energy*, 2018, **3**, 30–36.

(93) M. R. Lukatskaya, D. Feng, S.-M. Bak, J. W. F. To, X.-Q. Yang, Y. Cui, J. I. Feldblyum, and Z. Bao, *ACS Nano*, 2020, **14**, 15919–15925.

(94) H. Banda, J.-H. Dou, T. Chen, N. J. Libretto, M. Chaudhary, G. M. Bernard, J. T. Miller, V. K. Michaelis, and M. Dincă, *J. Am. Chem. Soc.*, 2021, **143**, 2285–2292.

(95) H. Banda, J.-H. Dou, T. Chen, Y. Zhang, and M. Dincă, *Angew. Chem. Int. Ed.*, 2021, **60**, 27119–27125.

(96) J. Ferraris, D. O. Cowan, V. Walatka, and J. H. Perlstein, *J. Am. Chem. Soc.*, 1973, **95**, 948–949.

(97) K. Bechgaard, C. S. Jacobsen, K. Mortensen, H. J. Pedersen, and N. Thorup, *Solid State Commun.*, 1980, **33**, 1119–1125.

(98) A. M. Kini, U. Geiser, H. H. Wang, K. D. Carlson, J. M. Williams, W. K. Kwok, K. G. Vandervoort, J. E. Thompson, and D. L. Stupka, *Inorg. Chem.*, 1990, **29**, 2555–2557.

(99) H. Shirakawa, E. J. Louis, A. G. MacDiarmid, C. K. Chiang, and A. J. Heeger, *J. Chem. Soc., Chem. Commun.*, 1977, 578–580.

(100) Y. Kobayashi, T. Terauchi, S. Sumi, and Y. Matsushita, *Nat. Mater.*, 2017, **16**, 109–114.

(101) Y. Kobayashi, K. Hirata, S. N. Hood, H. Yang, A. Walsh, Y. Matsushita, and K. Ishioka, *Chem. Sci.*, 2020, **11**, 11699–11704.

(102) P. W. Fritz, and A. Coskun, *Chem. Eur. J.*, 2021, **27**, 7489–7501.

(103) T. Zhang, G. Xing, W. Chen, and L. Chen, *Mater. Chem. Front.*, 2020, **4**, 332–353.

(104) C. D. Wood, B. Tan, A. Trewin, H. J. Niu, D. Bradshaw, M. J. Rosseinsky, Y. Z. Khimyak, N. L. Campbell, R. Kirk, E. Stockel, and A. I. Cooper, *Chem. Mater.*, 2007, **19**, 2034–2048.

(105) N. B. McKeown, and P. M. Budd, *Chem. Soc. Rev.*, 2006, **35**, 675–683.

(106) A. I. Cooper, *Adv. Mater.*, 2009, **21**, 1291–1295.

(107) Y. Xu, S. Jin, H. Xu, A. Nagai, and D. Jiang, *Chem. Soc. Rev.*, 2013, **42**, 8012–8031.

(108) J.-S. M. Lee, and A. I. Cooper, *Chem. Rev.*, 2020, **120**, 2171–2214.

(109) T. Ben, H. Ren, S. Ma, D. Cao, J. Lan, X. Jing, W. Wang, J. Xu, F. Deng, J. M. Simmons, S. Qiu, and G. Zhu, *Angew. Chem. Int. Ed.*, 2009, **48**, 9457–9460.

(110) Y. Tian, and G. Zhu, *Chem. Rev.,* 2020, **120**, 16, 8934–8986.

(111) H. M. El-Kaderi, J. R. Hunt, J. L. Mendoza-Cortes, A. P. Cote, R. E. Taylor, M. O'Keeffe, and O. M. Yaghi, *Science*, 2007, **316**, 268–272.

(112) P. Kuhn, M. Antonietti, and A. Thomas, *Angew. Chem. Int. Ed.*, 2008, **47**, 3450–3453.

(113) X. Feng, X. Ding, and D. Jiang, *Chem. Soc. Rev.*, 2012, **41**, 6010–6022.

(114) C. S. Diercks, and O. M. Yaghi, *Science*, 2017, **355**, eaal1585.

(115) Z. Luo, L. Liu, J. Ning, K. Lei, Y. Lu, F. Li, and J. Chen, *Angew. Chem. Int. Ed.*, 2018, **57**, 9443–9446.

(116) F. Xu, S. Jin, H. Zhong, D. Wu, X. Yang, X. Chen, H. Wei, R. Fu, and D. Jiang, *Sci. Rep.*, 2015, **5**, 8225.

(117) Z. Lei, Q. Yang, Y. Xu, S. Guo, W. Sun, H. Liu, L. P. Lv, Y. Zhang, and Y. Wang, *Nat. Commun.*, 2018, **9**, 576.

(118) S. Xu, G. Wang, B. P. Biswal, M. Addicoat, S. Paasch, W. Sheng, X. Zhuang, E. Brunner, T. Heine, R. Berger, and X. Feng, *Angew. Chem. Int. Ed.*, 2019, **58**, 849–853.

(119) C. R. Mulzer, L. Shen, R. P. Bisbey, J. R. McKone, N. Zhang, H. D. Abruña, and W. R. Dichtel, *ACS Cent. Sci.*, 2016, **2**, 667–673.

(120) Y. Wu, D. Yan, Z. Zhang, M. M. Matsushita, and K. Awaga, *ACS Appl. Mater. Interfaces*, 2019, **11**, 7661–7665.

(121) M. Souto, and D. F. Perepichka, *J. Mater. Chem. C*, 2021, **9**, 10668–10676.

(122) S. Duhovic, and M. Dincă, *Chem. Mater.,* 2015, **27**, 5487–5490.

(123) X. Feng, L. Liu, Y. Honsho, A. Saeki, S. Seki, S. Irle, Y. Dong, A. Nagai, and D. Jiang, *Angew. Chem. Int. Ed.,* 2012, **51**, 2618–2622.

(124) V. Lakshmi, C. H. Liu, M. Rajeswara Rao, Y. Chen, Y. Fang, A. Dadvand, E. Hamzehpoor, Y. Sakai-Otsuka, R. S. Stein, and D. F. Perepichka, *J. Am. Chem. Soc.*, 2020, **142**, 2155–2160.

(125) J. M. Rotter, R. Guntermann, M. Auth, A. Mähringer, A. Sperlich, V. Dyakonov, D. D. Medina, and T. Bein, *Chem. Sci.*, 2020, **11**, 12843–12853.

(126) R. Ghosh, and F. Paesani, *Chem. Sci.*, 2021, **12**, 8373–8384.

(127) T. Ben, K. Shi, Y. Cui, C. Pei, Y. Zuo, H. Guo, D. Zhang, J. Xu, F. Deng, Z. Tian, and S. Qiu, *J. Mater. Chem.*, 2011, **21**, 18208–18214.

(128) E. Jin, M. Asada, Q. Xu, S. Dalapati, M. A. Addicoat, M. A. Brady, H. Xu, T. Nakamura, T. Heine, Q. Chen, and D. Jiang, *Science*, 2017, **357**, 673–676.

(129) H. Lyu, C. S. Diercks, C. Zhu, and O. M. Yaghi, *J. Am. Chem. Soc.*, 2019, **141**, 6848−6852.

(130) A. Acharjya, L. Longworth-Dunbar, J. Roeser, P. Pachfule, and A. Thomas, *J. Am. Chem. Soc.*, 2020, **142**, 14033−14038.

(131) J. Guo, Y. Xu, S. Jin, L. Chen, T. Kaji, Y. Honsho, M. A. Addicoat, J. Kim, A. Saeki, H. Ihee, S. Seki, S. Irle, M. Hiramoto, J. Gao, and D. Jiang, *Nat. Commun.*, 2013, **4**, 2736.

(132) J. Mahmood, E. K. Lee, M. Jung, D. Shin, I.-Y. Jeon, S.-M. Jung, H.-J. Choi, J.-M. Seo, S.-Y. Bae, S.-D. Sohn, N. Park, J. H. Oh, H.-J. Shin, and J.-B. Baek, *Nat. Commun.*, 2015, **6**, 6486.

(133) S. Jhulki, J. Kim, I.-C. Hwang, G. Haider, J. Park, J. Y. Park, Y. Lee, W. Hwang, A. A. Dar, B. Dhara, S. H. Lee, J. Kim, J. Y. Koo, M. H. Jo, C.-C. Hwang, Y. H. Jung, Y. Park, M. Kataria, Y.-F. Chen, S.-H. Jhi, M.-H. Baik, K. Baek, and K. Kim, *Chem* 2020, **6**, 2035.

(134) M. Wang, M. Ballabio, M. Wang, H. H. Lin, B. P. Biswal, X. Han, S. Paasch, E. Brunner, P. Liu, M. Chen, M. Bonn, T. Heine, S. Zhou, E. Canovas, R. Dong, and X. Feng, *J. Am. Chem. Soc.*, 2019, **141**, 16810–16816.

(135) Z. Meng, R. M. Stolz, and K. A. Mirica, *J. Am. Chem. Soc.*, 2019, **141**, 11929–11937.

(136) Y. Yue, H. Li, H. Chen, and N. Huang, *J. Am. Chem. Soc.*, 2022, **144**, 2873–2878.

(137) H. Li, J. Chang, S. Li, X. Guan, D. Li, C. Li, L. Tang, M. Xue, Y. Yan, V. Valtchev, S. Qiu, and Q. Fang, *J. Am. Chem. Soc.*, 2019, **141**, 13324–13329.

(138) T. Li, W. Zhu, R. Shen, H.-Y. Wang, W. Chen, S.-J. Hao, Y. Li, Z.-G. Gu, and Z. Li, *New J. Chem.*, 2018, **42**, 6247–6255.

(139) S. Wang, L. Da, J. Hao, J. Li, M. Wang, Y. Huang, Z. Li, Z. Liu, and D. Cao, *Angew. Chem. Int. Ed.*, 2021, **60**, 9321–9325.

(140) Y. Byun, L. S. Xie, P. Fritz, T. Ashirov, M. Dincă, and A. Coskun, *Angew. Chem. Int. Ed.*, 2020, **59**, 15166–15170.

(141) C. Wang, B. Chen, Y. Yu, Y. Wang, and W. Zhang, *J. Clean. Prod.,* 2017, **163**, 241–251.

(142) H. Ambrose, and A. Kendall, *Transp. Res. D* 2016, **47**, 182–194.

(143) Y. Lu, Q. Zhang, L. Li, Z. Niu, and J. Chen, *Chem*, 2018, **4**, 2786–2813.

(144) P. Poizot, J. Gaubicher, S. Renault, L. Dubois, Y. Liang, and Y. Yao, *Chem. Rev.*, 2020, **120**, 6490–6557.

(145) Y. Lu, and J. Chen, *Nat. Rev. Chem.*, 2020, **4**, 127–142.

(146) T. B. Schon, B. T. McAllister, P.–F. Li, and D. S. Seferos, *Chem. Soc. Rev.*, 2016, **45**, 6345–6404.

(147) D. I. Williams, J. J. Byrne, and J. S. Driscoll, *J. Electrochem. Soc.*, 1969, **116**, 2–4.

(148) H. Alt, H. Binder, A. Köhling, and G. Sandstede, *Electrochim. Acta*, 1972, **17**, 873–887.

(149) D. MacInnes Jr., M. A. Druy, P. J. Nigrey, D. P. Nairns, A. G. MacDiarmid, and A. J. Heeger, *J. Chem. Soc. Chem. Commun.*, 1981, **7**, 317–319.

(150) P. Novák, K. Müller, K. S. V. Santhanam, and O. Haas, *Chem. Rev.*, 1997, **97**, 207–282.

(151) X. Jia, Y. Ge, L. Shao, C. Wang, and G. G. Wallace, *ACS Sustain. Chem. Eng.*, 2019, **7**, 14321–14340.

(152) T. Matsunaga, H. Daifuku, T. Nakajima, and T. Kawagoe, *Poly. Adv. Technol.*, 1990, **1**, 33–39.

(153) K. Nakahara, S. Iwasa, M. Satoh, Y. Morioka, J. Iriyama, M. Suguro, and E. Hasegawa, *Chem. Phys. Lett.*, 2002, **359**, 351–354.

(154) T. Suga, Y.-J. Pu, K. Oyaizu, and H. Nishide, *Bull. Chem. Soc. Japan.*, 2004, **77**, 2203–2204.

(155) M. Armand, and J.-M. Tarascon, *Nature*, 2008, **451**, 652–657.

(156) Z. Song, Y. Qian, T. Zhang, M. Otani, and H. Zhou, *Adv. Sci.*, 2015, **2**, 1500124.

Chapter 2. Continuous Electrical Conductivity Variation in M_3(hexaiminotriphenylene)$_2$ (M = Co, Ni, Cu) MOF Alloys

2.1 Abstract

MOFs with higher electrical conductivity do not always exhibit the best performance. Instead, MOFs with their electrical conductivity and/or band structures tailored to match the requirements of certain applications have the greatest potential to perform well. Therefore, strategies to effectively tune the electrical conductivity and/or band structures are highly desired. One of the simplest but probably most effective strategies is compositional tuning. Here, we report continuous fine-scale tuning of band gaps over 0.4 eV and of electrical conductivity over four orders of magnitude in a series of highly crystalline binary alloys of two-dimensional electrically conducting metal-organic frameworks M_3(HITP)$_2$ (M = Co, Ni, Cu; HITP = 2,3,6,7,10,11-hexaiminotriphenylene). Isostructurality in the M_3(HITP)$_2$ series permits the direct synthesis of binary alloys $(M_xM'_{3-x})$(HITP)$_2$ (MM' = CuNi, CoNi, and CoCu) with metal compositions precisely controlled by precursor ratios. We attribute the continuous tuning of both band gaps and electrical conductivity to changes in free carrier concentrations and to subtle differences in interlayer displacement (D) or spacing (S), both of which are defined by metal substitution. The activation energy of (Co_xNi_{3-x})(HITP)$_2$ alloys scales inversely with increasing the Ni percentage, confirming thermally-activated bulk transport.

2.2 Introduction

The ability to change the electronic energy levels of the valence and conduction bands in semiconductors is one of the foundational principles of modern electronics. In principle, the same applies to electrically conducting metal-organic frameworks (MOFs), a class of emerging crystalline porous conductors.[1,2] Finely tuning their electronic properties, be it their absolute conductivity or the activation energy for charge transport, is crucial for optimizing their performance as active materials in supercapacitors,[3–5] batteries,[6] electrocatalysis,[7–11] chemiresistive sensors,[12–17] and thermoelectrics.[18,19] However, this has proven difficult in conducting MOFs, where changes in conductivity are most often enacted by varying structure rather than composition. Whereas different structures indeed lead to different conductivities, structural changes rarely allow for continuous fine tuning of electronic energy levels. Notable exceptions involve redox doping,[20] such as in tetracyanoquinodimethane-doped $Cu_3(BTC)_2$ (1,3,5-benzenetricarboxylate), a system that allows smooth variation of conductivity over six orders of magnitude,[21] or more commonly via I_2 doping of relatively insulating host frameworks.[17]

In inorganic semiconductors, a much more successful strategy towards band engineering is isostructural alloying, such as in $Si_{1-x}Ge_x$. We show here that one of the prototypical electrically conducting MOFs, $Ni_3(HITP)_2$ (HITP = 2,3,6,7,10,11-hexaiminotriphenylene), is amenable to similar compositional tuning. Binary alloys $(M_xM'_{3-x})(HITP)_2)$ (MM' = CuNi, CoNi, and CoCu) allow precise control over the M/M' ratios and are isostructural with the parent compounds $M_3(HITP)_2$ (M = Co, Ni, Cu), here reported with significantly improved crystallinity compared to published procedures. Alloying enables continuous variation of electrical conductivity over 4 orders of magnitude from 5.8×10^{-3} S cm^{-1} to 55.4 S cm^{-1}.
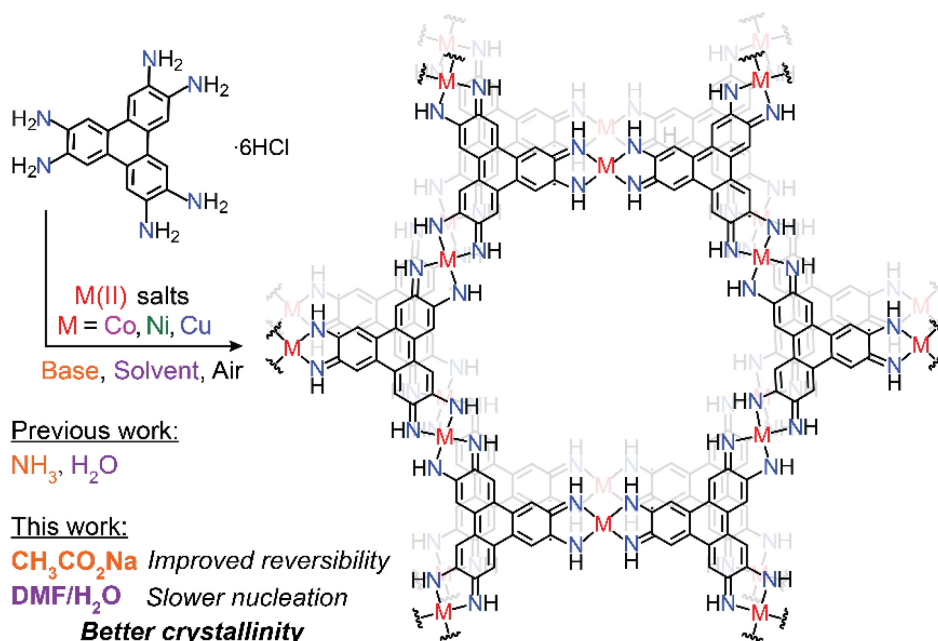
Figure 2.1. Synthesis of $M_3(HITP)_2$ (M = Co, Ni, Cu) and $(M_xM'_{3-x})(HITP)_2$ alloys.

Figure 2.2. The demonstration of the indispensability of air during the synthesis of $Co_3(HITP)_2$. The reaction mixture containing HATP·6HCl, $Co(OAc)_2$·$4H_2O$, NaOAc (2 M) in Milli-Q water/DMF is still clear without any precipitate after three-hour stirring under N_2 atmosphere at room temperature.

2.3 Results and Discussion

Although pure $M_3(HITP)_2$ (M = Ni, Cu, Co) have been reported with varying degrees of crystallinity and porosity,[9,12,22] systematic investigations of potential mixed-metal phases required the development of consistent synthetic procedures for high quality crystalline and porous powders of all three MOFs (Figure 2.1). Generally, the synthesis of $M_3(HITP)_2$ involves coordination of amino groups to metal ions, subsequent deprotonation of amino groups (typically by aqueous ammonia), followed by oxidation in air. The absence of air prevents the formation of any precipitate (Figure 2.2) and is thus considered critical. However, replacing ammonia with a weaker base, such as CH_3CO_2Na led to significant improvements in crystallinity for $Ni_3(HITP)_2$ and $Cu_3(HITP)_2$ (Figures 2.3, 2.4). Most strikingly, $Co_3(HITP)_2$ crystallizes only in the presence of CH_3CO_2Na, with ammonia yielding an essentially amorphous phase (Figures 2.5, 2.6). The crystallinity of all three compounds can be further improved by employing coordinating solvents/H_2O mixtures (e.g., *N,N*-dimethylformamide (DMF) for $Co_3(HITP)_2$, dimethyl sulfoxide (DMSO) for $Ni_3(HITP)_2$, and *N,N*-dimethylacetamide (DMA) for $Cu_3(HITP)_2$). The organic co-solvents modulate the rate of deprotonation, thereby retarding nucleation,[23] and have higher donicity/donor numbers than water,[24] which affects the reversibility of the metal-ligand bond formation and further controls crystal growth.[23]
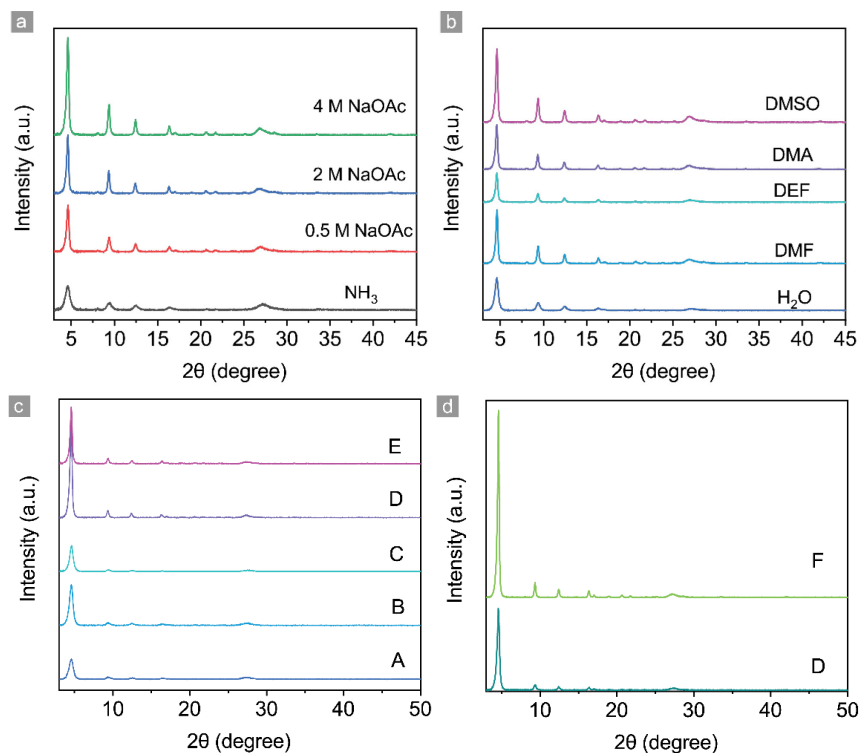
Figure 2.3. Optimization of the synthesis of $Ni_3(HITP)_2$. (a) PXRD patterns of $Ni_3(HITP)_2$ synthesized using different base in water-only solvent system are presented. A significant improvement of crystallinity was observed when using NaOAc as the base. 4 M NaOAc solution was found to be optimal for the synthesis of $Ni_3(HITP)_2$. (b) PXRD patterns of $Ni_3(HITP)_2$ synthesized using different solvent combinations (from bottom to top: water, DMF/H_2O, DEF/H_2O, DMA/H_2O, DMSO/H_2O), revealing the influence of coordinating solvents on the crystallinity of $Ni_3(HITP)_2$. DMSO was found to be optimal for the synthesis of $Ni_3(HITP)_2$. (c) The influence of the amount of DMSO. From A to E, the amount of DMSO is 0.5 mL, 0.75 mL, 1 mL, 1.5 mL, 3 mL. (d) Comparison of the synthetic procedure in 2.5.2.
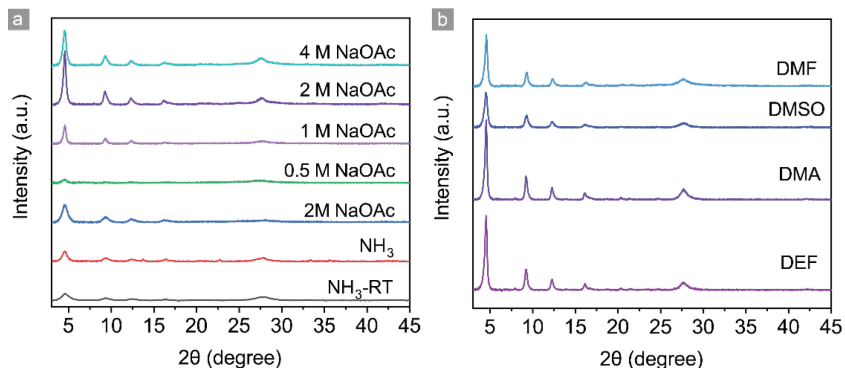
Figure 2.4. Optimization of the synthesis of $Cu_3(HITP)_2$. (a) PXRD patterns of $Cu_3(HITP)_2$ synthesized using different base are presented. A water-only solvent system was used for the bottom three traces, whereas DMF/H_2O solvent system (v/v = 3:7) was used for the top four traces. Significant improvement of the crystallinity was observed when using appropriate amount of NaOAc as the base and DMF/H_2O as the solvent. (b) PXRD patterns of $Cu_3(HITP)_2$ synthesized using different solvent combinations (from bottom to top: DEF/H_2O, DMA/H_2O, DMSO/H_2O, DMF/H_2O; v/v = 3:7), revealing the influence of coordinating solvents on the crystallinity of $Cu_3(HITP)_2$. DMA was found to be optimal for the synthesis of $Cu_3(HITP)_2$. Regarding the synthesis of $Cu_3(HITP)_2$, dark mixture is formed immediately after mixing HATP aqueous solution and $CuSO_4$ solution, which is different from both $Co_3(HITP)_2$ and $Ni_3(HITP)_2$. This indicates that the interaction between Cu^{2+} and HATP is strong even without deprotonation, impeding the formation of highly crystalline material. Therefore, DMA is used as one of the solvent components since $CuSO_4 \cdot 5H_2O$ barely dissolve in DMA, which results in the low Cu^{2+} concentration in the reaction mixture. Thus, slower formation of $Cu_3(HITP)_2$ and significantly improved crystallinity can be realized.
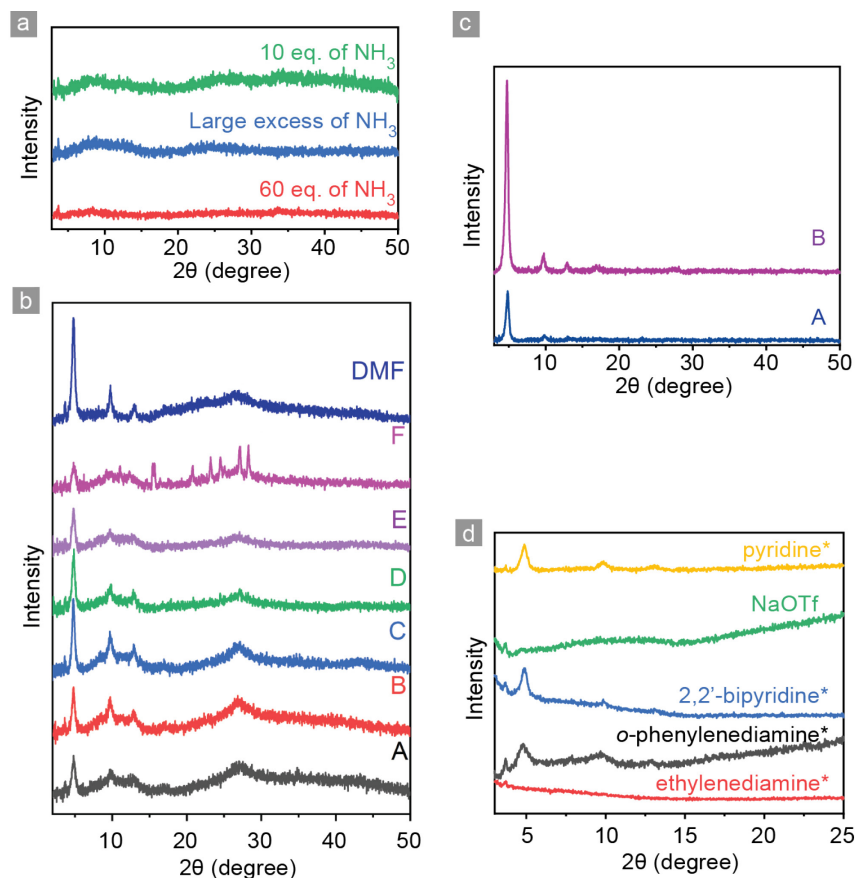
Figure 2.5. Optimization of the synthesis of Co$_3$(HITP)$_2$. Equivalence corresponds to HATP·6HCl. (a) amorphous Co$_3$(HITP)$_2$ obtained by using ammonia as base. (b) PXRD patterns of Co$_3$(HITP)$_2$ synthesized using different amount of NaOAc (A to F: 860, 650, 430, 270, 120, 75 eq.) with water-only solvent system are presented, indicating the amount of NaOAc needs to be appropriate to obtain of Co$_3$(HITP)$_2$ with good quality. As shown by the top trace, using DMF/H$_2$O (v/v = 3:7) mixture as the solvent further improves the crystallinity. (c) Trace A: Co$_3$(HITP)$_2$ synthesized using the procedure described in 2.5.2; Trace B: Co$_3$(HITP)$_2$ synthesized using the alternative procedure described in 2.5.2. The improvement of crystallinity using condition B demonstrates that NaOAc serves not only as a base, but also as a modulator. (d) PXRD patterns of Co$_3$(HITP)$_2$ synthesized using different weak bases. *: 3 eq. of the corresponding base was added as a modulator to the reaction mixture with Co salts, HATP, and excess amount of NaOAc.
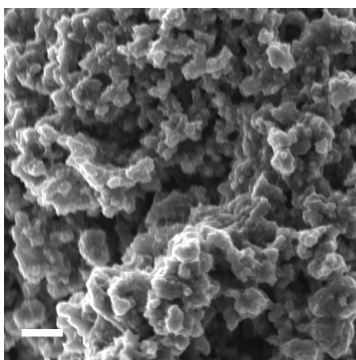
Figure 2.6. SEM images of amorphous Co$_3$(HITP)$_2$ synthesized by using aqueous NH$_3$ as the base. Irregular shaped particles were observed. Scale bar: 500 nm.

Crystallinity improvements also correlate with enhanced permanent porosity. N_2 adsorption isotherms at 77 K for $M_3(HITP)_2$ samples activated by heating at 90 °C under dynamic vacuum gave Brunauer-Emmett-Teller (BET) surface areas of 805.5±0.5 m²/g, 884.7±0.9 m²/g, and 495.4±1.3 m²/g for the Co, Ni, and Cu materials, respectively (Figure 2.7a-c). These are considerably higher than previously reported values and confirm the improved synthetic procedures and material quality developed here.[9,18] Uniform pore size distributions were found in $M_3(HITP)_2$ by pore size distribution analysis (Figure 2.8). Thermogravimetric analysis (TGA) revealed that $M_3(HITP)_2$ undergo pronounced weight losses above 200 °C, likely due to decomposition (Figure 2.9).
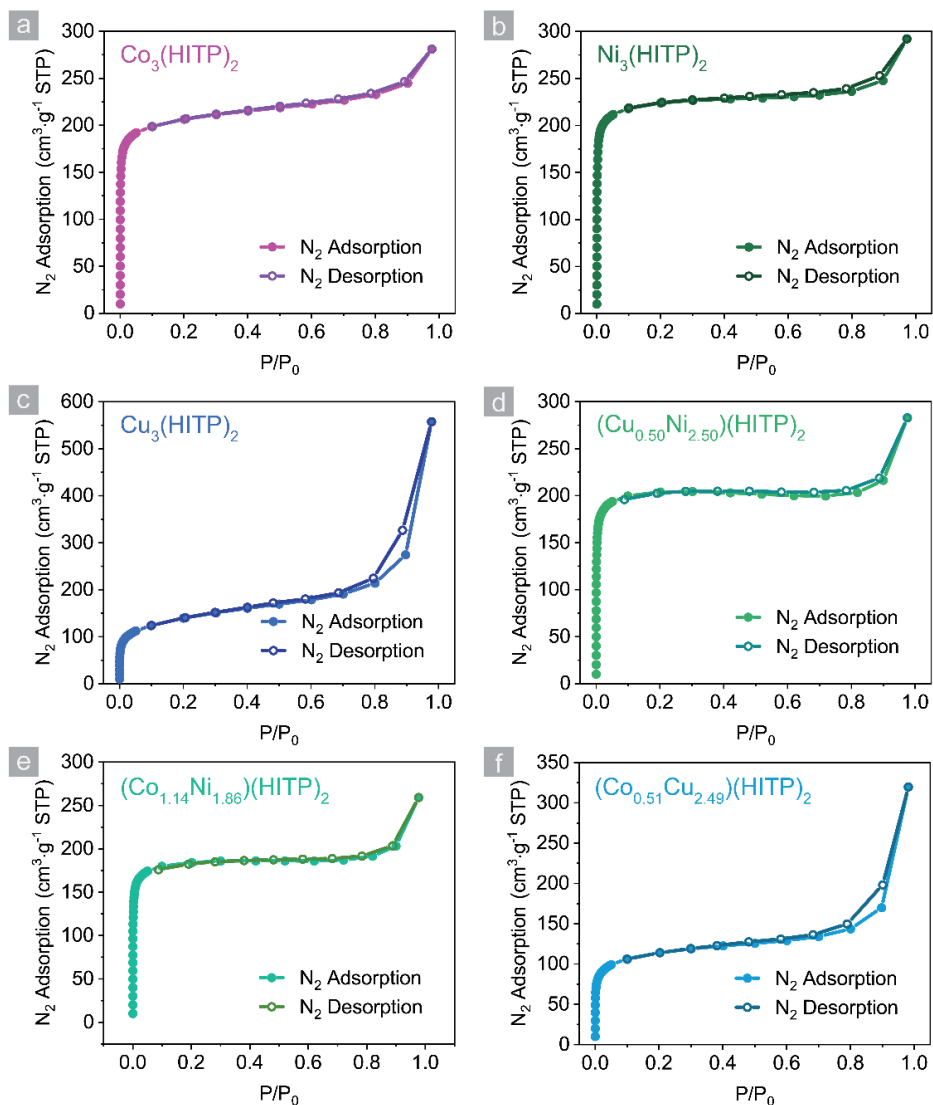
Figure 2.7. N_2 adsorption isotherms of $M_3(HITP)_2$ (M = Co (a), Ni (b), and Cu (c)) and representative $(M_xM'_{3-x})(HITP)_2$ $((Cu_{0.50}Ni_{2.50})(HITP)_2$ (d), $(Co_{1.14}Ni_{1.86})(HITP)_2$ (e), and $(Co_{0.51}Cu_{2.49})(HITP)_2$ (f)) at 77 K. The linear BET fit of these N_2 adsorption isotherms gave BET surface area of 805.4861±0.5152 m²/g for $Co_3(HITP)_2$, 884.6592±0.8542 m²/g for $Ni_3(HITP)_2$, 495.3837±1.2717 m²/g for $Cu_3(HITP)_2$, 814.8304±0.4478 m²/g for $(Cu_{0.50}Ni_{2.50})(HITP)_2$, 731.7164 ± 0.4050 m²/g for $(Co_{1.14}Ni_{1.86})(HITP)_2$, and 426.9539±0.6385 m²/g for $(Co_{0.51}Cu_{2.49})(HITP)_2$. The BET SSA values of $(M_xM'_{3-x})(HITP)_2$ alloys measured suggest the possibility of controlling the porosity by changing the composition of $(M_xM'_{3-x})(HITP)_2$ alloys.
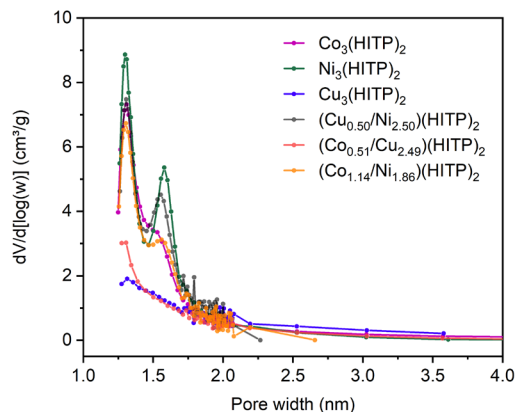
Figure 2.8. The pore size distribution (PSD) of $M_3(HITP)_2$ (M = Co, Ni, and Cu) and representative $(M_xM'_{3-x})(HITP)_2$ alloys $((Cu_{0.50}Ni_{2.50})(HITP)_2$, $(Co_{0.51}Cu_{2.49})(HITP)_2$, and $(Co_{1.14}Ni_{1.86})(HITP)_2)$ calculated using BJH model. The maximums in PSD of $M_3(HITP)_2$ and $(M_xM'_{3-x})(HITP)_2$ alloys are at pore width of around 1.3 nm and 1.6 nm, which is consistent with the crystal structures.
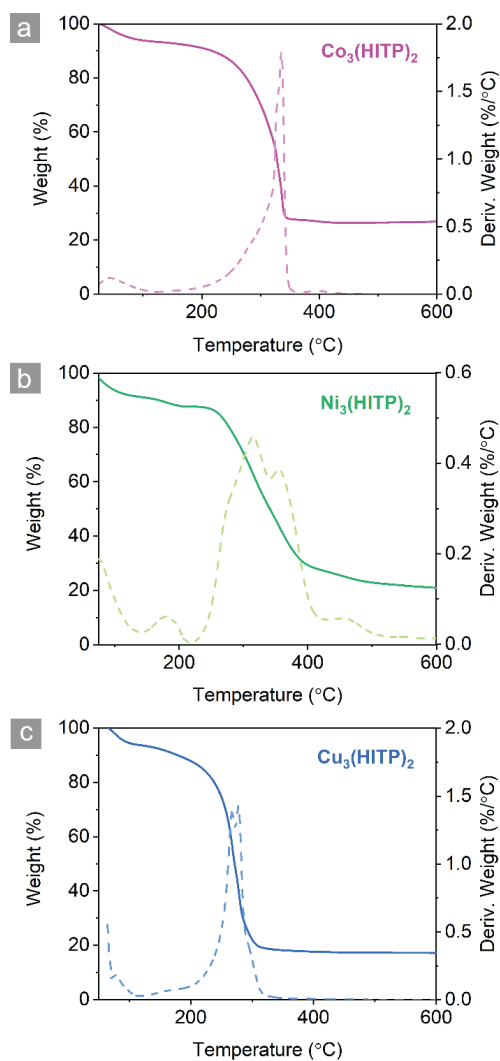
Figure 2.9. TGA of $M_3(HITP)_2$ MOFs. Thermograms (straight line) and derivative curve (dashed line) of $Co_3(HITP)_2$ (a), $Ni_3(HITP)_2$ (b), and $Cu_3(HITP)_2$ (c) in air. Pronounced weight losses above 200 °C were observed in all cases.

65

Scanning electron microscopy (SEM) revealed that black $Ni_3(HITP)_2$ and $Cu_3(HITP)_2$ powders consist of hexagonal, 1-2 μm-long rod-like crystals, whereas $Co_3(HITP)_2$ consists of polycrystalline flakes several hundreds of nanometers wide (Figures 2.10-2.11). All materials exhibit sufficiently high crystallinity for Pawley refinement of their respective powder X-ray diffraction (PXRD) data (Figure 2.12a). Surprisingly, PXRD data for all materials gave best fits for the orthorhombic space group Cmcm (Figure 2.12a and Table 2.1), confirming a lower symmetry than the previously reported hexagonal systems.[12,22] The lower symmetry is also a consequence of improved crystallinity and indicates less averaging of the stacking arrangement in the c direction. Indeed, the synchrotron PXRD data (Figure 2.13) allows observation of subtle differences among the three materials for both the interlayer displacement (D) along the b direction and the interlayer spacing (S) along the c direction. Thus, $Ni_3(HITP)_2$ exhibits the largest D value, 1.56(2) Å, whereas $Cu_3(HITP)_2$ has the smallest S value of only 3.16(8) Å. The latter is significantly smaller than the previously reported value, 3.30 Å, which was derived from a more poorly crystalline sample.[11] The S spacing is evidently connected with the strength of interaction between the 2D sheets, which has recently been shown to contribute significantly to electrical conductivity in layered lanthanide MOFs;[25] precise measurements of this value are important for future computations involving these materials.
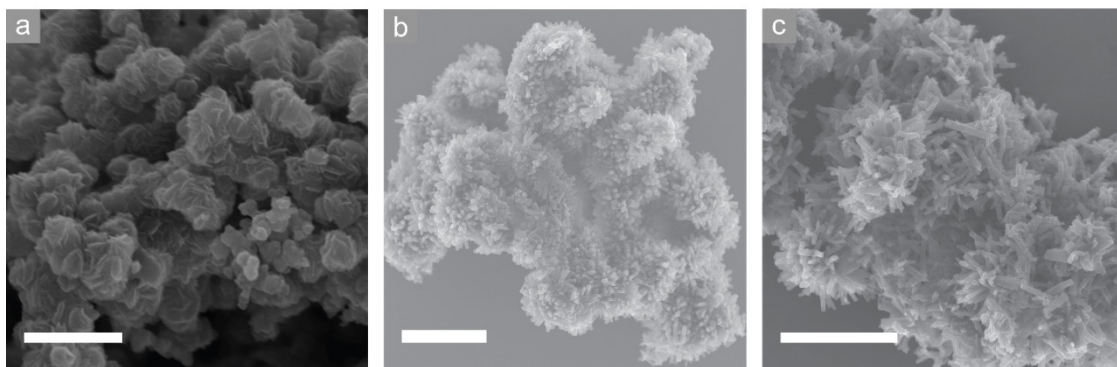
Figure 2.10. SEM images of micro- and nano-crystals of $Co_3(HITP)_2$ (a), $Ni_3(HITP)_2$ (b), and $Cu_3(HITP)_2$ (c) 2D MOFs, indicating the uniformity of morphology. Scale bars: 500 nm (a), 2 μm (b, c).
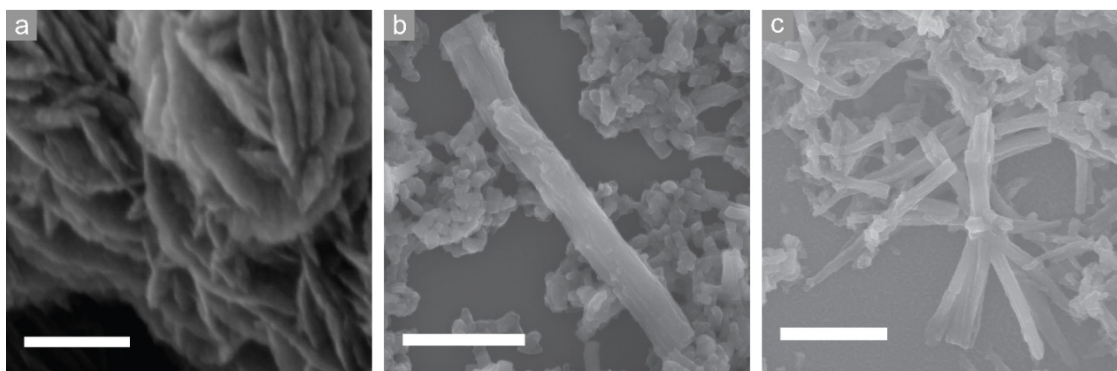
Figure 2.11. Zoom-in SEM images of micro- and nano-crystals of $Co_3(HITP)_2$ (a), and $Ni_3(HITP)_2$ (b) 2D MOFs, demonstrating their high crystallinity. Scale bars: 100 nm (a), 2 μm (b, c).
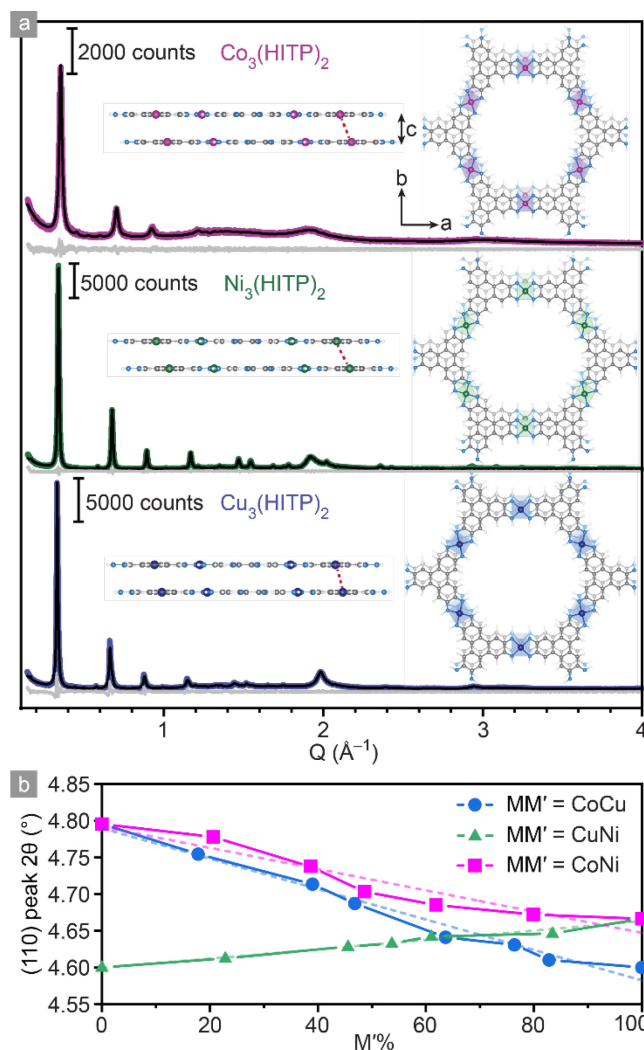
Figure 2.12. (a) Synchrotron PXRD patterns and corresponding Pawley refinements for $Co_3(HITP)_2$, $Ni_3(HITP)_2$, and $Cu_3(HITP)_2$. Insets show the simulated structures (both ab direction and c direction). The red dashed lines indicate interlayer displacement. (b) Continuous changes of the crystal lattice parameters as evidenced by shifts in the (110) peak position for $(Co_x/Cu_{3-x})(HITP)_2$, $(Co_xNi_{3-x})(HITP)_2$, and $(Cu_xNi_{3-x})(HITP)_2$ alloys. Solid lines are the guide to the eye; dashed lines are the linear fit to the Vegard's law, with R^2 of 0.98, 0.92, and 0.98, respectively.

Table 2.1. Lattice parameters obtained by Pawley refinements of synchrotron PXRD patterns of $M_3(HITP)_2$ (M = Co, Ni, Cu). Pawley refinements gave best fits for the orthorhombic space group Cmcm for $M_3(HITP)_2$.

$Co_3(HITP)_2$	$Ni_3(HITP)_2$	$Cu_3(HITP)_2$
a = 35.750861 Å b = 22.189065 Å c = 6.595006 Å $\alpha = \beta = \gamma = 90°$	a = 37.418502 Å b = 21.521620 Å c = 6.476743 Å $\alpha = \beta = \gamma = 90°$	a = 37.963930 Å b = 21.325635 Å c = 6.336320 Å $\alpha = \beta = \gamma = 90°$
Interlayer spacing (S): 3.29(8) Å Co-Co distance: 3.579 Å Interlayer displacement (D): 1.390 Å	Interlayer spacing (S): 3.23(8) Å Ni-Ni distance: 3.595 Å Interlayer displacement (D): 1.562 Å	Interlayer spacing (S): 3.16(8) Å Cu-Cu distance: 3.285 Å Interlayer displacement (D): 0.869 Å
Pawley refinement R_{wp} = 4.23%	Pawley refinement R_{wp} = 4.83%	Pawley refinement R_{wp} = 5.93%
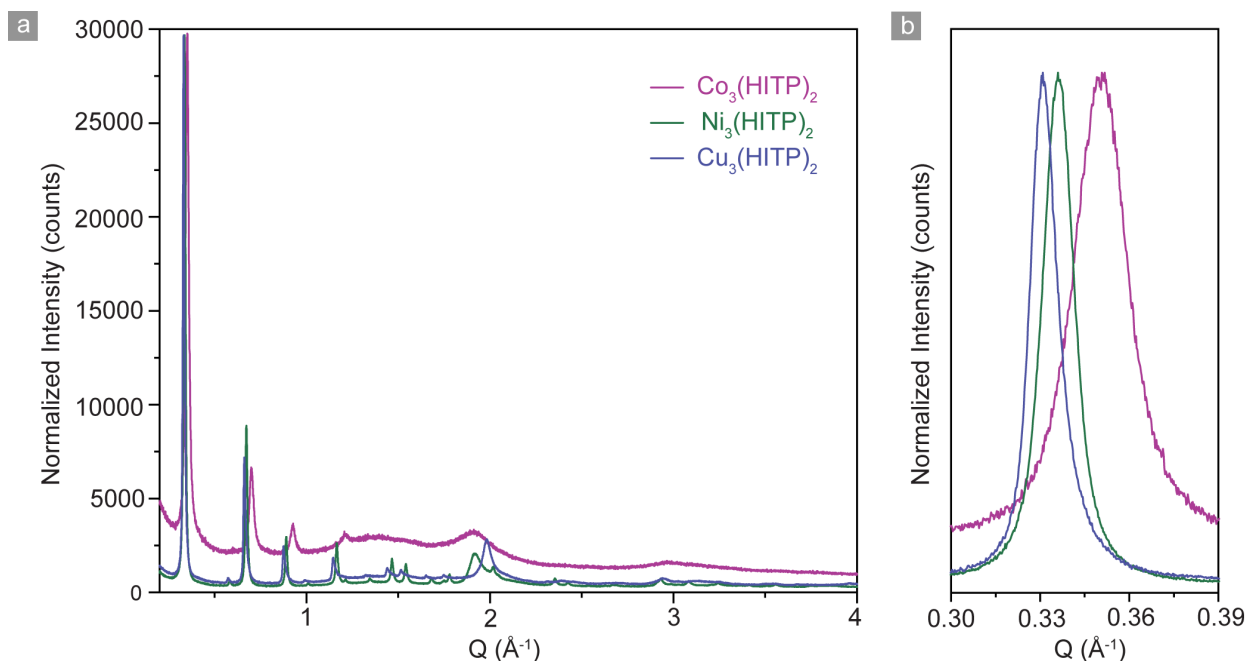
Figure 2.13. Synchrotron PXRD patterns $M_3(HITP)_2$ (M = Co, Ni, Cu) (a) and zoomed-in region of (110) peaks.

Structural details from the Pawley refinements were confirmed by high resolution transmission electron microscopy (HRTEM), with all three materials exhibiting hexagonal lattices (Figure 2.14). Importantly, Fast-Fourier transform (FFT) analysis of the HRTEM micrographs provided lattice parameters which are in excellent agreement with those obtained from PXRD (Tables 2.2-2.4). HRTEM also allows precise measurements of π-π stacking distances of 3.25 Å for $Ni_3(HITP)_2$ and 3.12 Å for $Cu_3(HITP)_2$, again in excellent agreement with those obtained from PXRD analysis (Figures 2.15-2.17).
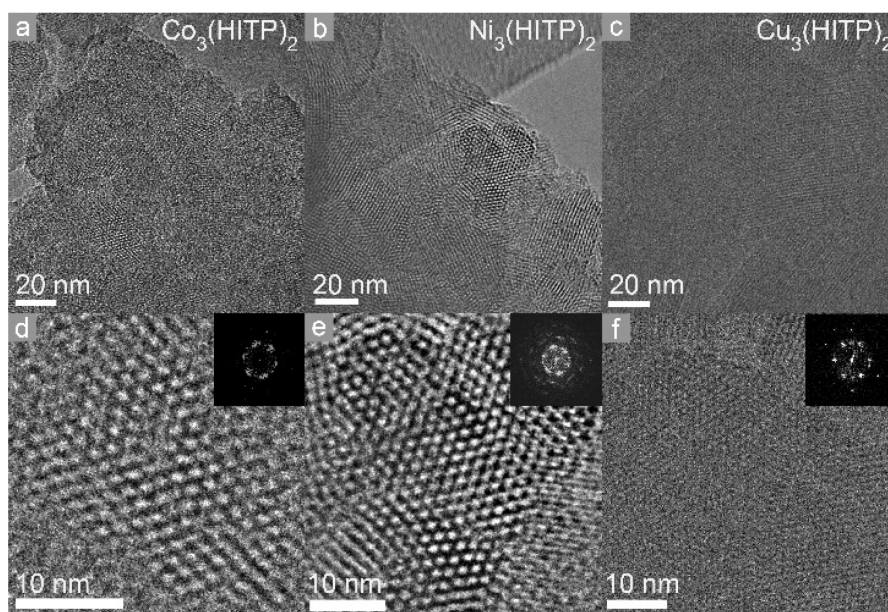
Figure 2.14. HRTEM images of $Co_3(HITP)_2$ (a, d), $Ni_3(HITP)_2$ (b, e), and $Cu_3(HITP)_2$ (c, f). Insets show FFT analysis of the micrographs in (d), (e), and (f).

Table 2.2. *d*-spacing extracted from FFT of TEM images (Observed), calculated based on the refined structure of $Co_3(HITP)_2$ with unit cell parameters of $a = 35.75$ Å, $b = 22.19$ Å, $c = 6.59$ Å (X-ray), and indices corresponding to the *d*-spacing (Index). Although the π-stacking layers can be seen, interlayer distance cannot be obtained due to the insufficiency of image quality.

Observed (Å)	X-ray (Å)	Index
17.2	18.9	110

Table 2.3. *d*-spacing extracted from FFT of TEM images (Observed), calculated based on the refined structure of $Ni_3(HITP)_2$ with unit cell parameters of $a = 37.42$ Å, $b = 21.52$ Å, $c = 6.48$ Å (X-ray), and indices corresponding to the *d*-spacing (Index).

Observed (Å)	X-ray (Å)	Index
18.5	18.7	110
3.25	3.24	002

Table 2.4. *d*-spacing extracted from FFT of TEM images (Observed), calculated based on the refined structure of $Cu_3(HITP)_2$ with unit cell parameters of $a = 37.96$ Å, $b = 21.33$ Å, $c = 6.34$ Å (X-ray), and indices corresponding to the *d*-spacing (Index).

Observed (Å)	X-ray (Å)	Index
18.6	18.5	110
3.12	3.17	002
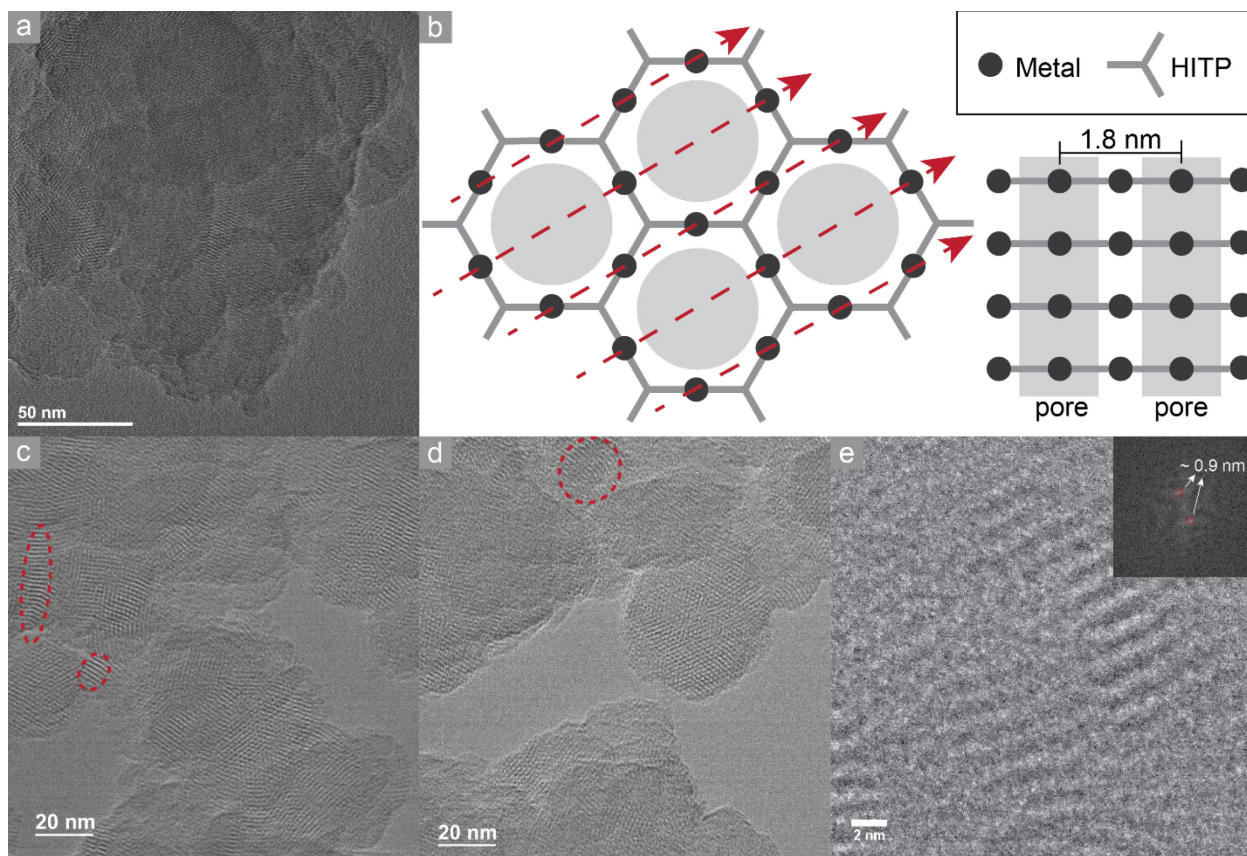
Figure 2.15. TEM images of $Co_3(HITP)_2$ nanocrystalline powder. (a) Flakes about 50 nanometers wide stack together to form bulk $Co_3(HITP)_2$, whereas rod-like morphology can be hardly seen. (b) Left: schematic representation of one layer of $M_3(HITP)_2$ (M = Co, Ni, Cu) and the pore arrangement that observed under TEM. Right: schematic representation of a stacking configuration of four layers of $M_3(HITP)_2$ parallel to 2D layers. Red dashed arrows in the left scheme indicate the direction of viewing for the right scheme. (c, d) Thin films of $Co_3(HITP)_2$ showing hexagonal pores. Red dashed circles indicate the rod-like fragments formed during sonication of $Co_3(HITP)_2$ flakes. (e) Interlayer π-stacking of layers of $Co_3(HITP)_2$. Inset shows the corresponding FFT.
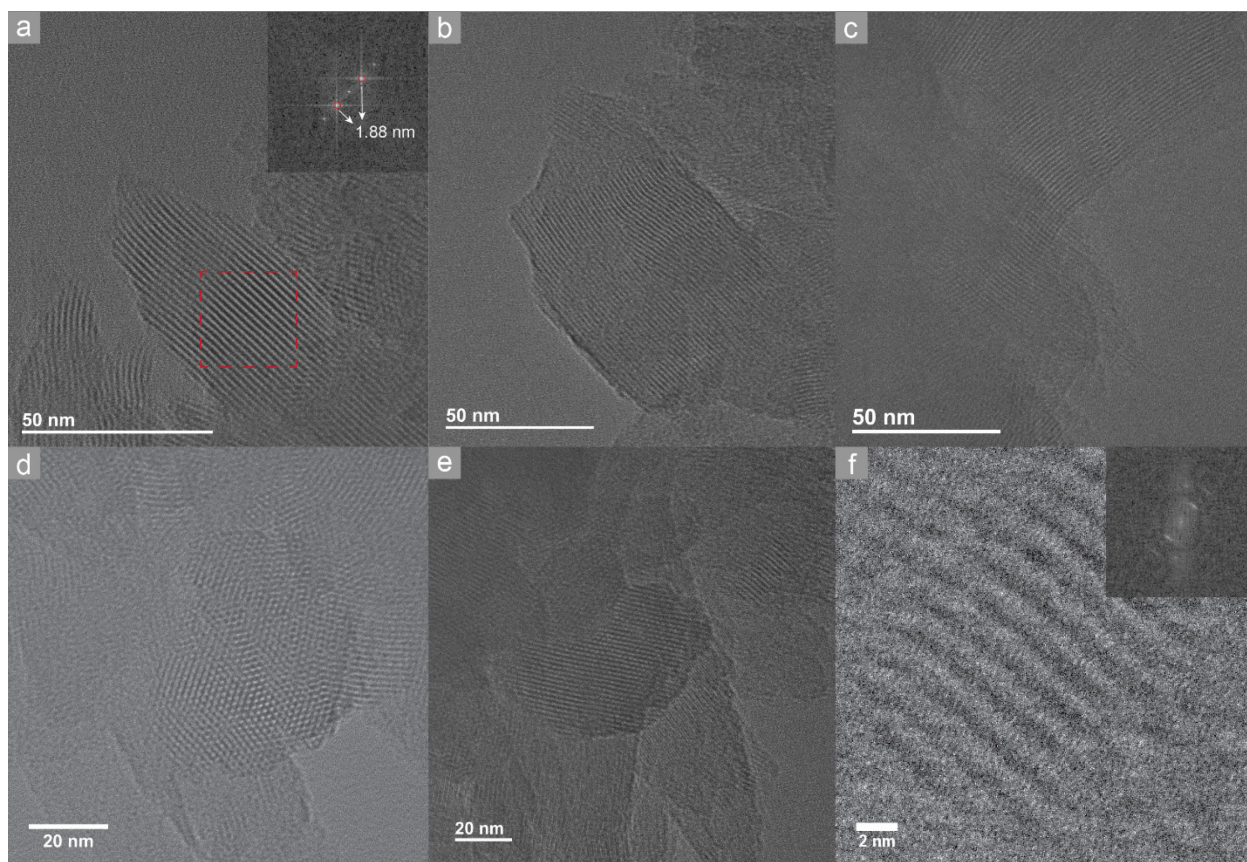
Figure 2.16. TEM images of $Ni_3(HITP)_2$ microcrystalline powder. (a, b, c) Rods of $Ni_3(HITP)_2$ with diameters more than 50 nanometers. Well-aligned fringes indicate the ordered 1D pore structure of $Ni_3(HITP)_2$, which has been schematically illustrated in Figure 2.15b. Inset shows the corresponding FFT. (d, e) Hexagonal $Ni_3(HITP)_2$ films show hexagonal pore structures. (f) Interlayer π-stacking of layers of $Ni_3(HITP)_2$. Inset shows the corresponding FFT.
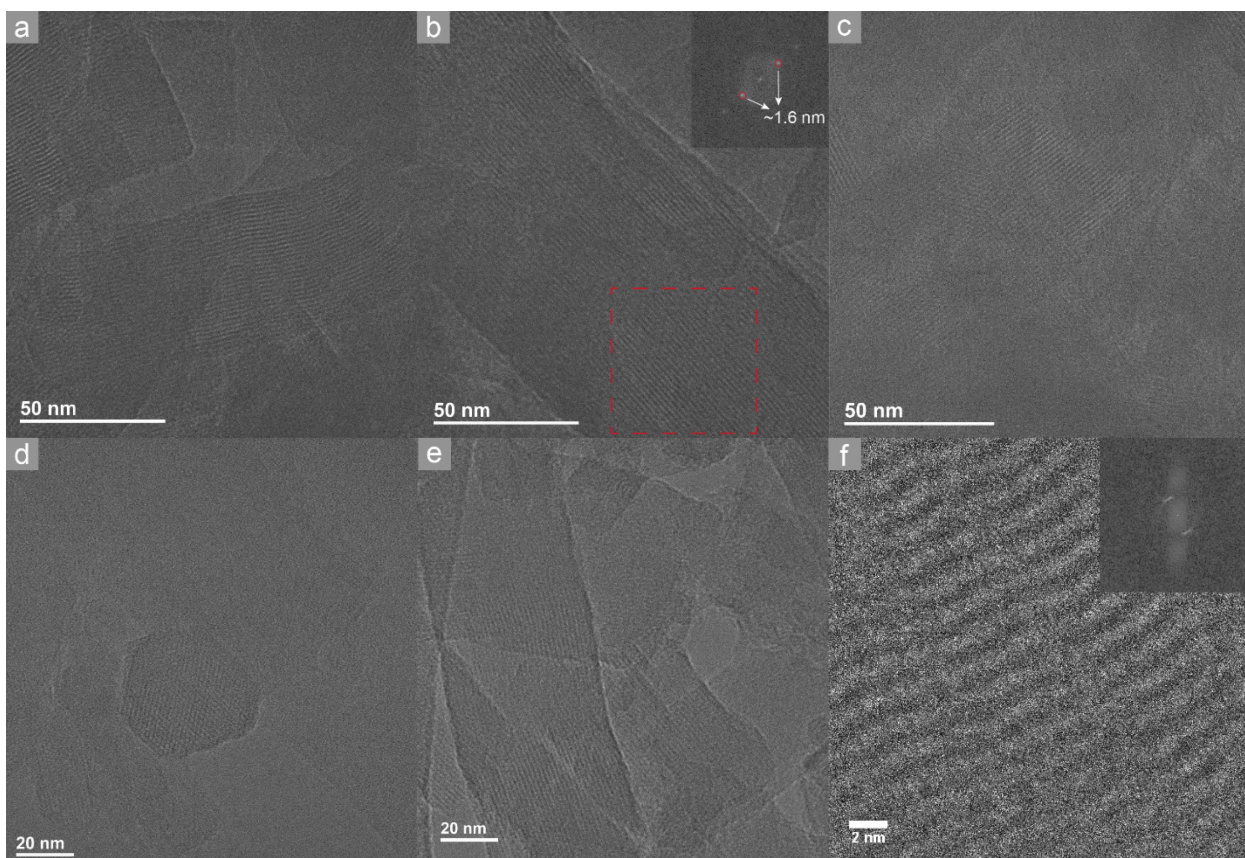
Figure 2.17. TEM images of $Cu_3(HITP)_2$ microcrystalline powder. (a, b, c, e) Rods of $Cu_3(HITP)_2$ with diameters vary from around 50 to over 100 nanometers. Well-aligned fringes indicate the ordered 1D pore structure of $Cu_3(HITP)_2$, which has been schematically illustrated in Figure 2.15b. Inset shows the corresponding FFT. (d) Hexagonal $Cu_3(HITP)_2$ films. (f) Interlayer π-stacking of layers of $Cu_3(HITP)_2$. Inset shows the corresponding FFT.

Owing to their nearly identical structures, $M_3(HITP)_2$ (M = Co, Ni, Cu) can be produced from binary mixtures of metal precursors with continuously variable compositions. To illustrate this, we targeted three binary series $(M_xM'_{3-x})(HITP)_2$: 5 compositions in the Cu/Ni space, 5 for Co/Ni, and 6 for Co/Cu. The final M/M' ratios were determined by inductively coupled plasma-mass spectrometry (ICP-MS), X-ray photoelectron spectroscopy (XPS), and/or energy-dispersive X-ray spectroscopy (EDS). All confirmed that the final metal compositions were similar to those of the precursors (Figure 2.18).

A series of spectroscopic and analytical techniques confirmed the uniform composition of the MOF alloys, with $(Co_xNi_{3-x})(HITP)_2$ as a representative example. STEM elemental mapping of $(Co_xNi_{3-x})(HITP)_2$ samples revealed uniform distribution of Co and Ni atoms within single crystallites/grains, confirming the formation of true mixed phases rather than individual particles or phase-segregated islets of $Co_3(HITP)_2$ and $Ni_3(HITP)_2$ (Figures 2.19-2.24). Tellingly, the morphology of $(Co_xNi_{3-x})(HITP)_2$ particles also evolve gradually from nano-flakes for the cobalt-rich $(Co_{2.38}Ni_{0.62})(HITP)_2$ to nano-rods for the nickel-rich $(Co_{0.60}Ni_{2.40})(HITP)_2$ (Figures 2.25, 2.26). Finally, monotonous shifts of the (110) peak position in the corresponding PXRD patterns confirm a systematic increase in the b unit cell parameter of

$(Co_xNi_{3-x})(HITP)_2$ with increasing Ni content (Figure 2.12b). Similar changes are found in the $(Cu_xNi_{3-x})(HITP)_2$ and $(Co_xCu_{3-x})(HITP)_2$ series (Figures 2.12b, 2.27); all follow Vegard's law, an empirical formula describing solid solutions.[26]
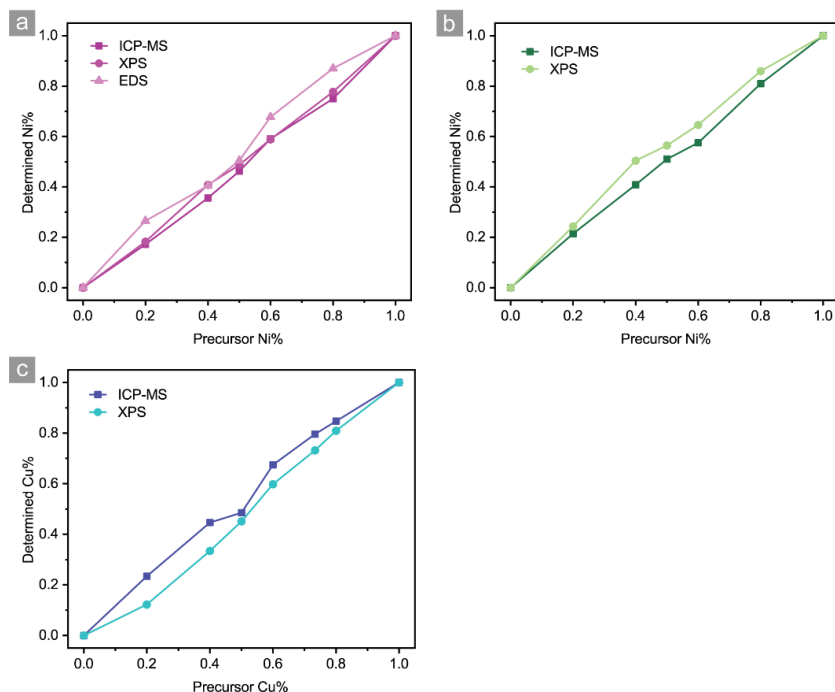
Figure 2.18. Summary of metal composition determinations by different methods. a) $(Co_xNi_{3-x})(HITP)_2$ alloys; b) $(Cu_xNi_{3-x})(HITP)_2$ alloys; c) $(Co_xCu_{3-x})(HITP)_2$ alloys. The metal compositions of $(M_xM'_{3-x})(HITP)_2$ alloys were determined by ICP-MS, XPS, and EDS. Regarding the metal composition determinations by XPS, the binary mixtures of cobalt phthalocyanine (CoPc), nickel phthalocyanine (NiPc), and cupper phthalocyanine (CuPc) were used as standards to calibrate the RSF values of each element.
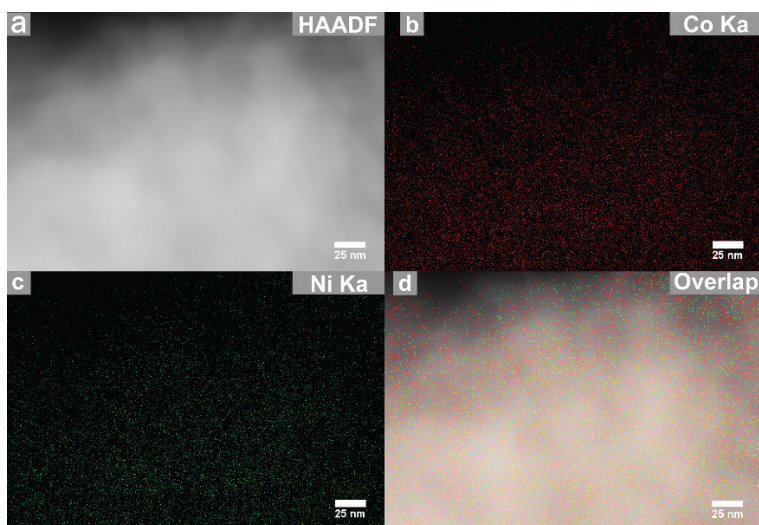
Figure 2.19. HAADF-STEM image of $(Co_{2.38}Ni_{0.62})(HITP)_2$. (a), and the corresponding elemental mapping of Co (b) and Ni (c). The overlap (d) shows the uniform distribution of Co and Ni in this material. All of the 5 $(Co_xNi_{3-x})(HITP)_2$ alloys with different Co: Ni ratios show uniform distribution of Co and Ni verified by energy-dispersive X-ray spectroscopy (EDS), indicating the absence of phase separation. Importantly, the yellow spots in the overlap diagrams demonstrate the presence of both Co and Ni within 1×1 nm^2 area, indicating the good mixing of Co and Ni.
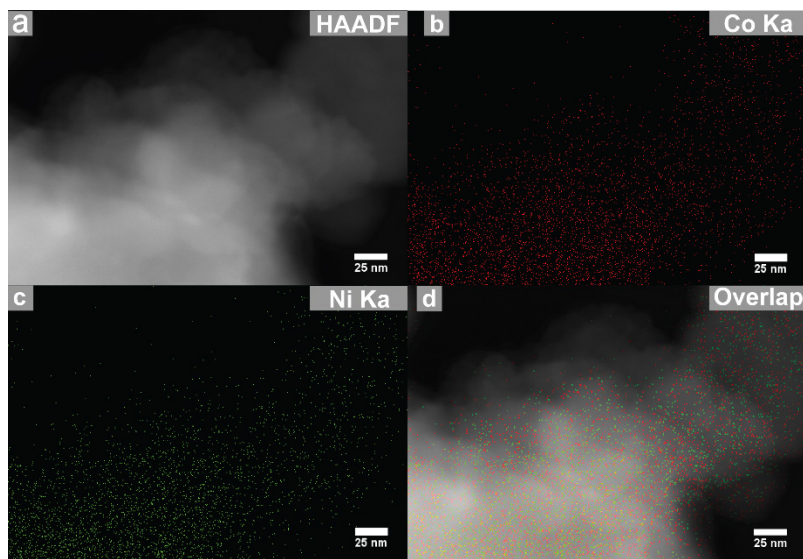
Figure 2.20. HAADF-STEM image of $(Co_{1.83}Ni_{1.17})(HITP)_2$. (a), and the corresponding elemental mapping of Co (b) and Ni (c). The overlap (d) shows the uniform distribution of Co and Ni in this material.
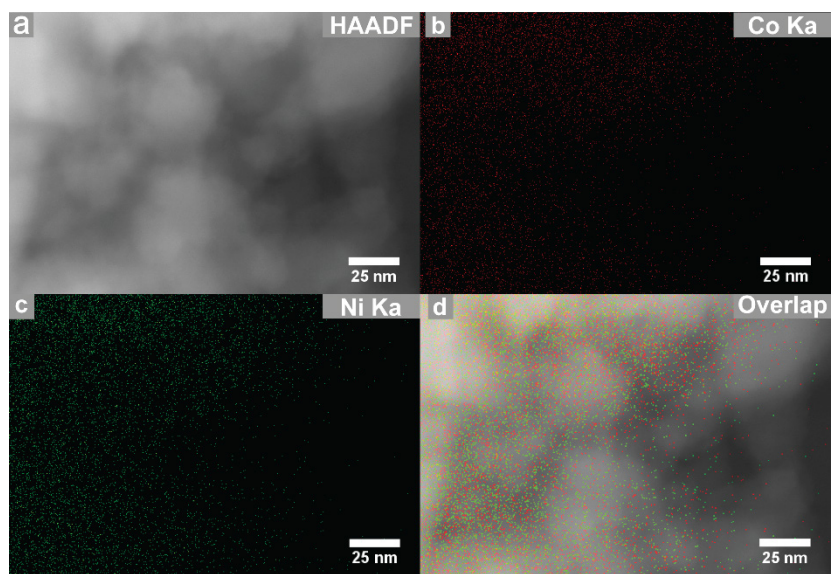
Figure 2.21. HAADF-STEM image of $(Co_{1.54}Ni_{1.45})(HITP)_2$. (a), and the corresponding elemental mapping of Co (b) and Ni (c). The overlap (d) shows the uniform distribution of Co and Ni in this material.
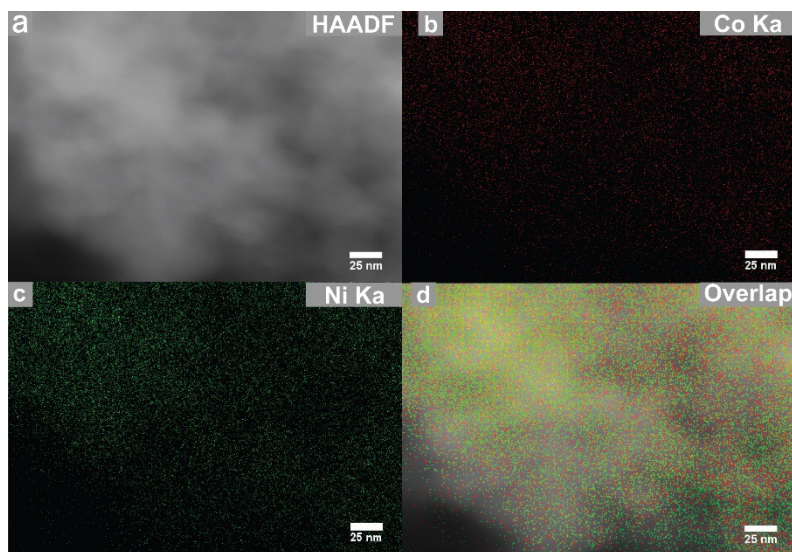
Figure 2.22. HAADF-STEM image of $(Co_{1.14}Ni_{1.86})(HITP)_2$. (a), and the corresponding elemental mapping of Co (b) and Ni (c). The overlap (d) shows the uniform distribution of Co and Ni in this material.
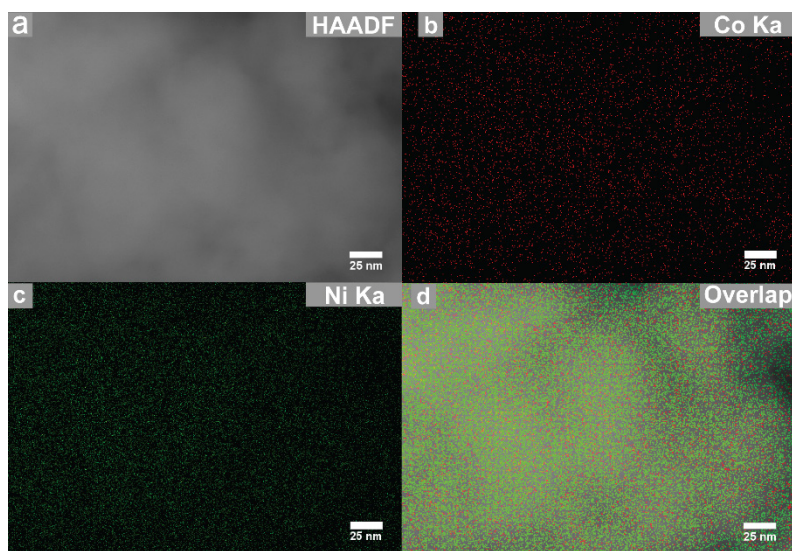
Figure 2.23. HAADF-STEM image of $(Co_{0.60}Ni_{2.40})(HITP)_2$. (a), and the corresponding elemental mapping of Co (b) and Ni (c). The overlap (d) shows the uniform distribution of Co and Ni in this material.
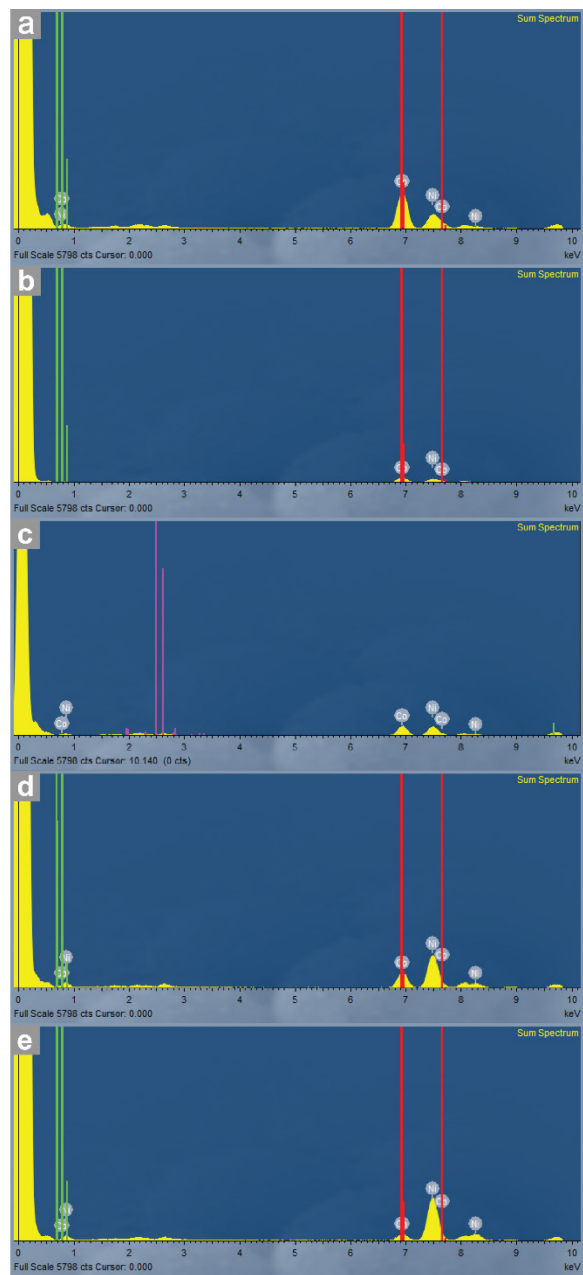
Figure 2.24. EDS spectra of $(Co_{2.38}Ni_{0.62})(HITP)_2$ (a), $(Co_{1.83}Ni_{1.17})(HITP)_2$ (b), $(Co_{1.54}Ni_{1.45})(HITP)_2$ (c), $(Co_{1.14}Ni_{1.86})(HITP)_2$ (d), and $(Co_{0.60}Ni_{2.40})(HITP)_2$ (e).
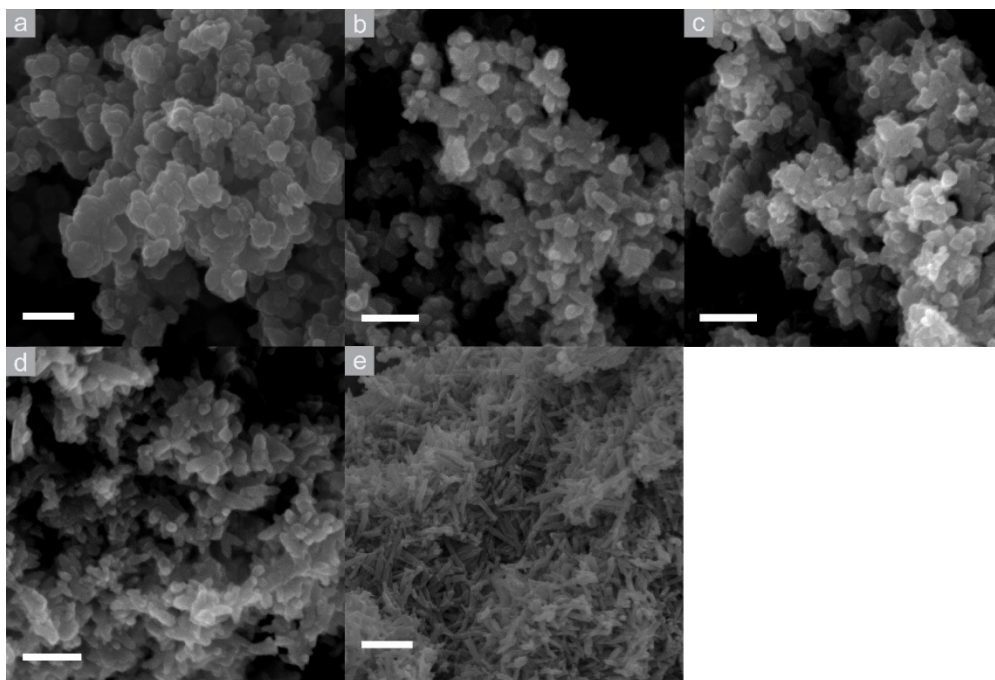
Figure 2.25. SEM images of $(Co_xNi_{3-x})(HITP)_2$ alloys. From (a) to (e): $(Co_{2.38}Ni_{0.62})(HITP)_2$ to $(Co_{0.60}Ni_{2.40})(HITP)_2$. Scale bars: 200 nm (a-d), 500 nm (e). The phase purity was confirmed by exhaustive SEM imaging of the $(Co_xNi_{3-x})(HITP)_2$ alloy samples from multiple batches where only one morphologically unique crystallite could be found for each composition.
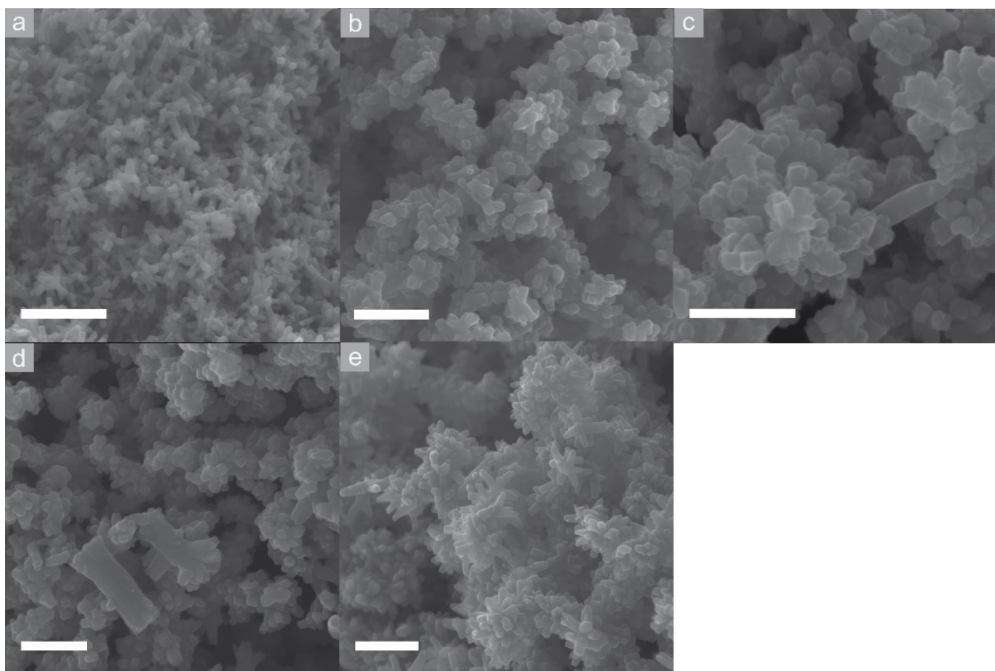
Figure 2.26. SEM images of $(Cu_xNi_{3-x})(HITP)_2$ alloys. From (a) to (e): $(Cu_{2.32}/Ni_{0.68})(HITP)_2$ to $(Cu_{0.50}/Ni_{2.50})(HITP)_2$. Scale bars: 500 nm. The phase purity was confirmed by exhaustive SEM imaging of the $(Cu_xNi_{3-x})(HITP)_2$ alloy samples from multiple batches where only one morphologically unique crystallite could be found for each composition.
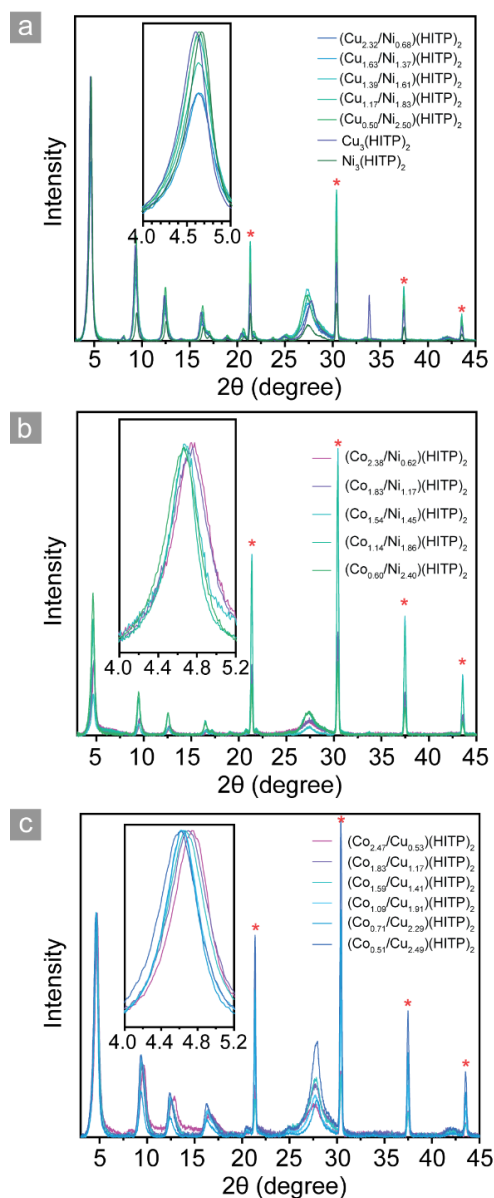
Figure 2.27. PXRD of (a) $(Cu_xNi_{3-x})(HITP)_2$ alloys, (b) $(Co_xNi_{3-x})(HITP)_2$ alloys, and (c) $(Co_xCu_{3-x})(HITP)_2$ alloys. All PXRD patterns are calibrated by internal standard LaB_6, whose diffraction peaks are marked by $\star$.

XPS and X-ray absorption spectroscopy (XAS) confirmed that all metals are in the +2 formal oxidation state and exhibit square-planar coordination geometry. The XPS Co $2p_{3/2}$ peak of $Co_3(HITP)_2$ has a binding energy of 780.9 eV with a prominent satellite at 786.7 eV. These are consistent with Co^{2+} compounds, as satellite features rarely appear for Co^{3+} compounds.[4,27] Furthermore, $Co_3(HITP)_2$ resides in Co(II) region in the Wagner plot[28] of Co based on the Co $2p_{3/2}$ binding energy and Co LMM kinetic energy (769.7 eV, Figure 2.28). The XPS spectra of $Ni_3(HITP)_2$ and $Cu_3(HITP)_2$ exhibit single Ni $2p_{3/2}$ and Cu $2p_{3/2}$ peaks at 855.2 eV and 933.5 eV, respectively, as expected for Ni^{2+} and Cu^{2+} (Figure 2.29).[29,30] The weak satellite accompanying the Ni $2p_{3/2}$ peak suggests Ni^{2+} is diamagnetic in $Ni_3(HITP)_2$.[31] The complementary Cu

LMM peak with a kinetic energy of 918.2 eV also locates $Cu_3(HITP)_2$ in the Cu(II) region of the Wagner plot of Cu (Figure 2.30). We note that the improved synthesis of $Cu_3(HITP)_2$ leads to pure Cu(II) samples, in contrast with previous reports where mixed valence contributions to conductivity could not be ruled out.[12] XPS N 1s spectra of $M_3(HITP)_2$ can be deconvoluted into two peaks at 399.6 eV and 397.9 eV which are attributed to the anilinic amine (–NH–) and the quinoid imine (=N–),[32,33] and correlate well with the proposed partial oxidation of HATP to form HITP (Figure 2.29). The resulting charge neutrality of the frameworks is demonstrated by the absence of possible additional charge-balancing ions (e.g., Na^+ and OAc^-; Figures 2.31, 2.32).
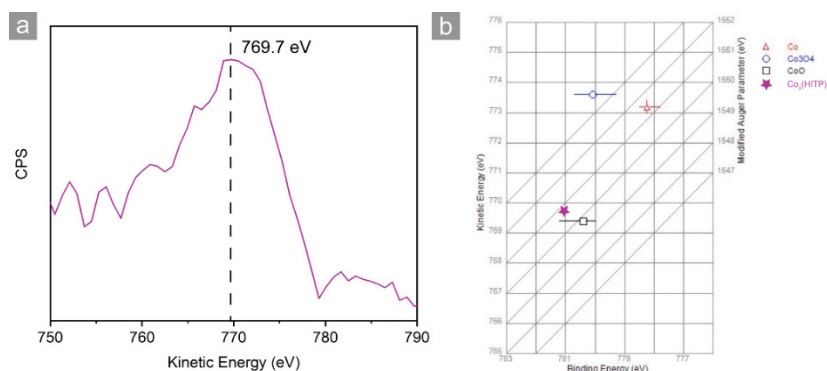
Figure 2.28. a) Co LMM region of $Co_3(HITP)_2$, the kinetic energy 769.7 eV is typical for Co^{2+}. b) Wagner plot of Co, indicating that $Co_3(HITP)_2$ only has Co^{2+}. The Wagner plot is generated using NIST XPS Data Base.
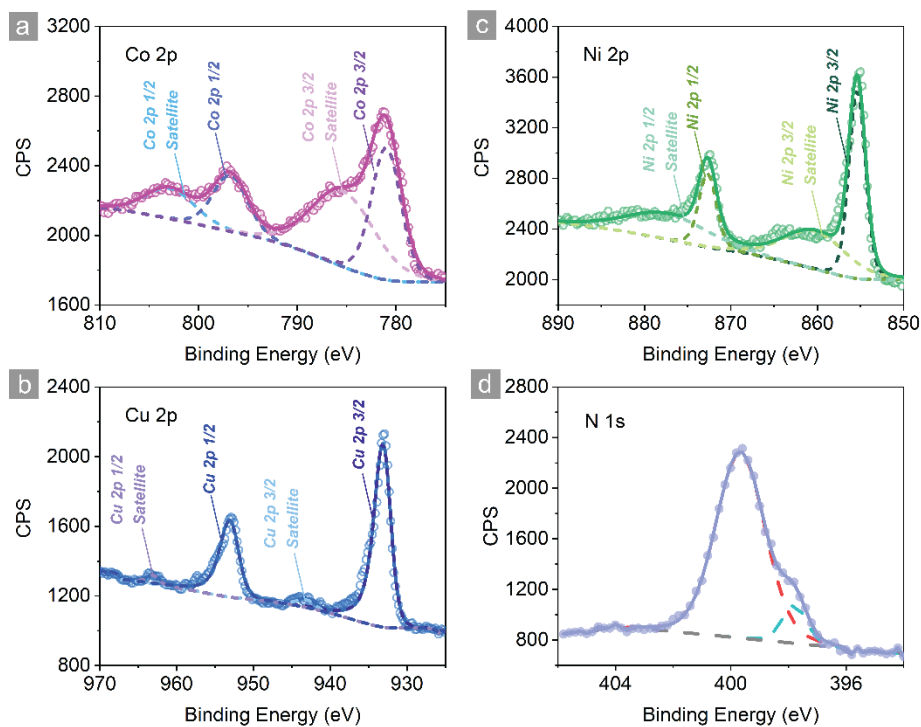
Figure 2.29. XPS high resolution spectra of a) Co 2p region of $Co_3(HITP)_2$, b) Cu 2p region of $Cu_3(HITP)_2$, c) Ni 2p region of $Ni_3(HITP)_2$, and typical N 1s region of $M_3(HITP)_2$ MOFs. Circles represent the experimental data, the solid lines are the envelope of fitting, and the dash lines are backgrounds and fitting components.
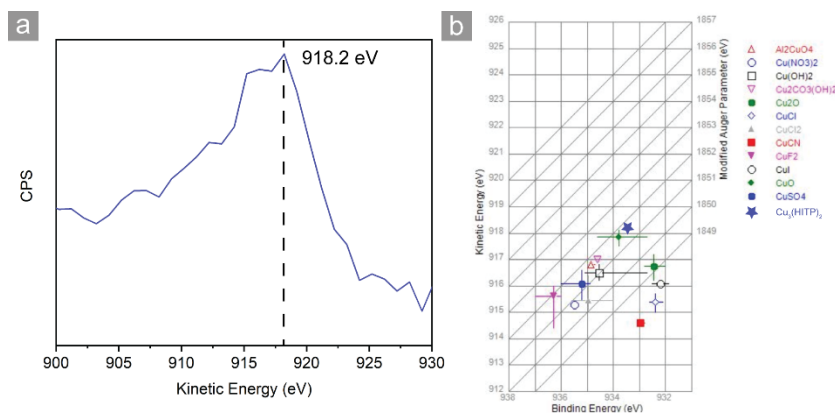
Figure 2.30. a) Cu LMM region of $Cu_3(HITP)_2$, the kinetic energy 918.2 eV is typical for Cu^{2+}. b) Wagner plot of Cu, indicating that $Cu_3(HITP)_2$ only has Cu^{2+}. The Wagner plot is generated using NIST XPS Data Base.
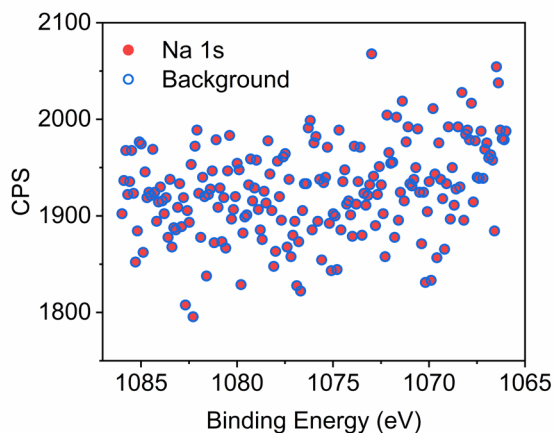
Figure 2.31. The absence of Na^+ in the as-synthesized $Co_3(HITP)_2$ verified by XPS, indicating that the framework is neutral in charge.

X-ray absorption near edge structure (XANES) analysis of $Co_3(HITP)_2$ revealed a pre-edge feature at 7.7092 keV and an edge energy of 7.7204 keV, well matched with the value expected for Co^{2+} (Figure 2.33). The weak pre-edge feature at 8.9712 keV in the XANES spectrum of $Cu_3(HITP)_2$ (Figure 2.34) is characteristic of Cu^{2+}, which has been unambiguously assigned to a 1s→3d transition. This transition is not observed in Cu^+ with fully occupied 3d orbitals.[34–36] The XANES spectra of $M_3(HITP)_2$ and corresponding model complexes MPc (Pc = phthalocyanine) exhibit similar features, indicating they have similar square-planar coordination environment (Figures 2.33-2.36). The fit for the extended X-ray absorption fine structure (EXAFS) spectrum of $Co_3(HITP)_2$ demonstrates the square-planar coordination mode of Co with four Co–N bonds (fitted coordination number of 3.9, Table 2.5) of 1.84 Å (Figure 2.35), matching well with the structure modeled from PXRD data. The simulated Co–N bond length is also comparable to the 1.824(5) Å averaged Co–N bond length of $Co(II)(s\text{-}bqdi)_2$ complex (s-bqdi = semi-*o*-benzoquinonediimine).[37] Importantly, the +2 oxidation states and square-planar coordination environment of the metal ions are conserved in all $(M_xM'_{3–x})(HITP)_2$ alloys, as verified by XPS (Figure 2.37-2.39).
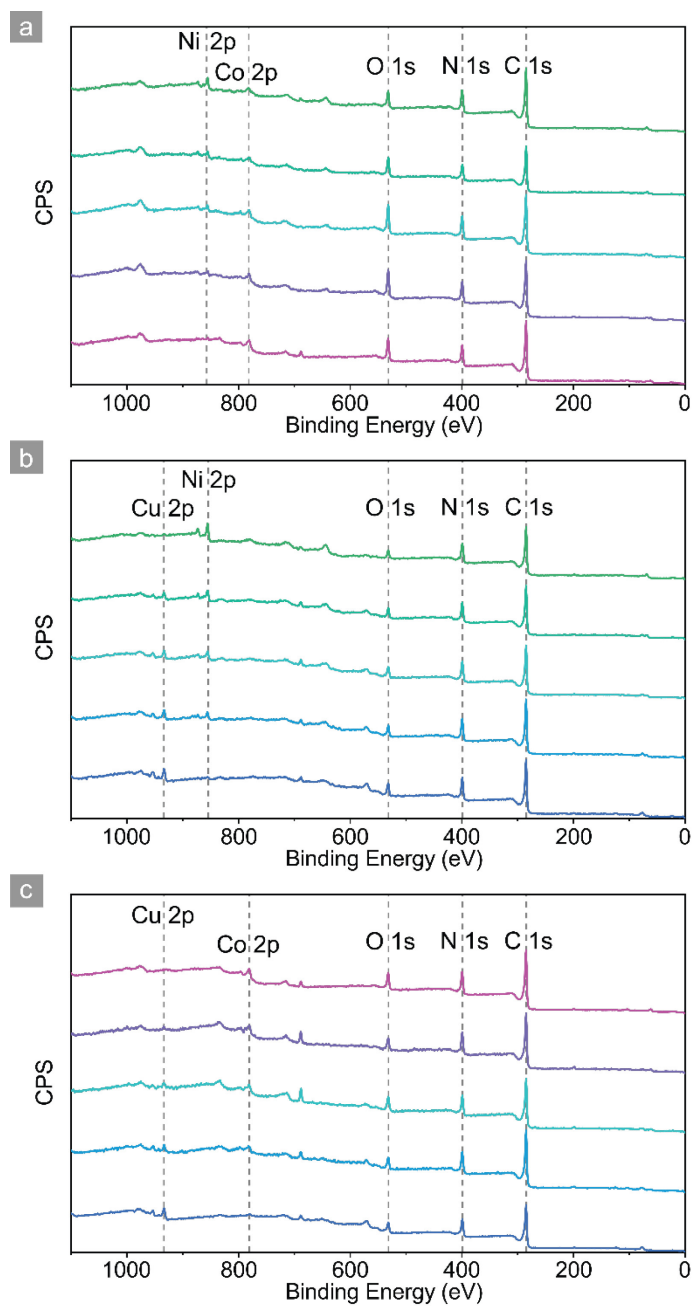
Figure 2.32. XPS survey spectra of $(M_xM'_{3-x})(HITP)_2$ alloys (MM' = CoNi (a), CuNi (b), and CoCu (c)). (a) From top to bottom: $(Co_{0.60}Ni_{2.40})(HITP)_2$ to $(Co_{2.38}Ni_{0.62})(HITP)_2$. (b) From top to bottom: $(Cu_{0.50}Ni_{2.50})(HITP)_2$ to $(Cu_{2.32}Ni_{0.68})(HITP)_2$. (c) From top to bottom: $(Co_{2.47}Cu_{0.53})(HITP)_2$ to $(Co_{0.51}Cu_{2.49})(HITP)_2$.
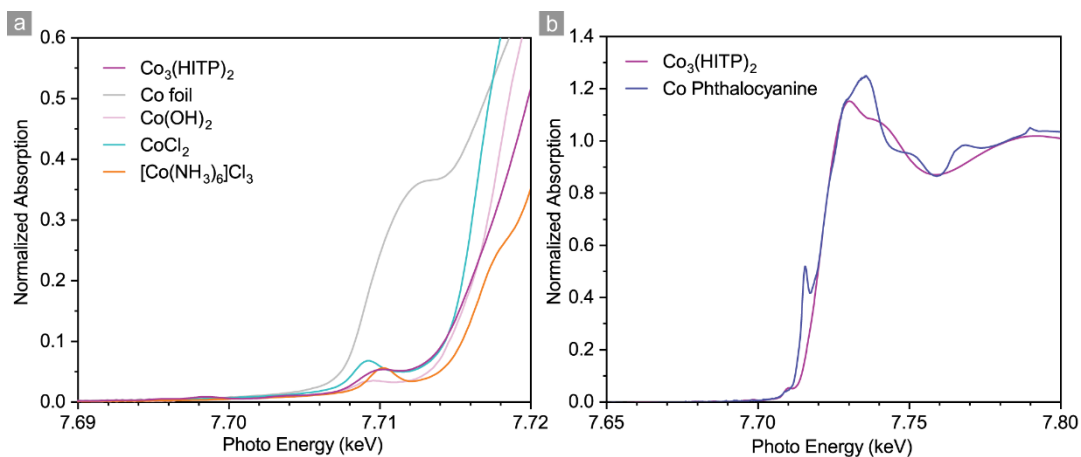
Figure 2.33. XANES spectra of Co$_3$(HITP)$_2$ and reference Co complexes. A pre-edge feature of Co$_3$(HITP)$_2$ at 7.7092 keV and a K-edge energy of 7.7204 keV.
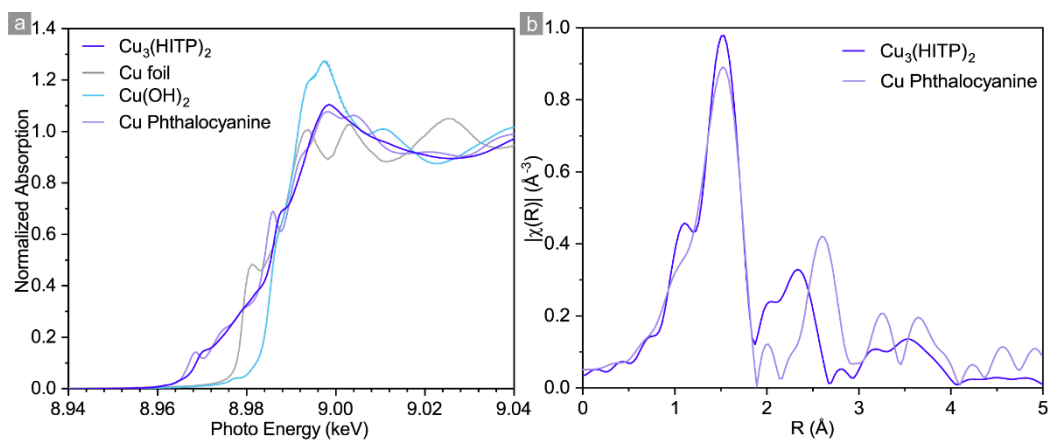
Figure 2.34. (a) XANES spectra of Cu$_3$(HITP)$_2$ and reference Cu complexes. Note that Cu$_3$(HITP)$_2$ and Cu phthalocyanine (CuPc) have similar XANES features, indicating they have similar coordination environment, which is consistent with the Cu$_3$(HITP)$_2$ structure obtained from PXRD refinement. (b) EXAFS of Cu$_3$(HITP)$_2$ and CuPc. Cu$_3$(HITP)$_2$ has similar Cu–N bond length as CuPc (1.934(5) Å).
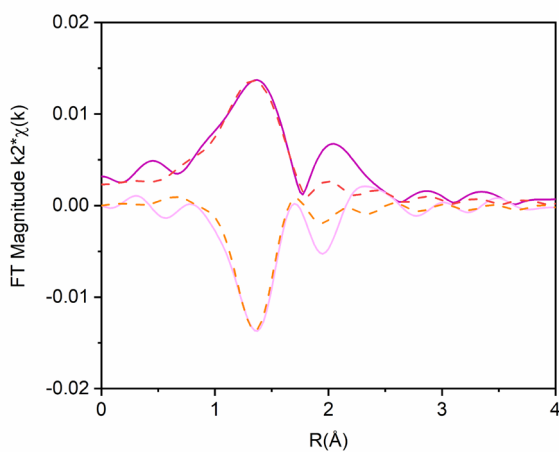
Figure 2.35. EXAFS fitting of Co$_3$(HITP)$_2$. Solid lines represent the experimental data and dashed lines are fitting curves.

Table 2.5. EXAFS fitting parameters over a Fourier transform range of 2.7 to 10.0 $Å^{-1}$ at the Co K edge. Note that Co–N bond length in $Co_3(HITP)_2$ is shorter than that Co phthalocyanine (1.908(5) Å).

Sample	Pre-edge energy (keV)	XANES energy (keV)	Scattering Pair	CN	R (Å)	σ^2 (Å^2)	ΔE_o (eV)	
$Co_3(HITP)_2$	7.7092	7.7204	Co–N	3.9	1.84	0.006	-7.1	Co^{2+}
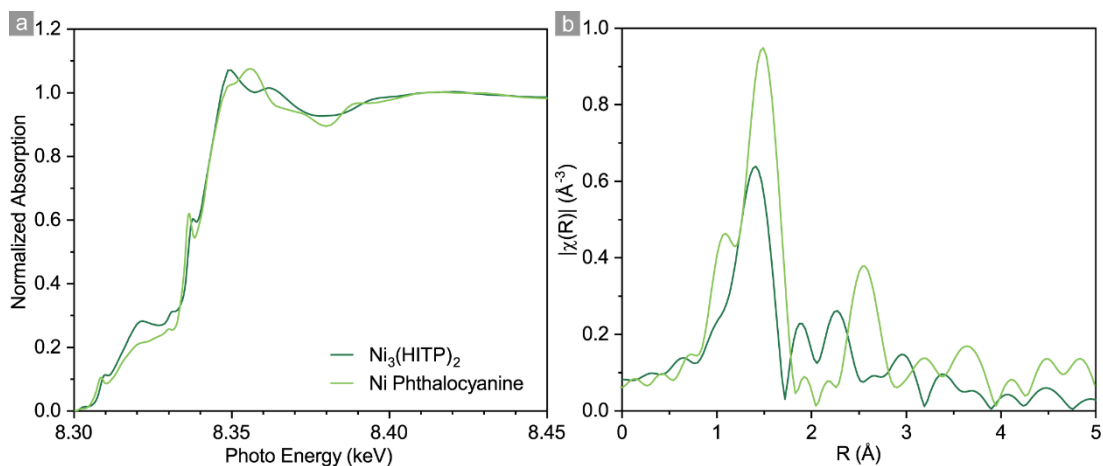
Figure 2.36. (a) XANES spectra of $Ni_3(HITP)_2$ and reference Ni phthalocyanine (NiPc). They have similar XANES features, indicating $Ni_3(HITP)_2$ and NiPc have similar coordination environment, which is consistent with the $Ni_3(HITP)_2$ structure obtained from PXRD refinement. (b) EXAFS of $Ni_3(HITP)_2$ and NiPc. $Ni_3(HITP)_2$ has shorter Ni–N bond length than NiPc.
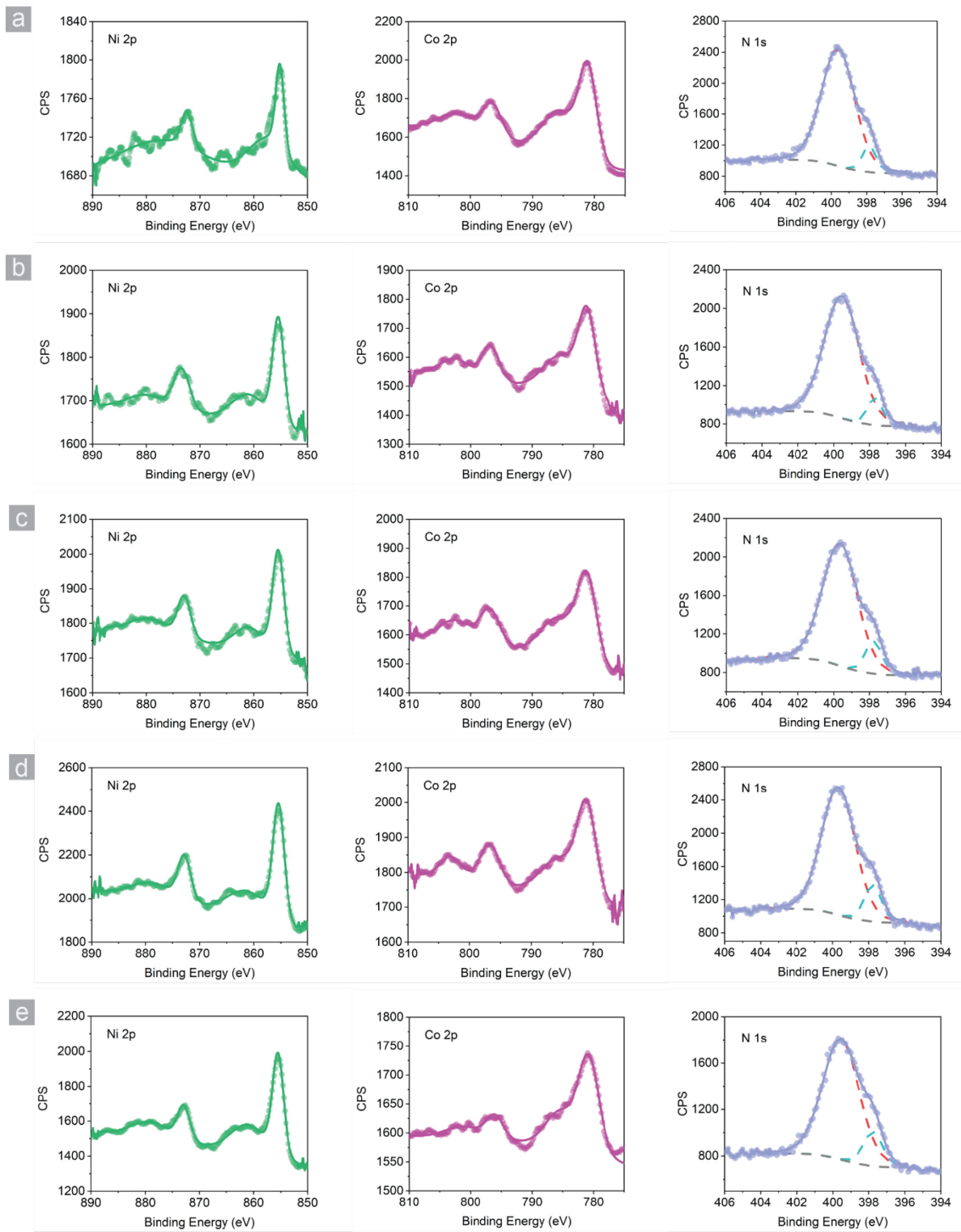
Figure 2.37. XPS Ni 2p (green), Co 2p (magenta), and N 1s (light purple) regions of $(Co_xNi_{3-x})(HITP)_2$ alloys. From (a) to (e): $(Co_{2.38}Ni_{0.62})(HITP)_2$ to $(Co_{0.60}Ni_{2.40})(HITP)_2$. Solid circles represent experimental data, while solid and dash lines are the fitting.
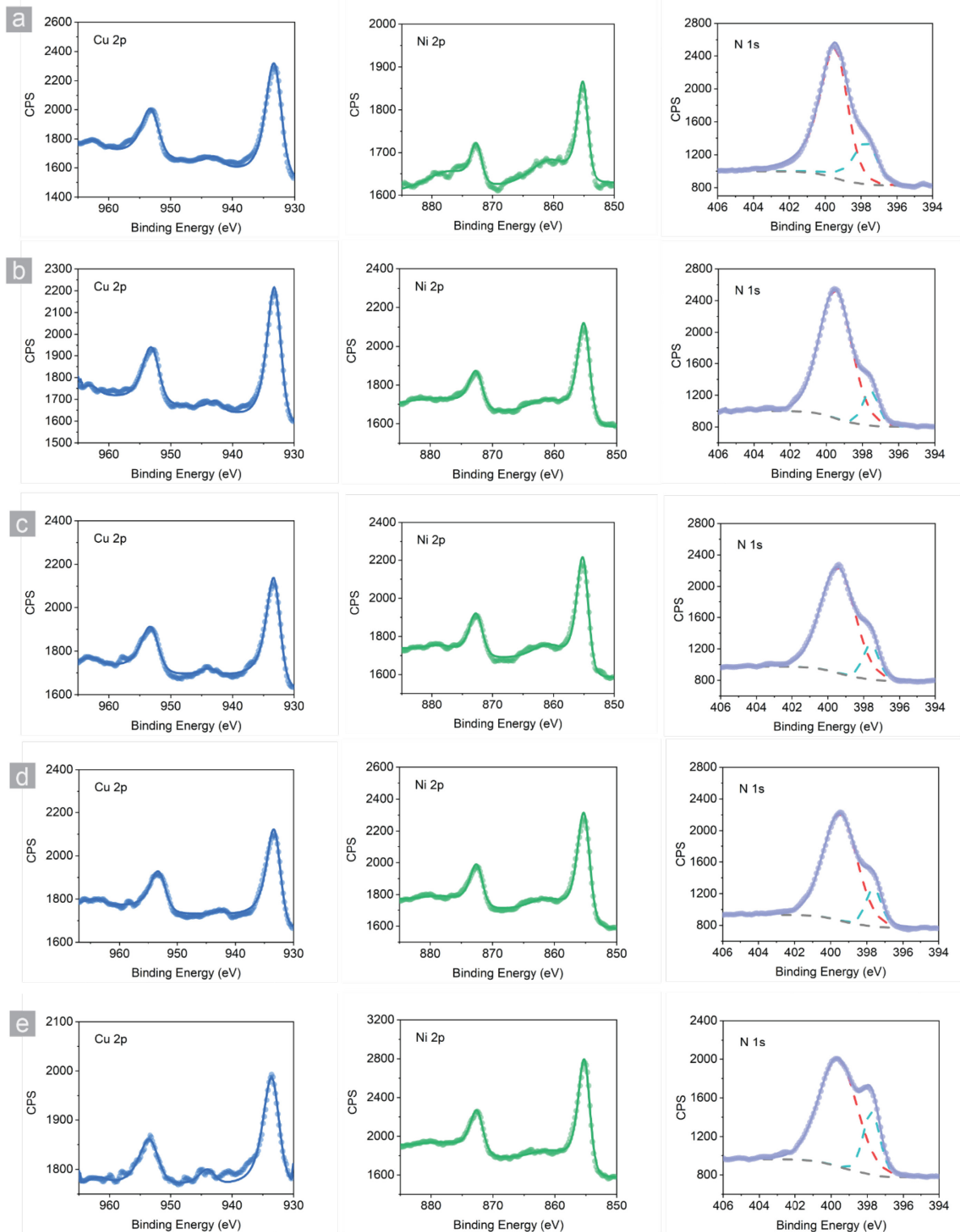
Figure 2.38. XPS Cu 2p (deep blue), Ni 2p (green), and N 1s (light purple) regions of $(Cu_xNi_{3-x})(HITP)_2$ alloys. From (a) to (e): $(Cu_{2.32}Ni_{0.68})(HITP)_2$ to $(Cu_{0.50}Ni_{2.50})(HITP)_2$. Solid circles represent experimental data, while solid and dash lines are the fitting.
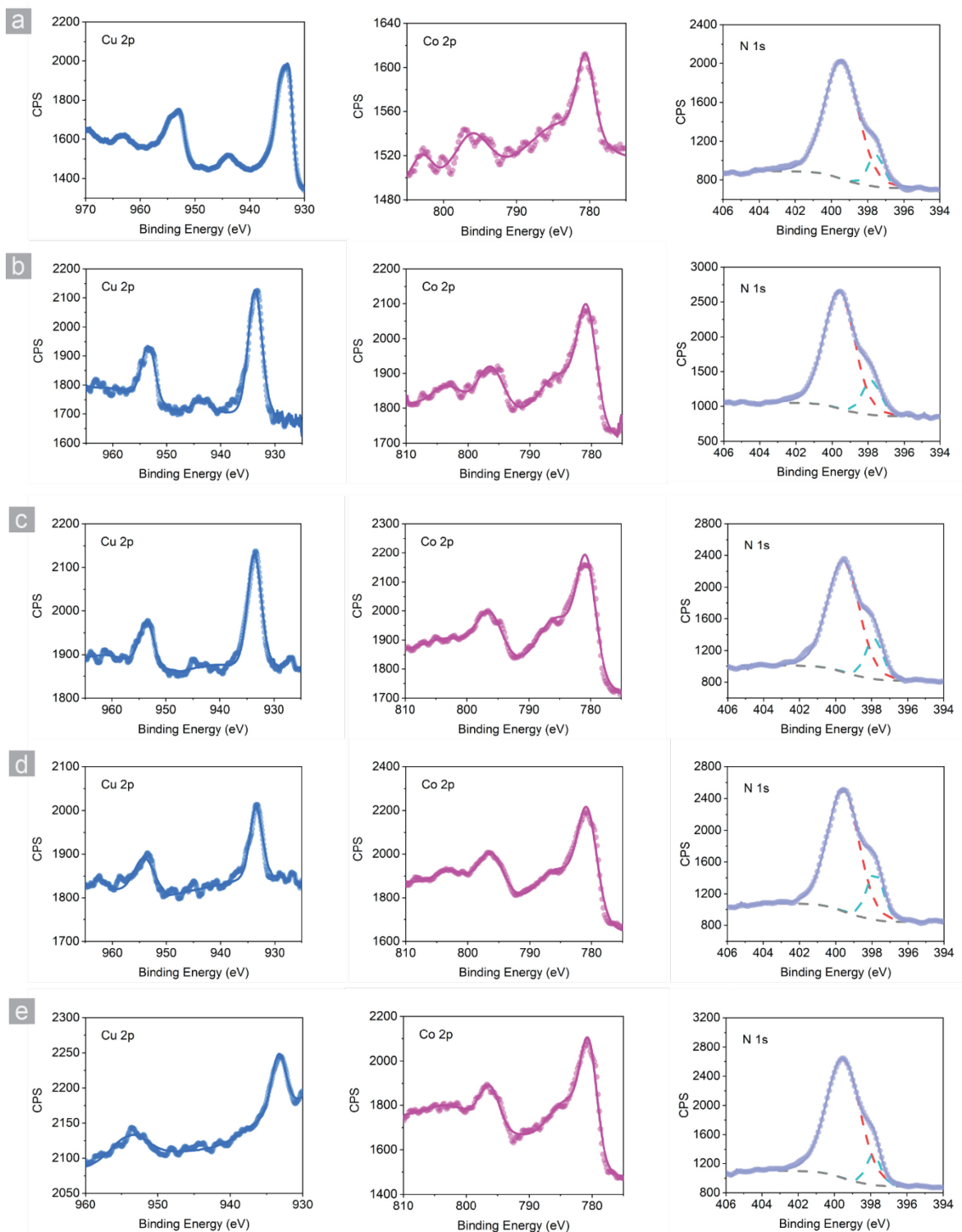
Figure 2.39. XPS Cu 2p (deep blue), Co 2p (magenta), and N 1s (light purple) regions of $(Co_xCu_{3-x})(HITP)_2$ alloys. From (a) to (e): $(Co_{0.51}Cu_{2.49})(HITP)_2$ to $(Co_{2.47}Cu_{0.53})(HITP)_2$. Solid circles represent experimental data, while solid and dash lines are the fitting.

X-band electron paramagnetic resonance (EPR) spectroscopy confirmed the presence of HITP-centered organic radicals with g = 2.00. Peaks at g = 5.64 and $\cong$1.9 in the EPR spectrum of $Co_3(HITP)_2$

are typical for high-spin Co^{2+} ions.[38] Similarly, g peaks at 2.17 and 2.02 observed for $Cu_3(HITP)_2$ are typical for square-planar Cu^{2+} ions.[39] Expectedly for non-Kramers Ni^{2+} ions, the X-band EPR spectrum of $Ni_3(HITP)_2$ exhibits only the signal for the ligand-based radical (Figure 2.40).
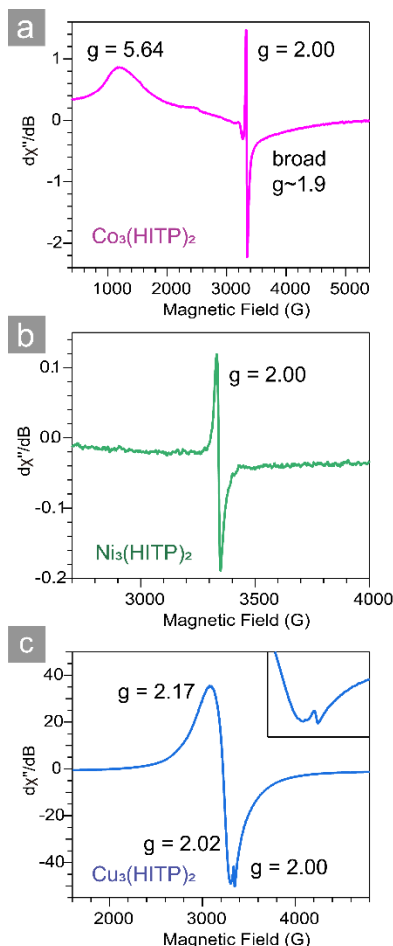
Figure 2.40. EPR spectra of (a) $Co_3(HITP)_2$, (b) $Ni_3(HITP)_2$, and (c) $Cu_3(HITP)_2$ recorded at 5 K. The inset is a zoom-in view of the $Cu_3(HITP)_2$ trace. g at 5.64 and ~1.9 matches well with typical spectra of high spin Co^{2+} with zero-field splitting. A signal for organic radical with g = 2.00 can also been seen, corresponding to HITP-centered radical. Only the signal for HITP-based organic radical with g = 2.00 can be seen in $Ni_3(HITP)_2$, while low spin Ni^{2+}-based transition cannot be observed under experimental condition. g = [2.17, 2.02] matches well with typical spectra for square-planar Cu^{2+}.

Optical spectroscopy provided additional insight into the electronic structures of $(M_xM'_{3-x})(HITP)_2$. Diffuse reflectance UV-visible (DR-UV-Vis) spectroscopy revealed a clear absorption edge for $Co_3(HITP)_2$, with broader absorption edges in the near-infrared (IR) region for $Ni_3(HITP)_2$ and $Cu_3(HITP)_2$ (Figure 2.41). The increase of the background IR absorption, generally associated with free carrier absorption in degenerate or narrow-gap semiconductors,[40] suggests an enhancement of the free carrier concentration from $Co_3(HITP)_2$ to $Ni_3(HITP)_2$ (Figure 2.41a). Indeed, diffuse reflectance infrared Fourier transform spectra (DRIFTS) of $(M_x/M'_{3-x})(HITP)_2$ also reveal a continuous increase of background absorption with increasing Cu or Ni content, suggesting the continuous elevation of free carrier

concentration (Figure 2.42). Plotting the DR-UV-Vis spectra of $M_3(HITP)_2$ in Tauc coordinates[41–43] revealed optical band gaps E_o of 0.719 eV, 0.429 eV, and 0.291 eV for $Co_3(HITP)_2$, $Cu_3(HITP)_2$, and $Ni_3(HITP)_2$, respectively. The progressively narrower band gap when transitioning from Co to Cu and Ni is also in agreement with a decreased free carrier concentration for the pure cobalt MOF. Most importantly, DR-UV-Vis spectra of $(M_xM'_{3-x})(HITP)_2$ (Figure 2.42), confirm that the optical band gaps of the alloys can also be continuously tuned over 0.4 eV (cf. Moss−Burstein shift).[41,44] They narrow progressively from 0.662 eV for $(Co_{2.38}Ni_{0.62})(HITP)_2$ to 0.395 eV for $(Co_{0.60}Ni_{2.40})(HITP)_2$ in the CoNi series, from 0.762 eV for $(Co_{2.47}Cu_{0.53})(HITP)_2$ to 0.513 eV for $(Co_{0.52}Cu_{2.48})(HITP)_2$ in the CoCu series, and from 0.392 eV for $(Cu_{2.32}Ni_{0.68})(HITP)_2$ to 0.326 eV for $(Cu_{0.50}Ni_{2.50})(HITP)_2$ in the CuNi series (Figure 2.41c). Finally, DRIFTS analysis of $M_3(HITP)_2$ and $(M_xM'_{3-x})(HITP)_2$ showed the expected vibrational bands corresponding to HITP, but no features related to electronic transitions below the absorption edges. The influence of defects on optical properties is thus negligible.
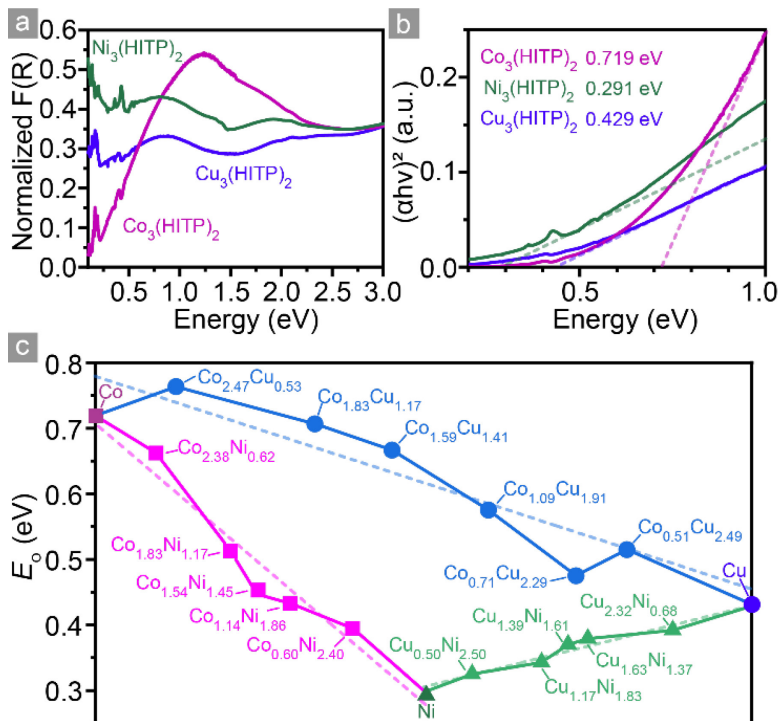
Figure 2.41. DR-UV-Vis and DRIFT spectra of $M_3(HITP)_2$ and $(M_xM'_{3-x})(HITP)_2$. (a) Normalized Kubelka–Munk-transformed spectra of $M_3(HITP)_2$. (b) Normalized Tauc plots from the spectra in (a). Dashed lines indicate best linear fits to the absorption edges. (c) Optical band gaps, E_o, of $(M_xM'_{3-x})(HITP)_2$. Solid lines are guides to the eye; dashed lines are linear fits of E_o.
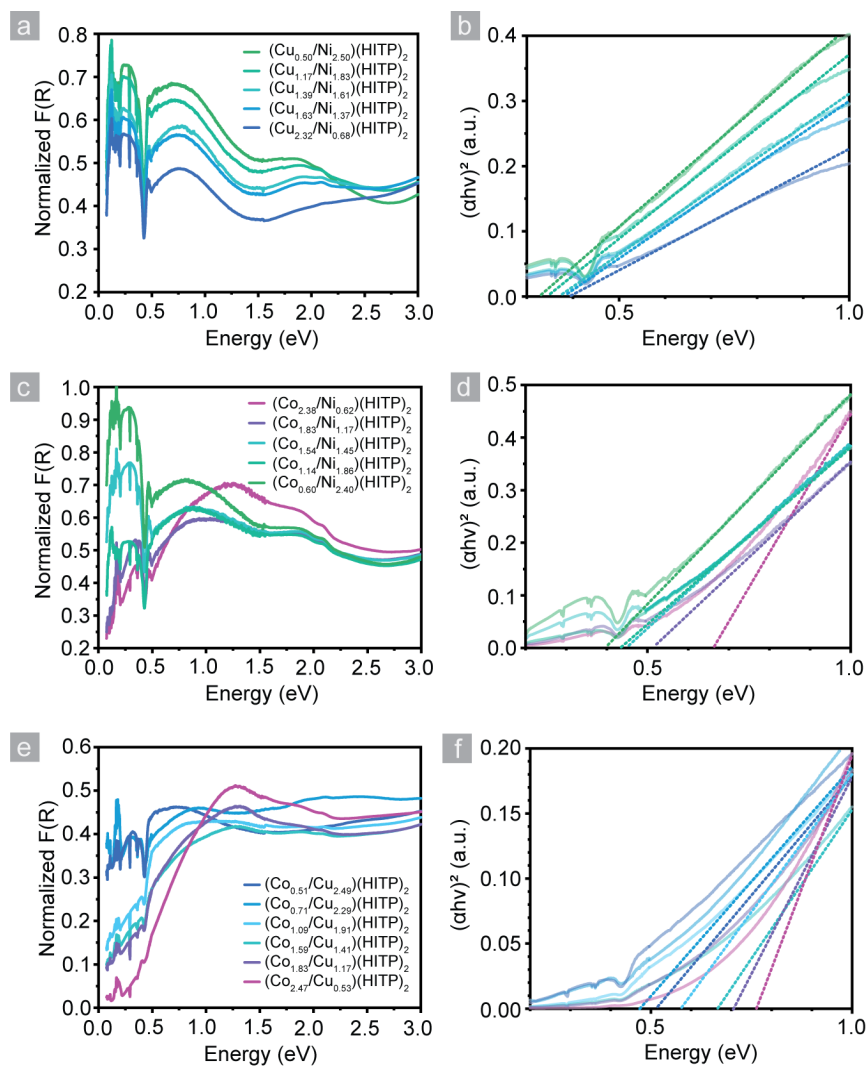
Figure 2.42. Diffuse reflectance spectra of (a) $(Cu_xNi_{3-x})(HITP)_2$ alloys, (c) $(Co_xNi_{3-x})(HITP)_2$ alloys, and (d) $(Co_xCu_{3-x})(HITP)_2$ alloys, and corresponding Tauc fits of optical band gaps (b, d, and f).

The smooth variation in electronic structures derived from optical spectroscopy is also reflected in electrical conductivity measurements for the phase-pure $M_3(HITP)_2$ and the $(M_xM'_{3-x})(HITP)_2$ alloys. Four-contact probe measurements of polycrystalline pellets of $M_3(HITP)_2$ revealed bulk conductivity values, σ, of 0.024 S cm^{-1}, 0.75 S cm^{-1}, and 55.4 S cm^{-1} for the pure Co, Cu, and Ni MOFs, respectively, at 296 K. These are higher than the bulk conductivities reported previously for the same compounds,[12,22] which were already among the most conductive MOFs. The metal ions exert an obvious influence on electrical conductivity, at least partially by contributing to different extents to the valence and conduction bands density of states. The electronic nature of the metal ion notwithstanding, we attribute the differences in σ to the slight structural variations among the three materials. In particular, the interlayer displacement, D, and stacking, S, exert an important effect on transport normal to the sheets. D appears to be optimal in $Ni_3(HITP)_2$ (D $\cong$ 1.7 Å in the optimized calculated structure[22]), which also shows the highest bulk

conductivity. With D deviating to 1.39(0) Å for $Co_3(HITP)_2$ and 0.86(9) Å for $Cu_3(HITP)_2$, these materials exhibit lower conductivities. Similarly, the higher σ of $Cu_3(HITP)_2$ relative to $Co_3(HITP)_2$ can be traced to its smaller interlayer spacing, 3.16(8) Å, compared to 3.29(8) Å for $Co_3(HITP)_2$.

In line with the spectroscopic and electrical data for the pure phases, the conductivity of $(M_xM'_{3-x})(HITP)_2$ alloys can be tuned precisely over 4 orders of magnitude from 5.8×10^{-3} S cm^{-1} in $(Co_{2.47}Cu_{0.53})(HITP)_2$ to 55.4 S cm^{-1} in $Ni_3(HITP)_2$ (Figure 2.43a, 2.44). Variations in electrical conductivity among the 16 different compositional alloys are in line with all of the discussions above and can be traced to combinations of systematic changes in optical band gaps, E_o, free carrier concentrations, and structural parameters S and D. For instance, increasing Ni content in the $(Co_xNi_{3-x})(HITP)_2$ series shifts the D and S values in such a way as to enhance interlayer π-π interactions, which in turn leads to higher σ. Apparent deviations from these trends, such as with $(Co_{2.47}Cu_{0.53})(HITP)_2$, are also in line with slightly lower crystallinity for that particular composition, itself likely a result of the relatively more pronounced structural mismatch between $Co_3(HITP)_2$ and $Cu_3(HITP)_2$ (Table 2.1, Figure 2.27).
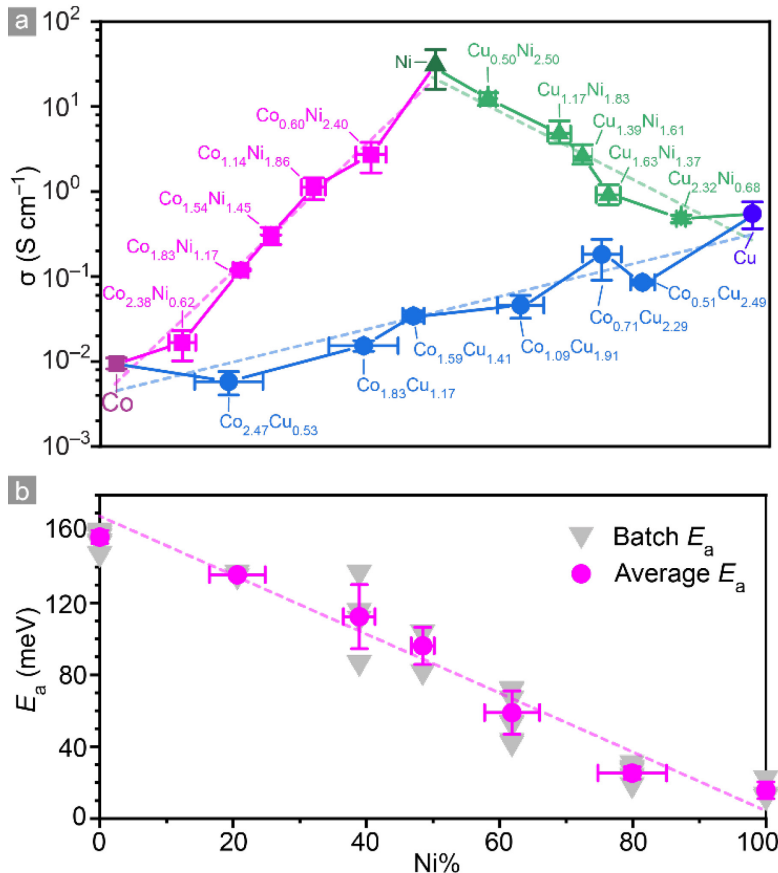
Figure 2.43. (a) Electrical conductivity data for $(M_xM'_{3-x})(HITP)_2$. Solid lines are guides to the eye; dashed lines are linear fits. (b) Continuous changes of E_a in $(Co_xNi_{3-x})(HITP)_2$. The dashed line is a linear fit with $R^2 = 0.98$.
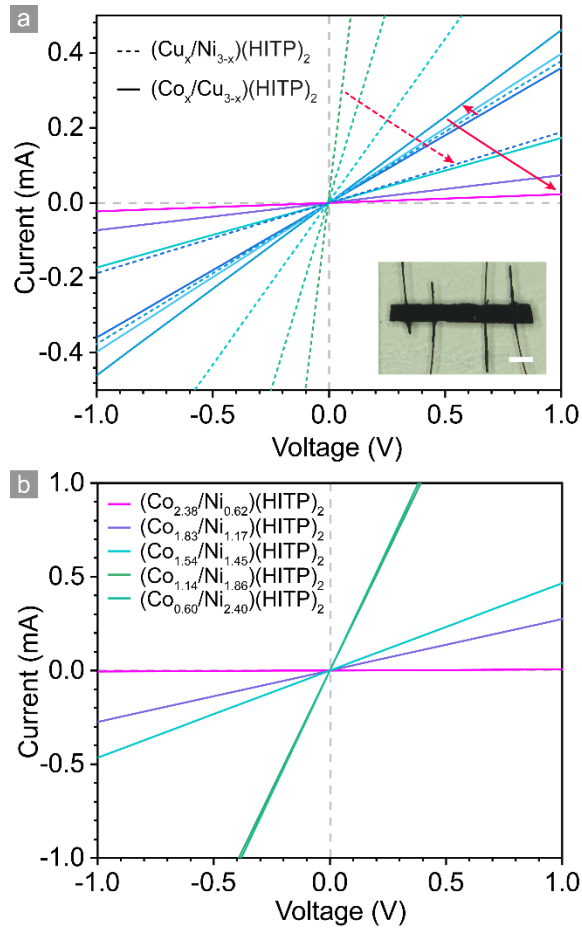
Figure 2.44. I-V curves of pressed pellets of $(M_xM'_{3-x})(HITP)_2$ alloys. (a) $(Cu_xNi_{3-x})(HITP)_2$ alloys (dotted lines) and $(Co_xCu_{3-x})(HITP)_2$ alloys (solid lines). Dotted arrows and solid arrows are guides of the eye, indicating the change of M' concentrations from high to low. Inset figure shows a typical device of 4-contact electrical conductivity measurement (scale bar: 1 mm). (b) $(Co_xNi_{3-x})(HITP)_2$ alloys.

Notably, control measurements of mechanically blended mixtures of phase-pure $M_3(HITP)_2$ samples behave differently than the alloyed phases, with the more abundant sample dominating transport in non-linear fashion. For instance, mixtures of $Co_3(HITP)_2$ and $Ni_3(HITP)_2$ are nearly as conductive as the former when the Ni% is low, and jump to a conductivity closer to that of the latter when the Ni% reaches 40%. Surprisingly, all blended $Co_3(HITP)_2:Cu_3(HITP)_2$ mixtures exhibit lower σ than $Co_3(HITP)_2$, likely a consequence of work function/energy level mismatch between individual particles of the two pure phases, which increases the grain boundary resistance (Figure 2.45, 2.46).

Variable-temperature (VT) conductivity measurements, performed for the pure phases and for $(Co_xNi_{3-x})(HITP)_2$ as a representative example of the alloyed samples, revealed temperature-activated bulk transport from 200 K to 350 K in all cases (Figure 2.47). The corresponding activation energies for transport, E_a, correlate well with the σ values: 157 meV for $Co_3(HITP)_2$, 65.3 meV for $Cu_3(HITP)_2$, and 15.7 meV for $Ni_3(HITP)_2$. E_a values for $(Co_xNi_{3-x})(HITP)_2$ alloys vary linearly with the Ni content (Figure

2.43b), decreasing from 136 meV for $(Co_{2.38}Ni_{0.62})(HITP)_2$ to 25.4 meV for $(Co_{0.60}Ni_{2.40})(HITP)_2$, providing a final confirmation of continuous compositional band engineering through metal substitution.
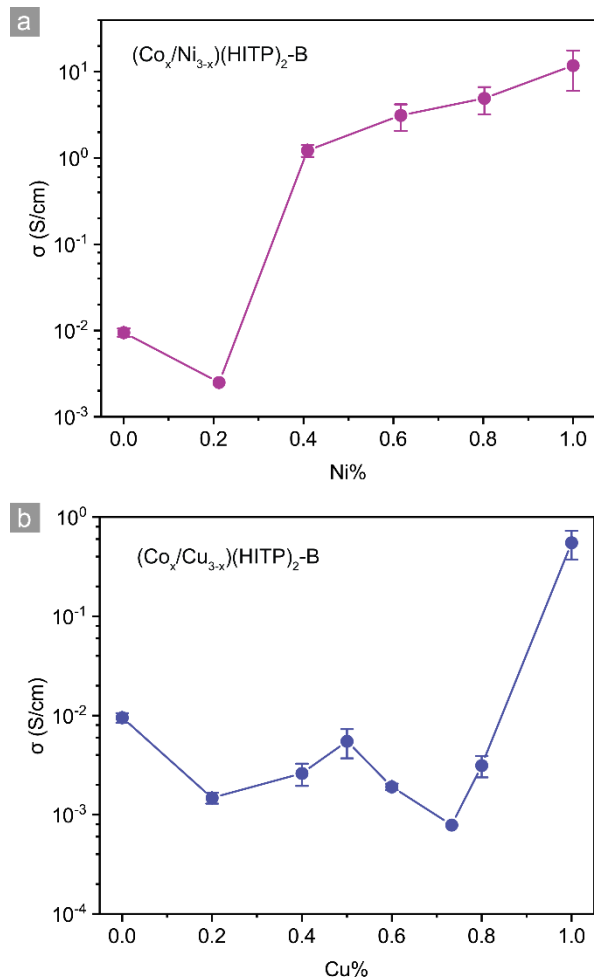
Figure 2.45. 4-Probe electrical conductivity of $(Co_xNi_{3-x})(HITP)_2$-Blend (a) and $(Co_xCu_{3-x})(HITP)_2$-Blend (b) produced by simple blending method described in 2.5.2. In contrast to $(Co_xNi_{3-x})(HITP)_2$ alloys and $(Co_xCu_{3-x})(HITP)_2$ alloys, no obvious trend of electrical conductivity was observed. For $(Co_xNi_{3-x})(HITP)_2$-Blend samples, the conductivity is dominated by $Co_3(HITP)_2$ when Ni% is low since $Co_3(HITP)_2$ is intrinsically less conductive. Whereas the conductivity is dominated by $Ni_3(HITP)_2$ when Ni% reaches 40%, which we assume is due to the formation of continuous pathways for carrier conduction by touching $Ni_3(HITP)_2$ grains. These results indicate that the variation of conductivity follows Percolation Theory[10] rather than continuously varying the energy level.
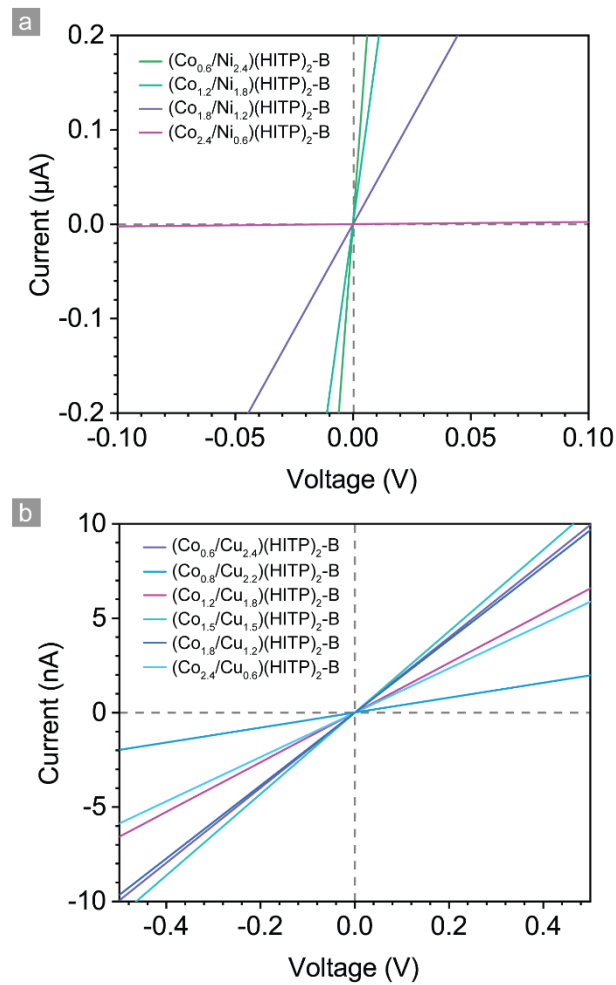
Figure 2.46. I-V curves of 4-Probe devices of $(Co_xNi_{3-x})(HITP)_2$-Blend (a) and $(Co_xCu_{3-x})(HITP)_2$-Blend (b) produced by simple blending method described above.
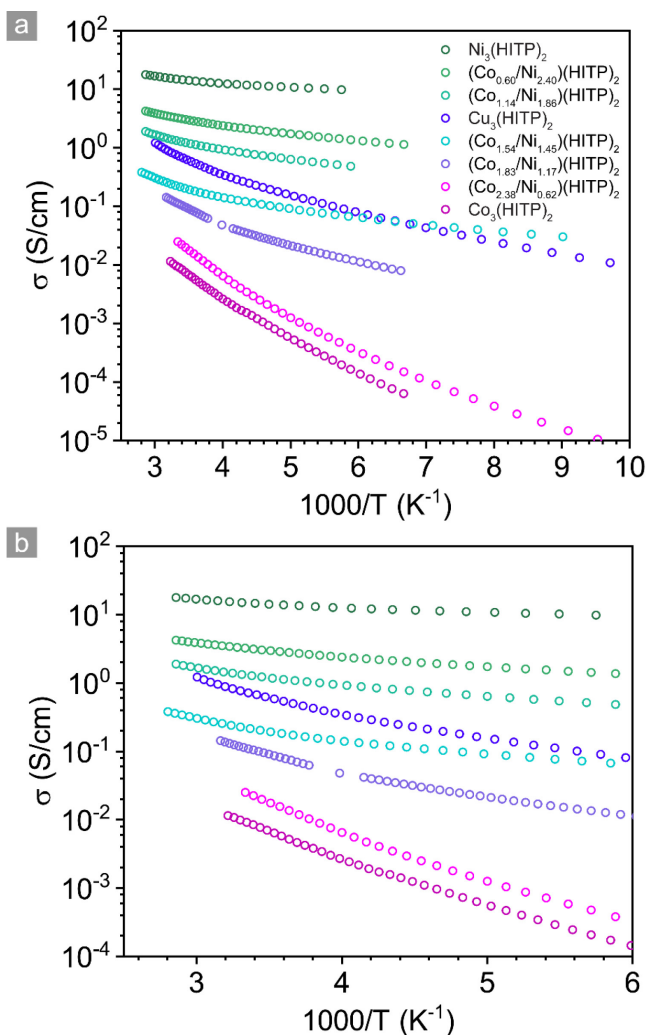
Figure 2.47. Temperature dependence of electrical conductivity of $M_3(HITP)_2$ (M = Co, Ni, Cu) and $(Co_xNi_{3-x})(HITP)_2$ alloys. Both large (a) and small (b) temperature ranges are shown. Good overlap of electrical conductivity of $M_3(HITP)_2$ (M = Co, Ni, Cu) and $(Co_xNi_{3-x})(HITP)_2$ alloys during cooling and heating were observed.

2.4 Conclusions

A considerable need exists for improved synthesis of conductive MOFs. Here, synthetic improvements in the production of phase-pure $M_3(HITP)_2$ (M = Co, Ni, Cu) led to more crystalline and porous materials with higher conductivity values than previously reported. These advances also enable a systematic investigation into the influence of the metal ion on physical properties in $(M_xM'_{3-x})(HITP)_2$ alloys, which allow continuous tuning of optical and electronic band gaps, and precise modulation of electrical conductivity over four orders of magnitude. These results highlight the importance of synthetic advances for a deeper understanding of structure-function relationships that are crucial for further material developments in this field.

2.5 Methods and Materials

2.5.1 Materials

Ni(OAc)$_2$·4H$_2$O (Strem), CuSO$_4$·5H$_2$O (Alfa Aesar), Co(NO$_3$)$_2$·6H$_2$O (Alfa Aesar), Ni(NO$_3$)$_2$·6H$_2$O (Strem), NiSO$_4$·6H$_2$O (Alfa Aesar), CuCl$_2$·2H$_2$O (Alfa Aesar), Co(OAc)$_2$·4H$_2$O (Alfa Aesar), and NaOAc (Alfa Aesar) were used without further purification. 2,3,6,7,10,11-hexaaminotriphenylene hexahydrochloride (HATP·6HCl), was prepared according to a published procedure. *N,N*-dimethylformamide (DMF), *N,N*-diethylformamide (DEF), *N,N*-dimethylacetamide (DMA), dimethyl sulfoxide (DMSO), and methanol were used as received without further purification.

2.5.2 Synthetic Methods

Ni$_3$(HITP)$_2$ rods

1.5 mL of the stock solution (9.31 mmol·L^{-1}, 1.5 eq.) of nickel(II) acetate tetrahydrate (Ni(OAc)$_2$·4H$_2$O) in DMSO was preheated at 65 °C, to which was added a solution of 5 mg (0.0093 mmol, 1 eq.) of HATP·6HCl in 1.5 mL of water. To this was added 2 mL of NaOAc aqueous solution (4 mol·L^{-1}), and this mixture was heated in a 20 mL open glass vial with stirring for 2 hours at 65 °C. The resulting black powder was filtered, washed with large amount of water and methanol, and dried under vacuum.

Alternative synthetic procedure which gives more crystalline material:

6 mL of the stock solution (2.33 mmol·L^{-1}, 1.5 eq.) of nickel(II) acetate tetrahydrate (Ni(OAc)$_2$·4H$_2$O) in DMF/DMA (v/v = 1:1) was preheated at 65 °C, to which was added 4 mL of NaOAc aqueous solution (2 mol·L^{-1}). To this was added a solution of 5 mg (0.0093 mmol, 1 eq.) of HATP·6HCl in 1.5 mL of water, and this mixture was heated in a 20 mL open glass vial while stirring for 2 hours at 65 °C. The resulting black powder was filtered, washed with large amount of water and methanol, and dried under vacuum.

Cu$_3$(HITP)$_2$ rods

3.5 mg (0.014 mmol, 1.5 eq.) of copper(II) sulfate pentahydrate (CuSO$_4$·5H$_2$O) was suspended in 1.5 mL of DMA and sonicated for 10 min. Then a solution of 5 mg (0.0093 mmol, 1 eq.) of HATP·6HCl in 1.5 mL of water was added and sonicated for 5 min. To this was added 2 mL of NaOAc aqueous solution (2 mol·L^{-1}) at room temperature, and this mixture was heated in a 20 mL open glass vial with stirring for 2 hours at 65 °C. The resulting black powder was filtered, washed with large amount of water and methanol, and dried under vacuum.

Co$_3$(HITP)$_2$ particles

1.5 mL of the stock solution (62.1 mmol·L^{-1}, 10 eq.) of cobalt(II) nitrate hexahydrate (Co(NO$_3$)$_2$·6H$_2$O) in DMF was preheated at 65 °C, to which was added a solution of 5 mg (0.0093 mmol, 1 eq.) of HATP·6HCl in 1.5 mL of water. To this was added 2 mL of NaOAc aqueous solution (2 mol·L^{-1}), and

this mixture was heated in a 20 mL open glass vial with stirring for 2 hours at 65 °C. The resulting black powder was filtered, washed with large amount of water and methanol, and dried under vacuum.

Alternative synthetic procedure which gives more crystalline material:

1.5 mL of the stock solution (62.1 mmol·L^{-1}, 10 eq.) of cobalt(II) nitrate hexahydrate (Co(NO$_3$)$_2$·6H$_2$O) in DMF was preheated at 65 °C, to which was added 2 mL of NaOAc aqueous solution (2 mol·L^{-1}). To this was added a solution of 5 mg (0.0093 mmol, 1 eq.) of HATP·6HCl in 1.5 mL of water, and this mixture was heated in a 20 mL open glass vial while stirring for 2 hours at 65 °C. The resulting black powder was filtered, washed with large amount of water and methanol, and dried under vacuum.

(Cu$_x$Ni$_{3-x}$)(HITP)$_2$ alloys

6 mL of the Cu/Ni mixed salts stock solution (CuSO$_4$·5H$_2$O and Ni(OAc)$_2$·4H$_2$O with 4:1, 3:2, 1:1, 2:3, and 1:4 mole ratios in DMF/DMA (v/v = 1/1); the total concentration of metal ions is 2.33 mmol·L^{-1}) was added to a 20 mL glass vial, to which was added 4 mL of NaOAc aqueous solution (2 mol·L^{-1}). To this was added a solution of 5 mg (0.0093 mmol, 1 eq.) of HATP·6HCl in 1.5 mL of water, and this mixture was heated in a 20 mL open glass vial with stirring for 2 hours at 65 °C. The resulting black powder was filtered, washed with large amount of water and methanol, and dried under vacuum.

(Co$_x$Ni$_{3-x}$)(HITP)$_2$ alloys

3 mL of the Co/Ni mixed salts stock solution (Co(NO$_3$)$_2$·6H$_2$O and Ni(OAc)$_2$·4H$_2$O with 4:1, 3:2, 1:1, 2:3, and 1:4 mole ratios in DMF; the total concentration of metal ions is 4.66 mmol·L^{-1}) was added to a 20 mL glass vial, to which 5 mg (0.0093 mmol, 1 eq.) of HATP·6HCl in 1.5 mL of water was added. To this was added 2 mL of NaOAc aqueous solution (2 mol·L^{-1}), and the mixture was heated at 65 °C with stirring for 2 hours. The resulting black powder was filtered, washed with large amount of water and methanol, and dried under vacuum.

(Co$_x$Cu$_{3-x}$)(HITP)$_2$ alloys

3 mL of the Co/Cu mixed salts stock solution was (Co(NO$_3$)$_2$·6H$_2$O and CuSO$_4$·5H$_2$O with 4:1, 3:2, 1:1, 2:3, 4:11, and 1:4 mole ratios in DMF; the total concentration of metal ions is 4.66 mmol·L^{-1}) was added to a 20 mL glass vial, to which 5 mg (0.0093 mmol, 1 eq.) added to a 20 mL glass vial, followed by the addition of 1 mL of DMA. The 5 mg (0.0093 mmol, 1 eq.) of HATP·6HCl in 1.5 mL of water was added to the vial, resulting in a deep blue solution. To this was added 2 mL of NaOAc aqueous solution (2 mol·L^{-1}), and the mixture was sonicated for 1 minute and then heated at 65 °C with stirring for 2 hours. The resulting black powder was filtered, washed with large amount of water and methanol, and dried under vacuum.

(Co$_x$/Ni$_{3-x}$)(HITP)$_2$-Blend

Using a pestle and mortar to blend the mixture of Co$_3$(HITP)$_2$ and Ni$_3$(HITP)$_2$ with 4:1, 3:2, 1:1, 2:3, and 1:4 mole ratios.

(Co$_x$/Cu$_{3-x}$)(HITP)$_2$-Blend

Using a pestle and mortar to blend the mixture of Co$_3$(HITP)$_2$ and Cu$_3$(HITP)$_2$ with 4:1, 3:2, 1:1, 2:3, 4:11, and 1:4 mole ratios.

2.5.3 Physical Characterization Methods

Laboratory powder X-ray diffraction (PXRD)

PXRD patterns were recorded using a Bruker Advance II diffractometer equipped with a $\theta/2\theta$ reflection geometry and Ni-filtered Cu Kα radiation (Kα_1 = 1.5406 Å, Kα_2 = 1.5444 Å, Kα_2/ Kα_1 = 0.5). The tube voltage and current were 40 kV and 40 mA, respectively. Samples for PXRD were prepared by placing a thin layer of the appropriate material on a zero-background silicon crystal plate.

High-resolution synchrotron PXRD

Data were collected at 100 K in beamline 11-BM at the Advanced Photon Source (APS), Argonne National Laboratory using the Debye-Scherrer geometry and an average wavelength of 0.457840 Å. Discrete detectors covering an angular range from –6 to 28° 2θ are scanned over a 34° 2θ range, with data points collected every 0.001° 2θ (actual 2θ/step is 0.0009984375°) and scan speed of 0.1 s/step. The 11-BM instrument uses X-ray optics with two platinum-striped mirrors and a double-crystal Si(111) monochromator, where the second crystal has an adjustable sagittal bend. Ion chambers monitor incident flux. A vertical Huber 480 goniometer, equipped with a Heidenhain encoder, positions an analyzer system comprised of twelve perfect Si(111) analyzers and twelve Oxford-Danfysik LaCl$_3$ scintillators, with a spacing of 2° 2θ. Analyzer orientation can be adjusted individually on two axes. A three-axis translation stage holds the sample mounting and allows it to be spun, typically at ~5400 RPM (90 Hz). A Mitsubishi robotic arm is used to mount and dismount samples on the diffractometer. Oxford Cryosystems Cryostream Plus device allows sample temperatures to be controlled over the range 80-500 K when the robot is used. The diffractometer is controlled via EPICS. Data are collected while continually scanning the diffractometer 2θ arm. A mixture of NIST standard reference materials, Si (SRM 640c) and Al$_2$O$_3$ (SRM 676) is used to calibrate the instrument, where the Si lattice constant determines the wavelength for each detector. Corrections are applied for detector sensitivity, 2θ offset, small differences in wavelength between detectors, and the source intensity, as noted by the ion chamber before merging the data into a single set of intensities evenly spaced in 2θ.

N$_2$ adsorption isotherms

Isotherms were measured by a volumetric method using a Micromeritics ASAP 2020 Plus gas sorption analyzer. An oven-dried sample tube equipped with a TranSeal^{TM} (Micromeritics) was evacuated and tared. The sample was transferred to the sample tube, which was then capped with a TranSeal^{TM}. The sample was activated at 90 °C under high dynamic vacuum ($< 10^{-4}$ mbar) for 24 hours before analysis. The N$_2$

isotherm was measured using a liquid nitrogen bath at 77 K. Ultrahigh purity grade (99.999% purity) N_2, oil-free valves and gas regulators were used for all the free space correction and measurements. Fits to the Brunauer-Emmett-Teller (BET) equation satisfied the published consistency criteria.

Thermogravimetric analysis (TGA)

TGA was performed on a TA Instruments Q500 Thermogravimetric Analyzer at a heating rate of 2.0 °C/min under air gas flow of 5 mL/min on a platinum pan from room temperature to 600 °C.

Elemental analyses

Elemental analyses were performed by Robertson Microlit Laboratories, Ledgewood, New Jersey.

X-ray photoelectron spectroscopy (XPS)

XPS measurements were performed at the MIT MRSEC (formerly the Center for Materials Science and Engineering, or CMSE) using a Physical Electronics PHI Versaprobe II X-ray photoelectron spectrometer equipped with an Al anode source. Powder samples were pressed on copper tapes with full coverage. Charge shift was calibrated by setting surface adventitious carbon C1s peak to 284.8 eV. Regarding the metal composition determinations by XPS, the binary mixtures of cobalt phthalocyanine (CoPc), nickel phthalocyanine (NiPc), and cupper phthalocyanine (CuPc) were used as standards to calibrate the RSF values of each element, as suggested by CasaXPS Manual. The mixtures of MPc were made by thoroughly blending MPc powders using a pestle and mortar.

Inductively coupled plasma mass spectrometry (ICP-MS)

ICP-MS was performed to quantify the metal composition of $(M_xM'_{3-x})(HITP)_2$ alloys (MM' = CoCu, CuNi, and CoNi) using Agilent 7900 inductively coupled plasma mass spectrometer. ~5 mg sample was weighed and digested using concentrated nitric acid (67~70% w/v %, BDH Aristar) by a Milestone UltraWave microwave digester. Metal concentrations of the resulting solution were determined using calibration curves constructed from standard solutions (ICP-MS certified reference standards, VWR).

Scanning electron microscopy (SEM)

SEM images were conducted at MIT MRSEC (formerly the Center for Materials Science and Engineering, or CMSE) on a Zeiss Merlin high-resolution scanning electron microscope with an InLens detector at an operating voltage of 3 or 4 kV.

High Resolution Transmission Electron Microscopy (HRTEM)

HRTEM images were obtained with a spherical aberration corrected FEI Titan 80-300, operated at an accelerating voltage of 300 kV equipped with a Gatan K2 in-situ direct electron detector (at the Center for Functional Nanomaterials (CFN), Brookhaven National Laboratory (BNL)). Samples were drop-cast onto Cu TEM grids from powder dispersed in methanol. The dose rate used was 5.3 $e^-/Å^2/s$ for high-magnification (115 kx) images, with an image exposure of time of 5 s (~26.5 $e^-/Å^2$ cumulative dose per image). The dose rate was not directly measured for low magnification images, but the dose rate was orders

magnitude lower for those images than for the high magnification images with 1 s exposure time. All image acquisition was done using DigitalMicrograph software. TEM grids of 3 samples ($Co_3(HITP)_2$ flakes, $Ni_3(HITP)_2$ rods, and $Cu_3(HITP)_2$ rods) were prepared by drop-casting 0.5 mL of the respective sample suspensions onto [Cu-mesh] lacey-C substrate grids. The suspension of samples were prepared by sonicating ~1 mg of powder sample in ~5 mL of isopropanol for 30 s. The droplets of sample were allowed to sit on the grids in ambient conditions for ~20–30 s, and were then wicked dry with filter paper.

High-angle Annular Dark-Field Scanning Transmission Electron Microscopy (HAADF-STEM)

HAADF-STEM images and energy dispersive spectroscopy elemental mapping were collected at the MIT MRSEC (formerly the Center for Materials Science and Engineering, or CMSE) on a JEOL 2010 FEG Analytical Electron Microscope with a spot size of 1 nm^2.

Energy dispersive X-ray spectroscopy (EDS)

EDS analyses were performed under HAADF-STEM mode. Every sample was measured twice in different randomly chosen areas.

X-ray absorption spectroscopy (XAS)

XAS measurements were conducted at the Co (7.709 keV), Ni (8.333 keV), and Cu (8.979 keV) K-edges in the fluorescence mode at the Inner-Shell Spectroscopy Beamline, 8-ID, of the Brookhaven National Laboratory NSLS-II synchrotron. The intensity of the incident beam I_0 and the beam transmitted through the sample and the reference (I_t and I_r, respectively) were monitored by ionization chambers. For ex-situ samples with higher metal concentration (5 wt.% or more) material was diluted with polyethylene glycol and pressed into a 1.3 cm pellet to give optimal data quality (high signal to noise ratio). Each scan took 30-60 s to obtain high quality data. All data were collected at room temperature and spectra were closely monitored for radiation damage. For reference, the locations of the white line and X-ray absorption near-edge spectroscopy (XANES) energy (inflection point of the leading edge) are noted for representative spectra at each edge. The XANES measurements of the compounds provide critical information about the oxidation states of the metal centers.

Diffuse reflectance infrared Fourier transform spectroscopy (DRIFTS)

DRIFTS measurements were performed on a Bruker Tensor 37 (MIR source and KBr beam splitter) with a mercury cadmium telluride (MCT, cooled with liquid nitrogen) detector utilizing the DiffusIR™ accessory (Pike Technologies). To ensure air-free measurement a sealable environmental chamber equipped with ZnSe window (Pike Technologies) was used. Samples were ground in air with dry potassium bromide in a mortar and pestle (99.9%, Pike technologies) to produce 0.5-1 wt.% MOF mixtures. The data was averaged over 32 scans between 4000 – 600 cm^{-1} with the resolution of 4 cm^{-1}. Each of the Kubelka-Munk function transformed DRIFTS spectra were normalized with respect to the DRUV–vis–

NIR data by matching the DRIFTS value of F(R) at 4000 cm^{-1} with the DRUV–vis–NIR value of F(R) of the same sample at 4000 cm^{-1}.

Diffuse reflectance UV-vis-NIR spectra (DRUV–Vis–NIR)

DRUV-Vis-NIR spectra between 200 and 2500 nm were collected on a Cary 5000i spectrophotometer, fitted with the UV-Vis DiffusIR accessory (Pike Technologies), at the scan rate of 200 nm/min under ambient conditions. A KBr baseline and a zero-background correction were collected prior to the sample measurements. Samples were prepared as described above for the DRIFTS measurements. For the Tauc plots and the determination of the optical bandgaps, the UV-vis-NIR spectra were stitched manually with the DRIFTS spectra obtained for the same samples.

Room temperature (RT) electrical conductivity measurements

RT electrical conductivity measurements were carried out at 296 K in ambient atmosphere on pressed pellets using a 4-probe probe setup. Pressed pellets of MOF samples were made by adding MOF powders into a 6 mm inner-diameter trapezoidal split sleeve pressing die (Across International) and pressing the die set by a hydraulic pump (MTI corporation) for 5 min. The applied pressure was approximately 1 GPa. The pellet thicknesses were measured after the measurement using a micrometer (Mitutoyo). The resulting pellet was cut into a cuboid by a blade and placed onto a piece of dry glass slide with thermally conductive and electrically insulating grease (DuPont Krytox). Four parallel copper wire contacts were attached to the cuboid by carbon paste. The other end of the gold wire was pasted onto the glass slide by carbon paste. The device is shown in Figure 2.44. The device was mounted onto the sample chuck of a probe station (Janis Cryogenics ST-500) equipped with four micro-manipulators that allowed us to control the position of the probes with a resolution of 5 μm. The temperature of the device was balanced by the heater of the probe station chuck and the environment was controlled at 296 K by a temperature controller (Scientific Instrument model 9700). Electrical contacts were made by gently pressing gold-plated tungsten probes (Janis 7B-100G) into the carbon paste that was on the glass slide. Probes were connected to a sourcemeter (Keithley model 2450) through triax cables (Keithley model 7078-TRX-10). The chamber of the probe station was covered by a stainless-steel lid. This lid had a quartz window in the center, which was covered by a black plastic cover to keep the device in the dark. Linear I–V curves were obtained by supplying the current and measuring the voltage. The current was duel-swept through the outer two probes, while voltage was measured through the inner two probes. The specific lengths of the conduction channel were measured by a Leica S6 E stereoscopic microscope and calibrated by an external ruler of known distances. At least three pellets from four separate batches of each sample were measured. For each sample, the conductivity values were averaged to give the average conductivity value and a standard error which was used for the error estimation on the average conductivity value for each sample.

Variable temperature electrical conductivity

Data were collected from 150 to 350 K or 400 K using a Quantum Design PPMS DynaCool equipped with the Electrical Transport Option. A four-contact probe cell was manufactured for the measurements using the same preparation method as described in room temperature electrical conductivity measurements. The copper wires were soldered to the copper current collector of the sample puck. For each sample, the measurement procedure consisted of two cycles of heating and cooling. The temperature was first varied from 300 K to 350 K or 400 K at 5 K/min, measuring the resistance in AC mode every 1 K. Then the temperature was varied from 350 K or 400 K to 150 K at 5 K/min, measuring the resistance in AC mode every 1 K. The measurement was repeated. The phase remained within 1° for the temperature range presented in the manuscript. The activation energy E_a was calculated using the equation $ln\sigma = ln\sigma_0 - \frac{E_a}{k_B T}$, where E_a was extracted from the linear least squares fit of $ln\sigma$ vs. 1/T.

Optical microscopy (OM)

OM images were obtained by Leica S6 E stereoscopic microscope.

Electron paramagnetic resonance spectroscopy (EPR)

EPR measurements were performed on activated samples packed under nitrogen in septum-sealed quartz tubes using a Bruker EMX spectrometer equipped with an ER 4199HS cavity and Gunn diode microwave source at ~5 K, with a microwave frequency of 9.37 GHz, power of 0.100 mW, and attenuation of 33.0 dB. The measurements were taken in perpendicular mode. Simulations of EPR were performed with the EasySpin package4 in Matlab (R2018b). For $Co_3(HITP)_2$ and $Cu_3(HITP)_2$, pure MOF powder samples were used, while for $Ni_3(HITP)_2$, MOF powder was ground with KBr in a mortar and pestle to give a 5 wt.% dilution mixture.

2.6 References

(1) Sun, L.; Campbell, M. G.; Dincă, M. Electrically Conductive Porous Metal–Organic Frameworks. *Angew. Chem., Int. Ed.* **2016**, *55*, 3566–3579.

(2) Xie, L. S.; Skorupskii, G.; Dincă, M. Electrically Conductive Metal–Organic Frameworks. *Chem. Rev.* **2020**, *120*, in press.

(3) Sheberla, D.; Bachman, J. C.; Elias, J. S.; Sun, C.-J.; Shao-Horn, Y.; Dincă, M. Conductive MOF Electrodes for Stable Supercapacitors with High Areal Capacitance. *Nat. Mater.* **2017**, *16*, 220–224.

(4) Park, J.; Lee, M.; Feng, D.; Huang, Z.; Hinckley, A. C.; Yakovenko, A.; Zou, X.; Cui, Y.; Bao, Z. Stabilization of Hexaaminobenzene in a 2D Conductive Metal-Organic Framework for High Power Sodium Storage. *J. Am. Chem. Soc.* **2018**, *140*, 10315–10323.

(5) Feng, D.; Lei, T.; Lukatskaya, M. R.; Park, J.; Huang, Z.; Lee, M.; Shaw, L.; Chen, S.; Yakovenko, A. A.; Kulkarni, A.; Xiao, J.; Fredrickson, K.; Tok, J. B.; Zou, X.; Cui, Y.; Bao, Z. Robust and Conductive Two-Dimensional Metal-Organic Frameworks with Exceptionally High Volumetric and Areal Capacitance. *Nat. Energy* **2018**, *3*, 30–36.

(6) Shinde, S. S.; Lee, C. H.; Jung, J.-Y.; Wagh, N. K.; Kim, S.-H.; Kim, D.-H.; Lin, C.; Lee, S. U.; Lee, J.-H. Unveiling Dual-Linkage 3D Hexaiminobenzene Metal-Organic Frameworks towards Long-Lasting Advanced Reversible Zn-Air Batteries. *Energy Environ. Sci.* **2019**, *12*, 727–738.

(7) Clough, A. J.; Yoo, J. W.; Mecklenburg, M. H.; Marinescu, S. C. Two-Dimensional Metal–Organic Surfaces for Efficient Hydrogen Evolution from Water. *J. Am. Chem. Soc.* **2015**, *137*, 118–121.

(8) Miner, E. M.; Fukushima, T.; Sheberla, D.; Sun, L.; Surendranath, Y.; Dincă, M. Electrochemical Oxygen Reduction Catalysed by Ni_3(Hexaiminotriphenylene)$_2$. *Nat. Commun.* **2016**, *7*, 10942.

(9) Dong, R.; Zheng, Z.; Tranca, D. C.; Zhang, J.; Chandrasekhar, N.; Liu, S.; Zhuang, X.; Seifert, G.; Feng, X. Immobilizing Molecular Metal Dithiolene–Diamine Complexes on 2D Metal–Organic Frameworks for Electrocatalytic H_2 Production. *Chem. Eur. J.* **2017**, *23*, 2255–2260.

(10) Downes, C. A.; Clough, A. J.; Chen, K.; Yoo, J. W.; Marinescu, S. C. Evaluation of the H_2 Evolving Activity of Benzenehexathiolate Coordination Frameworks and the Effect of Film Thickness on H_2 Production. *ACS Appl. Mater. Interfaces* **2018**, *10*, 1719–1727.

(11) Miner, E. M.; Wang, L.; Dincă, M. Modular O_2 Electroreduction Activity in Triphenylene-Based Metal-Organic Frameworks. *Chem. Sci.* **2018**, *9*, 6286–6291.

(12) Campbell, M. G.; Sheberla, D.; Liu, S. F.; Swager, T. M.; Dincă, M. Cu_3(Hexaiminotriphenylene)$_2$: An Electrically Conductive 2D Metal-Organic Framework for Chemiresistive Sensing. *Angew. Chem., Int. Ed.* **2015**, *54*, 4349–4352.

(13) Campbell, M. G.; Liu, S. F.; Swager, T. M.; Dincă, M. Chemiresistive Sensor Arrays from Conductive 2D Metal-Organic Frameworks. *J. Am. Chem. Soc.* **2015**, *137*, 13780–13783.

(14) Smith, M. K.; Mirica, K. A. Self-Organized Frameworks on Textiles (SOFT): Conductive Fabrics for Simultaneous Sensing, Capture, and Filtration of Gases. *J. Am. Chem. Soc.* **2017**, *139*, 16759–16767.

(15) Rubio-Gimenez, V.; Almora-Barrios, N.; Escorcia-Ariza, G.; Galbiati, M.; Sessolo, M.; Tatay, S.; Marti-Gastaldo, C. Origin of the Chemiresistive Response of Ultrathin Films of Conductive Metal-Organic Frameworks. *Angew. Chem., Int. Ed.* **2018**, *57*, 15086–15090.

(16) Meng, Z.; Aykanat, A.; Mirica, K. A. Welding Metallophthalocyanines into Bimetallic Molecular Meshes for Ultrasensitive, Low-Power Chemiresistive Detection of Gases. *J. Am. Chem. Soc.* **2019**, *141*, 2046–2053.

(17) Aubrey, M. L.; Kapelewski, M. T.; Melville, J. F.; Oktawiec, J.; Presti, D.; Gagliardi, L.; Long, J. R. Chemiresistive Detection of Gaseous Hydrocarbons and Interrogation of Charge Transport in Cu[Ni(2,3-Pyrazinedithiolate)$_2$] by Gas Adsorption. *J. Am. Chem. Soc.* **2019**, *141*, 5005–5013.

(18) Sun, L.; Liao, B.; Sheberla, D.; Kraemer, D.; Zhou, J.; Stach, E.A.; Zakharov, D.; Stavila, V.; Talin, A. A.; Ge, Y.; Allendorf, M. D.; Chen, G.; Léonard, F.; Dincă, M. A microporous and naturally nanostructured thermoelectric metal-organic framework with ultralow thermal conductivity. *Joule* **2017**, *1*, 168-177.

(19) Erickson, K. J.; Léonard, F.; Stavila, V.; Foster, M. E.; Spataru, C. D.; Jones, R. E.; Foley, B. M.; Hopkins, P. E.; Allendorf, M. D.; Talin, A. A. Thin Film Thermoelectric Metal–Organic Framework with High Seebeck Coefficient and Low Thermal Conductivity. *Adv. Mater.* **2015**, *27*, 3453-3459.

(20) Xie, L. S.; Sun, L.; Wan, R.; Park, S. S.; DeGayner, J. A.; Hendon, C. H.; Dincă, M. Tunable Mixed-Valence Doping Toward Record Electrical Conductivity in a Three-Dimensional Metal–Organic Framework. *J. Am. Chem. Soc.* **2018**, *140*, 7411-7414.

(21) Talin, A. A.; Centrone, A.; Ford, A. C.; Foster, M. E.; Stavila, V.; Haney, P.; Kinney, R. A.; Szalai, V.; El Gabaly, F.; Yoon, H. P.; Léonard, F.; Allendorf, M. D. Tunable Electrical Conductivity in Metal-Organic Framework Thin-Film Devices. *Science* **2014**, *343*, 66–69.

(22) Sheberla, D.; Sun, L.; Blood-Forsythe, M. A.; Er, S.; Wade, C. R.; Brozek, C. K.; Aspuru-Guzik, A.; Dincă, M. High Electrical Condutivity in Ni$_3$(2,3,6,7,10,11-Hexaiminotriphenylene)$_2$, a Semiconducting Metal–Organic Graphene Analogue. *J. Am. Chem. Soc.* **2014**, *136*, 8859–8862.

(23) Van Vleet, M. J.; Weng, T.; Li, X.; Schmidt, J. R. In Situ, Time-Resolved, and Mechanistic Studies of Metal–Organic Framework Nucleation and Growth. *Chem. Rev.* **2018**, *118*, 3681-3721.

(24) Marcus, Y. The Effectivity of Solvents as Electron Pair Donors. *J. Sol. Chem.* **1984**, *13*, 599-624.

(25) Skorupskii, G.; Trump, B. A.; Kasel, T. W.; Brown, C. M.; Hendon, C. H.; Dincă, M. Efficient and Tunable One-Dimensional Charge Transport in Layered Lanthanide Metal–Organic Frameworks. *Nat. Chem.* **2020**, *12*, 131-136.

(26) Denton, A. R.; Ashcroft, N. W. Vegard's Law. *Phys. Rev. A* **1991**, *43*, 3161-3164.

(27) McIntyre, N. S.; Cook, M. G. X-ray Photoelectron Studies on Some Oxides and Hydroxides of Cobalt, Nickel, and Copper. *Anal. Chem.* **1975**, *47*, 2208-2213.

(28) Moretti, G. Auger Parameter and Wagner Plot in the Characterization of Chemical States by X-ray Photoelectron Spectroscopy: A Review. *J. Electron Spectrosc.* **1998**, *95*, 95-144.

(29) Matienzo, J.; Yin, L. I.; Grim, S. O.; Swartz Jr, W. E. X-ray Photoelectron Spectroscopy of Nickel Compounds. *Inorg. Chem.* **1973**, *12*, 2762-2769.

(30) Frost, D. C.; Ishitani, A.; McDowell, C. A. X-ray Photoelectron Spectroscopy of Copper Compounds. *Mol. Phys.* **1972**, *24*, 861-877.

(31) Yin, L.; Adler, I.; Tsang, T.; Matienzo, L. J.; Grim, S. O. Paramagnetism and Shake-up Satellites in X-ray Photoelectron Spectra. *Chem. Phys. Lett.* **1974**, *24*, 81-84.

(32) Tan, K. L.; Tan, B. T. G.; Kang, E. T.; Neoh, K. G. X-ray Photoelectron Spectroscopy Studies of the Chemical Structure of Polyaniline. *Phys. Rev. B* **1989**, *39*, 8070-8073.

(33) Mohtasebi, A.; Chowdhury, T.; Hsu, L. H.; Biesinger, M. C.; Kruse, P. Interfacial Charge Transfer Between Phenyl-capped Aniline Tetramer Films and Iron Oxide Surfaces. *J. Phys. Chem. C* **2016**, *120*, 29248-29263.

(34) Bair, R. A.; Goddard III, W. A. *Ab initio* Studies of the X-ray Absorption Edge in Copper Complexes. I. Atomic Cu^{2+} and $Cu(II)Cl_2$. *Phys. Rev. B* **1980**, *22*, 2767-2776.

(35) Sano, M.; Komorita, S.; Yamatera, H. XANES Spectra of Copper (II) Complexes: Correlation of the Intensity of the 1s → 3d Transition and the Shape of the Complex. *Inorg. Chem.* **1992**, *31*, 459-463.

(36) Chaboy, J.; Muñoz-Páez, A.; Carrera, F.; Merkling, P.; Marcos, E. S. *Ab initio* X-ray Absorption Study of Copper K-edge XANES Spectra in Cu(II) Compounds. *Phys. Rev. B* **2005**, *71*, 134208.

(37) Peng, S.-M.; Chen, C.-T.; Liaw, D.-S.; Chen, C.-I.; Wang, Y. Establishment of the Bond Patterns of *o*-Benzoquinonediimine and Semi-*o*-Benzoquinonediimine: Crystal Structures of Metal Complexes, $[Fe^{II}(bqdi)_3](PF_6)_2, [Co^{II}(s-bqdi)_2]$ and $[Co^{III}Cl(s-bqdi)_2)]$. *Inorg. Chim. Acta* **1985**, *101*, L31-L33.

(38) Jiménez, H. R.; Salgado, J.; Moratal, J. M.; Morgenstern-Badarau, I. EPR and Magnetic Susceptibility Studies of Cobalt (II)-and Nickel (II)-substituted Azurins from Pseudomonas Aeruginosa. Electronic Structure of the Active Sites. *Inorg. Chem.* **1996**, *35*, 2737-2741.

(39) Garribba, E.; Micera, G. The Determination of the Geometry of Cu (II) Complexes: An EPR Spectroscopy Experiment. *J. Chem. Educ.* **2006**, *83*, 1229-1232.

(40) Amalric Popescu, D.; Herrmann, J.-M.; Ensuque, A.; Bozon-Verduraz, F. Nanosized Tin Dioxide: Spectroscopic (UV-Vis, NIR, EPR) and Electrical Conductivity Studies. *Phys. Chem. Chem. Phys.* **2001**, *3*, 2522-2530.

(41) Chu, J.; Sher, A. Physics and Properties of Narrow Gap Semiconductors. New York: Springer, **2008**.

(42) Nowak, M.; Kauch, B.; Szperlich, P. Determination of Energy Band Gap of Nanocrystalline SbSI Using Diffuse Reflectance Spectroscopy. *Rev. Sci. Instrum.* **2009**, *80*, 046107.

(43) Gibbs, Z. M.; LaLonde, A.; Snyder, G. J. Optical Band Gap and the Burstein-Moss Effect in Iodine Doped PbTe Using Diffuse Reflectance Infrared Fourier Transform Spectroscopy. *New J. Phys.* **2013**, *15*, 075020.

(44) Kudman, I.; Seidel, T. Absorption Edge in Degenerate p–Type GaAs. *J. Appl. Phys.* **1962**, *33*, 771-773.

Chapter 3. Dimensionality Modulates Electrical Conductivity in Compositionally Constant One-, Two-, and Three-Dimensional Frameworks

3.1 Abstract

Electrically conductive porous metal-organic frameworks (MOFs) and non-porous conjugated coordination polymers (CCPs) have attracted considerable interest, as they have exhibited great potential in various applications such as supercapacitors and electrocatalysis. However, a considerable need exists for improving the understanding of the relationship between compositional, structural characteristics, and charge transport. In Chapter 2, we have presented the study of composition-properties relationship of a class of isostructural 2D layered conductive MOFs. In this chapter, we reveal the construction of compositionally constant Ni-based metal-organic frameworks (MOFs) and conjugated coordination polymers (CCPs) with different structural dimensionality, including closely π-stacked 1D chains (**Ni-1D**), aggregated 2D layers (**Ni-2D**), and a 3D framework (**Ni-3D**), based on 2,3,5,6-tetraamino-1,4-hydroquinone (TAHQ) and its various oxidized forms. These materials have the same metal-ligand composition, but exhibit distinct electronic properties caused by different dimensionality and supramolecular interactions between SBUs, ligands, and structural motifs. The electrical conductivities of these materials span nearly 8 orders of magnitude, approaching 0.3 S/cm, which benefitted from the better energy level matching of organic linker to metal ions and strong donor-acceptor (D-A) π-π stacking due to the electron deficient character.

3.2 Introduction

Interest in electrically conducting metal-organic frameworks (MOFs)[1,2] and non-porous conjugated coordination polymers (CCPs)[3] is growing, not least because they have shown potential applications as active materials for supercapacitors,[4–6] batteries,[7,8] electrocatalysis,[9–11] chemiresistive sensors,[12–14] and thermoelectrics,[15,16] among others. Electrical conductivities that span more than 10 orders of magnitude have been reported for these materials, but systematic advances in understanding structure-function relationships in this class are rare, even when similar building blocks are employed. For instance, use of the common hexahydroxytriphenylene (HHTP) or hexaiminotriphenylene (HITP) ligands leads to some of the highest electrical conductivities (> 100 S/cm),[17,18] but also very low conductivities (< 10^{-7} S/cm).[19] Evidently, these vast differences are related to both structure and composition. Whereas identical structures with different compositions naturally give rise to different electrical properties,[11,20,21] probing the opposite: how electrical properties change when composition is constant, but the structure changes, has not been possible thus far.

Here, we employ 2,3,5,6-tetraamino-1,4-hydroquinone (TAHQ) and its various oxidized forms to isolate three distinct porous and non-porous Ni-based frameworks that share the same 1:1 metal: ligand ratio, but exhibit structures with one-, two-, and three-dimensional connectivities. Their electrical conductivities span nearly 8 orders of magnitude, reaching 0.3 S/cm.

3.3 Results and Discussion

3.3.1 Ligand Choice

Several features of TAHQ are attractive from a coordination standpoint. In its most reduced form, TAHQ is essentially a hydroquinone with two 1,2-phenylenediamine moieties on either side of the phenol groups. Electron-rich TAHQ readily oxidizes to produce the quinone form tetraaminobenzoquinone (TABQ, Figure 3.1a; see 3.5.2 for synthetic details). Whereas both phenol and amino groups can engage in metal coordination in TAHQ, the significantly reduced electron density of the quinone groups makes them poor ligands, and TABQ typically coordinates metals only through its amino groups (Figure 3.1b). Electrostatic potential (ESP) surfaces of the two redox partners (Figure 3.1a) highlight additional distinguishing features that arise in TABQ upon oxidation: a significantly reduced HOMO-LUMO gap level relative to TAHQ, and a reduced electron density on the quinone carbons. These establish donor-acceptor (D-A) interactions that could further influence framework structure, as is the case in molecular TABQ crystals (Figure 3.2).[22] Indeed, D-A alignment is often used to tailor the solid state packing of conducting polymer chains, where it also functions to lower the band gap and promote charge transport.[23]
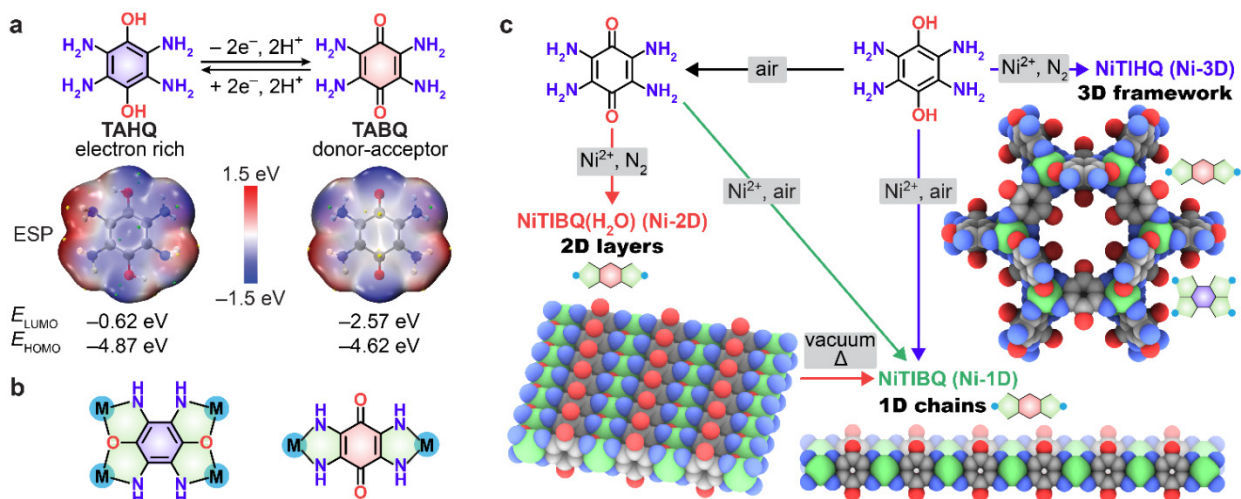
Figure 3.1. Ligand choice and synthetic conditions of Ni-based frameworks. (a) Chemical structures of TAHQ and TABQ with electrostatic potential (ESP) surfaces and HOMO and LUMO energies (at B3LYP/def2-QZVP level). (b) Different connectivities of TAHQ (left) and TABQ (right) towards metals. (c) Schematic illustration of the synthetic details and transformation of **Ni-1D**, **Ni-2D**, and **Ni-3D**.
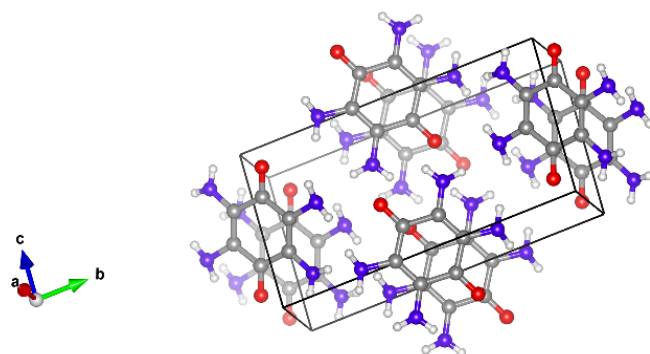
Figure 3.2. The solid-state packing of TABQ molecules shows the intermolecular D-A interaction, where electron-rich O atoms have close contact with electron-deficient carbonyl C atoms.
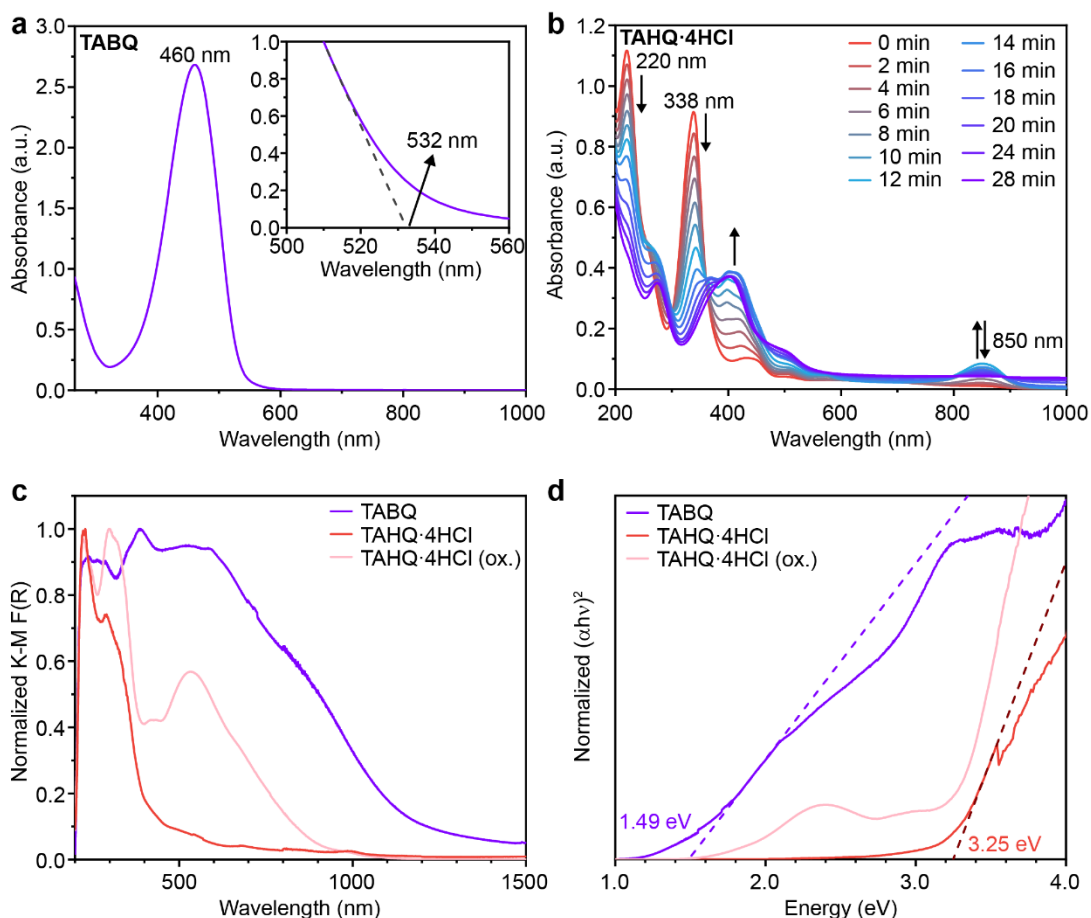
Figure 3.3 UV-Vis spectra of ligands. (a) UV-Vis spectrum of TABQ in dilute DMF solution, showing an intense absorption peak at 460 nm with an absorption tail at 532 nm. (b) Evolution of UV-Vis spectra of TAHQ·4HCl in dilute MeOH solution upon air exposure. Arrows represent the growing or diminishing of absorption bands. (c) Normalized DRUV-Vis spectra of TABQ, TAHQ·4HCl, and partially oxidized TAHQ·4HCl (TAHQ·4HCl (ox.)). The spectrum of TAHQ·4HCl shows an intense absorption at 291 nm and an absorption shoulder at 327 nm, which are assigned to the $\pi{\rightarrow}\pi^*$ absorption of TAHQ aromatic core. TABQ shows intense NIR absorptions. (d) DRUV-Vis spectra of TABQ, TAHQ·4HCl, and TAHQ·4HCl (ox.) plotted in the Tauc coordinate for direct allowed transition. Optical gaps of 1.49 eV and 3.25 eV are obtained for TABQ and TAHQ·4HCl, respectively, by fitting the linear regions. Oxidation clearly decreases the gap of TAHQ·4HCl.

The electronic features of TAHQ and TABQ are best probed by UV-Vis spectroscopy. A solution UV-Vis spectrum of TABQ shows an intense intraquinone transition at 460 nm,[24,25] with an absorption onset at 532 nm (Figure 3.3a). The optical gap is thus calculated to be 2.33 eV, close to the computed HOMO-LUMO gap of 2.05 eV. In comparison, the spectrum of TAHQ taken under an atmosphere of N$_2$ exhibits an absorption band for the hydroquinone π–π^* transition at 338 nm, whose onset gives an optical gap of 3.45 eV.[26] Although the solution of TAHQ rapidly and completely oxidizes to TABQ within half an hour upon exposure to air, as evidenced by the evolution of the UV-Vis spectra (Figure 3.3b), no isosbestic points are observed, suggesting that oxidation proceeds via an intermediate species.[27] A clue to this intermediate being the tetraamino-semiquinone radical comes from the growing and diminishing of a broad absorption at ~850 nm during the oxidation.[28] The D-A nature of TABQ is best revealed in the solid-

state diffuse reflectance UV-Vis spectrum (DRUV-Vis, Figure 3.3c), which reveals a broad absorption from mid-visible to beyond 1000 nm. This feature is absent in the solution spectrum and is commonly associated with intermolecular charge transfer interactions. It gives an optical gap of 1.49 eV, significantly smaller than the solution value (Figure 3.3d). UV-Vis spectroscopy did not reveal any packing effects for TAHQ, whose spectra were qualitatively identical between solution and solid-state.
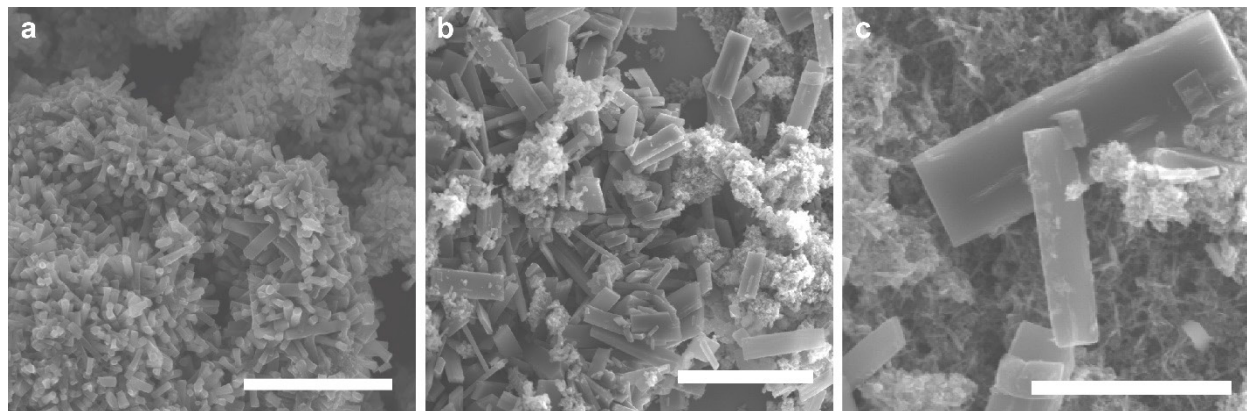
Figure 3.4. SEM images of **Ni-2D** showing nano-crystalline (a) and micro-crystalline (b, c) rods. Scale bars: (a), (c): 1 μm; (b): 2 μm.

3.3.2 Ni-Based Non-porous Frameworks

Solvothermal reaction between TABQ and $Ni(OAc)_2 \cdot 4H_2O$ in degassed concentrated aqueous ammonia under inert atmosphere at 120 °C yields $NiC_6H_4O_3N_4$ ($NiTIBQ(H_2O)$, **Ni-2D**) as a black microcrystalline powder consisting of rectangular rod-like crystals with lengths varying between 0.5 μm and 1.5 μm (Figure 3.4). The structure of **Ni-2D** was determined by continuous rotation electron diffraction (cRED) with an *ab initio* method.[29] The resolution of the cRED datasets was measured up to 0.72 Å, allowing the location of all non-hydrogen atomic positions in **Ni-2D** with atomic precision (Figures 3.5d, 3.6-3.7, and Table 3.4). The four amino groups in TABQ are deprotonated and chelate square-planar Ni^{2+} ions to form 1D chains of alternating tetra*imino*-benzoquinone (TIBQ) moieties and Ni^{2+}. The 1D chains are connected through bridging H_2O molecules to form 2D layers, where TIBQ moieties stack along the crystallographic *c*-axis in a fully eclipsed manner and a π-π stacking distance of 3.34(5) Å (Figures 3.5a, 3.5b). This distance is very close to the interlayer spacing of graphene sheets in graphite[30] and the interlayer spacing of highly conducting 2D MOFs.[20] The presence of bridging H_2O rather than OH^- or O^{2-} was further confirmed by O1s X-ray photoelectron spectroscopy (XPS), which shows a characteristic water O1s binding energy of 535.4 eV (Figure 3.8),[31,32] and by attenuated total reflection (ATR)-FTIR, which reveals the characteristic water O–H stretching band at 3406 cm^{-1} (Figure 3.9 and the discussion in the caption).[33] 2D layers of **Ni-2D** are staggered, likely due to the electrostatic repulsion of carbonyl O atoms, and crystallize in the orthorhombic space group *Immm* (Figure 3.5b, 3.5c), with the shortest interlayer Ni···Ni distance of 7.52 Å.
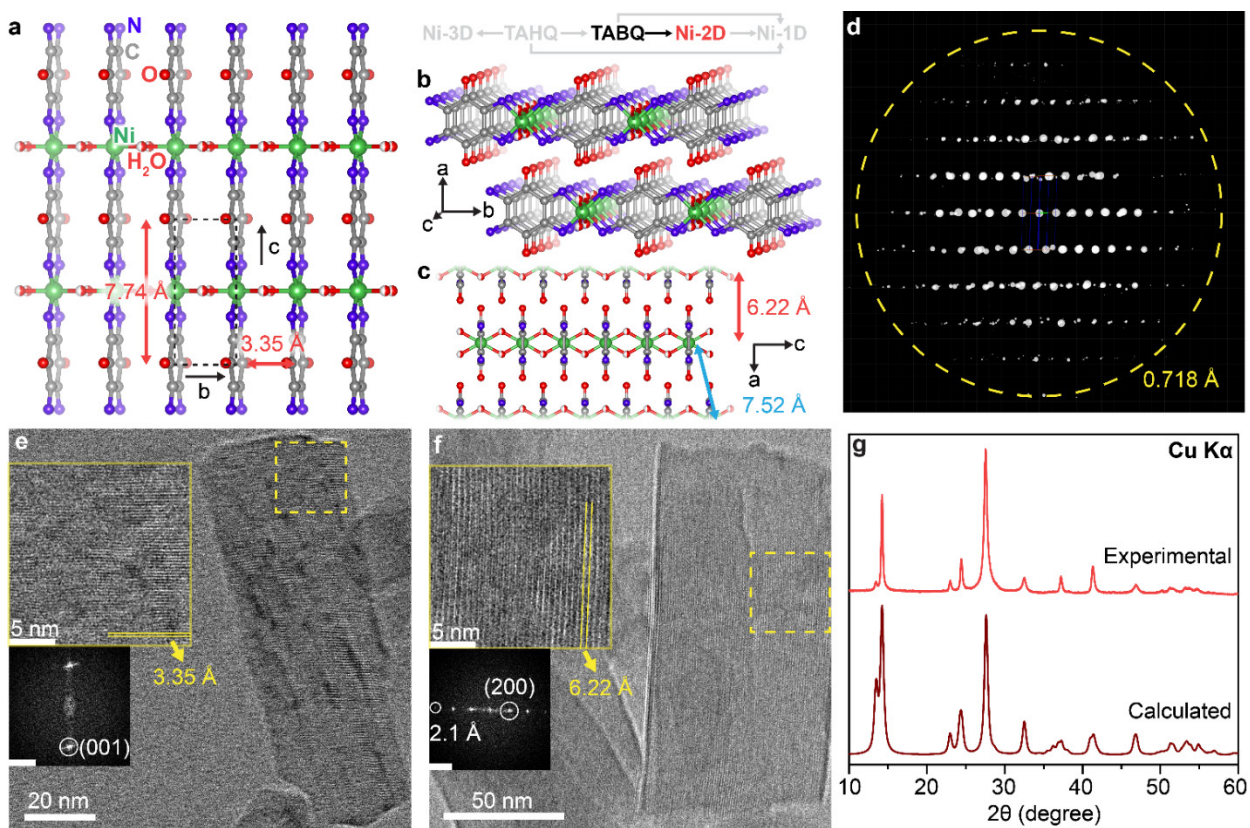
Figure 3.5. Structural characterizations of **Ni-2D**. (a) Part of a 2D layer of **Ni-2D**. Half-filled spheres represent the bridging H_2O molecules with 50% occupancy. Hydrogen atoms are omitted for clarity. The black dashed lines represent a unit cell. (b, c) The stacking of 2D layers. (d) 3D reciprocal lattices of a **Ni-2D** rod with a resolution down to 0.72 Å. (e) A Cryo-EM image of a **Ni-2D** rod, showing the π-π stacking of TIBQ ligands within 2D layers across the whole rod. Upper and lower inset, the high-magnification image and FFT of the yellow dashed square. (f) A Cryo-EM image of a **Ni-2D** rod, revealing interlayer stacking across the whole rod. Upper and lower inset, the high-magnification image and FFT of the yellow dashed square. Scale bars of FFTs, 2 nm^{-1}. (g) Experimental and calculated PXRD patterns of **Ni-2D**.
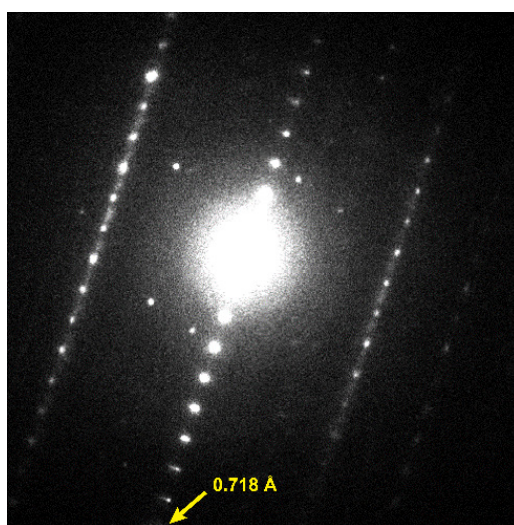
Figure 3.6. Typical SAED pattern of **Ni-2D** with high resolution of 0.718 Å.
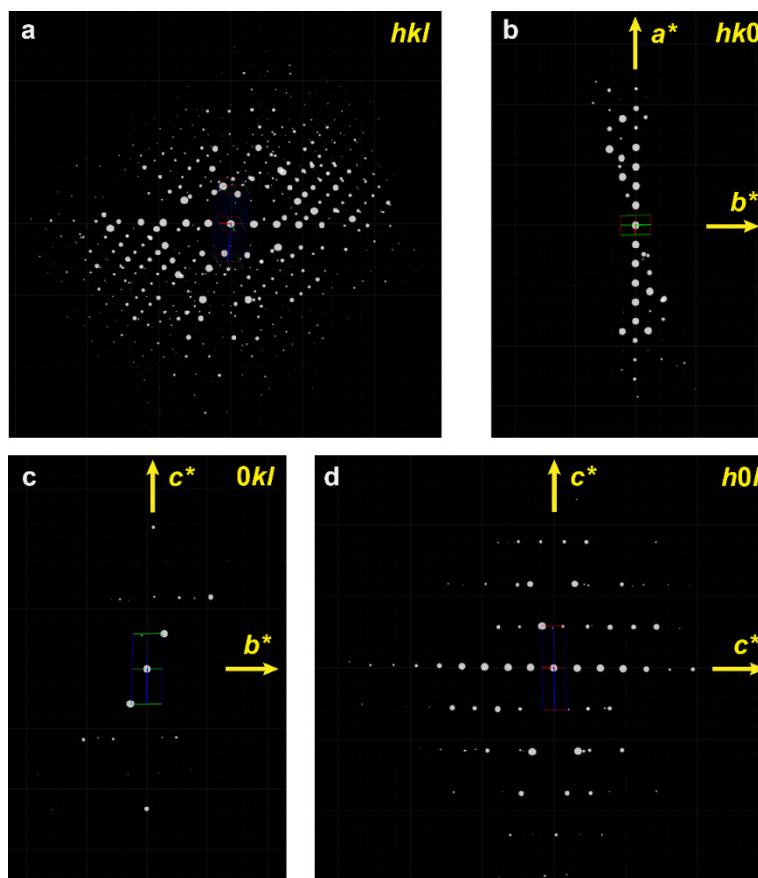
Figure 3.7. Reconstructed 3D cRED data of **Ni-2D** indexed with orthorhombic symmetry: (a) overview (*hkl*), and selected planes in the reciprocal lattice corresponding to (b) *hk*0, (c) 0*kl* and (d) *h*0*l*.
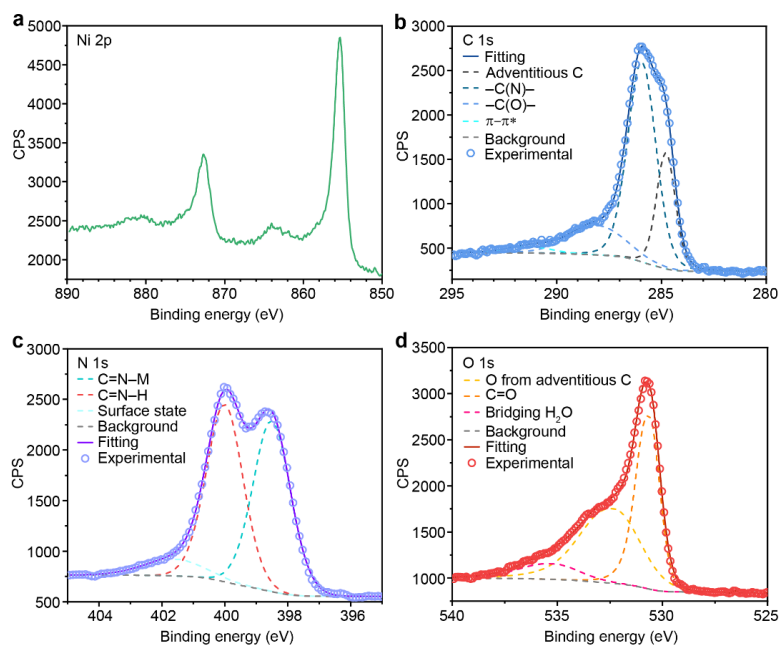
Figure 3.8. High resolution XPS spectra of **Ni-2D**. (a) Ni 2p region shows BE of Ni $2p_{3/2}$ is 855.3 eV. (b) C 1s region and the corresponding deconvolution. (c) N 1s region and the corresponding deconvolution. (d) O 1s region and the corresponding deconvolution.

113
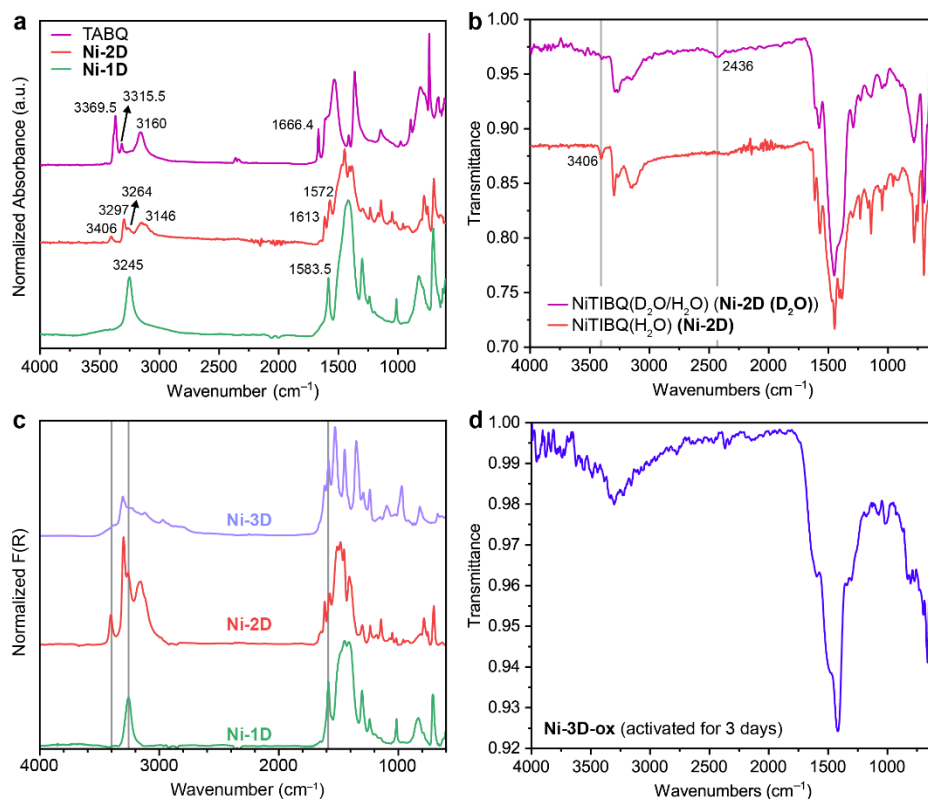
Figure 3.9. (a) ATR-FTIR of TABQ, **Ni-2D**, and **Ni-1D**. (b) Comparison of ATR-FTIR of **Ni-2D** and **Ni-2D (D$_2$O/H$_2$O)** which is synthesized using D$_2$O (see Synthetic procedures). The measurement was done in an ATR-FTIR instrument in a N$_2$ glove box. (c) DRIFTS of **Ni-3D**, **Ni-2D**, and **Ni-1D**. The presence of solvent molecules (likely water molecules) within the hydrophilic 1D pores of as-synthesized **Ni-3D** under inert atmosphere was supported by the broad O–H stretching feature spanning from 2500 cm^{-1} to 3600 cm^{-1}, with the presence of sharp peaks that are indicative for the presence of hydrogen bonding network. (d) ATR-FTIR of **Ni-3D-ox** activated at 110 °C under dynamic vacuum for 3 days, still exhibiting the presence of hydrogen bonding network given the broad O–H stretching band between 2500 cm^{-1} and 3600 cm^{-1}. The measurement was done in an ATR-FTIR instrument in a N$_2$ glove box. The ligand TABQ showed a strong C=O stretching peak at 1666 cm^{-1}, but **Ni-1D** and **Ni-2D** both exhibited red-shifted C=O stretching peak at 1583 cm^{-1} and 1613 cm^{-1}, respectively, indicating the extended delocalization of their structures, with the former exhibiting slightly higher degree of delocalization (Figure 3.9a). Only one broad N–H stretching band was observed for **Ni-1D**, which is in great agreement with the remarkable bond equalization within the 5c-6π subsystems revealed by the XRD analysis. ATR-FTIR spectroscopy was used to provide evidence for the presence of bridging water molecules in **Ni-2D**. Based on the cRED analysis, we located O atoms that bridge Ni^{2+} ions. However, the chemical identity of the O-containing species was not resolved by cRED analysis. O^{2-}, does not show any O–H stretching features, whereas OH$^-$ and H$_2$O exhibit distinct O–H stretching frequencies. The vibrational mode at 3406 cm^{-1} is assigned to the O–H stretching of bridging water molecules, given that the O–H stretching of Ni–OH–Ni is generally above 3600 cm^{-1}. To further support our assignment, we synthesized **Ni-2D (D$_2$O/H$_2$O)** which should contain both D$_2$O and H$_2$O. Indeed, the intensity of O–H stretching band at 3406 cm^{-1} decreases, while a new peak at 2436 cm^{-1} shows up, which originates from the O–D stretching of bridging D$_2$O (Figure 3.9b).
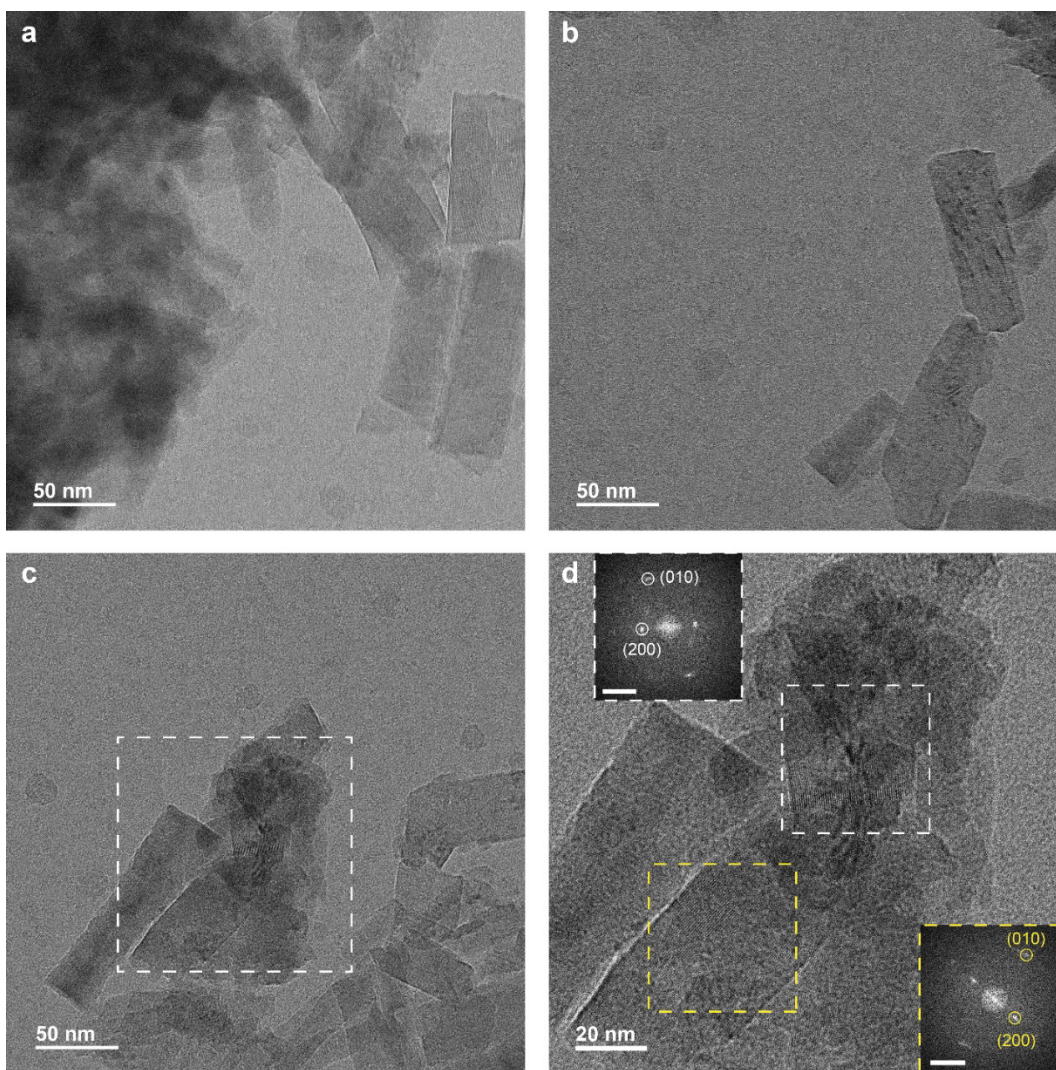
Figure 3.10. Low magnification Cryo-EM images of individual and aggregated **Ni-2D** crystals (a, b, c) show rod-like morphology and crystallite sizes up to 200 nm. (d) High magnification Cryo-EM image of the highlighted area in (c). Insets are the FFT of corresponding highlighted areas. (010) Bragg planes have the d-spacing of 3.34(6) Å; (200) Bragg planes have the d-spacing of 6.2216) Å. Scale bars of insets are 2 nm^{-1}.

The structural features of **Ni-2D** were also confirmed by high-resolution Cryo-EM down to a resolution of 2.1 Å, which is prominent given the well-known beam sensitivity of similar hybrid materials.[34] The Cryo-EM images showed that crystals of **Ni-2D** exhibit long-range ordering across the whole crystallite (Figures 3.5e, f, 3.10). Micrographs investigating the *b* crystallographic direction (Figures 3.5e, 3.10d) revealed the eclipsed π-π stacking of TIBQ–Ni chains within 2D layers of **Ni-2D**. A stacking distance of 3.35 Å was obtained by analyzing the Fast-Fourier transform (FFT, Figure 3.5e lower inset) of the highlighted area. Micrographs exploring the *a* crystallographic direction (Figures 3.5f, 3.10) showed 2D layers oriented parallel to the long side of the rod crystals with an interlayer spacing of 6.22 Å. Altogether, the Cryo-EM data are in excellent agreement with the crystal structure derived from cRED.

115

The excellent match between calculated and experimental powder X-ray diffraction (PXRD) patterns further confirmed the crystal structure and phase purity of the bulk material (Figure 3.5g).

Remarkably, repeating the synthetic conditions for Ni-2D in the presence of air produced $NiC_6H_4O_2N_4$ (NiTIBQ, **Ni-1D**), another black microcrystalline material that proved to be structurally distinct from **Ni-2D**.[35] Polycrystalline **Ni-1D** can also be synthesized from TAHQ·4HCl under aerobic conditions (Figure 3.11) and consists of sharp-edged rectangular bricks and rods (Figures 3.12c-d, 3.13) up to 500 nm long. Because cRED caused electron beam damage in this case, the crystal structure of **Ni-1D** was solved by Rietveld refinement from high resolution synchrotron PXRD data (Figure 3.12e).[36] As in **Ni-2D**, **Ni-1D** is formed from chains of TIBQ and Ni^{2+}, formed by concomitant deprotonation and oxidation of TABQ or TAHQ under reaction conditions. The main structural difference between **Ni-2D** and **Ni-1D** is the absence of bridging water, which changes the packing of Ni-TIBQ chains from 2D layers in the former to brick-wall packing in the latter (Figure 3.12a).[37] This type of packing has been observed in organic semiconductors with high carrier mobility,[38] and may be attributed here to interchain D-A interactions between partially oxidized TIBQ moieties (Figure 3.12b). The packing in **Ni-1D** leads to an interchain π-π stacking distance of 3.11 Å at 100 K, significantly shorter than that in **Ni-2D**, where bridging water molecules disrupt the D-A alignment. Notably, such close π-π stacking is rarely seen in conjugated metal-organic materials.[39] Interchain hydrogen bonding through –NH and C=O is also favorable given the appropriate alignment of chains (Figure 3.12b). The combination and balance between interchain D-A alignment and hydrogen bonding may also account for the two distinct morphologies observed for **Ni-1D**: parallelepipeds and rods, which can be explained by the Bravais-Friedel-Donnay-Harker (BFDH) law, and further verified by high-resolution Cryo-EM.
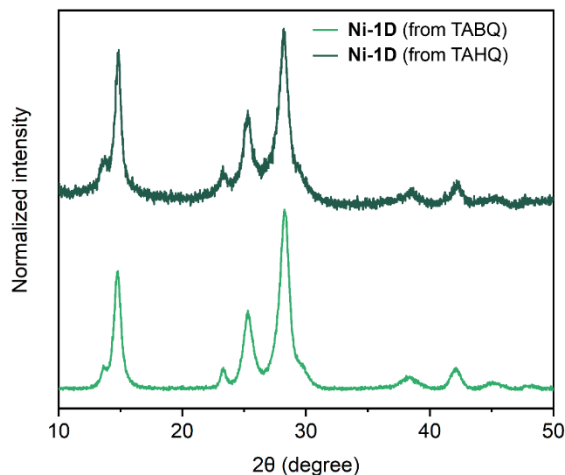
Figure 3.11. PXRD patterns of **Ni-1D** obtained from TABQ and TAHQ·4HCl using the same synthetic procedure.
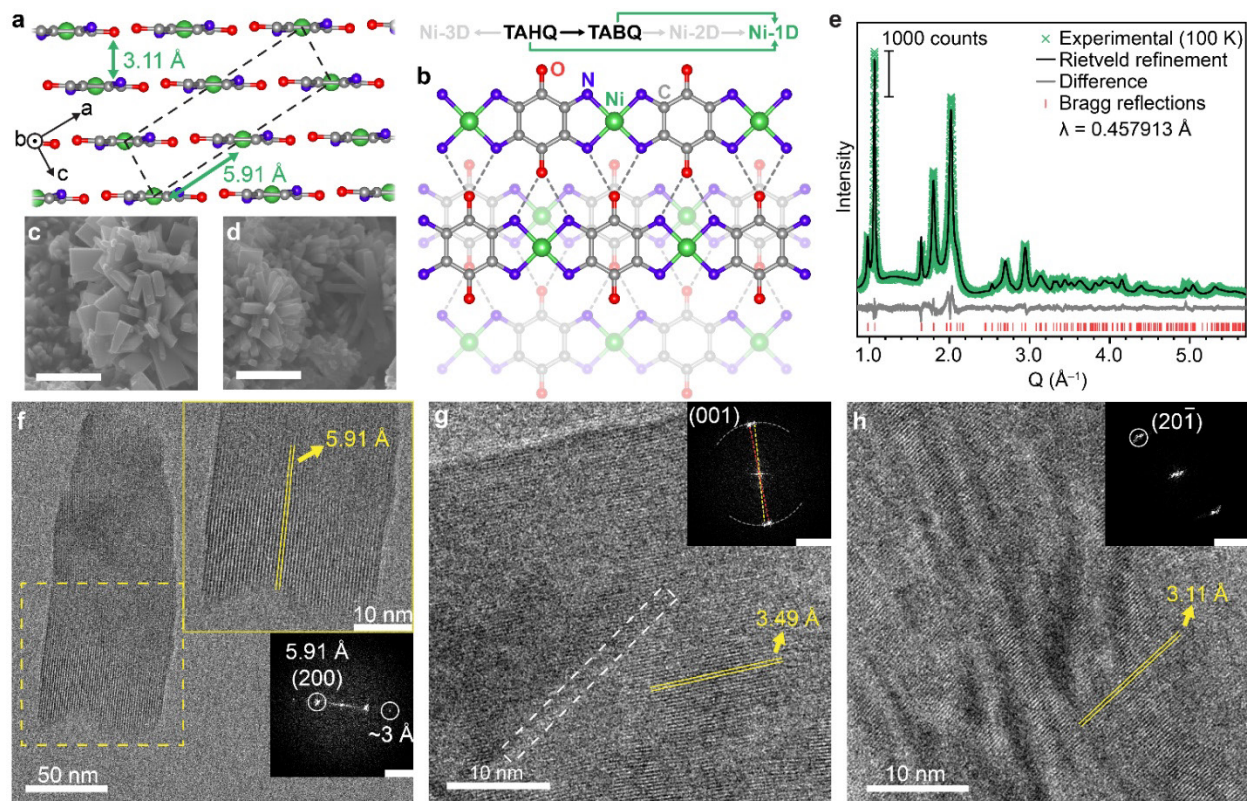
Figure 3.12. Structural characterizations of **Ni-1D**. (a) The interchain D-A π-π stacking of **Ni-1D**. Hydrogen atoms are omitted for clarity. The black dashed lines represent a unit cell. (b) Top-down view of the interchain D-A π-π stacking and interchain hydrogen bonding between –NH and C=O (gray dashed lines). (c, d) SEM images of **Ni-1D** microcrystals. Scale bars, 500 nm. (e) Rietveld refinement of the synchrotron PXRD pattern of **Ni-1D**, with R_p = 4.17%, R_{wp} = 5.34%, and GoF = 1.39. (f) A Cryo-EM image of a single **Ni-1D** rod, showing TIBQ–Ni chains aligning along the a-axis. Upper and lower inset, high-magnification image and FFT of the yellow dashed square. (g) A high magnification Cryo-EM image of a part of a **Ni-1D** rod, revealing TIBQ–Ni chains aligning along the c-axis. A grain boundary was highlighted by the white dashed rectangle. Inset, FFT of the mircrograph. White dashed arcs indicate a Debye-Scherrer ring. Yellow and red dashed lines indicate two sets of diffraction spots. (h) A high magnification Cryo-EM image of a part of a **Ni-1D** rod exhibiting interchain π-π stacking. Inset, FFT of the mircrograph. Scale bars of FFTs, 2 nm^{-1}.
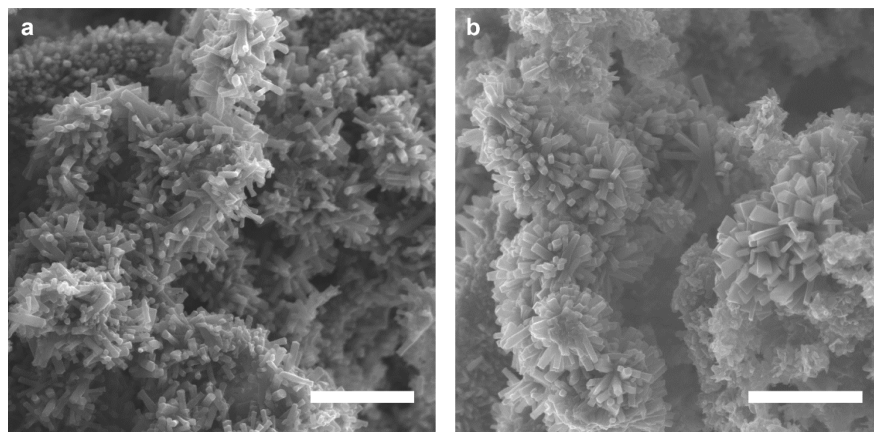
Figure 3.13. SEM images of **Ni-1D** showing both rod-like (a, b) and brick-like (b) shapes. Scale bars: 1 μm.

117
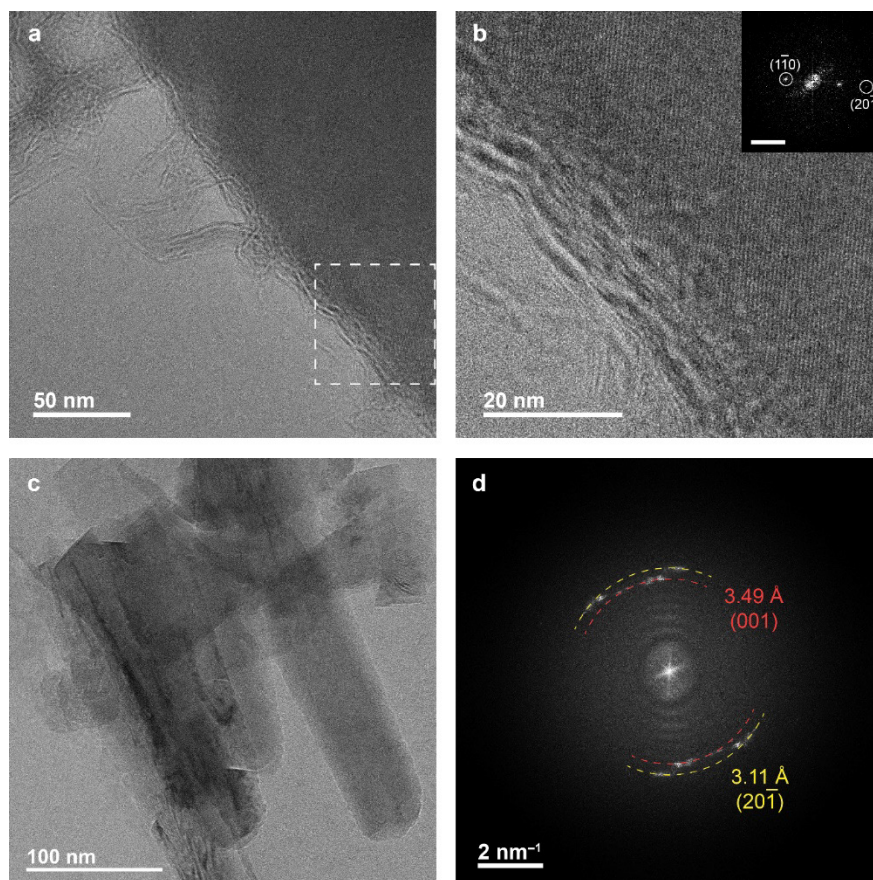
Figure. 3.14. (a) Low magnification Cryo-EM image of a rod-like crystal of **Ni-1D**. (b) High magnification Cryo-EM image of the selected area in (a) highlighted by a dashed square. Inset is the fast Fourier transform (FFT) of (b), showing diffraction spots corresponding to $(1\bar{1}0)$ and $(20\bar{1})$ Bragg planes. Scale bar, 2 nm^{-1}. (c) Low magnification Cryo-EM image of aggregated rod-like crystals of Ni-1D. (d) FFT of (c), showing two sets of diffraction spots which correspond to the *d*-spacing of (001) Bragg planes (3.49 Å) and $(20\bar{1})$ Bragg planes (3.11 Å), respectively.

A micrograph of a **Ni-1D** single rod longer than 200 nm showed the long-range ordering of TIBQ–Ni chains across the whole crystallite down to a resolution of 3.0 Å, with an interchain spacing of 5.91 Å along the *a*-axis (Figure 3.12f). Cryo-EM also revealed the close packing enabled by D-A alignment along the *c* crystallographic direction, with an interchain spacing of ~3.5 Å (Figures 3.12g, 3.14) and the close π-π stacking with a distance of ~3.1 Å (Figures 3.12h, 3.14d). Cryo-EM also revealed structural features that Rietveld refinement did not. Remarkably, a grain boundary formed by a subtle misalignment of the 1D chains was recognized by the presence of two sets of diffraction spots located on the same Debye-Scherrer ring with a misalignment angle of 5.8° (Figure 3.12g, inset). Grain boundaries can significantly affect charge transport in semiconductors, and are often invoked, but have not yet been structurally resolved in conducting MOFs or CCPs.
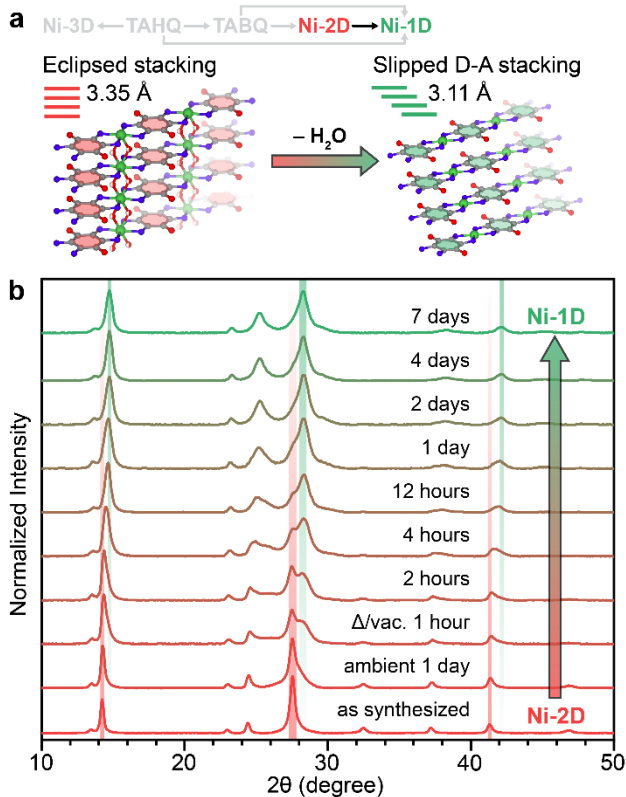
Figure 3.15. (a) Scheme and (b) *ex-situ* PXRD patterns for the transformation from **Ni-2D** to **Ni-1D**.

Given the structural similarities between **Ni-1D** and Ni-2D, it is perhaps not surprising that the latter can transform into the former through loss of bridging water. Albeit slowly, **Ni-2D** spontaneously transforms into **Ni-1D** over weeks under ambient conditions, suggesting that the D-A slipped π-stacking in Ni-1D is favorable energetically (Figure 3.15a). Lower temperature suppresses the transformation, whereas heating to 100 °C under dynamic vacuum considerably accelerates it (Figures 3.15b, 3.16). Continued heating of **Ni-1D** showed no further changes in its PXRD, attesting to its excellent thermal stability. The gradual removal of bridging water molecules was confirmed spectroscopically by ATR-FTIR (Figure 3.17), which revealed a gradual reduction in the intensity of the O–H stretching band for bridging water at 3406 cm^{-1}. The two N–H stretching bands of **Ni-2D** at 3297 cm^{-1} and 3264 cm^{-1} also merge into a single N–H band at 3245 cm^{-1} that coincides with that observed for **Ni-1D**. Unlike **Ni-2D**, **Ni-1D** is stable in strong acid (e.g., 4 M HCl (aq.)) and base (e.g., 1 M KOH (aq.)) (Figure 3.18), a rare feature in electrically conductive CCPs.[3]

119
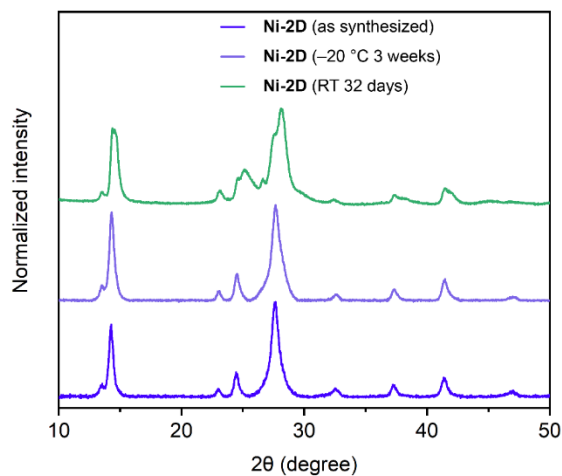
Figure 3.16. The comparison of PXRD patterns of **Ni-2D** that is just synthesized, kept at –20 °C for 3 weeks, and kept at RT for 32 days, indicating that low temperature can slow down the transformation from **Ni-2D** to **Ni-1D**.
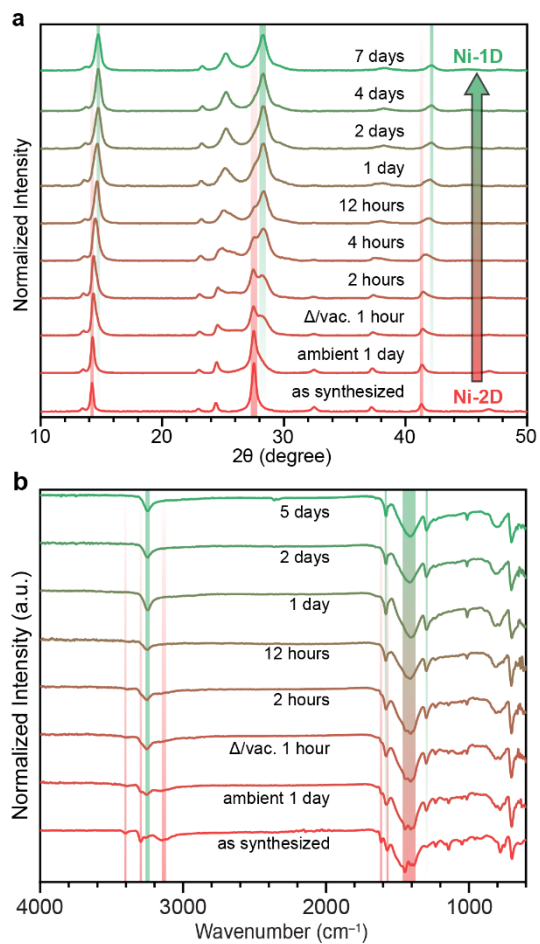
Figure 3.17. The transformation of **Ni-2D** to **Ni-1D** monitored by *ex-situ* PXRD (a) and ATR-FTIR spectroscopy (b). Δ/vac.: heating and dynamic vacuum.
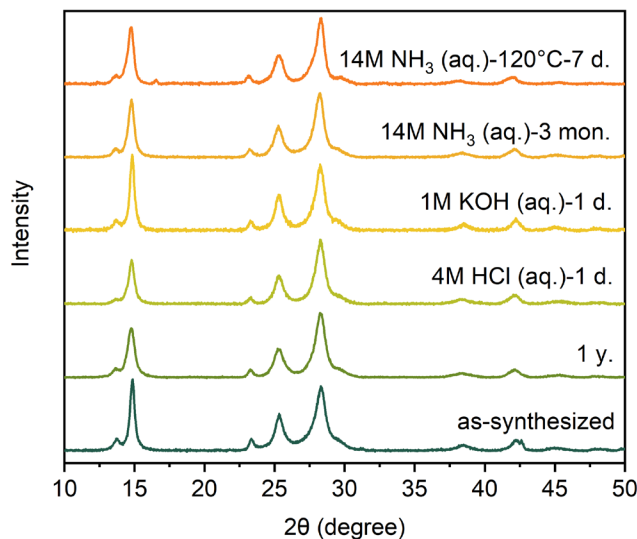
Figure 3.18. Excellent stability of **Ni-1D**. The crystallinity of **Ni-1D** retains after one year in ambient condition, soaked in 4M HCl (aq.) or 1M KOH (aq.) at room temperature for one day, soaked in 14M NH$_3$ (aq.) at room temperature for 3 months, or 120 °C for 7 days.

3.3.3 A Three-Dimensional, Porous Ni-TIHQ Framework

The reaction of TAHQ·4HCl with Ni(OAc)$_2$·4H$_2$O in degassed concentrated aqueous ammonia at 120 °C under N$_2$ yields brown hexagonal rod-like crystals of a Ni-TIHQ framework (**Ni-3D**) up to 40 μm long (Figures 3.19d inset, 3.20). **Ni-3D** undergoes a rapid color change from brown to black within half an hour of exposure to air (Figure 3.21), even though PXRD reveals no changes during this time (Figure 3.22). cRED analysis down to a resolution of 0.767 Å (Figures 3.19d, 3.23, 3.24, and Table 3.4) showed that crystals of oxidized **Ni-3D** (NiC$_6$H$_4$O$_2$N$_4$, **Ni-3D-ox**) belong to the trigonal space group $R\bar{3}m$. As with **Ni-2D**, the high quality cRED data allowed direct location of all non-hydrogen atoms in **Ni-3D-ox** and reveals helical 1D rod secondary building units (SBUs) parallel to the c-axis (Figure 3.19b).[40] The SBUs consist of slightly distorted [NiN$_4$O$_2$] octahedra sharing two axial vertices, and located on 3$_1$ screw axes (Figure 3.19b). The SBUs are connected by TIHQ ligands into a hexagonal lattice (Figure 3.19a), where every Ni^{2+} is coordinated by two μ^4-TIHQ and one μ^2-TIHQ linkers. The μ^4-TIHQ linkers use all six heteroatoms to chelate four independent Ni^{2+} ions from two adjacent SBUs, where each N atom binds to one Ni^{2+} and each O atom bridges two Ni^{2+} ions on the same SBU. This coordination mode is particularly notable because planar hexa-substituted triphenylenes and benzenes have thus far almost exclusively given rise to planar 2D MOFs with trigonal symmetry, with very few exceptions.[41,42] The μ^2-TIHQ linkers bridge two Ni^{2+} ions from two adjacent SBUs through four N atoms, similar to the coordination modes observed in **Ni-1D** and **Ni-2D**. Interestingly, the uncoordinated O atoms from μ^2-TIHQ linkers point towards the center of the 1D hexagonal pores, leading to a highly hydrophilic pore environment (Figure 3.19a).

121

Altogether, the overall topology of **Ni-3D(-ox)** is *fog* (Figure 3.25), and is one of the two distinct (3,4)-c derived nets of the basic 4-c *nbo* net.[43]
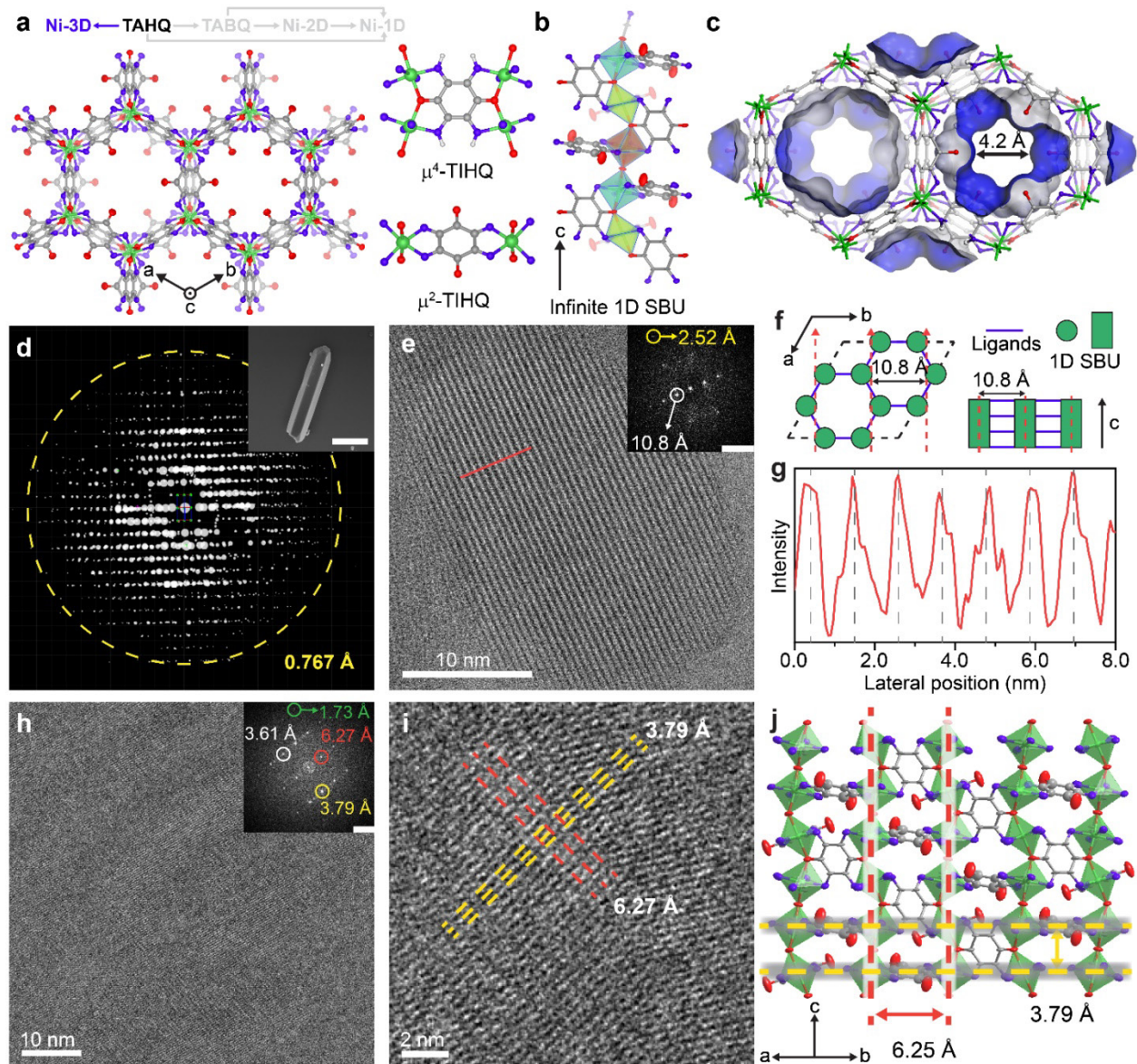
Figure 3.19. Structural characterization of **Ni-3D-ox**. (a) Portions of the crystal structure of **Ni-3D-ox**, built from octahedral [NiN$_4$O$_2$] nodes, μ^4-TIHQ linkers and μ^2-TIHQ linkers. (b) A portion of an infinite 1D rod SBU along the c crystallographic axis formed by octahedral [NiN$_4$O$_2$] nodes through vertices sharing. (c) The Connolly surface of a unit cell of **Ni-3D-ox** viewing along the c-axis. (d) 3D reciprocal lattices of a **Ni-3D-ox** rod with a maximum resolution of 0.77 Å. Inset, a single hexagonal rod of **Ni-3D-ox**. Scale bar, 5 μm. (e) A high-magnification Cryo-EM image of a part of a **Ni-3D-ox** rod, showing well-aligned 1D SBUs. Inset, FFT of the micrograph. (f) Schematic representation of **Ni-3D-ox** structure to illustrate the 1D SBUs alignment in (e). Red arrows and dashed lines indicate the viewing direction. (g) Intensity profile of the red solid line in (e), normal to the c-direction. Gray dashed lines with an even spacing of 10.9 Å are guide to the eye. (h) A Cryo-EM image of a portion of a **Ni-3D-ox** single crystal. Inset, FFT of the micrograph. (i) A high magnification Cryo-EM image of the same crystal in (h), showing individual [NiN$_4$O$_2$] nodes. Orthogonal yellow and red dashed lines indicate the packing of [NiN$_4$O$_2$] nodes shown in (j). Scale bars for FFT, 2nm^{-1}.
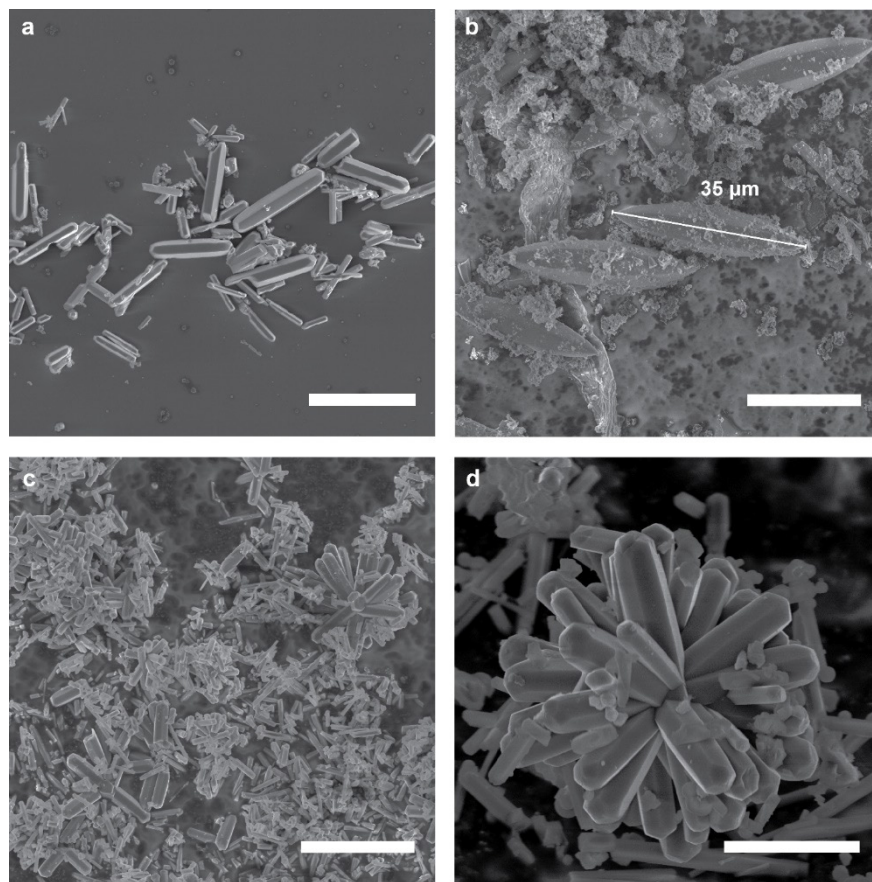
Figure 3.20. SEM images of **Ni-3D** and **Ni-3D-ox** crystals. (a) Hexagonal rod-like crystals of **Ni-3D**. (b) Hexagonal spindly crystals of **Ni-3D** with ~35 μm length. Hexagonal rod-like crystals of **Ni-3D-ox** after activated at 110 ℃ (c) or 130 ℃ (d) under dynamic vacuum for 3 days. Scale bars: (a) 15 μm; (b) 20 μm; (c) 10 μm; (d) 3 μm.
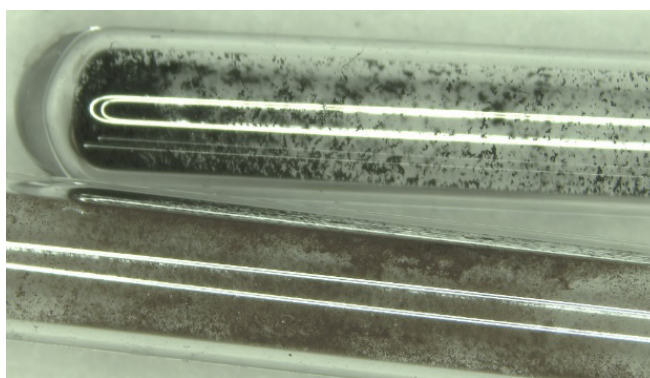
Figure 3.21. Optical microscope images of **Ni-3D** in quartz EPR tubes before (lower) and after (upper) being exposed to air (**Ni-3D-ox**). A color change from brown to black can be clearly seen, indicating the oxidation of **Ni-3D** to **Ni-3D-ox**.
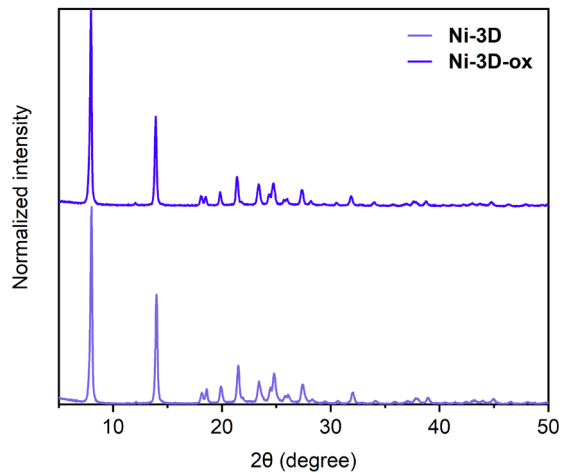
Figure 3.22. The PXRD patterns of **Ni-3D** (obtained by work-up under inert atmosphere) and **Ni-3D-ox** (obtained by work-up under air).
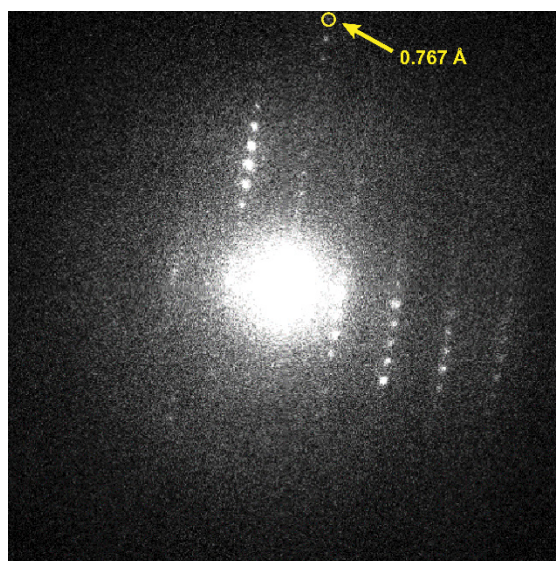
Figure 3.23. Typical SAED pattern of **Ni-3D-ox** with high resolution of 0.767 Å.
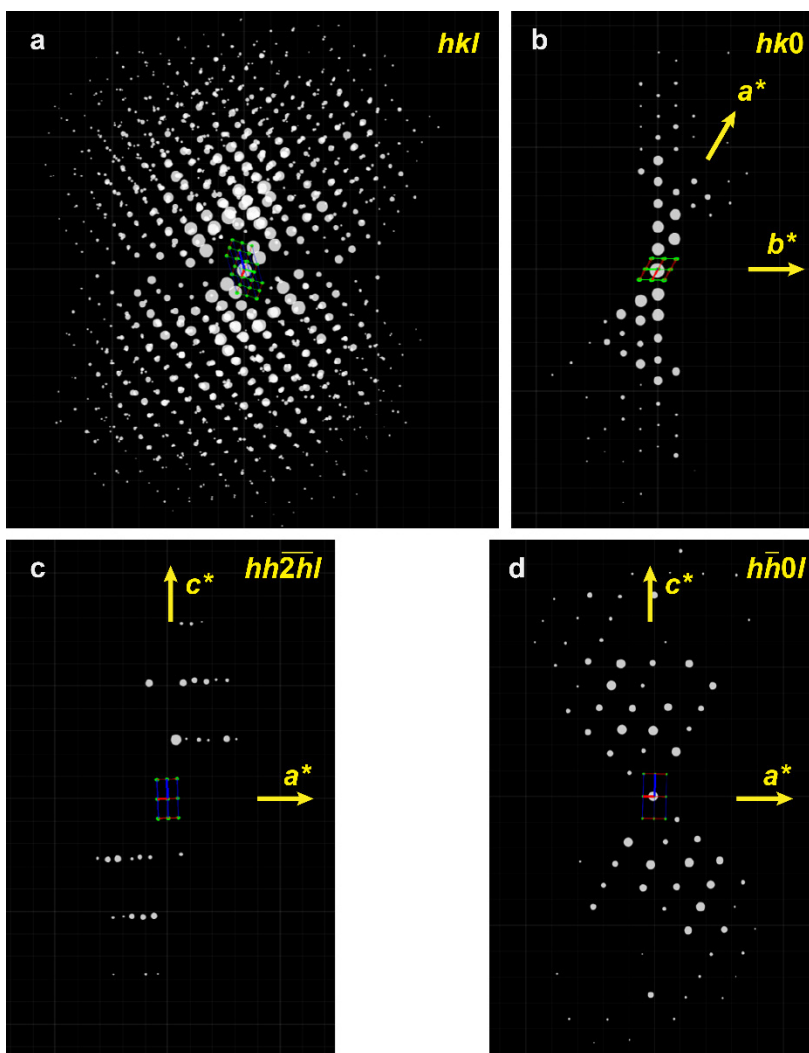
Figure 3.24. Reconstructed 3D cRED data of **Ni-3D-ox** indexed with rhombohedral symmetry: (a) overview (hkl), and selected planes in the reciprocal lattice corresponding to (b) $hk0$, (c) $hh\overline{2h}l$ and (d) $h\overline{h}0l$.
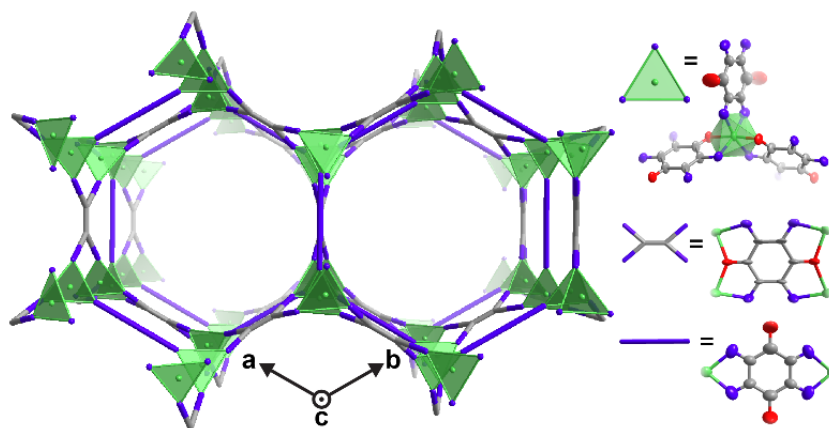
Figure 3.25. Topological analysis of **Ni-3D-ox** crystal structure, showing a ***fog*** net.

In contrast to the dense nature of **Ni-1D** and **Ni-2D** (Figure 3.26a), **Ni-3D-ox** is intrinsically ultra-microporous with 1D pores of ~4.2 Å in diameter, as indicated by the calculated Connolly surface (Figures

125

3.19c, 3.27). Indeed, a N_2 adsorption isotherm of activated **Ni-3D-ox** at 77 K gives a Brunauer−Emmett−Teller (BET) apparent surface area of 120 m^2/g (Figure 3.26b). We note, however, that there is likely a substantial amount of H_2O that persists in the pores even after prolonged activation at 110 °C (Figure 3.28) as suggested by a continued weight loss observed by thermogravimetric analysis upon heating from 100 °C to 300 °C before eventual decomposition (Figure 3.29, Tables 3.1-3.3). In contrast, no significant weight losses were observed between 100 °C and 300 °C for either **Ni-1D** or **Ni-2D** (Figures 3.30, 3.31).
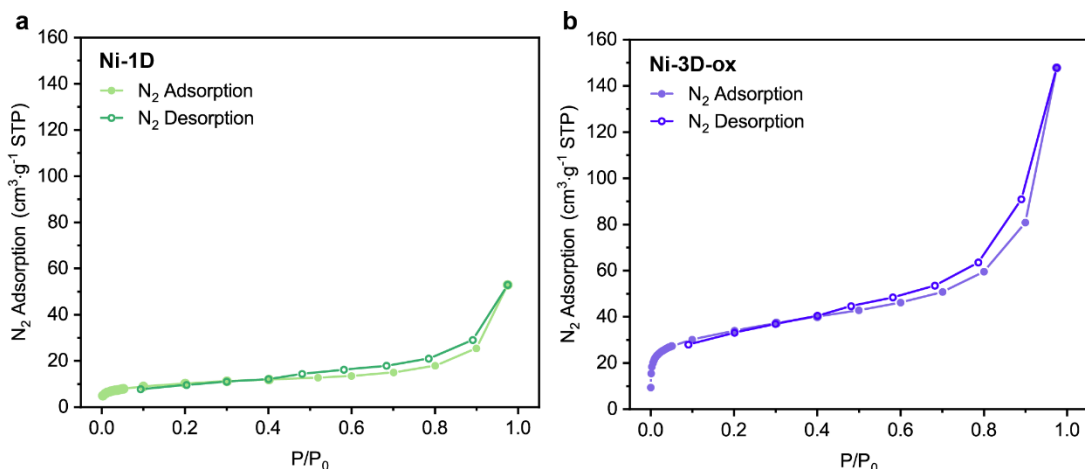
Figure 3.26. N_2 isotherms of **Ni-1D** (a), and **Ni-3D-ox** (b) measured at 77 K. The BET surface area of **Ni-1D**, and **Ni-3D-ox** are 33.57±0.28 m^2/g, and 119.61±0.46 m^2/g, respectively, in great agreement with the non-porous structure of the former and the ultra-microporous structure of the latter.
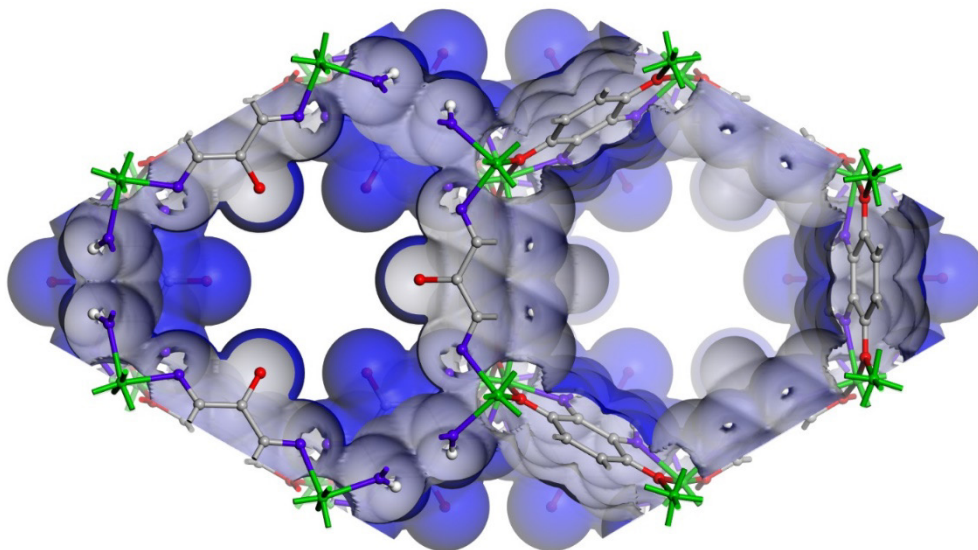
Figure 3.27. van der Waals surface of a unit cell of crystal structure of **Ni-3D-ox** viewing along the *c* crystallographic axis (generated using Materials Studio). The theoretical solvent accessible surface area (ASA) is 518 m^2/g calculated using Zeo++ (http://www.zeoplusplus.org/). The calculated diameters of, respectively, the largest included sphere, the largest free sphere and the largest included sphere along free sphere path are 8.4 Å, 4.2 Å, and 8.4 Å. This indicates that there are H_2O molecules in the pores to form the hydrogen-bonding network.
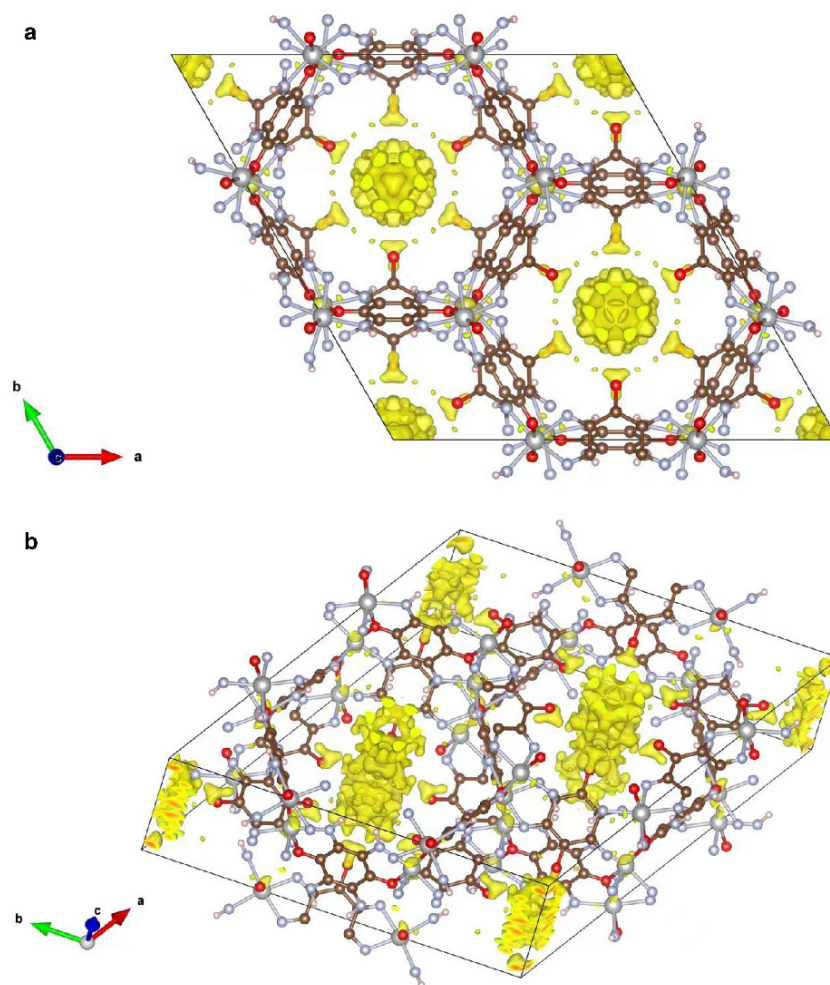
Figure 3.28. Residual electron density in the pores of **Ni-3D-ox**, suggesting the presence of significant amount of solvents in the pores. The solvents are likely water molecules forming hydrogen bonding network with the hydrophilic framework.

Table 3.1. Elemental analysis of **Ni-1D**.

	C%	H%	N%
Found [a]	32.68	1.64	25.48
Calculated [a]	32.34	1.81	25.15
Found [b]	32.64	1.84	25.12
Calculated [b]	32.34	1.81	25.15

[a] Synthesized by the preparation method mentioned in the Synthetic procedures section. Based on the formula $NiC_6H_4N_4O_2$. [b] Synthesized by heating **Ni-2D** at 110 °C under dynamic vacuum for 3 days.

Table 3.2. Elemental analysis of **Ni-2D**.

	C%	H%	N%
Found	30.18	1.69	23.46
Calculated [a]	29.92	2.51	23.26

[a] Based on the formula $NiC_6H_2N_4O_2 \cdot H_2O$.

Table 3.3. Elemental analysis of **Ni-3D-ox**.

	C%	H%	N%
Found [a]	21.46	3.54	15.43
Calculated [a]	21.78	4.87	16.93
Found [b]	23.78	2.60	15.62
Calculated [b]	23.71	4.31	18.44

[a] **Ni-3D-ox** dried at room temperature under dynamic vacuum for 3 days. The calculated EA result is based on the formula $NiC_6H_4N_4O_2 \cdot 6H_2O$. [b] **Ni-3D-ox** activated at 130 °C under dynamic vacuum for 3 days. The calculated EA result is based on the formula $NiC_6H_4N_4O_2 \cdot 4.5H_2O$. The slightly lower N% compared with that from calculated formula is common in hexaiminobenzene-based, and hexaiminotriphenylene-based 2D conductive MOFs, or tetraiminobenzene-based conjugated coordination polymers.
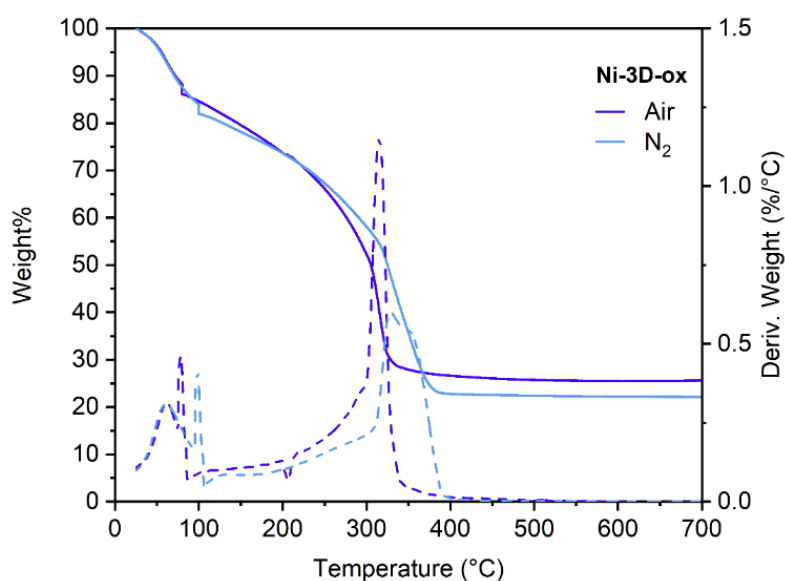
Figure 3.29. TGA of **Ni-3D-ox** under air and N_2, respectively. Pronounced weight losses above around 300 °C were observed in both cases. The absorbed water molecules in the pores were gradually removed upon heating until around 300 °C, which followed by a pronounced weight loss. The metal weight% can be calculated using the average remaining weight% (NiO, 25.6% in air, 22.2% in N_2). The Ni% can be calculated as 18.78%, which matches well with the formula calculated from EA result (Table 3.3): $C_6H_4N_4O_2Ni \cdot 6H_2O$ (17.85%).
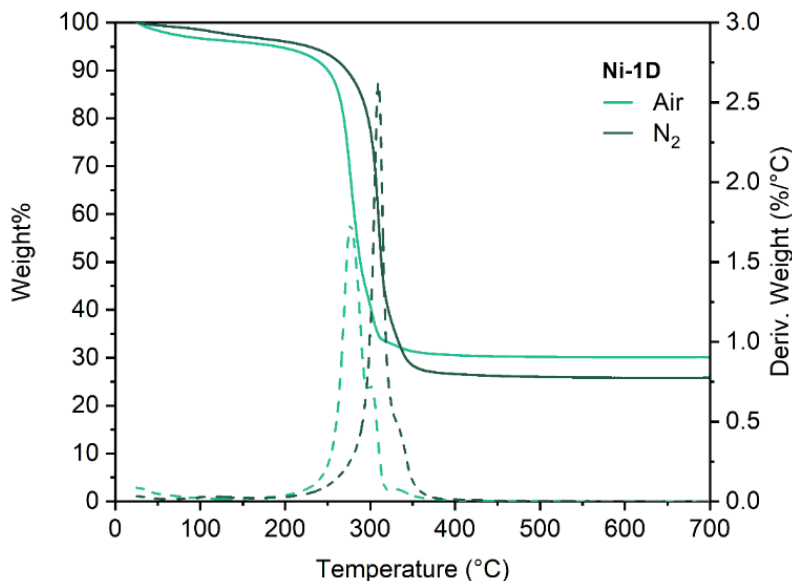
Figure 3.30. TGA of **Ni-1D** under air and N_2, respectively. Pronounced weight losses above around 300 °C were observed in both cases. The metal weight% can be calculated using the remaining weight% of TGA under air. We set the weight% at the plateau (96.2%) to 100% to accommodate the initial residual solvent lost. Therefore, we can have weight% of remaining solid of 31.3%, which turns out to be NiO. The Ni% can be calculated as 24.7%, which matches well with the theoretical value of 26.3%.
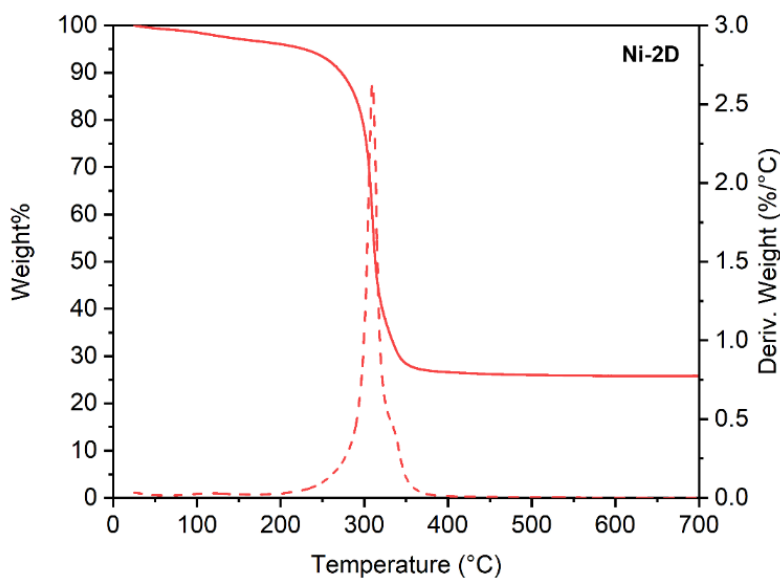
Figure 3.31. TGA of **Ni-2D** under air. Pronounced weight losses above around 300 °C were observed in both cases. The metal weight% can be calculated using the remaining weight% of TGA under air. We set the weight% at the plateau (96.7%) to 100% to accommodate the initial residual solvent lost. Therefore, we can have weight% of remaining solid of 26.7%, which turns out to be NiO. The Ni% can be calculated as 21.0%, which matches well with the theoretical value of 24.6%.

129
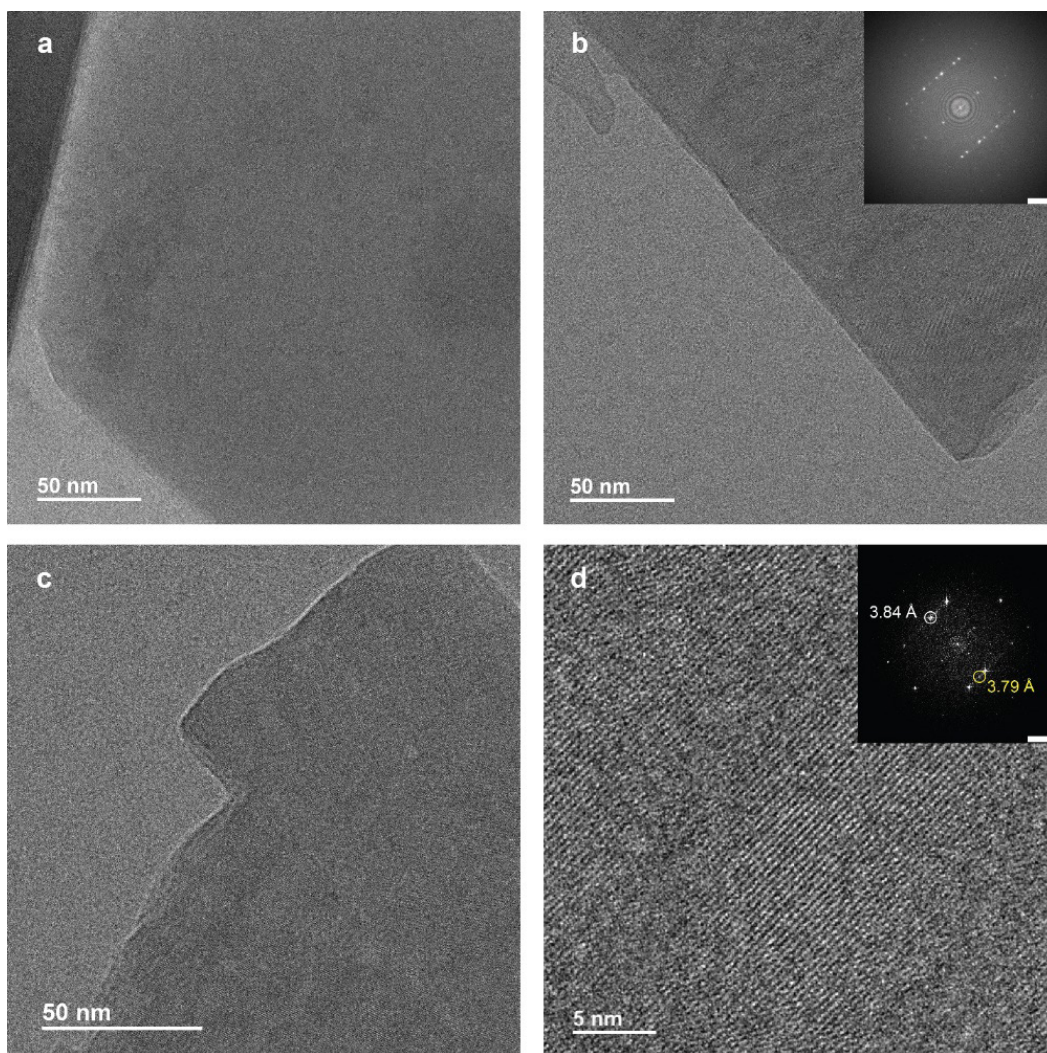
Figure 3.32. Cryo-EM images of **Ni-3D-ox**. (a) Low magnification Cryo-EM image of a large hexagonal crystal. (b) Low magnification Cryo-EM image of a large rod-like crystal. Individual [NiO$_2$N$_4$] octahedrons can be clearly seen. Inset is the FFT of b. (c) Low magnification Cryo-EM image of two aggregated large rod-like crystals. (d) High magnification Cryo-EM image of a selected area in c. Inset is the FFT of d. 3.84 Å corresponds to the Ni-Ni distance between adjacent [NiO$_2$N$_4$] octahedrons within one infinite 1D metal node. 3.79 Å corresponds to the *d*-spacing of (003) Bragg planes. Scale bars of insets are 2 nm^{-1}.

As with the previous materials, the structure of **Ni-3D-ox** was confirmed by near atomic-resolution Cryo-EM, down to 1.7 Å (Figure 3.19h). Long-range ordering of the SBUs was revealed by the evenly spaced high-contrast lattice fringes that align parallel to the *c*-axis (Figures 3.19e, 3.19f) with a spacing of 10.8 Å, confirmed by both FFT (Figure 3.19e, inset) and line intensity profile normal to the *c*-axis (Figure 3.19g). Micrographs exploring the crystallographic orientation shown in Figure 3.19j exhibited highly ordered packing of [NiN$_4$O$_2$] nodes across the whole crystal (Figure 3.19h, Figure 3.32). Individual [NiN$_4$O$_2$] octahedrons were clearly observed in the high-magnification micrograph of a portion of another **Ni-3D-ox** single crystal (Figure 3.32c), arranging as an orthogonal array with two average internode

distances of 6.27 Å and 3.79 Å (Figure 3.19i), matched perfectly with the crystal structure solved by cRED. Bulk phase purity of **Ni-3D-ox** was verified by PXRD (Figure 3.33).
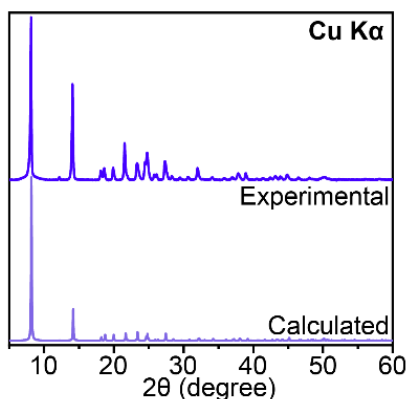
Figure 3.33. Experimental and calculated PXRD pattern of **Ni-3D-ox**. Cu kα X-ray source was used. An excellent agreement was obtained.

3.3.4 Assessing the Formal Oxidation States of the Ligands

The physical and structural details of the three Ni materials are determined exclusively by the formal oxidation state of their linkers. Indeed, XPS confirmed that the Ni ions in all materials are divalent, with essentially identical Ni $2p_{3/2}$ binding energies (Figures 3.8, 3.34, 3.35).[44] A first indication of the degree of ligand oxidation came from comparing the C–C, C–O, and C–N bond lengths across the three materials. Because the TIBQ linkers in **Ni-1D** can be thought of as two N–C–C–C–N 5-center, 6π (5c-6π) subsystems, the C–C and C–N distances here are remarkably similar, 1.384 Å and 1.393 Å, respectively (Figure 3.36a). The 6π systems further functions as a particularly effective electronic communication bridge between two Ni^{2+} centers. The two C–C bonds connecting the two 6π subsystems (C1–C3' and C1'–C3 in Figure 3.37a) show more pronounced single bond character and an elongated bond distance of 1.454 Å, significantly longer than in the free ligand TABQ, 1.360 Å. Similar structural distortions have been observed in 2,5-diaminobenzoquinonediimine (DABQDI) metal complexes, such as planar Ni-DABQDI tapes,[24] and oxidized TABQ derivatives.[45] The C=O bond in **Ni-1D** is also slightly more extended to 1.261 Å relative to the free TABQ ligand, 1.237 Å, likely due to partial participation in the 6π subunit. In contrast, the C=O bond length in **Ni-2D** remains nearly unchanged compared to the free ligand, at 1.232 Å, remained unchanged in **Ni-2D**, while the C–C distances undergo significant elongation to an average of 1.497 Å, closer to the single-bond character of C–C bonds in cyclohexane (1.53 Å) than the C–C bonds in aromatic rings (Figure 3.36c). The C–N bonds in **Ni-2D** show both C=NH and C=N⁻ character with an average C–N distance of 1.375 Å (Figure 3.37b). Altogether, the structural details point to a more oxidized form of TIBQ and a more localized electronic structure in **Ni-2D** than in **Ni-1D**.
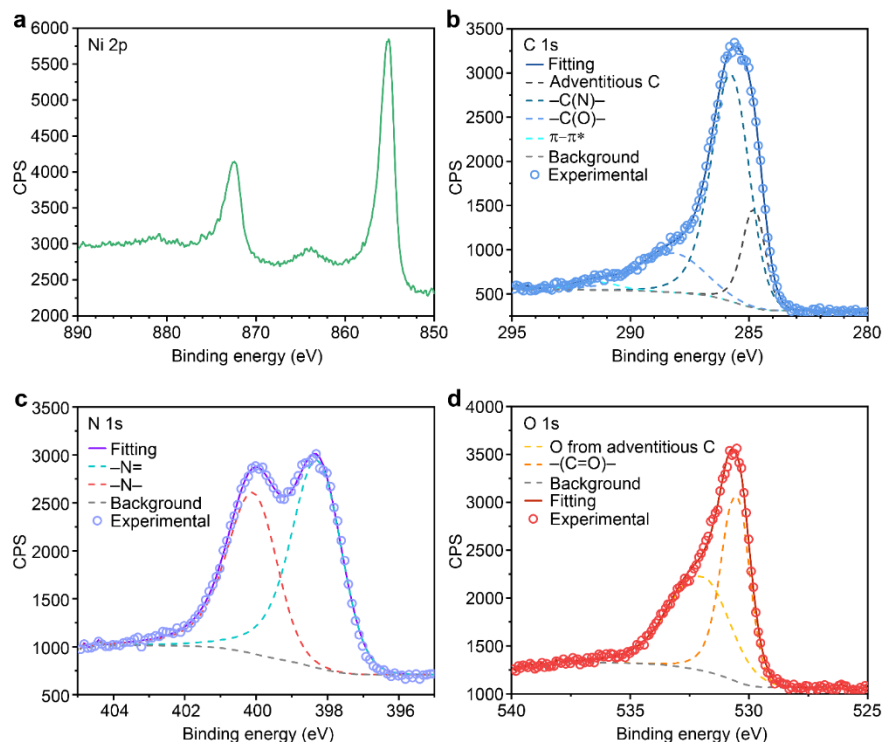
Figure 3.34. High resolution XPS spectra of **Ni-1D**. (a) Ni 2p region shows BE of Ni $2p_{3/2}$ is 855.1 eV. (b) C 1s region and the corresponding deconvolution. (c) N 1s region and the corresponding deconvolution. (d) O 1s region and the corresponding deconvolution.
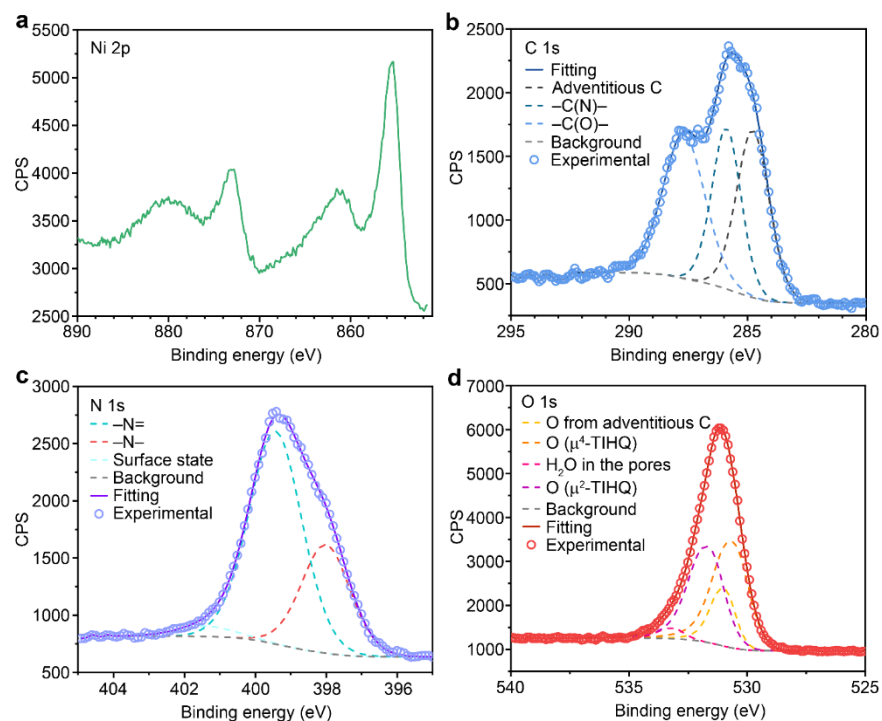
Figure 3.35. High resolution XPS spectra of **Ni-3D-ox**. (a) Ni 2p region shows BE of Ni $2p_{3/2}$ is 855.4 eV. Strong satellite features (~6 eV higher BE than the main peaks) were observed for both Ni $2p_{3/2}$ and Ni $2p_{1/2}$ transitions. (b) C 1s region and the corresponding deconvolution. (c) N 1s region and the corresponding deconvolution. (d) O 1s region and the corresponding deconvolution.
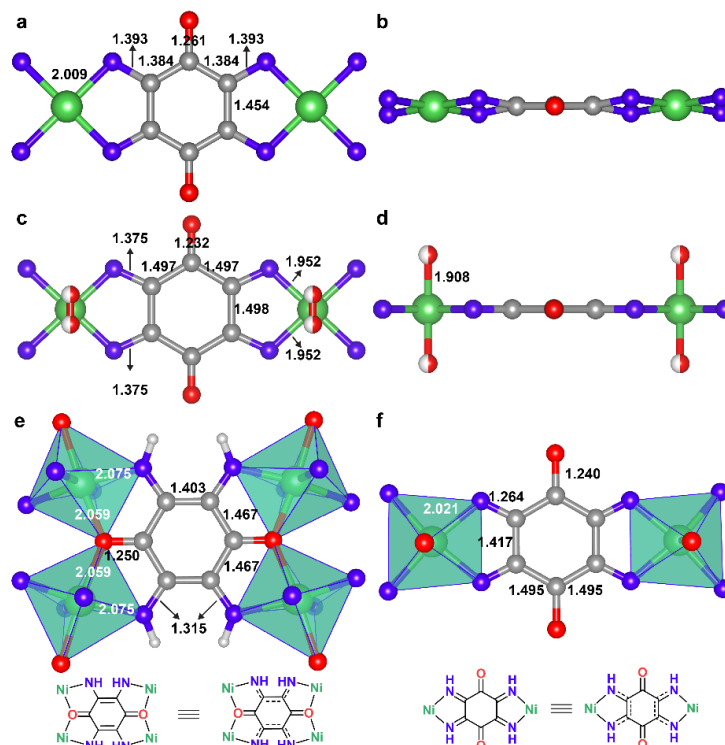
Figure 3.36. Selected bond lengths (Å) of ligands in **Ni-1D** (a, b), **Ni-2D** (c, d), and **Ni-3D-ox** (e, f). Lewis structures of **Ni-3D-ox** were shown in (e) and (f). Gray spheres: C; blue spheres: N; red spheres: O; white spheres: H; half-filled red spheres: O from bridging H_2O with an occupancy of 50%. The average bond lengths of C–C, C–N, C–O of TABQ, **Ni-1D**, **Ni-2D**, and **Ni-3D-ox** are 1.387 Å, 1.378 Å, 1.412 Å, and 1.370/1.362 Å (μ^4-TIHQ/μ^2-TIHQ).
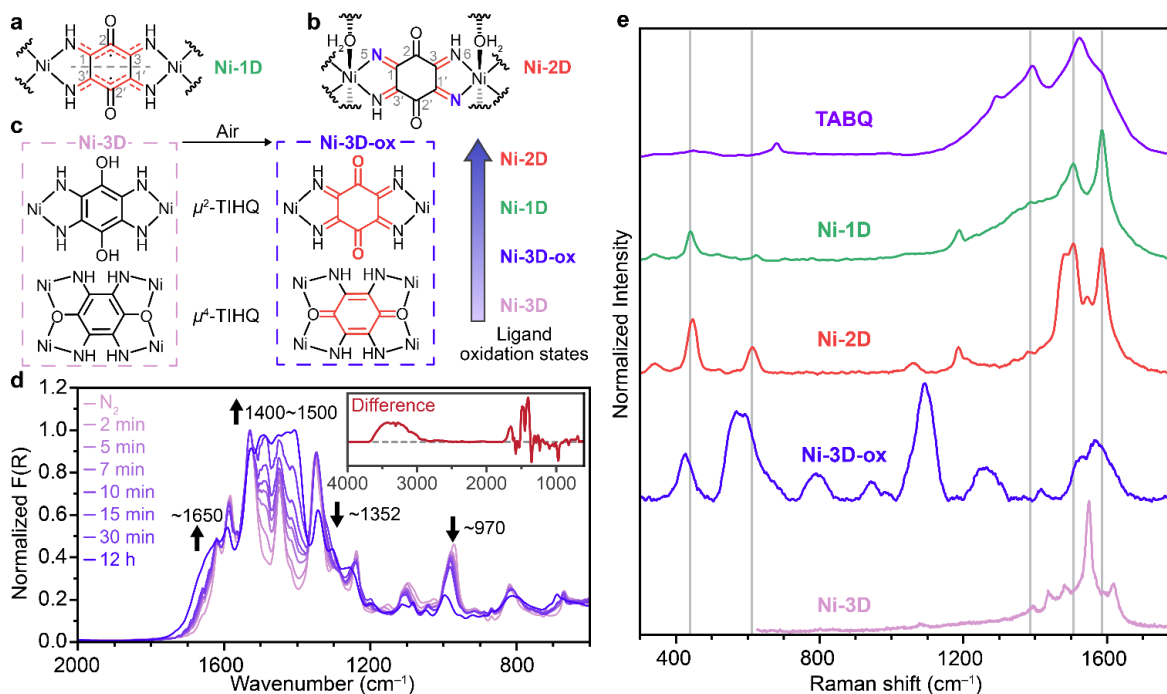
Figure 3.37. Characterization of ligand oxidation states. Lewis structures that can best describe (a) **Ni-1D**, (b) **Ni-2D**, (c) **Ni-3D** and **Ni-3D-ox**. (d) *In-situ* DRIFTS of **Ni-3D** upon exposure to air. Inset, the difference spectrum. (e) 532-nm Raman spectra of TABQ, **Ni-1D**, **Ni-2D**, **Ni-3D-ox**, and **Ni-3D**.

The color change accompanying the oxidation of **Ni-3D** to **Ni-3D-ox** likewise corresponds to the oxidation of TIHQ. Indeed, monitoring this rapid oxidation by *in-situ* diffuse reflectance infrared Fourier transform spectroscopy (DRIFTS), showed gradually diminishing C–N and C–O stretching bands, and concomitant growth of C=N and C=O stretching bands (Figure 3.37d). Thus, although TIHQ linkers in as-synthesized **Ni-3D** retain their hydroquinone character (Figure 3.37c), μ^2-TIHQ and μ^4-TIHQ in **Ni-3D-ox** are best described as being neutral and bearing a –4 negative charge, respectively, to give an overall neutral framework. Indeed, the C–O, C–C, and C–N distances and μ^4-TIHQ in **Ni-3D-ox** are similar to that of free TABQ (which can be thought of as bearing a –4 charge balanced by 4 protons). Conversely, the C–O and C–N distances of 1.240 Å and 1.264 Å for μ^2-TIHQ are typical for carbonyl C=O and imine C=NH moieties, respectively (Figure 3.36). Therefore, μ^2-TIHQ linkers are best described as 1,2,4,5-tetraimino-3,6-diketocyclohexane (Figure 3.37c), a neutral ligand that has also been reported as such in a binuclear Ru complex.[46] Overall, the structural data reveal a redox ladder wherein the ligand is progressively oxidized in moving from **Ni-3D** to **Ni-3D-ox**, **Ni-1D**, and **Ni-2D** (Figure 3.37c).

The oxidation state of linkers was further confirmed by Raman spectroscopy, as the C–C, C–O, and C–N vibrational modes are highly sensitive to the ligand oxidation state.[47] The intense C=O stretching bands at ~1587 cm^{-1} for both **Ni-1D** and **Ni-2D** are slightly red shifted relative to TABQ, 1595 cm^{-1} (Figure 3.37e). The broad C–N stretching band at 1387 cm^{-1} observed for **Ni-1D** can be explained by the highly delocalized nature of the 6π subsystems.[48] In comparison, the two bands at 1506 cm^{-1} and 1547 cm^{-1} observed for **Ni-2D**, corresponding to C=NH and C=N$^-$ stretching modes, attest to the more oxidized ligand in this material.[48] Notably, benzene ring breathing bands at 1619 cm^{-1} and 1551 cm^{-1} for **Ni-3D** shift and merge into a new C–C stretching band at 1531 cm^{-1} upon formation of **Ni-3D-ox**, confirming the oxidation of TIHQ linkers (Figures 3.37e, 3.38). The Raman bands between 400 cm^{-1} and 650 cm^{-1} in all spectra correspond to Ni–N and/or Ni–O bonds.
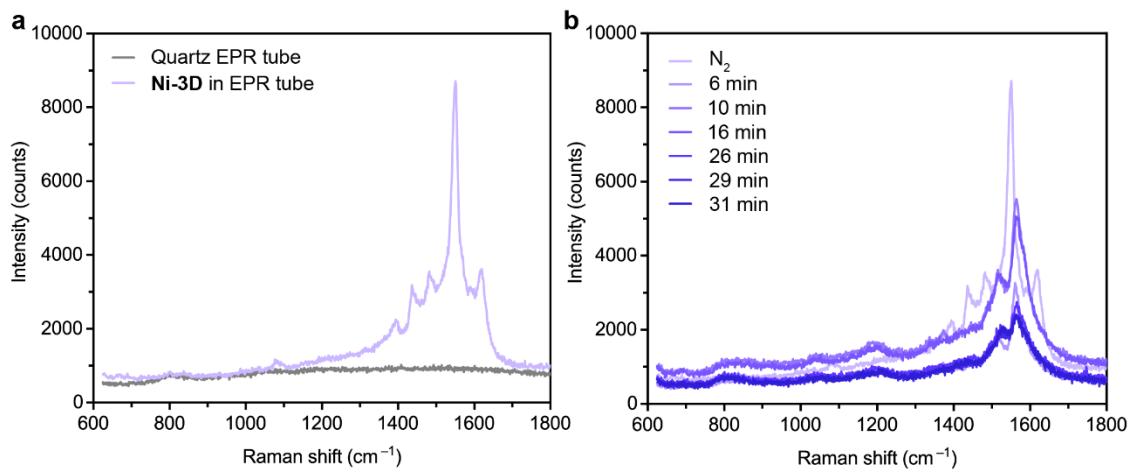
Figure 3.38. (a) Raman spectra of quartz EPR tube and **Ni-3D** in the EPR tube. (b) *in-situ* Raman spectra of **Ni-3D** upon exposure to air.

3.3.5 Electronic Structures of Ni-Frameworks

Initial assessment for the degree of charge delocalization and metal-ligand conjugation in the three Ni frameworks came from electronic structure investigations by DRUV-Vis and magnetometry. Both **Ni-1D** and **Ni-2D** exhibit strong electronic absorptions around 500 nm, corresponding to ligand-centered (LC) π-π^* intraquinone excitations (Figures 3.39a, 3.40).[24,25] The absorption maximum of **Ni-1D**, 503 nm, is slightly red-shifted compared to **Ni-2D**, 475 nm, consistent with the higher degree of delocalization in the former. In contrast, **Ni-3D** shows a hydroquinone-based LC π-π^* transition at 344 nm.[26] Broad metal-to-ligand charge transfer (MLCT) bands centered around 750 nm and 732 nm were observed for **Ni-1D** and **Ni-2D**,[24] respectively. These absorptions are significantly red-shifted compared with that in related 2,5-diamino-1,4-diiminobenzoquinone complexes,[49–51] and indicate significant electronic delocalization between Ni^{2+} and TIBQ orbitals. The two broad NIR bands, centered at 1172 nm for **Ni-1D** and 1081 nm for **Ni-2D**, stem from extended intrachain metal-ligand d-π conjugation and strong interchain stacking. In contrast, **Ni-3D** exhibits essentially no MLCT features or NIR bands, which suggests that it lacks intrinsic charge delocalization. However, oxidation to **Ni-3D-ox** coincides with the gradual growth of MLCT bands centered around 506 nm and 660 nm (Figure 3.39b), suggesting substantially enhanced metal-ligand electronic communication with oxidation of TIHQ. Although the NIR region in **Ni-3D-ox** gains intensity relative to **Ni-3D**, indicating the increase of free carrier concentration and electronic delocalization,[52] it is still much weaker than the NIR features of **Ni-2D** and **Ni-1D**. Extracting optical band-gaps (E_o) from the DRUV-Vis spectra by way of Tauc plots revealed decreasing values of 2.06 eV, 1.60 eV, 0.82 eV, and 0.70 eV for **Ni-3D**, **Ni-3D-ox**, **Ni-2D**, and **Ni-1D** respectively (Figures 3.39c-d).
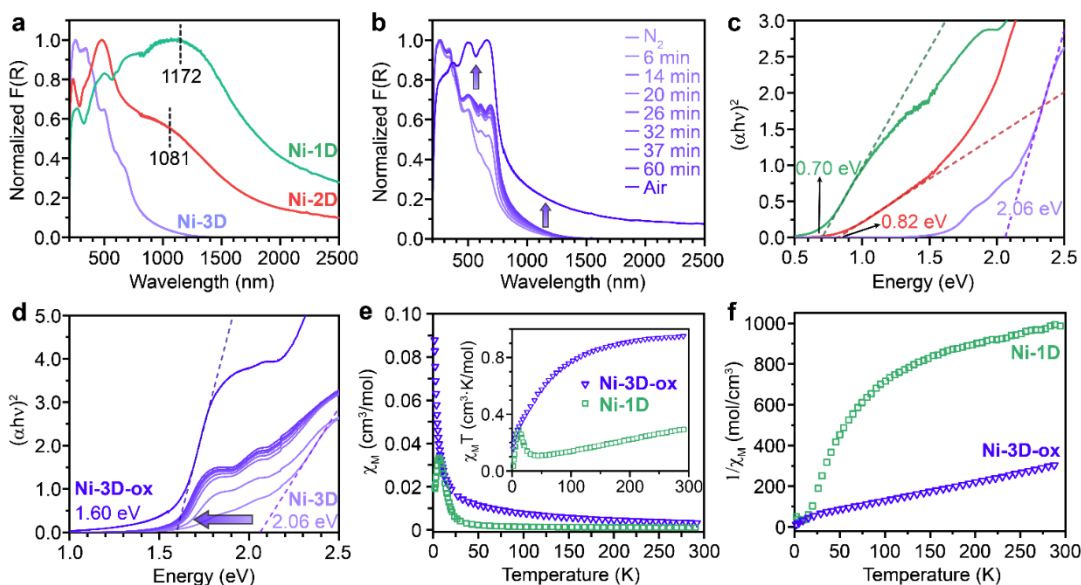
Figure 3.39. (a) Normalized DRUV-Vis spectra and (c) Tauc plots of **Ni-1D**, **Ni-2D**, and **Ni-3D**. (b) *In-situ* DRUV-Vis spectra and (d) Tauc plots of **Ni-3D** upon exposure to air. Dashed lines indicate the best linear fits to the absorption edges. (e, f) Temperature dependence of χ_M, $\chi_M T$, and χ_M^{-1} (H = 1.0 kOe) for **Ni-1D** and **Ni-3D-ox**.
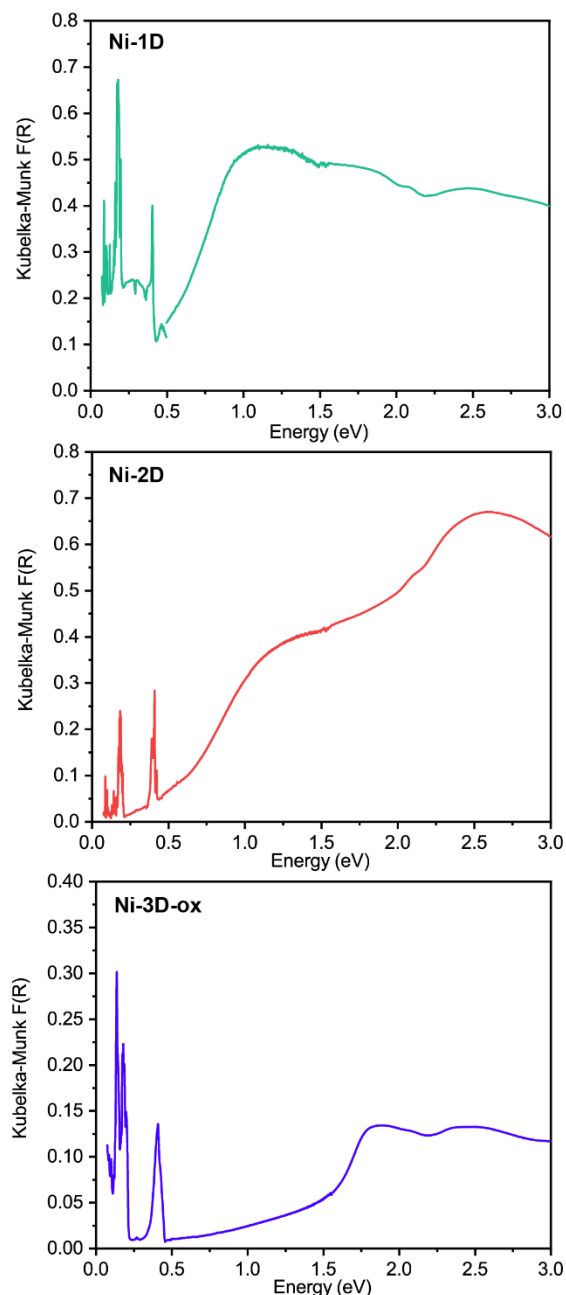
Figure 3.40. DRUV-Vis and DRIFTS spectra of **Ni-1D**, **Ni-2D**, and **Ni-3D-ox** in energy scale that are matched together.

Magnetometry provided critical insight into the electronic communication between metals and/or ligands. Direct current (DC) magnetic susceptibilities were measured for polycrystalline samples of **Ni-1D** and **Ni-3D-ox**[53] from 1.8 K to 293 K under an applied field of 1 kOe (Figure 3.39e). **Ni-1D** has $\chi_M T$ of 0.30 cm^3 K mol^{-1} per Ni-TIBQ unit at 293 K, much lower than the value of 1 cm^3 K mol^{-1} expected for high-spin Ni^{2+} centers with S = 1. $\chi_M T$ for **Ni-1D** gradually decreases with decreasing temperature, but sees a sharp increase between 45 K and 11 K. This behavior is consistent with the presence of both ferromagnetic and antiferromagnetic exchange pathways. For structurally closely-related molecular

136

analogs, such as Ni(isq)$_2$ (isq = o-diiminobenzosemiquinonate) complexes,[54,55] square-planar Ni^{2+} ions typically exhibit closed-shell S = 0 configurations. Therefore, the antiferromagnetic coupling here likely arises from the Ni-mediated interaction between TIBQ-centered radicals (Figure 3.41), again in close analogy to the Ni(isq)$_2$ complexes.[56]
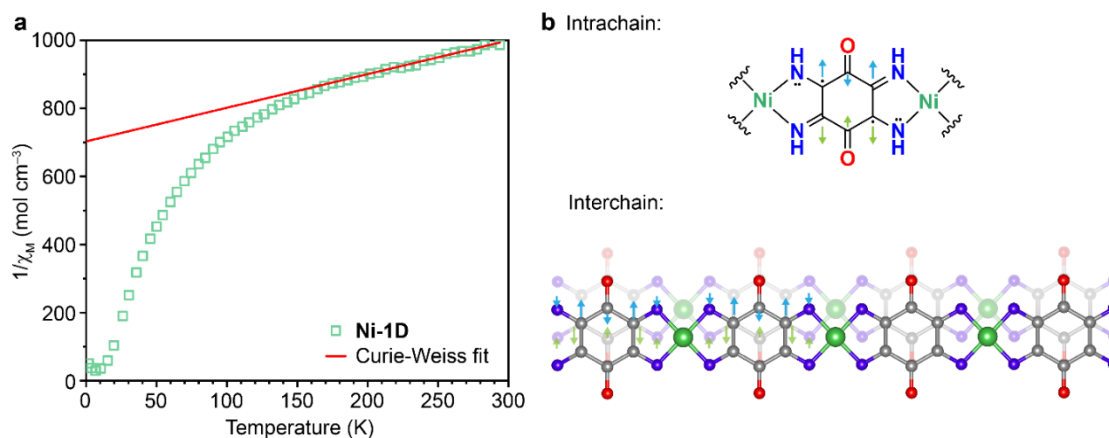
Figure 3.41. (a) The $1/\chi_M$ vs. T plot. The red solid line is the best Curie-Weiss fit using the data between 175 K and 300 K, where Curie Constant C is 0.993 cm^3 K mol^{-1}, and the Weiss temperature θ is –693 K, indicative of strong antiferromagnetic interactions. (b) Schematic representation of spin polarization in **Ni-1D**, showing intrachain and interchain antiparallel spin alignment.
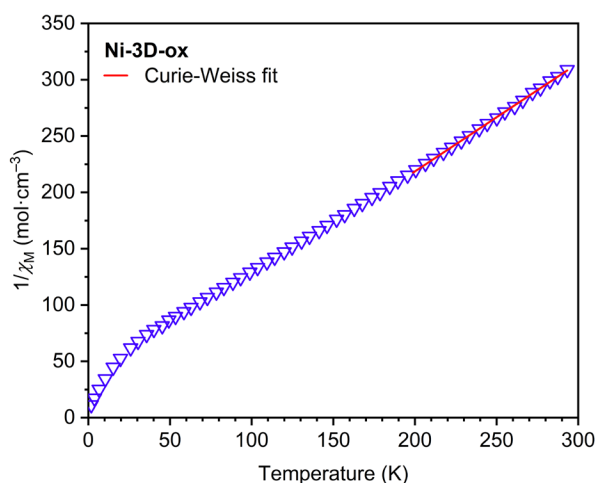
Figure 3.42. The $1/\chi_M$ vs. T plot of **Ni-3D-ox**. The red solid line represents the best Curie-Weiss fit ($R^2 = 0.9996$) using the high temperature data between 200 K and 300 K, where Curie Constant C is 1.04 cm^3 K mol^{-1}, and the Weiss temperature θ is –25.44 K, indicative of a $S = 1$ spin system and dominant antiferromagnetic interactions.

Ni-3D-ox exhibits a $\chi_M T$ value of 0.95 cm^3 K mol^{-1} per Ni-TIHQ unit at 293 K, very close to the value expected for an Ni^{2+}-centered S = 1 spin and a closed-shell TIHQ linker (1 cm^3 K mol^{-1} for g = 2.0). The $\chi_M T$ value gradually decreases to 0.158 cm^3 K mol^{-1} at 1.8 K, suggesting overall antiferromagnetic coupling between the Ni-centered spins. Fitting the χ_M^{-1} vs. T curve in the high-temperature region to the Curie-Weiss law gives a Curie constant C of 1.04 cm^3 K mol^{-1} and a Weiss temperature $\theta = –25.4$ K (Figures 3.39f, 3.42). In contrast to **Ni-1D**, **Ni-3D-ox** can be described as a network of isolated S = 1 spins

centered on Ni^{2+}, coupled by weak antiferromagnetic interactions. The weak antiferromagnetic coupling observed here further point to the absence of TIHQ-centered radicals, whose presence would have enabled strong exchange coupling with Ni-centered spin systems by analogy with molecular complexes.[28,57] The presence of organic radicals in **Ni-1D** and **Ni-2D** and absence thereof in **Ni-3D-ox** was confirmed by electron paramagnetic resonance (EPR) spectroscopy. Characteristic signal at g = 2.05 and 2.08 observed for **Ni-1D** and **Ni-2D**, respectively, is ~200 times weaker in **Ni-3D-ox** (Figure 3.43).
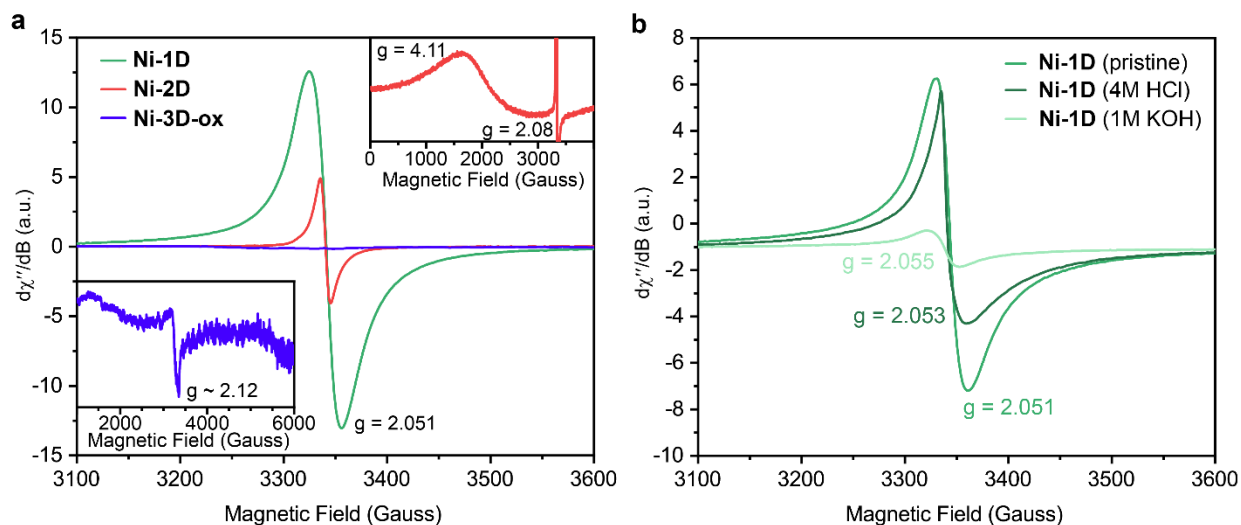
Figure 3.43. (a) EPR spectra of **Ni-1D** (green), **Ni-2D** (red), and **Ni-3D-ox** (blue) at ~4.5 K with similar mass loading. (b) EPR spectra of pristine **Ni-1D**, **Ni-1D** soaked in 4M HCl (aq.), and **Ni-1D** soaked in 1M KOH (MeOH solution) at ~4.5 K, exhibiting *g* values of 2.051, 2.053, and 2.055, respectively. We attribute the paramagnetism of **Ni-1D** to TIBQ-based radicals. The intense isotropic signal at g = 2.051 deviates slightly from that of cation-stabilized radicals (g ~ 2.003), suggesting the participation of Ni *d* orbitals in the TIBQ-centered molecular orbital of the odd spin.

3.3.6 Electrical Conductivities of Ni-Frameworks

The distinct electronic structures of **Ni-1D**, **Ni-2D**, and **Ni-3D(-ox)** give rise to electrical conductivities that span almost 8 orders of magnitude, from 10^{-9} S cm^{-1} to nearly 1 S cm^{-1}. Four-contact probe measurements of polycrystalline pellets of **Ni-1D** and **Ni-2D** revealed bulk electrical conductivities reaching 0.19 S cm^{-1} ($\bar{\sigma} = (0.16 \pm 0.02)$ S cm^{-1}), and 0.067 S cm^{-1} ($\bar{\sigma} = (0.054 \pm 0.009)$ S cm^{-1}), respectively, at room temperature (RT), which are on par with the most conductive 1D CCPs to date.[3] Interestingly, the conductivity of **Ni-1D** increased by about 60% to 0.27 S cm^{-1} after treatment with HCl (Figures 3.44, 3.45), similar to the *p*-doping of polyaniline. The transformation of **Ni-2D** to **Ni-1D** at RT over the course of several (Covid-induced lockdown) months coincided with a gradual increase in electrical conductivity (Figures 3.46a, 3.47-3.50). Given the similar crystallite size and the same metal-ligand connectivity in these two materials, we attribute the higherelectrical conductivity of **Ni-1D** to its interchain D-A stacking and its shorter π-π stacking distance.
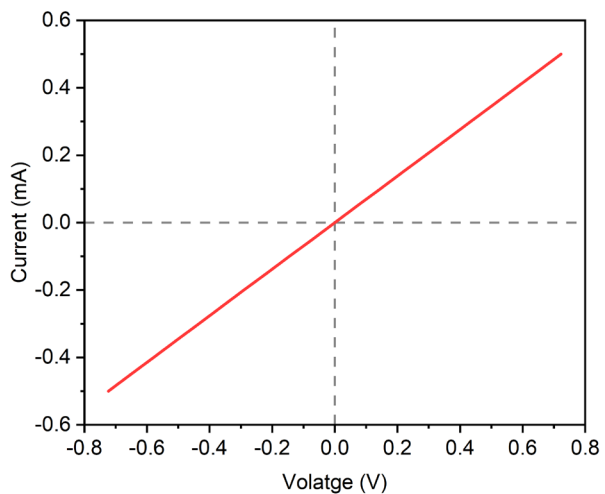
Figure 3.44. The linear I-V curve of a 4-probe device of **Ni-1D**, giving the conductivity value of 0.158 S/cm.
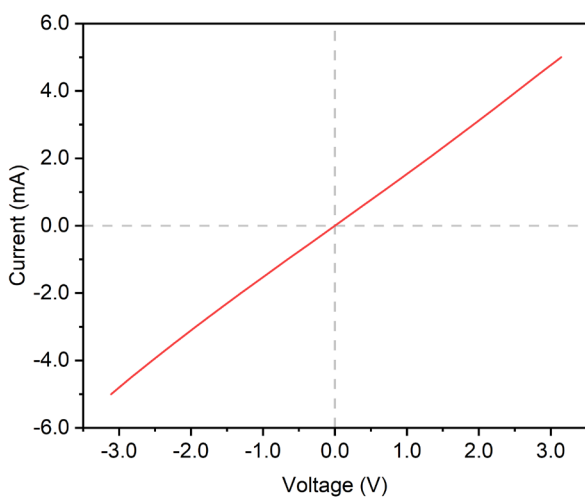
Figure 3.45. The linear I-V curve of a 4-probe device of 4 M HCl soaked **Ni-1D**, giving the conductivity value of 0.267 S/cm, which is about 1.6 times higher than **Ni-1D**.
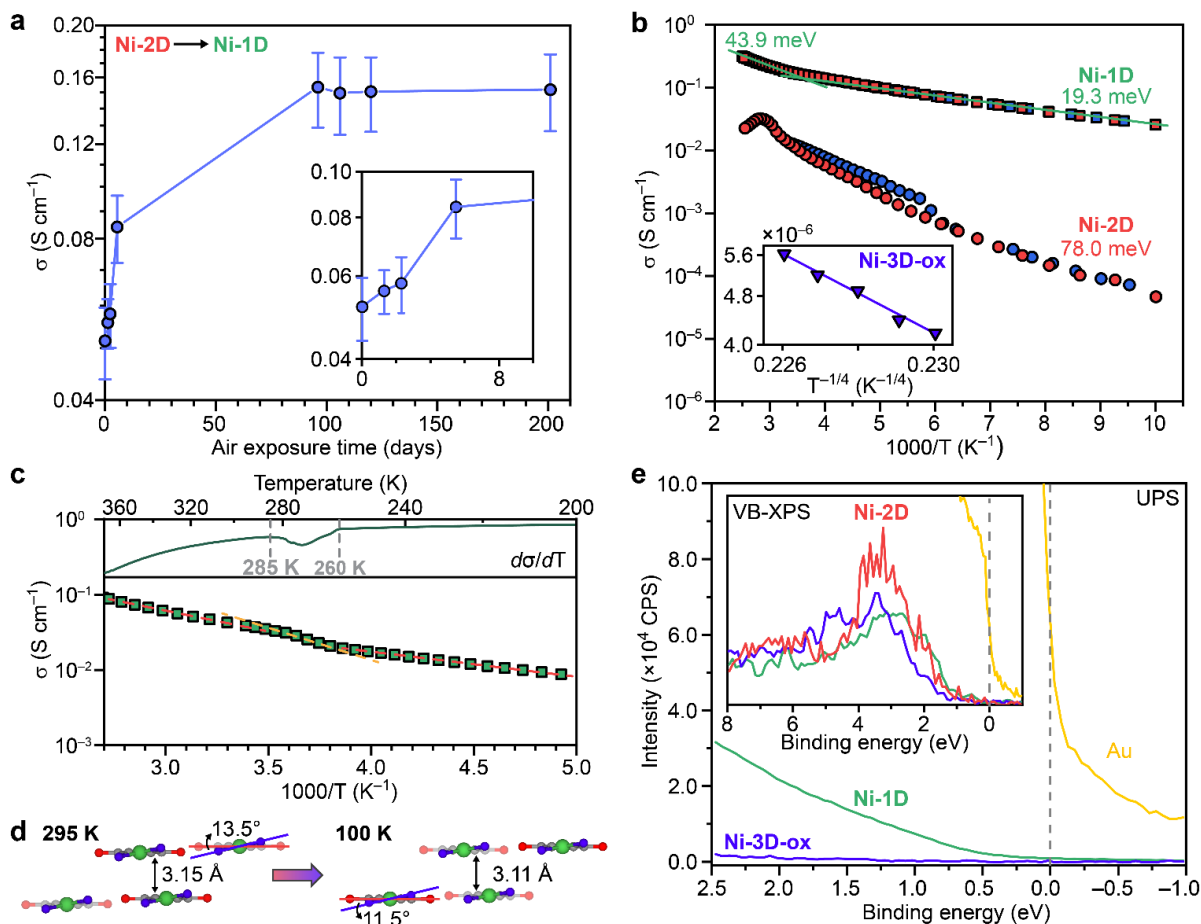
Figure 3.46. Electrical conductivity. (a) Conductivity increases during the transformation from **Ni-2D** to **Ni-1D** at ambient condition. Solid lines are guides to the eye. (b) Temperature dependence of four-probe conductivities of **Ni-1D**, **Ni-2D**, and **Ni-3D-ox**. Red, heating; blue, cooling. Solid lines are the best linear fit. (c) Reversible E_A change of **Ni-1D**. Inset, the first derivative of temperature dependence of electrical conductivity ($d\sigma/dT$). (d) Crystal structures of **Ni-1D** at 295 K and 100 K. (e) Fermi edge region of UPS and VB-XPS. Gray dashed lines are the Fermi edge calibrated by sputtering cleaned polycrystalline Au reference.
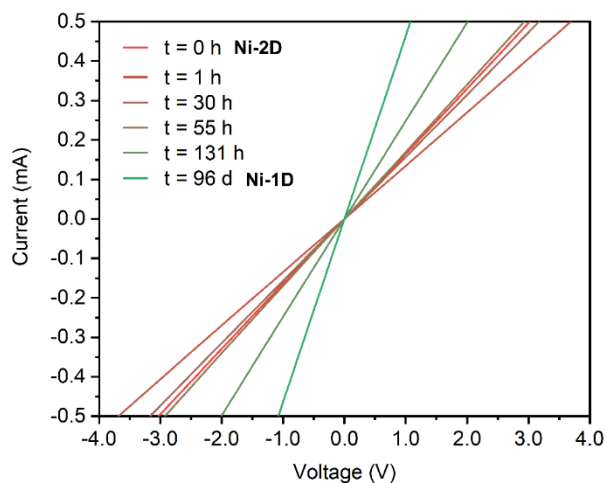
Figure 3.47. Linear I-V curves of a 4-probe device (device 1) of **Ni-2D** during the transformation to **Ni-1D**, giving the initial conductivity value (**Ni-2D**) of 0.0667 S cm^{-1}, which finally increased to 0.188 S cm^{-1} after 96 days under ambient condition.

140
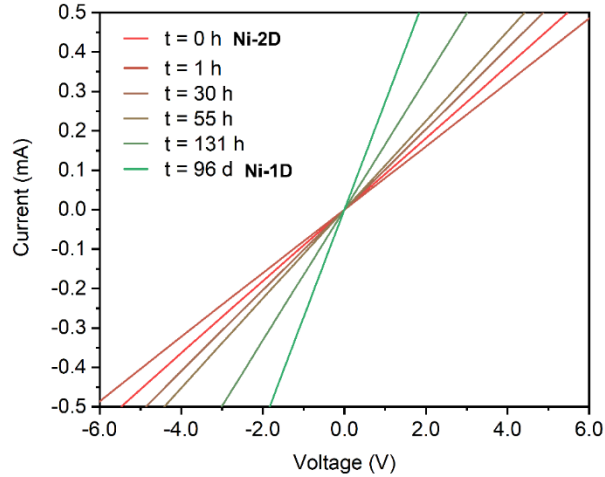
Figure 3.48. Linear I-V curves of a 4-probe device (device 2) of **Ni-2D** during the transformation to **Ni-1D**, giving the initial conductivity of 0.0439 S cm^{-1}, which increased to 0.132 S cm^{-1} after 96 days under ambient condition.
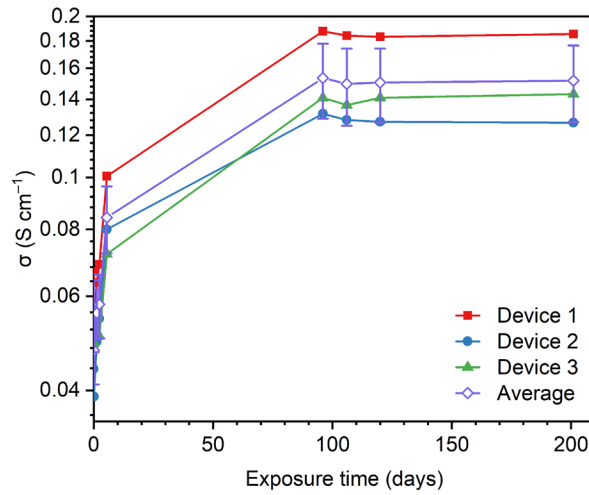
Figure 3.49. Electrical conductivity changes of three 4-probe devices during the **Ni-2D** to **Ni-1D** transformation.
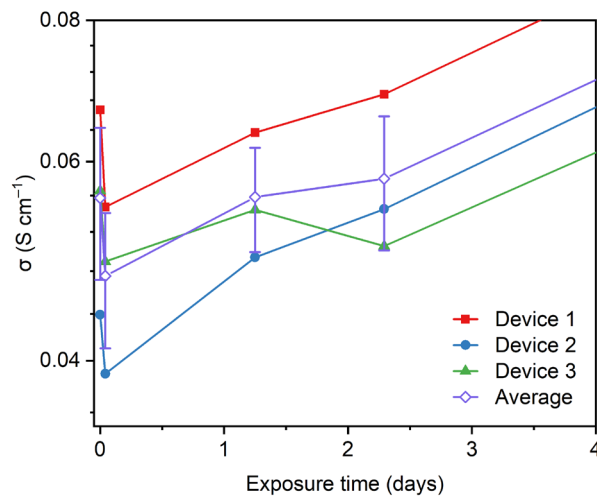
Figure 3.50. The initial decrease of electrical conductivity of the 4-probe devices. We hypothesized that the initial loss of bridging water molecules induced substantial amount of deep carrier traps originated from structural defects, according to the Multiple Trap and thermally Release (MTR) model, leading to the decrease of electrical conductivity. A similar feature was also observed in the variable temperature conductivity measurement of **Ni-2D**.

Under anaerobic conditions, **Ni-3D** exhibits a two-probe electrical conductivity of 6.2×10^{-9} S cm^{-1}, as may be expected in the absence of π-π stacking and weak covalency of the metal-ligand bond.[1,2] Upon exposure to air, the conductivity increases to 6.7×10^{-7} S cm^{-1} after 12-hours, to finally reach a maximum conductivity of 2.9×10^{-5} S cm^{-1} for **Ni-3D-ox**, a remarkable value for 3D-connected, porous MOFs.[58] The increase in conductivity in going from **Ni-3D** to **Ni-3D-ox** is paralleled by a substantial decrease of E_o (~0.5 eV). This implies that increasing the ligand oxidation state modifies the electronic structure of the framework, which translates to improved charge transport.

Variable-temperature conductivity measurements revealed semiconducting behavior for all three materials (Figure 3.46b). **Ni-1D** and **Ni-2D** exhibit Arrhenius-type dependence of the conductivity with temperature T:

$$\sigma_{e,T} = \sigma_{e,\infty} \exp\left(-\frac{E_A}{k_B T}\right)$$

where $\sigma_{e,\infty}$ is the temperature-independent prefactor, and E_A is the thermal activation energy. This behavior is typical for doped organic semiconductors and conductive MOFs with band-like charge transport.[1,2,59]

A notable increase in E_A for **Ni-1D** from 19.3 meV at T < ~260 K to 43.9 meV at T > ~285 K (Figures 3.46c, 3.51) is correlated with a reversible structural change that occurs at approximately 270 K (Figures 3.46c, 3.52). Indeed, Rietveld refinement of synchrotron PXRD data for **Ni-1D** at 295 K (Figure 3.53) revealed a longer interchain π-π stacking distance of 3.15 Å (3.11 Å at 100 K) and a larger dihedral angle of 13.5° between the six-membered carbon ring and five-membered Ni chelating ring (11.5° at 100 K) (Figure 3.46d), suggesting that the interchain and intrachain transport are both weakened, in agreement with the higher E_A.
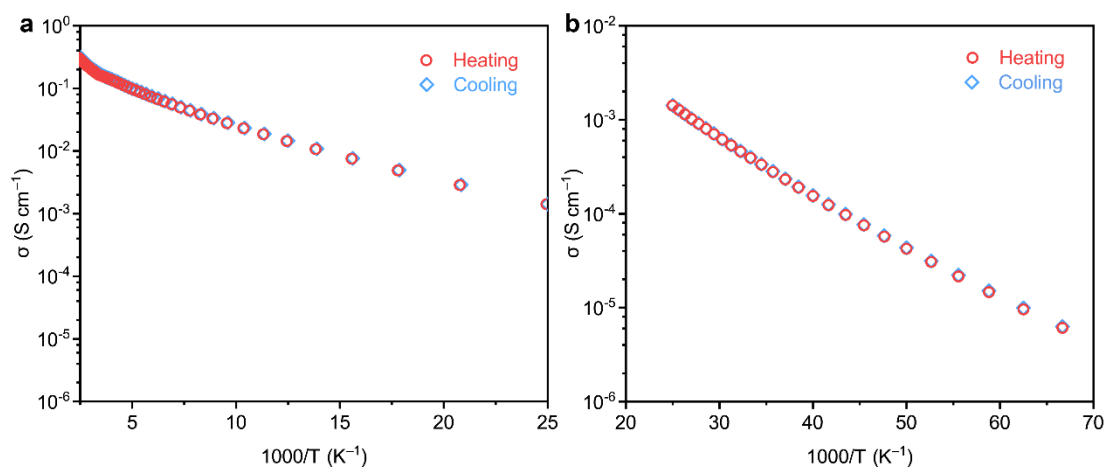
Figure 3.51. Variable temperature electrical conductivity measurement of a 4-probe device of **Ni-1D**. (a) 400 K to 40 K. (b) 40 K to 15 K. We observed a subtle E_A decreasing with temperature decreasing. For example, fitting the data between 40 K and 15 K to Arrhenius equation gave an E_A of 11.4 meV, which is slightly lower than the E_A obtained by fitting the 400 K to 100 K data.
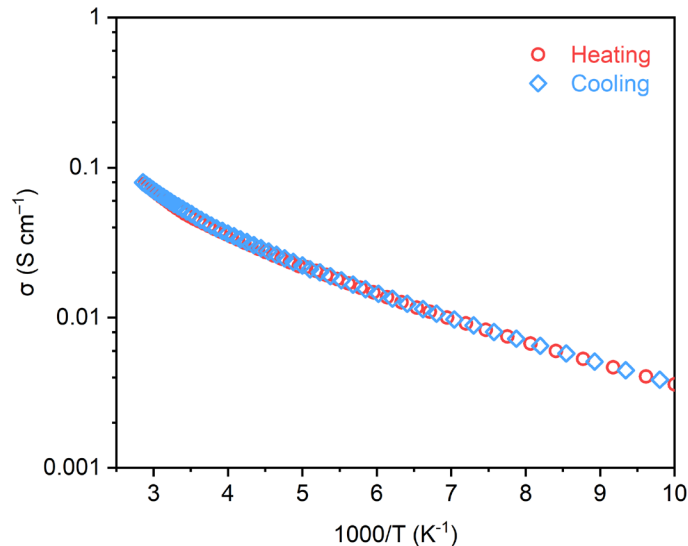
Figure 3.52. Variable temperature electrical conductivity measurement of another 4-probe device of **Ni-1D**. The reversible structural change was also observed.

Ni-2D showed significantly higher E_A of 78.0 meV in the temperature range 100–300 K (Figure 3.46b). The apparent decrease in conductivity above 60 °C is *not* an indication of transition to a temperature-deactivated transport. Rather, we attribute it to partial transformation of **Ni-2D** to **Ni-1D**; the associated disorder accompanying this transformation is the more likely cause of decreasing electrical conductivity with temperature (Figure 3.54). For context, these E_A values are still smaller than that observed for heavily *n*-doped C_{60}, one of the most conductive doped organic semiconductors, and suggest exceptional electronic coupling and small energetic disorder in our materials.[59]
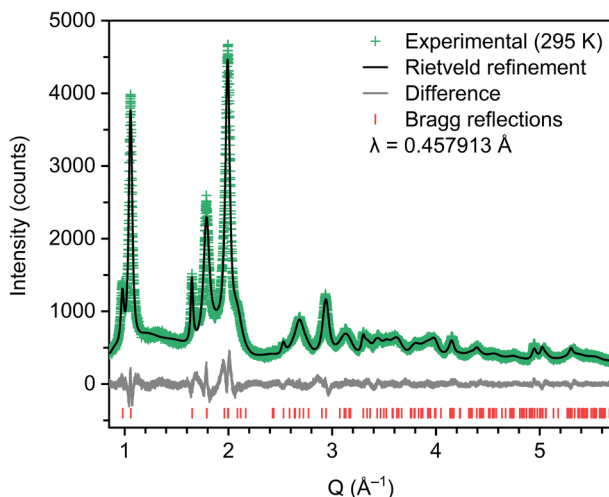
Figure 3.53. Rietveld refinement of synchrotron PXRD data of **Ni-1D** at 295 K. R_p=4.30%, R_{wp}=5.29%, R_{exp}=3.69%, and GoF=1.43. The resulting lattice parameters are: a = 11.92 Å, b = 7.62 Å, c = 3.52 Å; $\alpha = \gamma = 90°$, $\beta = 95.385°$. Space group remained the same: C2/m.
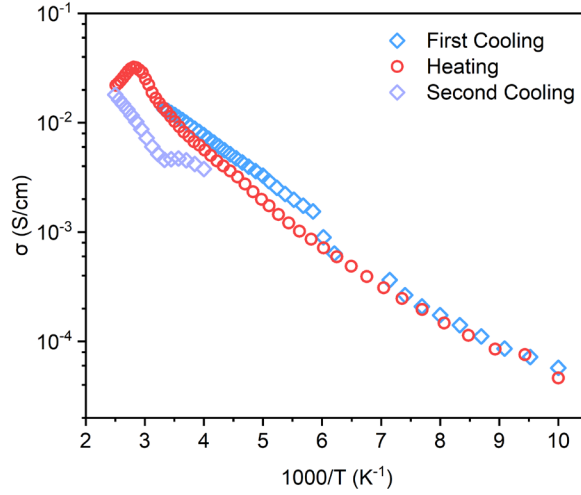
Figure 3.54. Variable temperature electrical conductivity measurement of a 4-probe device of **Ni-2D**. Cooling sequence was applied first to prevent its transformation to **Ni-1D**. However, the transformation happened during the heating sequence above RT. Therefore, a hysteresis-like feature was observed that actually resulted from the chemical transformation.

In contrast to the lower dimensionality structures, **Ni-3D-ox** shows variable-range hopping (VRH) transport, which is best described by Mott's VRH theory (Figures 3.46b inset, 3.55),[60]

$$\sigma_{e,T} = \sigma_{e,0}\exp\left[-\left(\frac{T_0}{T}\right)^{\frac{1}{d+1}}\right]$$

where d is the dimensionality of transport (d = 3 for **Ni-3D-ox**), $\sigma_{e,0}$ is the temperature-independent constant and equals the T→∞ value of $\sigma_{e,T}$, and T_0 is the Mott temperature. The latter is related to the charge carrier concentration and carrier hopping length between adjacent localized states. We believe that the increased conductivity of Ni-3D-ox relative to Ni-3D is due to ligand oxidation, which generates charge carriers and localized sites that overall decrease the hopping distance. We note that VRH theory also fits the variable temperature conductivity data for **Ni-2D** (with d = 2), indicating that the charge transport in this material occurs primarily within the 2D layers and that interlayer electronic interactions are weak (Figure 3.56).
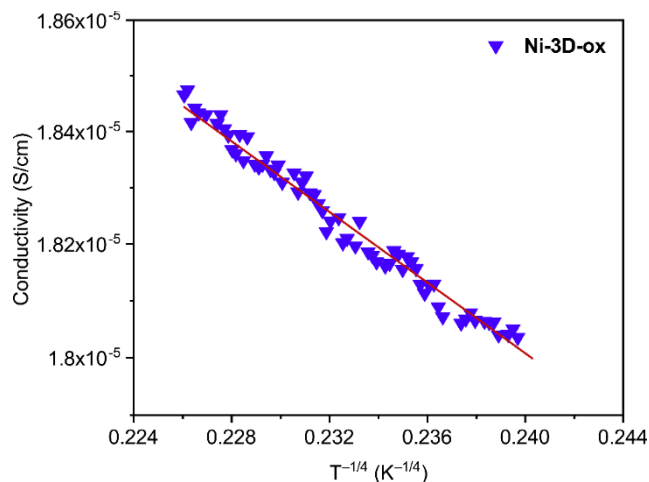
Figure 3.55. Variable temperature electrical conductivity measurement of a 2-probe device of **Ni-3D-ox**. Red solid line represented the best fit.
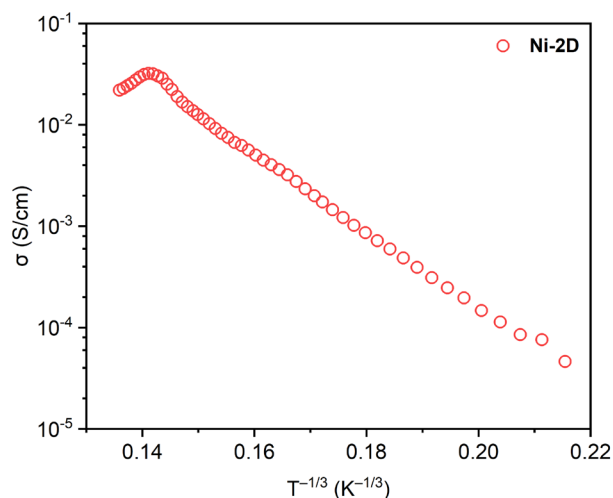
Figure 3.56. Variable temperature electrical conductivity of **Ni-2D** plotted for 2D VRH theory, revealing excellent linear relationship between 300 K and 100 K.

Valence-band XPS (VB-XPS) and ultraviolet photoelectron spectroscopy (UPS) corroborate the electronic structure insights afforded by conductivity measurements. The highest occupied states (HOS) of **Ni-1D** and **Ni-3D-ox** revealed by UPS are, respectively, ~0.45 eV and ~1.3 eV below the Fermi level E_F (Figures 3.46e, 3.57). Fitting of the VB-XPS edge gives higher HOS level for **Ni-1D**, which is only about ~0.2 eV below E_F, indicating the substantial contribution of Ni orbitals to the density of states (DOS) near the valence band maximum (VBM) and the close match of ligand and metal energy levels (Figure 3.58). The shallow HOS below E_F of **Ni-1D** is consistent with its high electrical conductivity. **Ni-2D** exhibits moderate HOS (~0.6 eV below E_F), again in good agreement with its slightly lower conductivity relative to **Ni-1D.**
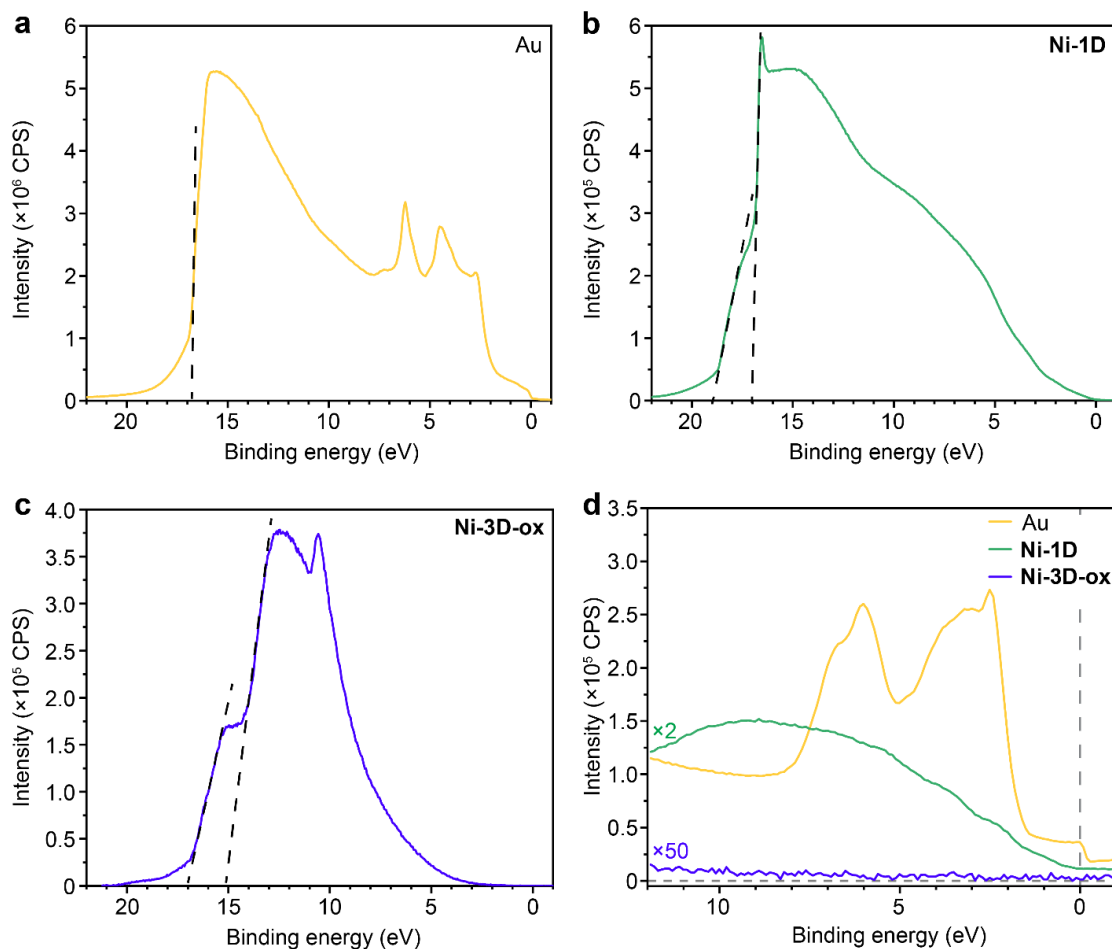
Figure 3.57. Secondary electron cut-off regions of UPS (He I) of Au reference (a), **Ni-1D** (b), and **Ni-3D-ox** (c). The shoulder-like cut-off feature in both **Ni-1D** and **Ni-3D-ox** is likely related to the presence of different vacuum state (E_{vac}) due to surface state of these materials, resulting in localized smaller work functions. (d) He II UPS spectra of Au reference, **Ni-1D**, and **Ni-3D-ox**. The Φ_{Au} was calculated to be 4.24 eV, which is typical for polycrystalline Au that has been exposed to air. For **Ni-1D**, the main cutoff is ~17.4 eV with an additional feature at ~19.3 eV, corresponding to local E_{vac} difference. Therefore, $\Phi_{\text{Ni-1D}}$ was calculated to be 3.8 eV, similar to that obtained from VB-XPS. **Ni-3D-ox** has the primary cutoff at ~15.0 eV, and the additional cutoff is at ~17.0 eV. The work function is ~6.2 eV, similar to that of Co_3O_4 and MoO_2. The HOS of **Ni-1D** obtained from UPS is ~0.45eV below Fermi level. VB-XPS fitting gave higher HOS level, which is only about ~0.2 eV below Fermi level. The HOS of **Ni-3D-ox** obtained from UPS is ~1.3 eV, calculated by plotting its UPS spectrum in the log scale. The IE of **Ni-1D** obtained from UPS is calculated as 4.25 eV, and the IE of **Ni-3D-ox** is 7.5 eV.

146
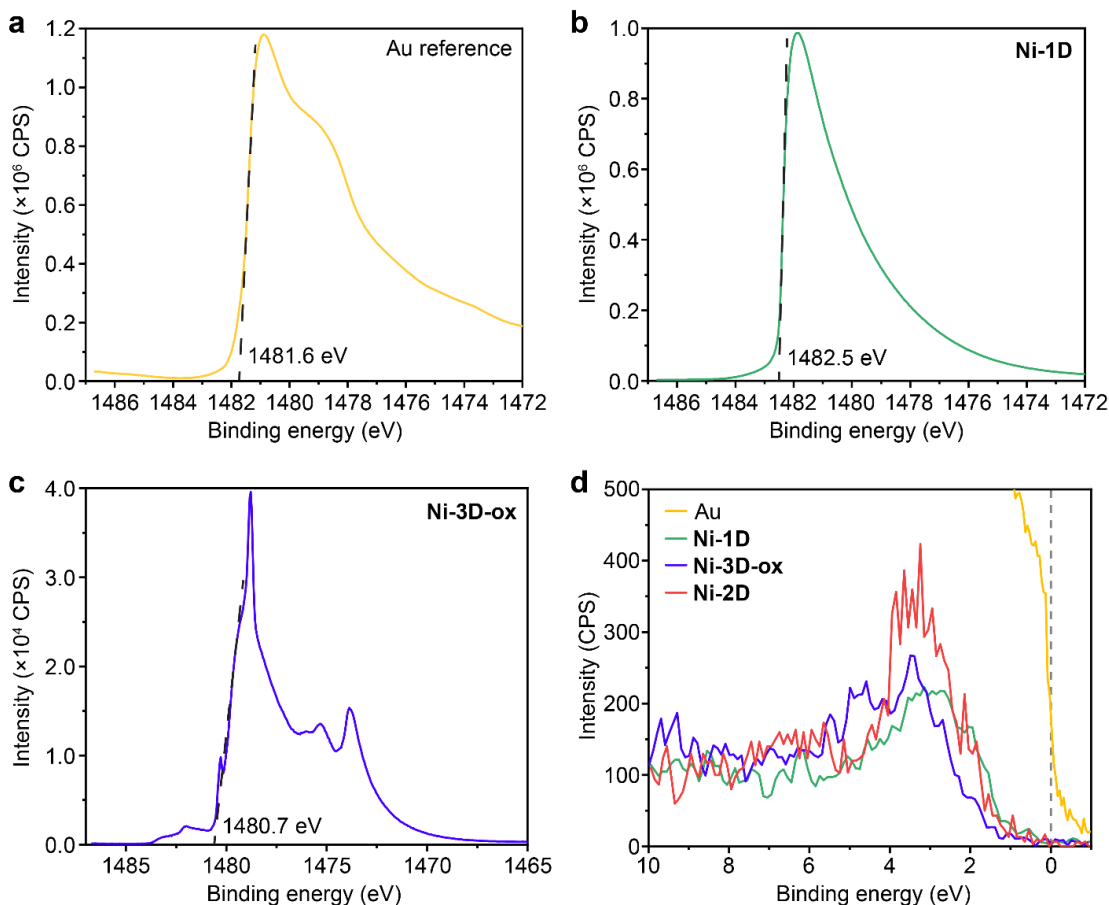
Figure 3.58. Cut-off region of VB-XPS of Au reference (a), **Ni-1D** (b), and **Ni-3D-ox** (c). (d) Fermi edge region of VB-XPS. The Fermi edges of materials were aligned to E_F of Au reference since they are all attached on the same biasing stage. Fitting the cut-off region gives the position of second-electron cut-off for calculating the work function (Φ): $\Phi = E_{photon} - E_{cut\text{-}off}$. Therefore, Φ_{Au} was calculated as 1486.7 eV – 1481.6 eV = 5.1 eV. Although slightly smaller than the literature reported value 5.3 eV, it is commonly observed for polycrystalline gold when atomically clean and ordered under ultra-high vacuum. $\Phi_{Ni\text{-}1D}$ and $\Phi_{Ni\text{-}3D\text{-}ox}$ were also calculated to be 4.2 eV and 6.0 eV, respectively. The highest occupied state (HOS) or valence band maximum (VBM) of **Ni-1D** is ~0.2 eV below the Fermi level referenced by Au, whereas that of oxidized **Ni-3D-ox** is ~1.3 eV. The HOS of **Ni-2D** is ~0.6 eV below E_F. Therefore, combined with the work functions, the ionization energies (*IE*) of **Ni-1D** and **Ni-3D-ox** were determined to be 4.4 eV and 7.3 eV, respectively. We note that the *IE* of **Ni-1D** is similar to that of highly conductive heavily n-doped ZnPc and C_{60}, whereas the *IE* of **Ni-3D-ox** is similar to that of semiconducting transition metal oxides such as NiO and TiO_2.

3.4 Conclusions and Outlook

Despite the considerable interest in electronic properties of MOFs and coordination polymers, it has been difficult to design systems that enable correlations between physical properties and structure. Indeed, when structure-function relationships are discussed in this context, changes in structure usually are also accompanied or caused by compositional changes.[61–63] Here, we showed that owing to their multiple redox states and metal binding preference, the redox series comprising TAHQ, TABQ, and TIBQ provides a unique platform to study structure-function relationships in essentially isomeric Ni MOFs/coordination

147

polymers. These results thus provide important insight into how dimensionality and various supramolecular interactions between SBUs, ligands, and structural motifs (i.e. D-A, hydrogen bonding, and π-π stacking) lead to differences of nearly 8 orders of magnitude in electrical conductivity. Ligands that combine similar breadth of redox states and metal-chelating motifs should provide inspiration for future material design.

3.5 Methods and Materials

3.5.1 Materials

Ni(OAc)$_2$·4H$_2$O (Strem), potassium phthalimide (Sigma Aldrich), tetrachloro-p-benzoquinone (Sigma Aldrich), hydrazine monohydrate (80.0 wt.%, TCI America), concentrated aqueous ammonia (~14 M), SnCl$_2$·2H$_2$O (Alfa Aesar), concentrated HCl (~36%), N,N-dimethylformamide (DMF), ethanol (EtOH), acetonitrile (ACN) and methanol (MeOH) were used as received without further purification. House DI water and house nitrogen were used during the synthesis. NMR solvents were purchased from Cambridge Isotope Laboratory.

3.5.2 Synthetic Methods
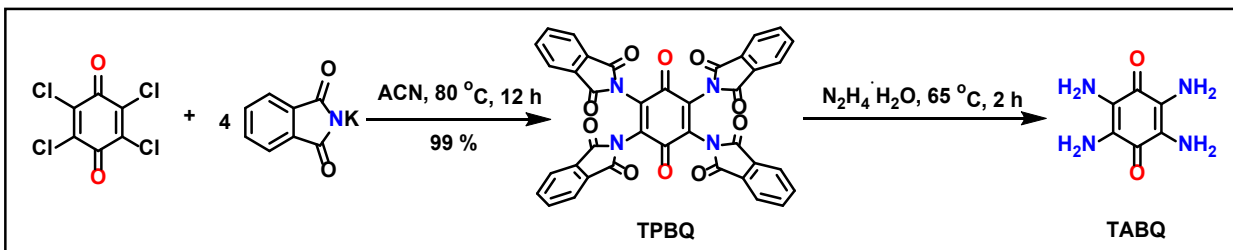
Scheme 3.1. Overview of the synthesis of tetraamino-p-benzoquinone (TABQ). The synthesis was modified based on previous literature reports.

Tetra(phthalimido)-p-benzoquinone (TPBQ)

To a stirred solution of tetrachloro-p-benzoquinone (25 g) in 250 mL acetonitrile, potassium phthalimide (75 g) was added. The reaction mixture was heated at 80 °C and refluxing for 12 h under N$_2$ atmosphere, after which the reaction mixture was cooled down to room temperature and filtered. The resulting solid was washed with 300 mL of acetonitrile and then suspended in 100 mL of DMF. The dark colored suspension was heated at 100 °C and stirred for 30 min, which was followed by hot filtration to obtain brown solid. The resulting solid was suspended in DMF/EtOH (v/v = 1:1), and the mixture was sonicated for 1 hour, and then filtered to obtain pale tan solid with quantitative yield (69.3 g, 99%). The purity of TPBQ was verified by ATR-FTIR (Figure 3.59), given the insolubility of TPBQ preventing any solution NMR characterizations.
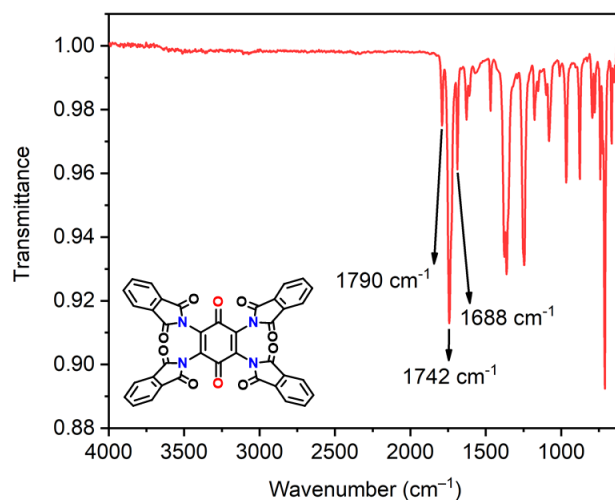
Figure 3.59. ATR-FTIR spectrum of TPB, matching the results from previous literature reports.

Tetraamino-p-benzoquinone (TABQ)

To a 500 mL round bottom flask was added 35 g of TPBQ, followed by the addition of 125 mL of hydrazine hydrate (80.0 wt%). The reaction mixture was heated at 65 °C for 2 hours, after which it was cooled to room temperature, filtered and washed with DI water until the filtrate coming out is colorless. The resulting deep purple crystalline solid (3.77 g, 44%) was deemed to be pure TABQ by ^{1}H-NMR (Figure 3.60) and ^{13}C-NMR (Figure 3.61).
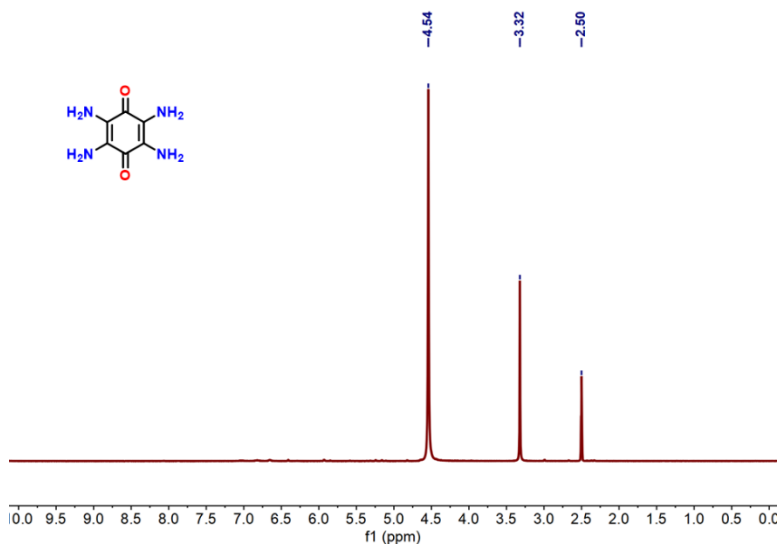
Figure 3.60. ^{1}H-NMR spectrum of TABQ.

149
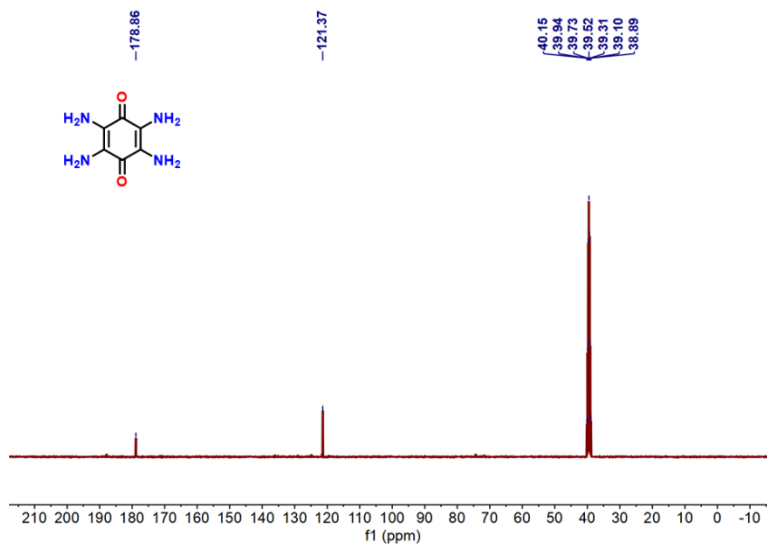
Figure 3.61. ^{13}C-NMR spectrum of TABQ.
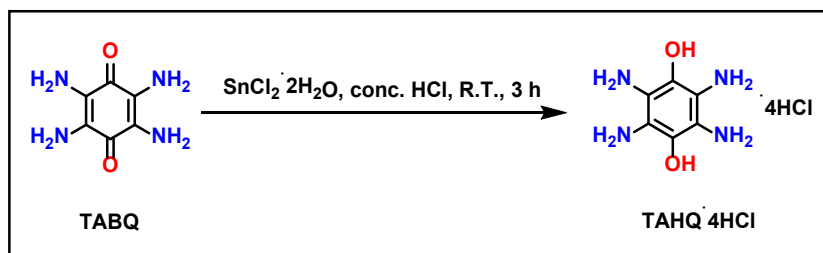
Scheme 3.2. Overview of the synthesis of tetraamino-*p*-hydroquinone tetrahydrochloride (TAHQ·4HCl). The synthesis was modified based on previous literature reports.
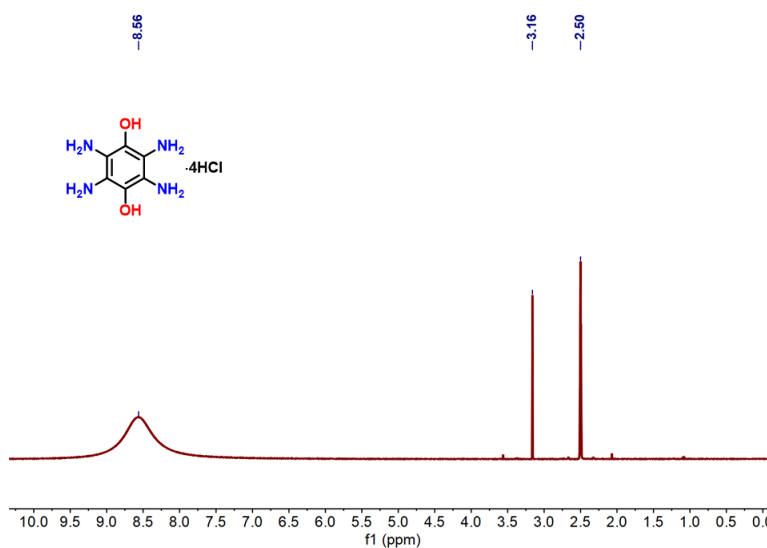
Figure 3.62. ^{1}H-NMR spectrum of TAHQ·4HCl.

Tetraamino-*p*-hydroquinone tetrahydrochloride (TAHQ·4HCl)

825 mg of TABQ (very fine powdered), 1.68 g of $SnCl_2·2H_2O$ (1.5-fold excess), and 10 mL of conc. hydrochloric acid were stirred in a 25 mL Schlenk flask at room temperature under N_2 atmosphere for 3 hours. The resulting reaction mixture was filtered by vacuum filtration in a nitrogen-purging box and washed twice with degassed anhydrous methanol. The resulting solid was collected and transferred into a glove box for drying and storage. 1.24 g of gray solid (TAHQ·4HCl) was obtained at a yield of 80%. Pale pink colored solid (TAHQ·4HCl (pink)) was obtained when conducting filtration and washing steps without the protection of N_2 atmosphere, which represents the partially oxidized TAHQ·4HCl.

Synthesis of Ni-2D Rods

In a N_2 purging box, 20 mg of TABQ and 44 mg of $Ni(OAc)_2·4H_2O$ were transferred into a 15 mL thick-wall pressure tube, followed by the addition of 0.5 mL of degassed DI water and 2.4 mL of degassed concentrated aqueous ammonia solution. The pressure tube was sealed and heated at 120 ℃ in an isothermal oven for 2 days, after which the tube was cooled down to room temperature. The resulting crystalline precipitate was filtered under N_2 atmosphere and washed with a large amount of degassed DI water. The solid was briefly dried under the N_2 flow on the filtration setup and was used immediately for further characterization.

Synthesis of NiTIBQ(D$_2$O/H$_2$O) Rods

In a N_2 purging box, 20 mg of TABQ and 44 mg of $Ni(OAc)_2·4H_2O$ were transferred into a 15 mL thick-wall pressure tube, followed by the addition of 0.5 mL of degassed D_2O and 2.4 mL of degassed concentrated aqueous ammonia solution. The pressure tube was sealed and heated at 120 ℃ in an isothermal oven for 2 days, after which the tube was cooled down to room temperature. The crystalline precipitate was filtered under N_2 atmosphere and washed with large amount of degassed D_2O. The solid was briefly dried under N_2 flow on the filtration setup and was used immediately for ATR-FTIR and PXRD. The resulting bulk solid contains both bridging H_2O and D_2O.

Synthesis of Ni-1D Rods/Bricks

Under the ambient condition, 20 mg of TABQ and 44 mg of $Ni(OAc)_2·4H_2O$ were transferred into a 15 mL thick-wall pressure tube, followed by the addition of 0.5 mL of DI water and 2.4 mL of concentrated aqueous ammonia solution. The pressure tube was sealed (the atmosphere inside the tube is air) and heated at 120 ℃ in an isothermal oven for 2 days, after which the tube was cooled down to room temperature. The resulting black crystalline precipitate was filtered under ambient condition and washed with large amount of DI water and methanol. The solid was dried at room temperature under a dynamic vacuum for at least 24 hours.

Synthesis of Ni-3D Rods

In a N_2 purging box, 15 mg of TAHQ·4HCl and 18 mg of $Ni(OAc)_2$·$4H_2O$ were transferred into a 15 mL thick-wall pressure tube, followed by the addition of 1 mL of degassed concentrated aqueous ammonia solution. The pressure tube was sealed and heated at 120 °C in an isothermal oven for 1 day, after which the tube was cooled down to room temperature and transferred into a N_2 glove box. The reaction mixture was transferred to a 20 mL glass vial and the supernatant was decanted to obtain **brown** crystals at the bottom of the vial. The resulting solid was washed with degassed DI water at least 3 times and was dried under N_2 flow.

Workup in the ambient condition gives **Ni-3D-ox**:

After cooled down to room temperature, the reaction mixture was filtered and washed with large amount of DI water. The resulting **black** solid was dried under air flow on the filtration setup. The black color of the resulting solid indicates the air oxidation of the framework.

3.5.3 Physical Characterization Methods

Laboratory powder X-ray diffraction (PXRD)

PXRD patterns were recorded using a Bruker Advance II diffractometer equipped with a θ/2θ reflection geometry and Ni-filtered Cu Kα radiation (Kα$_1$ = 1.5406 Å, Kα$_2$ = 1.5444 Å, Kα$_2$/ Kα$_1$ = 0.5). The tube voltage and current were 40 kV and 40 mA, respectively. Samples for PXRD were prepared by placing a thin layer of the appropriate material on a zero-background silicon crystal plate.

cRED data collection, procession, and structure solution of Ni-2D and Ni-3D-ox

The crystals were dispersed in ethanol and ultrasonication for 5 min. A droplet of suspension was then transferred on a copper grid with carbon film. The cRED data were collected on 200kV JEOL JEM-2100 transmission electron microscope equipped with a quad hybrid pixel detector (Timepix, 512 × 512 pixels, pixel size 55 μm, Amsterdam Sci. Ins.). Before data collection, the sample was cooled down to 96 K by using Gatan cryo-transfer tomography holder. During the data collection, the goniometer was rotated continuously while the selected area electron diffraction (ED) patterns were captured from the crystal simultaneous by using the software of *instamatic*. In order to balance the intensity of electron diffraction and resolution, all the ED patterns were recorded under the spot size 3 with the exposure time 0.5 s. The 3D reciprocal lattice was reconstructed by the software REDp, which was very useful for indexing and obtaining the reflection conditions.

For the structure solution of **Ni-2D**, five crystals were measured and indexed with orthorhombic symmetry, leading to mean lattice parameters of a = 12.442(3) Å, b = 7.7419(15) Å, c = 3.3457(7) Å in space group *Immm* (Figure 3.7, reflection condition: $hk0, h + k = 2n, h0l, h = 2n, 0k0, k = 2n$). The X-ray crystallography software package *XDS* was used for data processing to estimate integrated diffraction

intensities. To improve the completeness, *XSCALE* was then applied for data merging, which resulted in a completeness of 88.9% by merging the five datasets. The SHELX software package was used for structural analysis, where SHELXT was used for structure solution. As the resolution of cRED datasets was measured down to 0.718 Å (Figure 3.6), all non-hydrogen atomic positions in **Ni-2D** framework were located directly by *ab initial* method. The SHELXL was used for structure refinement using electron scattering factors for all the atoms. The atomic displacement parameters (ADPs) for all framework atoms were refined anisotropically.

For the structure solution of **Ni-3D-ox**, four cRED datasets were collected on individual crystals with a resolution down to 0.767 Å (Figure 3.23). The cRED data were indexed with hexagonal symmetry, resulting in mean lattice parameters of a = 21.656(3) Å, c = 11.399(2) Å, in space group $R\bar{3}m$. (Figure 3.24, reflection condition: $hkil$, $-h + k + l$ = 3n, $h\bar{h}0l$, $h + l$ = 3n, $hh\overline{2h}l$ l = 3n, 000l, l = 3n). As with **Ni-2D**, the cRED data procession and structure solution for **Ni-3D-ox** were conducted using XDS and SHELX software based on the merged four datasets. The completeness of merged datasets for the **Ni-3D-ox** was up to 99.4%. To deduct the contribution of diffraction from the disordered guest molecules in the pores, the PLATON/SQUEEZE procedure was conducted during the refinement for **Ni-3D-ox** (Figure 3.28). Crystallographic details of **Ni-2D** and **Ni-3D-ox** are summarized in Table 3.4.

High-resolution synchrotron PXRD

Data were collected at 100 K or 295 K in beamline 11-BM at the Advanced Photon Source (APS), Argonne National Laboratory using the Debye-Scherrer geometry and an average wavelength of 0.457840 Å. Discrete detectors covering an angular range from -6 to 28° 2θ are scanned over a 34° 2θ range, with data points collected every 0.001° 2θ (actual 2θ/step is 0.0009984375°) and scan speed of 0.1 s/step. The 11-BM instrument uses X-ray optics with two platinum-striped mirrors and a double-crystal Si(111) monochromator, where the second crystal has an adjustable sagittal bend. Ion chambers monitor incident flux. A vertical Huber 480 goniometer, equipped with a Heidenhain encoder, positions an analyzer system comprised of twelve perfect Si(111) analyzers and twelve Oxford-Danfysik $LaCl_3$ scintillators, with a spacing of 2° 2θ. Analyzer orientation can be adjusted individually on two axes. A three-axis translation stage holds the sample mounting and allows it to be spun, typically at ~5400 RPM (90 Hz). A Mitsubishi robotic arm is used to mount and dismount samples on the diffractometer. Oxford Cryosystems Cryostream Plus device allows sample temperatures to be controlled over the range 80-500 K when the robot is used. The diffractometer is controlled via EPICS. Data are collected while continually scanning the diffractometer 2θ arm. A mixture of NIST standard reference materials, Si (SRM 640c) and Al_2O_3 (SRM 676) is used to calibrate the instrument, where the Si lattice constant determines the wavelength for each detector. Corrections are applied for detector sensitivity, 2θ offset, small differences in wavelength

between detectors, and the source intensity, as noted by the ion chamber before merging the data into a single set of intensities evenly spaced in 2θ.

Structure determination of Ni-1D

Rietveld refinements of synchrotron PXRD data were conducted using TOPAS Academic (version 6). The refined lattice parameters of **Ni-1D** at 100 K are a = 11.8228(45) Å, b = 7.6175(52) Å, c = 3.4942(2) Å, β = 94.656° in the space group C2/m, with R_{wp} = 5.336, R_{exp} = 3.843, R_p = 4.17, and GoF = 1.388. The refined lattice parameters of Ni-1D at 295 K are a = 11.9231(38) Å, b = 7.6170(96) Å, c = 3.5210(23) Å, β = 94.385(1)° in the same space group C2/m, with R_{wp} = 5.289, R_{exp} = 3.692, R_p = 4.296, and GoF = 1.433.

N₂ adsorption isotherms

Isotherms were measured by a volumetric method using a Micromeritics ASAP 2020 Plus gas sorption analyzer. An oven-dried sample tube equipped with a TranSeal™ (Micromeritics) was evacuated and tared. The sample was transferred to the sample tube, which was then capped with a TranSeal™. The sample was activated at 100 °C under high dynamic vacuum (< 10^{-4} mbar) for 24 hours before analysis. The N_2 isotherm was measured using a liquid nitrogen bath at 77 K. Ultrahigh purity grade (99.999% purity) N_2, oil-free valves and gas regulators were used for all the free space correction and measurements. Fits to the Brunauer-Emmett-Teller (BET) equation satisfied the published consistency criteria.

Thermogravimetric analysis (TGA)

TGA was performed on a TA Instruments Q500 Thermogravimetric Analyzer at a heating rate of 2.0 °C/min under air or N_2 gas flow of 5 mL/min on a platinum pan from room temperature to 700 °C.

Elemental analyses

Elemental analyses were performed by Robertson Microlit Laboratories, Ledgewood, New Jersey.

X-ray photoelectron spectroscopy (XPS)

XPS measurements were performed at the MIT MRSEC (formerly the Center for Materials Science and Engineering, or CMSE) using a Physical Electronics PHI Versaprobe II X-ray photoelectron spectrometer equipped with a monochromatic Al anode X-ray source. The main chamber pressure was in the 10^{-10} Torr range. MOF powder samples were pressed on copper tapes with full coverage. Survey spectra were collected from 0~1100 eV in binding energy (BE), with a resolution of 0.8 eV. High resolution spectra of C1s, N1s, and M2p regions were collected with a resolution of 0.1 eV. BE calibration was carried out by shifting the adventitious carbon C1s peak to 284.8 eV. Deconvolution of the C1s spectra were conducted before BE calibration to find out the adventitious carbon C1s peak, given that the MOF samples also contain significant amount of carbon. Gaussian-Lorentzian product function with 30% of Lorentzian component was used for the line shapes during fitting, which is commonly used for C1s. The lineshape used for fitting O 1s spectra is GL(30)T(2). Valence band XPS (VB-XPS) was collected with a resolution of 0.05 eV.

Ultraviolet photoelectron spectroscopy (UPS)

XPS measurements were performed at the Harvard CNS using Thermo Scientific Nexsa XPS equipped with a monochromated, micro-focused, and low power Al Kα X-ray source (1486.7 eV) and helium discharge lamp for UPS (He I: 21.2 eV; He II: 40.8 eV). Pressed pellets of Ni-1D and Ni-3D-ox were loaded onto a biasing sample stage. A –10 V bias was applied for secondary electron cut-off measurements (i.e., work function measurement). The pellets were sputtered clean before acquiring spectra. A polycrystalline Au film was used to calibrate the position of Fermi level. The work function measurement using XPS also used the biasing stage and a –10 V bias was applied during the measurement.

Scanning electron microscopy (SEM)

SEM images were collected at MIT MRSEC (formerly the Center for Materials Science and Engineering, or CMSE) on a Zeiss Merlin high-resolution scanning electron microscope with an InLens detector at an operating voltage of 3 or 4 kV.

Cryo-HRTEM

Cryo-HRTEM images were obtained at the Automated Cryogenic Electron Microscopy Facility in MIT.nano on a Talos Arctica G2 microscope operated at an accelerating voltage of 200 kV with a Falcon3EC direct electron detector. Samples were prepared by sonicating MOF/CCP powders in isopropanol for 5 to 10 seconds. Specimens were prepared by drop-casting sonicated samples onto C-flat^{TM} Cu grids with holey carbon for Cryo-EM. All image acquisition was done using EPU at an exposure time of 1 s, with focusing done adjacent to the region imaged to minimize beam exposure prior to image acquisition (standard low dose imaging protocols). Analysis of the raw HRTEM data was done using Gatan Microscopy Suite software (GMS 3). For **Ni-2D**, the specimens were prepared right after its synthesis and cooled down to LN_2 temperature to prevent any bridging water loss.

Diffuse reflectance infrared Fourier transform spectroscopy (DRIFTS)

DRIFTS was performed on a Bruker Tensor 37 (MIR source and KBr beam splitter) with a mercury cadmium telluride (MCT, cooled with LN_2) detector utilizing the DiffusIR™ accessory (Pike Technologies). To ensure air-free measurement, a sealable environmental chamber equipped with ZnSe window (Pike Technologies) was used. Samples were ground in air with dry KBr in a mortar and pestle (99.9%, Pike technologies) to produce 0.5-1 wt.% MOF or CCP mixtures. The data was averaged over 64 scans between 4000 – 600 cm^{-1} with the resolution of 4 cm^{-1}. Each of the Kubelka-Munk function-transformed DRIFTS spectra were normalized with respect to the DRUV–vis–NIR data by matching the DRIFTS value of F(R) at 4000 cm^{-1} with the DRUV–vis–NIR value of F(R) of the same sample at 4000 cm^{-1}. Air-free measurements were done by preparing the samples inside a N_2 glove box. *In-situ* monitoring of the air-exposure of **Ni-3D** was done after the air-free measurement by opening the valve of the environmental chamber to air.

Diffuse reflectance UV-vis-NIR spectra (DRUV–vis–NIR)

DRUV-Vis-NIR spectra between 200 and 2500 nm were collected on a Cary 5000i spectrophotometer, fitted with the UV-Vis DiffusIR accessory (Pike Technologies), at a scan rate of 600 nm/min under ambient conditions. A KBr baseline and a zero-background correction were collected prior to the sample measurements. Samples were prepared as described above for the DRIFTS measurements. For the Tauc plots and the determination of the optical bandgaps, the UV-vis-NIR spectra were stitched manually with the DRIFTS spectra obtained for the same samples. Air-free and *in-situ* measurements of **Ni-3D** used similar protocols to the DRIFTS measurements, but a quartz window instead of the ZnSe window was used.

Raman spectroscopy

Raman spectra of solid samples were measured using a Renishaw Invia Reflex Raman Confocal Microscope under the excitation laser of 473 nm, 532 nm, or 785 nm, with the laser not exceeding 5% of the full power. Air-free measurement of **Ni-3D** was done by encapsulating the solid sample into a sealed quartz tube inside a N_2 glove box and measuring the tube and sample together. Quartz is Raman transparent at the Raman shift range of interest.

Room temperature electrical conductivity measurements

Room temperature electrical conductivity measurements were carried out at 296 K in ambient atmosphere on pressed pellets using a 4-probe probe setup. Pressed pellets of MOF or CCP samples were made by adding powders into a 6 mm inner-diameter trapezoidal split sleeve pressing die (Across International) and pressing the die set by a hydraulic pump (MTI corporation) for 1 min. The applied pressure was approximately 1 GPa. The pellet thicknesses were measured after the measurement using a micrometer (Mitutoyo). The resulting pellet was cut into a cuboid by a blade and placed onto a piece of dry glass slide with thermally conductive and electrically insulating grease (DuPont Krytox). Four parallel copper wire contacts were attached to the cuboid by carbon paste. The other end of the copper wire was pasted onto the glass slide by carbon paste. The device was mounted onto the sample chuck of a probe station (Janis Cryogenics ST-500) equipped with four micro-manipulators that allowed us to control the position of the probes with a resolution of 5 μm. The temperature of the device was balanced by the heater of the probe station chuck and the environment and was controlled at 296 K by a temperature controller (Scientific Instrument model 9700). Electrical contacts were made by gently pressing gold-plated tungsten probes (Janis 7B-100G) into the carbon paste that was on the glass slide. Probes were connected to a sourcemeter (Keithley model 2450) through triax cables (Keithley model 7078-TRX-10). The chamber of the probe station was covered by a stainless-steel lid. This lid had a quartz window in the center, which was covered by black plastic to keep the device in the dark. Linear I–V curves were obtained by supplying the current and measuring the voltage. The current was duel-swept through the outer two probes, while

voltage was measured through the inner two probes. The specific lengths of the conduction channel were measured by a Leica S6 E stereoscopic microscope and calibrated by an external ruler of known distances. At least three pellets from four separate batches of each sample were measured. For each sample, the conductivity values were averaged to give the average conductivity value and a standard error which was used for the error estimation on the average conductivity value for each sample.

Variable temperature electrical conductivity data

Variable temperature electrical conductivity data were collected from 15 K or 100 K to 350 K or 400 K using a Quantum Design PPMS DynaCool equipped with the Electrical Transport Option. A four-contact probe cell was manufactured for the measurements using the same preparation method as described in room temperature electrical conductivity measurements. The copper wires were soldered to the copper current collector of the sample puck. For each sample, the measurement procedure consisted of two cycles of heating and cooling. The temperature was first varied from 300 K to 350 K or 400 K at 5 K/min, measuring the resistance in AC mode every 1 K. Then the temperature was varied from 350 K or 400 K to 150 K at 5 K/min, measuring the resistance in AC mode every 1 K. The measurement was repeated. The phase angle remained within 1°, which means that the difference of AC and DC resistance is below 1%. For **Ni-2D**, the cooling sequence was applied first instead of heating sequence to prevent its transformation to **Ni-1D**.

Optical microscopy (OM)

OM images were obtained by Leica S6 E stereoscopic microscope.

Electron paramagnetic resonance spectroscopy (EPR) measurements

EPR spectra were performed under nitrogen in septum-sealed quartz tubes using a Bruker EMX spectrometer equipped with an ER 4199HS cavity and Gunn diode microwave source at ~5 K, with a microwave frequency of 9.37 GHz, power of 0.100 mW, and attenuation of 33.0 dB. The measurements were taken in perpendicular mode. Pure MOF and CCP powder samples were used for the measurements.

Magnetic measurements

Magnetic measurements were performed on microcrystalline samples with a Quantum Design Dynacool D-209 Physical Property Measurement System (PPMS). Magnetization measurements were performed at 1.8 K in the field range of ±90 kOe. Susceptibility measurements were performed under 1 kOe external field in temperature range of 1.8–300 K. Experimental data were corrected for diamagnetic contribution based on blank sample holder measurements and Pascal's constants.

DFT calculations

DFT calculations were performed at either B3LYP/6-311G(d,p) or B3LYP/def2-QZVP level using ORCA. The wave-function analysis was done by Multiwfn.

3.5.4 Crystallographic Data

Table 3.4. cRED: Experimental parameters, crystallographic data, and structure refinement details.

Experimental parameters and crystallographic data		
Material code	**Ni-2D**	**Ni-3D-ox**
Number of datasets	5	4
Tilt step	0.23°	0.23°
Wavelength	0.0251 Å	0.0251 Å
Program for data procession	*XDS*	*XDS*
Program for structure solution	ShelxT	ShelxT
Crystal system	Orthorhombic	Hexagonal
Unit cell dimensions	a= 12.442(3) Å, b= 7.7419(15) Å, c= 3.3457(7) Å	a= 21.656(3) Å, c= 11.399(2) Å
Possible space group	*Immm*	$R\bar{3}m$
Resolution	0.718 Å	0.767 Å
Completeness	88.9%	99.4%
R_{int}	23.26%	50.97%
No. of reflections	1145	12870
No. of unique reflections	198	1185
Structure refinement against cRED data		
Formula	$NiC_6N_4O_3$	$NiC_6N_4O_2H_2$
Crystal system	Orthorhombic	Hexagonal
Space group	*Immm*	$R\bar{3}m$
Unit cell dimensions	a= 12.442(3) Å, b= 7.7419(15) Å, c= 3.3457(7) Å	a= 21.656(3) Å, c= 11.399(2) Å
Volume	322.28(11)Å^3	4629.8(16) Å^3
Z	4	18
ρ (g/cm^3)	4.839	1.426
F(000)	53	822
Dataset (*h,k l*)	–15~15, –9~9, –4~4	–27~27, –27~27, –13~13
Tot., Uniq. Data, Rint	1145, 198, 23.26%	12870, 1185, 50.97%
Observed Data [Fo > 4sig(Fo)]	159	425
$N_{reflections}$, $N_{parameters}$, $N_{restraints}$	198, 11, 24	1185, 68, 1
R_1, wR_2, *Gof*	0.3440, 0.6266, 2.367	0.1896, 0.4902, 1.079
I/σ	4.4	2.9
ρ_{min}, ρ_{max} (e$^-$ /Å^3)	–0.2/0.2	–0.2/0.2

3.6 References

(1) Sun, L.; Campbell, M. G.; Dincă, M. Electrically Conductive Porous Metal-Organic Frameworks. *Angew. Chemie - Int. Ed.* **2016**, *55* (11), 3566–3579.

(2) Xie, L. S.; Skorupskii, G.; Dincă, M. Electrically Conductive Metal-Organic Frameworks. *Chem. Rev.* **2020**, *120* (16), 8536–8580.

(3) Givaja, G.; Amo-Ochoa, P.; Gómez-García, C. J.; Zamora, F. Electrical Conductive Coordination Polymers. *Chem. Soc. Rev.* **2012**, *41* (1), 115–147.

(4) Sheberla, D.; Bachman, J. C.; Elias, J. S.; Sun, C. J.; Shao-Horn, Y.; Dincă, M. Conductive MOF Electrodes for Stable Supercapacitors with High Areal Capacitance. *Nat. Mater.* **2017**, *16* (2), 220–224.

(5) Feng, D.; Lei, T.; Lukatskaya, M. R.; Park, J.; Huang, Z.; Lee, M.; Shaw, L.; Chen, S.; Yakovenko, A. A.; Kulkarni, A.; Xiao, J.; Fredrickson, K.; Tok, J. B.; Zou, X.; Cui, Y.; Bao, Z. Robust and Conductive Two-Dimensional Metal-Organic Frameworks with Exceptionally High Volumetric and Areal Capacitance. *Nat. Energy* **2018**, *3* (1), 30–36.

(6) Banda, H.; Dou, J.-H.; Chen, T.; Libretto, N. J.; Chaudhary, M.; Bernard, G. M.; Miller, J. T.; Michaelis, V. K.; Dincă, M. High-Capacitance Pseudocapacitors from Li^+ Ion Intercalation in Nonporous, Electrically Conductive 2D Coordination Polymers. *J. Am. Chem. Soc.* **2021**, *143*, 2285–2292.

(7) Shinde, S. S.; Lee, C. H.; Jung, J. Y.; Wagh, N. K.; Kim, S. H.; Kim, D. H.; Lin, C.; Lee, S. U.; Lee, J. H. Unveiling Dual-Linkage 3D Hexaminobenzene Metal-Organic Frameworks towards Long-Lasting Advanced Reversible Zn-Air Batteries. *Energy Environ. Sci.* **2019**, *12* (2), 727–738.

(8) Nam, K. W.; Park, S. S.; dos Reis, R.; Dravid, V. P.; Kim, H.; Mirkin, C. A.; Stoddart, J. F. Conductive 2D Metal–Organic Framework for High-Performance Cathodes in Aqueous Rechargeable Zinc Batteries. *Nat. Commun.* **2019**, *10*, 4948.

(9) Clough, A. J.; Yoo, J. W.; Mecklenburg, M. H.; Marinescu, S. C. Two-Dimensional Metal−Organic Surfaces for Efficient Hydrogen Evolution from Water. *J. Am. Chem. Soc.* **2015**, *137* (1), 118–121.

(10) Miner, E. M.; Fukushima, T.; Sheberla, D.; Sun, L.; Surendranath, Y.; Dincă, M. Electrochemical Oxygen Reduction Catalysed by Ni_3(Hexaiminotriphenylene)$_2$. *Nat. Commun.* **2016**, *7*, 10942.

(11) Miner, E. M.; Wang, L.; Dincă, M. Modular O2 Electroreduction Activity in Triphenylene-Based Metal–Organic Frameworks. *Chem. Sci.* **2018**, *9*, 6286–6291.

(12) Campbell, M. G.; Sheberla, D.; Liu, S. F.; Swager, T. M.; Dincă, M. Cu_3(Hexaiminotriphenylene)$_2$: An Electrically Conductive 2D Metal–Organic Framework for Chemiresistive Sensing. *Angew. Chem. Int. Ed.* **2015**, *54* (14), 4349–4352.

(13) Campbell, M. G.; Liu, S. F.; Swager, T. M.; Dincă, M. Chemiresistive Sensor Arrays from Conductive 2D Metal−Organic Frameworks. *J. Am. Chem. Soc.* **2015**, *137* (43), 13780–13783.

(14) Stassen, I.; Dou, J.-H.; Hendon, C.; Dincă, M. Chemiresistive Sensing of Ambient CO2 by an Autogenously Hydrated Cu3(Hexaiminobenzene)2 Framework. *ACS Cent. Sci.* **2019**, *5* (8), 1425–1431.

(15) Sun, L.; Liao, B.; Sun, L.; Liao, B.; Sheberla, D.; Kraemer, D.; Zhou, J.; Stach, E. A.; Zakharov, D.; Stavila, V.; Talin, A. A.; Ge, Y.; Allendorf, M. D.; Chen, G.; Léonard, F.; Dincă, M. A Microporous and Naturally Nanostructured Thermoelectric Metal-Organic Framework with Ultralow Thermal Conductivity. *Joule* **2017**, *1* (1), 168–177.

(16) Erickson, K. J.; Léonard, F.; Stavila, V.; Foster, M. E.; Spataru, C. D.; Jones, R. E.; Foley, B. M.; Hopkins, P. E.; Allendorf, M. D.; Talin, A. A. Thin Film Thermoelectric Metal–Organic Framework with High Seebeck Coefficient and Low Thermal Conductivity. *Adv. Mater.* **2015**, *27* (22), 3453–3459.

(17) Sheberla, D.; Sun, L.; Blood-forsythe, M. A.; Er, S.; Wade, C. R.; Brozek, C. K.; Aspuru-Guzik, A.; Dincă, M. High Electrical Conductivity in Ni3(2,3,6,7,10,11- Hexaiminotriphenylene)2, a Semiconducting Metal−Organic Graphene Analogue. *J. Am. Chem. Soc.* **2014**, *136* (25), 8859–8862.

(18) Day, R. W.; Bediako, D. K.; Rezaee, M.; Parent, L. R.; Skorupskii, G.; Arguilla, M. Q.; Hendon, C. H.; Stassen, I.; Gianneschi, N. C.; Kim, P.; Dincă, M. Single Crystals of Electrically Conductive Two-Dimensional Metal−Organic Frameworks: Structural and Electrical Transport Properties. *ACS Cent. Sci.* **2019**, *5* (12), 1959–1964.

(19) Park, J.; Hinckley, A. C.; Huang, Z.; Feng, D.; Yakovenko, A. A.; Lee, M.; Chen, S.; Zou, X.; Bao, Z. Synthetic Routes for a 2D Semiconductive Copper Hexahydroxybenzene Metal–Organic Framework. *J. Am. Chem. Soc.* **2018**, *140* (44), 14533–14537.

(20) Chen, T.; Dou, J.-H.; Yang, L.; Sun, C.; Libretto, N. J.; Skorupskii, G.; Miller, J. T.; Dincă, M. Continuous Electrical Conductivity Variation in M3(Hexaiminotriphenylene)2 (M = Co, Ni, Cu) MOF Alloys. *J. Am. Chem. Soc.* **2020**, *142* (28), 12367–12373.

(21) Meng, Z.; Luo, J.; Li, W.; Mirica, K. Hierarchical Tuning of the Performance of Electrochemical Carbon Dioxide Reduction Using Conductive Two-Dimensional Metallophthalocyanine Based Metal−Organic Frameworks. *J. Am. Chem. Soc.* **2020**, *142* (52), 21656–21669.

(22) Sato, M.; Takeda, T.; Hoshino, N.; Akutagawa, T. Electronic and Crystal Structures of 1,2,3-Triazole-Fused p-Benzoquinone Derivatives. *CrystEngComm* **2017**, *19* (6), 910–917.

(23) Müllen, K.; Pisula, W. Donor−Acceptor Polymers. *J. Am. Chem. Soc.* **2015**, *137* (30), 9503–9505.

(24) Audi, H.; Chen, Z.; Charaf-Eddin, A.; D'Aléo, A.; Canard, G.; Jacquemin, D.; Siri, O. Extendable Nickel Complex Tapes That Reach NIR Absorptions. *Chem. Commun.* **2014**, *50* (96), 15111–15272.

(25) Rall, J.; Stange, A. F.; Hübler, K.; Kaim, W. A Coordination-Induced 1,4→1,2-Quinonediimine Isomerization. *Angew. Chem. Int. Ed.* **1998**, *37* (19), 2681–2682.

(26) Yamamoto, T.; Kimura, T.; Shiraishi, K. Preparation of π-Conjugated Polymers Composed of Hydroquinone , p-Benzoquinone , and p-Diacetoxyphenylene Units. Optical and Redox Properties of the Polymers. *Macromolecules* **1999**, *32* (26), 8886–8896.

(27) Metcalfe, R. A.; Vasconcellos, L. C. G.; Mirza, H.; Franco, D. W.; Lever, A. B. P. Synthesis and Characterization of Dinuclear Complexes of 3,3',4,4'-Tetraminobiphenyl with Tetramminoruthenium and Bis(bipyridine)ruthenium Residues and Their Two- and Four-Electron Oxidized Products Including a ZINDO Study of Orbital Mixing as a Function of Ligand Oxidation State. *J. Chem. Soc. Dalt. Trans.* **1999**, *16*, 2653–2667.

(28) Chakarawet, K.; Harris, T. D.; Long, J. R. Semiquinone Radical-Bridged M_2(M = Fe, Co, Ni) Complexes with Strong Magnetic Exchange Giving Rise to Slow Magnetic Relaxation. *Chem. Sci.* **2020**, *11* (31), 8196–8203.

(29) Huang, Z.; Grape, E. S.; Li, J.; Inge, A. K.; Zou, X. 3D Electron Diffraction as an Important Technique for Structure Elucidation of Metal-Organic Frameworks and Covalent Organic Frameworks. *Coord. Chem. Rev.* **2021**, *427*, 213583.

(30) Trucano, P.; Chen, R. Structure of Graphite by Neutron Diffraction. *Nature* **1975**, *258* (5531), 136–137.

(31) Beamson, G.; Briggs, D. *High Resolution XPS of Organic Polymers: The Scienta ESCA 300 Database*; Wiley: New York, NY, 1992.

(32) Trotochaud, L.; Head, A. R.; Pletincx, S.; Karsl, O.; Yu, Y.; Waldner, A.; Kyhl, L.; Hau, T.; Terryn, H.; Eichhorn, B.; Bluhm, H. Water Adsorption and Dissociation on Polycrystalline Copper Oxides : Effects of Environmental Contamination and Experimental Protocol. *J. Phys. Chem. B* **2018**, *122* (2), 1000–1008.

(33) Gu, S.; Du, J.; Huang, J.; Guo, Y.; Yang, L.; Xu, W.; Chen, W. Unsymmetrical NCN-Pincer Mononuclear and Dinuclear Nickel(II) Complexes of N-Heterocyclic Carbene (NHC): Synthesis, Structure and Catalysis for Suzuki–Miyaura Cross-Coupling. *Dalt. Trans.* **2017**, *46* (2), 586–594.

(34) Zhang, D.; Zhu, Y.; Ying, X.; Hsiung, C.; Sougrat, R.; Li, K.; Han, Y. Atomic-Resolution Transmission Electron Microscopy of Electron Beam – Sensitive Crystalline Materials. *Science* **2018**, *359* (6376), 675–679.

(35) Wang, L.; Ni, Y.; Hou, X.; Chen, L.; Li, F.; Chen, J. A Two-Dimensional Metal–Organic Polymer Enabled by Robust Nickel–Nitrogen and Hydrogen Bonds for Exceptional Sodium Ion Storage. *Angew. Chem. Int. Ed.* **2020**, *59* (49), 22126–22131.

(36) Rietveld, H. M. A Profile Refinement Method for Nuclear and Magnetic Structures. *J. Appl. Crystallogr.* **1969**, *2* (2), 65–71.

(37) Fratini, S.; Nikolka, M.; Salleo, A.; Schweicher, G.; Sirringhaus, H. Charge Transport in High-Mobility Conjugated Polymers and Molecular Semiconductors. *Nat. Mater.* **2020**, *19* (5), 491–502.

(38) Anthony, J. E.; Brooks, J. S.; Eaton, D. L.; Parkin, S. R. Functionalized Pentacene: Improved Electronic Properties from Control of Solid-State Order. *J. Am. Chem. Soc.* **2001**, *123* (38), 9482–9483.

(39) Skorupskii, G.; Trump, B. A.; Kasel, T. W.; Brown, C. M.; Hendon, C. H.; Dincă, M. Efficient and Tunable One-Dimensional Charge Transport in Layered Lanthanide Metal–Organic Frameworks. *Nat. Chem.* **2020**, *12* (2), 131–136.

(40) Schoedel, A.; Li, M.; Li, D.; Kee, M. O.; Yaghi, O. M. Structures of Metal−Organic Frameworks with Rod Secondary Building Units. *Chem. Rev.* **2016**, *116* (19), 12466–12535.

(41) Wu, X.; Qiu, Y.; Chen, Z.; Guan, B.; Hao, X.; Rykov, A. I.; Sun, Y.; Liu, L.; Zou, Y.; Sun, J.; Xu, W.; Zhu, D. Paramagnetic Conducting Metal–Organic Frameworks with Three- Dimensional Structure. *Angew. Chem. Int. Ed.* **2020**, *132* (47), 21059–21064.

(42) Chen, G.; Gee, L. B.; Xu, W.; Zhu, Y.; Lezama-pacheco, J. S.; Huang, Z.; Li, Z.; Babicz, T.; Choudhury, S.; Chang, T.; Reed, E.; Solomon, E. I.; Bao, Z. Valence-Dependent Electrical Conductivity in a 3D Tetrahydroxyquinone-Based Metal−Organic Framework. *J. Am. Chem. Soc.* **2020**, *142* (51), 21243–21248.

(43) Li, M.; Li, D.; Kee, M. O.; Yaghi, O. M. Topological Analysis of Metal−Organic Frameworks with Polytopic Linkers and/or Multiple Building Units and the Minimal Transitivity Principle. *Chem. Rev.* **2014**, *114* (2), 1343–1370.

(44) Grosvenor, A. P.; Biesinger, M. C.; Smart, R. S. C.; Mcintyre, N. S. New Interpretations of XPS Spectra of Nickel Metal and Oxides. *Surf. Sci.* **2006**, *600* (9), 1771–1779.

(45) Stang, S.; Lebkücher, A.; Walter, P.; Kaifer, E.; Himmel, H. Redox-Active Guanidine Ligands with Pyridine and p-Benzoquinone Backbones. *Eur. J. Inorg. Chem.* **2012**, *30*, 4833–4845.

(46) Masui, H.; Freda, A. L.; Zerner, M. C.; Lever, A. B. P. Binuclear 1,2,4,5-Tetraimino-3,6-Diketocyclohexane Bis[bis(bipyridine)ruthenium(II)] Redox Series. *Inorg. Chem.* **2000**, *39* (1), 141–152.

(47) Vlček Jr, A. Metal and Ligand Oxidation States in Dioxolene Complexes: Meaning, Assignment and Control. *Comments Inorg. Chem.* **1994**, *16* (4), 207–228.

(48) Bernard, M.; Goff, A. H. Raman Spectroscopy for the Study of Polyaniline. *Synth. Met.* **1997**, *85* (1-3), 1145–1146.

(49) Siri, O.; Taquet, J.; Collin, J.; Rohmer, M. Tunable Charge Delocalization in Dinickel Quinonoid Complexes. *Chem. Eur. J.* **2005**, *11* (24), 7247–7253.

(50) Taquet, J.; Siri, O.; Braunstein, P.; Welter, R. Dinuclear Nickel and Palladium Complexes with Bridging 2,5-Diamino-1,4-benzoquinonediimines: Synthesis, Structures, and Catalytic Oligomerization of Ethylene. *Inorg. Chem.* **2006**, *45* (12), 4668–4676.

(51) Jeon, I.; Park, J. G.; Xiao, D. J.; Harris, T. D. An Azophenine Radical-Bridged Fe_2 Single-Molecule Magnet with Record Magnetic Exchange Coupling. *J. Am. Chem. Soc.* **2013**, *135* (45), 16845–16848.

(52) Popescu, D. A.; Herrmann, J. M.; Ensuque, A.; Bozon-Verduraz, F. Nanosized Tin Dioxide : Spectroscopic (UV – VIS , NIR , EPR) and Electrical Conductivity Studies. *Phys. Chem. Chem. Phys.* **2001**, *3* (12), 2522–2530.

(53) **Ni-2D** is too unstable to do magnetometry measurements.

(54) Herebian, D.; Wieghardt, K. E.; Neese, F. Analysis and Interpretation of Metal-Radical Coupling in a Series of Square Planar Nickel Complexes: Correlated Ab Initio and Density Functional Investigation of $[Ni(L^{ISQ})_2]$ (L^{ISQ}: 3,5-Di-Tert-Butyl-o-Diiminobenzosemiquinonate(1-)). *J. Am. Chem. Soc.* **2003**, *125* (8), 10997–11005.

(55) Chłopek, K.; Bothe, E.; Neese, F.; Weyhermu, T.; Wieghardt, K. Molecular and Electronic Structures of Tetrahedral Complexes of Nickel and Cobalt Containing N,N′-Disubstituted, Bulky o-Diiminobenzosemiquinonate (1−) π-Radical Ligands. *Inorg. Chem.* **2006**, *45* (16), 6298–6307.

(56) Balch, A. L.; Holm, R. H. Complete Electron-Transfer Series of the $[M-N_4]$ Type. *J. Am. Chem. Soc.* **1966**, *88* (22), 5201–5209.

(57) Bencini, A.; Carbonera, C.; Dei, A.; Vaz, M. G. F. Magnetic Exchange Interaction between Paramagnetic Transition Metal Ions and Radical Ligands. A 9,10-Dioxophenanthrenesemiquinonato Adduct of a Nickel(II)-Tetraazamacrocycle Complex and DFT Description. *Dalt. Trans.* **2003**, *9*, 1701–1706.

(58) Skorupskii, G.; Dincă, M. Electrical Conductivity in a Porous, Cubic Rare-Earth Catecholate. *J. Am. Chem. Soc.* **2020**, *142* (15), 6920–6924.

(59) Schwarze, M.; Gaul, C.; Scholz, R.; Bussolotti, F.; Hofacker, A.; Schellhammer, K. S.; Nell, B.; Naab, B. D.; Bao, Z.; Spoltore, D.; Vandewal, K.; Widmer, J.; Kera, S.; Ueno, N.; Ortmann, F.; Leo, K. Molecular Parameters Responsible for Thermally Activated Transport in Doped Organic Semiconductors. *Nat. Mater.* **2019**, *18* (5), 242–248.

(60) Mott, N. F. Conduction in Glasses Containing Transition Metal Ions. *J. Non. Cryst. Solids* **1968**, *1* (1), 1–17.

(61) Park, S. S.; Hontz, E. R.; Sun, L.; Hendon, C. H.; Walsh, A.; Voorhis, T. Van; Dincă, M. Cation-Dependent Intrinsic Electrical Conductivity in Isostructural Tetrathiafulvalene-Based Microporous Metal−Organic Frameworks. *J. Am. Chem. Soc.* **2015**, *137* (5), 1774–1777.

(62) Xie, L. S.; Dincă, M. Novel Topology in Semiconducting Tetrathiafulvalene Lanthanide Metal-Organic Frameworks. *Isr. J. Chem.* **2018**, *58* (9-10), 1119–1122.

(63) Ko, M.; Mendecki, L.; Eagleton, A. M.; Durbin, C. G.; Stolz, R. M.; Meng, Z.; Mirica, K. A. Employing Conductive Metal−Organic Frameworks for Voltammetric Detection of Neurochemicals. *J. Am. Chem. Soc.* **2020**, *142* (27), 11717–11733.

Chapter 4. Fully Conjugated Tetraoxa[8]circulene-Based Porous Semiconducting Polymers

4.1 Abstract

Tetraoxa[8]circulenes (TOCs) are a class of hetero[8]circulenes featuring a planar cyclooctatetraene core with a mixed aromatic/antiaromatic motif that governs their electronic properties. Polymeric TOCs (pTOCs) have been the subject of several computational simulations because they are predicted to be low-band-gap semiconductors, but they have not been available synthetically yet. Here, we report the first example of pTOCs, a new family of porous semiconductors, synthesized under ionothermal conditions through the intermolecular cyclization of 1,4,5,8-anthracenetetrone. pTOCs are porous, with surface areas up to 1656 m^2 g^{-1}, and exhibit light-switchable and tunable semiconducting properties.

4.2 Introduction

Porous organic polymers (POPs) and covalent organic frameworks (COFs) have attracted considerable interest due to their permanent porosity, chemical and structural tunability, and the potential for charge transport. Whereas, COFs are often perceived to have an inherent advantage over POPs in terms of electrical conductivity due to their crystallinity, many COFs involve polarized linkages,[1] such as B–O and C=N, which naturally leads to decreased conjugation both energetically and spatially, and may hinder through-bond carrier migration.[2] POPs, on the other hand, are often obtained under kinetically controlled reaction conditions that involve a broad range of bond connections, including nonpolarized C–C and C=C bonds, thus facilitating the formation of semiconducting materials with low bandgaps even when amorphous materials are formed.[3] A variety of strategies can be applied to tune the electronic structures, band gaps, and thus the charge transport properties of POPs. To this end, among many others,[3b,4] Coskun et al. have recently reported a facile strategy to tune the band gap of POPs based on an acid catalyzed cyclization reaction.[5]

Hetero[8]circulenes have received substantial interest due to their optoelectronic properties, enabling their use as active materials in OLEDs[6] and OFETs.[7] One of the archetypal classes of hetero[8]circulenes, tetraoxa[8]circulenes (TOCs), feature a planar structure and an antiaromatic cyclooctatetraene (COT) core,[8] resulting in unique electronic structures and redox switchable aromatic motifs.[9] The aromaticity of TOCs has been extensively studied both computationally[10] and experimentally[11] in molecular systems. Recently, a series of triptycene-bearing TOCs were reported and proposed as chemical sensors and as host materials for fullerenes.[12] Given its rigid molecular structure and exceptional conjugation, we envisioned TOC to be a promising building block for electrically conductive POPs featuring the intrinsic properties of TOCs as predicted by several computational studies.[13]

Herein, we report a polymerized version of TOC, pTOC. To our knowledge, this is the first example of a polymeric structure with this unique building block. The pTOC exhibits a two-dimensional (2D) extended ladder-type polymeric structure with three-dimensional (3D) characteristics. With a porosity of up to 1656 m^2 g^{-1}, pTOCs exhibit intrinsic electrical conductivity ranging from 1.0×10^{-6} S cm^{-1} to 1.7×10^{-5} S cm^{-1}, which varies with the synthesis temperatures.
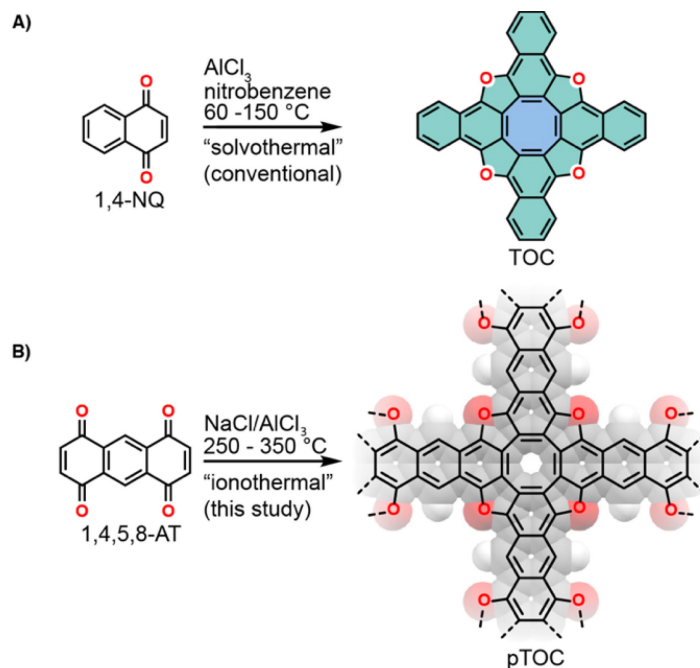
Figure 4.1. A) Cyclooligomerization of naphthoquinone under Lewis acidic conditions. The aromatic part of the molecule is highlighted in green and the antiaromatic COT-core in blue. B) Polymerization of 1,4,5,8-anthracene tetrone (AT) under ionothermal conditions. The structure of pTOC is shown along with its model structure as an overlay.

4.3 Results and Discussion

Our initial attempts to obtain pTOCs mimicked the 1970 Högberg TOC synthesis based on the cyclization of 1,4-naphthoquinone[14] (Figure 4.1A). However, the treatment of 1,4,5,8-anthracenetetrone (AT)[15] with Lewis acids such as $AlCl_3$ and BF_3OEt_2 under solvothermal conditions did not yield any precipitate despite extensive screening of reaction temperatures, duration, or solvents (Table 4.1, 4.2). Early research on TOCs suggested that dihydroxy species are formed as intermediates prior to dehydration and subsequent cyclization. Considering the likely poor solubility of the intermediates in our case, we surmised that the reaction temperature was not high enough to facilitate cyclization. To enable more facile dehydration and hence induce condensation, we thus moved from a solvothermal approach to an ionothermal approach. Indeed, heating AT in a eutectic mixture of $AlCl_3/NaCl$[16] at temperatures ranging from 250 to 350 °C produced black solids, named pTOC-*temp*, where *temp* represents the reaction temperature, in 80–90% yield (Figure 4.1B). The temperature range was specifically chosen to avoid carbonization, which is commonly reported to take place above 400 °C under ionothermal conditions.[17]

Table 4.1. Reaction conditions of the attempted solvothermal conditions in nitrobenzene for the synthesis of pTOCs.

	eq. of AlCl₃	Time (h)	Temperature (°C)
a	1.4	1	60
b	2.8	1	60
c	2.8	2	60
d	1.4	6	150
e	1.4	6	125
f	1.4	6	100
g	2.8	6	100

Table 4.2. Reaction conditions of solvothermal reactions with different solvents and Lewis acids.

	Lewis acid	solvent	eq. Acid	time (h)	Temperature (°C)
h	AlCl₃	toluene	2.8	6	125
i	AlCl₃	DMSO	2.8	6	125
j	BF₃·OEt₂	dry ether	100	72	40
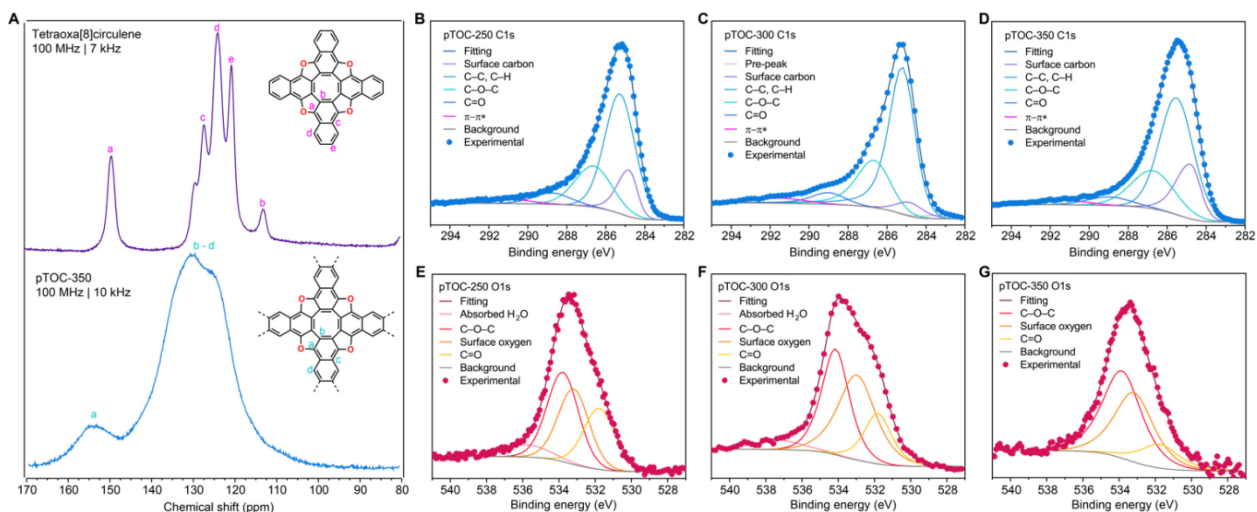
Figure 4.2. Spectroscopic characterization of pTOCs. A) Solid-state CP-MAS ^{13}C NMR spectra of tetraoxa[8]circulene (purple) and pTOC-350 (blue). B-D) C1s XPS spectra and deconvolution of the pTOCs. E-G) O1s XPS spectra and deconvolution of the pTOCs.

Solid-state (SS) Solid-state (SS) cross-polarization magic-angle spinning (CP-MAS) ^{13}C-NMR analysis of TOC and pTOC-350 confirmed the formation of pTOCs (Figure 4.2A, 4.3). The ^{13}C-NMR spectrum of TOC shows two peaks at 149 ppm (C atoms attached to the O) and 112 ppm (C atoms of the COT core), whereas the bulk of aromatic C atoms are located at 127, 123, and 120 ppm. In contrast, the ^{13}C spectrum of pTOC-350 shows broader features, implying the formation of an extended structure. Although the peaks shift slightly to a lower field upon polymerization, the peak positions are still in agreement with the TOC. The broad features in the pTOC-350 spectrum are also expected given its

amorphous nature (Figure 4.4). Electron paramagnetic resonance (EPR) of pTOC-350 confirms the presence of organic radicals with an isotropic signal at $g = 2.007$ (Figure 4.5). These radicals are likely localized on defects such as unreacted/terminal carbonyl moieties and contribute to the electron conduction given that the EPR signal has Lorentzian line broadening.[18] Indeed, the ^{13}C SS-NMR spectrum of pTOCs also shows a peak at 182 ppm, indicative of residual/terminal carbonyl moieties (Figure 4.3).
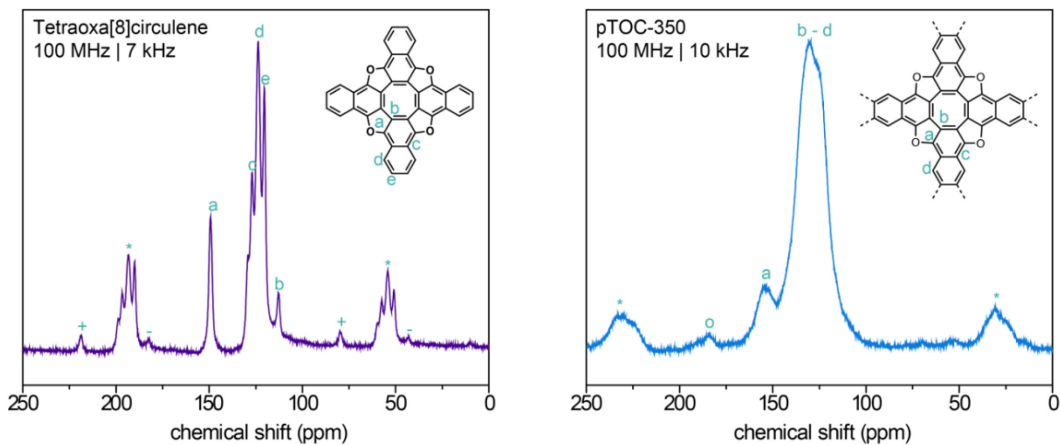
Figure 4.3. ^{13}C CP-MAS solid-state NMR spectra of TOC (purple) and pTOC-350 (blue). Side bands are indicated by symbols for TOC (*, +, -) and pTOC-350 (*). The spectrum of pTOC-350 shows a terminal/residual carbonyl peak indicated with "o" at 183 ppm.
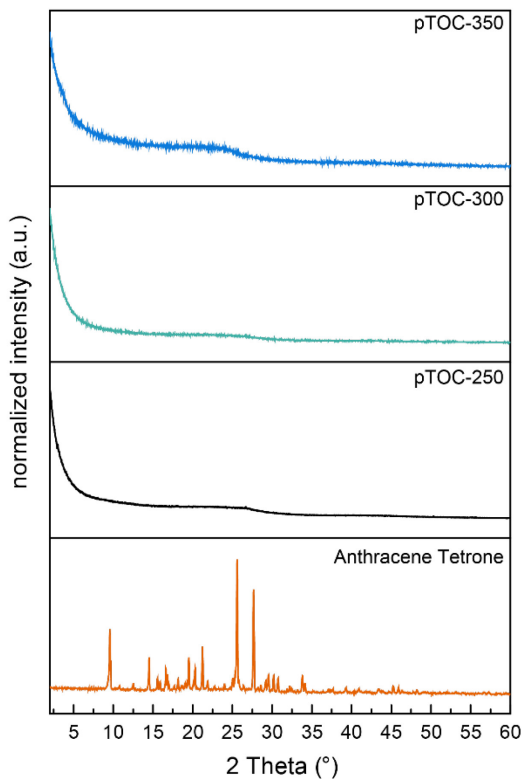
Figure 4.4. Powder X-ray diffractograms of anthracene-tetrone (orange), pTOC-250 (black), pTOC-300 (green) and pTOC-350 (blue).
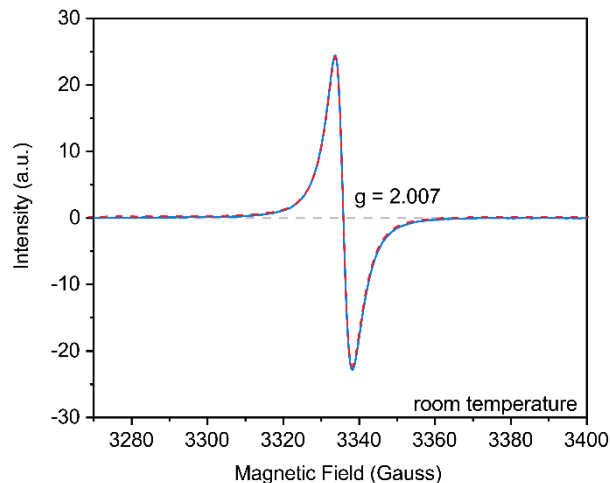
Figure 4.5. EPR spectrum of pTOC-350 at room temperature. The microwave frequency is 9.37 GHz, power is 0.005 mW, and attenuation is 10.0 dB. An isotropic organic radical signal at g = 2.007 is observed. Red dashed line is simulated EPR spectrum of an isotropic S = ½ spin with g = 2.007 and Lorentzian line broadening (peak-to-peak (PP) line width equals to 0.5 mT).

Fourier-transform infrared (FT-IR) spectroscopy, recorded in transmission mode with KBr pellets and in ATR mode (Figure 4.6A-C), revealed the expected C–O stretching bands at 660 and 850 cm^{-1}, and confirmed residual carbonyl bands at 1660 cm^{-1}.[19] Additional bands at 3050 and 1600 cm^{-1} correspond to C–H and C=C stretching modes, respectively. Absorbed water molecules in pTOCs result in very broad bands spanning the ~1800 cm^{-1} – 4000 cm^{-1} range, which are diminished in the spectra recorded by diffuse reflectance infrared Fourier-transform spectroscopy (DRIFTS) under N_2 (Figure 4.7). DRIFTS also shows that the intensity of the residual carbonyl vibrational bands between 1800 cm^{-1} and 1650 cm^{-1} decreases with higher reaction temperature, consistent with a higher degree of polymerization.
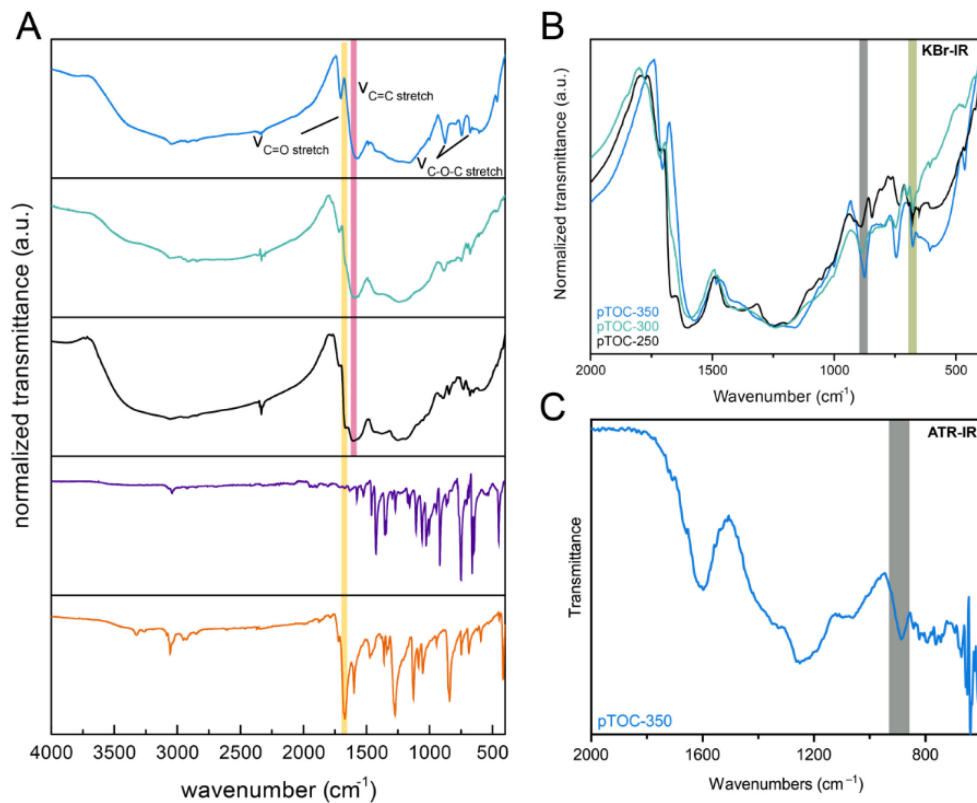
Figure 4.6. Infrared spectroscopy of pTOCs, TOC and precursor. A) FTIR spectra of anthracene tetrone (orange), TOC (purple), pTOC-250 (black), pTOC-300 (green) and pTOC-350 (blue). Characteristic modes are highlighted in yellow (C=O stretch) and pink (C=C stretch). Obtained using KBr pellets in the transmission mode. B) Zoomed region of the pTOCs in the range of 2000 – 400 cm^{-1} with highlights of the C-O stretching modes. C) Zoomed ATR-IR spectrum of pTOC-350 in the range of 2000 – 600 cm^{-1} with highlights of the C–O stretching modes.
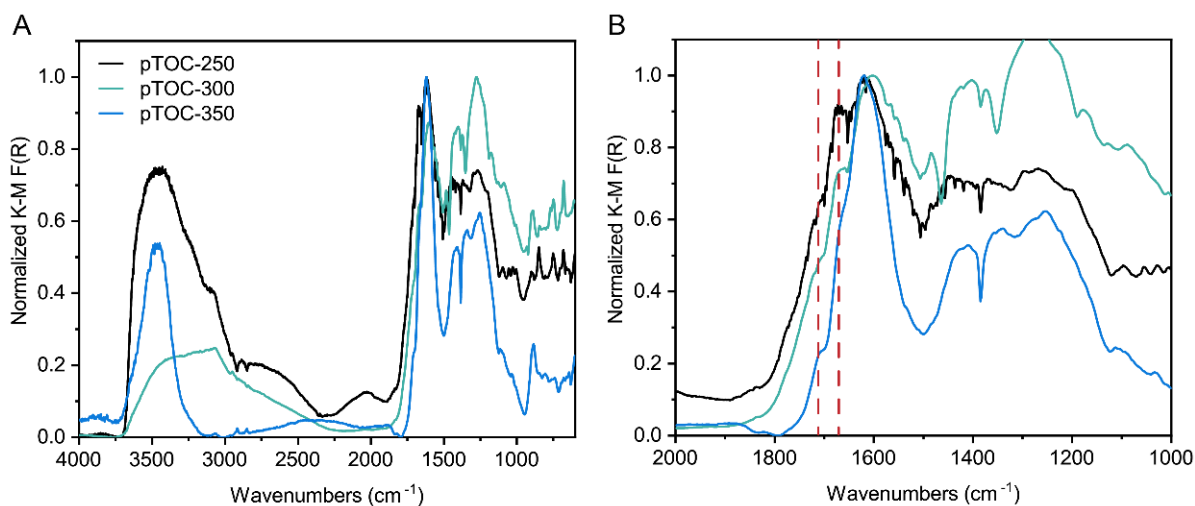
Figure 4.7. A) DRIFTS of pTOC-250 (black), pTOC-300 (green) and pTOC-350 (blue). B) DRIFTS normalized by the intensity of C=C stretching at ~1600 cm^{-1}, highlighting that the intensity of residual C=O stretching (marked by red dashed lines) decreased significantly from pTOC-250 to pTOC-350.

171
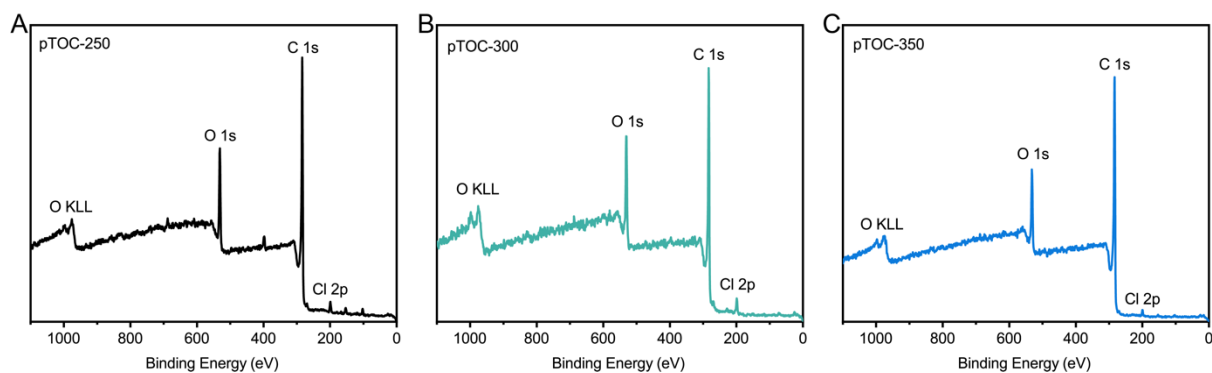
Figure 4.8. XPS survey spectra of pTOC-250 (A), pTOC-300 (B), pTOC-350 (C).

Table 4.3. Atomic compositions of pTOCs obtained by XPS survey spectra.

Materials	C At%	O At%	C/O ratio
pTOC-250	82.11	11.91	6.89
pTOC-300	83.11	14.64	5.68
pTOC-350	86.99	11.63	7.48

The composition of pTOCs was confirmed by X-ray photoelectron spectroscopy (XPS), which revealed that the C/O ratio varied with the reaction temperature (Figure 4.8, Table 4.3). Thus, pTOC-350 exhibits the highest C/O ratio of 7.48, close to the theoretical value of 7. This corresponds to the highest degree of polymerization among all pTOCs and is in agreement with the DRIFTS data. The slight deviation from the theoretical C/O value can be attributed to the cleavage of oxygen moieties at high reaction temperatures. With a C/O ratio of 6.89, pTOC-250 likely maintains extra oxygen atoms due to incomplete polymerization. The deconvolution of the C1s signal in high-resolution XPS spectra of pTOCs showed C–O–C components of the furane moieties at ≈286.7 eV that are consistent with literature values,[20] further verifying the *in-situ* formation of tetraoxa[8]circulene moieties (Figure 4.2B-D, Tables 4.3-4.10). The ratio of the C=O to C–O–C intensity decreases with increasing reaction temperature (Tables 4.4-4.6, 4.8) and is consistent with the higher degree of polymerization in pTOC-350. This result is further verified by the deconvolution of the O1s region, where the C=O component is almost negligible for pTOC-350 (Figure 4.2E-G, Table 4.7-4.9), confirming that a higher reaction temperature is necessary to facilitate dehydration and subsequent aromatization of the polymer backbone (Figure 4.2B-G).

Table 4.4. Deconvolution details of C1s XPS spectrum of pTOC-350.

Name	Position (eV)	FWHM (eV)	Line Shape	%Area
Adventitious carbon	284.80	1.25	LA(4.2, 9, 4)	18.35
C–H, C–C	285.52	2.04	GL(30)	51.97
C–O–C	286.72	2.62	GL(30)	21.74
C=O	289.95	2.62	GL(30)	4.87
π–π*	291.43	3.00	GL(30)	3.08

172

Table 4.5. Deconvolution details of C1s XPS spectrum of pTOC-300.[a]

Name	Position (eV)	FWHM (eV)	Line Shape	%Area
Adventitious carbon	284.85	1.59	LA(4.2, 9, 4)	6.04
C–H, C–C	285.22	1.51	A(0.35, 0.2, 0)GL(30)[b]	58.08
C–O–C	286.67	1.96	A(0.35, 0.2, 0)GL(30)[b]	24.27
C=O	289.00	1.96	A(0.35, 0.2, 0)GL(30)[b]	5.98
π–π*	291.41	2.87	GL(30)	3.72

[a]A small C1s pre-peak at BE of 283.15 eV was needed for the deconvolution. [b]An asymmetric feature was needed for the line shape of (C–H, C–C), C–O–C, and C=O components to get a reasonable fit.

Table 4.6. Deconvolution details of C1s XPS spectrum of pTOC-250.

Name	Position (eV)	FWHM (eV)	Line Shape	%Area
Adventitious carbon	284.80	1.00	LA(4.2, 9, 4)	14.09
C–H, C–C	285.27	1.83	GL(30)	53.54
C–O–C	286.62	2.24	GL(30)	22.57
C=O	288.76	2.24	GL(30)	6.22
π–π*	291.30	3.00	GL(30)	3.58

Table 4.7. Deconvolution details of O1s XPS spectrum of pTOC-350.

Name	Position (eV)	FWHM (eV)	Line Shape	%Area
C=O[a]	531.76	2.54	GL(70)	13.14
Surface O	533.17	2.54	GL(70)	38.48
C–O–C	533.85	2.54	GL(70)	48.37
Absorbed H_2O[b]	-	-	-	-

[a]The BE of C=O peak is consistent with the literature values of aromatic C=O. [b]A peak of absorbed H_2O is needed for pTOC-300 and pTOC-250, but is not necessary for pTOC-350.

Table 4.8. Deconvolution details of O1s XPS spectrum of pTOC-300.

Name	Position (eV)	FWHM (eV)	Line Shape	%Area
C=O[a]	531.80	1.79	GL(70)	17.58
Surface O	532.97	2.43	GL(70)	40.05
C–O–C	534.15	1.79	GL(70)	36.76
Absorbed H_2O	537.28	3.00	GL(70)	5.60

[a]The BE of C=O peak is consistent with the literature values of aromatic C=O.

Table 4.9. Deconvolution details of O1s XPS spectrum of pTOC-250.

Name	Position (eV)	FWHM (eV)	Line Shape	%Area
C=O[a]	531.80	2.04	GL(70)	25.17
Surface O	532.97	2.01	GL(70)	30.66
C–O–C	534.15	2.04	GL(70)	36.81
Absorbed H_2O	537.28	3.00	GL(70)	7.35

[a]The BE of C=O peak is consistent with the literature values of aromatic C=O.

Table 4.10. Area ratio analysis based on deconvolution of C1s and O1s XPS spectra.

Materials	(C–H,C–C)/C–O–C	C=O/C–O–C (C1s)	C=O/C–O–C (O1s)
pTOC-250	2.37	0.276	0.684
pTOC-300	2.39	0.246	0.478
pTOC-350	2.39	0.224	0.272

Raman spectra of the pTOCs were recorded using a Raman microscope at an excitation wavelength of 535 nm. The polymers showed two strong peaks at 1365 cm^{-1} and 1595 cm^{-1} (Figure 4.9) assigned as D (defect) and G (graphene) bands, respectively. This behavior has also been observed in fully conjugated systems prepared under solvothermal conditions.[3a,21] The I_D/I_G ratio decreases with increasing reaction temperature, from 0.75 for pTOC-250 to 0.62 for pTOC-350, indicating both the increased proportion of fused aromatic rings and decreased defects with increasing reaction temperature.[22] These compositional changes were also reflected macroscopically in the morphology of the various pTOCs. Thus, scanning electron microscopy (SEM) revealed that samples produced at elevated temperatures present as much smoother, more regular particles that contrast with the irregular, highly corrugated microparticles produced at lower temperatures (Figure 4.10). The polymeric samples are consistent in their thermal behavior: pTOCs do not exhibit any mass loss below 450 °C (decomposition temperature, T_d>450 °C) except for the initial removal of moisture absorbed from ambient air (Figure 4.11). By contrast, the AT precursor loses significant mass below 200°C.
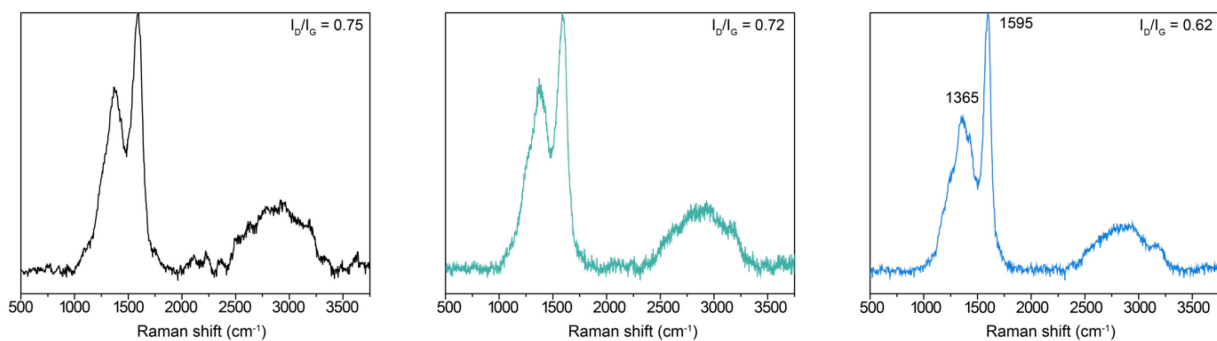
Figure 4.9. Raman spectra of pTOC-250 (black), pTOC-300 (green) and pTOC-350 (blue).
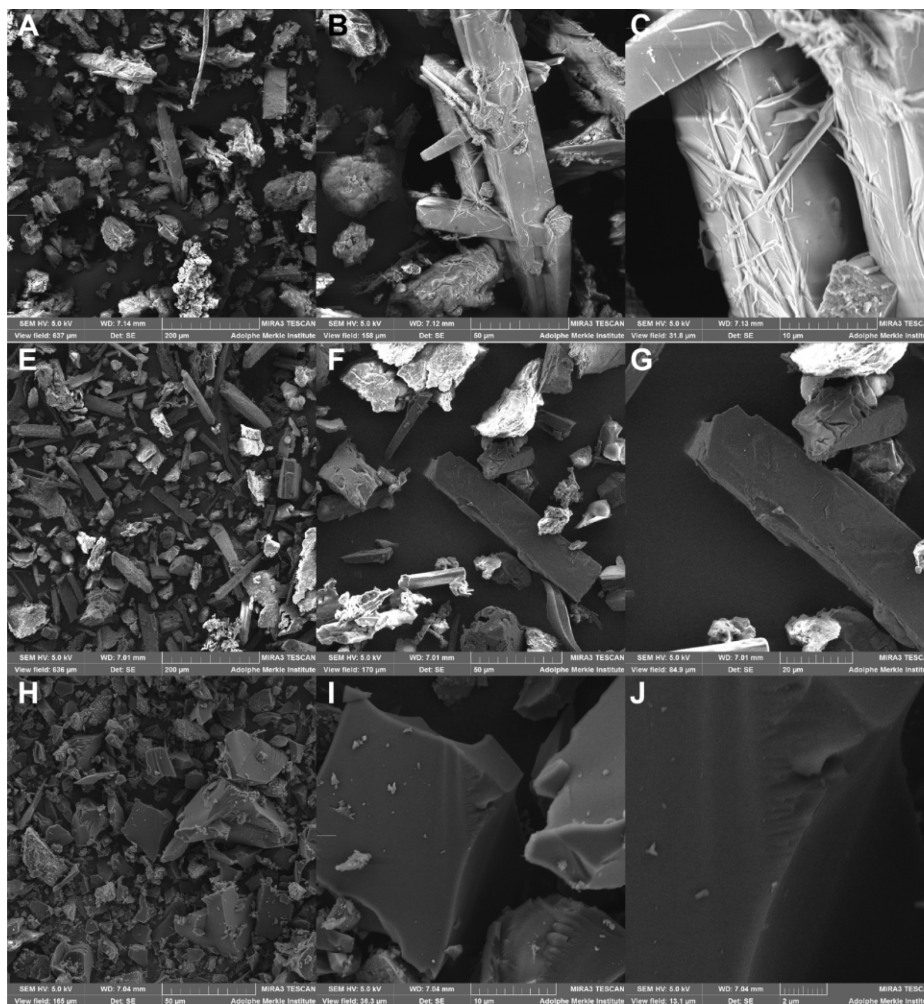
Figure 4.10. SEM micrographs of A-C) pTOC-250, D-E) pTOC-300 and H-J) pTOC-350 at various magnifications.
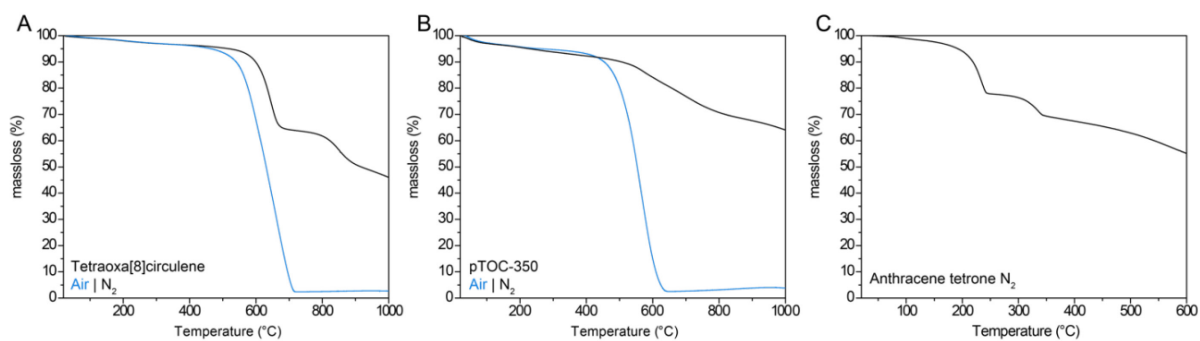
Figure 4.11. Thermogravimetric analysis of (A) tetraoxa[8]circulene under air (blue) and nitrogen (black), (B) pTOC-350 under air (blue) and nitrogen (black) and (C) AT under nitrogen.
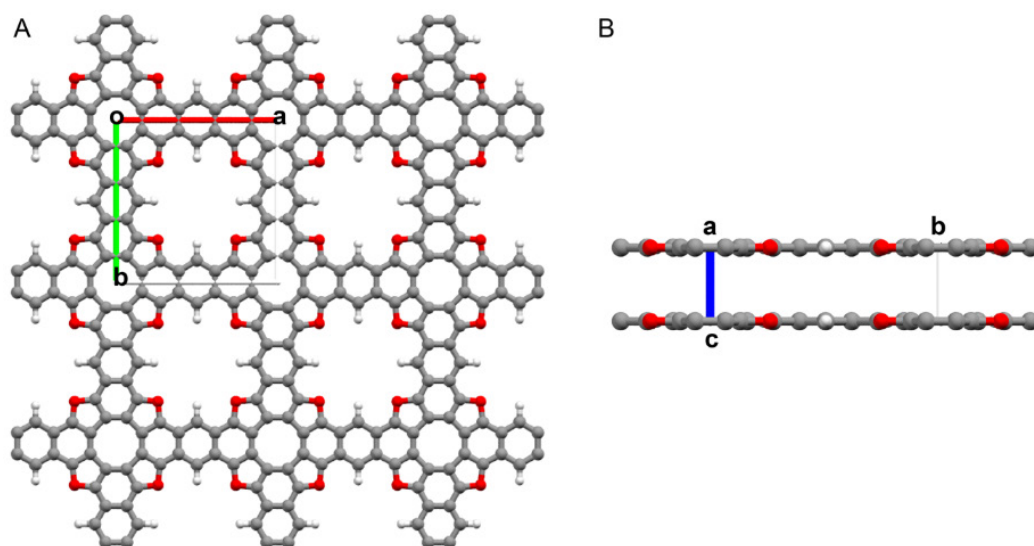
Figure 4.12. Simulated structure of pTOC using Materials Studio (P4/mmm space group). (A) Layered structure of pTOC, a = b = 10.74 Å. (B) Stacking of pTOC layers, exhibiting an interlayer spacing of 3.42 Å.
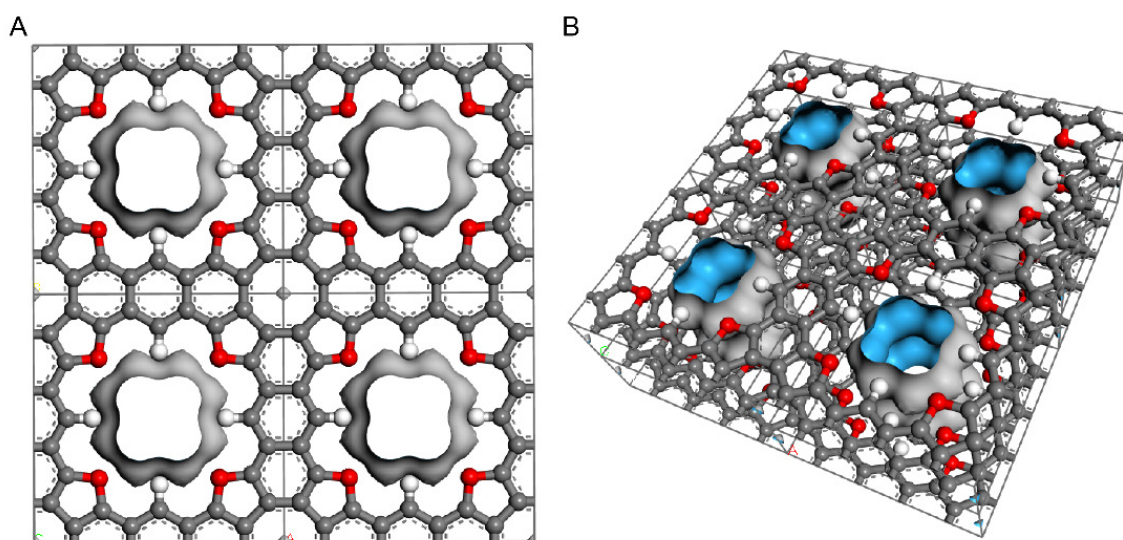
Figure 4.13. Connolly surface of the simulated structure of pTOC. The analysis showed that the actual pore diameter is around 5 Å. The gray lines represent the unit cell boundaries.

An idealized, defect-free structure of pTOC was modeled using Materials Studio assumed a square 2D lattice, which gave a π–π stacking distance of ≈3.4 Å (Figure 4.12). A Connolly surface analysis of this structure gave micropores with a diameter of approximately 5 Å (Figure 4.13). N_2 sorption isotherms (Figure 4.14A) at 77 K provided experimental evidence for permanent microporosity: all pTOCs exhibited type I isotherms with significant adsorption at low partial pressures below 0.11 P/P_0 (Figure 4.15). A slight desorption hysteresis at higher relative pressures indicated the presence of mesopores, most likely due to the imperfect stacking and the amorphous nature of the samples. Interestingly, the surface area, obtained by fitting the isotherms to the Brunauer–Emmett–Teller (BET) model, increased with the reaction

176

temperature from 411 m^2 g^{-1} to 1075 m^2 g^{-1} and 1656 m^2 g^{-1} for pTOC-250, pTOC-300, and pTOC-350, respectively (Table 4.11). Analyzing the N$_2$ isotherm data with nonlocal density functional theory (NLDFT) (Figure 4.14B) confirmed non-uniform pore size distributions with peaks at 0.53 nm, 0.97 nm, and larger pores ranging from 1.3 nm to 4 nm. Remarkably, the smallest pore size obtained from NLDFT analysis is in good agreement with the value observed in the idealized structure. As such, we propose that the smallest pores originate from the stacked 2D layers of various sizes, and they interconnect to form an overall amorphous structure that gives rise to larger micropores and mesopores. This hypothesis is in line with the higher porosity for pTOC-350 and is further supported by the fact that the proportion of 0.5 nm relative to 0.9 nm pores increases with temperature.
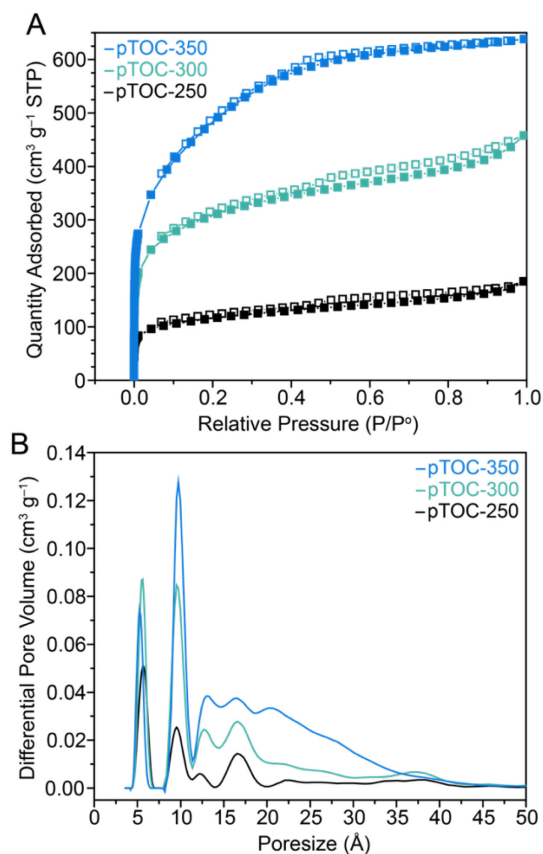
Figure 4.14. Gas sorption analysis of pTOCs: A) N$_2$ isotherms of pTOC-250 (black), pTOC-300 (green) and pTOC-350 (blue) at 77 K. Filled and empty symbols represent adsorption and desorption, respectively. B) NLDFT pore size distribution of pTOC-250 (black), pTOC-300 (green) and pTOC-350 (blue).
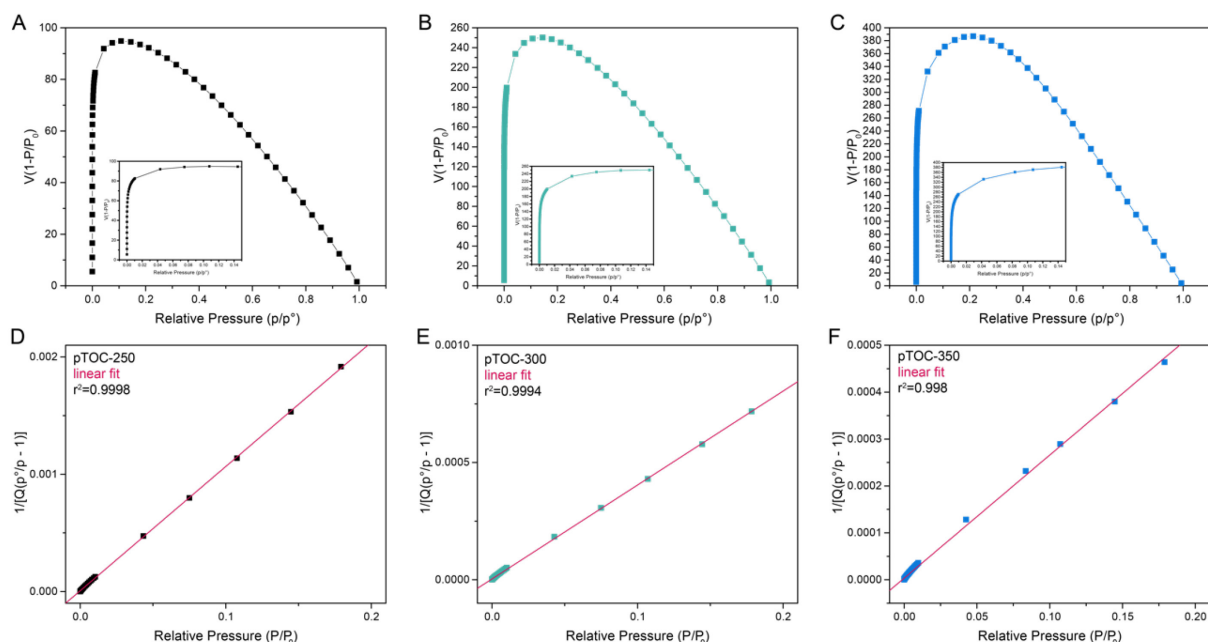
Figure 4.15. A-C) Calculated Rouquerol plot for the pTOCs (Inset: enlarged plot) along with the pressure ranges used for the BET surface area calculations (pTOC-250 (black), pTOC-300 (green) and pTOC-350 (blue)). The pressure range where the $Q(1-P/P_0)$ term increases continuously with P/P_0 for the surface area calculations. (D-F) BET plot of the pTOCs obtained from N_2 isotherms at 77 K.

Table 4.11. N_2 sorption data for pTOCs at 77 K.

Sample	BET[a] $(m^2\ g^{-1})$	S_{micro}[b] $(m^2\ g^{-1})$	S_{ext}[c] $(m^2\ g^{-1})$	V_{total}[d] $(cm^3\ g^{-1})$	V_{micro}[e] $(cm^3\ g^{-1})$	V_{ext}[f] $(cm^3\ g^{-1})$	Ratio of 0.5/0.9 nm pores[g]
pTOC-250	411	200	211	0.286	0.086	0.200	1.50
pTOC-300	1075	481	594	0.710	0.215	0.495	0.66
pTOC-350	1656	530	1126	0.989	0.245	0.664	0.36

[a]BET surface areas calculated over the pressure range (P/P_0) of $0.01 - 0.11$. [b]Micropore surface area calculated using the t-plot method. [c]$S_{ext} = S_{total} - S_{micro}$. [d]Total pore volume obtained at $P/P_0 = 0.99$. [e]Micropore volume calculated using the t-plot method. [f]$V_{ext} = V_{total} - V_{micro}$. [g]Ratio of 0.5/0.9 nm pores calculated from the integral of the pore size distribution (PSD) plots.

A first hint for the degree ofconjugation in pTOC comes from diffuse-reflectance UV-Vis (DRUV-Vis) spectroscopy. DRUV-Vis spectra of pTOC powders diluted in KBr show broad absorption that tails significantly into the near infrared (NIR) region, suggesting the formation of extended structures (Figure 4.16A). The absence of sharp absorption edges is likely the result of the disordered structure of polymers. Interestingly, both pTOC-250 and pTOC-300 exhibit absorption maxima at around 500 nm with shoulders at 800 nm, substantially red-shifted relative to the absorption maximum of ≈350 nm for pTOC-350, despite their lower degree of polymerization. These differences likely stem from different interlayer interactions in the three samples. Plotted in Tauc coordinates, the DRUV/Vis spectra reveal optical band gaps (E_o) of

1.31 eV, 1.49 eV and 1.88 eV for pTOC-250, pTOC-300 and pTOC-350, respectively (Figure 4.16B). Notably, the band gaps of pTOC-250 and pTOC-300 are significantly smaller than the theoretical value for a single layer of pTOC (i.e., no inter-layer interaction), whereas that of pTOC-350 is quite similar.[13c] Encouraged by the broad optical absorption and relatively low E_o of pTOCs, two-probe electrical conductivity measurements of pressed pellets were performed (Table 4.12, Figure 4.17). Consistent with E_o progression, pTOC-250 and pTOC-300 showed higher average conductivities of $1.7×10^{-5}$ S cm^{-1} and $1.2×10^{-5}$ S cm^{-1}, respectively, whereas pTOC-350 had a maximal average conductivity of $3.3×10^{-6}$ S cm^{-1}, when the synthesis time was increased from 3 to 5 days (Figure 4.18). These results indicate that there is no correlation between the synthesis temperature and the conductivities of pTOCs. Four-probe devices of pTOC-350 exhibited a very similar conductivity value of $1.19×10^{-6}$ S cm^{-1}, indicating the negligible influence of contact resistance. Whereas most COFs are based on polarized linkages, a few examples of fully conjugated COFs through pyrazine, cyano-vinylene or vinylene linkages have also been reported recently.[23] Compared to these, pTOCs maintain a higher degree of sp^2 conjugation without strongly polarizing functionalities or building blocks and furthermore demonstrate the realization of electrical conductivity with highly tunable porosity (Table 4.13). To prove that the residual Cl$^-$ ions are not contributing to the conductivity of the pTOCs, we conducted conductivity measurements of pTOC-350 after doping with NaCl, which showed a slightly reduced conductivity of $1.8×10^{-7}$ S cm^{-1} (Figure 4.19).
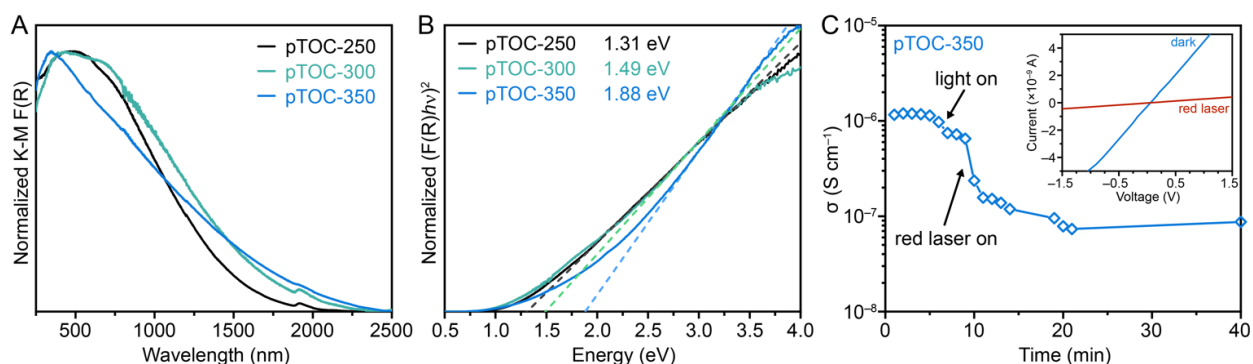
Figure 4.16. Spectroscopic analysis of pTOCs: A) DRUV spectra of pTOC-250 (black), pTOC-300 (green), and pTOC-350 (blue) diluted in KBr, respectively. B) Tauc plots of the DRUV spectra. C) The evolution of electrical conductivity of pTOC-350 when exposed to light and red laser (<5 mW).

Table 4.12. Average room-temperature conductivities of pTOCs.

Materials	Conductivity (S cm^{-1})
pTOC-250	$1.7×10^{-5}$
pTOC-300	$1.2×10^{-5}$
pTOC-350	$1.0×10^{-6}$
pTOC-350-LR	$1.2×10^{-5}$
pTOC-350-I$_2$ (RT doping)	$5.0×10^{-6}$
pTOC-350- I$_2$ (50 °C doping)	$4.1×10^{-4}$

179
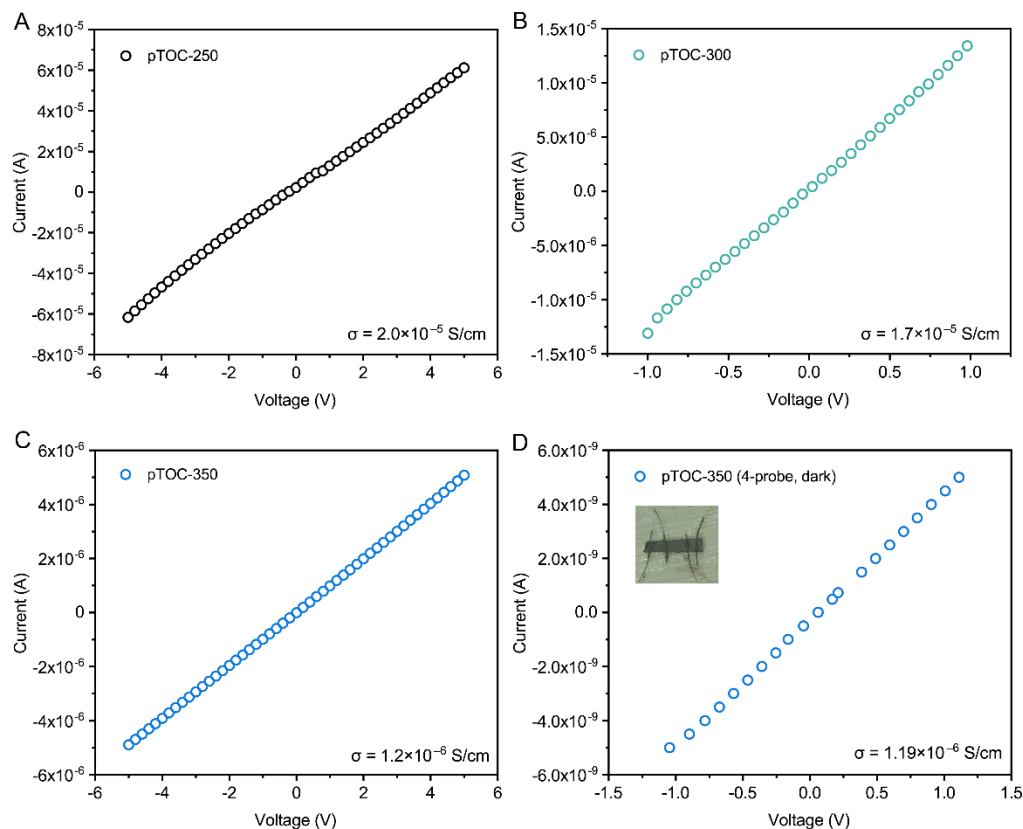
Figure 4.17. Typical linear I-V curves of two-probe (A-C) and four-probe (D) electrical conductivity measurements of pTOCs, suggesting ohmic contact for all devices. The contact resistance in the conductivity measurements of pTOCs has little influence on the results, as suggested by the almost same conductivity values of two-probe and four-probe measurements of pTOC-350. The average electrical conductivities of pTOC-250, pTOC-300, and pTOC-350 are 1.7×10^{-5} S/cm, 1.2×10^{-5} S/cm, and 1.0×10^{-6} S/cm. Inset of D shows the image of a typical four-probe device.
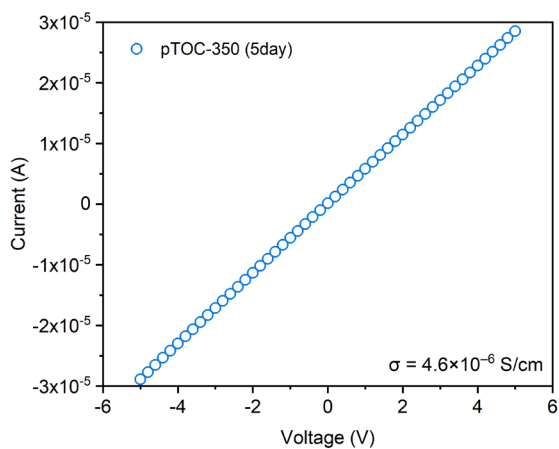
Figure 4.18. A typical I-V curve of two-probe electrical conductivity measurement of pTOC-350 synthesized by a 120-hour reaction. The average conductivity is 3.3×10^{-6} S/cm, which is slightly higher than that of pTOC-350 synthesized over 72h.

Table 4.13. Conductivity and surface area data for POPs and COFs.

Material	Description	Crystallinity	Conductivity (S cm^{-1})	BET SA (m^2 g^{-1})	References
pTOC-250	-	-	1.7×10^{-5}	411	this work
pTOC-300	-	-	1.2×10^{-5}	1075	this work
pTOC-350	-	-	1.0×10^{-6}	1656	this work
pTOC-350	ox (I$_2$)	-	4.1×10^{-4}	n.a.	this work
pTOC-350	LR[a]	-	1.2×10^{-5}	n.a.	this work
3D ep-POP	-	-	8×10^{-10}	779	3a
3D p-POP	-	-	5×10^{-8}	801	3a
3D p-POP	ox (I$_2$)	-	6×10^{-4}	n.a.	3a
SP-BTT	-	-	4.2×10^{-6}	356	4a
SP-BTT-HCl	H$^+$	-	1×10^{-4}	n.a.	4a
1-S	-	x	3.7×10^{-10}	1424	24
1-Se	-	x	8.4×10^{-9}	1634	24
1-Te	-	x	1.3×10^{-7}	352	24
sp^{2}c-COF	-	x	6.1×10^{-16}	692	25
sp^{2}c-COF	ox (I$_2$)	x	7.1×10^{-4}	n.a.	25
BUCT-COF-1	-	x	1.6×10^{-7}	976	23b
BUCT-COF-4	-	x	5.8×10^{-8}	477	23a
BUCT-COF-4	ox (I$_2$)	x	2.8×10^{-6}	n.a.	23a
ZnPc-pz-I$_2$	ox (I$_2$)	x	3.1×10^{-4}	225	23c
CuPc-pz	-	x	3.3×10^{-7}	485	23d
ZnPc-pz	-	x	7×10^{-7}	487	23d
P2PV	-	x	1×10^{-9}	880	26
P3PcB	-	x	1×10^{-9}	1073	26

[a] LR = Lawesson Reagent
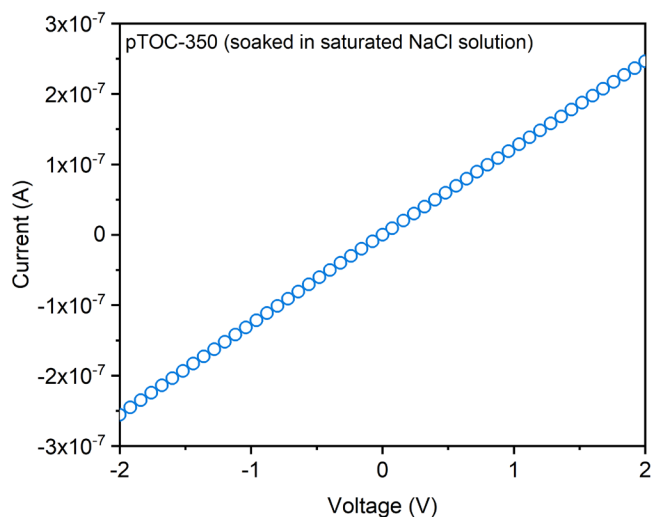
Figure 4.19. I-V curve of two-probe electrical conductivity measurement of pTOC-350 synthesized by a 72-hour reaction. The sample was doped by soaking in saturated sodium chloride solution. These measurements were conducted to prove that chloride ions are not acting as dopants in pTOCs. We hypothesize that the Cl could be 1) Cl⁻ remaining in the framework, or 2) C–Cl moieties generated during synthesis as defects. Assuming hypothesis 1 is true, we performed conductivity measurements of pTOC-350 soaked in NaCl aqueous solution, which exhibit 2-probe electrical conductivity of 1.8×10^{-7} S/cm. This value is slightly lower than that of pristine pTOC-350 (1.0×10^{-6} S/cm), and we thus prove that Cl⁻, if present in the material, cannot promote charge transport of pTOCs. On the other hand, assuming the presence of C–Cl moieties, the in-plane π-conjugation will be significantly interrupted, leading to lower electrical conductivity. Therefore, we conclude that the presence of trace chlorine in pTOCs, being either chloride or organic chlorine, does not act as a doping agent and cannot promote charge transport of pTOCs.

Interestingly, the electrical conductivity of pTOCs revealed negative photo-response, decreasing by more than one order of magnitude after the four-probe device was exposed to light and low-intensity red laser (630–670 nm) (Figures 4.16C, 4.20). We note that although a photo-response is not unusual for organic electronic materials, the majority are positively photo-conductive, whereas negative photoconductivity is much less common.[27] We attribute it to the light-induced generation of shallow trap states that impedes the transport of charge carriers.[28] To verify the stability of pTOCs under photo-irradiation, we conducted long-term exposure experiments followed by characterization via HRXPS (Figure 4.21 and Table 4.14-4.15) and DRUV-Vis (Figure 4.22) spectroscopy, the results of which indicate that the chemical structure of pTOC remains unchanged. With well-defined residual carbonyl defects present, post-synthetic modification (PSM) of these sites allows the tuning of electronic properties of pTOCs. We conducted PSM of residual carbonyls in pTOC-350 using Lawesson's reagent (LR) (Figure 4.23A). This treatment transforms C=O groups to C=S groups, as confirmed by the reduced intensity of residual C=O and the appearance of C=S vibrational bands in DRIFTS (Figure 4.24), and the presence of sulfur, as revealed by XPS analysis (Figures 4.25, 4.26). Treatment with the LR increases the conductivity of pTOC-350 by nearly one order of magnitude to 1.2×10^{-5} S cm⁻¹ (Table 4.12). pTOCs also provide a promising platform for bulk doping given their high porosity and high heteroatom content. The bulk

182

doping of pTOC-350 was realized upon exposure to I_2 vapor at room temperature and the incorporation of iodine again confirmed by XPS (Figure 4.27). Two different iodine-containing species were found at binding energies of 619.1 eV and 620.6 eV ($3d_{5/2}$ transition of iodine), which are assigned to reduced species and trapped I_2, respectively. pTOC-350-I_2 showed a slight increase of conductivity to 5.0×10^{-6} S cm^{-1} (Figure 4.28). Notably, the conductivity of pTOC-350 enhanced substantially to 4.1×10^{-4} S cm^{-1} after exposure to I_2 at 50 °C, a value that is in line with some of the most conductive POPs.[2] DRIFTS of pTOC-350-I_2 revealed negligible changes except for the appearance of intense Drude-type background absorption(Figure 4.29), suggesting a significant increase in free carrier concentration upon I_2 doping.
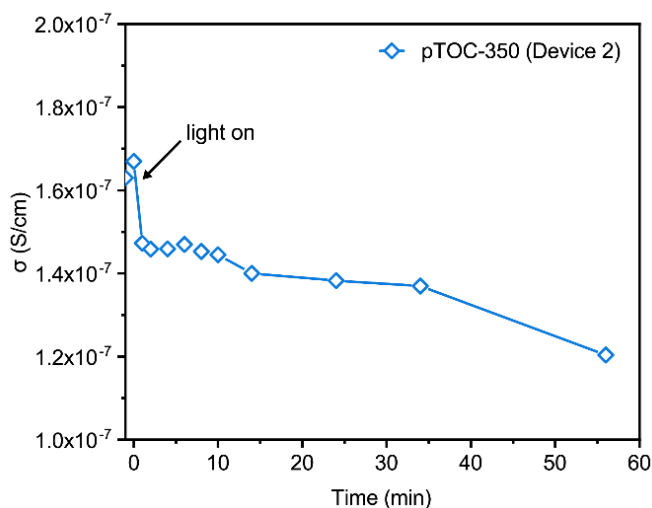
Figure 4.20. Negative photoconductivity of another four-probe device of pTOC-350, exhibiting moderate to significant electrical conductivity drop upon light exposure.
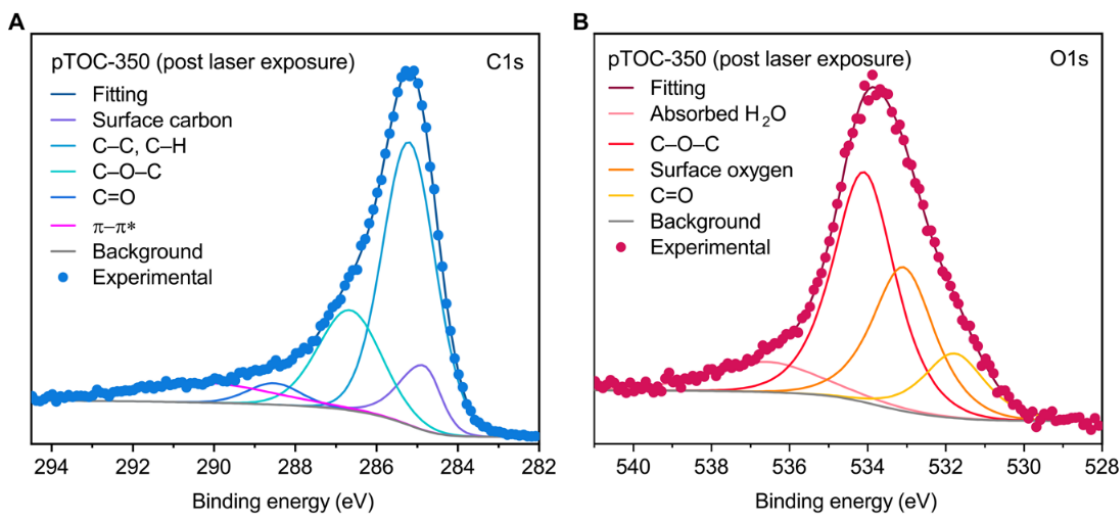
Figure 4.21. High-resolution C1s (A) and O1s (B) XPS spectra of laser-exposed pTOC-350 and the corresponding deconvolutions.

Table 4.14. Deconvolution details of C1s XPS spectrum of pTOC-350 (laser exposed).

Name	Position (eV)	FWHM (eV)	Line Shape	%Area
Adventitious carbon	284.83	1.00	LA(4.2, 9, 4)	9.88
C–H, C–C	285.20	1.53	GL(30)	53.53
C–O–C	286.66	1.84	GL(30)	22.76
C=O	288.52	1.53	GL(30)	4.04
π -π*	290.31	4.00	GL(30)	9.79

Table 4.15. Deconvolution details of O1s XPS spectrum of pTOC-350 (laser exposed).

Name	Position (eV)	FWHM (eV)	Line Shape	%Area
C=O[a]	531.78	2.54	GL(70)	13.16
Surface O	533.09	2.54	GL(70)	29.30
C-O-C	534.10	2.54	GL(70)	46.89
Absorbed H_2O[b]	536.59	3.22	GL(70)	10.65

[a]The BE of C=O peak is consistent with the literature values of aromatic C=O. [b]Absorbed H_2O is needed for fitting.
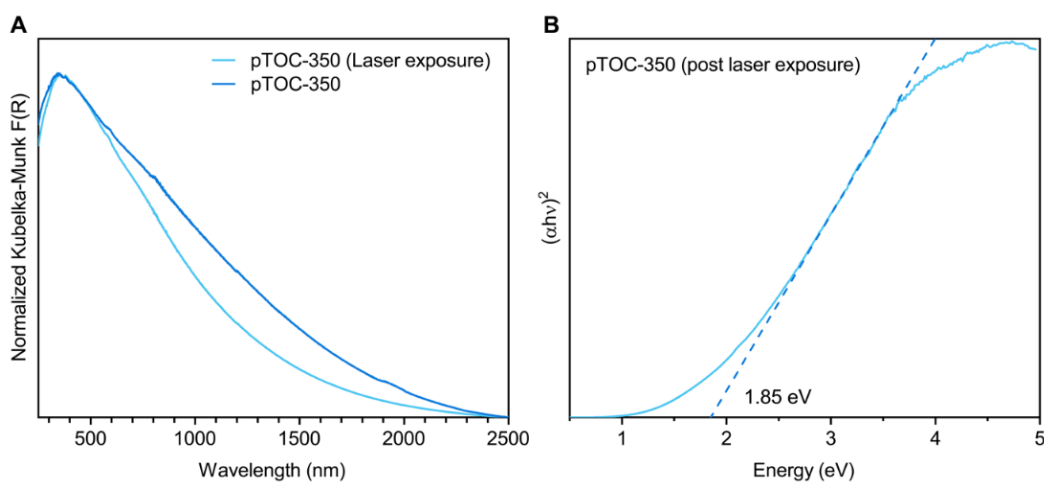
Figure 4.22. (A) DRUV-Vis spectra of pristine pTOC-350 and pTOC-350 exposed to laser. (B) Tauc plot of the DRUV-Vis spectrum of pTOC-350 exposed to laser. The dashed line is the linear fitting, revealing an optical band gap of 1.85 eV.
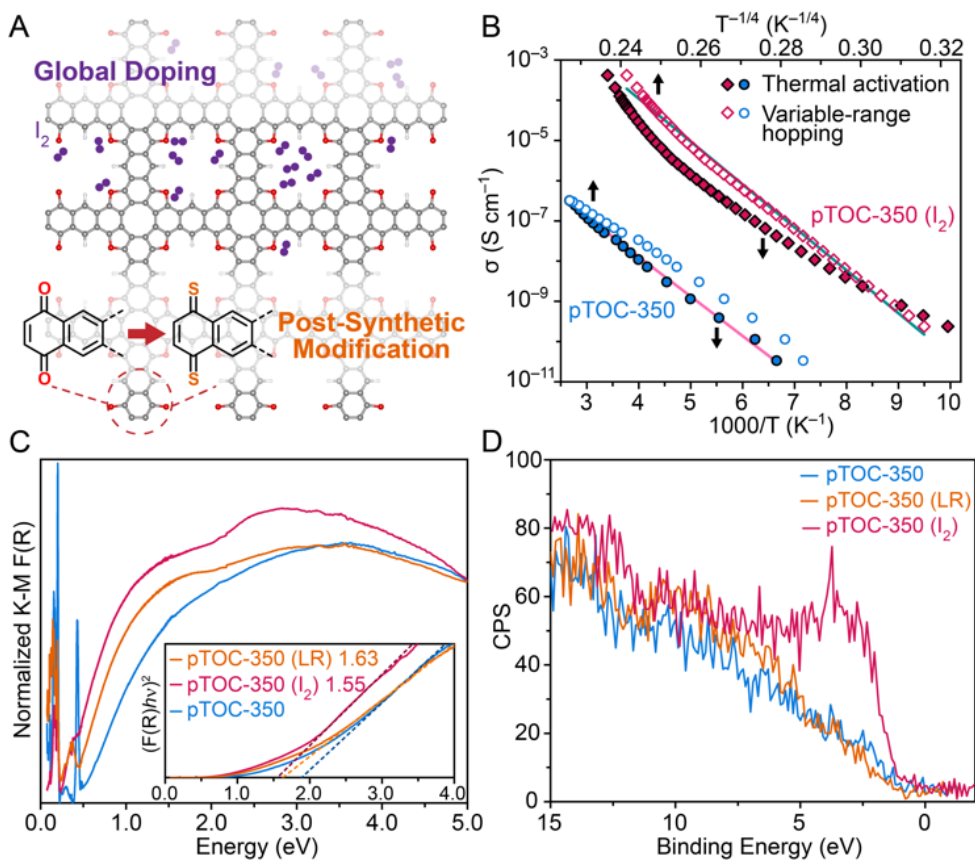
Figure 4.23. Doping and post-synthetic modification. A) Schematic representations of PSM and bulk doping. B) Variable-temperature electrical conductivity measurements of pTOC-350 and pTOC-350-I_2. Solid and hollow symbols represent data plotted for the thermal hopping model and the VRH model, respectively. Solid lines are the best fits. C) Diffuse reflectance UV/Vis-NIR and DRIFTS spectra of pTOC-350 (blue), pTOC-350-LR (orange), and pTOC-350-I_2 (red). D) VB-XPS of the samples shown in (C).
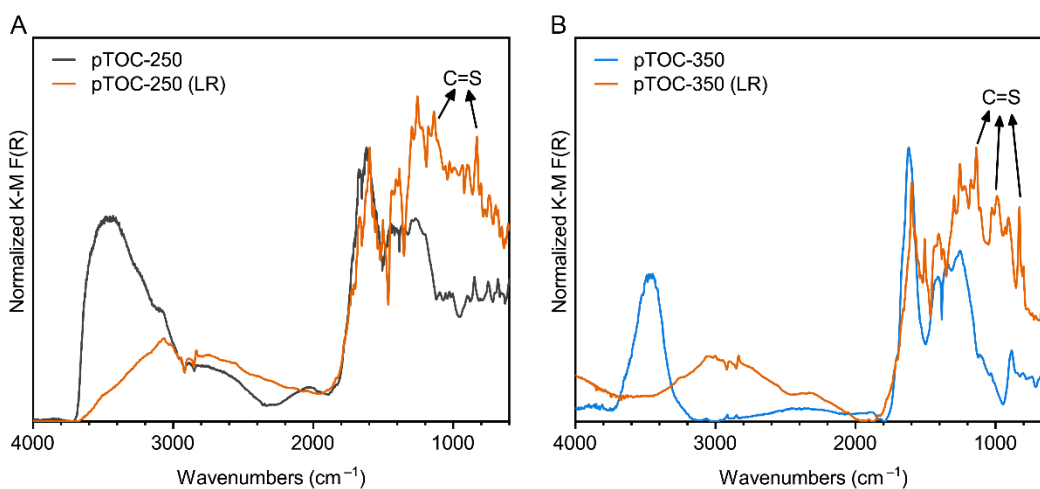
Figure 4.24. The comparison of DRIFTS of pristine pTOCs and pTOCs (LR). The decrease in the intensity of residual carbonyl moiety was observed along with the appearance of new peaks between 1200 cm^{-1} and 800 cm^{-1}, which were tentatively assigned to C=S stretching modes.
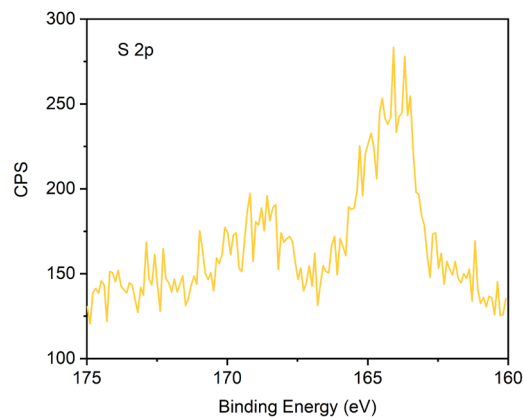
Figure 4.25. S2p XPS spectrum of pTOC-350 reacted with LR.
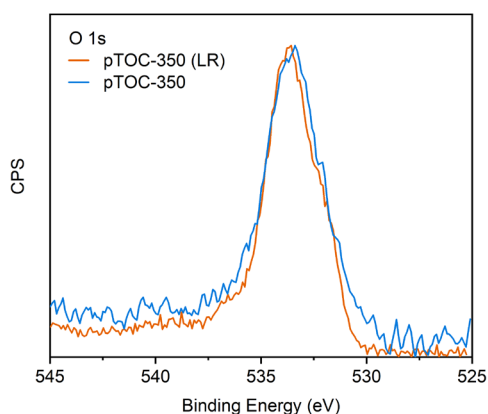
Figure 4.26. O1s XPS spectrum of pristine pTOC-350 and pTOC-350 (LR). According to the O1s deconvolution of pTOCs, the lower intensity at lower BE of pTOC-350 (LR) indicates the decrease of residual carbonyl groups.
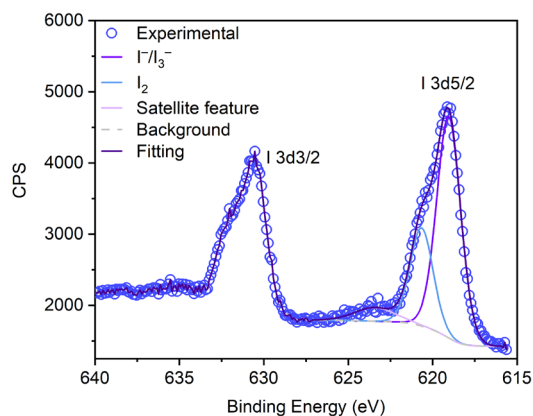
Figure 4.27. I 3d XPS spectrum of pTOC-350 doped with I_2. The presence of iodine was clearly seen even under ultrahigh vacuum (~10^{-10} Torr), suggesting that the iodine-containing species present in the doped material indeed interact with the framework. Deconvolution of the I 3d5/2 region resulted in three components (65.5% : 27.8% : 6.7%). The species with BE of 619.05 eV has oxidation states lower than I_2, which normally shows a BE of 620.2±0.5 eV. We attribute this species to the product obtained after redox reaction between I_2 and pTOC-350 and/or I_2 molecules that are strongly interacting with the framework, given that previous literature has reported that I_2 chemisorbed on Ag surface also exhibited a BE of 619.3 eV. The component with a BE of 620.6 eV is assigned to trapped iodine. The broad peak with a BE of 623.4 eV is the result of satellite features.
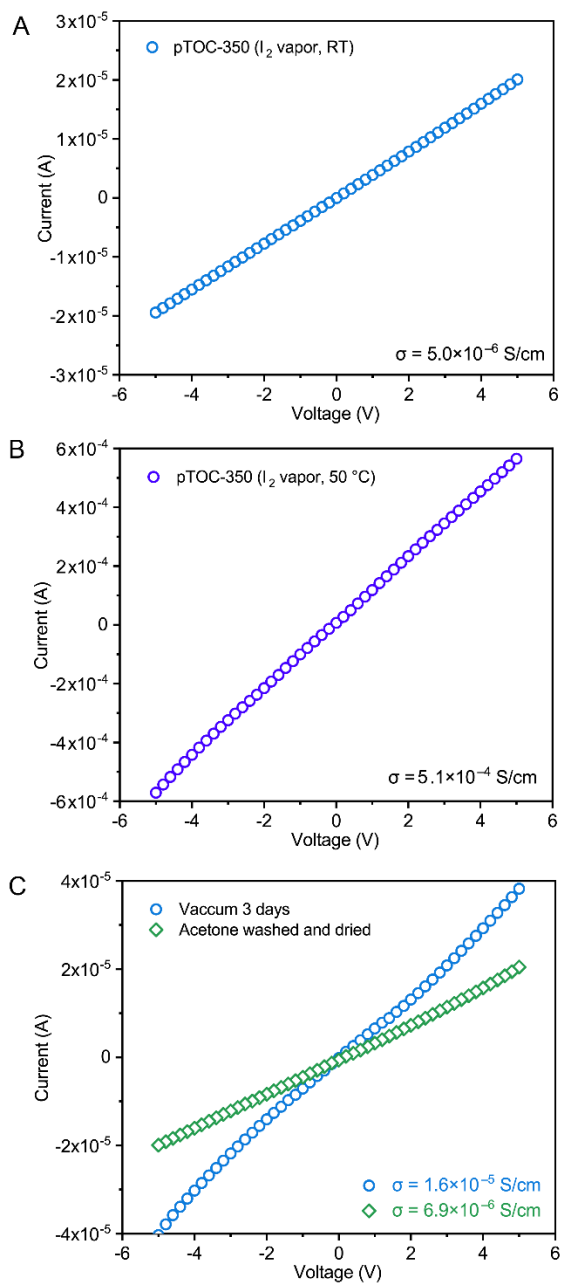
Figure 4.28. The typical *I-V* curves of two-probe electrical conductivity measurements of pTOC-350 doped with I_2 vapor at RT (A), and 50 °C (B). The average conductivity of pTOC-350 doped at 50 °C for 6 h and 18 h are 1.9×10^{-4} S/cm and 5.1×10^{-4} S/cm, respectively. (C) IV curves of pTOC-350-I_2 which are either evacuated under dynamic vacuum for 3 days (blue circles) or washed with acetone and dried (green squares), showing decreased conductivity of $1.6 \times \times 10^{-5}$ S/cm and 6.9×10^{-6} S/cm, respectively. However, these values are still obviously higher than the pristine pTOC-350, suggesting the increased conductivity is robust in pTOC-350-I_2.
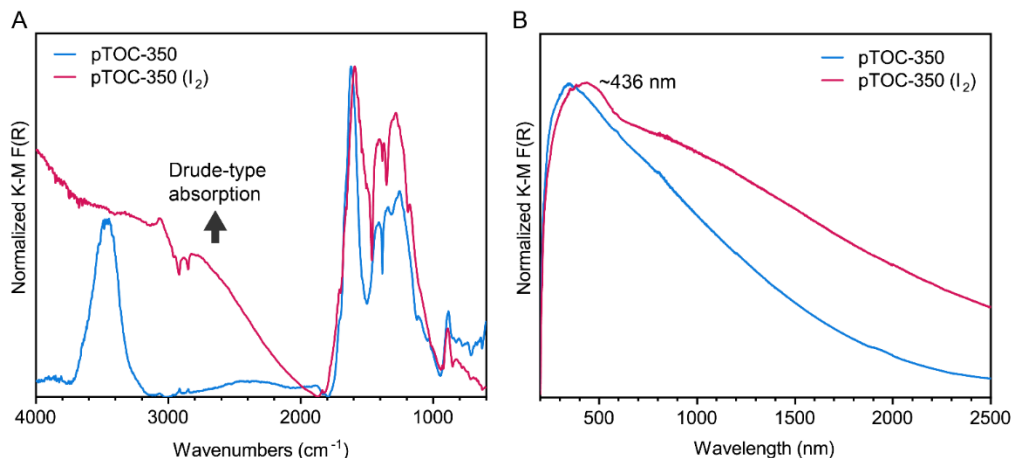
Figure 4.29. (A) The comparison of DRIFTS of pristine pTOC-350 and pTOC-350 (I_2). The peak profiles did not change, however, the Drude-type absorption became significant after I_2 doping, suggesting the substantial increase of free carrier concentration. This is likely the result of redox doping that generated a lot of carriers. (B) The comparison of DRUV (plotted in the wavelength scale) of pristine pTOC-350 and pTOC-350 (I_2). The absorption maximum red shifted almost 100 nm to ~436 nm, suggesting a smaller band gap. The growth of a broad NIR band was also observed, which we attribute to the polaronic transition that caused by I_2 doping. The intense background absorption matches well with DRIFTS.
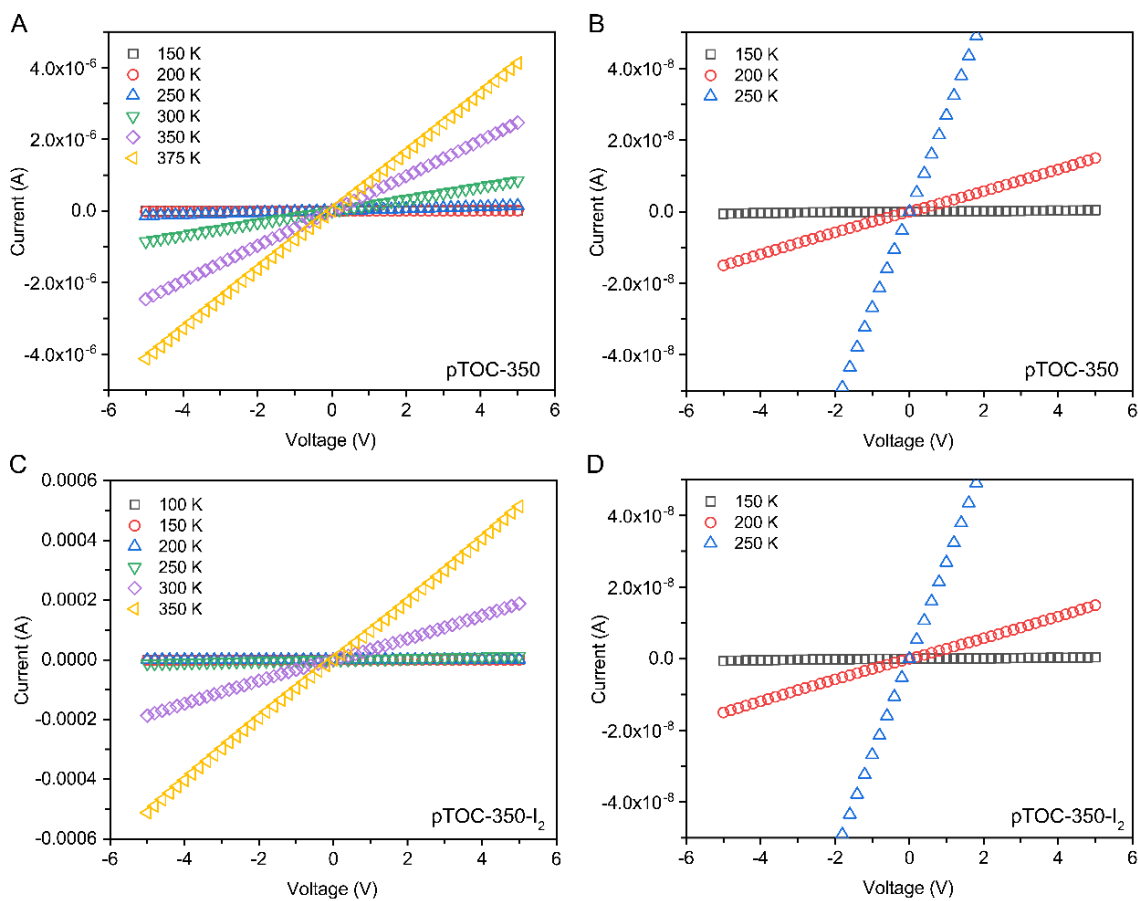
Figure 4.30. *I–V* curves for a two-probe pressed pellet of (A, B) pTOC-350 and (C, D) pTOC-350-I_2 taken at different temperatures.
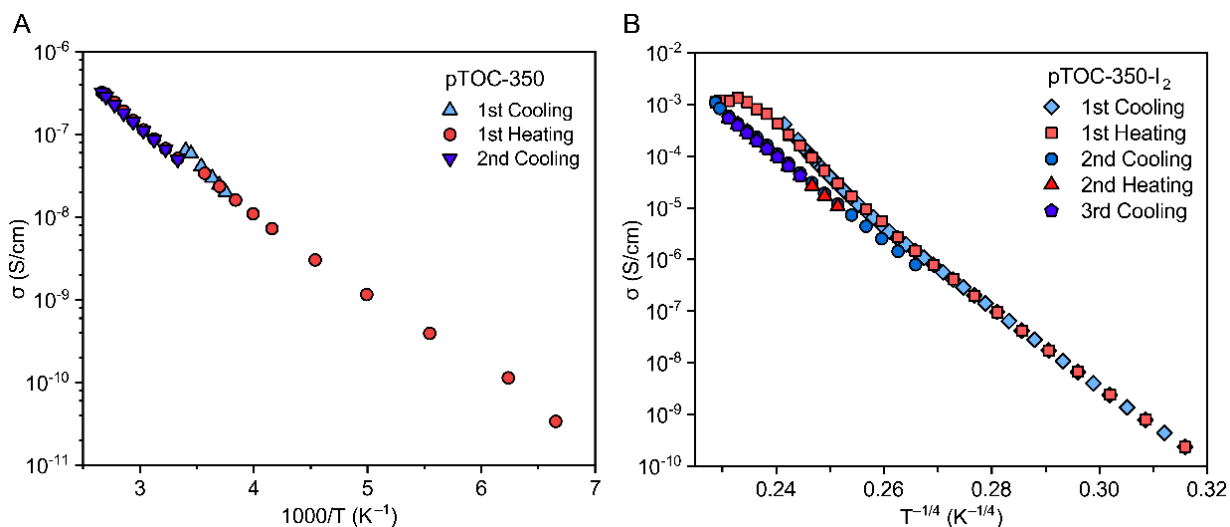
Figure 4.31. Multiple cycles of VT electrical conductivity data of pTOC-350 plotted for thermally activated hopping transport (A) and pTOC-350-I_2 plotted for 3D VRH mechanism (B). The conductivity of pTOC-350-I_2 only decreased very slightly after the first heating measurement that went to 375 K under high vacuum, confirming that the I_2 doping of pTOC-350 is robust.

Variable-temperature (VT) conductivity measurements (Figures 4.30, 4.31) revealed semiconducting behavior for pTOC-350 and pTOC-350-I_2 between 375 K and 100 K (Figure 4.23B). Fitting the data of pTOC-350 to the Arrhenius equation for conventional thermally activated hopping transport between the nearest-neighbor localized states, $\sigma = \sigma_0\exp(-E_a/k_BT)$, where σ is the electrical conductivity, σ_0 is a material-based prefactor, k_B is the Boltzmann constant, and T is the absolute temperature, yielded the activation energy for hopping, $E_a = 0.195$ eV. This value is lower than that of a 3D fully sp^2-hybridized graphitic polymer (3D-p-POP) we reported previously.[3a] However, the variable temperature conductivity data for pTOC-350-I_2 deviates significantly from linear behavior when modeled by thermally activated hopping (Figure 4.32). Instead, the data fits better to the variable-range hopping (VRH) model, $\sigma = \sigma_0\exp[-(T_0/T)^{1/4}]$, where σ_0 is the conductivity at infinite temperature, and T_0 is the Mott temperature.[29] The better fit to the VRH model suggests that in the I_2-doped sample, more delocalized electronic states and/or better overlap of charge carrier wavefunctions dominate transport.[30]

To understand the change in the electronic structures of pTOCs upon post-synthetic modification and doping, we conducted DRUV-Vis and valence-band XPS (VB-XPS). pTOC-350-LR and pTOC-350-I_2 both exhibit red-shifted absorption (Figure 4.23C) and a decrease in E_o from 1.88 eV to 1.63 eV, and 1.55 eV, respectively, accompanied by an increase in the background absorption and the appearance of a broad NIR band owing to the polaronic transitions and/or interlayer interactions (Figure 4.33). The absorption maximum of pTOC-350-I_2 red-shifted to ≈436 nm, as might be expected for significantly delocalized electronic states revealed by VT conductivity measurements. The main absorption band for pTOC-350-LR showed no change, highlighting the different outcomes between bulk doping and post-synthetic modification. VB-XPS, which reports on the density of states (DOS) near the Fermi level E_F, revealed a

189

significant increase of DOS for pTOC-350-I_2, further substantiating the increase in carrier concentration (Figure 4.23D, 4.34) upon I_2 doping, contrasting with the minimal changes observed for the LR-treated sample.
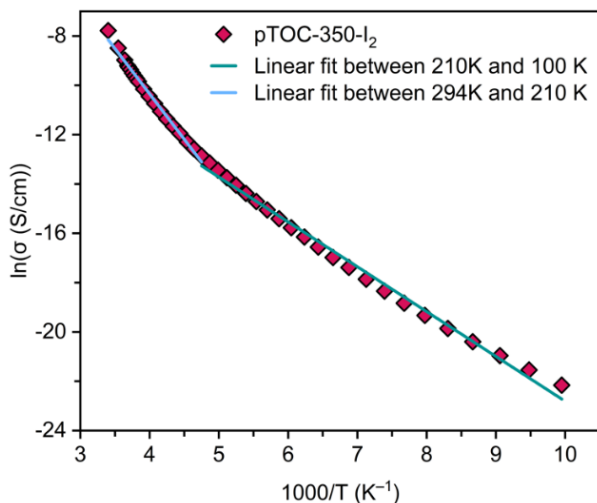
Figure 4.32. The VT electrical conductivity data of pTOC-350-I_2 plotted for thermally activated hopping transport ($\ln(\sigma)$ versus T^{-1}) from 294 K to 100 K. The linear fittings of low temperatures (210 K to 100 K) or high temperatures (294 K to 210 K) both revealed deviation of the experimental data from linear behaviour, although with $R^2 \sim 0.99$. The linear fitting of the full temperature range (100 K to 294 K, not shown for clarity) gave a R^2 of 0.97, indicating poor correlation.
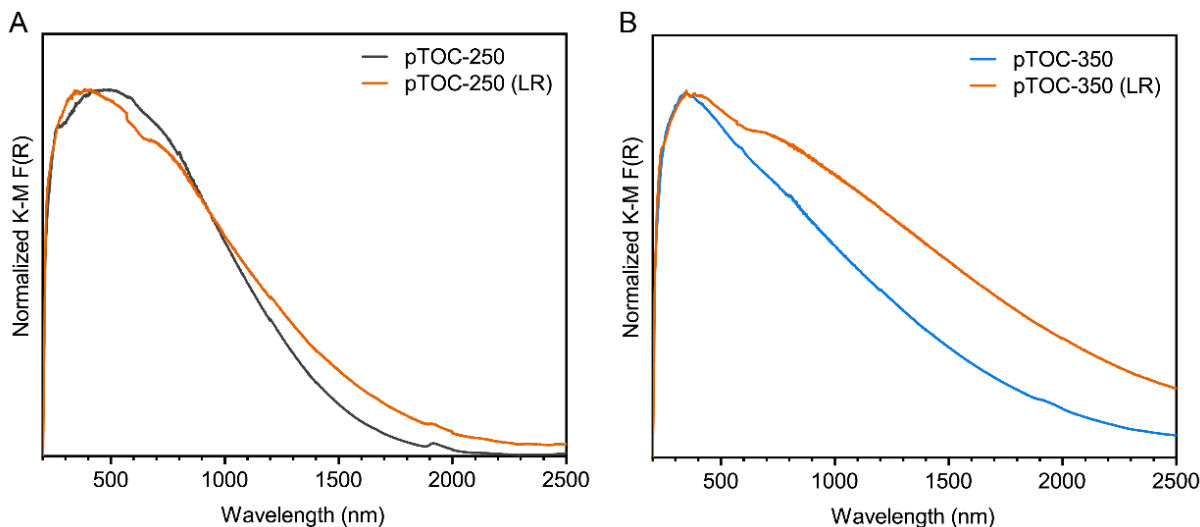
Figure 4.33. The comparison of DRUV (plotted in the wavelength scale) of pristine pTOCs and pTOCs (LR). The absorption maximum of pTOC-250 significantly blue shifted to ~385 nm upon LR treatment, indicating that the extended conjugation might be interrupted by defect engineering. However, a slight increase of the background absorption was observed, implying the small increase of free carrier concentration. On the other hand, the DRUV spectrum of pTOC-350 changed substantially upon LR treatment. Although the main absorption changed little, which in fact is in great agreement with the defect engineer strategy rather than global doping, the NIR band centered close to 800 nm significantly gained intensity, indicating that the incorporation of heavier atoms (S in this case) can assist intermolecular interactions. The background absorption also increased a lot for pTOC-350. The changes of electronic structure reflected well on the electrical conductivity changes.
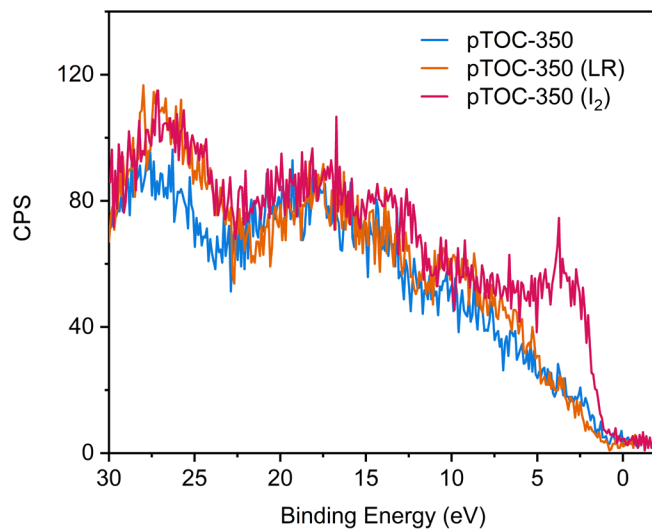
Figure 4.34. Valence-band (VB) XPS of pristine pTOC-350 (blue), pTOC-350 (LR) (orange), and pTOC-350 (I_2) (red). A significant increase of DOS near Fermi level was observed for pTOC-350 (I_2), suggesting the increase of carrier concentration.

4.4 Conclusions

In summary, we have introduced a new class of semiconducting two-dimensional porous organic polymers featuring tetraoxa[8]circulene building blocks, which—to date—were only envisioned in theoretical simulations. The polymers, obtained via ionothermal synthesis, feature high porosity, semiconductor behavior, and unusual negative photoconductivity. The conductivity of the pTOCs can be tuned through both post-synthetic modification and bulk doping, where both their carrier concentration and electronic band structures are readily controlled. Altogether, these results highlight the potential of pTOCs as a new family of porous semiconductors.

4.5 Methods and Materials

4.5.1 Materials

All chemicals and solvents were purchased and used without any further purification. 1,8-Dihydroxy-9,10-anthraquinone (95%), aluminium(III)chloride (98.5%), sodium chloride (99.5%) and nitrobenzene (99%) were purchased from Acros Organics. Potassium carbonate (99%), dichloromethane (99%), magnesium sulfate, silica (60A, 35-70 micron), methanol, THF and hydrochloric acid (37%) were purchased from Fisher Chemicals. Dimethylsulfate (99.5%), zinc powder and ceric(IV)ammoniumnitrate (98.5%) were purchased from Sigma Aldrich. Acetone was purchased from Thommen Furler. Sodium hydroxide was purchased from Reactolab SA. N-bromosuccinimde was purchased from Fluorochem. Pyridine was purchased from Roth.

4.5.2 Synthetic Methods
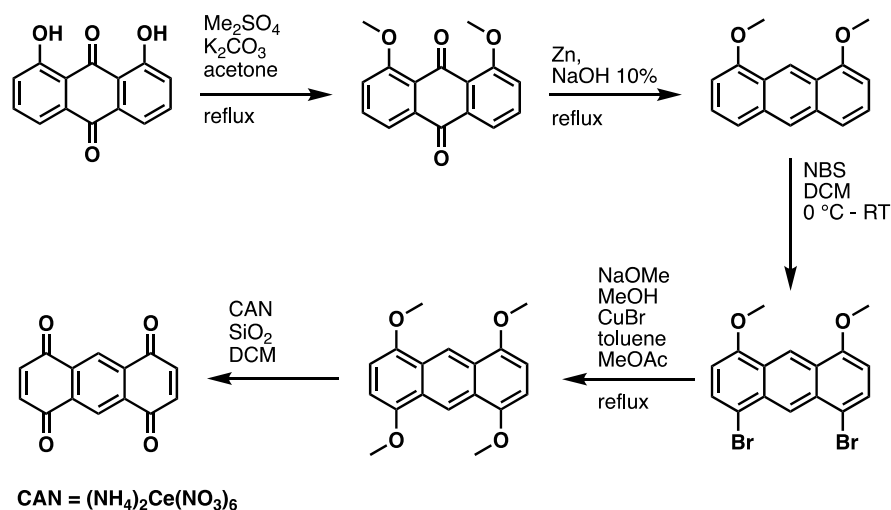
Scheme 4.1. Reaction scheme for the preparation of 1,4,5,8-anthracenetetrone starting from 1,8-dihydroxy-9,10-anthraquinone.

1,8-Dimethoxy-9,10-anthraquinone (1)

A 500 mL two-neck round bottomed flask was flushed with argon and charged with 1,8-dihydroxy-9,10-anthraquinone (15.5 g, 64.5 mmol, 1 eq.) and K_2CO_3 (24.1 g, 174.2 mmol, 2.7 eq.) and acetone (400 mL) before heating to reflux for 30 minutes. Subsequently, dimethyl sulfate (15.26 mL, 161.3 mmol, 2.5 eq.) in acetone (50 mL) was slowly added over the course of 30 minutes. The obtained solution was subsequently refluxed for 48 h. After cooling to RT, the suspension was filtered, and the purple residue washed with 3×150 mL CH_2Cl_2. The combined organic phases were passed through silica and the pad was washed with 3×100 mL CH_2Cl_2. The solvents were removed under reduced pressure and the obtained residues were subsequently stirred in 2N NaOH for 30 minutes to remove residual dimethyl sulfate. Subsequently, the aqueous layers were extracted with CH_2Cl_2. After removing the solvents, the product was obtained as a yellow solid. Yield: 15.8 g (91.3 %); yellow solid. ^{1}H NMR (400 MHz, Chloroform-d) δ 7.84 (dd, J = 7.7, 1.1 Hz, 1H), 7.64 (dd, J = 8.4, 7.7 Hz, 1H), 7.30 (dd, J = 8.4, 1.1 Hz, 1H), 4.01 (s, 3H).

1,8-Dimethoxyanthracene (2)

A 500 mL two-neck flask was flushed with argon and charged with **2** (5.00 g, 18.6 mmol, 1.00 eq.), 10% aq. NaOH (125 mL) and zinc powder (7.31 g, 111.8 mmol, 6.0 eq.). The obtained mixture was heated under vigorous stirring for 24 h. The suspension was filtered, and the filtrate washed with 3 x 100 mL water before drying under vacuum. The obtained yellow–grey precipitate was dissolved in CH_2Cl_2 (500 mL) and was passed through a short pad of silica before removing the solvents under reduced pressure. Yield: 3.9 g (89.6 %); yellow solid. ^{1}H NMR (400 MHz, Chloroform-d) δ 9.24 (d, J = 1.0 Hz, 1H), 8.31 (s, 1H), 7.56 (dq, J = 8.6, 0.8 Hz, 2H), 7.37 (dd, J = 8.5, 7.4 Hz, 2H), 6.73 (dd, J = 7.5, 0.8 Hz, 2H), 4.09 (s, 6H).

1,8-Dibromo-4,5-dimethoxyanthracene (3)

A 250 mL two-neck flask was flushed with argon and charged with **3** (1.0 g, 4.2 mmol, 1.0 eq.) in 50 mL CH_2Cl_2 before cooling to 0 °C with an ice bath. Subsequently, NBS (1.5 g, 8.6 mmol, 2.05 eq.) was added over 30 minutes and the solution was slowly allowed to warm to RT and was stirred for an additional 3 hours. After diluting the reaction mixture with CH_2Cl_2, the solution was washed with 2N NaOH (100 mL) and 3x150 mL water. The combined organic layers were dried over $MgSO_4$ and the solvents evaporated under reduced pressure. Yield: 1.1 g (66.2 %); green solid. ^{1}H NMR (400 MHz, Chloroform-*d*) δ 9.26 (d, *J* = 0.9 Hz, 1H), 9.01 (d, *J* = 0.9 Hz, 1H), 7.72 (d, *J* = 8.1 Hz, 2H), 6.63 (d, *J* = 8.0 Hz, 2H), 4.07 (s, 6H).

1,4,5,8-Tetramethoxyanthracene (4)

A 500 mL two-neck flask was flushed with argon and charged with methanol (200 mL). Freshly cut sodium (23.2 g, 1.01 mol, 100 eq.) was slowly added over the course of 1 hour. Towards the end of the addition the solution was heated to reflux before adding **3** (4.0 g, 10.1 mmol, 1.0 eq.), dry toluene (100 mL), MeOAc (9.52 g, 10.0 mL, 126.2 mmol, 12.5 eq.) and copper (I) bromide (1.4 g, 10.1 mmol, 1.0 eq.), successively. The obtained suspension was heated to reflux for 48 h. After cooling to RT, the solvents were removed under reduced pressure and the residue was carefully dissolved with CH_2Cl_2 (300 mL) and washed with 10% HCl followed by water (3x 200 mL). The organic layers were dried over $MgSO_4$ and the solvents evaporated under reduced pressure. The obtained solid was triturated with hot chloroform to afford **4** as a pale-yellow solid. Yield: 1.8 g (59.7 %); pale-yellow solid. ^{1}H NMR (400 MHz, Chloroform-*d*) δ 9.10 (s, 2H), 6.63 (s, 4H), 4.03 (s, 12H).

1,4,5,8-Anthracenetetrone (5)

A 500 mL two-neck flask was charged with silica (50.0 g) before slowly adding ceric ammonium nitrate (23.3 g, 42.4 mmol, 5.5 eq.) dissolved in 37 mL of H_2O. The mixture was stirred till a yellow free-flowing solid was obtained. Subsequently, 300 mL CH_2Cl_2 was added before adding **4** (2.3 g, 7.7 mmol, 1.0 eq.) dissolved in CH_2Cl_2 (50 mL) was added dropwise and stirred for 2 h. The obtained suspension was filtered, and the residues washed with CH_2Cl_2 (200 mL). The combined organic layers were dried over $MgSO_4$ and the solvents evaporated under reduced pressure. The obtained solid was purified via column chromatography with 4:1 CH_2Cl_2:hexanes as an eluent. Yield: 1.35 g (73.5 %); red crystals. ^{1}H NMR (400 MHz, Chloroform-*d*) δ 8.82 (s, 2H), 7.14 (s, 4H).

Ionothermal synthesis of pTOC-350

A 20 mL glass ampule was charged with ground sodium chloride (86.4 mg, 1.48 mmol, 1.76 eq.) before transferring to a glovebox. Subsequently, **5** (200.0 mg, 0.84 mmol, 1.00 eq.) and aluminum chloride (313.5 mg, 2.35 mmol, 2.8 eq.) were added and the ampule was evacuated to an internal pressure of 0.15

mbar for 45 min before flame-sealing the ampule. The mixture was heated to 350 °C for 72h or 120h. After cooling to RT the obtained black solid was stirred in a 1:1 mixture of water and methanol for 24h followed by 2N HCl for 48h. The solid was subsequently filtered using a POR4 fritted glass filter and washed with water, methanol, acetone, pyridine and THF. The polymer was subsequently stirred in a 1:1 water-ethanol mixture overnight followed by stirring in 2N HCl overnight. Finally, the polymers were filtered over a POR4 fritted glass, washed with water and acetone before being dried at 90 °C under vacuum. Yield: 147 mg (88 %); black powder.

pTOC-250 and -300 were synthesized by following same procedure at 250 and 300 ºC, respectively.

Solvothermal synthesis of pTOCs

A 20 mL microwave vial was charged with **5** (50.0 mg, 0.21 mmol, 1.00 eq.), aluminum chloride (39.2 mg, 0.29 mmol, 1.4 eq.) and nitrobenzene (5 mL) in a glovebox before heating to reaction temperature (100, 125, 150 and 175 °C) for 6 hours. After cooling to RT the obtained suspension was filtered over a POR4 fritted glass filter and subsequently washed with ethanol, 2N HCl, ethanol, pyridine and ethanol. Yield: 0 g (0 %).

Solvothermal synthesis of TOC

A 10 mL microwave vial was charged with previously sublimed naphthoquinone (100.0 mg, 0.63 mmol, 1.00 eq.), aluminum chloride (118.0 mg, 0.885 mmol, 1.4 eq.) and nitrobenzene (5 mL) in a glovebox before heating in a microwave to 60 °C for 1 hour. After cooling to RT the obtained suspension was filtered over a POR4 fritted glass filter and subsequently washed with ethanol, 2N HCl, ethanol, pyridine and ethanol. Yield: 80.6 mg (91.0 %); yellow powder.

Doping of pTOCs

I_2 vapor doping: 10 mg of pTOCs placed in a 4 mL vial, and then this vial was placed into a 20 mL vial with 10 mg of I_2. The small vial was left open, while the large vial was sealed. The vapor doping set-up kept at room temperature or elevated temperature for 6~12 hours.

KOH or HCl doping: To a 20 mL vial with 20 mg of pTOCs was added 5~10 mL of aqueous KOH or HCl solution. The vial was sealed and kept at room temperature overnight. The reaction mixture was then filtered and washed with DI water and acetone and dried over air flow.

Post-synthetic modification of the unreacted carbonyl groups in pTOCs using Lawesson's reagent: In a N_2-filled glove box, 15 mg of pTOCs and 15 mg of Lawesson's reagent were transferred into a 20 mL glass pressure tube, followed by the addition of 5 mL toluene. The pressure tube was then transferred out of the glove box and heated at 120 °C for 12 hours. After cooling down to room temperature, the reaction mixture was filtered and washed with toluene. The resulting black solid was dried under air flow.

4.5.3 Physical Characterization Methods

FTIR spectra were recorded on a PerkinElmer Frontier spectrometer equipped with a PIKE GladiATR module in the range of 4000-400 cm^{-1} at a scanning rate of 2 cm^{-1}.

Liquid phase NMR spectra were recorded on a Bruker Ascend 400 MHz spectrometer using deuterated solvents.

CP-MAS ^{13}C solid-state NMR spectra were recorded on a Bruker Avance Neo 400 MHz spectrometer using 7 kHz or 10 kHz spinning rate and a 5.0 s relaxation delay.

PXRD patterns were recorded on a STOE STADI-P system using Cu Kα1 incident beam. The diffractograms were recorded between 2θ 2-60° and 0.015°/step using a DECTRIS MYTHEN 1K detector.

TGA analysis was recorded on a Mettler-Toledo TGA/DSC 3+ instrument using standard 70 μL alumina and 40 μL aluminium crucibles. The flowrate of the respective gas (nitrogen or air) was set to 10 mL/min and the heating rate was set to 5 °C/min for the 600 °C measurements under nitrogen and to 10 °C/min for the 1000 °C measurements under nitrogen or air.

Nitrogen and CO_2 sorption measurements were performed at 77 and 273 K, respectively, using Micromeritics 3Flex instrument, after evacuation of the samples at 363 K for 24 h. The pore size distribution was determined *via* NLDFT using carbon heterogeneous surface as model.

Field emission SEM images were obtained using a TESCAN MIRA3. Prior to the SEM measurements, the samples were coated with 1.5 nm of gold using a Cressington 208HR sputter coater.

Raman spectra were recorded on an Alpha 300R Raman microscope with a UHTS 300 spectrometer using 535 nm laser excitation.

XPS measurements were performed at the MIT MRSEC (formerly the Center for Materials Science and Engineering, or CMSE) using a Physical Electronics PHI Versaprobe II X-ray photoelectron spectrometer equipped with a monochromatic Al anode X-ray source. The main chamber pressure was in the 10^{-10} Torr range. pTOC powder samples were pressed on copper tapes with full coverage. Survey spectra were collected from 0~1100 eV in binding energy (BE), with a resolution of 0.8 eV. High resolution spectra of C1s and O1s regions were collected with a resolution of 0.1 eV. BE calibration was carried out by shifting the adventitious carbon C1s peak to 284.8 eV. Deconvolution of the C1s spectra were conducted before BE calibration to find out the adventitious carbon C1s peak, given that the samples also contain significant amount of carbon. Gaussian-Lorentzian product function, with exponential tailing for asymmetrical peak shape if necessary, was used for the line shapes during fitting, which is commonly used for C1s and O1s. Valence-band XPS was measured at a resolution of 0.1 eV.

DRIFTS measurements were performed on a Bruker Tensor 37 (MIR source and KBr beam splitter) with a mercury cadmium telluride (MCT, cooled with liquid nitrogen) detector utilizing the DiffusIR™ accessory (Pike Technologies). A sealable environmental chamber equipped with ZnSe window (Pike

Technologies) was used. Samples were ground in air with dry potassium bromide (99.9%, Pike technologies) in a mortar and pestle to produce ~1 wt.% pTOC mixtures. The data was averaged over 32 scans between 4000 – 600 cm^{-1} with the resolution of 4 cm^{-1}.

DRUV-Vis spectra between 200 and 2500 nm were collected on a Cary 5000i spectrophotometer, fitted with the UV-Vis DiffusIR accessory (Pike Technologies), at the scan rate of 200 nm/min under ambient conditions. A KBr baseline and a zero-background correction were collected prior to the sample measurements. Samples were prepared as described above for the DRIFTS measurements.

Room temperature electrical conductivity measurements were carried out in an ambient atmosphere on pressed pellets using either the 2-probe or 4-probe setup. For the 2-probe measurements, a home-made press was used, which has two probes that could be connected to source meter. Powder samples were transferred into a glass or PTFE tube and sandwiched between two stainless steel rod leads. The whole set-up was held by an IR press. For the 4-probe measurements, pressed pellets were prepared by adding sample powders into a 6 mm inner-diameter trapezoidal split sleeve pressing (Across International) and pressing the die set by a hydraulic pump (MTI corporation) for 1 min. The applied pressure was approximately 1 GPa. The pellet thicknesses were measured after the measurement using a micrometer (Mitutoyo). The resulting pellet was cut into a cuboid by a blade and placed onto a piece of dry glass slide with thermally conductive and electrically insulating grease (DuPont Krytox). Four parallel copper wire contacts were attached to the cuboid by carbon paste. The other end of the copper wire was pasted onto the glass slide by carbon paste. The device was mounted onto the sample chuck of a probe station (Janis Cryogenics ST-500) equipped with four micro-manipulators that allowed us to control the position of the probes with a resolution of 5 μm. Electrical contacts were made by gently pressing gold-plated tungsten probes (Janis 7B-100G) into the carbon paste that was on the glass slide. For both configurations, probes were connected to a sourcemeter (Keithley model 2450), either through normal wires for 2-probe or through triax cables (Keithley model 7078-TRX-10) for 4-probe. The chamber of the probe station was covered by a stainless-steel lid to keep the device in the dark. Linear I–V curves were obtained by (1) supplying the voltage and measuring the current for 2-probe configuration; (2) supplying the current and measuring the voltage for 4-probe configuration. At least three parallel measurements were conducted for each sample, and the conductivity values were averaged to give the average conductivity value. The light response was investigated using a four-probe configuration employing a 5 mW 650 nm laser. For the negative photoconductivity experiments, the samples were kept in a vial and irradiated for a specific amount of time – 1h or 24h for the actual experiments and stability evaluation respectively.

Variable temperature electrical conductivity data were collected from 150 K to 375 K for pTOC-350, from 100 K to 375 K for pTOC-350-I_2 using a home-built two-probe in situ screw press set-up. Electrical contacts were made by touching the short screw or the inner plate of the sample mounting chuck by gold-

coated tungsten probes. Probes were connected to a sourcemeter (Keithley model 2450) through triax cables described above. Temperature was balanced by the heater of the probe station chuck and liquid nitrogen that were regulated by a temperature controller (Scientific Instruments 9700). All measurements were performed under dynamic vacuum ($\sim 10^{-5}$ Torr). I–V curves were collected by sweeping voltage while scanning temperatures with a step size of 5 K or 10 K and at least 30 minutes per step. Two I–V curves were measured for a given temperature to confirm the stability of temperature. The final measurement at each temperature was used to calculate the conductivity of the device.

The model structure of pTOC was built by Materials Studio using Forcite module and the Universal forcefield, based on the crystal structure of molecular TOC (CCDC 887700). Ultra-fine level of calculation was employed.

Reactions utilizing microwave irradiation were carried out in an Anton Paar Monowave 400 microwave reactor. Heating was performed as fast as possible while after reaching reaction temperature power was regulated by the system to keep temperature constant.

Electron paramagnetic resonance spectroscopy (EPR) measurement was performed on pTOC-350 powder packed under nitrogen in a septum-sealed quartz tube using a Bruker EMX spectrometer equipped with an ER 4199HS cavity and Gunn diode microwave source at room temperature, with a microwave frequency of 9.37 GHz, power of 0.005 mW, and attenuation of 33.0 dB. The measurement was taken in perpendicular mode. Fitting and simulation of EPR spectrum was conducted using EasySpin (https://easyspin.org/).

4.6 References

(1) T. Joshi, C. Chen, H. Li, C. S. Diercks, G. Wang, P. J. Waller, H. Li, J.-L. Bredas, O. M. Yaghi, M. F. Crommie, *Adv. Mater.* **2019**, *31*, 1805941.

(2) P. W. Fritz, A. Coskun, *Chem. Eur. J.* **2021**, *27*, 7489–7501.

(3) a) Y. Byun, L. S. Xie, P. Fritz, T. Ashirov, M. Dincă, A. Coskun, *Angew. Chem. Int. Ed.* **2020**, *59*, 15166–15170; *Angew. Chem.* **2020**, *132*, 15278–15282; b) Y. S. Kochergin, D. Schwarz, A. Acharjya, A. Ichangi, R. Kulkarni, P. Eliášová, J. Vacek, J. Schmidt, A. Thomas, M. J. Bojdys, *Angew. Chem. Int. Ed.* **2018**, *57*, 14188–14192; *Angew. Chem.* **2018**, *130*, 14384–14388.

(4) a) Y. S. Kochergin, Y. Noda, R. Kulkarni, K. Škodáková, J. Tarábek, J. Schmidt, M. J. Bojdys, *Macromolecules* **2019**, *52*, 7696–7703; b) B. Bonillo, R. S. Sprick, A. I. Cooper, *Chem. Mater.* **2016**, *28*, 3469–3480.

(5) J. Lee, O. Buyukcakir, T.-w. Kwon, A. Coskun, *J. Am. Chem. Soc.* **2018**, *140*, 10937–10940.

(6) a) K. B. Ivaniuk, G. V. Baryshnikov, P. Y. Stakhira, S. K. Pedersen, M. Pittelkow, A. Lazauskas, D. Volyniuk, J. V. Grazulevicius, B. F. Minaev, H. Ågren, *J. Mater. Chem. C* **2017**, *5*, 4123–4128; b) R. R. Valiev, R. M. Gadirov, K. M. Degtyarenko, D. V. Grigoryev, R. T. Nasubullin, G. V. Baryshnikov, B. F. Minaev, S. K. Pedersen, M. Pittelkow, *Chem. Phys. Lett.* **2019**, *732*, 136667.

(7) A. Dadvand, F. Cicoira, K. Y. Chernichenko, E. S. Balenkova, R. M. Osuna, F. Rosei, V. G. Nenajdenko, D. F. Perepichka, *Chem. Commun.* **2008**, 5354–5356.

(8) F. Fouad, S. D. Bunge, B. D. Ellman, R. J. Twieg, *Acta Crystallogr. Sect. C* **2012**, *68*, 0465–0467.

(9) F. Chen, Y. S. Hong, S. Shimizu, D. Kim, T. Tanaka, A. Osuka, *Angew. Chem. Int. Ed.* **2015**, *54*, 10639–10642; *Angew. Chem.* **2015**, *127*, 10785–10788.

(10) a) C. B. Nielsen, T. Brock-Nannestad, P. Hammershoj, T. K. Reenberg, M. Schau-Magnussen, D. Trpcevski, T. Hensel, R. Salcedo, G. V. Baryshnikov, B. F. Minaev, M. Pittelkow, *Chem. Eur. J.* **2013**, *19*, 3898–3904; b) G. V. Baryshnikov, R. R. Valiev, N. N. Karaush, D. Sundholm, B. F. Minaev, *Phys. Chem. Chem. Phys.* **2016**, *18*, 8980–8992; c) G. V. Baryshnikov, R. R. Valiev, N. N. Karaush, V. A. Minaeva, A. N. Sinelnikov, S. K. Pedersen, M. Pittelkow, B. F. Minaev, H. Agren, *Phys. Chem. Chem. Phys.* **2016**, *18*, 28040–28051; d) S. Radenković, I. Gutman, P. Bultinck, *J. Phys. Chem. A* **2012**, *116*, 9421–9430.

(11) M. Pittelkow, T. Hensel, N. Andersen, M. Plesner, *Synlett* **2016**, *27*, 498–525.

(12) N. G. Petrov, P. Chartier, T. Maris, J. D. Wuest, *J. Am. Chem. Soc.* **2022**, *144*, 556–572.

(13) a) G. V. Baryshnikov, B. F. Minaev, N. N. Karaush, V. A. Minaeva, *RSC Adv.* **2014**, *4*, 25843–25851; b) G. V. Baryshnikov, B. F. Minaev, N. N. Karaush, V. A. Minaeva, *Phys. Chem. Chem. Phys.* **2014**, *16*, 6555–6559; c) A. V. Kuklin, G. V. Baryshnikov, B. F. Minaev, N. Ignatova, H. Ågren, *J. Phys. Chem. C* **2018**, *122*, 22216–22222; d) L. V. Begunovich, A. V. Kuklin, G. V. Baryshnikov, R. R. Valiev, H. Ågren, *Nanoscale* **2021**, *13*, 4799–4811.

(14) H. Erdtman, H. E. Hogberg, *Tetrahedron Lett.* **1970**, *11*, 3389–3392.

(15) F. Glocklhofer, B. Stoger, J. Frohlich, *Synth. Commun.* **2018**, *48*, 2358–2365.

(16) a) E. M. Levin, J. F. Kinney, R. D. Wells, J. T. Benedict, *J. Res. Natl. Bur. Stand. Sect. A* **1974**, *78*, 505–507; b) R. W. Berg, H. A. Hjuler, N. J. Bjerrum, *Inorg. Chem.* **1984**, *23*, 557–565.

(17) a) M. Liu, L. Guo, S. Jin, B. Tan, *J. Mater. Chem. A* **2019**, *7*, 5153–5172; b) K. Schwinghammer, S. Hug, M. B. Mesch, J. Senker, B. V. Lotsch, *Energy Environ. Sci.* **2015**, *8*, 3345–3353.

(18) K. Tadyszak, A. Musiał, A. Ostrowski, J. K. Wychowaniec, *Nanomaterials* **2020**, *10*, 798.

(19) J. Spanget-Larsen, D. Liang, E. Chen, E. Thulstrup, *Asian Chem. Lett.* **2000**, *4*, 121–134.

(20) G. Beamson, D. R. Briggs, *J. Chem. Educ.* **1993**, *70*, A25.

(21) S. Zheng, D. Shi, D. Yan, Q. Wang, T. Sun, T. Ma, L. Li, D. He, Z. Tao, J. Chen, *Angew. Chem. Int. Ed.* **2022**, *61*, e202117511; *Angew. Chem.* **2022**, *134*, e202117511.

(22) a) I. Childres, L. Jauregui, W. Park, H. Caoa, Y. P. Chena, *New Developments in Photon and Materials Research*, Nova, New York, **2013**, pp. 403–418; b) Y. Wang, D. C. Alsmeyer, R. L. McCreery, *Chem. Mater.* **1990**, *2*, 557–563.

(23) a) S. Wang, X.-X. Li, L. Da, Y. Wang, Z. Xiang, W. Wang, Y.-B. Zhang, D. Cao, *J. Am. Chem. Soc.* **2021**, *143*, 15562–15566; b) S. Wang, L. Da, J. Hao, J. Li, M. Wang, Y. Huang, Z. Li, Z. Liu, D. Cao, *Angew. Chem. Int. Ed.* **2021**, *60*, 9321–9325; *Angew. Chem.* **2021**, *133*, 9407–9411; c) M. Wang, M. Wang, H.-H. Lin, M. Ballabio, H. Zhong, M. Bonn, S. Zhou, T. Heine, E. Canovas, R. Dong, X. Feng, *J. Am. Chem. Soc.* **2020**, *142*, 21622–21627; d) M. Wang, M. Ballabio, M. Wang, H.-H. Lin, B. P. Biswal, X. Han, S. Paasch, E. Brunner, P. Liu, M. Chen, M. Bonn, T. Heine, S. Zhou, E. Cánovas, R. Dong, X. Feng, *J. Am. Chem. Soc.* **2019**, *141*, 16810–16816.

(24) S. Duhović, M. Dincă, *Chem. Mater.* **2015**, *27*, 5487-5490.

(25) E. Jin, M. Asada, Q. Xu, S. Dalapati, M. A. Addicoat, M. A. Brady, H. Xu, T. Nakamura, T. Heine, Q. Chen, D. Jiang, *Science* **2017**, *357*, 673-676.

(26) T. Jadhav, Y. Fang, C.-H. Liu, A. Dadvand, E. Hamzehpoor, W. Patterson, A. Jonderian, R. S. Stein, D. F. Perepichka, *J. Am. Chem. Soc.* **2020**, *142*, 8862-8870.

(27) K. Y. Law, *Chem. Rev.* **1993**, *93*, 449–486.

(28) a) A. S. Chaves, H. Chacham, *Appl. Phys. Lett.* **1995**, *66*, 727–729; b) M. A. C. Fox, D. A., *Adv. Mater.* **1991**, 381–385.

(29) N. F. D. Mott, A. Edward, *Electronic Processes in Non-Crystalline Materials*, Oxford University Press, Oxford, **1979**.

(30) H. Tanaka, M. Hirate, S. Watanabe, S.-i. Kuroda, *Adv. Mater.* **2014**, *26*, 2376–2383.

Chapter 5. High-rate, High-Capacity Electrochemical Energy Storage in Hydrogen-Bonded Fused Aromatics

5.1 Abstract

Designing materials for electrochemical energy storage with short charging times and high charge capacities is a longstanding challenge. The fundamental difficulty lies in installing a high density of redox couples into a stable material that can efficiently conduct both ions and electrons. We report all-organic, fused aromatic materials that store up to 310 mAh g^{-1} and charge in as little as 33 seconds. This performance stems from abundant quinone/imine functionalities that decorate an extended aromatic backbone, act as redox-active sites, engage in hydrogen bonding, and enable a delocalized high-rate energy storage with stability upon cycling. The extended conjugation and hydrogen bonding-assisted bulk charge storage contrasts with the surface-confined or hydration-dependent behavior of traditional inorganic electrodes. Materials with high capacity for electrical energy storage, such as the electrode materials in Li-ion batteries, typically need several hours for a full charge. Conversely, carbonaceous electrodes in electrochemical capacitors charge in few seconds, but store only a fraction of the energy in Li-ion batteries. Combining the merits of both batteries and capacitors into a single high-energy, high-power device represents a major scientific and technological challenge. From a design perspective, the difficulty lies in designing electrode materials with a high density of redox sites and excellent electron and ion conduction pathways. Here, we show that heteroatoms on fused aromatic molecules serve as multifunctional sites in enabling high-rate, high-capacity charge storage. Heteroatoms serve as redox-active sites that engage in hydrogen-bonding and induce electron delocalization for an excellent conduction of ions and electrons. These principles provide key blueprints toward the development of materials for high-energy, high-power storage devices.

5.2 Introduction

Growing demand for electrifying the transportation sector and decarbonizing the grid requires the development of electrochemical energy storage (EES) systems that cater to a wide variety of energy and power needs[1,2]. As the dominant EES devices, lithium-ion cells (LICs) and electrochemical capacitors typically only offer either high energy or high power[3]. Over the last decade, several attempts were made to achieve high power and energy densities in hybrid energy storage systems by integrating LICs and capacitors at the device level[4]. This approach represents a modular way of supplying high energy and high power to applications where power demands vary with time or the possibility to recover energy at high power is as important as power delivery itself. However, the complexity and costs involved in device-level engineering diminish the utility of hybrid energy storage systems in compact applications such as electric vehicles. This creates a strong incentive to develop electrode materials that combine the high charge capacity of LICs with the fast charging and long cycling life of capacitors.

The combination of high capacity and high power in a single electrode material mandates that the material possesses abundant redox-active sites and that it promotes rapid transport of electrical and ionic charges throughout the electrode bulk. This charge storage mechanism, commonly known as pseudocapacitance, has primarily been identified in redox-active transition metal oxides/nitrides/carbides, which exhibit short charge diffusion lengths when fabricated as thin films[5]. However, when film thickness increases with these materials, as required for practically-relevant mass loadings, ion and electron transport dramatically decreases, leading to sub-optimal performance[6]. Overcoming this challenge typically requires composite synthesis[7] and nano-engineering[8].
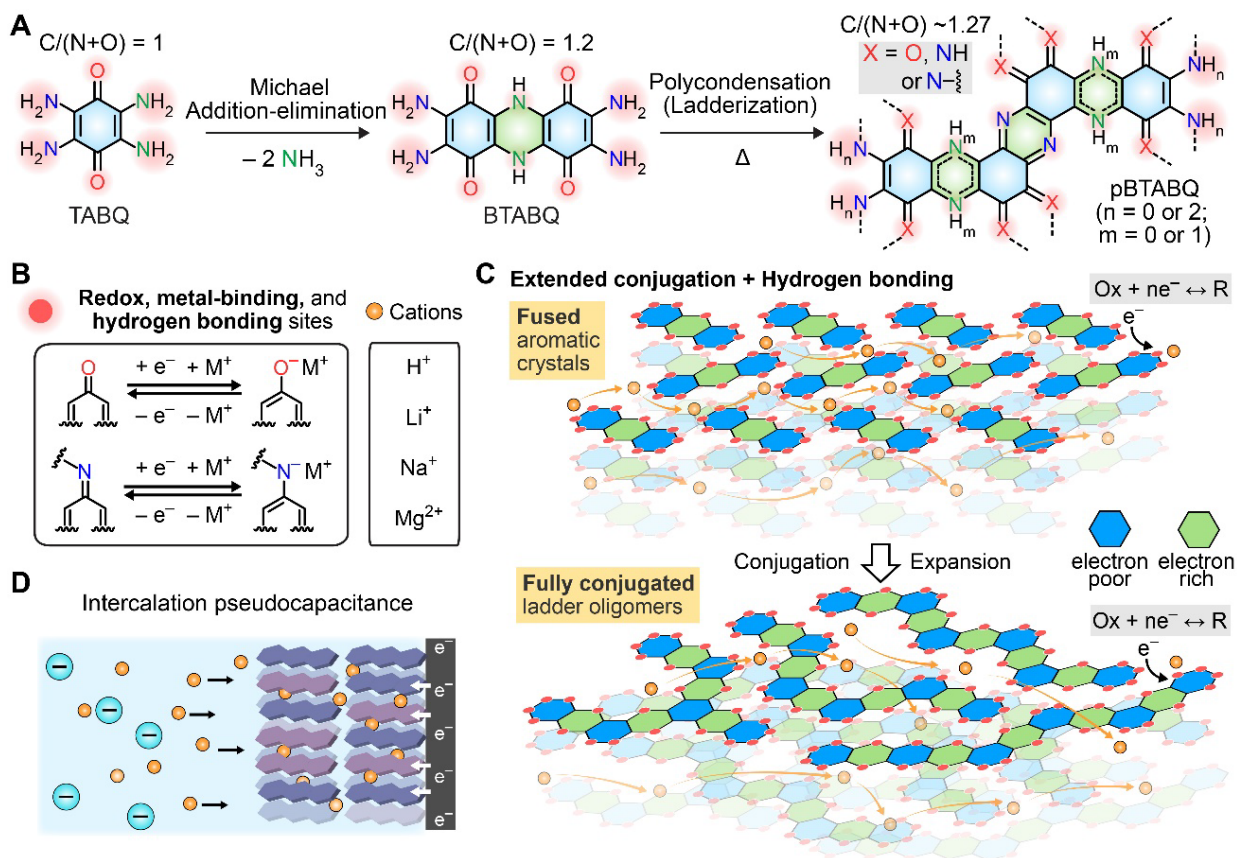
Figure 5.1. Charge storage in fused aromatic materials. (A) One-step syntheses of BTABQ and pBTABQ. (B, C) Schematic depiction of fused aromatic molecular crystals and their conversion to conjugated ladder oligomers through self-condensation. The high density of redox-active sites (carbonyl and amine/imine groups) enable an alternating arrangement of electron donor (D) and acceptor (A) moieties. The resulting extended conjugation, strong D-A π-π interactions, and hydrogen bonding facilitate electronic charge delocalization and diffusion of ionic charges. (D) Representation of pseudocapacitive intercalation of various cations into fused aromatic materials.

Organic materials offer an alternative, more compositionally diverse materials space for designing pseudocapacitive electrodes from earth-abundant elements. However, they typically suffer from poor intrinsic electrical conductivity, a result of limited electronic delocalization, and high solubility in electrolytes, which leads to poor cyclability. These combine to deliver inferior electrochemical performance compared to the inorganic alternatives[9]. Although strategies such as polymerization and compositing organic molecules with insoluble admixers can limit electrode dissolution, designing organic materials that are themselves insoluble but still allow swift charge transport and storage is difficult[10]. Here, we report bis-tetraaminobenzoquinone (BTABQ) and its polymeric analogue (pBTABQ) as new pseudocapacitive organic materials for EES (Figure 5.1A). They exhibit a high density of redox-active quinone and imine groups (Figure 5.1B) and aromatic backbones with extended conjugation. Owing to strong intermolecular hydrogen bonding and donor-acceptor (D-A) π-π interactions, they are insoluble in both organic and aqueous media (Figure 5.1C). BTABQ and pBTABQ exhibit high charge storage capacities at high charge-discharge rates, which can be associated with rapid pseudocapacitive

intercalation processes (Figure 5.1D). Charge storage and transport occurs throughout the electrode bulk, even at practical mass loadings, due to extended electronic delocalization and facile ion transport.

5.3 Results and Discussion

5.3.1 Synthesis and Characterization

BTABQ is accessible in gram-quantities by one-step Michael condensation of commercially available tetraamino-*p*-benzoquinone (TABQ) (Figures 5.1A, 5.2). Although it is highly insoluble in water and common organic solvents such as acetonitrile, dimethylformamide (DMF), N-methyl-2-pyrrolidone (NMP), and propylene carbonate (PC) (Figure 5.3), BTABQ forms as highly crystalline micro-rods (Figures 5.4, 5.5, 5.6A). The addition of tetrabutylammonium chloride (TBACl) to the reaction mixture is important for growing BTABQ micro-crystals, as suggested by SEM images (Figure 5.4) and the substantial decrease of full width at half maximum of PXRD reflections (Figure 5.5D). Given that smaller cations, such as tetramethylammonium (TMA$^+$) and Li$^+$, led to less improvement of crystallinity, we hypothesize that the TBA cations act as buffers between BTABQ molecules, leading to slower and more reversible crystallization (Figure 5.5A).
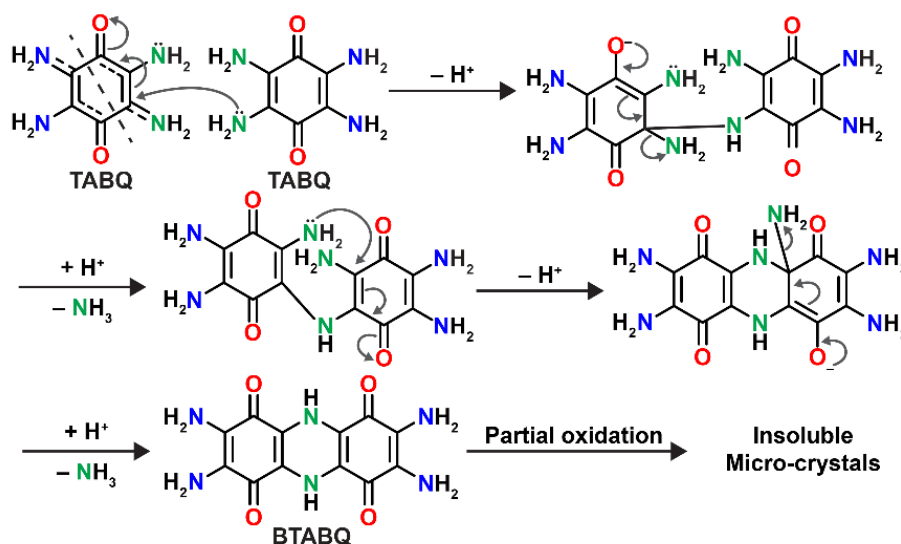
Figure 5.2. The proposed mechanism of the formation of BTABQ. The proposed mechanism of the formation of BTABQ via 1,4-Michael addition/elimination between two TABQ molecules. TABQ can be considered as two head-to-tail connected α,β-unsaturated ketone based on its reported crystal structure.
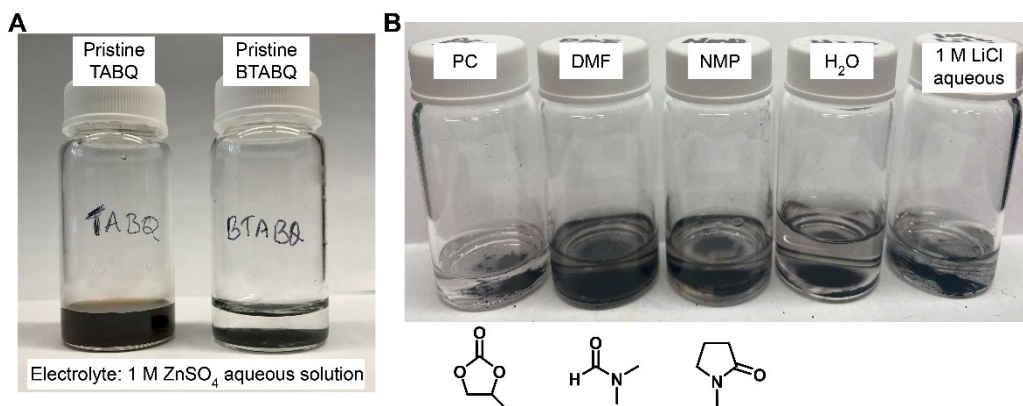
Figure 5.3. The solubility tests of BTABQ in a variety of organic solvents and aqueous electrolytes. (A) the comparison of the solubility of TABQ, a small organic molecule, and BTABQ in 1 M $ZnSO_4$ aqueous electrolyte. TABQ readily dissolves in the 1 M $ZnSO_4$ aqueous electrolyte even without electrochemical polarization, whereas BTABQ is insoluble in the same electrolyte. (B) BTABQ exhibits low solubility in propylene carbonate (PC), dimethylformamide (DMF); N-methyl-2-pyrrolidone (NMP), water, and 1 M LiCl aqueous solution.
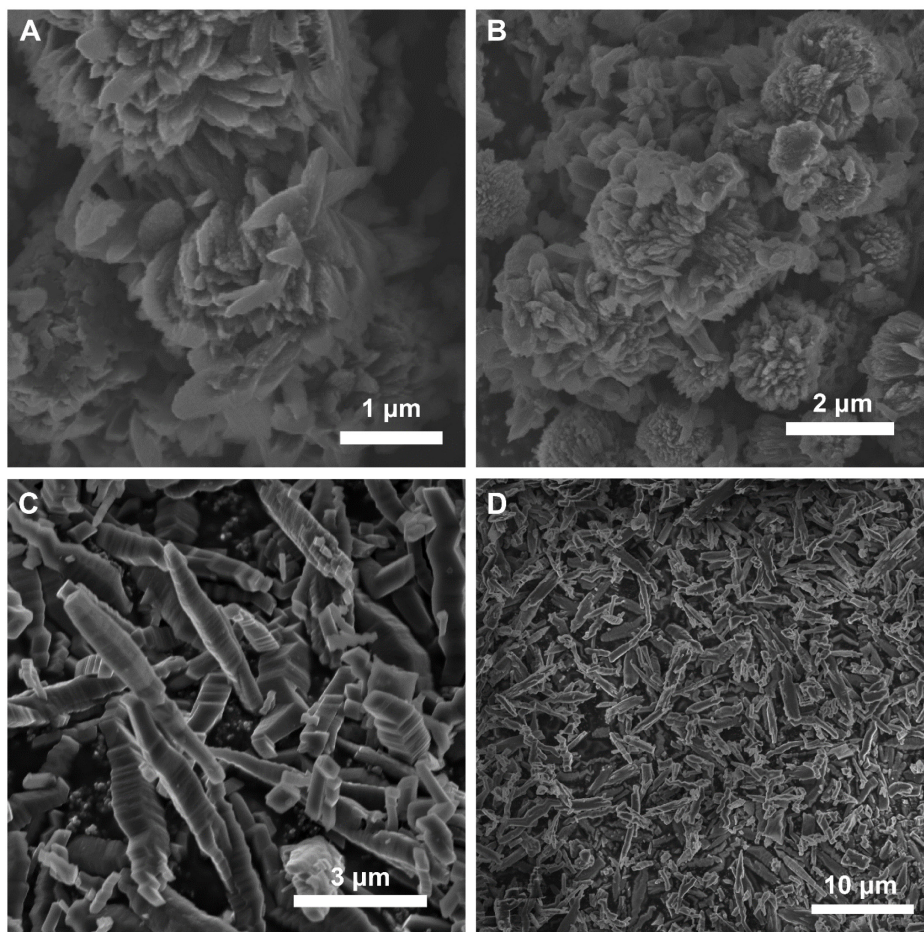
Figure 5.4. SEM images of BTABQ. (A, B) SEM images of BTABQ synthesized without TBACl. (C, D) SEM images of BTABQ synthesized with TBACl. The particle sizes increase significantly by using TBACl during synthesis, suggesting the improvement of crystallinity.

205
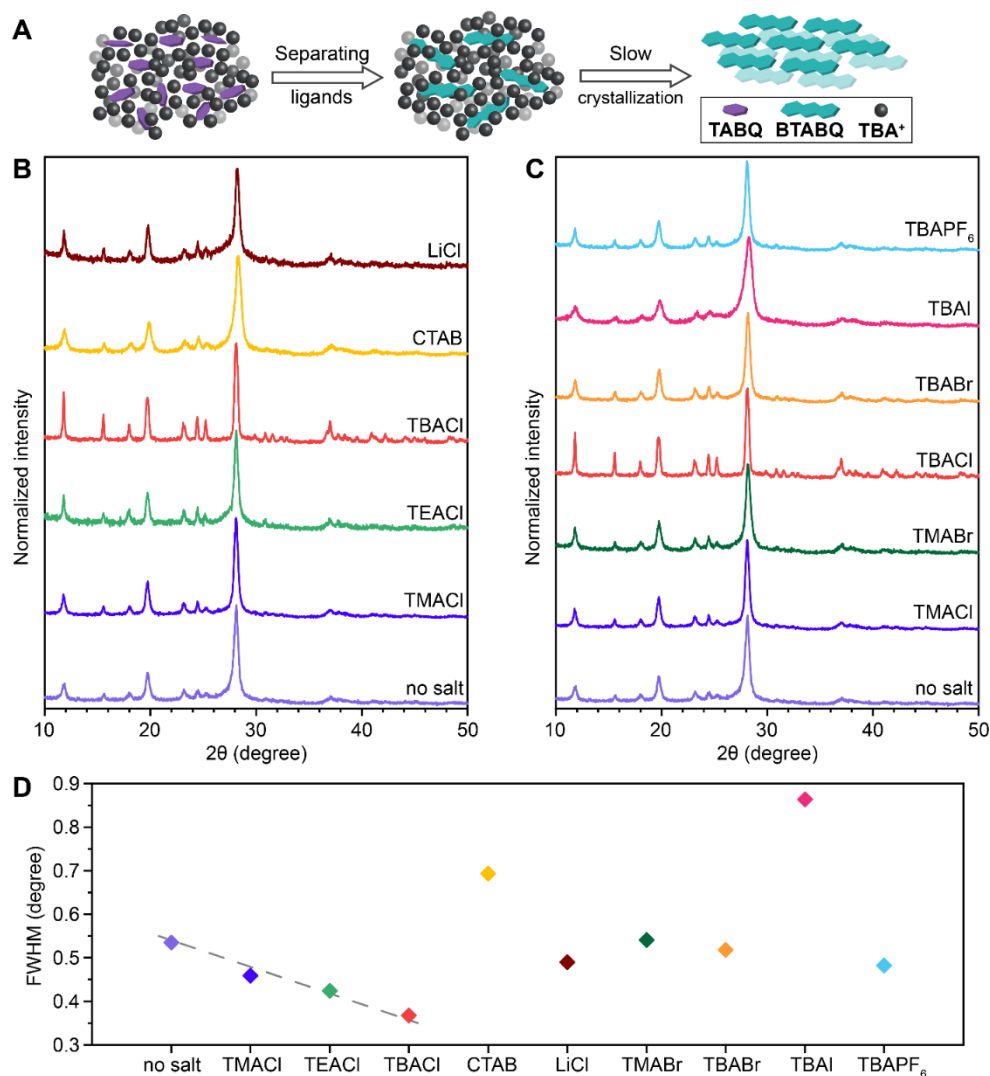
Figure 5.5. (A) Schematic showing the proposed mechanism of TBACl slowing down the crystallization of BTABQ. (B, C) PXRD patterns of BTABQ synthesized using different salts, revealing the influence of different cations (B) and anions (C) on the crystallinity. (D) FWHM of the (102) reflection (2θ ~28.3°) of all PXRD patterns. Gray dashed line is guide to eye. The crystallinity increases with the cation size, from Li^+ and TMA^+ to TBA^+, whereas the crystallinity decreases with halide anion size, from Cl^- to I^-.

The crystal structure of BTABQ was obtained from continuous rotation electron diffraction (cRED) using an ab initio method (Figure 5.6A)[11], following Pawley refinement of the unit cell parameters from synchrotron powder X-ray diffraction (PXRD) data (Figure 5.7). High-resolution cRED datasets, down to 0.625 Å, allowed direct location of all non-hydrogen atoms (Figure 5.8, 5.9, Table 5.4). BTABQ has a planar, fused tricyclic aromatic backbone with two diaminobenzoquinone moieties bridged by a dihydro-pyrazine core. A closer look at its bond lengths reveals that the two C–NH_2 bonds exhibit partial double bond character, while the two carbonyl bonds exhibit partial single bond character (Figure 5.6B), indicating the presence of significant keto-enol tautomerization (Figure 5.6C). The partial imine character is further verified by the imine carbon chemical shift at 146.4 ppm in the ^{13}C solid-state nuclear magnetic

resonance (ssNMR) spectrum (Figure 5.10), and the C=N stretching band in the Fourier-transform infrared (FTIR) spectrum of BTABQ (Figure 5.11)[12]. Each BTABQ molecule engages in hydrogen bonding interactions with six neighboring molecules to form two-dimensional (2D) layers (Figure 5.6D). The 2D layers stack through short D-A π-π interactions, along the (102) crystallographic direction (Figure 5.12), to give an interlayer separation of only 3.14 Å (Figures 5.6E, 5.6F). The integrity of the 2D layers is maintained upon exfoliation, as evidenced by scanning electron microscopy (SEM, Figure 5.13).

B

Bond length (Å)

C2–N8	1.331[a]	C1–O7	1.236[c]
C3–N9	1.438[b]	C4–O10	1.302[d]
C5–N11	1.406[b]	C–C (average)	
C6–N12	1.413[b]		1.390

[a] partial double; [b] single; [c] double; [d] partial single
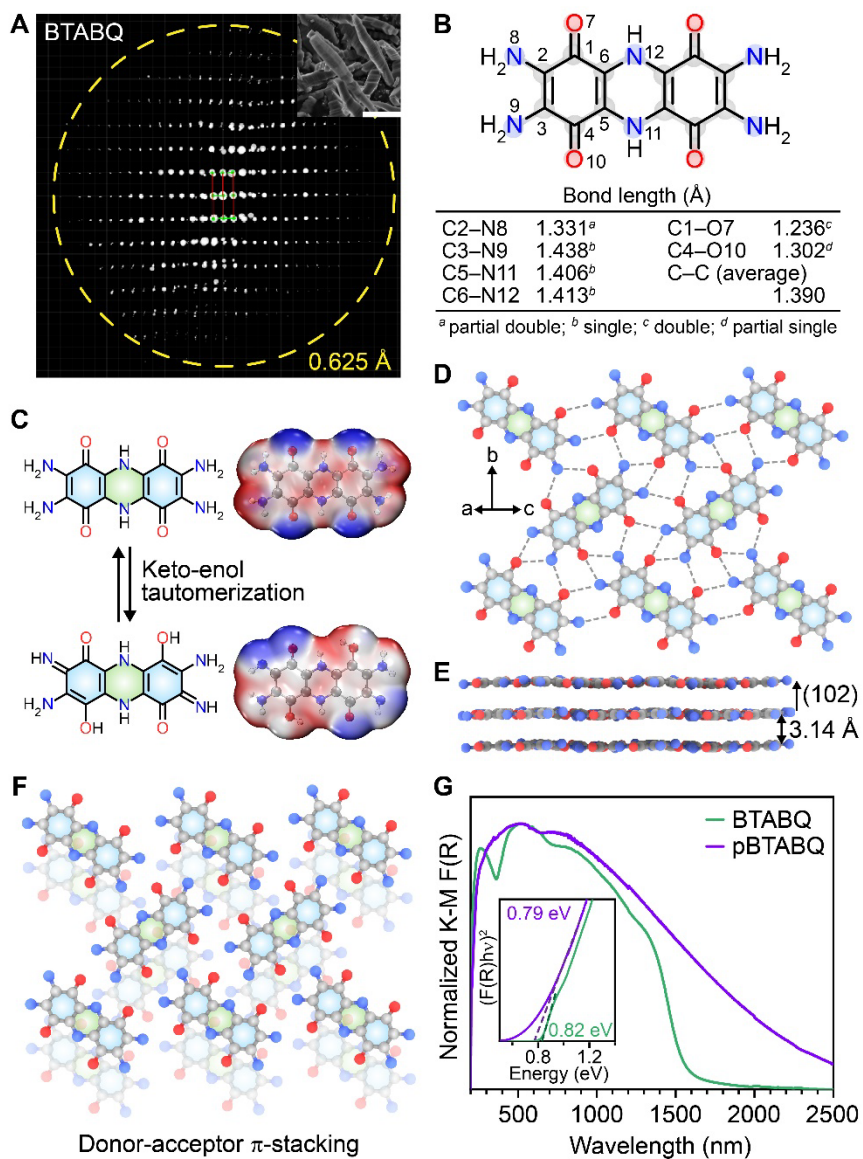
Figure 5.6. Characterization of BTABQ and pBTABQ. (A) Projection of 3D reciprocal lattice reconstructed from the cRED dataset of BTABQ with a maximum resolution of 0.625 Å. Inset shows a SEM image of BTABQ rods. Scale bar: 2μm. (B) Bond lengths in BTABQ. (C) Keto-enol tautomerization of BTABQ, and the electrostatic potential maps of the two tautomers. (D) A 2D layer of BTABQ molecules formed by hydrogen bonding interactions (dashed lines) between carbonyl and amine/imine groups. The N···O (2.89 Å) and N···N (3.04 Å) distances are shorter than the sum of their van der Waals radii 3.15 Å and 3.20 Å, respectively. (E) π-π stacking of 2D layers of BTABQ with an interlayer distance of 3.14 Å. (F) D-A alignment of 2D layers. (G) DRUV-Vis-NIR spectra of BTABQ and pBTABQ. Inset shows respective optical band gaps.
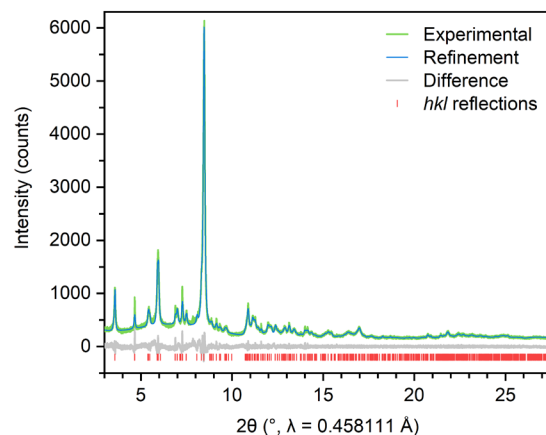
Figure 5.7. Pawley refinement of the synchrotron PXRD data of BTABQ. The data was collected at 100 K with an X-ray wavelength of 0.458111 Å. The refined lattice parameters are a = 4.8923(1) Å, b = 11.2897(3) Å, c = 9.9041(4) Å, β = 101.67° in the space group P2$_1$/c, with R_{wp} = 5.828%, R_{exp} = 5.248%, R_p = 4.667%, and GoF = 1.11.
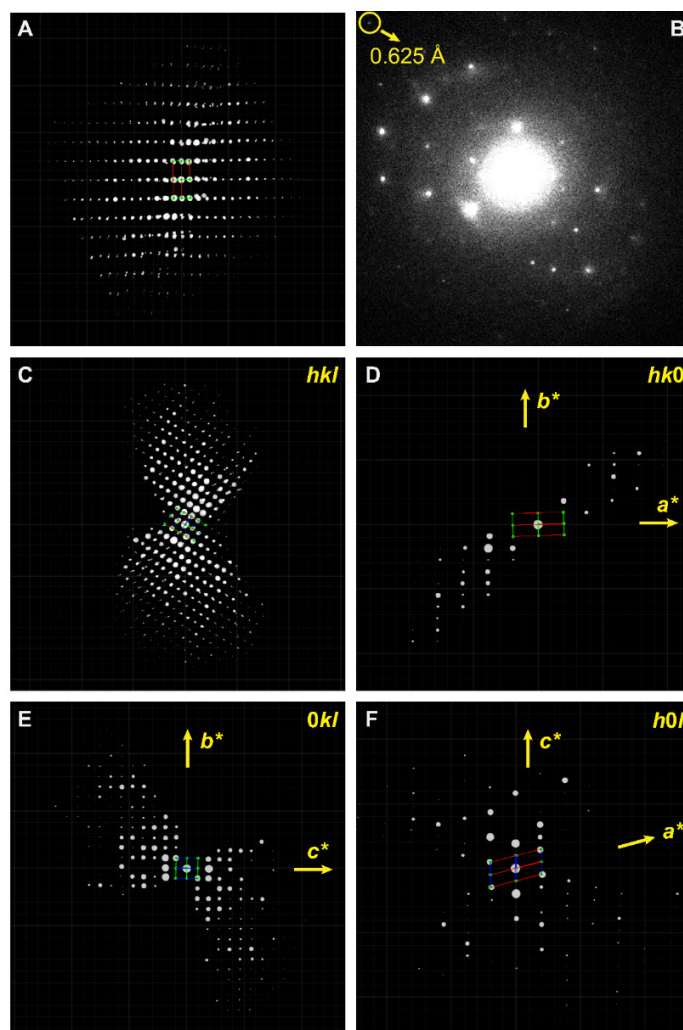
Figure 5.8. Pawley refinement cRED data of BTABQ. (A) 3D reciprocal lattices of BTABQ. (B) Typical selected area electron diffraction (SAED) pattern of BTABQ with a resolution as high as 0.625 Å. (C-F) Reconstructed 3D cRED data of BTABQ indexed with monoclinic symmetry (space group P2$_1$/c): overview (*hkl*) (C), and selected planes in the reciprocal lattice corresponding to *hk*0 (D), 0*kl* (E) and *h*0*l* (F).
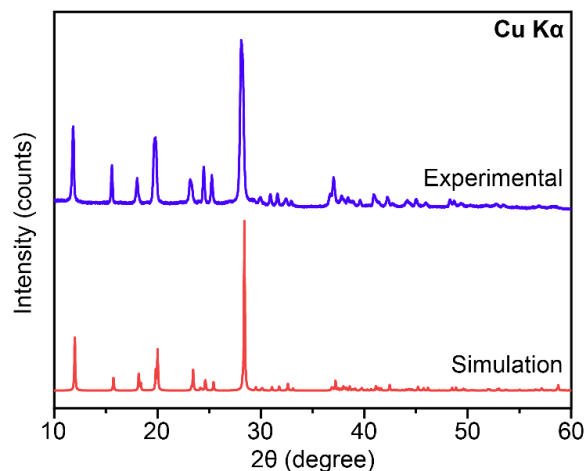
Figure 5.9. Comparison between experimental PXRD pattern and simulated pattern based on the determined crystal structure based on cRED data. Excellent agreement between the two patterns is observed, indicating the bulk phase purity of obtained as-synthesized BTABQ.
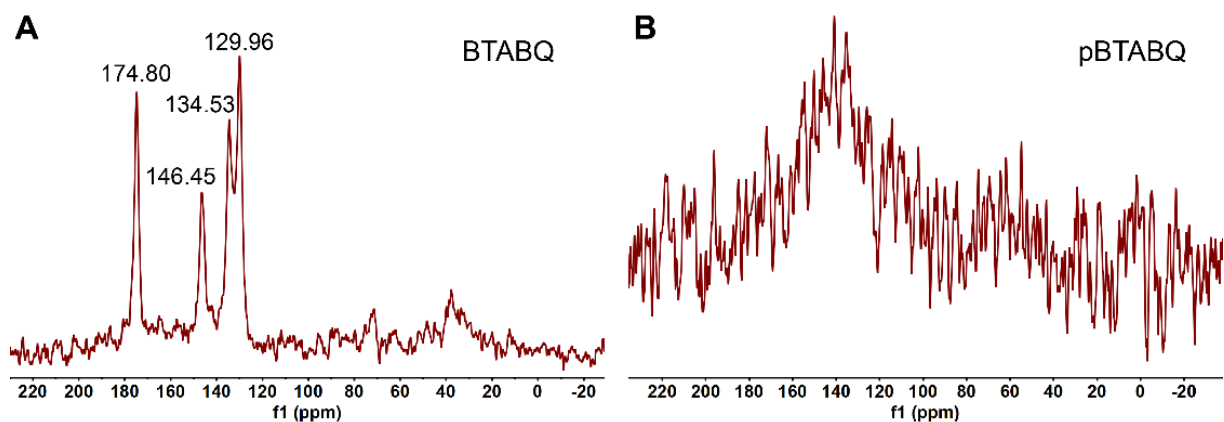
Figure 5.10. ^{13}C ss-NMR spectra of BTABQ and pBTABQ. (A) Solid-state ^{13}C NMR spectrum of BTABQ. (B) Solid-state ^{13}C NMR spectrum of pBTABQ. The ssNMR spectrum of BTABQ exhibits peaks at 174.8 ppm (C=O), 146.4 ppm (C=N), and 134.5 ppm/129.9 ppm (C–N/C–O). The ssNMR spectrum of pBTABQ exhibits a broad peak centered at 140 ppm. The broadness of the peak in the ssNMR spectrum of pBTABQ is mainly because pBTABQ has significant presence of organic radicals and these radicals delocalize among the bulk material since pBTABQ has a high degree of electronic delocalization. A less important reason for the broadness is the amorphous nature of pBTABQ.
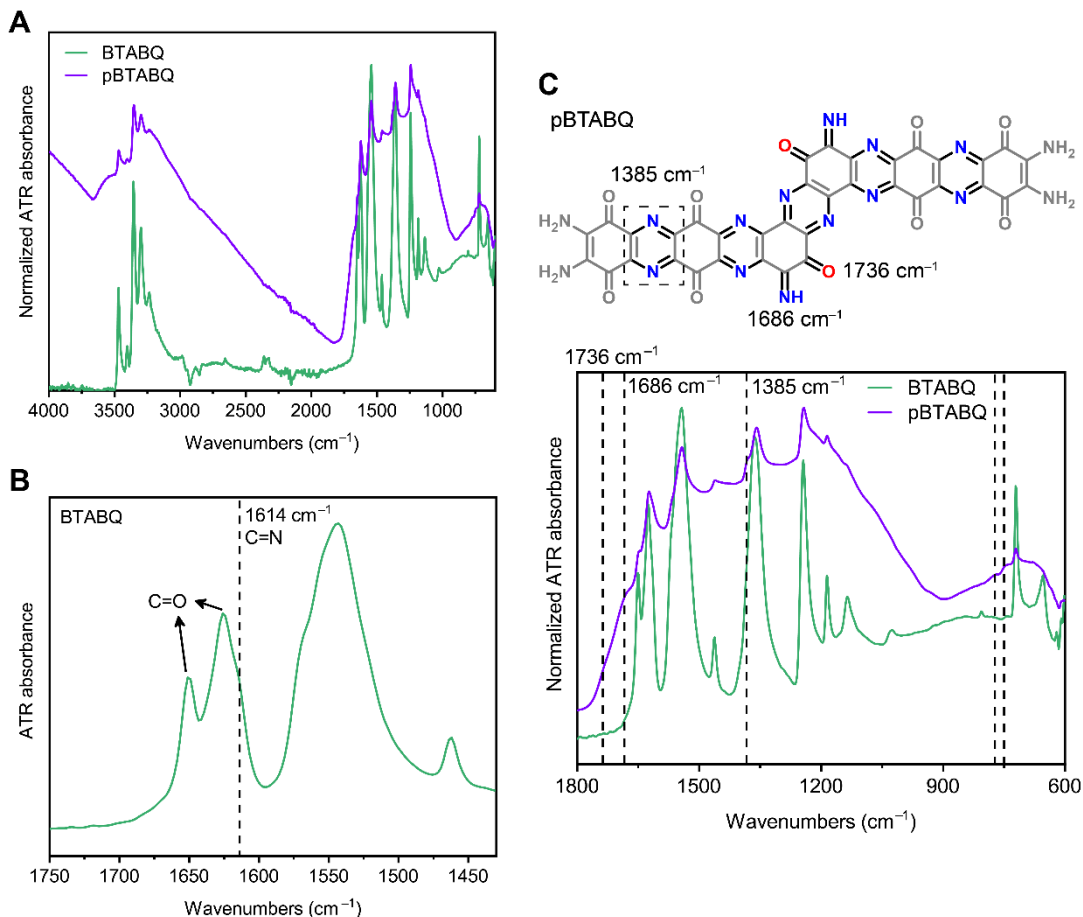
Figure 5.11. ATR-FTIR spectra of BTABQ and pBTABQ. (A) ATR-FTIR spectra of BTABQ and pBTABQ. The sharp peaks between 3000 cm^{-1} and 3500 cm^{-1} indicate the presence of hydrogen bonding network in both materials. (B) The presence of carbonyl (C=O) groups and C=N stretching band (as a shoulder feature at 1614 cm^{-1}) in BTABQ. (C) Detailed comparison of ATR-FTIR spectra of BTABQ and pBTABQ. BTABQ and pBTABQ show largely similar infrared features (although the latter is much broader), which is mainly because they have very similar chemical structures. However, the ATR-FTIR spectrum of pBTABQ shows a vibrational band at 1385 cm^{-1}, which is characteristic for pyrazine moieties[1]. The new bands between 750 cm^{-1} and 800 cm^{-1} in the ATR-FTIR spectrum of pBTABQ are also characteristic for ring motions of the pyrazine rings. In addition, two new shoulder bands at ~1736 cm^{-1} and 1686 cm^{-1} correspond to the highlighted C=O and C=NH groups, respectively, in the proposed molecular structure of pBTABQ.
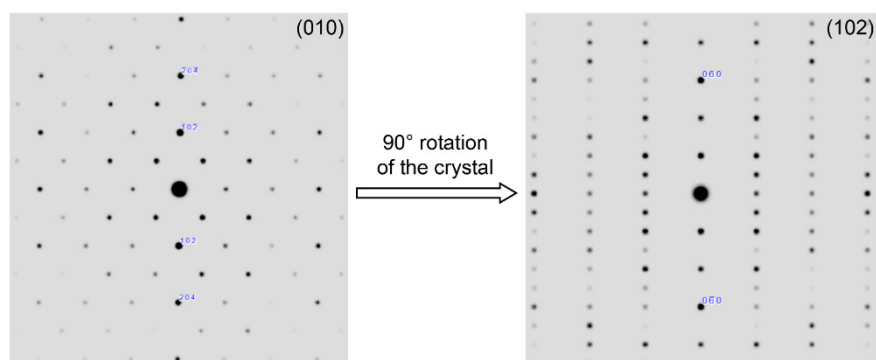
Figure 5.12. Simulated indexing of BTABQ crystal structure based on electron diffraction data. (010) Bragg planes superimpose with 2D layers of BTABQ, and these 2D layers stack along the (102) crystallographic direction.

210
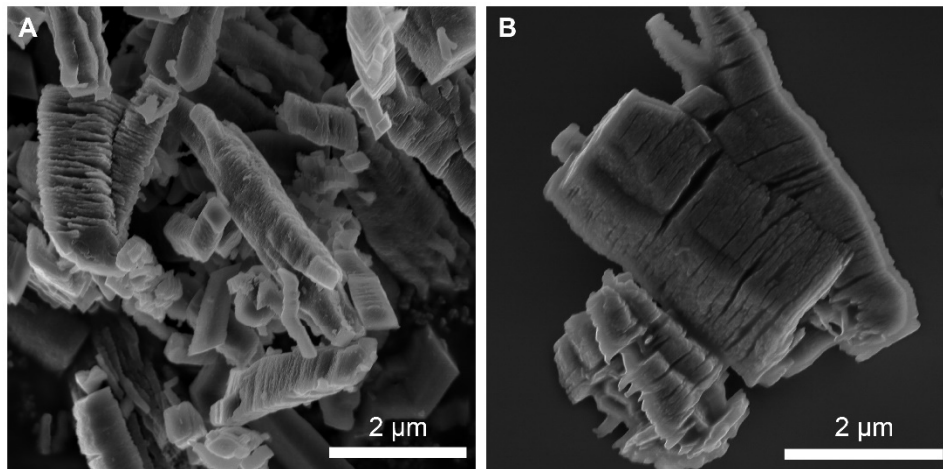
Figure 5.13. SEM images of exfoliated BTABQ. (A, B) SEM images of exfoliated BTABQ crystals after one-hour sonication in chlorobenzene, showing 2D layered character, similar to the accordion-like morphology of exfoliated MXenes.

Thermogravimetric analysis and differential scanning calorimetry of BTABQ revealed an endothermic weight loss event around 300 ℃ (Figures 5.14, 5.15). Given the proximity of amino and carbonyl groups in the solid-state structure of BTABQ, we surmised that this process may be associated with further condensation between neighboring BTABQ molecules. Indeed, heating bulk BTABQ at ~300 ℃ under dynamic vacuum for 2 days yields an amorphous solid with unchanged particle size and morphology (Figures 5.16–5.18). This solid, termed poly(bis-tetraaminobenzoquinone) (pBTABQ) and accessible in gram-quantities, has a significantly higher molecular weight (Figure 5.19) and lower oxygen and nitrogen content than BTABQ (Figure 5.20, Tables 5.1, 5.2), indicating that ladderization/polymerization of BTABQ with concomitant loss of water and ammonia (Figure 5.21) produces a molecular backbone with large extended conjugation[13]. Pair distribution function analyses of both materials reveal similar local structures, confirming that despite the lack of long-range ordering, pBTABQ has a dense solid-state arrangement of molecular fragments analogous to BTABQ (Figure 5.22). The presence of intermolecular π-π stacking in pBTABQ, itself likely enabled by D-A interactions (Figure 5.23) was further confirmed by high magnification Cryo-EM data (Figure 5.18). Importantly, similar to FTIR spectra, Raman spectroscopy revealed significant resonances between 2500 cm^{-1} and 3100 cm^{-1} for both BTABQ and pBTABQ, suggesting that the polymer maintains a significant degree of hydrogen bonding (Figure 5.24). N$_2$ sorption studies indicate that both materials are non-porous, with similarly low specific surface areas of ~15-20 m^2 g^{-1} (Figure 5.25).
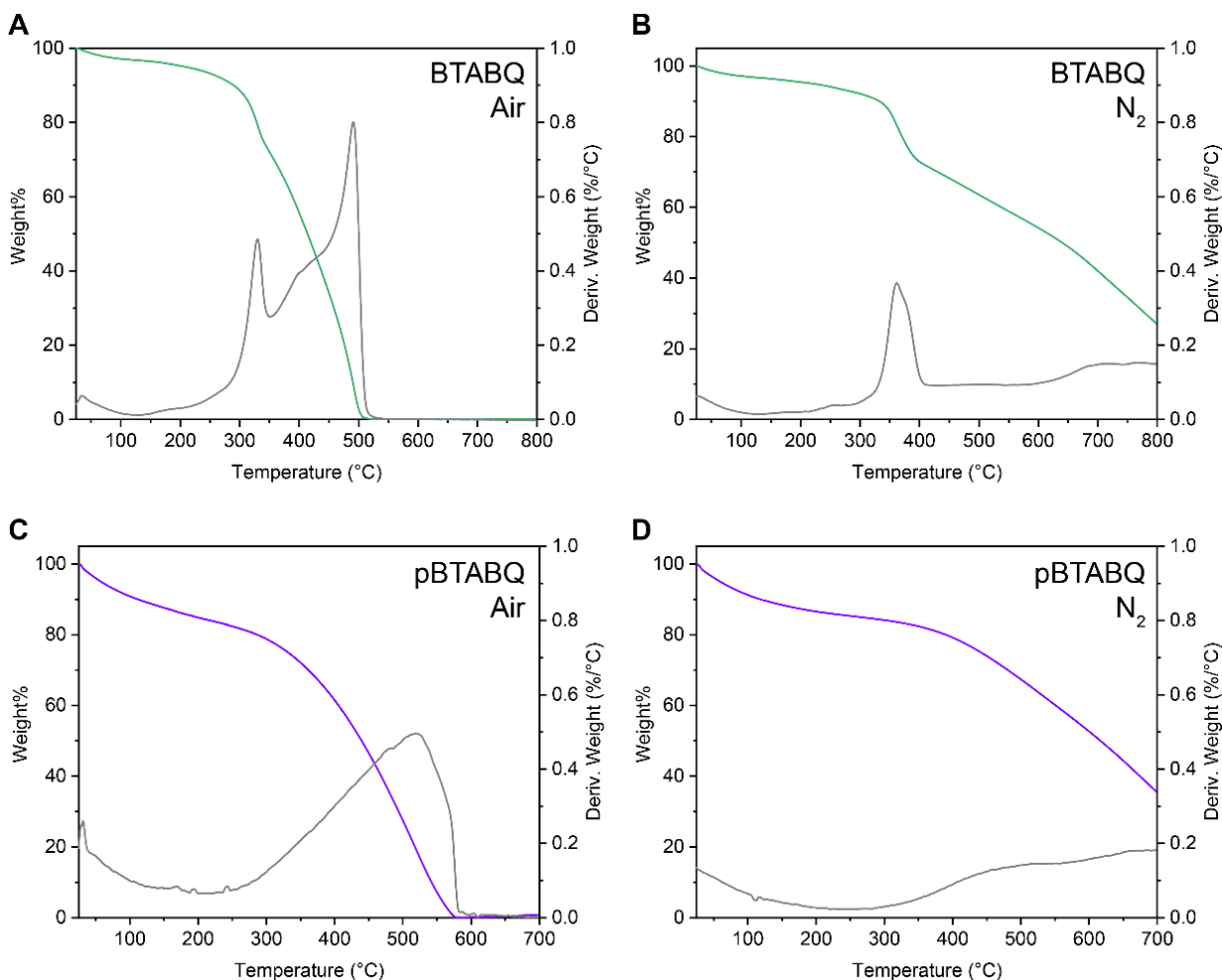
Figure 5.14. Thermogravimetric analysis of BTABQ and pBTABQ. (A, B) Thermogravimetric analysis of BTABQ under air or N_2 flow. (C, D) Thermogravimetric analysis of pBTABQ under air or N_2 flow. Both BTABQ and pBTABQ show an initial gradual weight loss at low temperatures, which is likely resulted from the removal of surface-absorbed water, given that both materials are hydrophilic due to the presence of hydrogen bonding network. A significant weight loss is seen slightly above 300 °C in the thermogravimetric analysis of BTABQ under either air (A) or N_2 (B) due to the ladderization of BTABQ to form pBTABQ. However, this sharp weight loss is absent from the thermogravimetric analysis of pBTABQ (C, D), confirming that pBTABQ is formed by solid-state polycondensation/ladderization of BTABQ. The gradual weight loss starting between 350 °C and 400 °C in all thermogravimetric analysis is due to thermolysis of materials. BTABQ and pBTABQ completely burned under air flow beyond 500 °C and ~570 °C, respectively.
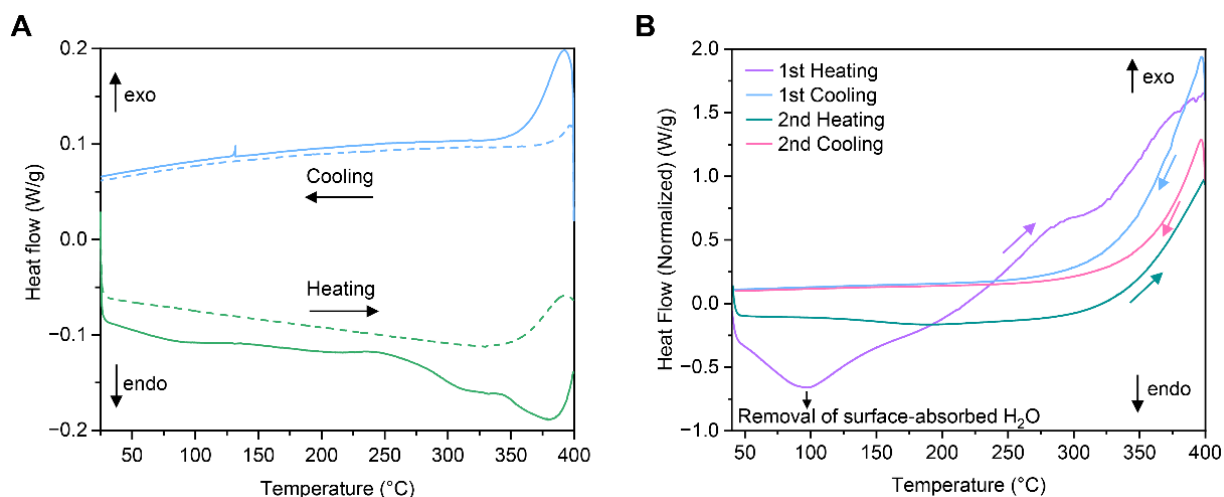
Figure 5.15. Differential scanning calorimetry of BTABQ. (A) Differential scanning calorimetry (DSC) of BTABQ in a hermetically sealed Al pan with a pinhole lid. Solid and dashed lines represent the first and second heating/cooling cycles, respectively. The broad feature observed at around 100 °C in the first heating scan is due to the removal of surface absorbed water, which is consistent with TGA data. A significant endothermic event starts to occur at ~250 °C during the first heating scan, reaches a plateau at ~310 °C (the temperature at which pBTABQ is synthesized), and then reaches a peak at ~380 °C. The back cooling scan shows background feature at ~310 °C, indicating the endothermic event in the heating scan is irreversible, and likely due to chemical transformation. Although the polycondensation reaction of BTABQ is exothermic, NH_3 and H_2O formed during the reaction escape from the hermetically sealed Al pan with a pinhole lid, leading to the overall endothermic feature. The broad endothermic event is absent in the second heating scan, proving that the polycondensation of BTABQ indeed happened in the first heating scan. (B) DSC data of BTABQ in a pinhole-free hermetically sealed Al pan. A significant broad exothermic event was observed around 300 °C. The broadness of this event is due to the slow kinetics of BTABQ condensation into pBTABQ.
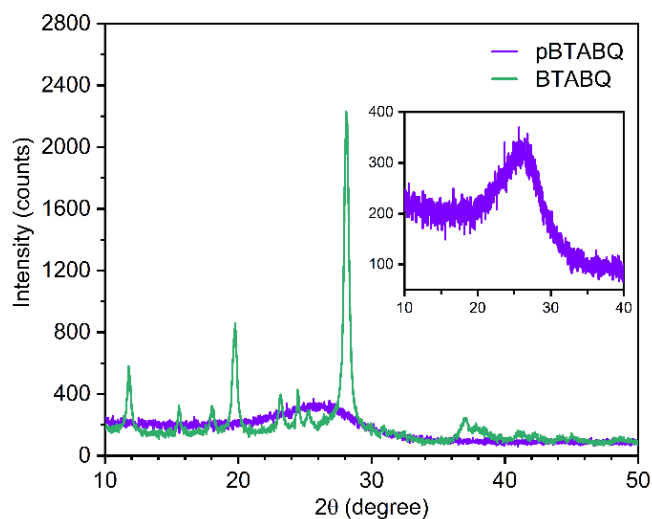
Figure 5.16. In-house PXRD patterns of BTABQ pBTABQ. The PXRD pattern of pBTABQ only exhibits a broad reflection centered around $2\theta = 26.2°$, corresponding to a d spacing around 3.4 Å. This broad reflection originates from the disordered π–π stacking of pBTABQ.

213
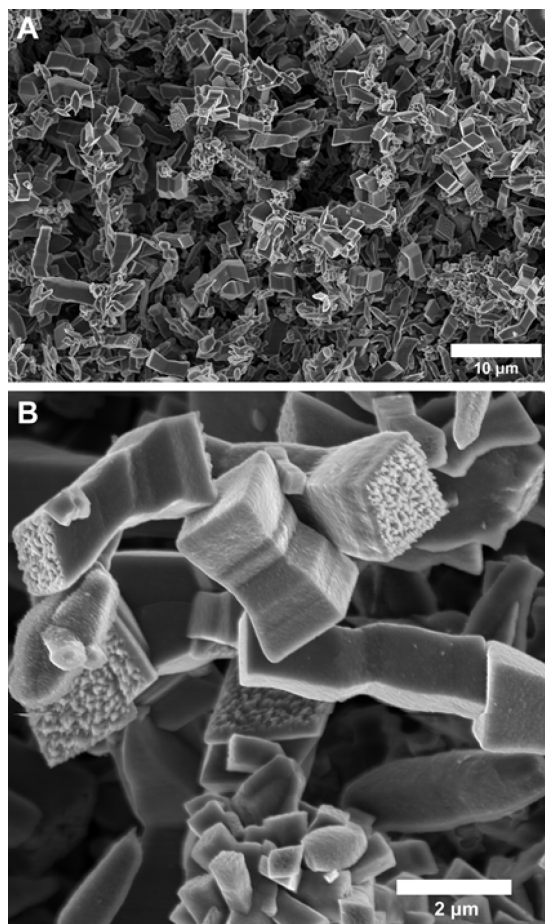
Figure 5.17. SEM images of pBTABQ. The morphology remained the same as its precursor BTABQ, but the particle surfaces became very rough, indicating amorphization.
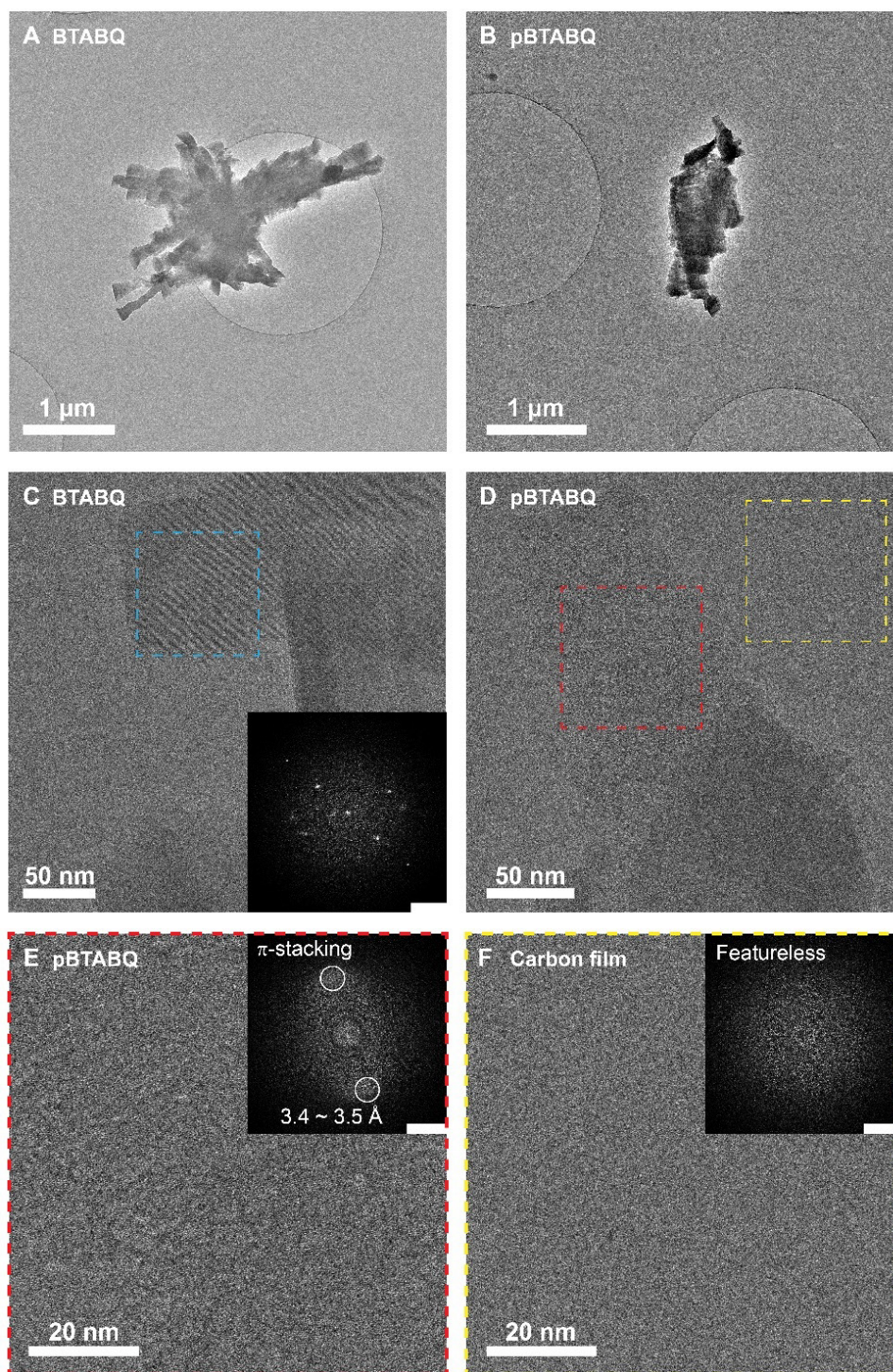
Figure 5.18. Cryo-EM images of BTABQ and pBTABQ. (A) A Cryo-EM image of BTABQ. (B) A Cryo-EM image of pBTABQ. Both materials show a similar particle morphology. (C) A high resolution Cryo-EM image of BTABQ. Inset, Fast-Fourier Transform (FFT) of the area in blue dashed square. (D) A high resolution Cryo-EM image of pBTABQ. (E, F) Zoomed-in images of areas in red (pBTABQ) and yellow (carbon film on the grid) dashed squares, respectively. Insets are the FFT. Scale bars for FFT: 2 nm^{-1}. Clear lattice fringes can be seen in the Cryo-EM image of BTABQ, consistent with its high crystallinity. No lattice fringes can be seen for pBTABQ, also consistent with its amorphous nature. However, unidirectional disordered π-π stacking of pBTABQ with d spacings ranging from 3.4 Å to 3.5 Å can be seen in FFT of (E).
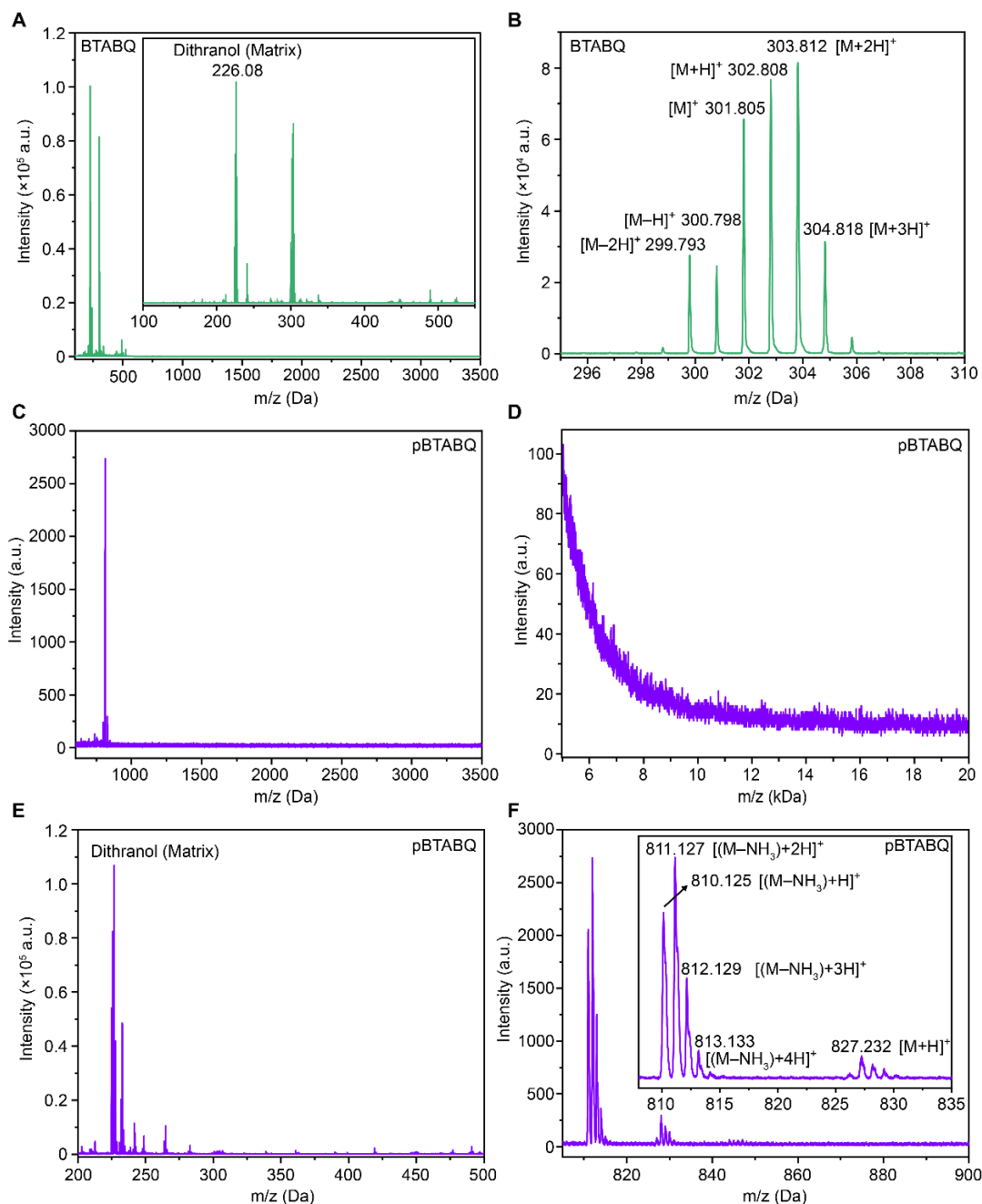
Figure 5.19. Cryo-EM images of MALDI-TOF mass spectrometry of BTABQ and pBTABQ. (A, B) MALDI-TOF mass spectrometry of BTABQ. (C–F) MALDI-TOF mass spectrometry of pBTABQ. Dithranol ([M]$^+$, 226.08 Da) is used as the matrix. No internal standard was used during measurements. The m/z values are therefore calibrated using the m/z value of dithranol, and as a result, errors within ±1 Da are expected. The data confirmed that BTABQ has a dihydropyrazine core. Amino-containing organic molecules usually show significant signal for [M]$^+$ in MALDI-TOF mass spectrometry[2]. The experimental m/z value of [M]$^+$ of BTABQ is 301.805 Da, which matches quite well with the theoretical value of 303.08 Da. [M+H]$^+$ peak of BTABQ can also be clearly observed at 302.808 Da. Molecules with abundant amino groups can also readily undergo dehydrogenation or hydrogenation during MALDI-TOF measurements[3]. Therefore, [M–H]$^+$, [M–2H]$^+$, [M+2H]$^+$, and [M+3H]$^+$ signals can all be observed in the mass spectrum of BTABQ. The mass spectra of pBTABQ clearly reveal the absence of BTABQ upon heating, given that no peaks at ~300 Da were observed. The condensation/ladderization of BTABQ is also confirmed according to the significantly higher m/z values observed for pBTABQ. The m/z value of [M+H]$^+$, 827.232 Da, also matches well with our proposed molecular structure with a theoretical m/z value of 827.1 Da.

216
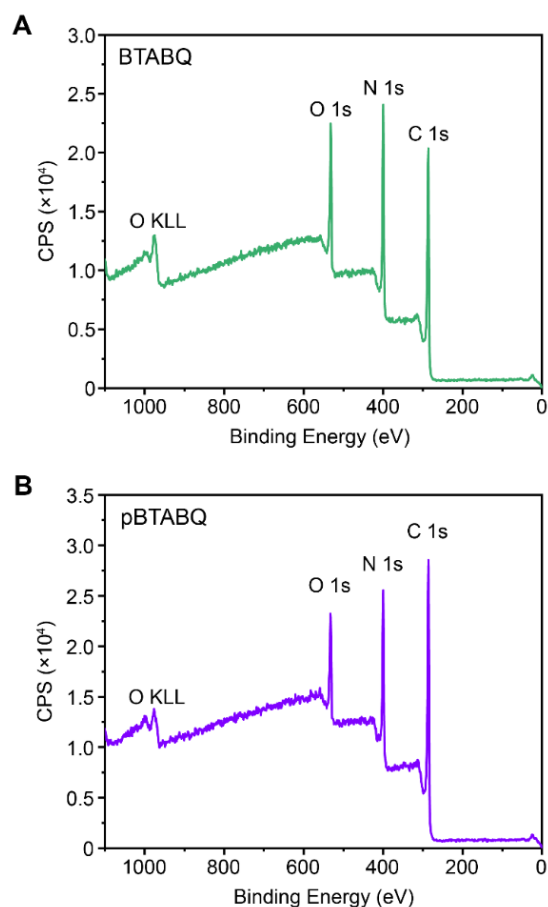
Figure 5.20. XPS survey spectra of BTABQ and pBTABQ. pBTABQ has significantly lower O atomic composition and slightly lower N atomic composition than BTABQ.

Table 5.1. Atomic composition of BTABQ and pBTABQ, as determined by XPS survey spectra. The elemental composition results shown above suggest that O at% decreases significantly upon heating.

Sample	C (At%)	N (At%)	O (At%)
BTABQ-theoretical	54.55	27.27	18.18
BTABQ-experimental	56.39	27.19	16.42
pBTABQ	65.27	24.34	10.39

Table 5.2. Elemental analysis of BTABQ and pBTABQ.

Materials	C% (f)[a]	H% (f)[a]	N% (f)[a]	C% (c)[a]	H% (c)[a]	N% (c)[a]	O% (c)[a]
BTABQ[b]	47.14	2.84	26.06	47.69	3.33	27.81	21.17
pBTABQ[c]	52.48	1.44	26.34	52.31	1.22	27.11	19.36

[a] f: found values; c: calculated values. [b] Based on the chemical formula $C_{12}H_{10}O_4N_6$. c Based on the chemical formula $C_{36}H_{10}N_{16}O_{10}$.
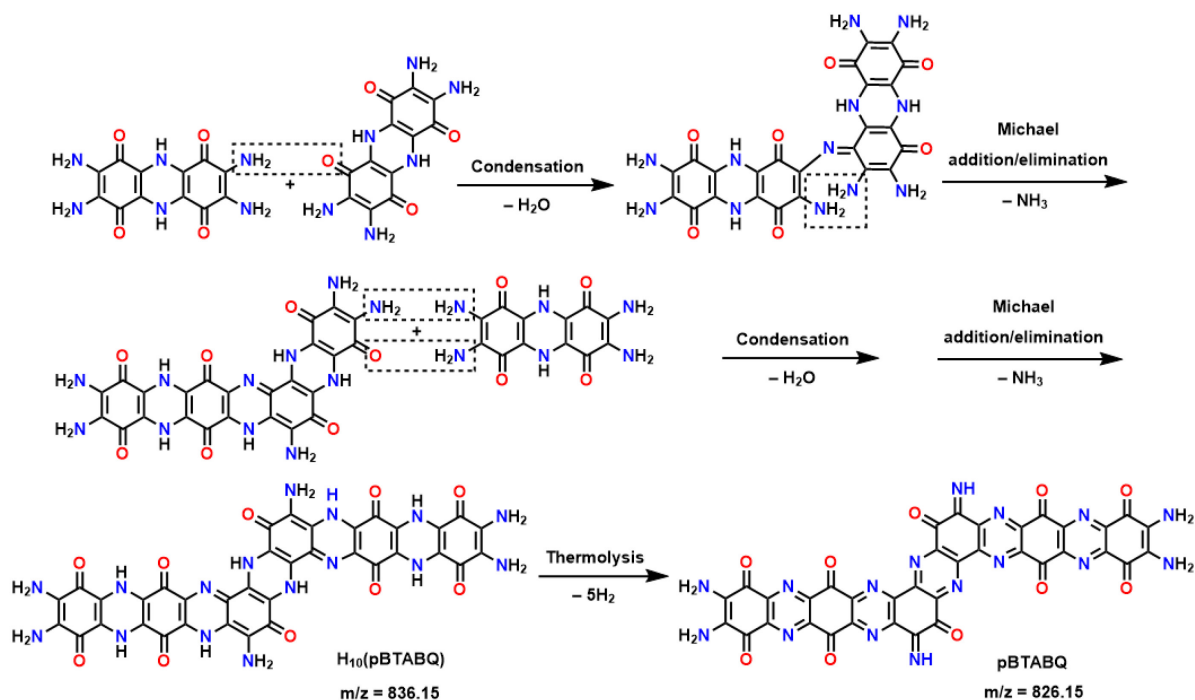
Figure 5.21. Proposed mechanism of the formation of pBTABQ. pBTABQ is synthesized upon heating BTABQ at 300~310 °C under vacuum. The formation of pBTABQ involves condensation between carbonyl and amino groups, and Michael addition/elimination which is also seen in the synthesis of BTABQ from TABQ. The resulting molecule, H_{10}(pBTABQ) (m/z = 836.15 Da) undergoes thermal dehydrogenation to give the final pBTABQ (m/z = 827.15 Da for $[M+H]^+$, matches with the MALDI-TOF result). The driving force of this dehydrogenation is its large positive entropy $\Delta_r S_m$ (solid to solid transformation with the formation of 5 eq. H_2 (g)).
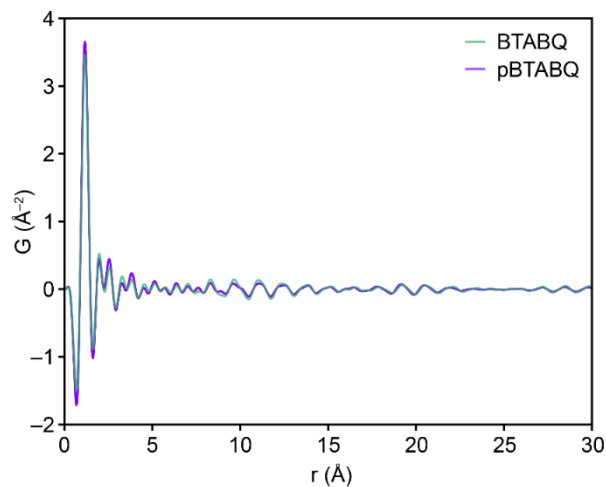
Figure 5.22. Pair distribution function measurements of BTABQ and pBTABQ. PDF results of BTABQ (green) and pBTABQ (purple) show very similar inter-atomic distance distributions, which suggests that they have almost identical local structure. Although ladderization inevitably results in more extended backbones in pBTABQ and disordered solid-state structure, the solid-state packing is still very similar by virtue of strong π-π interactions and intermolecular hydrogen bonding.

218
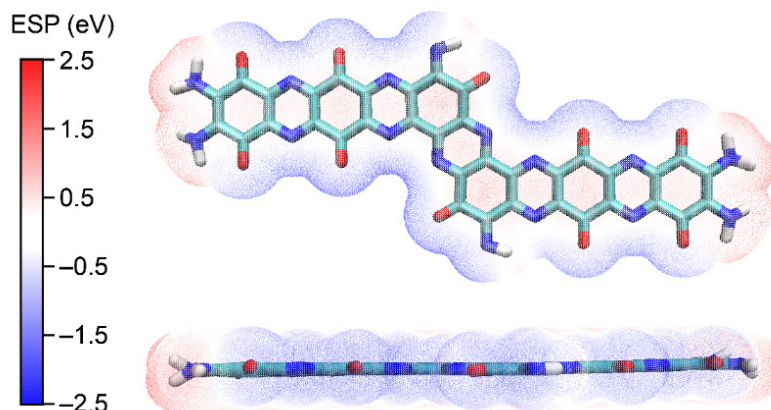
Figure 5.23. Electrostatic potential (ESP) maps of a representative structure of pBTABQ. The pBTABQ molecule is calculated using DFT at the B3LYP/def2-TZVP level. The fused extended aromatic backbone is completely flat, indicating good electronic delocalization. Similar to BTABQ, the donor-acceptor interaction in pBTABQ is also mainly formed between the electron-rich heteroatoms, including O from carbonyl groups and N from amine/imine groups (shown as blue color in the ESP map), and the relative electron-poor aromatic backbone (shown as red color in the ESP map). According to the ESP map, the pyrazine rings are not as electron-poor as the benzoquinone rings. Meanwhile, the pyrazine N atoms also have less negative electrostatic potential than the carbonyl O atoms and amino/imine N atoms. Therefore, we can conclude that although the pyrazine rings can participate in the donor-acceptor interactions between pBTABQ molecules, their contribution to the overall donor-acceptor interactions is insignificant.
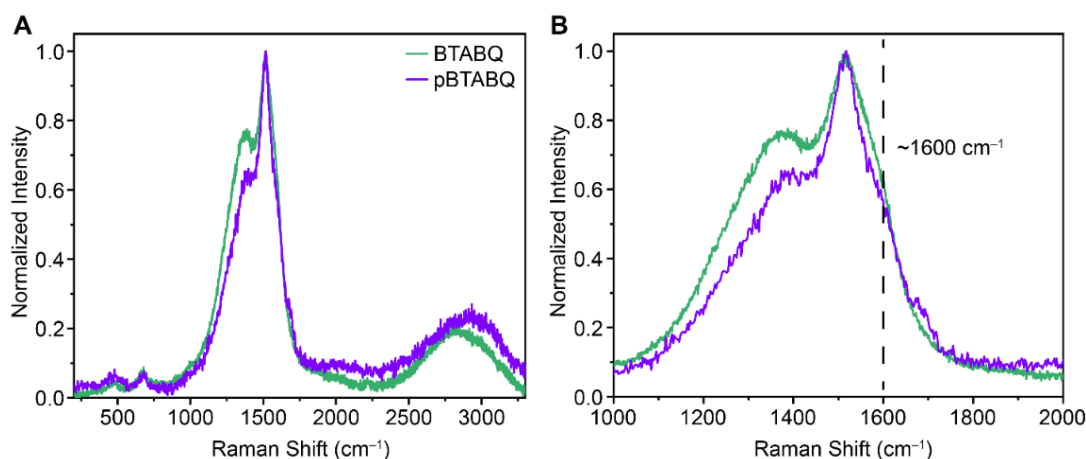
Figure 5.24. Raman spectra of BTABQ, and pBTABQ. The broad bands around 3000 cm^{-1} can be assigned to an extended hydrogen bonding network. We assign the shoulder around 1600 cm^{-1} in the Raman spectrum of BTABQ to C=O bonds, whose intensity decreases in the spectrum of pBTABQ. We also assign the shoulder between 1200 cm^{-1} and 1300 cm^{-1} in the BTABQ spectrum to C–N bonds, whose intensity decreases in the pBTABQ spectrum. This evidence agrees well with our hypothesis that amino-carbonyl addition and β-elimination reactions take place during heating, leading to higher degree of ring fusion and more extended conjugation. The broad bands at around 1400 cm^{-1} are assigned to C=N. The high ratio of C–N/C=N to C=O band intensity suggests the presence of strong intermolecular hydrogen bonding in all materials. The main peaks around 1515 cm^{-1} are assigned to C=C bonds.

219
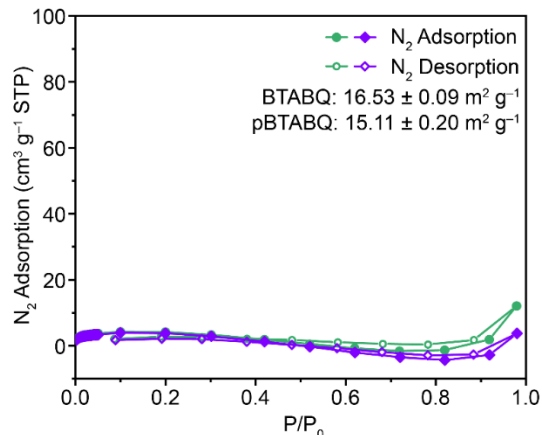
Figure 5.25. N$_2$ isotherms at 77 K of BTABQ (green circles), and pBTABQ (purple diamonds). Solid symbols represent the N$_2$ adsorption processes, whereas hollow symbols represent N$_2$ desorption processes. The solid lines are the guide to the eye. Specific surface area was calculated by fitting isotherms to the BET equation. Both materials are non-porous.
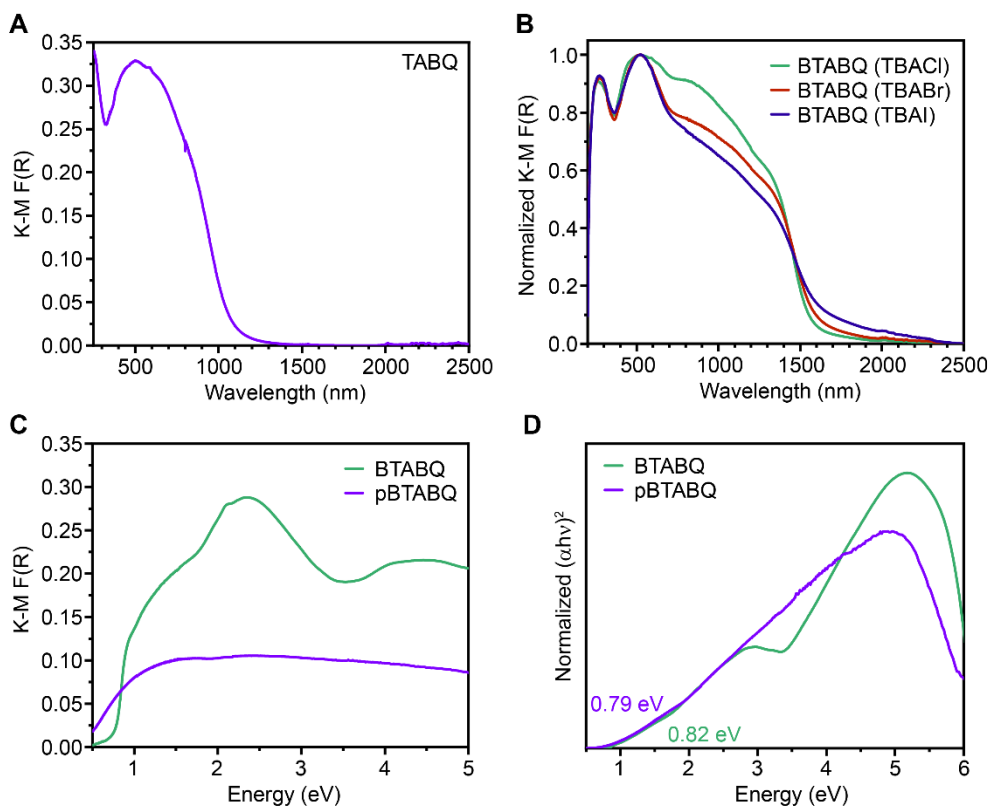
Figure 5.26. DRUV-Vis-NIR spectra of TABQ, BTABQ, and pBTABQ. (A) DRUV-Vis-NIR spectrum of TABQ, showing intra-quinone transition band at ~500 nm. (B) DRUV-Vis-NIR spectra of BTABQ synthesized using TBACl, TBABr, and TBAI (see Figure S4), suggesting that more ordered intermolecular packing (i.e., higher crystallinity) results in stronger visible and NIR absorption and more clear vibronic fine structure. (C) DRUV-Vis-NIR spectra of BTABQ and pBTABQ in energy scale, revealing the presence of very intense polaron bands (above ~1.5 eV) and bipolaron bands (below ~1 eV). The spectrum of pBTABQ is significantly broader than that of BTABQ, which we attribute to (1) the enhanced delocalization of polarons, polaron pairs and bipolarons caused by ladderization, and (2) disordered nature of pBTABQ. The considerable background absorption of pBTABQ close to 0.5 eV (Mid-IR) is characteristic of a free carrier response. (D) Normalized Tauc plots of DRUV-Vis-NIR spectra of BTABQ and pBTABQ, revealing their optical band gaps of 0.82 eV and 0.79 eV, respectively.

Diffuse-reflectance UV-Vis (DRUV-Vis) spectroscopy revealed that both materials exhibit broad absorption peaks centered around 520 and 800 nm (Figure 5.6G). The former is typical for π-π* intra-quinone electronic transitions (Figure 5.26A), while extended conjugation within fused aromatic backbones of BTABQ and pBTABQ accounts for the latter[14]. Although both materials display significant absorptions in the near-infrared region (NIR), leading to narrow optical band gaps of 0.82 eV and 0.79 eV (Figure 5.6G, 5.26D) for BTABQ and pBTABQ, respectively, only the latter has a strong absorption tail into the Mid-IR region. This low energy absorption, rare in organic materials, is indicative of the greater extent of conjugation in pBTABQ relative to BTABQ. Their significant intermolecular electronic delocalization is assisted by strong hydrogen bonding[15] and π-π stacking. Altogether, the various analytical data confirm that pBTABQ is a disordered oligomeric analog of BTABQ that has an extended, fused aromatic backbone, maintains a high density of carbonyl/imine redox sites, and supports a persistent hydrogen bonding network in its solid-state packing.

Due to the irreversible solid-state condensation reaction upon heating BTABQ solid, pBTABQ consists of fused aromatic molecules that can be described as oligomeric analog of BTABQ. Based on elemental analysis results (Table 5.2), MALDI-TOF mass spectrometry data (Figure 5.19), and XPS analysis of pBTABQ, pBTABQ can be best described as the chemical structure shown in Scheme 5.1, which formed due to cascade carbonyl-amino condensation reactions and Michael condensation reactions (Figure 5.21).
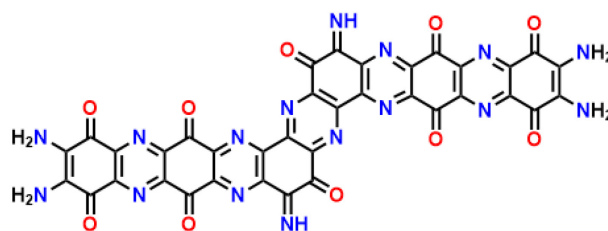
Scheme 5.1. The best molecular structure representative of pBTABQ.

BTABQ and pBTABQ exhibit similar bulk electrical conductivities of 2.4×10^{-5} S cm^{-1} ($\bar{\sigma} = 2.33 \times 10^{-5}$ S cm^{-1}) and 0.79×10^{-6} S cm^{-1} ($\bar{\sigma} = 0.40 \times 10^{-6}$ S cm^{-1}) at room temperature, respectively (Figure 5.27). Despite its larger aromatic backbone, pBTABQ is less conductive than BTABQ likely due to its disordered solid-state packing. Electron paramagnetic resonance spectra exhibit intense isotropic signals that are consistent with the presence of organic radicals in both materials (Figure 5.28), likely stemming from redox-active quinone/imine moieties or the fused heterocyclic systems within BTABQ units. Overall, the presence of a high density of diverse redox sites in extended conjugated materials with efficient electronic delocalization makes BTABQ and pBTABQ promising candidates for high-rate EES.
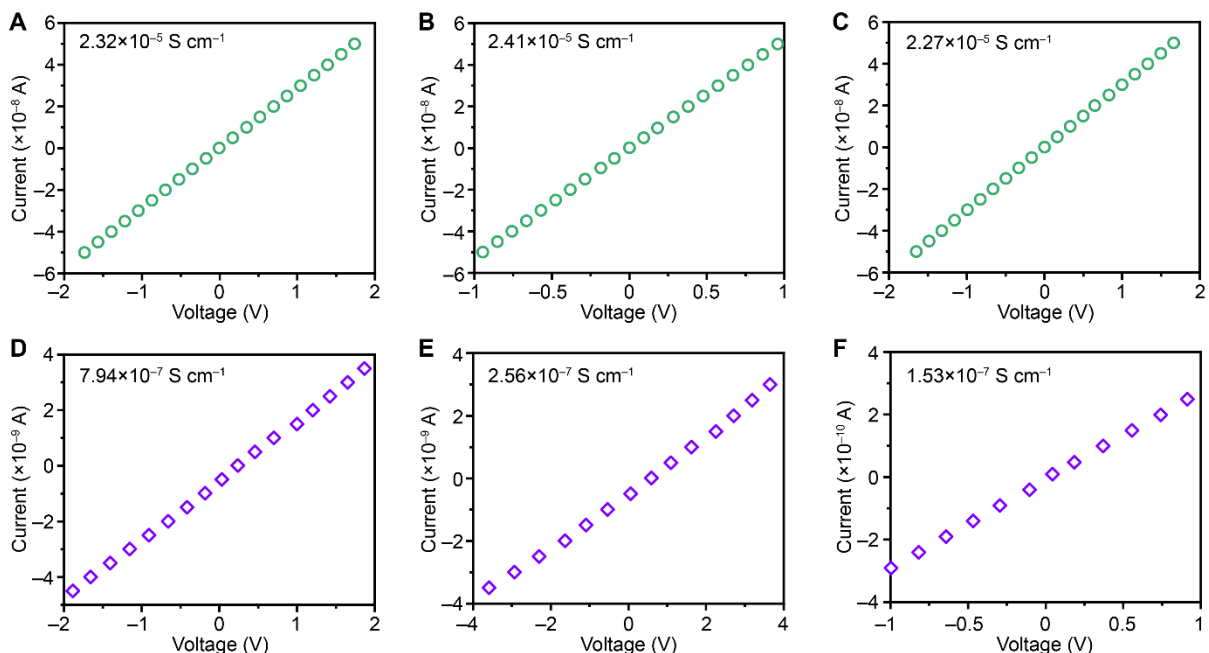
Figure 5.27. Electrical conductivity measurements of BTABQ and pBTABQ. (A-C) I-V curves of four-contact devices of BTABQ for room temperature electrical conductivity measurements. (D-F) I-V curves of four-contact devices of pBTABQ for room temperature electrical conductivity measurements. The electrical conductivity value of each device is presented in the top left corner of each figure. The <u>average</u> bulk electrical conductivity of BTABQ is 2.33×10^{-5} S cm^{-1}. The <u>average</u> bulk electrical conductivity of pBTABQ is 0.40×10^{-6} S cm^{-1}. The bulk electrical conductivity of a material is not only determined by the molecular structure and the concentration of radical concentration, but also significantly affected by the crystallinity, grain boundaries, and carrier mobility. Thus, although pBTABQ may well have more extended intramolecular π-conjugation, its amorphous nature and disordered intermolecular packing hinders the transport of transport of charge carriers. A similar and well-known example is the difference between crystalline silicon and amorphous silicon: the former has significantly higher carrier mobility.
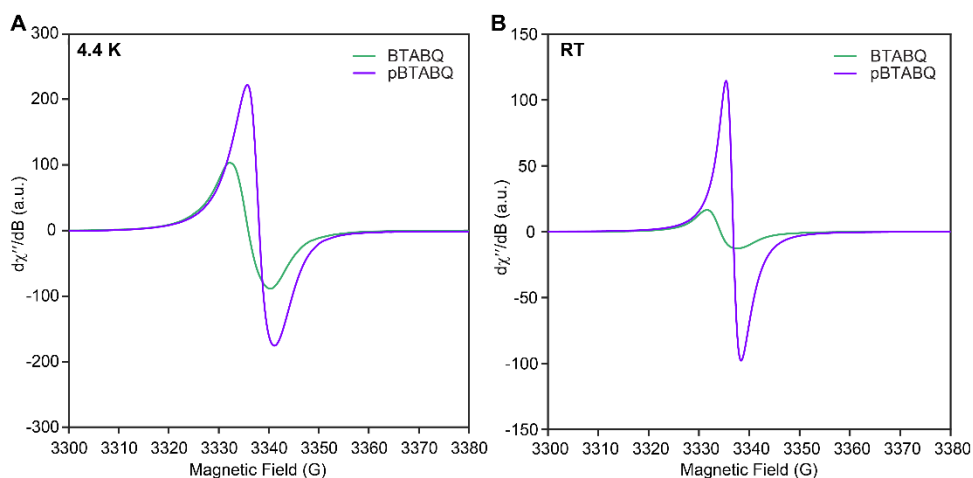
Figure 5.28. EPR spectra of BTABQ and pBTABQ. (A) EPR spectra of BTABQ and pBTABQ at 4.4 K. (B) EPR spectra of BTABQ and pBTABQ at RT. Both samples have approximately the same mass loading, and they exhibit strong and almost isotropic signals due to the presence of stable organic radicals, which is likely formed due to partial oxidation in the presence of air. The g values at 4.4 K are 2.0069 and 2.0055 for BTABQ and pBTABQ, respectively, which changed slightly to 2.0078, and 2.0063 at RT. The significantly enhanced intensity of EPR signal for pBTABQ suggests its higher radical concentration.

222

5.3.2 Electrochemical Performance in Neutral Electrolytes

Cyclic voltammograms (CVs) of BTABQ and pBTABQ, obtained in a three-electrode configuration in a 1 M aqueous solution of LiCl (see 5.4.2), display quasi-rectangular curves at scan rates ranging from 0.2 to 30 mV s^{-1} (Figures 5.29A, 5.30). Under cathodic polarization, BTABQ and pBTABQ display stable potential windows of 0.5 V and 1.0 V, respectively (Figure 5.31). An analysis of the CV currents (*i*) at different scan rates (*v*) using the power law equation ($i = av^b$) reveals *b* values close to unity for both materials (Figure 5.29C), indicating that the charge storage processes are rapid and are not limited by ion diffusion[16]. Altogether, the electrochemical behaviors of BTABQ and pBTABQ diverge from the sharp redox features and the diffusion-limited behaviors ($b = 0.5$) generally observed for organic battery electrodes[10,17] such as tetraamino-*p*-benzoquinone (TABQ), 5,7,12,14-pentancetetrone (PT) (Figure 5.29B, 5.29C), signaling an intrinsically different charge storage mechanism. Significantly, their behavior resembles that reported for inorganic materials such as $RuO_2 \cdot nH_2O$[18,19] and MXenes[20–22]. That is, they behave like capacitors but exhibit a rapid redox-based charge storage mechanism known as pseudocapacitance. Indeed, both BTABQ and pBTABQ have low specific surface areas (<20 m^2 g^{-1}), but exhibit high gravimetric specific capacitances of ~ 510 F g^{-1} at 0.2 mV s^{-1} and ~ 300 F g^{-1} at 10 mV s^{-1} (Figure 5.29D inset), consistent with a pseudocapacitive charge storage mechanism[23]. Notably, BTABQ and pBTABQ deliver these capacitances at high average discharge potentials of, 3.21 V and 2.96 V vs. Li$^+$/Li, respectively (Figure 5.29A). Galvanostatic charge-discharge (GCD) experiments at current densities ranging from 2 to 10 A g^{-1} display triangular (i.e. capacitive) voltage vs. time profiles (Figure 5.32). Additionally, both materials display excellent retention of capacitance over 20,000 CV cycles at a scan rate of 30 mV s^{-1} (Figure 5.29D). Furthermore, pBTABQ shows $\sim 96\%$ retention in GCD experiments at a current density of 10 A g^{-1} for at least 100,000 cycles (Figure 5.33). Both materials are stable after long cycling, as verified by XPS of cycled electrodes (Figure 5.34, 5.35). However, BTABQ undergoes in-situ exfoliation during the first 10 cycles to a stable, crystalline exfoliated microstructure that remains unchanged upon subsequent cycling (Figures 5.36A–D, 5.37A, 5.38). In contrast, the morphology and particle size of pBTABQ remain unchanged even after prolonged cycling (Figures 5.36F–H, 5.37B, 5.39).
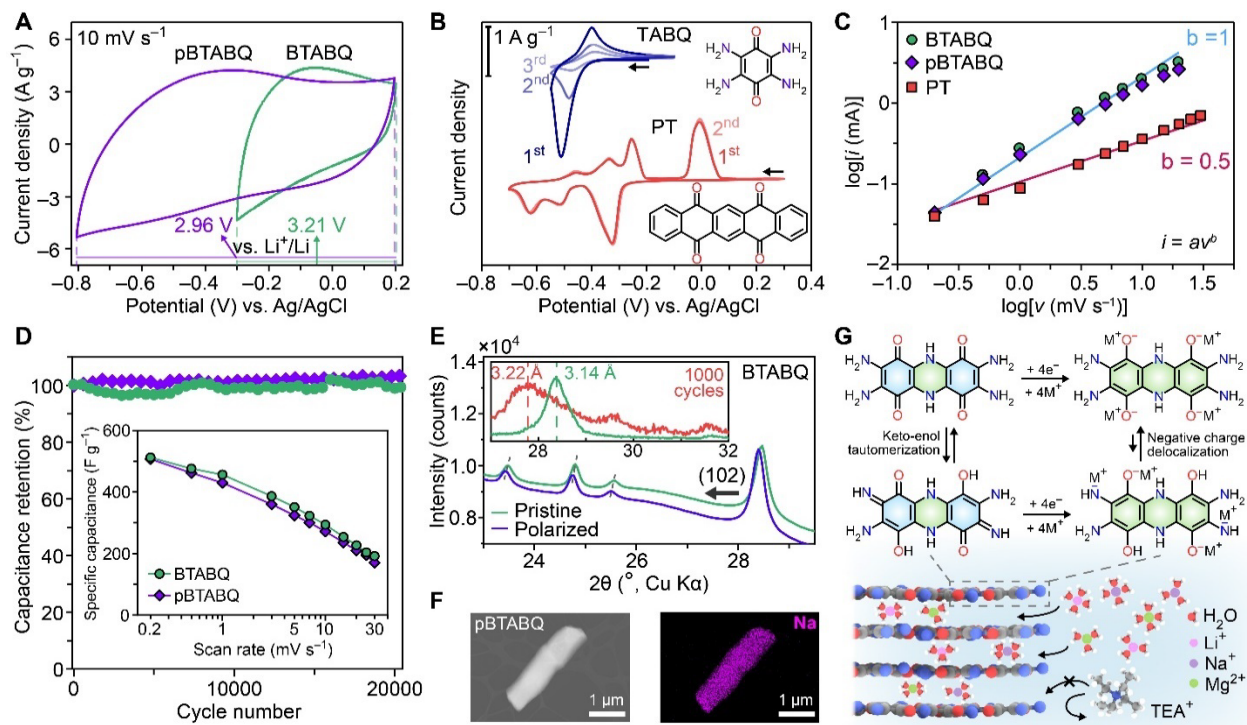
Figure 5.29. Charge storage in neutral electrolytes. (A) CVs of BTABQ and pBTABQ obtained at a scan rate of 10 mV s^{-1} using 1 M LiCl aqueous electrolyte. The nominal voltages vs. Li$^+$/Li are noted for both materials. (B) CVs of TABQ and PT obtained at a scan rate of 10 mV s^{-1} using 1 M LiCl aqueous electrolyte. (C) Current versus scan rate analysis of CVs of BTABQ, pBTABQ, and PT using the power law equation. (D) BTABQ and pBTABQ retain ~98% of their capacitance over 20000 CV cycles. Inset shows gravimetric specific capacitances at scan rates ranging from 0.2 to 30 mV s^{-1}. (E) In-situ WAXS patterns of pristine and negatively polarized BTABQ reveal lattice expansion, indicating intercalation of electrolytic ions under polarization. (F) Ex-situ EDS mapping of pBTABQ shows the presence of Na$^+$ ions throughout the bulk of a negatively polarized particle. (G) Schematic representation of redox mechanism of BTABQ and pseudocapacitive intercalation of hydrated ions into BTABQ.
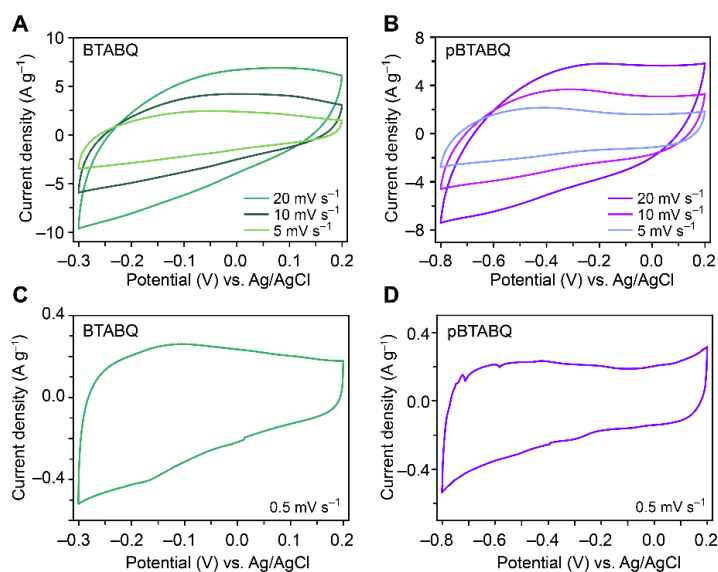
Figure 5.30. Cyclic voltammograms of BTABQ and pBTABQ in aqueous electrolytes. (A, C) Cyclic voltammograms (CVs) of BTABQ in 1 M LiCl aqueous electrolyte at various scan rates. (B, D) CVs of pBTABQ in 1 M LiCl aqueous electrolyte at various scan rates. All CVs display quasi-rectangular curves.
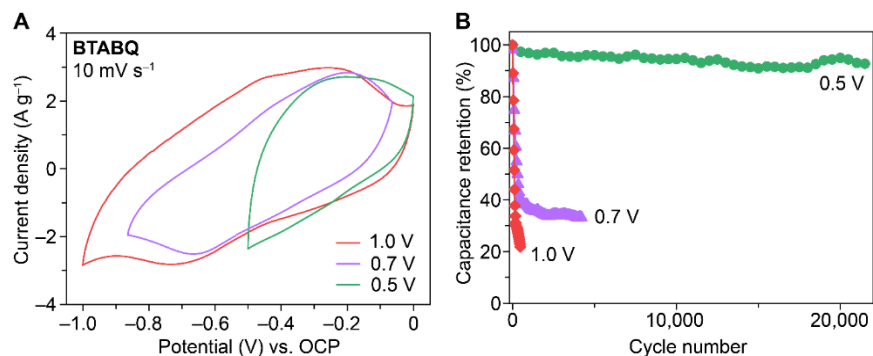
Figure 5.31. Determination of stable operating voltage window of BTABQ. (A) CVs of BTABQ in 1 M LiCl aqueous electrolyte cycled in increasingly reducing potential windows of 0.5, 0.7 and 1.0 V vs. open circuit potentials (OCP). (B) Capacitance retention of BTABQ over repeated cycling in the different potential windows. Experiments aimed at finding the stable electrochemical potential window of operation for BTABQ, have shown quasi-rectangular CVs in reductive potential windows of 0.5, 0.7 and 1 V. These quasi-rectangular CVs indicate that BTABQ maintains similar specific capacitances (in F g^{-1}) in increasingly large voltage windows. Consequently, in terms of specific charge capacity mAh g^{-1}, BTABQ stores twice the amount of charge in a 1 V window relative to a 0.5 V window, delivering values closer to its theoretical specific capacity. However, repeated cycling of BTABQ in the potential ranges beyond 0.5 V have found a significant loss in discharge capacities within the first few hundred cycles. Although stable cycling even over a few hundred cycles is considered good for a battery material, our focus is on maximizing cycling stability for a pseudocapacitor application. Hence, we have chosen to use 0.5 V scan windows for all our electrochemical studies on BTABQ.
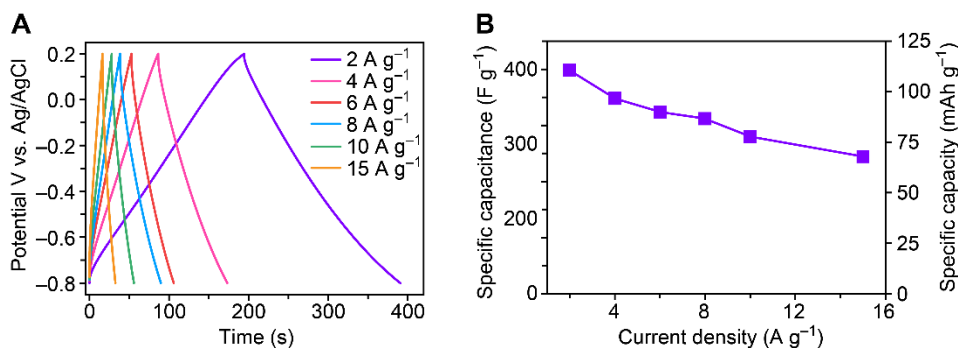
Figure 5.32. Rate capability of Galvanostatic charge-discharge of pBTABQ. (A) Galvanostatic charge-discharge (GCD) curves of pBTABQ in 1 M LiCl aqueous electrolyte at various current densities from 2 to 15 A g^{-1}. (B) Corresponding gravimetric specific capacitance and specific capacity.
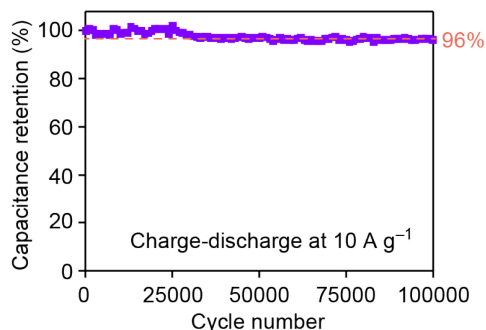
Figure 5.33. Galvanostatic charge-discharge cycling of pBTABQ in 1 M LiCl aqueous electrolyte. An excellent capacitance retention of over 96% was noted after 100,000 cycles of repeated charge-discharge. A variety of factors, primarily the strong hydrogen bonding network and intermolecular π-stacking contribute to extreme insolubility of both materials in all common solvents.
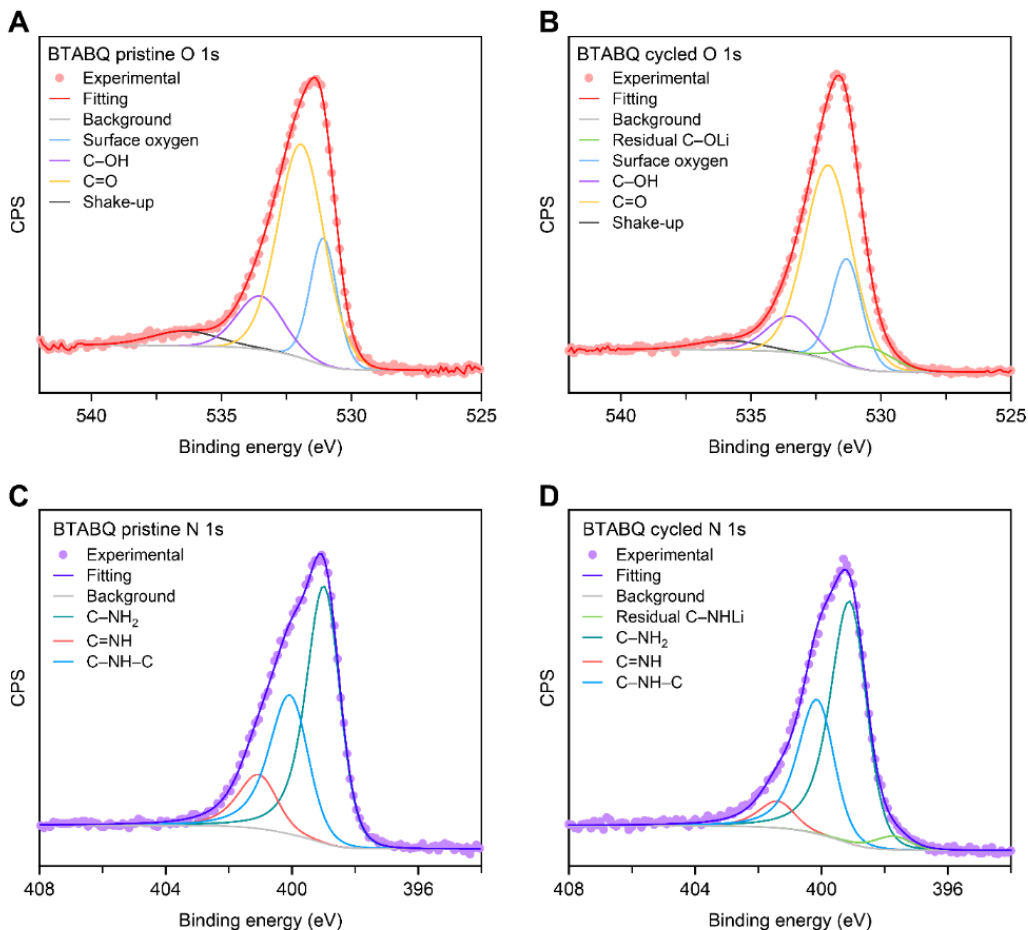
Figure 5.34. *Ex-situ* high-resolution XPS spectra of pristine and cycled BTABQ electrodes. (A, B) Ex-situ XPS O (1s) region of pristine and cycled BTABQ electrodes, respectively. (C, D) Ex-situ XPS N (1s) region pristine and cycled BTABQ electrodes, respectively. The electrode measured has been cycled 1000 times in 1 M LiCl aqueous electrolyte before the ex-situ measurements. We note that a small amount of residual $C–O–Li^+$ and $C–NH–Li^+$ were observed in O (1s) and N (1s) spectra, respectively, because this cycling experiment was not stopped exactly at OCP after cycling. Despite this slight difference, pristine and cycled BTABQ exhibit essentially identical O (1s) and N (1s) peaks and deconvolutions, indicating the chemical composition of BTABQ remains unchanged upon cycling.

Electrochemical impedance spectroscopy (EIS) provided additional information on the charge storage behavior under dynamic conditions. Nyquist plots of impedance for both BTABQ and pBTABQ (Figure 5.40) display typical capacitor-like features with low equivalent series resistances (~1–2 Ω), short semicircles and 45° transition regions along with an extended 90° capacitive region at low frequencies. Meanwhile, semicircles in the high frequency region reveal decreasing diameters with applied negative potentials, confirming that fast charge transfer events accompany charge storage in both materials[24]. In contrast, EIS of PT reveals typical battery-like features where charge storage is limited by ion diffusion (Figure 5.41). Overall, EIS and CVs of BTABQ and pBTABQ display capacitor-like features and highlight a possibility of pseudocapacitive charge storage that is distinct from common organic battery materials.
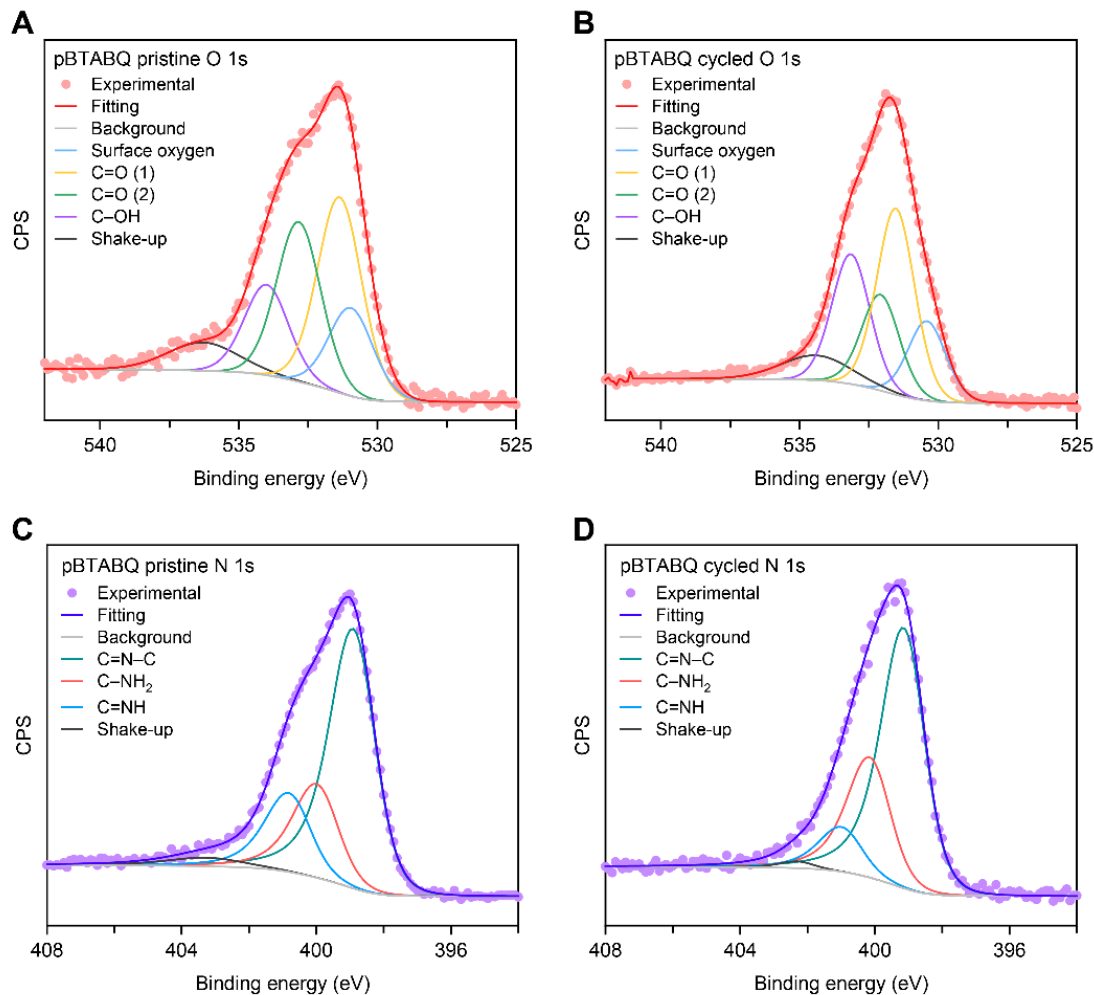
Figure 5.35. *Ex-situ* high resolution XPS spectra of pristine and cycled pBTABQ electrodes. (A, B) Ex-situ XPS O (1s) region of pristine and cycled pBTABQ electrodes, respectively. (C, D) Ex-situ XPS N (1s) region pristine and cycled pBTABQ electrodes. The electrode measured has been cycled 1000 times in 1 M LiCl aqueous electrolyte before the ex-situ measurements. Pristine and cycled pBTABQ exhibit essentially identical O (1s) and N (1s) peaks and deconvolutions, indicating the chemical composition of pBTABQ exhibit minimal changes upon cycling.
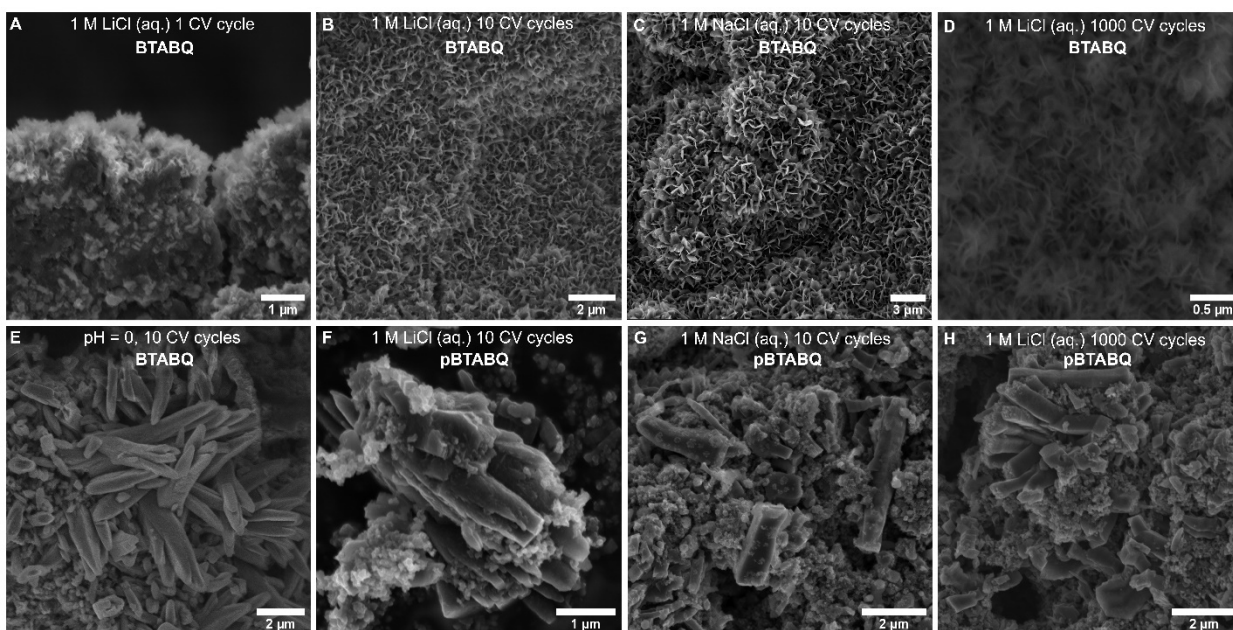
Figure 5.36. *Ex-situ* SEM images of BTABQ and pBTABQ electrodes. (A, B, C, D, E) Ex-situ SEM images of BTABQ electrodes obtained after recording CVs under different electrochemical conditions using a 10 mV s^{-1} scan rate. A, B and D correspond to BTABQ electrodes after 1, 10 and 1000 CV cycles, respectively, in 1 M LiCl aqueous electrolyte. Whereas C and E correspond to BTABQ electrodes after 10 CV cycles in 1 M NaCl neutral and 1 M NaCl (pH = 0) aqueous electrolytes, respectively. (F, G, H) Ex-situ SEM images of pBTABQ electrodes obtained after recording CVs under different electrochemical conditions using a 10 mV s^{-1} scan rate. F and H correspond to pBTABQ electrodes after 10 and 1000 CV cycles, respectively, in 1 M LiCl aqueous electrolyte. Whereas G corresponds to pBTABQ electrode after 10 CV cycles in 1 M NaCl neutral aqueous electrolyte. BTABQ undergoes in-situ exfoliation, even just after 1 CV cycle, in neutral electrolytes, but not in acidic conditions. In great contrast, pBTABQ does not exfoliate even in neutral conditions after long cycling.
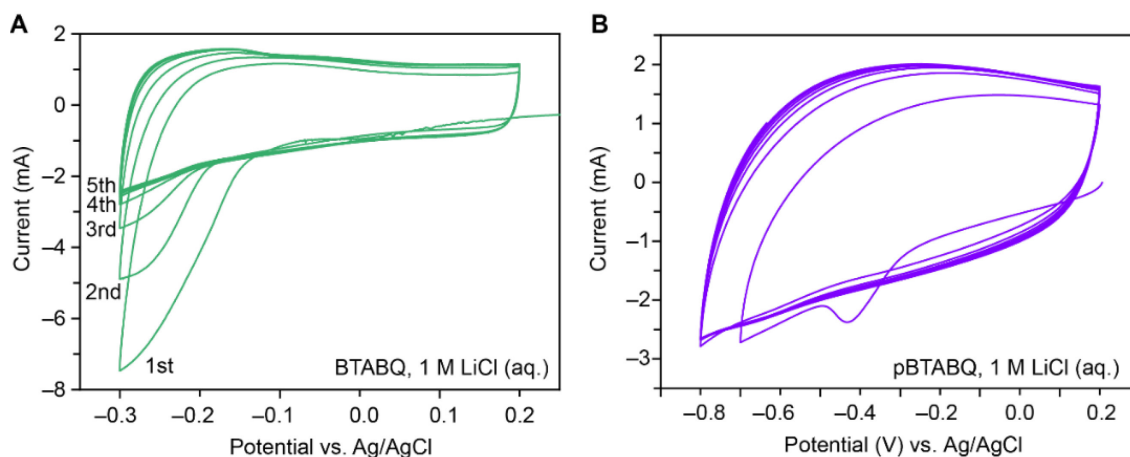
Figure 5.37. CV profiles of BTABQ and pBTABQ. (A) CV cycles of BTABQ electrodes in 1 M LiCl aqueous electrolyte at 10 mV s^{-1}. (B) CV cycles of pBTABQ electrodes in 1 M LiCl aqueous electrolyte at 10 mV s^{-1}. BTABQ displays irreversible currents in the first 5 CV cycles, indicative for intercalation and exfoliation. On the other hand, pBTABQ does not show a similar significant current drop in the first few CV cycles.

228
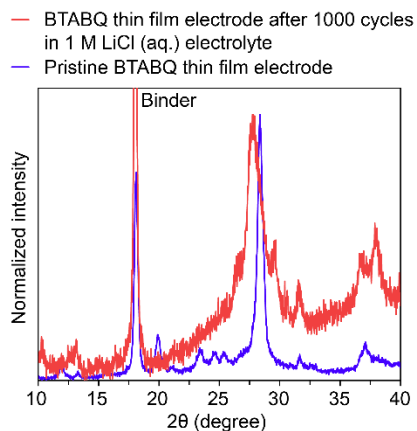
Figure 5.38. *Ex-situ* PXRD patterns of pristine BTABQ electrode and BTABQ electrode after 1000 cycles in 1 M LiCl aqueous electrolyte.
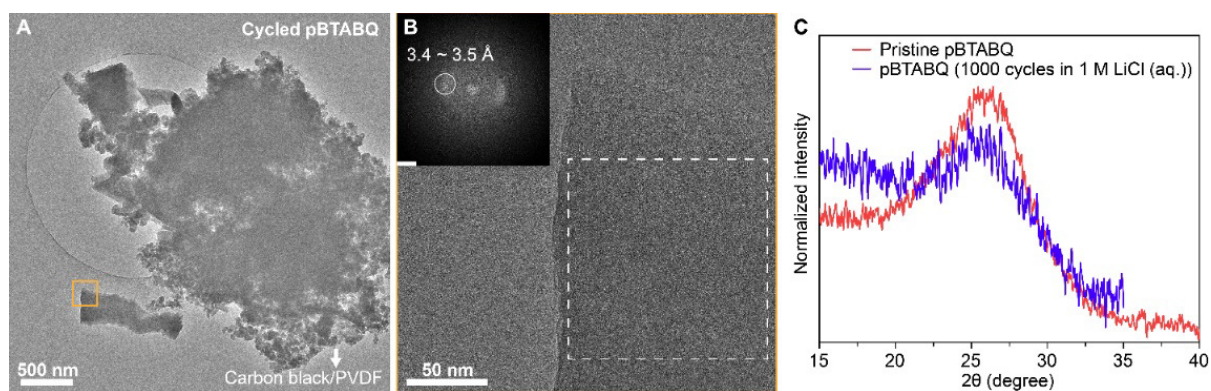
Figure 5.39. Morphological and structural characterizations of cycled pBTABQ. (A) Ex-situ Cryo-EM image of pBTABQ electrode after 1000 cycles in 1 M LiCl aqueous electrolyte. The morphology of pBTABQ particles remains unchanged upon cycling. (B) A high magnification Cyro-EM image of the highlighted area in (A), revealing the closely packed nature of pBTABQ particle after cycling. Inset: FFT of the area highlighted by a white dashed square, showing d-spacing of 3.4 Å ~ 3.5 Å, similar to that of pristine pBTABQ (Figure S16). (C) Ex-situ PXRD patterns of pristine pBTABQ electrode and pBTABQ electrode after 1000 cycles in 1 M LiCl aqueous electrolyte.
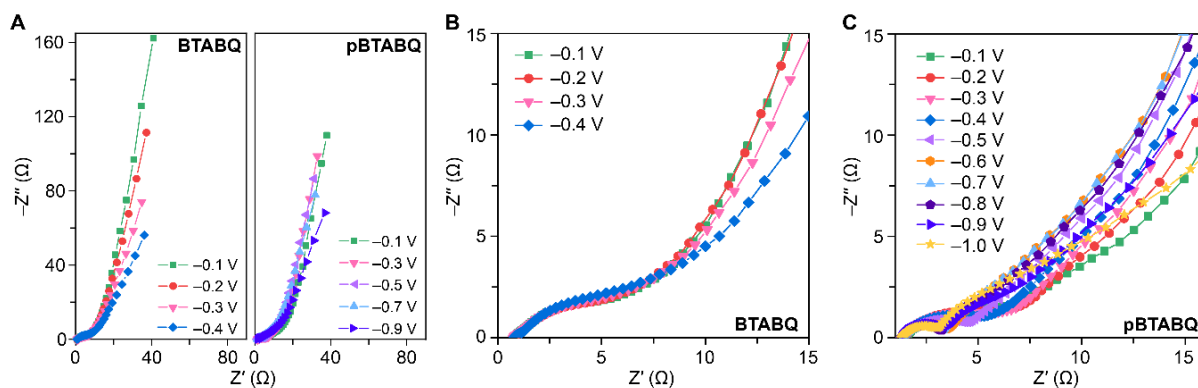
Figure 5.40. Electrochemical impedance spectra of BTABQ and pBTABQ in an aqueous 1 M LiCl electrolyte under various negative polarization relative to their open circuit potentials.

229
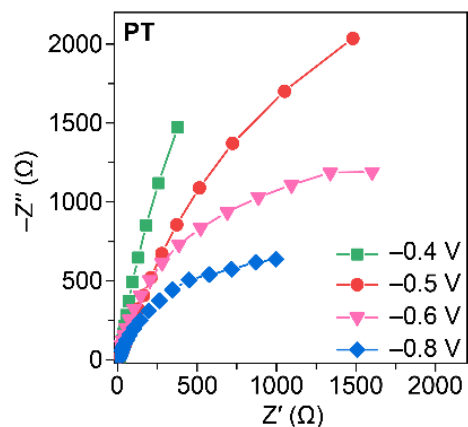
Figure 5.41. Electrochemical impedance spectra of PT in an aqueous 1 M LiCl electrolyte under various negative polarization. PT shows typical battery-like electrochemical kinetics where charge storage is limited by ion diffusion.

Redox processes during charge storage were analyzed through ex-situ X-ray photoelectron spectroscopy (XPS) and ssNMR studies of pristine and negatively polarized electrodes. Deconvolution of O (1s) XPS spectra of polarized electrodes reveal a significant decrease in the intensity of the C=O peak and the appearance of a C–O$^-$ peak, indicating the reduction of carbonyl groups (Figure 5.42). Deconvolution of N (1s) spectra indicates the disappearance of imine component and the growth of a benzoid-amine component upon reduction. The ssNMR spectrum of polarized BTABQ (Figure 5.43) further supports that both carbonyl and imine groups are reduced and are thus likely responsible for charge storage in BTABQ and pBTABQ (Figure 5.29G). Charges stored at these redox sites are delocalized both intramolecularly within the fused aromatic backbones, and intermolecularly through hydrogen bonding and D-A π-π stacking, manifesting in distinctly quasi-rectangular CVs, rapid electrode kinetics, and high-rate performance. In contrast, small organic molecules that display intermolecular hydrogen bonding but lack extended conjugation, such as TABQ (Figure 5.44)[25], and molecules with extensive conjugation but lacking intermolecular hydrogen bonding, such as PT[26,27], exhibit localized electronic states and display well-defined redox features that are limited by ion diffusion (Figure 5.26, 5.45)[9,10]. These comparisons suggest that the combination of all features: fused aromatic backbone with extended conjugation, hydrogen bonding, and π-π stacking are key to pseudocapacitive charge storage in organic materials.
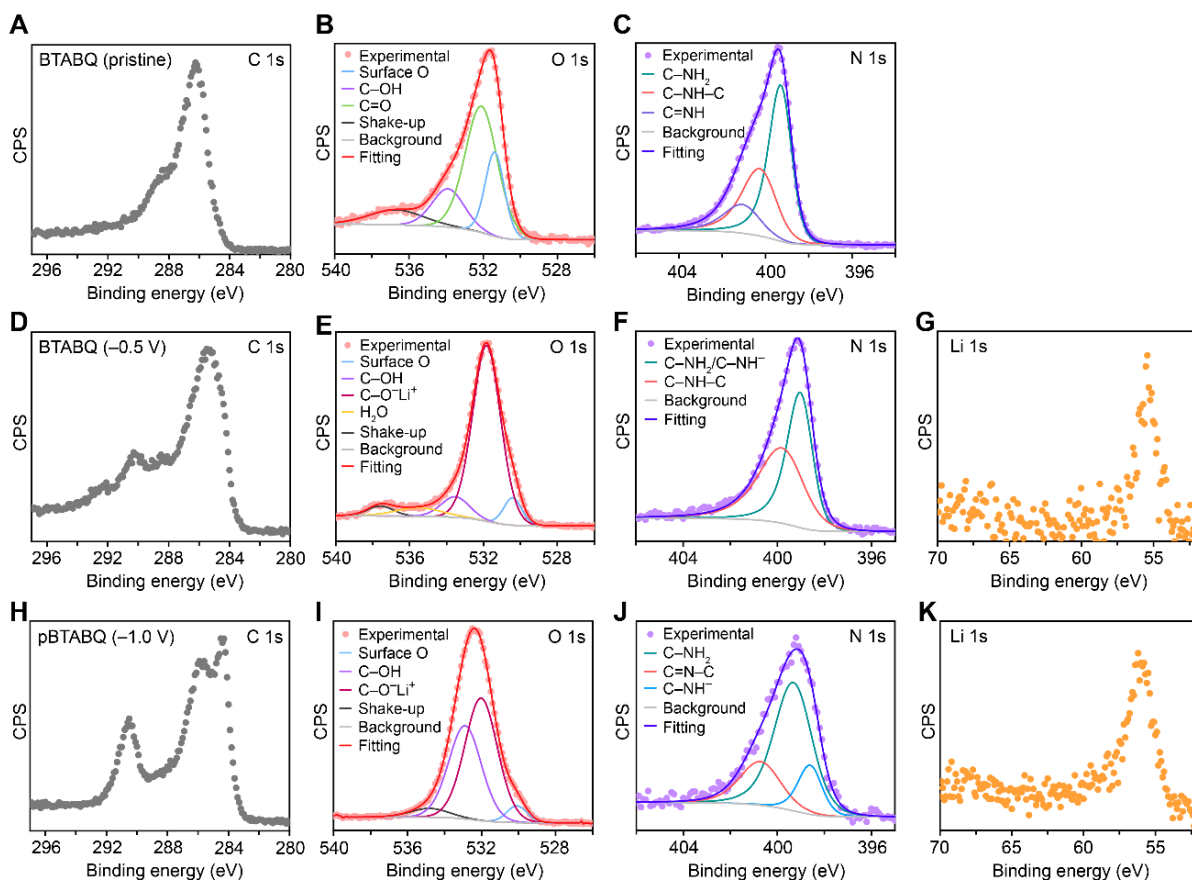
Figure 5.42. *Ex-situ* high resolution XPS spectra of pristine and negatively polarized BTABQ and pBTABQ electrodes. (A–C) High resolution XPS spectra of pristine BTABQ. (D–G) High resolution XPS spectra of negatively polarized BTABQ in 1M LiCl aqueous neutral electrolyte. (H–K) High resolution XPS spectra of negatively polarized pBTABQ. The deconvolution of O (1s) (B) and N (1s) (C) spectra of pristine BTABQ showed the presence of C–OH and C=NH, consistent with the presence of keto-enol tautomerization. Negatively polarized BTABQ and pBTABQ show the diminishing of C=O component and the growth of C–O⁻ component. Similarly, negatively polarized BTABQ and pBTABQ show the diminishing of C=N component and the growth of C–NH⁻ component. Significant signals of Li (1s) were observed for both negatively polarized BTABQ and pBTABQ.
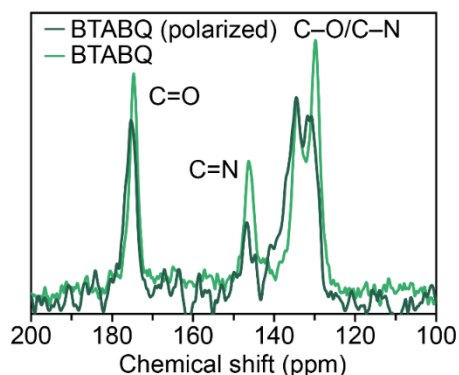
Figure 5.43. ^{13}C ss-NMR spectra of pristine and negatively polarized BTABQ electrodes. The strong signal of C=N (~146 ppm) in the spectrum of pristine BTABQ is consistent with its keto-enol tautomerization. The polarized sample showed significantly decreased intensity of C=N and slightly decreased intensity of C=O peaks.

231
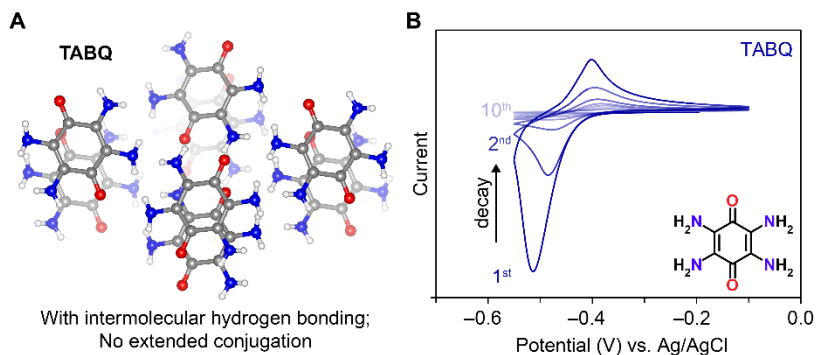
Figure 5.44. Structure and electrochemical behaviors of TABQ. (A) Crystal structure of TABQ (CCDC 1409346). (B) CV curves of TABQ in 1 M LiCl aqueous electrolyte at a scan rate of 10 mV s^{-1}, revealing well-defined redox peaks and battery-like diffusion-controlled features. A significant current drop was observed at the second cycle relative to the first one, and the drop in currents continues during subsequent cycling, which is due to the dissolution of TABQ electrode into electrolyte. Electrode dissolution is one of the major challenges for using organic small molecules for electrochemical charge storage.
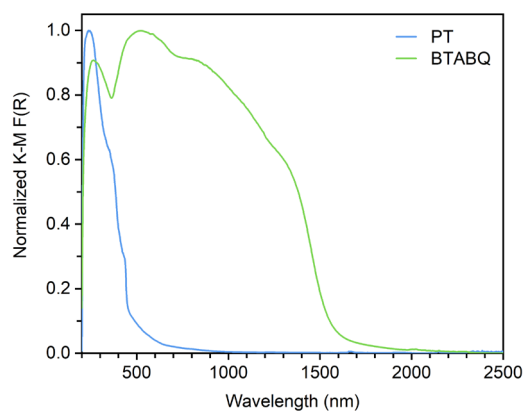
Figure 5.45. DRUV-Vis-NIR spectra of 5,7,12,14-pentancetetrone (PT) and BTABQ. While BTABQ exhibits significant absorption in NIR, PT shows negligible absorption beyond 500 nm, indicating limited charge delocalization and localized electronic states.

Wide-angle X-ray scattering (WAXS), PXRD, energy-dispersive X-ray spectroscopy (EDS) and angle-resolved XPS (ARXPS) coupled with depth profiling provided insight into whether the pseudocapacitance in BTABQ and pBTABQ is best described as surface-confined or as an intercalation-based bulk process[5]. WAXS patterns for BTABQ electrodes negatively polarized in-situ display a notable shift of the (102) reflection (Figure 5.6E) toward a lower 2θ value (Figure 5.29E, 5.46, 5.47). A PXRD pattern of BTABQ polarized after 1000 CV cycles revealed a more pronounced shift, corresponding to an increase in interlayer spacing from 3.14 Å to 3.22 Å during insertion of electrolytic Li$^+$ ions (Figure 5.29E inset), and supports an intercalation-based charge storage mechanism. Remarkably, other cations such as Na$^+$ and Mg^{2+} can also intercalate into both materials, as verified by ex-situ EDS studies of negatively polarized samples (Figure 5.29F, 5.48, 5.49). Elemental mapping indicates that a significant amount of metal cations distributes throughout the particles (Table 5.3), confirming charge storage in the bulk of both BTABQ and pBTABQ electrodes. ARXPS (Figure 5.50) and XPS depth profiling (Figure 5.51) for

polarized BTABQ and pBTABQ revealed that the amount of metal ions (Li^+ or Na^+) increases with increasing detection depth, confirming that the charge storage occurs via bulk pseudocapacitive intercalation rather than surface-confinement.
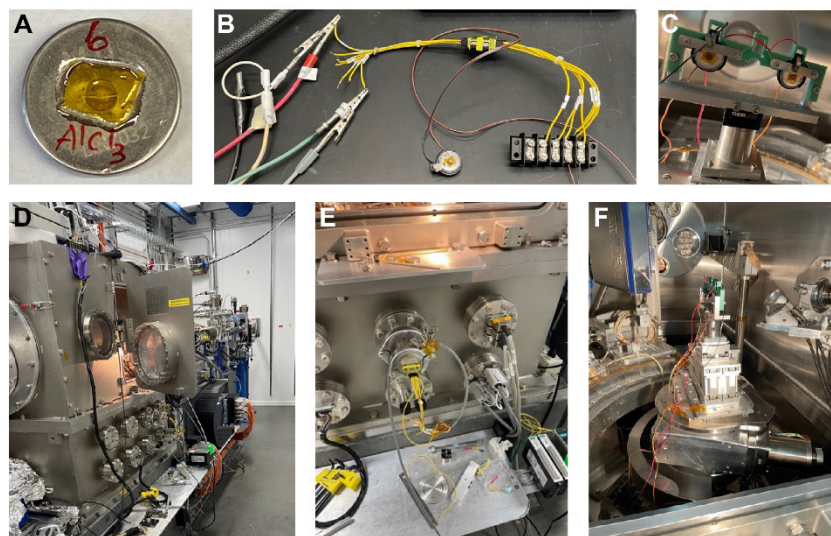
Figure 5.46. DRUV-Vis-NIR spectra In-situ WAXS measurements setup. (A) Customized coin cell. (B, C) Coin cell holders and wire connections. (D) Vacuum chamber. (E) Electric connection of the coin cells and the potential stat. (F) Sample stage.
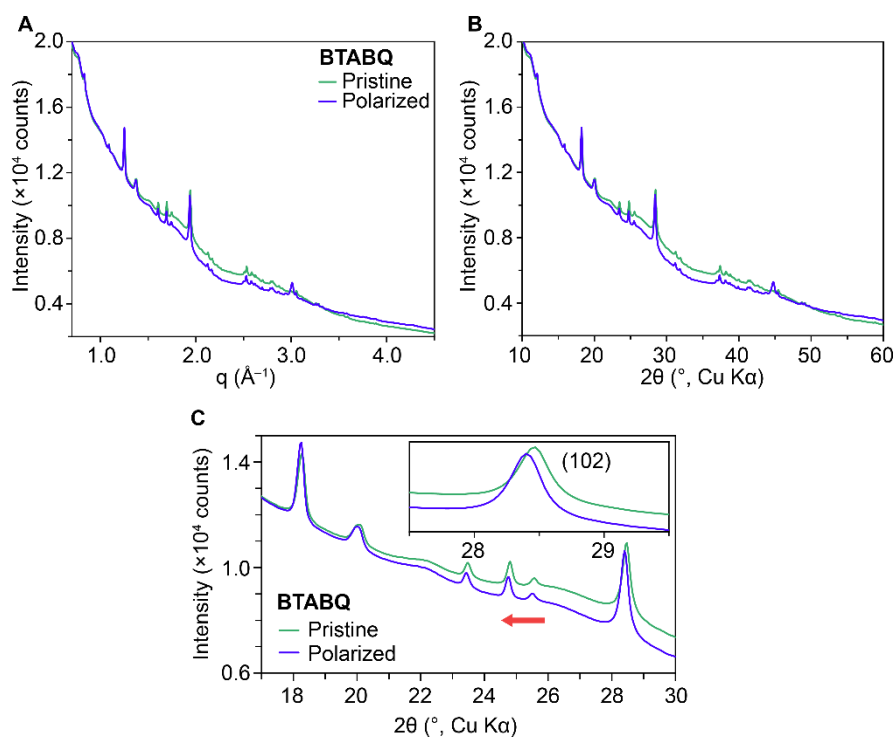
Figure 5.47. *In-situ* WAXS patterns of BTABQ cell. (A, B) In-situ WAXS patterns of BTABQ electrode before and after 30-min negative polarization in q space (A) and 2θ (Cu Kα, B). (C) Zoomed-in region where the shift of (102) reflection can be clearly observed.
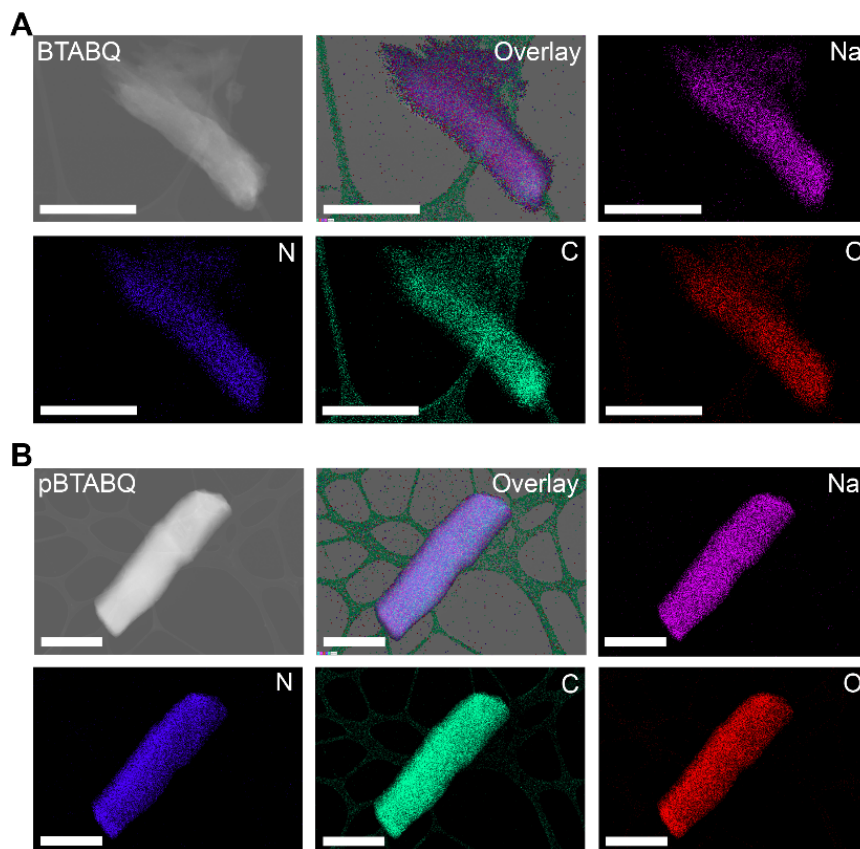
Figure 5.48. *Ex-situ* HAADF-STEM EDS mapping of negatively polarized BTABQ and pBTABQ. 1 M NaCl aqueous electrolyte was used. Scale bars: (A) 500 nm; (B) 1 μm.
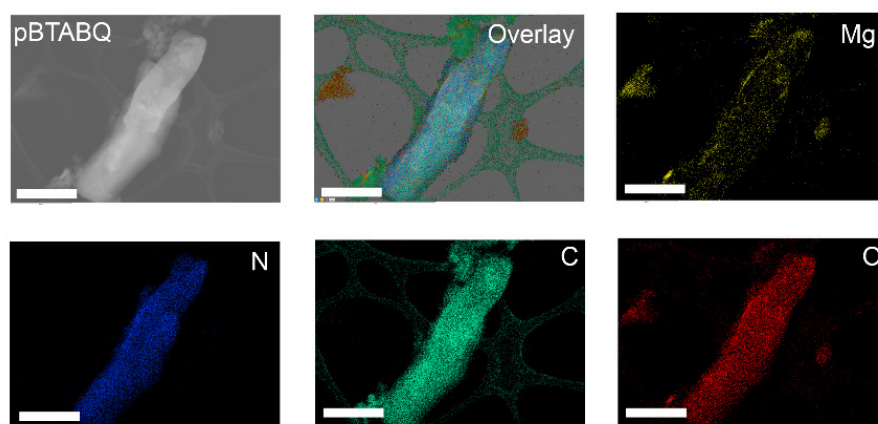
Figure 5.49. *Ex-situ* HAADF-STEM EDS mapping of negatively polarized pBTABQ in 0.5 M $MgCl_2$ aqueous electrolyte. Scale bars: 500 nm.

Table 5.3. Atomic composition[a] of negatively polarized BTABQ and pBTABQ in various electrolyte[b] obtained from ex-situ EDS mapping.

Sample	N (At%)	O (At%)	Na (At%)	Cap_{exp}/Cap_{theo}
BTABQ (neutral)	43.7	36.9	19.5	60%
pBTABQ (neutral)	51.1	35.5	13.5	34%
BTABQ (pH = 14.7)	36.4	36.9	26.6	87%
pBTABQ (pH = 0)	64.9	34.0	1.0[c]	-
pBTABQ (pH = 14.7)	32.2	41.8	26.0	76%
pBTABQ (17 m NaClO$_4$)[d]	39.3	34.1	26.7	79%
pBTABQ (neutral, MgCl$_2$)	61.5	33.8	4.7[d]	21%

[a] Only consider N, O, and Na. [b] Except further notice, the electrolytes are 1 M NaCl aqueous solution at various pH values. [c] Noise level. [d] WiSE. [e] At% of Mg. Essentially no Na$^+$ signal was observed in negatively polarized pBTABQ at pH = 0. Significantly larger amount of Na$^+$ was observed, for both negatively polarized BTABQ and pBTABQ, at pH = 14.7 relative to the values observed at neutral conditions. Significantly larger amount of Na$^+$ was observed for negatively polarized pBTABQ in WiSE relative to the value observed for pBTABQ in 1 M NaCl solution at pH = 7. The ratio of experimentally observed charge capacity vs. theoretical value (Cap_{exp}/Cap_{theo}) is calculated based on the equations: $Cap_{exp}/Cap_{theo} = 2 \times At\%(Na) / (At\%(N) \times 2/3 + At\%(O))$ for BTABQ; $Cap_{exp}/Cap_{theo} = At\%(Na)/ (12/26 \times (At\%(N) + At\%(O)))$ for pBTABQ.
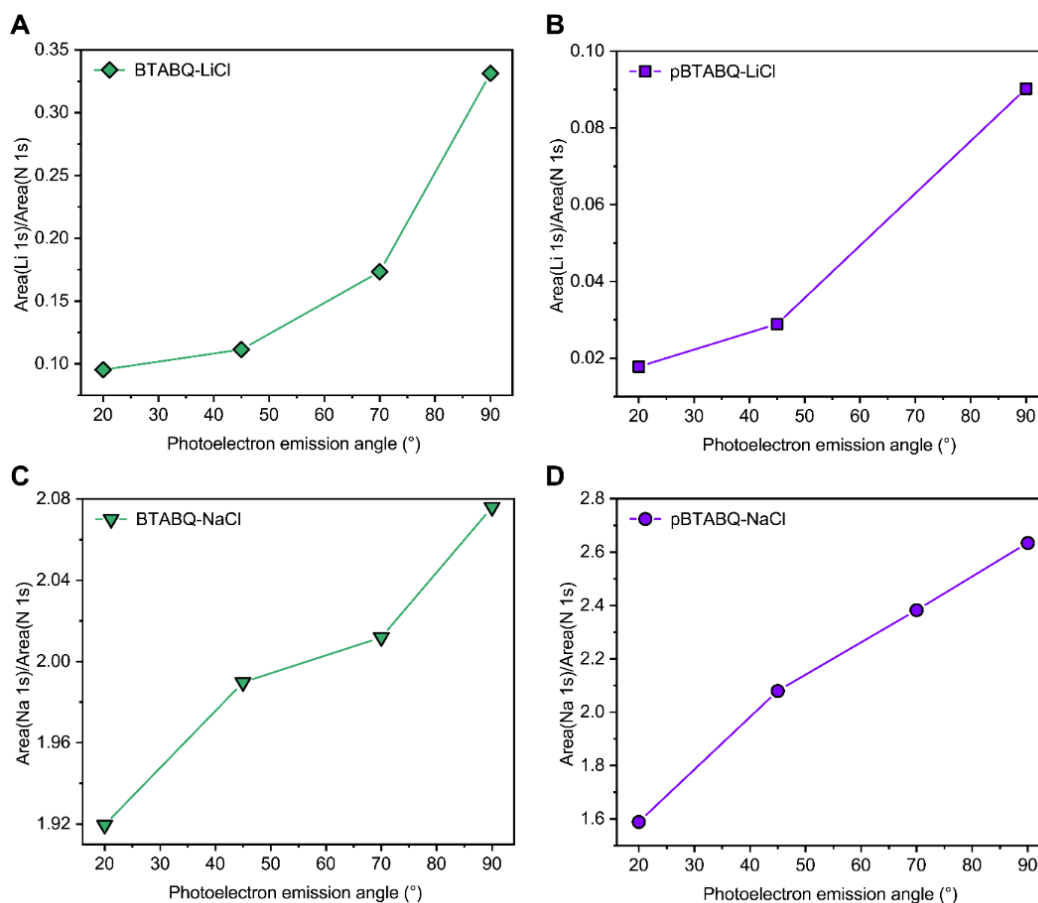
Figure 5.50. *Ex-situ* angle-resolved XPS results of negatively polarized BTABQ and pBTABQ electrodes. Dependence of detected metal ion (Li^+ or Na^+) amount on photoelectron emission angle obtained by ex-situ ARXPS spectroscopy of negatively polarized BTABQ and pBTABQ electrodes on CFP. Either 1 M LiCl or 1 M NaCl aqueous electrolyte was used for CV cycling. ARXPS is a XPS technique that varies the emission angle at which the photoelectrons are collected, thus enabling electron detection from different depths of samples. The higher electron emission angle leads to larger penetration depth. Therefore, if the charge storage is only surface-based, the metal ions will accumulate only on or near the surface, and in principle, the intensity of XPS signal of metal ions will not change upon changing the electron emission angle since the surface is always probed regardless of the electron emission angle. In contrast, if charge storage involves pseudocapacitive intercalation, metal ions will go deep inside the electrode material, and the intensity of the XPS signal for these ions will increase upon increasing the electron emission angle. Experimentally, we use the ratio of the area of metal signal (Li (1s) or Na (1s)) to the area of N (1s) signal as the indicator of the amount of metal ion detected, since the N composition is uniform across the whole electrode material. Figures above reveals that the amount of detected metal ions (Li^+ or Na^+) increases with increasing photoelectron emission angle. Therefore, the ARXPS results support the pseudocapacitive intercalation mechanism seen in both BTABQ and pBTABQ.
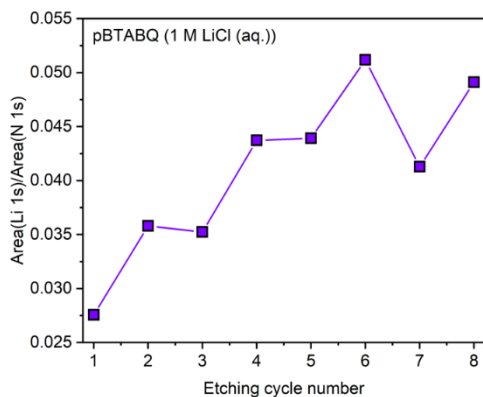
Figure 5.51. *Ex-situ* XPS Depth profiling result of negatively polarized pBTABQ electrode. Dependence of detected metal ion (Li^+ or Na^+) amount upon Ar ion etching obtained by ex-situ XPS depth profiling of negatively polarized pBTABQ electrode on CFP in 1 M LiCl aqueous electrolyte. The XPS depth profiling correlates between metal ion amount and depth from the surface. An Ar ion gun was used for etching, and a 60-second etching process was conducted between every two XPS measurements. Increasing amount of Li^+ deeper into the electrode, with a plateau reached after 5 etching cycles. Therefore, the depth profiling result agrees with the ARXPS data and supports charge storage by pseudocapacitive intercalation in pBTABQ.

Studies in a series of different electrolyte solutions provided important information on the role of electrolytic ions on intercalation. Various alkali or alkaline earth metal ions did not cause significant changes in the CVs for both the monomer and the polymer (Figure 5.52). However, markedly lower currents were observed with electrolytes containing tetraethylammonium (TEA^+) (Figure 5.53). Partially substituting TEA^+ with increasing amounts of Li^+ led to corresponding increases in current. Altogether, these results show that both materials can intercalate a variety of hydrated alkali and alkaline earth ions but exclude larger TEA^+ ions, presumably based on size (Figure 5.29G). The ability of BTABQ and pBTABQ to intercalate multiple ions and display size-differentiated pseudocapacitive behavior mimics that of MXenes[20,22] and coordination polymers[28]. Interestingly, the CV shape noted for the BTABQ in tests using Mg^{2+} diverges from a recent report on its use in Zn^{2+} batteries[17], warranting further focused investigations.
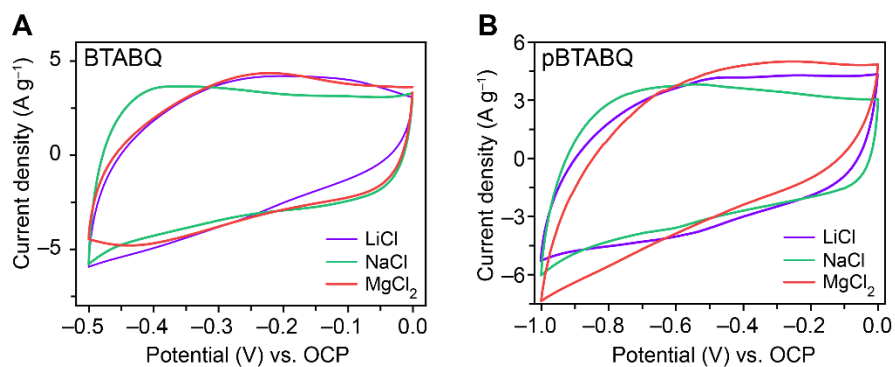
Figure 5.52. CVs of BTABQ and pBTABQ in a variety of aqueous electrolytes. (A, B) The cyclic voltammograms of BTABQ and pBTABQ in 1 M LiCl, NaCl, or $MgCl_2$ aqueous electrolyte at a scan rate of 10 mV s^{-1}, respectively. Potentials are applied and shown here with respect to the open circuit potentials (OCP) of each cell because of the minor electrolyte-dependent variations of measured potentials vs. AgCl/Ag.
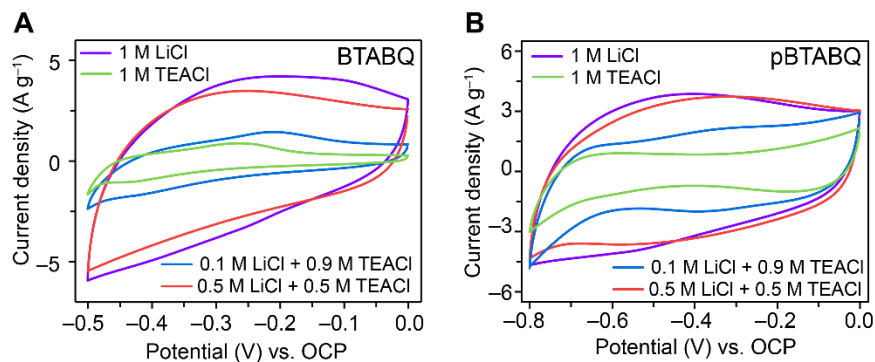
Figure 5.53. CVs of BTABQ and pBTABQ in mixtures of LiCl and TEACl aqueous electrolytes. (A, B) The cyclic voltammograms of BTABQ and pBTABQ in 1 M tetraethylammonium chloride (TEACl), 0.1 M LiCl/0.9 M TEACl, 0.5 M LiCl/0.5 M TEACl, and 1 M LiCl aqueous electrolytes at a scan rate of 10 mV s^{−1}, respectively. The current densities increased significantly by adding LiCl to TEACl aqueous electrolyte. Potentials are applied and shown here with respect to the open circuit potentials (OCP) of each cell because of the minor electrolyte-dependent variations of measured potentials vs. AgCl/Ag.

5.3.3 Influence of pH on Charge Storage

The pH of electrolytes often strongly modulates the charge storage behavior of pseudocapacitive materials[19,29]. With evidence in hand that both hydrogen bonding and ion sizes critically influence the electrochemical response of both BTABQ and pBTABQ, we evaluated the influence of pH using aqueous NaCl electrolytes in the pH range 0 – 14.7 (see 5.4.3). Although both materials exhibit similar dependence on pH, the discussion below is primarily focused on pBTABQ, given its larger electrochemical stability window (1.0 V).

CVs recorded in electrolytes with intermediate pH (3.0 – 12.0) remain quasi-rectangular, whereas CVs recorded under highly acidic or alkaline conditions exhibit broad redox features with small peak separations and markedly increased current (Figure 5.54A). Specifically, two sets of broad redox peaks are noted at pH = 0 – 1, whereas a single broad redox feature is observed at pH > 13 (Figure 5.55–5.57). Analysis of peak currents vs. scan rates (vide supra) finds b values of ~0.9 at pH < 1 and pH > 13 (Figure 5.54B), indicating that even at these pH extremes, charge storage is not limited by bulk ion diffusion. The total amount of charge stored at different pH, calculated as gravimetric specific capacity (mAh g^{−1}) from CVs at 0.2 mV s^{−1}, increases from ~160 mAh g^{−1} at intermediate pHs to 272 and 310 mAh g^{−1} at pH of 14.7 and 0, respectively (Figure 5.54C, 5.58). This "U-shaped" pH-dependence of specific capacities has previously been observed for $RuO_2 \cdot xH_2O$[19], but, to our knowledge, is a first in organic systems. The observed capacities are substantially higher than state-of-the-art inorganic pseudocapacitive electrodes and higher even than LIC cathodes that function at comparable electrochemical potentials[5,30]. Moreover, high capacities of 225 mAh g^{−1} (pH = 0), 135 mAh g^{−1} (pH = 14.7), and 72 mAh g^{−1} (pH = 7.3) can be accessed at fast rates, within 33 seconds (Figure 5.59). pBTABQ exhibits best rate capability at pH = 0, with

retention of 96%, 90% and 70 % capacities relative to the highest experimental capacity of 320 mAh g^{-1} (Q$_{max}$, 0.05 mV s^{-1}, Figure 5.60), at increasing scan rates of 0.2, 5 and 100 mV s^{-1}, respectively (Figure 5.59). Assuming a minimum of three BTABQ units in every oligomeric pBTABQ unit, one can estimate a 12-electron reduction and a theoretical maximum capacity of 389 mAh g^{-1} for pBTABQ (see 5.4.5), such that the experimental bulk utility of pBTABQ at pH = 0 is 82%. Remarkably, GCD tests at pH = 0 under high current densities of 2-10 A g^{-1} also deliver capacities greater than 200 mAh g^{-1} at rates corresponding to 6-50 C (1 C = discharge in 1 hour), and capacity retention of ~90% after 30,000 cycles (Figure 5.61). Cycling of pBTABQ at pH = 14 also exhibits ~90% of capacity retention after 10,000 cycles (Figure 5.62), further demonstrating the chemical and cycling stability of pBTABQ.
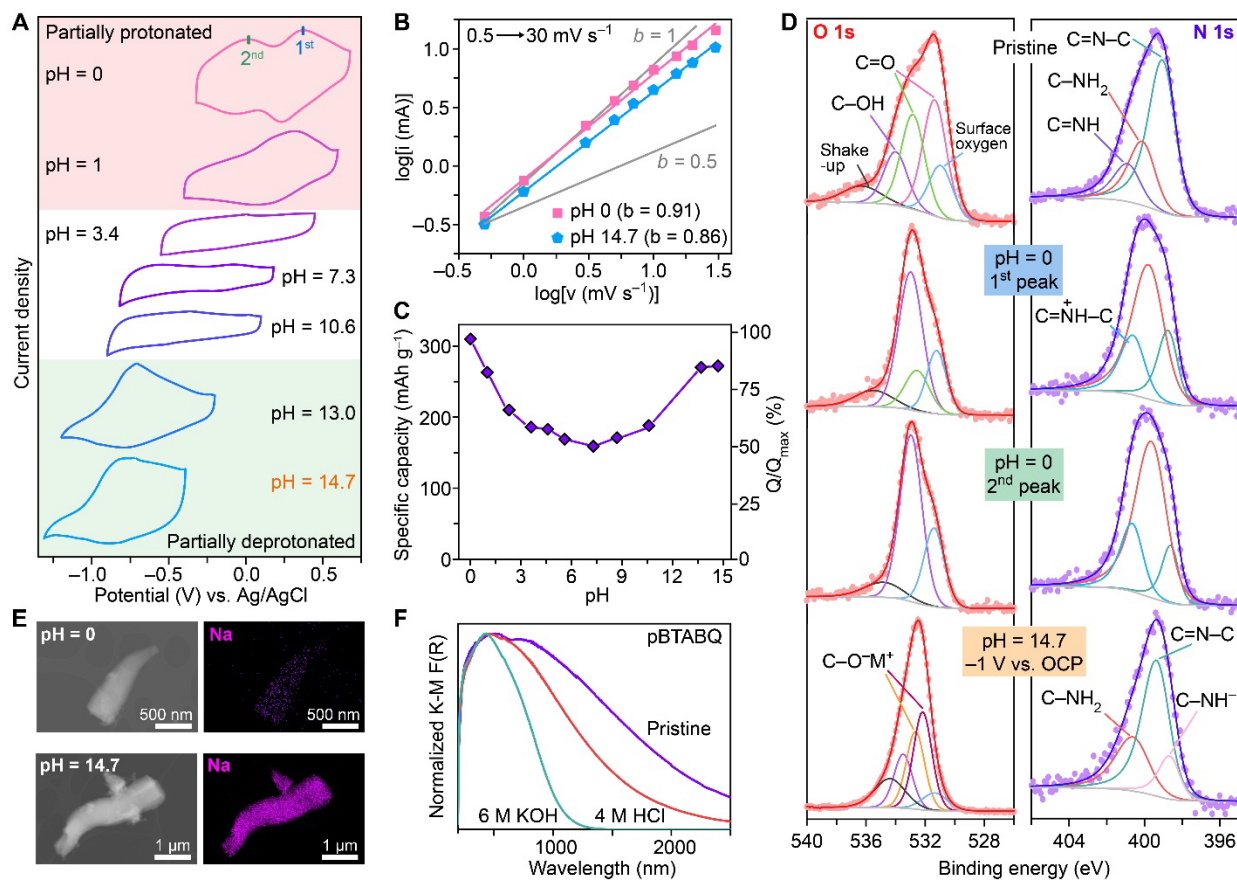
Figure 5.54. Role of pH on charge storage in pBTABQ. (A) CVs obtained at a scan rate of 5 mV s^{-1} in aqueous 1 M NaCl electrolyte solutions buffered at pH values ranging from 0 to 14.7. (B) Peak current versus scan rate analysis of the observed peaks under highly acidic and alkaline conditions reveal b values close to unity. (C) Plot of gravimetric specific capacities as a function of electrolyte pH obtained from CVs at a scan rate of 0.2 mV s^{-1}. (D) Ex-situ high resolution O (1s) and N (1s) XPS of polarized electrodes highlight changes at C=O and C=N groups at pH = 0 and 14.7. (E) EDS mappings of polarized pBTABQ under at pH = 0 and 14.7. (F) DRUV-Vis spectra of pristine and pBTABQ and after soaking in aqueous solutions of 4 M HCl or 6 M KOH.
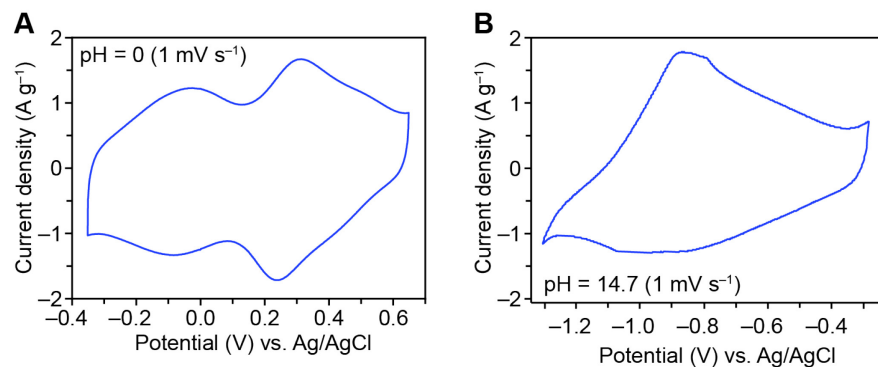
Figure 5.55. CVs of pBTABQ in highly acidic or basic electrolytes. (A) A cyclic voltammogram of pBTABQ in 1 M NaCl aqueous electrolyte with pH = 0. (B) A cyclic voltammogram of pBTABQ in 1 M NaCl aqueous electrolyte with pH = 14.7. The scan rate is 1 mV s^{-1}.
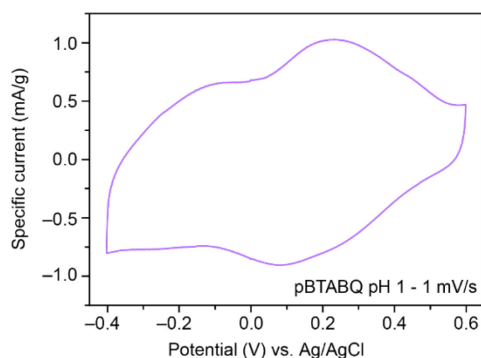
Figure 5.56. The cyclic voltammogram of pBTABQ recorded at a scan rate of 1 mV s^{-1} in 1 M NaCl electrolyte adjusted to pH = 1. Two sets of redox peaks can be noted here, whereas the second set of redox peaks is not obvious in the CV curve for pH = 1 shown in the main text due to higher scan rate (5 mV s^{-1}).
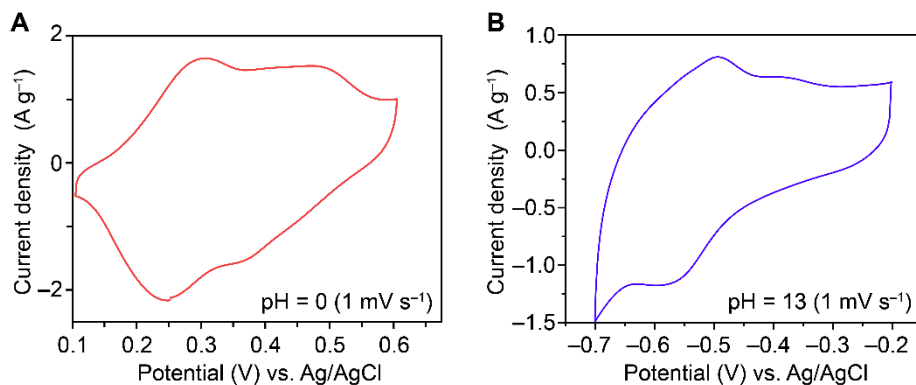
Figure 5.57. CVs of BTABQ in highly acidic or basic electrolytes. (A) A cyclic voltammogram of BTABQ in 1 M NaCl aqueous electrolyte with pH = 0. (B) A cyclic voltammogram of BTABQ in 1 M NaCl aqueous electrolyte with pH = 13. The scan rate is 1 mV s^{-1}.
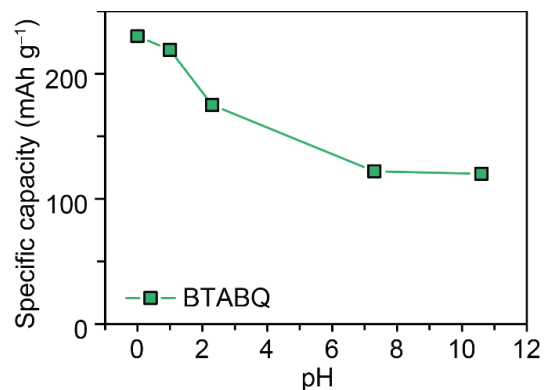
Figure 5.58. pH-dependence of charge storage performance of BTABQ. A plot of gravimetric specific capacities versus electrolyte pH obtained from CVs at a scan rate of 0.2 mV s^{-1} for BTABQ. At pH > 11.5, BTABQ start to dissolve in the electrolyte very slowly upon electrochemical polarization. We note that the charge capacity of BTABQ at pH = 0 condition (0.2 mV s^{-1}), 230 mAh g^{-1}, corresponds to 1656 F g^{-1} in capacitance.
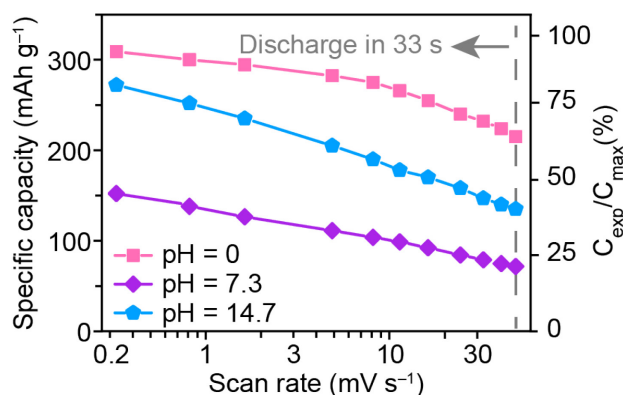
Figure 5.59. Rate capability of pBTABQ electrodes tested under different pH values. Left y-axis shows specific capacity, while the right y-axis shows the capacity retention at different scan rates. A good retention of specific capacity even at very short discharge time (i.e. high scan rate) highlights the power capability of pBTABQ.
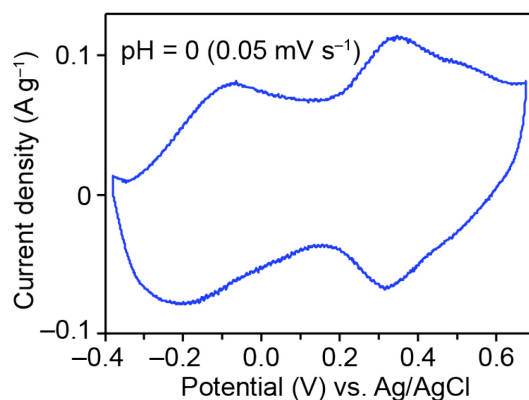
Figure 5.60. Cyclic voltammogram of pBTABQ in 1 M NaCl aqueous electrolyte with pH = 0 at a slow scan rate of 0.05 mV s^{-1}. Capacity calculated from this CV (320 mAh g^{-1}) was used as the experimental maximum value (C$_{max}$) of capacity in Figure 5.58.

241
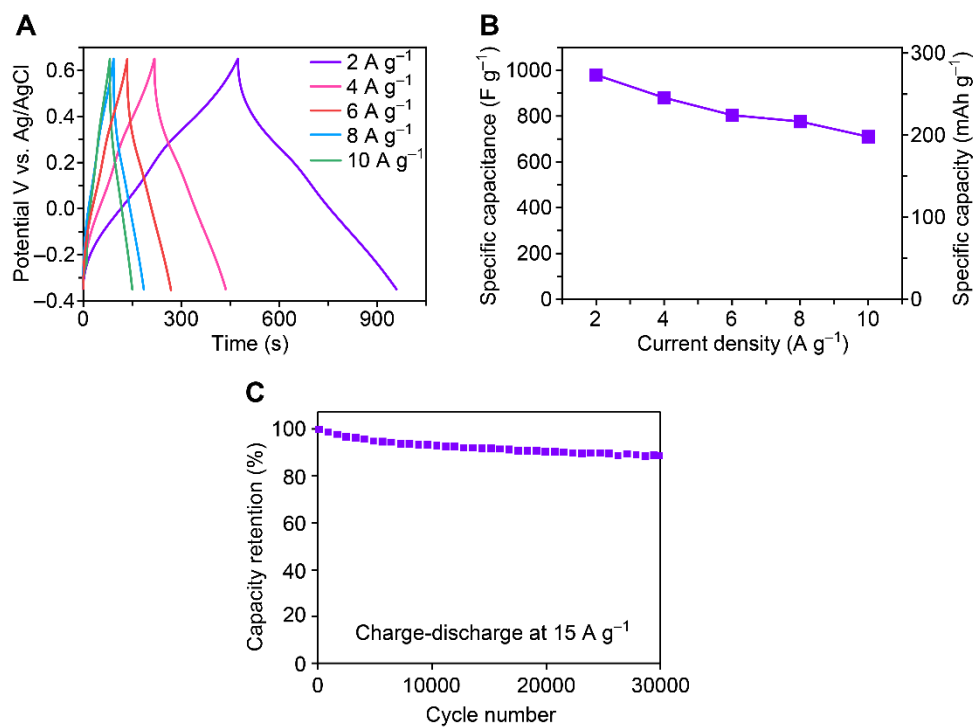
Figure 5.61. Galvanostatic charge-discharge studies of pBTABQ in acidic electrolyte. (A) GCD curves of pBTABQ in 1 M NaCl aqueous electrolyte at pH = 0 at various current densities from 2 to 10 A g^{-1}. (B) Corresponding gravimetric specific capacitance and specific capacity. (**C**) GCD cycling of pBTABQ in 1 M NaCl aqueous electrolyte with pH of 0 at a current density of 15 A g^{-1}. ~90% capacity retention is still observed after 30000 GCD cycles.
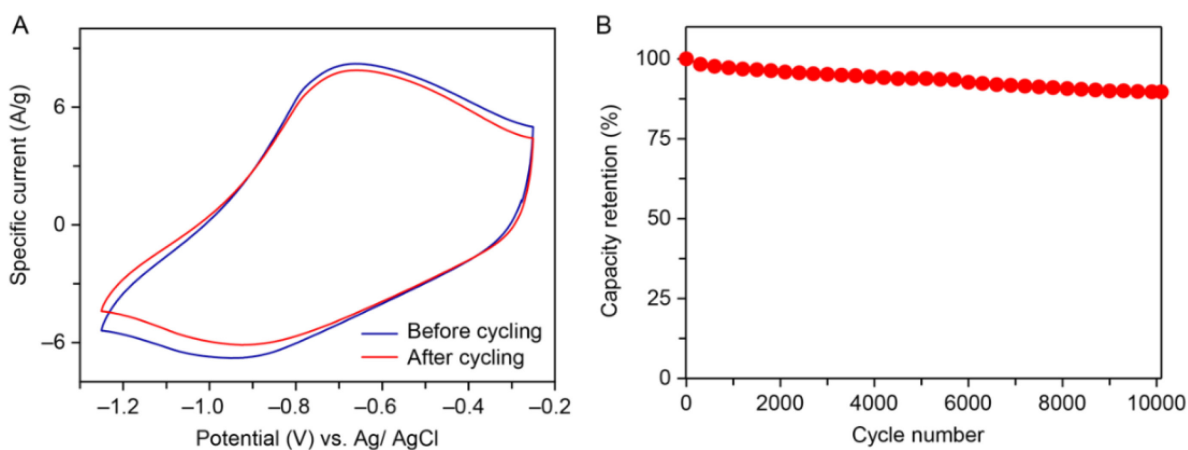
Figure 5.62. Charge storage performance of pBTABQ in basic electrolyte. (A) The cyclic voltammograms of pBTABQ in basic aqueous electrolyte (pH = 14) before and after cycling. (B) Capacity retention of pBTABQ during cycling.

Ex-situ studies on polarized electrodes provided information on the nature of the redox peaks leading to high capacities under acidic and alkaline conditions. First, a decrease in the intensity of the C=O and C=N components of the O (1s) and N (1s) XPS signals, respectively, upon polarization (Figure 5.54D) suggests that charge storage still occurs through the reduction of imines and carbonyls. A notable difference under highly acidic conditions is the absence of alkaline ions by elemental mapping (Figure

242

5.54E) and by XPS (Figure 5.63), which suggests that protons are exclusively responsible for charge storage under these conditions. Second, the emergence of distinguishable redox peaks suggests that redox states become more localized, likely arising from weakened electronic delocalization through partial protonation or deprotonation of pBTABQ under highly acidic or alkaline conditions. Indeed, soaking pBTABQ in strong acid and base leads to protonation and deprotonation, respectively, as verified by XPS (Figure 5.64). Concurrently, the UV-Vis spectra show significantly blue-shifted absorption (Figure 5.54F), as expected for diminished charge delocalization. XPS analysis (Figure 5.54D, 5.65) indicates that under acidic conditions, redox processes are proton-assisted, with the first peak involving both imines and carbonyls, and the second peak involving only carbonyl moieties. The broad peak observed under alkaline conditions can instead be assigned to the formation of enolates (Figure 5.54D). The exclusive involvement of protons at the expense of metal cations at high acidity implies excellent bulk proton diffusion under these conditions, as may be expected for Grotthuss transport through the extensive hydrogen bonding network of pBTABQ (Figure 5.66)[31]. The hydrogen bonding-assisted proton transport may also explain a lack of exfoliation of BTABQ in acidic electrolytes compared to neutral alkali electrolytes (*vide supra*) (Figure 5.54E). However, the same argument for the role of protons cannot explain the considerable increase in specific capacity of pBTABQ at pH > 13, where the concentration of protons is very low. Under these conditions, intercalation of hydrated Na^+ dominates, with a substantially larger amount of Na evident by EDS under alkaline conditions than under neutral conditions (Figure 5.54E, 5.67, 5.68, Table 5.3). The seemingly anomalous increase in capacities at the pH extremes highlights the importance of combining intercalation with a flexible hydrogen-bonded structure that either promotes proton transport at low pH, or allows deprotonation at high pH, thus allowing metal cation intercalation[31].
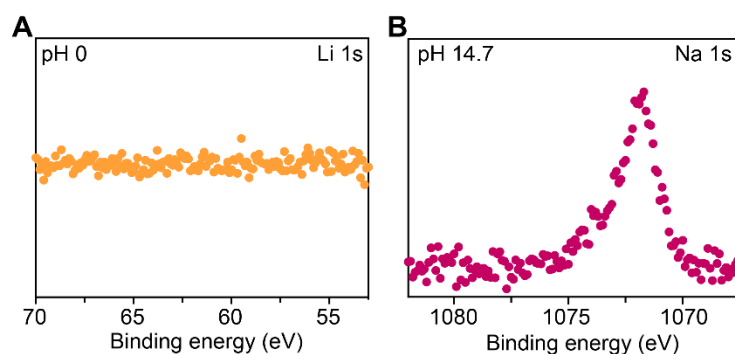
Figure 5.63. *Ex-situ* XPS scans at the metal region. (A) Li 1s region of ex-situ XPS of negatively polarized pBTABQ in 1 M LiCl aqueous electrolyte at pH = 0. (B) Na 1s region of ex-situ XPS of negatively polarized pBTABQ in 1 M NaCl aqueous electrolyte at pH = 14.7.
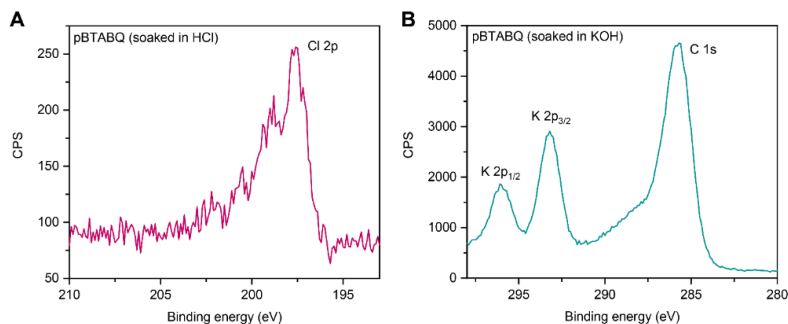
Figure 5.64. High resolution XPS spectra of acid- or base-treated pBTABQ. (A) Cl (2p) XPS spectrum of HCl-soaked pBTABQ. (B) K (2p) and C (1s) spectrum of KOH-soaked pBTABQ. The presence of Cl in HCl-soaked pBTABQ, and the presence of K in KOH-soaked pBTABQ prove that pBTABQ is protonated and deprotonated in highly acidic and basic electrolytes, respectively.
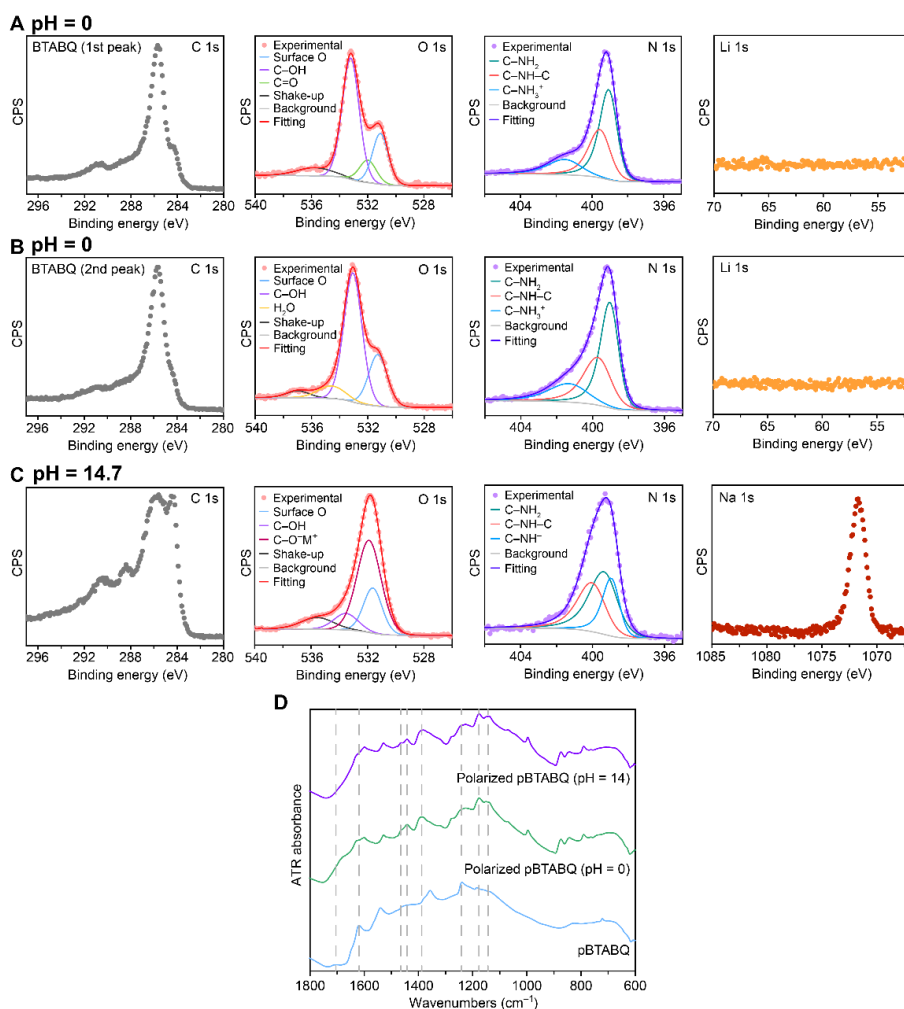
Figure 5.65. *Ex-situ* XPS and FTIR characterizations of negatively polarized BTABQ and pBTABQ. (A, B) *Ex-situ* high resolution XPS spectra of negatively polarized BTABQ in acidic aqueous electrolyte (LiCl/HCl, pH = 0). (C) *Ex-situ* high resolution XPS spectra of negatively polarized BTABQ in basic aqueous electrolyte (NaCl/NaOH, pH = 14.7). Similar redox response of BTABQ, relative to pBTABQ, toward electrolyte pH values is confirmed by ex-situ XPS data. (D) *Ex-situ* ATR-FTIR spectra of negatively polarized pBTABQ electrodes at pH = 0 or 14. Although notable changes can be seen, thorough interpretation of the changes of main bonds is complicated by the convoluted nature of FTIR spectra.

244
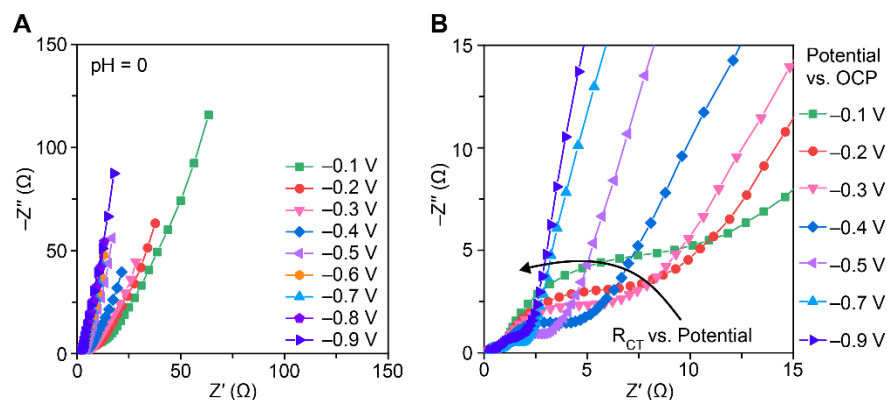
Figure 5.66. Electrochemical impedance spectra of pBTABQ in 1 M LiCl aqueous solution at pH = 0. Negative polarization at different potentials was applied during measurements. The Nyquist plots display typical capacitor-like features with low equivalent series resistances, short semicircles and 45° transition regions along with extended 90° capacitive regions at low frequencies (A). The charge-transfer resistances decreased with more negative potentials applied, suggesting that the redox processes became more facile upon polarization and the bulk of electrode was utilized for charge storage. Altogether, the charge storage is not limited by proton diffusion.
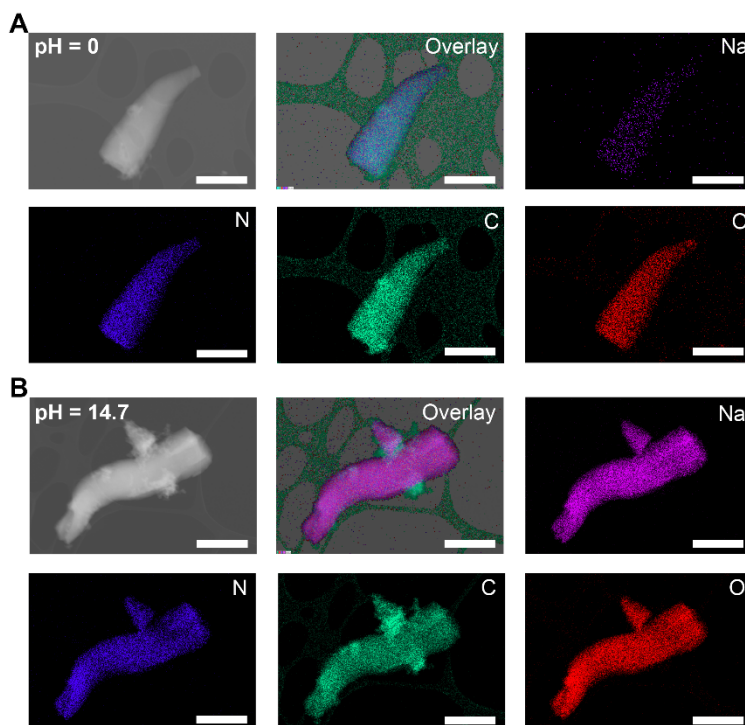
Figure 5.67. *Ex-situ* HAADF-STEM EDS mapping of negatively polarized pBTABQ in acidic and basic electrolytes. (A) Acidic aqueous electrolyte (1 M NaCl at pH = 0). (B) Basic aqueous electrolyte (1 M NaCl at pH = 14.7). Scale bars: (A) 500 nm; (B) 1 μm. A very small amount of Na (close to the noise level) was observed for polarized pBTABQ in acidic electrolyte.
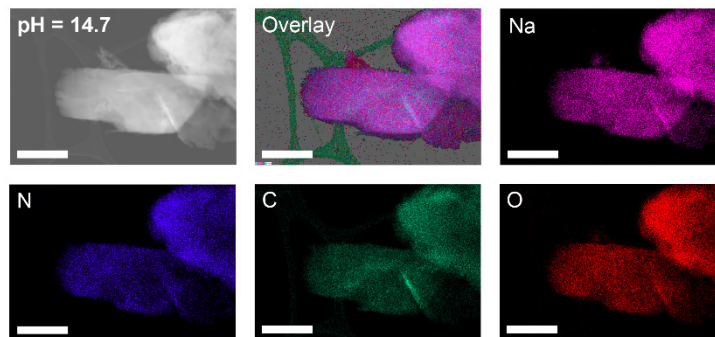
Figure 5.68. *Ex-situ* HAADF-STEM EDS mapping of negatively polarized BTABQ in basic electrolyte. The basic aqueous electrolyte is 1 M NaCl aqueous solution adjusted to pH = 14.7. Scale bars: 500 nm.

5.3.4 Deep Charge-Discharge Capability

Benefiting from the recent development of water-in-salt electrolytes (WiSE)[35,36], we explored deep charge-discharge capability of pBTABQ in a larger reductive potential window of 1.5 V. CVs recorded in 17 molal (m) $NaClO_4$ remain quasi-rectangular and deliver capacitances similar to those seen in aqueous neutral electrolytes, with over 90% capacity retention over 40,000 cycles (Figure 5.69A, 5.70). The corresponding Nyquist plots recorded under various negative polarizations confirm the capacitor-like features, as with those recorded in aqueous neutral electrolytes (Figure 5.71). Notably, EDS maps of polarized pBTABQ electrodes in WiSE reveal a significantly larger amount of intercalated Na^+ ions relative to that observed in neutral electrolyte (Figure 5.72, Table 5.3). This indeed is reflected in a higher charge capacity of 225 mAh g^{-1} for the WiSE system, a 50% increase relative to neutral aqueous electrolytes. Rate capability studies display ultrahigh-rate performance at various active material loadings as high as 6 mg cm^{-2}, a practical loading value (Figure 5.69B). For instance, discharge capacities greater than 100 mAh g^{-1} can be delivered within 60 seconds. A comparison between the performance of pBTABQ in acidic, alkaline, or WiSE electrolytes and state-of-the-art high-capacity LIC cathodes and high-rate pseudocapacitive electrodes is shown in Figure 5.69C (see also Figure 5.73). In a full cell, an asymmetric hybrid capacitor fabricated using pBTABQ as the negative electrode and porous activated carbon as the positive electrode delivers 2 V and cycles safely over 60,000 cycles with a capacitance retention of over 90% (Figure 5.74, 5.75). Optimization of the WiSE electrolyte (see supplemental experimental procedures)[37] further enhances the voltage window to 2.3 V (Figure 5.76). These preliminary full-cell data and the high average discharge voltage of pBTABQ vs. Li^+/Li (2.71 V, Figure 5.77) point to future opportunities for further optimizing asymmetric full-cells, for instance by using low voltage anodic materials such as lithium titanium oxide and graphite. Indeed, CVs of pBTABQ in several state-of-the-art WiSE formulations (Figure 5.78) that function well against lithium titanium oxide and graphite[38], show that our materials retain their performance in these electrochemical environments. Overall, the new

materials reported here, together with the structural and compositional principles underlining their electrochemical performance, provide important blueprints toward the use of organic pseudocapacitive materials in practical, high-rate, high-capacity EES devices.
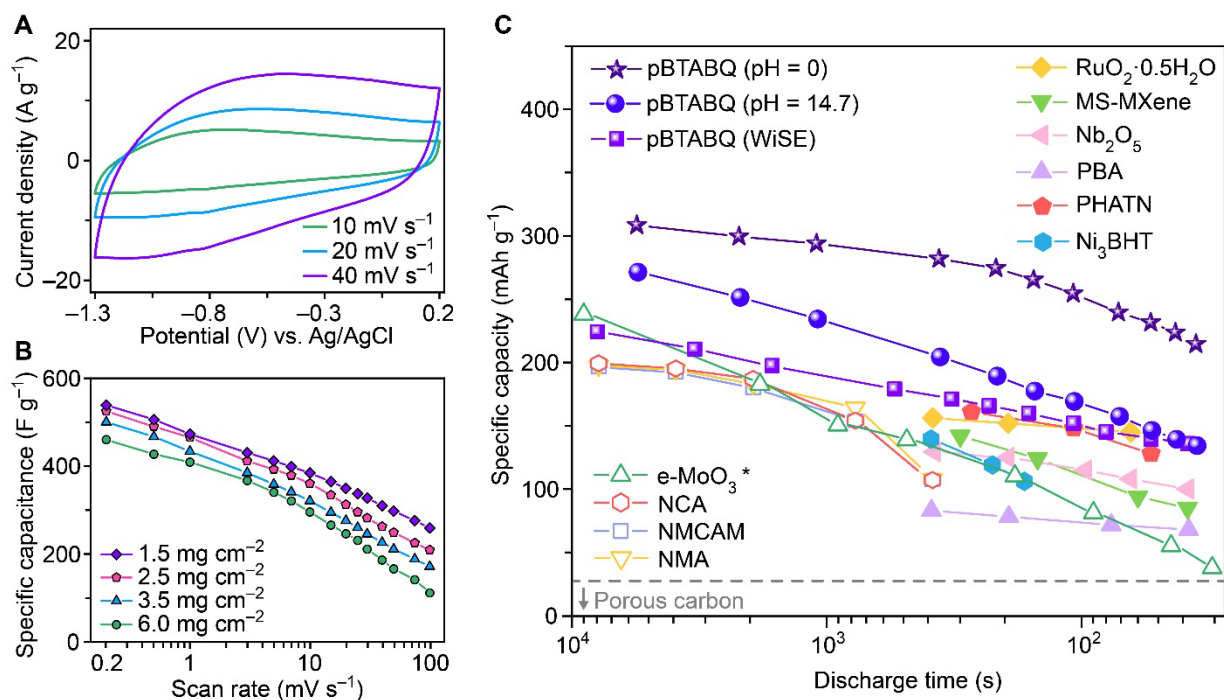
Figure 5.69. Electrochemical studies in water-in-salt electrolytes (WiSE) and performance benchmarking. (A) CVs of pBTABQ obtained at scan rates of 10, 20, and 40 mV s^{-1} using 17 m NaClO$_4$ WiSE electrolyte. (B) Power performance of pBTABQ in WiSE obtained from CVs at scan rates ranging from 0.2 to 100 mV s^{-1} on electrodes with active material loadings of 1.5, 2.5, 3.5, and 6.0 mg cm^{-2}. (C) Comparison of rate performances for pBTABQ and related state-of-the-art LIC cathodes[30,31] or pseudocapacitive[16,21,23,32–34] electrodes. Materials tested at potentials greater than 2 V vs. Li$^+$/Li and with a minimum active material loading of 1.5 mg cm^{-2} are chosen for comparison. MS-MXene: Ti$_3$C$_2$T$_x$ synthesized in molten alkali salts, PBA: Prussian blue analog, PHATN: perylene diimide–hexaazatrinaphthylene, NCA, NMCAM and NMA: Ni-rich analogues of LiNiO$_2$ doped with Al, Mn, Co and Mg, Ni$_3$BHT: Ni$_3$(benzenehexathiol), e-MoO$_3$: α-MoO$_3$ with expanded interlayer gaps, an example of extrinsic pseudocapacitive materials. (* mass loading ~0.6 mg cm^{-2}).
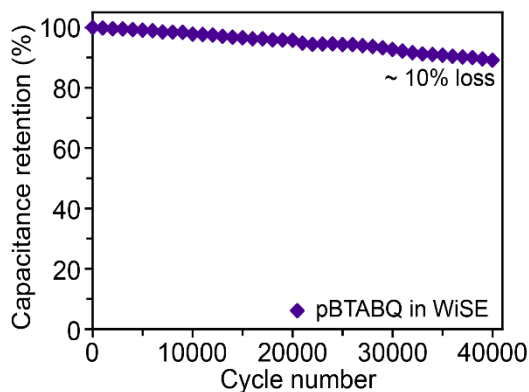
Figure 5.70. Cycling study of pBTABQ in 17 m NaClO$_4$ WiSE. ~90% of capacitance retention was obtained after 40,000 cycles.
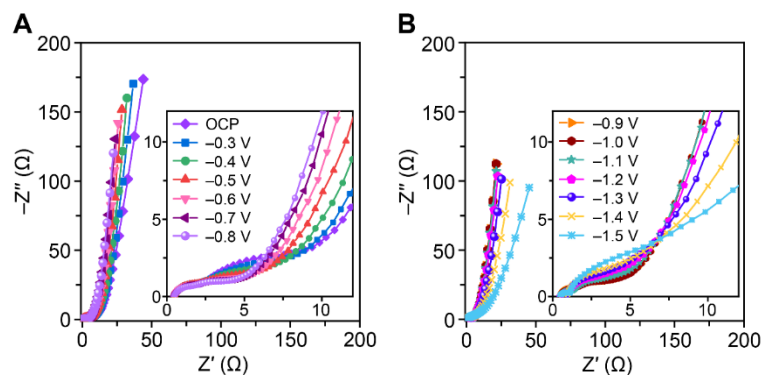
Figure 5.71. Electrochemical impedance spectra of pBTABQ in 17 m NaClO$_4$ WiSE. The Nyquist plots under various negative polarizations display typical capacitor-like features with low equivalent series resistances, short semicircles and 45° transition regions along with extended 90° capacitive regions at low frequencies.
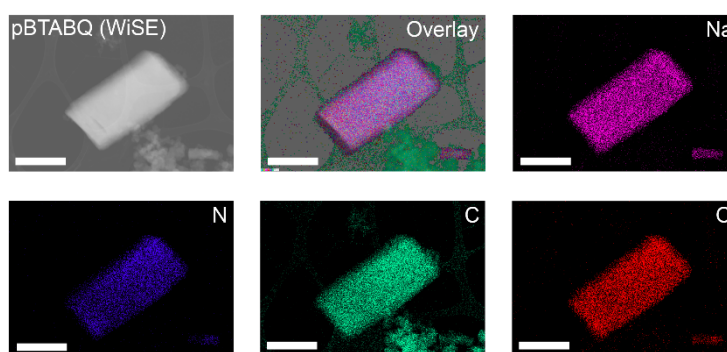
Figure 5.72. *Ex-situ* HAADF-STEM EDS maps of negatively polarized pBTABQ in 17 m NaClO$_4$ WiSE.
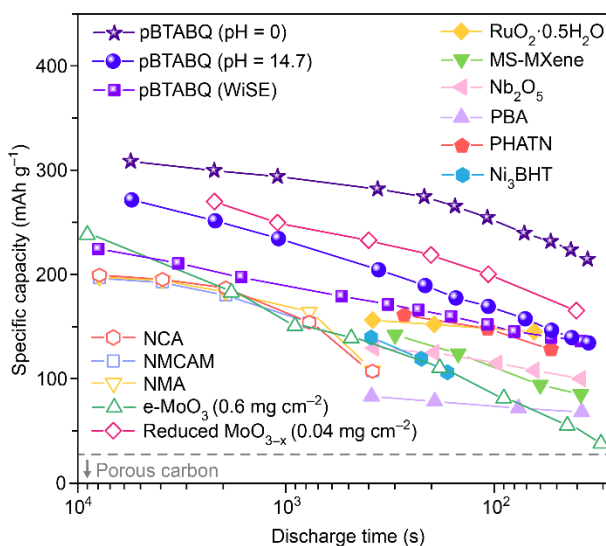
Figure 5.73. Comparison of specific capacities at various rates. Comparison of rate performances for pBTABQ and related state-of-the-art LIC cathodes or pseudocapacitive electrodes. Materials tested at potentials greater than 2 V vs. Li$^+$/Li and with a minimum active material loading of 1.5 mg cm^{-2} are chosen for comparison. MS-Mxene: Ti$_3$C$_2$T$_x$ synthesized using Molten alkali salts, PHATN: perylene diimide–hexaazatrinaphthylene, NCA, NMCAM and NMA: Ni-rich analogues of LiNiO$_2$ doped with Al, Mn, Co, and Mg, Ni$_3$BHT: Ni$_3$(benzenehexathiol), e-MoO$_3$: α-MoO$_3$, with expanded interlayer gaps, an example of extrinsic pseudocapacitive materials. Reduced MoO$_{3-x}$ data are not presented in the main text due to its ultra-low mass loading (two orders of magnitude lower than our materials).
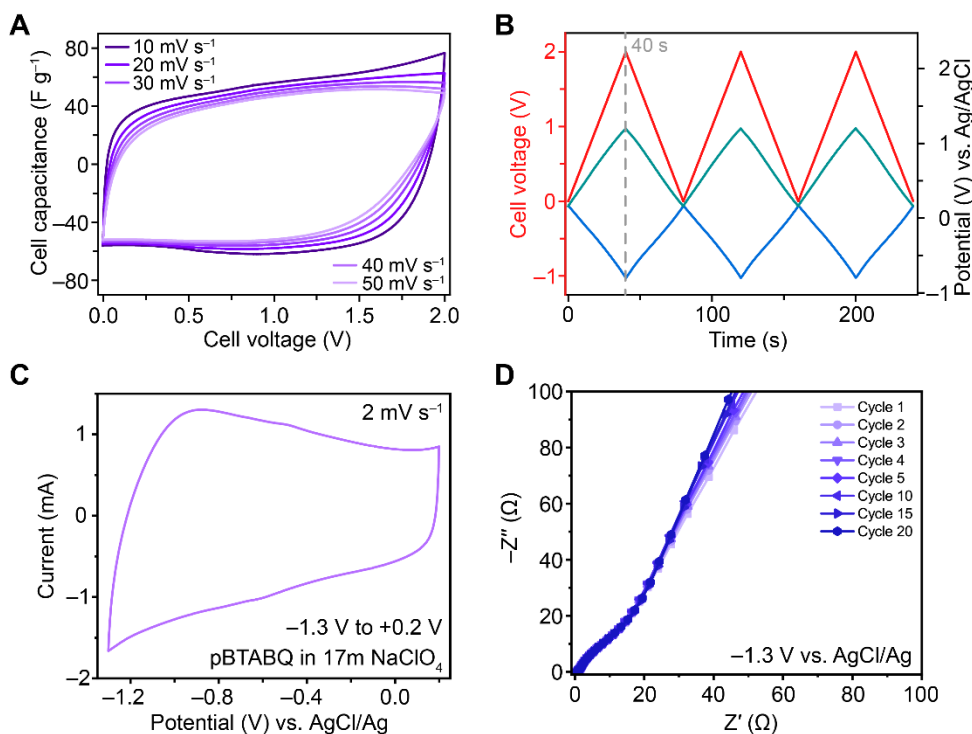
Figure 5.74. Electrochemical measurements of pBTABQ-based asymmetric EC and the stability test of pBTABQ in WiSE. (A) CV curves of an asymmetric electrochemical capacitor (EC) with pBTABQ and porous activated carbon (AC) as the negative and positive electrodes, respectively, and 17 m NaClO$_4$ WiSE. (B) Individual electrode potentials and full-cell potentials during cell operation from 0 to 2.0 V. Red lines: full-cell potential; blue lines: potential of the negative electrode (pBTABQ); cyan lines: potential of the positive electrode (AC). (C) A slow scan CV of a pBTABQ three-electrode cell using 17 m NaClO$_4$ WiSE, confirming the operating voltage window of pBTABQ (–1.3 V to +0.2 V vs. AgCl/Ag). (D) Constant voltage polarization of pBTABQ in a three-electrode cell using 17 m NaClO$_4$ WiSE. The potential of pBTABQ electrode was set at –1.3 V vs. AgCl/Ag. As each cycle takes about an hour and 15 minutes, 20 cycles mean that pBTABQ undergoes constant voltage polarization for 30 hours. The impedance show little change, especially in the semicircle region, upon long time polarization, proving that pBTABQ electrode has good stability in WiSE systems under operating conditions.
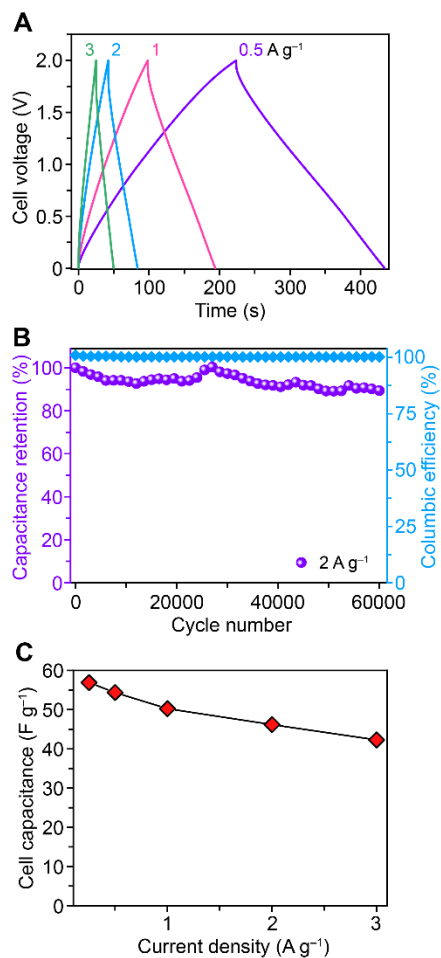
Figure 5.75. Galvanostatic charge-discharge cycling studies of pBTABQ-based asymmetric EC. (A) GCD curves of an asymmetric EC with pBTABQ as the negative electrode and porous activated carbon (AC) as the positive electrode, and 17 m NaClO$_4$ WiSE. (B) Cycling of the EC at a current density of 2 A g^{-1}. (C) Cell capacitance (based on the mass of **both electrodes**) retention at various current densities, suggesting the good rate capability of pBTABQ in a practical device.
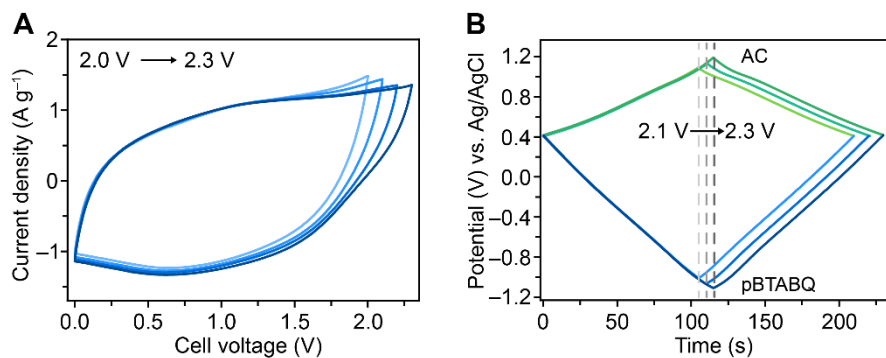
Figure 5.76. An pBTABQ-based an asymmetric EC with a voltage window of 2.3 V. (A) CV curves of an asymmetric EC with pBTABQ as the negative electrode and porous activated carbon (AC) as the positive electrode, and WiSE. The WiSE used here contains 12.5 m LiNO$_3$ in 1:1 weight ratio of water and 1,5-pentanediol. (B) Individual electrode potentials during cell operation from 0 to 2.1 V, 2.2 V, and 2.3 V, respectively.
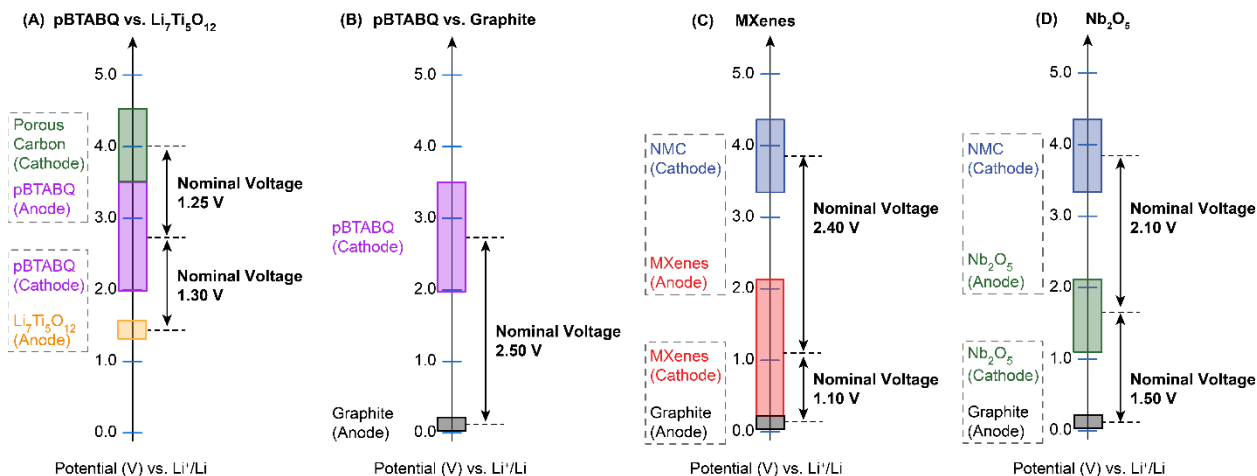
Figure 5.77. The comparison of operating voltage windows of pBTABQ and prototypical pseudocapacitive materials. pBTABQ functions in potentials from 1.91 – 3.51 V vs. Li$^+$/Li, leading to a nominal voltage of 2.71 V vs. Li$^+$/Li. This favorably high potentials of pBTABQ relative to MXenes and Nb$_2$O$_5$ allow fabrication of devices with higher nominal cell voltages. For instance, at a charge-discharge rate of 10 C, pristine MXenes and Nb$_2$O$_5$ deliver charge of ~150 mAh g^{-1} whereas, pBTABQ delivers 180 mAh g^{-1} using WiSE. More importantly, pBTBAQ delivers this capacitance at a much higher nominal voltage of 2.71 V vs. Li$^+$/Li relative to 1.2 V and 1.6 V vs. Li$^+$/Li for MXenes and Nb$_2$O$_5$, respectively (Figure 3). The substantially higher voltage of pBTABQ allows fabrication of an asymmetric pseudocapacitor full cell with lithium-titanium-oxide (LTO, ~1.5 V vs. Li$^+$/Li) as the anode, a prototypical high-rate pseudocapacitive material. Such a cell would offer a nominal voltage of 1.3 V with high-power characteristics and outperform a MXenes/Graphite hybrid cell both in terms of nominal voltage (1.1 V) and power capability. Alternatively, a pBTABQ/Graphite hybrid cell would deliver a nominal voltage of 2.5 V, more than double that of a MXenes/Graphite cell. Nominal voltage is calculated as the difference between the average discharge potentials of a cathode and an anode.
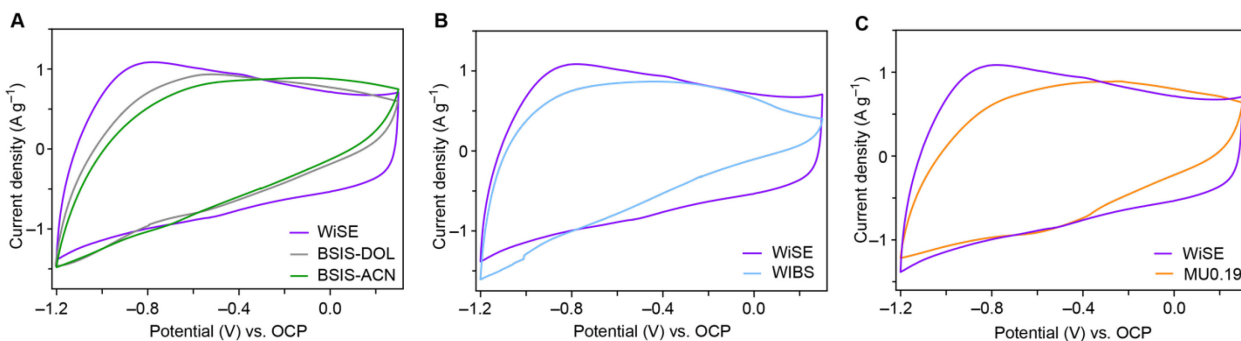
Figure 5.78. CVs of pBTABQ recorded in a variety of WiSE formulations. (A) CVs of pBTABQ recorded in a variety of WiSE formulations of Bisolvent in Salt (BSIS-DOL (Dioxolane), BSIS-ACN (Acetonitrile)). (B) CVs of pBTABQ recorded in Water-in-Bi-Salt (WIBS, LiTFSI and LiOTf). (C) CVs of pBTABQ recorded in WiSE containing asymmetric donor-acceptor methyl urea molecules (MU-0.19). A CV recorded in 17 m NaClO$_4$ WiSE were added to each panel for the reference (noted as "WiSE"). BSIS and MU-0.19 formulations are reported to form stable SEIs at deep reduction potentials corresponding to LTO. Whereas WIBS, together with fluorinated additives, are reported to enable Graphite anodes. pBTABQ performs well in all WiSE formulations, showcasing the potential to function in hybrid cells with either LTO or Graphite as the anode. The details of a variety of WiSE formulations are presented in supplemental experimental procedures.

5.4 Experimental Procedures

5.4.1 Data Availability

Crystallographic parameters for the structure of BTABQ are archived at the Cambridge Crystallographic Data Center (CCDC) (www.ccdc.cam.ac.uk) under the reference No. CCDC 2144223.

5.4.2 Materials and Synthetic Methods

Synthesis of bis-tetraaminobenzoquinone (BTABQ)

Precursor tetraamino-*p*-benzoquinone (TABQ) is synthesized using a previously reported procedure[39]. To a 15 mL pressure tube (ACE Glass, 150 psi) with 28.4 mg of TABQ and 220 mg of tetrabutylammonium chloride (TBACl, TCI) was added 6 mL of dimethylformamide (DMF, Sigma-Aldrich). The tube was capped under ambient condition, sonicated for 1 min, and then put into an isothermal oven at 120 °C. After 12 hours, the tube was cooled down to room temperature, and the reaction mixture was filtered and washed with DMF until the filtrate coming out became colorless. The resulting black solid was further washed with methanol (Sigma-Aldrich) and dried under air. 15.5 mg of BTABQ was obtained (60% yield). BTABQ is insoluble in common NMR solvents. Solid-state NMR of BTABQ (Figure 5.10): 174.8 ppm (C=O), 146.4 ppm (C=N), 134.5 ppm/129.9 ppm (C–N/C–O). Elemental analysis (Table 5.2): $C_{12}H_{10}O_4N_6$, found: C, 47.14%; H, 2.84%; N, 26.06%; calculated: C, 47.69%; H, 3.33%; N, 27.81%. MALDI-TOF: $[M+H]^+$: found, 302.808; calculated: 303.1; within the ±1 Da error of the instrument (Figure 5.19). FTIR (cm^{-1}): 3470, 3404, 3356, 3298, 3235, 1651, 1626, 1614, 1568, 1543, 1462, 1364, 1244, 1186, 1136, 721, 654. The crystallinity of BTABQ was characterized by PXRD (Figure 5.9). The synthesis of BTABQ can be scaled-up to gram scale. To a 250 mL Schlenk tube (ChemGlass) with 1.07 g of TABQ and 10.3 g of tetrabutylammonium bromide (TBABr, Sigma-Aldrich) was added 80 mL of DMF. The Schlenk tube was sealed under ambient conditions, sonicated for 1 min, and then put into an isothermal oven at 120 °C. After 12 hours, the Schlenk tube was cooled down to room temperature, and the reaction mixture was filtered and washed with DMF until the filtrate coming out became colorless. The resulting black solid was further washed with methanol and dried under air yielding 0.4 g of BTABQ (42% yield).

Synthesis of polymerized BTABQ (pBTABQ)

100 mg of BTABQ was transferred into a glass tube, heated at ~300 °C under vacuum for 2 days. 85 mg of pBTABQ was obtained as black solid. Elemental analysis: (Table 5.2): $C_{36}H_{10}O_{10}N_{16}$, found: C, 52.48%; H, 1.44%; N, 26.34%; calculated: C, 52.31%; H, 1.22%; N, 27.11%. MALDI-TOF: $[M+H]^+$: found, 827.232; calculated: 827.1; $[(M–NH_3)+H]^+$: found, 810.125; calculated: 810.1; within the ±1 Da error of the instrument (Figure 5.19). Solid-state NMR spectrum of pBTABQ exhibits a broad peak centered at 140 ppm (Figure 5.10). FTIR (cm^{-1}): 3468, 3404, 3352, 3298, 3236, 1736, 1686, 1647, 1624,

1543, 1460, 1385, 1358, 1242, 1184, 1134, 1068, 926, 770, 746, 721, 679, 633. The synthesis of pBTABQ can be scaled-up to gram scale. To a 25 mL thick-wall Schlenk tube (Synthware) was added 1.69 g of BTABQ, and the tube was heated at ~300 °C under vacuum for 2 days. 1.24 g of pBTABQ was obtained as a black solid.

Electrode and electrolyte preparations

The working electrodes were fabricated as a slurry by mixing active materials, polyvinylidene fluoride (PVDF) and acetylene black carbon in a ratio of 8:1:1 using dimethylformamide and were coated onto carbon fibre paper disk (Fuel Cell Earth). The as prepared electrodes were dried at 65 °C in air for 3 h prior to drying under vacuum at 120 °C overnight. The dried electrodes have loading densities of 1.5~6 mg cm^{-2}. 1.5~2 mg cm^{-2} loading was used for most of the three-electrode cells. 2.5, 3.5, and 6 mg cm^{-2} loadings were used for mass loading-performance studies shown in Figure 5. The activated carbon (YP50) counter electrodes were prepared as thin films by repeated kneading and rolling of a slurry of activated carbon, acetylene black and a polytetrafluoroethylene (PTFE) solution mixture, in a ratio of 8:1:1, with ethanol. The prepared films were dried at 120 °C overnight prior to use. The BTABQ electrodes for in house ex-situ PXRD and ss-NMR measurements were also made as thin films using the same method with the same component ratio. 1 M aqueous solutions of LiCl, NaCl, MgCl$_2$, and tetraethylammonium chloride (TEACl) were used for electrochemical tests in neutral conditions. Aqueous electrolytes with pH values ranging from 0 to 14.7, and water-in-salt electrolytes were prepared according to supplemental experimental procedures.

Preparation of electrolytes

Electrochemical tests in neutral conditions were performed using 1 M aqueous solutions of LiCl, NaCl, MgCl$_2$, tetraethylammonium chloride (TEACl) in deionized water. The role of pH on electrochemical performances was probed using electrolytes with pH values ranging from 0 to 14.7. Electrolytes with intermediate pH values between 2 and 13 were buffered, whereas highly acidic and basic solutions were unbuffered. While 1 M NaCl was used to maintain comparable ionic strengths, HCl and NaOH were used to adjust the pH of buffered solutions. A description of electrolytes and their constituents are given below:

Electrolyte pH	Electrolyte constituents
0	1 M HCl + 1 M NaCl
1	0.1 M HCl + 1 M NaCl
2.6	89 mL 0.1 M Citric acid + 11 mL 0.2 M Na$_2$HPO$_4$ + 1 M NaCl
3.4	71 mL 0.1 M Citric acid + 29 mL 0.2 M Na$_2$HPO$_4$ + 1 M NaCl
4.5	53 mL 0.1 M Citric acid + 47 mL 0.2 M Na$_2$HPO$_4$ + 1 M NaCl
5.4	44 mL 0.1 M Citric acid + 56 mL 0.2 M Na$_2$HPO$_4$ + 1 M NaCl

7.3	9 mL 0.1 M Citric acid + 91 mL 0.2 M Na_2HPO_4 + 1 M NaCl
9.0	10 mL 0.1 M Na_2CO_3 + 90 mL 0.1 M Na_2HCO_3 + 1 M NaCl
10.6	90 mL 0.1 M Na_2CO_3 + 10 mL 0.1 M Na_2HCO_3 + 1 M NaCl
13	0.1 M NaOH + 1 M NaCl
14.7	6 M NaOH + 1 M NaCl

Deep charge-discharge tests in water-in-salt electrolytes (WiSE) were done using 17 m (molality) $NaClO_4$ in three-electrode configuration. Two electrode devices were fabricated using both 17 m $NaClO_4$ WiSE and WiSE that contains 12.5 m $LiNO_3$ in 1:1 weight ratio of water and 1,5-pentanediol[40]. Detailed procedures for the preparation of WiSE formulations are available in references: Water-in-Bi-Salt (WIBS)[41], Bisolvent in Salt (BSIS-DOL[42], BSIS-ACN[43]), WiSE containing asymmetric donor-acceptor methyl urea molecules (MU-0.19)[44].

Supercapacitor assembly and electrochemical measurements

The electrode materials were first tested in a three-electrode supercapacitor configuration with porous activated carbon as counter, a leakless miniature AgCl/Ag (EDAQ, Leakless Miniature AgCl/Ag Reference Electrode, Model ET072) as the reference electrode and a 25 μm thick cellulose sheet as a separator. Porous activated carbon electrodes with excess weight were used to counter the charges and ensure distinct responses from the working electrodes. A custom-built T-shape Swagelok type cell was used to assemble the cell components[23]. Stainless steel rods are used as current collectors for cells using neutral or basic electrolytes. Titanium rods are used as current collectors for cells using acidic electrolytes. Aqueous solutions of various metal salts were used as electrolytes. Cells were assembled in a fume hood and allowed to rest for 12 h before electrochemical tests. All electrochemical measurements were carried out using a Biologic VSP-300 potentiostat controlled by the software *EC-Lab*. EIS measurements were performed using a multi-sinusoidal signal with an amplitude of 10 mV over a large frequency range of 10 mHz–200 kHz. Stability tests of pBTABQ-based three-electrode cells using water-in-salt electrolytes were performed by holding the potential of pBTABQ electrode at a voltage of –1.3 V (vs. AgCl/Ag) for an hour and measuring impedance (about 15 minutes). 20 cycles were performed, and equaled to about 30-hour potential hold at –1.3 V. Two-electrode asymmetric supercapacitors were fabricated by using BTABQ or pBTABQ electrode as the negative electrode, and porous activated carbon electrode as the positive electrode, with balanced weight according to their capacitance. The calculations of specific capacitance/capacity, and the analysis of electrode kinetics were detailed in supplemental experimental procedures.

5.4.3 Physical Characterization Methods

Powder X-ray diffraction (PXRD)

PXRD patterns were recorded using a Bruker Advance II diffractometer equipped with a θ/2θ reflection geometry and Ni-filtered Cu Kα radiation (Kα$_1$ = 1.5406 Å, Kα$_2$ = 1.5444 Å, Kα$_2$/ Kα$_1$ = 0.5). The tube voltage and current were 40 kV and 40 mA, respectively. Samples for PXRD were prepared by placing a thin layer of the appropriate material on a zero-background silicon crystal plate. For the ex-situ measurements of cycled BTABQ electrodes, the thin films were collected from the cycled cells, washed, and dried before being placed at the center of a zero-background silicon crystal plate. High-resolution synchrotron PXRD data were collected at 100 K in the 11-BM beamline at the Advanced Photon Source (APS), Argonne National Laboratory using the Debye-Scherrer geometry and an average calibrated wavelength of 0.458111 Å. Pawley refinement of synchrotron data of BTABQ was conducted using TOPAS Academic (version 6). The refined lattice parameters of BTABQ at 100 K (Figure 5.7) are a = 4.8923(1) Å, b = 11.2897(3) Å, c = 9.9041(4) Å, β = 101.67° in the space group P2$_1$/c, with R_{wp} = 5.828%, R_{exp} = 5.248%, R_p = 4.667%, and GoF = 1.11.

cRED data collection, procession and structure solution of BTABQ

The crystals were dispersed in ethanol and ultrasonication for 3 min. A droplet of suspension was then transferred on a copper grid with carbon film. The cRED data were collected on 200kV JEOL JEM-2100 transmission electron microscope equipped with a quad hybrid pixel detector (Timepix, 512 × 512 pixels, pixel size 55 μm, Amsterdam Sci. Ins.). Before data collection, the sample was cooled down to 96 K by using Gatan cryo-transfer tomography holder. During the data collection, the goniometer was rotated continuously while the selected area electron diffraction (ED) patterns were captured from the crystal simultaneously by using the software of *instamatic (Version 0.6)*[45]. To balance the intensity of electron diffraction and resolution, all the ED patterns were recorded under the spot size 3 with the exposure time 0.5 s. The 3D reciprocal lattice was reconstructed by the software REDp[46], which was very useful for indexing and obtaining the reflection conditions. For the structure solution of BTABQ, a total of 12 crystals were measured and indexed with monoclinic symmetry, with mean lattice parameters of a = 4.9172(10) Å, b = 11.2565(2) Å, c = 9.9400(2) Å, β = 101.123(3)° in space group of $P2_1/c$ (Figure 5.8, reflection condition: $h0l, l = 2n;\ 00l, l = 2n;\ 0k0, k = 2n$). The X-ray crystallography software package *XDS* was used for data processing to estimate integrated diffraction intensities[47]. To improve the completeness, *XSCALE* was then applied for data merging[47], which resulted in a completeness of 99.9% by merging the five datasets. The SHELX software package was used for structural analysis, whereas SHELXT was used for structure solution[48]. As the resolution of these cRED datasets was measured up to 0.625 Å (Figure 5.8), all non-hydrogen atomic positions in BTABQ can be located directly by an *ab initial* method. The SHELXL was used for structure refinement using electron scattering factors for all the atoms. The atomic displacement parameters (ADPs) for all framework atoms were refined anisotropically. Crystallographic details of BTABQ are summarized in Table 5.4.

Solid-state nuclear magnetic resonance (ss-NMR) spectroscopy

ss-NMR spectra were conducted on a three-channel Bruker Avance Neo spectrometer operating at 500.18 MHz and using a 3.2 mm HX solids probe capable of MAS (magic-angle spinning) speeds of up to 24 kHz. The solid samples were packed tightly into 3.2 mm ssNMR zirconia rotors and measured at a MAS speed of 17 kHz. The acquisition time of pristine BTABQ and negatively polarized BTABQ electrode film is about 2 hours. The acquisition time of pristine pBTABQ is about 12 hours.

X-ray photoelectron spectroscopy (XPS)

XPS measurements were performed using a Physical Electronics PHI Versaprobe II X-ray photoelectron spectrometer equipped with a monochromatic Al anode X-ray source. The main chamber pressure was in the 10^{-10} Torr range. BTABQ and pBTABQ powder samples were pressed on copper tapes with full coverage. Ex-situ samples were thoroughly washed after cell disassembly and were dried under vacuum before XPS measurements. Survey spectra were collected from 0~1100 eV in binding energy (BE), with a resolution of 0.8 eV. High resolution spectra of C (1s), N (1s), O (1s), and Li (1s) or Na (1s) (for negatively polarized samples) regions were collected with a resolution of 0.1 eV. BE calibration was not necessary, based on the deconvolution result of C (1s) region that gives adventitious carbon C1s peak around 284.8 eV. Deconvolution of the C (1s), N (1s), and O (1s) spectra were deconvoluted using CasaXPS. The FWHM of different components of each region were kept similar, except for the shake-up features which are intrinsically broad. Gaussian-Lorentzian product function with 30% of Lorentzian component (GL30) was used for the line shapes during the deconvolution of O (1s). LA(1.5, 2.44, 69) line shape was used for the deconvolution of N (1s) peaks. Angle-resolved XPS was conducted by tilting the sample stage to realize the change of photoelectron emission angles. Survey and high-resolution spectra of samples were taken at various emission angles, including 20°, 45° (normal XPS mode), 70° and 90°. Depth profiling of samples was conducted using Ar ion sputtering. Each etching cycle takes 60 seconds. XPS high resolution scans were conducted after every etching cycle.

Diffuse reflectance UV-Vis-NIR (DRUV–Vis–NIR) spectroscopy

DRUV-Vis-NIR spectra between 200 and 2500 nm were collected on a Cary 5000i spectrophotometer, fitted with the UV-Vis DiffusIR accessory (Pike Technologies), at the scan rate of 600 nm min^{-1} under ambient conditions. A KBr baseline and a zero-background correction were collected prior to the sample measurements. Samples were ground in air with dry KBr (99.9%, Pike technologies) in a mortar and pestle to produce 0.5-1 wt.% mixtures.

Room temperature electrical conductivity measurements

Measurements were carried out at 294 K in ambient atmosphere on pressed pellets using a 4-probe probe setup described previously[49]. For each sample, the conductivity values were averaged among at least 3 devices.

In-situ wide-angle X-ray scattering (WAXS) measurements

Measurements were conducted at the Soft Matter Interfaces beamline (12-ID) of the National Synchrotron Light Source II (NSLS-II) at Brookhaven National Laboratory with a beam energy of 16.1 keV and beam size of 200 × 20 μm. The coin cells were connected to the Princeton Applied Research Potentiostat (PARSTAT 2273) for in-situ bias controlling through metal wires. A home-made 3D printed holder was used to load the coin cell samples on the sample stage for transmission WAXS studies, ensuring that the cells were in the line of the beam. The Scattered data were collected in a vacuum with a PILATUS3 300 kW detector (Dectris, Switzerland), consisting of 0.172 mm square pixels in a 1475 × 195 array. To obtain a wide range of wave vector transfer (q), a series of 2D diffraction patterns were collected by rotating the detector on an arc with the sample-to-detector distance being 275 mm. Scattering patterns from each detector angle were stitched together using custom software and then reduced to 1D scattering intensity versus q curve by circular average. In-situ cells for WAXS were designed by machining commercial CR 2032 Coin cells. Specifically, a hole with a diameter of 3 mm was drilled into the top and bottom casings of the Coin cells. The holes were capped with a piece of Kapton tape and sealed with epoxy to facilitate transmission of X-rays and prevent electrolyte from leaking. Similar holes were also made in the separator and the porous carbon counter electrode. All cell components were arranged carefully into a stack to ensure a seamless transmission of X-ray beam through the BTABQ pellet. The fabricated cells were tested for their electrochemical performances using cyclic voltammetry prior to loading them in the WAXS chamber. Cells were tested at their corresponding rest potentials and then reversibly polarized to –0.9 V vs. OCP.

***Ex-situ* high-angle annular dark-field scanning transmission electron microscope (HAADF-STEM)**

HAADF-STEM images and energy dispersive spectroscopy elemental mapping were collected on a JEOL 2010 FEG Analytical Electron Microscope equipped with an Oxford Instrument ULTIM MAX detector. The measurements were conducted while the specimens were under a high vacuum. The specimens were prepared by drop-casting polarized samples onto Cu grids. The specimens were dried under vacuum overnight before measurements. The negatively polarized samples were thoroughly washed with water to remove any remaining salt before preparing the specimens.

DFT calculations

Calculations were performed at B3LYP/def2-QZVP level for the two tautomers of BTABQ and at B3LYP/def2-TZVP level for pBTABQ using ORCA. The wave-function analysis was done by Multiwfn[50,51].

N_2 adsorption isotherms

Isotherms were measured by a volumetric method using a Micromeritics ASAP 2020 Plus gas sorption analyzer. An oven-dried sample tube equipped with a TranSeal™ (Micromeritics) was evacuated and tared.

The sample was transferred to the sample tube, which was then capped with a TranSeal^{TM}. The sample was activated at 100 °C under high dynamic vacuum (< 10^{-4} mbar) for 24 hours before analysis. The N_2 isotherm was measured using a liquid nitrogen bath at 77 K. Ultrahigh purity grade (99.999% purity) N_2, oil-free valves and gas regulators were used for all the free space correction and measurements. Fits to the Brunauer-Emmett-Teller (BET) equation satisfied the published consistency criteria.

Thermogravimetric analysis (TGA)

TGA measurements were performed on a TA Instruments Q500 Thermogravimetric Analyzer at a heating rate of 2.0 °C/min under air or N_2 gas flow of 5 mL/min on a platinum pan from room temperature to 700 °C.

Differential Scanning Calorimetry (DSC)

DSC measurements were performed either on a Discovery 2500 DSC with a RCS 90 cooling system (TA Instruments). The DSC baseline and cell thermal parameters were calibrated using two sapphire discs. The temperature and cell constant were calibrated using an indium standard. ~ 6 mg of BTABQ was sealed under an atmosphere of N_2 and was hermetically sealed in Al pans with a pinhole lid (TA Instruments). Heating and cooling rates of 5 °C min^{-1} with 1-minute isothermal holds in between each ramp (the isothermal hold data not shown) were used with a 50 mL min^{-1} N_2 flow into the sample cell. An empty, hermetically sealed Al pan was used as a reference. Samples were scanned between 25 °C and 400 °C. The pans were loaded into the cell at 40 °C and cooled down to 25 °C before the start of measurements. The DSC data of BTABQ in a pinhole-free pan was collected using a Q100 DSC (TA Instruments). 8.4 mg of BTABQ was hermetically sealed at ambient condition. The sample was scanned between 40 °C and 400 °C.

Elemental analyses (EA)

EA were performed by Robertson Microlit Laboratories, Ledgewood, New Jersey.

Scanning electron microscopy (SEM)

SEM images were conducted at MIT MRSEC (formerly the Center for Materials Science and Engineering, or CMSE) on a Zeiss Merlin high-resolution scanning electron microscope with an InLens detector at an operating voltage of 3 or 4 kV.

MALDI-TOF mass spectrometry

Data was collected using a high-resolution Bruker Autoflex LRF Speed mass spectrometer in the positive linear mode. Measurement parameters were optimized separately for mass range 0–500 Da, 600–3500 Da, and 5–20 kDa, respectively. Slight difference of the intensity of background signal in different mass ranges is expected. Dithranol (m/z = 226.08 Da for [M]$^+$) was used as the Matrix. Powder samples were mixed with dithranol using mortar and pestle, and the mixtures were pressed into pellets for the

measurements. No internal standards were used; the spectra were calibrated using the mass of dithranol. Therefore, the mass accuracy is ±1 Da.

Pair-distribution function (PDF)

PDF measurements were conducted at beamline 28-ID-2 (XPD) of the National Synchrotron Light Source II (NSLS-II) at Brookhaven National Laboratory. The wavelength of the X-ray is 0.18423 Å, and the sample-to-detector distance is about 253 mm. The data was processed using the software PDFgetX3 (https://www.diffpy.org/index.html).

Cryo-HRTEM

Cryo-HRTEM images were obtained at the Automated Cryogenic Electron Microscopy Facility in MIT.nano on a Talos Arctica G2 microscope operated at an accelerating voltage of 200 kV with a Falcon3EC direct electron detector. Samples were prepared by sonicating powders in isopropanol for ~5 seconds. Specimens were prepared by drop-casting sonicated samples onto C-flat^{TM} Cu grids with holey carbon for Cryo-EM. All image acquisition was done using EPU at an exposure time of 1 s, with focusing done adjacent to the region imaged to minimize beam exposure prior to image acquisition (standard low dose imaging protocols). Analysis of the raw HRTEM data was done using Gatan Microscopy Suite software (GMS 3).

Attenuated total reflectance Fourier transform infrared spectroscopy (ATR-FTIR)

ATR-FTIR measurements were performed on a Bruker Tensor 37 (MIR source and KBr beam splitter) with a mercury cadmium telluride (MCT, cooled with LN$_2$) detector. Samples were placed onto the ATR crystal and pressed down using the swivel press to ensure optimal contact between samples and crystal. The data was averaged over 64 scans between 4000–600 cm^{-1} with the resolution of 4 cm^{-1}.

Raman spectroscopy

Raman spectra of solid samples were measured using a Renishaw Invia Reflex Raman Confocal Microscope under the excitation laser of 532 nm, with the laser not exceeding 5% of the full power.

Electron paramagnetic resonance spectroscopy (EPR)

EPR measurements were performed on activated samples packed under nitrogen in septum-sealed quartz tubes using a Bruker EMX spectrometer equipped with an ER 4199HS cavity and Gunn diode microwave source at ~5 K, with a microwave frequency of 9.37 GHz, power of 0.100 mW, and attenuation of 33.0 dB. The measurements were taken in perpendicular mode. Pure BTABQ and pBTABQ samples were used for the measurements.

5.4.4 Crystallographic Data

Table 5.4. cRED experimental parameters, crystallographic data and structure refinement details

Material code	BTABQ
Number of datasets	12
Tilt step	0.23°
Wavelength	0.0251 Å
Program for data procession	*XDS*
Program for structure solution	ShelxT
Crystal system	Monoclinic
Unit cell dimensions	a= 4.9172(10) Å,
	b= 11.2565(2) Å,
	c= 9.9400(2) Å
	β= 101.123(3)
Possible space group	*P2₁/c*
Resolution	0.625 Å
Completeness	99.9%
R_{int}	49.97%
No. of reflections	13148
No. of unique reflections	1161
Structure refinement against cRED data	
Formula	$C_{12}N_6O_4$
Crystal system	Monoclinic
Space group	*P2₁/c*
Unit cell dimensions	a= 4.8923(1) Å,
	b= 11.2897(3) Å,
	c= 9.9041(4) Å
	β= 101.67(3)°
Volume	535.72(6) Å³
Z	2
ρ (g/cm³)	1.811
F(000)	103
Dataset (*h,k l*)	–6~6, –14~14, –12~12
Tot., Uniq. Data, Rint	13148, 1161, 49.97%
Observed Data [$F_o > 4sig(F_o)$]	625
$N_{reflections}$, $N_{parameters}$, $N_{restraints}$	1161, 88, 0
R_1, wR_2, *Gof*	0.2797, 0.5946, 1.541
I/σ	3.4
ρ_{min}, ρ_{max} (e⁻ /Å³)	–0.4/0.2
CCDC number	2144223

5.4.5 Electrochemical Calculations

The specific gravimetric capacitance (C_g) was calculated from the discharge sequence of three-electrode CV curves using the equation below:

$$C_g = (\int (idv))/(2mvdV)$$

The specific gravimetric capacity (Q_g) was calculated from the discharge sequence of three-electrode CV curves using the equation below:

$$Q_g = (\int (idv))/(2mv)$$

The value was obtained in mAh g^{-1} by dividing the above value in Coulombs by 3.6.

The specific gravimetric capacitance (C_g) was calculated from the discharge sequence of a GCD curve using the equation below:

$$C_g = (idt)/(mdV)$$

The specific gravimetric capacity (Q_g) was calculated from the discharge sequence of a GCD curve using the equation below:

$$Q_g = (idt)/(m)$$

The value was obtained in mAh g^{-1} by dividing the above value in Coulombs by 3.6.

For two electrode cells, capacitances and capacities were calculated by considering the mass of the active materials on both electrodes. Above, i = current, t = time, m = mass of the working electrode, dV = discharge potential window, v = scan rate. CVs at different scan rates were compared by plotting their rate normalized currents: dividing current by the corresponding scan rates.

Kinetics of the electrochemical processes were analyzed using the power law equation:

$$i(v) = av^b$$

Plotting log(i) vs. log (v) allowed determination of b as the slope of the fit. Following this approach, b values were evaluated at various potentials on a CV over a range of scan rates using neutral, acidic, and basic electrolytes.

The theoretical capacity of a material is calculated by Faraday's law using the following equation:

$$Q_{theoretical} = \frac{nF}{3.6 \times MW} \text{ mAh g}^{-1}$$

where n is the number of electrons involved in the redox process, F is the Faraday constant (96485 s A mol^{-1}), and MW is the molecular weight of the material (g mol^{-1}).

For BTABQ, the theoretical capacity is calculated to be 355 mAh g^{-1}, based on the reduction of four carbonyl groups ($n = 4$). However, due to the keto-enol tautomerization of BTABQ, two amino groups out of four show significant imine character. Therefore, the reduction process happens on both imine and

carbonyl groups. Proposed reduction mechanism of BTABQ under cathodic electrochemical polarization is shown below. The presence of keto-enol tautomerization, extended conjugation, and hydrogen bonding lead to negative charge delocalization of in the reduced BTABQ species, accounting for the quasi-rectangular CV shape.
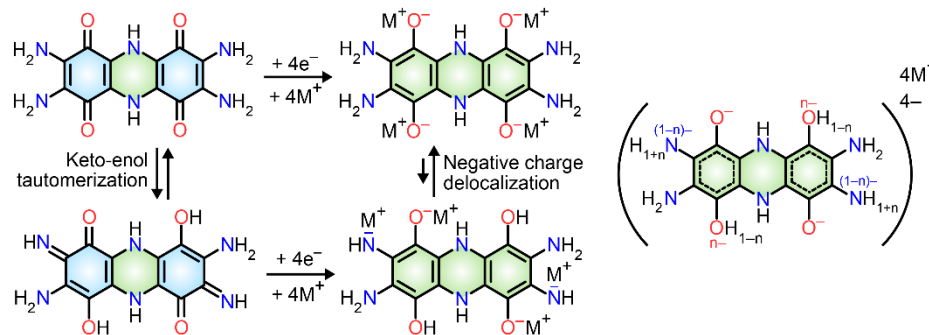
Scheme 5.2. Proposed charge storage mechanism of BTABQ.

For pBTABQ, the theoretical capacity is calculated to be 389 mAh g^{-1}, based on the chemical structure discussed above and the redox process shown below ($n = 12$; only one of the tautomers are shown):
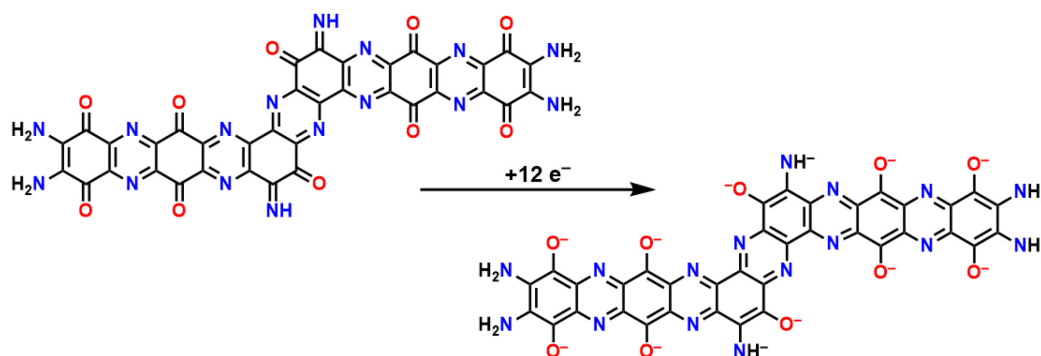
Scheme 5.3. Reduction of pBTABQ.

We note that the pyrazine moieties are not reduced within the potential window we study.

5.5 References

(1) Simon, P., and Gogotsi, Y., (2020). Perspectives for electrochemical capacitors and related devices. Nat. Mater. *19*, 1151–1163.

(2) Gür, T.M. (2018). Review of electrical energy storage technologies, materials and systems: challenges and prospects for large-scale grid storage. Energy Environ. Sci. *11*, 2696–2767.

(3) Simon, P., Gogotsi, Y., and Dunn, B. (2014). Where do batteries end and supercapacitors begin? Science *343*, 1210–1212.

(4) Zou, Z., Xu, J., Zeng, F., and Mei, X. (2019). A hybrid energy storage system for dual-motor driven electric vehicles. DEStech Trans. Environ. Energy Earth Sci. (iceee) 145–148.

(5) Choi, C., Ashby, D.S., Butts, D.M., DeBlock, R.H., Wei, Q., Lau, J., and Dunn, B. (2020). Achieving high energy density and high power density with pseudocapacitive materials. Nat. Rev. Mater. *5*, 5–19.

(6) Fleischmann, S., Mitchell, J.B., Wang, R., Zhan, C., Jiang, D.E., Presser, V., and Augustyn, V. (2020). Pseudocapacitance: from fundamental understanding to high power energy storage materials. Chem. Rev. *120*, 6738–6782.

(7) Sun, H., Mei, L., Liang, J., Zhao, Z., Lee, C., Fei, H., Ding, M., Lau, J., Li, M., Wang, C., and Xu, X. (2017). Three-dimensional holey-graphene/niobia composite architectures for ultrahigh-rate energy storage. Science *356*, 599–604.

(8) Xia, Y., Mathis, T.S., Zhao, M.Q., Anasori, B., Dang, A., Zhou, Z., Cho, H., Gogotsi, Y., and Yang, S. (2018). Thickness-independent capacitance of vertically aligned liquid-crystalline MXenes. Nature *557*, 409–412.

(9) Poizot, P., Gaubicher, J., Renault, S., Dubois, L., Liang, Y., and Yao, Y. (2020). Opportunities and challenges for organic electrodes in electrochemical energy storage. Chem. Rev. *120*, 6490–6557.

(10) Lu, Y., Zhang, Q., Li, L., Niu, Z., and Chen, J. (2018). Design strategies toward enhancing the performance of organic electrode materials in metal-ion batteries. Chem *4*, 2786–2813.

(11) Huang, Z., Grape, E.S., Li, J., Inge, A.K., and Zou, X. (2021). 3D electron diffraction as an important technique for structure elucidation of metal-organic frameworks and covalent organic frameworks. Coord. Chem. Rev. *427*, 213583.

(12) Waller, P.J., Lyle, S.J., Osborn Popp, T.M., Diercks, C.S., Reimer, J.A., and Yaghi, O.M. (2016). Chemical conversion of linkages in covalent organic frameworks. J. Am. Chem. Soc. *138*, 15519–15522.

(13) Lee, J., Kalin, A.J., Yuan, T., Al-Hashimi, M., and Fang, L. (2017). Fully conjugated ladder polymers. Chem. Sci. *8*, 2503–2521.

(14) Audi, H., Chen, Z., Charaf-Eddin, A., D'Aléo, A., Canard, G., Jacquemin, D., and Siri, O. (2014). Extendable nickel complex tapes that reach NIR absorptions. Chem. Commun. *50*, 15140–15143.

(15) Isono, T., Kamo, H., Ueda, A., Takahashi, K., Nakao, A., Kumai, R., Nakao, H., Kobayashi, K., Murakami, Y., and Mori, H. (2013). Hydrogen bond-promoted metallic state in a purely organic single-component conductor under pressure. Nat. Commun. *4*, 1344.

(16) Augustyn, V., Come, J., Lowe, M.A., Kim, J.W., Taberna, P.L., Tolbert, S.H., Abruña, H.D., Simon, P., and Dunn, B. (2013). High-rate electrochemical energy storage through Li^+ intercalation pseudocapacitance. Nat. Mater. *12*, 518–522.

(17) Lin, L., Lin, Z., Zhu, J., Wang, K., Wu, W., Qiu, T., and Sun, X. (2023). A semi-conductive organic cathode material enabled by extended conjugation for rechargeable aqueous zinc batteries. Energy Environ. Sci. *16*, 89–96.

(18) Zheng, J.P., Cygan, P.J., and Jow, T.R. (1995). Hydrous ruthenium oxide as an electrode material for electrochemical capacitors. J. Electroanal. Chem. *142*, 2699–2703.

(19) Burke, L.D., Murphy, O.J., O'Neill, J.F., and Venkatesan, S. (1977). The oxygen electrode. Part 8.—Oxygen evolution at ruthenium dioxide anodes. *J. Chem. Soc. Faraday Trans. 1. 73*, 1659–1671.

(20) Lukatskaya, M.R., Mashtalir, O., Ren, C.E., Dall′Agnese, Y., Rozier, P., Taberna, P.L., Naguib, M., Simon, P., Barsoum, M.W., and Gogotsi, Y. (2013). Cation intercalation and high volumetric capacitance of two-dimensional titanium carbide. Science *341*, 1502–1505.

(21) Li, Y., Shao, H., Lin, Z., Lu, J., Liu, L., Duployer, B., Persson, P.O., Eklund, P., Hultman, L., Li, M., Chen, K., et al. (2020). A general Lewis acidic etching route for preparing MXenes with enhanced electrochemical performance in non-aqueous electrolyte. Nat. Mater. *19*, 894–899.

(22) Wang, X., Mathis, T.S., Li, K., Lin, Z., Vlcek, L., Torita, T., Osti, N.C., Hatter, C., Urbankowski, P., Sarycheva, A., Tyagi, M., et al. (2019). Influences from solvents on charge storage in titanium carbide MXenes. Nat. Energy *4*, 241–248.

(23) Banda, H., Dou, J.H., Chen, T., Libretto, N.J., Chaudhary, M., Bernard, G.M., Miller, J.T., Michaelis, V.K., and Dincă, M. (2021). High-capacitance pseudocapacitors from Li^+ ion intercalation in nonporous, electrically conductive 2D coordination polymers. J. Am. Chem. Soc. *143*, 2285–2292.

(24) Mathis, T.S., Kurra, N., Wang, X., Pinto, D., Simon, P., and Gogotsi, Y. (2019). Energy storage data reporting in perspective—guidelines for interpreting the performance of electrochemical energy storage systems. Adv. Energy Mater. *9*, 1902007.

(25) Lin, Z., Shi, H.Y., Lin, L., Yang, X., Wu, W., and Sun, X. (2021). A high capacity small molecule quinone cathode for rechargeable aqueous zinc-organic batteries. Nat. Commun. *12*, 4424.

(26) Han, C., Li, H., Li, Y., Zhu, J., and Zhi, C. (2021). Proton-assisted calcium-ion storage in aromatic organic molecular crystal with coplanar stacked structure. Nat. Commun. *12*, 2400.

(27) Wang, C., Jiang, C., Xu, Y., Liang, L., Zhou, M., Jiang, J., Singh, S., Zhao, H., Schober, A., and Lei, Y. (2016). A selectively permeable membrane for enhancing cyclability of organic sodium‑ion batteries. Adv. Mater. *28*, 9182–9187.

(28) Banda, H., Dou, J.H., Chen, T., Zhang, Y., and Dincă, M. (2021). Dual-ion intercalation and high volumetric capacitance in a two- dimensional non-porous coordination polymer. Angew. Chem. Int. Ed. *60*, 27119–27125.

929) Wen, S., Lee, J.W., Yeo, I.H., Park, J., and Mho, S.I. (2004). The role of cations of the electrolyte for the pseudocapacitive behavior of metal oxide electrodes, MnO_2 and RuO_2. Electrochim. Acta *50*, 849–855.

(30) Li, W., Lee, S. and Manthiram, A. (2020). High‑nickel NMA: a cobalt‑free alternative to NMC and NCA cathodes for lithium‑ion batteries. Adv. Mater. *32*, 2002718.

(31) Wu, X., Hong, J.J., Shin, W., Ma, L., Liu, T., Bi, X., Yuan, Y., Qi, Y., Surta, T.W., Huang, W., Neuefeind, J., et al. (2019). Diffusion-free Grotthuss topochemistry for high-rate and long-life proton batteries. Nat. Energy *4*, 123–130.

(32) Russell, J.C., Posey, V.A., Gray, J., May, R., Reed, D.A., Zhang, H., Marbella, L.E., Steigerwald, M.L., Yang, Y., Roy, X., et al. (2021). High-performance organic pseudocapacitors via molecular contortion. Nat. Mater. *20*, 1136–1141.

(33) Ma, H., Kong, D., Xu, Y., Xie, X., Tao, Y., Xiao, Z., Lv, W., Jang, H.D., Huang, J., and Yang, Q.H. (2017). Disassembly–reassembly approach to RuO_2/graphene composites for ultrahigh volumetric capacitance supercapacitor. Small *13*, 1701026.

(34) Yu, M., Shao, H., Wang, G., Yang, F., Liang, C., Rozier, P., Wang, C.Z., Lu, X., Simon, P., and Feng, X. (2020). Interlayer gap widened α-phase molybdenum trioxide as high-rate anodes for dual-ion-intercalation energy storage devices. Nat. Commun. *11*, 1348.

(35) Suo, L., Borodin, O., Gao, T., Olguin, M., Ho, J., Fan, X., Luo, C., Wang, C., and Xu, K. (2015). "Water-in-salt" electrolyte enables high-voltage aqueous lithium-ion chemistries. Science *350*, 938–943.

(36) Chao, D., and Qiao, S.Z. (2020). Toward high-voltage aqueous batteries: super- or low-concentrated electrolyte?. Joule *4*, 1846–1851.

(37) Jaumaux, P., Yang, X., Zhang, B., Safaei, J., Tang, X., Zhou, D., Wang, C., and Wang, G. (2021). Localized water-in-salt electrolyte for aqueous lithium-ion batteries. Angew. Chem. Int. Ed. *60*, 19965–19973.

(38) Yang, C., Chen, J., Qing, T., Fan, X., Sun, W., Von Cresce, A., Ding, M.S., Borodin, O., Vatamanu, J., Schroeder, M.A., et al. (2017). 4.0 V aqueous Li-ion batteries. Joule *1*, 122–132.

(39) Chen, T., Dou, J-H., Yang, L., Sun, C., Oppenheim, J. J., Li, J., and Dincă, M. (2022). J. Am. Chem. Soc. *144*, 5583–5593.

(40) Jaumaux, P., Yang, X., Zhang, B., Safaei, J., Tang, X., Zhou, D., Wang, C., and Wang, G. (2021). Localized water-in-salt electrolyte for aqueous lithium-ion batteries. Angew. Chem. Int. Ed. *60*, 19965–19973.

(41) Yang, C., Chen, J., Qing, T., Fan, X., Sun, W., Von Cresce, A., Ding, M.S., Borodin, O., Vatamanu, J., Schroeder, M.A., et al. (2017). 4.0 V aqueous Li-ion batteries. Joule *1*, 122–132.

(42) Ma, Z., Chen, J., Vatamanu, J., Borodin, O., Bedrov, D., Zhou, X., Zhang, W., Li, W., Xu, K., and Xing, L. (2022). Expanding the low-temperature and high-voltage limits of aqueous lithium-ion battery. Energy Stor. Mater. *45*, 903–910.

(43) Chen, J., Vatamanu, J., Xing, L., Borodin, O., Chen, H., Guan, X., Liu, X., Xu, K., and Li, W. (2020). Improving electrochemical stability and low-temperature performance with water/acetonitrile hybrid electrolytes. Adv. Energy Mater. *10*, 1902654.

(44) Lin, R., Ke, C., Chen, J., Liu, S., and Wang, J. (2022). Asymmetric donor-acceptor molecule-regulated core-shell-solvation electrolyte for high-voltage aqueous batteries. Joule *6*, 399–417.

(45) Smeets, S., Wang, B., Cichocka, M.O., Angstrom, J., and Wan, W. (2018). Instamatic (Version 0.6) Zenodo, https://doi.org/10.5281/zenodo.1217026.

(46) Wan, W., Sun, J., Su, J., Hovmöller, S., and Zou, X. (2013). Three-dimensional rotation electron diffraction: software RED for automated data collection and data processing. J. Appl. Crystallogr. *46*, 1863–1873.

(47) Kabsch, W. (2010). Integration, scaling, space-group assignment and post-refinement. Acta Crystallogr. *D66*, 133–144.

(48) Sheldrick, G.M. (2008). A short history of SHELX. Acta Crystallogr. *A64*, 112–122.

(49) Sun, L., Park, S.S., Sheberla, D., and Dincă, M. (2016). Measuring and reporting electrical conductivity in metal−organic frameworks: Cd_2(TTFTB) as a case study. J. Am. Chem. Soc. *138*, 14772–14782.

(50) Lu, T., and Chen, F. (2012). Multiwfn: A multifunctional wavefunction analyzer. J. Comput. Chem. *33*, 580–592.

(51) Zhang, J., and Lu, T. (2021). Efficient evaluation of electrostatic potential with computerized optiÅmized code. Phys. Chem. Chem. Phys. *23*, 20323–20328.

Chapter 6. Fast-Charging, High-Energy, and Long-Lasting Practical Organic Li-ion Batteries

6.1 Abstract

Establishing sustainable value chains for battery materials is essential for global adoption of energy storage technologies.[1] State-of-the-art inorganic cathode materials face severe supply chain limitations due to limited abundance and geopolitical restrictions.[2,3] Organic electrode materials (OEMs), derived entirely from earth abundant elements, alleviate these concerns. OEMs provide additional environmental benefits owing to their less intensive mining requirements and lower temperature processing, which diminish their CO_2 footprint.[1,4] However, the OEMs' performance lags that of inorganic cathodes as shortcomings related to poor conductivity, low storage capacity, or short cycle-life impose impractically large needs for additives for stable operation.[5–7] Here we describe a small molecule fused aromatic compound (BTABQ) whose high electrical conductivity, high capacity for redox charge storage, and complete lack of solubility in any practical solvent allow it to reversibly intercalate Li^+ ions and function as a competitive cathode material for Li-ion batteries, even as a neat material. Optimized electrode formulations based on BTABQ exhibit gravimetric capacities up to 340 mAh g^{-1} at an average discharge voltage of 2.5 V vs. Li^+/Li and deliver an electrode-level energy density of 765 Wh kg^{-1}, higher than most cobalt-containing cathodes. BTABQ-based cathodes operate at high charge-discharge rates at practical mass loadings reaching 16 mg cm^{-2} or 3 mAh cm^{-2}. These results address longstanding challenges associated with OEMs and demonstrate operational competitiveness rivalling established inorganic cathode technologies.

6.2 Introduction

Lithium-ion batteries (LIBs) are becoming increasingly important as efficient energy storage solutions for electrifying the transportation sector and decarbonizing the grid. However, the important role of cobalt[8], a scarce and expensive metal that is often mined at high social costs (e.g., child labor), in battery cathodes has questioned the long-term sustainability, scalability and affordability of current battery technologies[1]. More generally, beyond cobalt-containing materials (e.g., $LiCoO_2$ (LCO), $Li[Ni_{1-x-y}Mn_xCo_y]O_2$ (NMC) and $Li[Ni_{1-x-y}Co_xAl_y]O_2$ (NCA)) [9–12], all current and next-generation cathode alternatives (e.g., $LiFePO_4$ (LFP), over-lithiated layered $Li_{1+x}M_{1-x}O_2$ (M = Mn, Ti, etc.)[13–15] are also based on metal oxides that involve mining, refining, transportation, and treatment of mineral ores at elevated temperatures[16,17]. Mining and processing, while contributing extensively to global carbon emissions and local air and water pollution, are inherently limited by the natural abundance, disparate geographical distribution, and geopolitical restrictions on the mineral ores[2,3]. Even LFP, a favorite for next-generation EV batteries that uses inexpensive Fe as the only cathode metal, is challenged by the disputed use of phosphate, a critical feedstock for agriculture with a high supply risk. These features of current cathode materials present a pressing need for sustainable alternatives that are sourced from inexpensive, abundant precursors and that can be scaled globally through more environmentally benign processes.

Organic molecules, derived entirely from earth abundant elements, benefit from excellent compositional diversity and structural tunability while offering requisite synthetic control for targeted designs as cathode materials for LIBs. Although the merits of replacing inorganic cathodes with organic counterparts have long been appreciated in the literature[5–7], material candidates that deliver comprehensive performance along all metrics relevant for practical batteries have remained elusive. From a design perspective, small organic molecules offer the highest specific capacities by virtue of a dense arrangement of redox sites and their low molar masses. However, small discrete molecules have a strong propensity to dissolve in battery electrolytes and have low intrinsic electrical conductivity, which lead to poor cycling stability and slow electrode kinetics[5]. These inherent issues are routinely managed through extrinsic, and often impractical, solutions that involve preparing electrodes with conducting and polymeric binder additives that often exceed 40 wt.% [18–25]. Alternative strategies to polymerize redox-active OEM candidates or immobilize them into frameworks often require compromise of one or more practical metrics[6]. As such, there continues to be a strong interest in designing intrinsically insoluble and electrically conducting molecular organics that exhibit high specific capacity at appropriate cathodic voltages for LIBs. To our knowledge, OEMs that fulfill all these criteria so as to rival inorganic cathodes are not known.

Here, we report the use of a fused aromatic molecule, bis-tetraaminobenzoquinone (BTABQ), as a molecular organic electrode material (OEM) for LIBs. BTABQ, recently reported by us[26], is characterized

with a dense arrangement of redox-active carbonyl (C=O) and imine (C=N) groups on an aromatic backbone and has a high theoretical specific capacity of 356 mAh g^{-1} via a four-electron reduction process. Strong intermolecular hydrogen bonding and donor-acceptor (D-A) π-π interactions in BTABQ render it insoluble in common battery electrolytes and impart extended bulk electronic delocalization. These favorable material features allow neat BTABQ electrodes (i.e., 100% active material) to reversibly store charge and cycle safely for hundreds of cycles, in stark contrast to the issues of electrode dissolution chronically experienced in reported OEMs. The two-dimensional (2D) layered arrangement of BTABQ molecules enables facile intercalation/de-intercalation of Li$^+$ between the 2D layers and delivers excellent rate capabilities even at short charging times of 3 minutes. Optimized electrode compositions of BTABQ deliver excellent performances even at high areal mass loadings of 16 mg cm^{-2}, comprehensively demonstrating the practical viability of BTABQ, and OEMs, in LIBs for the first time.

6.3 Results and Discussion

6.3.1 Synthesis, Crystal structure, and Electrical Conductivity of BTABQ

BTABQ is obtained in gram scale by Michael condensation of tetraaminobenzoquinone (Figure 6.1a; see 6.4.2) and as highly crystalline micro-rods, as verified by its wide-angle X-ray scattering (WAXS) pattern, scanning electron microscopy (SEM) and Cryogenic electron microscopy (Cryo-EM) images (Figure 6.2a-c). BTABQ exhibits significant keto-enol tautomerization through the conjugation of carbonyl and amino groups within the two diaminobenzoquinone moieties that are connected by a dihydro-pyrazine core, leading to both quinone and imine forms. The presence of imine tautomer in BTABQ is evidenced by the C=N signal at 140.8 ppm in its solid-state ^{13}C NMR spectrum (Figures 6.1b, 6.3) and from the partial double bond character of two C–NH$_2$ bonds according to its single crystal structure (Figure 6.2d). The dihydro-pyrazine linkage is crucial for BTABQ to exhibit significant degree of electronic delocalization between two diaminobenzoquinone moieties relative to the electronic localization within each diaminobenzoquinone moiety observed for tetraamino-phenazine-1,4,6,9-tetrone (Figure 6.4), leading to a considerably small HOMO-LUMO gap of 1.242 eV for BTABQ (Figure 6.1a), which is about 1 eV lower than that of tetraamino-phenazine-1,4,6,9-tetrone (Table 6.1).
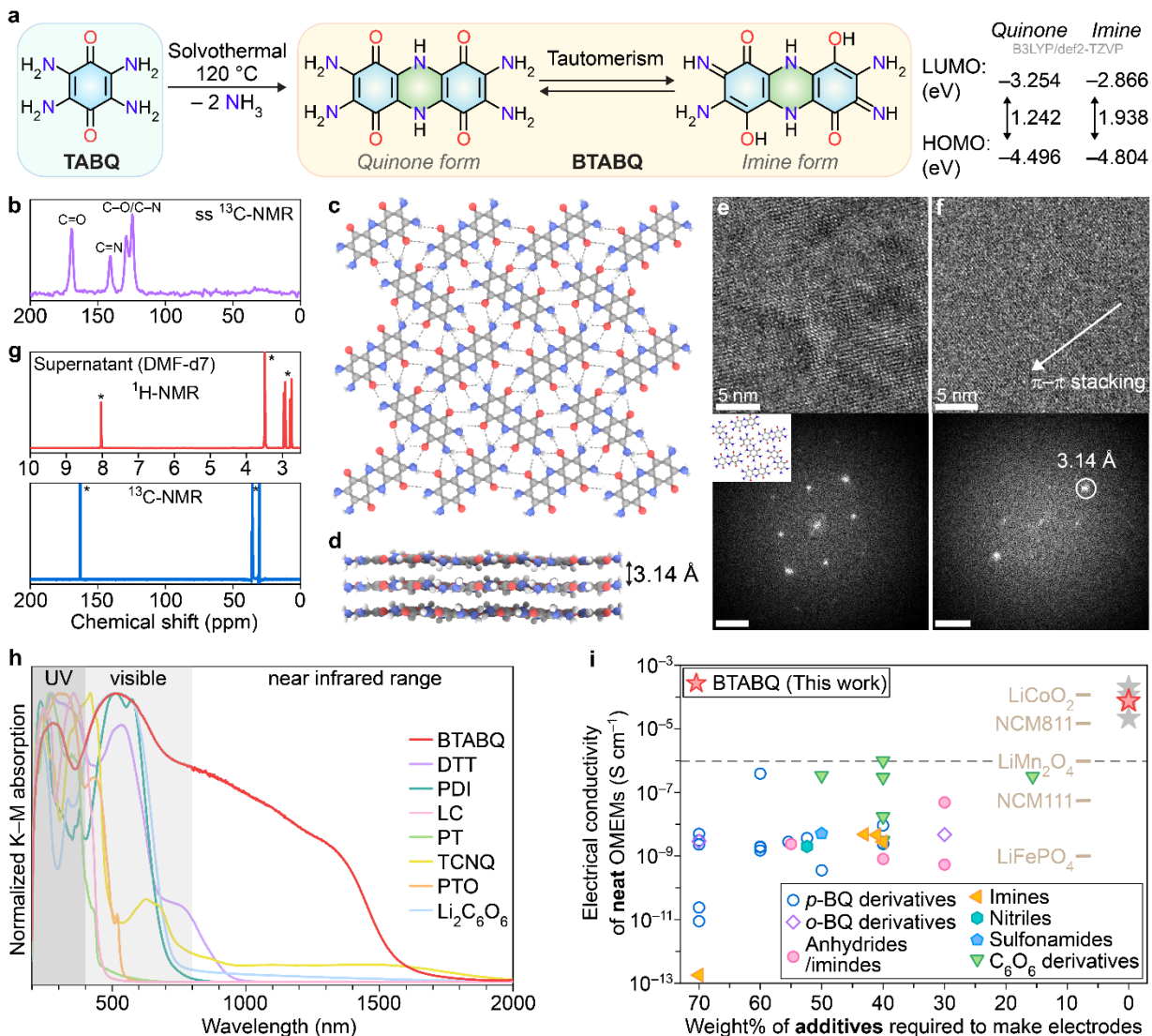
Figure 6.1. Characterization of BTABQ. **a,** One-step solvothermal synthesis of BTABQ. The keto-enol tautomerism of BTABQ is represented by both quinone and imine forms with different energy levels. **b,** Solid state ^{13}C-NMR spectrum of BTABQ confirms both quinone and imine forms. **c,** A 2D layer of BTABQ molecules formed by intermolecular hydrogen bonding (dashed lines). **d,** π-π stacking of BTABQ 2D layers with an interlayer spacing of 3.14 Å. **e,** In-plane and **f,** out-of-plane molecular packing of BTABQ directly seen in Cryo-EM images. **g,** ^{1}H and ^{13}C spectra of the supernatant obtained after heating BTABQ in deuterated *N,N*-dimethylformamide (DMF-d7) at 120 °C overnight. Asterisks indicate solvent peaks. **h,** DRUV-Vis spectra of BTABQ and other common OEMs. Only BTABQ shows significant NIR absorption. **i,** Electrical conductivities of different classes of OEMs, BTABQ and state-of-the-art inorganic electrode materials versus typical amounts of additives required for electrode fabrication.

Planar BTABQ molecules are surrounded by six neighbors and closely packed into two-dimensional layers through abundant intermolecular hydrogen bonding between carbonyl and amine/imine functional groups (Figure 6.1c). These layers stack through strong donor-acceptor π–π interactions with an interlayer distance, 3.14 Å (Figure 6.1d), which is substantially shorter than that of graphite (3.35 Å). Both the in-plane dense molecular packing and the out-of-plane close stacking of layers in BTABQ can be directly

seen in high-resolution Cryo-EM (Figures 6.1e, 6.1f, 6.5-6.7) images and their corresponding fast Fourier transform (FFT), in great agreement with its single crystal structure. Owing to its compact solid-state packing, BTABQ exhibits low solubility in common organic solvents and battery electrolytes (Figure 6.2e, 6.8). Notably, heating BTABQ in deuterated *N,N*-dimethylformamide at 120 °C overnight leads to little dissolution, as verified by the absence of BTABQ signals in the ^{1}H and ^{13}C spectra of the supernatant (Figure 6.1g). This uncommon insolubility, even at elevated temperatures, stands in stark contrast to other OEM reported for LIBs (Figure 6.8). Additionally, likely due to the combination of its intramolecular extended conjugation, intermolecular hydrogen bonding network, and interlayer π–π stacking, BTABQ exhibits broad absorption up to ~1600 nm in its diffuse-reflectance UV-Visible (DRUV-Vis) spectrum, indicating significant electronic delocalization. In comparison, other molecular OEMs, even those with extended aromatic cores, only show absorption below 800 nm (Figures 6.1h, 6.9a, 6.9b, 6.10), presenting a contrast to the unique electronic structure observed in BTABQ. Because of these features, BTABQ exhibits semiconducting behaviors with a transport activation energy of 319 meV and a champion room-temperature electrical conductivity of 2.1×10^{-4} S cm^{-1} (Figure 6.9c), substantially higher than the common molecular OEMs that are generally either poor conductors or insulators, including tetraamino-phenazine-1,4,6,9-tetrone (Figures 6.1i, 6.11, Table 6.2). Remarkably, the electrical conductivity of BTABQ is on par with that of LCO[27] and state-of-the-art NMC[28], and is about five orders of magnitude higher than that of LFP[29]. These favorable properties of BTABQ allow fabrication of battery electrodes with little to no conductive or binder additives and render great practical utility. In contrast, most, if not all, OEMs routinely need at least 40% of the total electrode weight for additives (Figures 6.1i, 6.9d)[7].
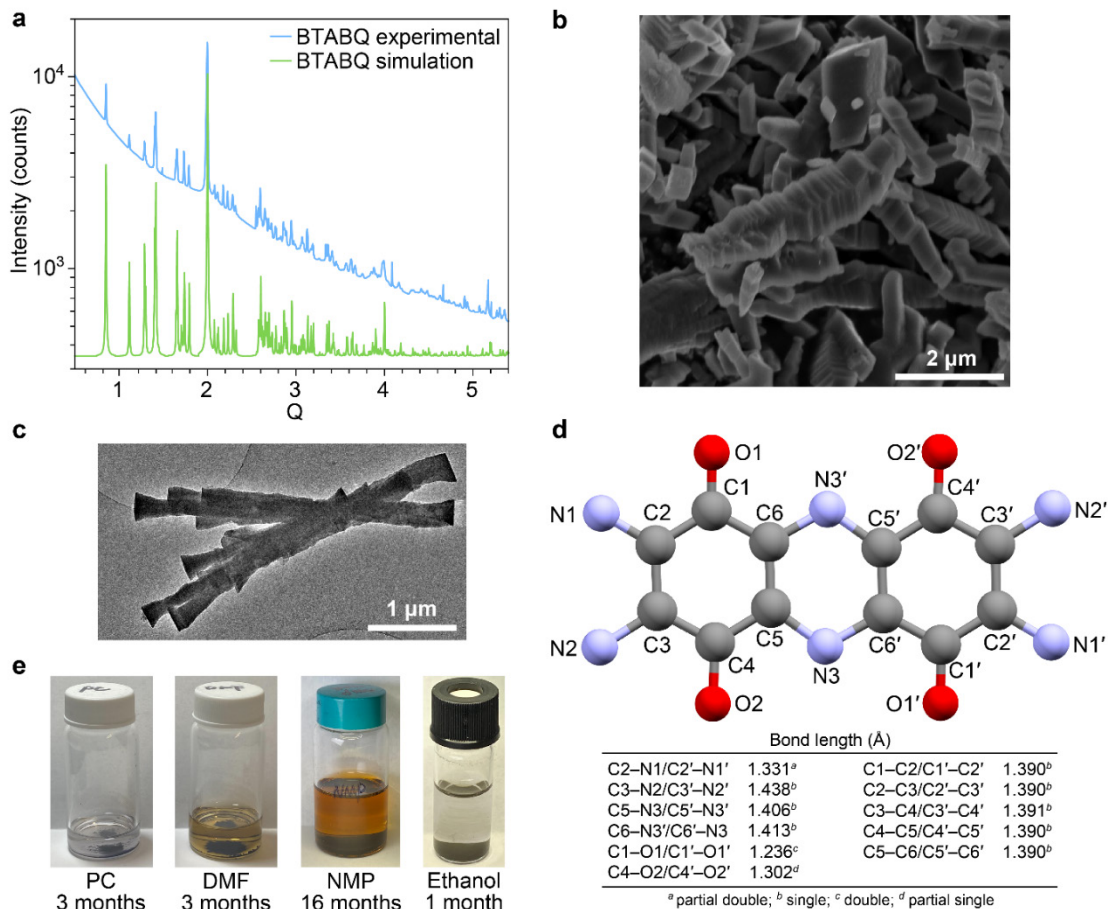
Figure 6.2. Characterizations of BTABQ and common molecular OEMs. **a,** Experimental and simulated WAXS patterns of BTABQ. **b,** A SEM image of BTABQ. **c,** A Cryo-EM image of BTABQ. **d,** Bond lengths of BTABQ obtained from its crystal structure. **e,** Solubility tests of BTABQ in common organic solvents.
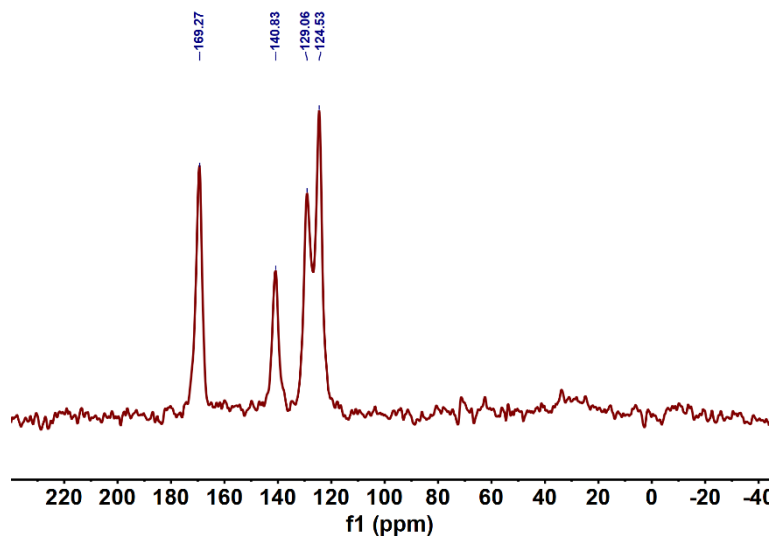

Figure 6.3. ^{13}C solid-state NMR spectrum of BTABQ. The peak at 140.83 ppm indicates the presence of C=NH, which is the result of keto-enol tautomerization of BTABQ. The peak at 169.27 ppm belongs to carbonyl groups, which have slightly lower chemical shift relative to common carbonyl signals (> 170 ppm) due to the excellent electronic delocalization in BTABQ molecules. The two peaks at 129.06 ppm and 124.53 ppm belong to C–N/C–O.
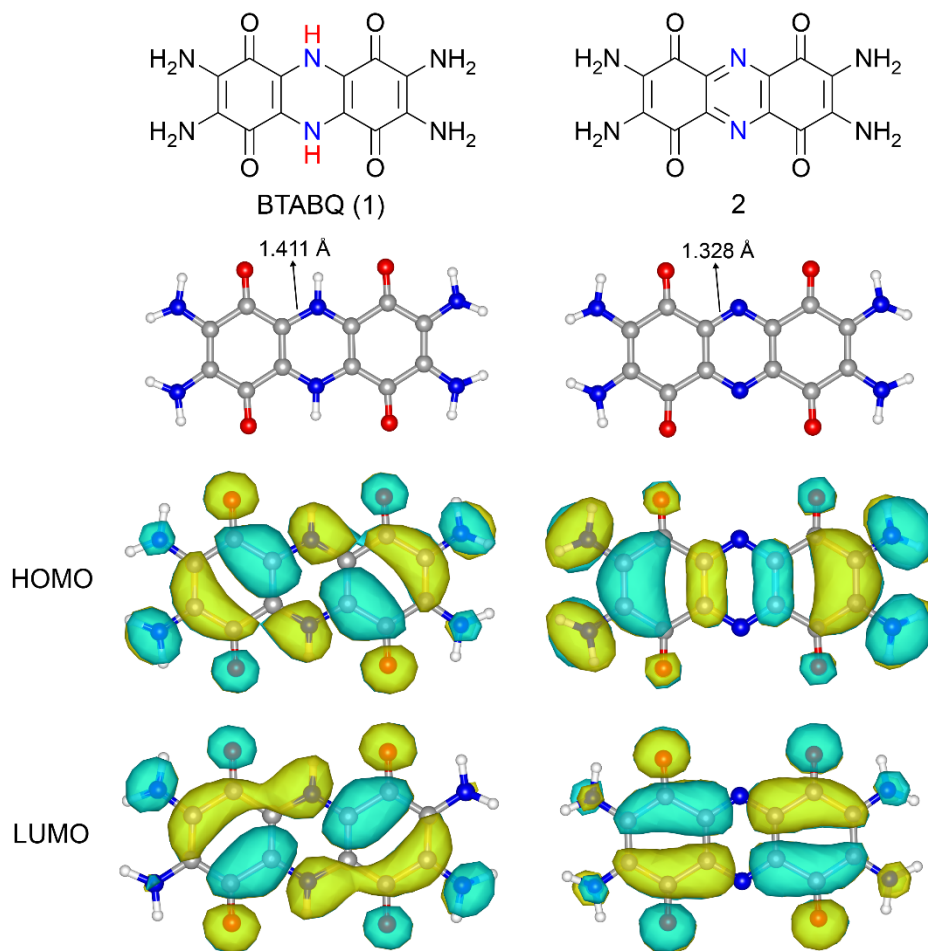
272

Figure 6.4. Molecular structure, and HOMO/LUMO orbital diagrams of BTABQ (1) and tetraamino-phenazine-1,4,6,9-tetrone (2) optimized by DFT calculations. The bond length of the marked C–N bond of BTABQ matches well with the experimental determined bond length (CCDC 2144223), whereas that of **2** is significantly shorter than the experimental values and is within the range of C=N. The frontier orbitals of BTABQ exhibit significantly better electronic delocalization compared with **2**, indicating better extended conjugation of BTABQ.

Table 6.1. HOMO and LUMO energies of both quinone and imine forms of BTABQ (1) and tetraamino-phenazine-1,4,6,9-tetrone (2).

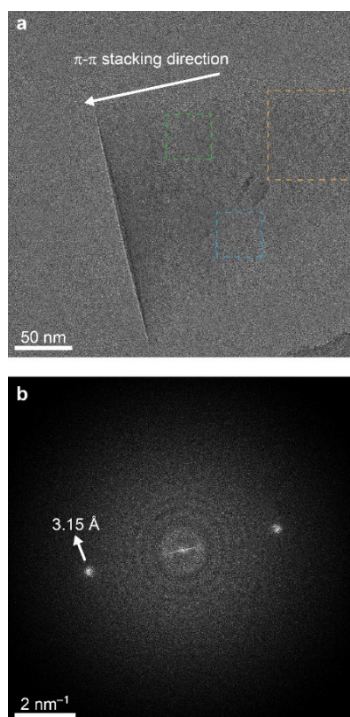|	B3LYP/ma-def2-QZVP			B3LYP/def2-TZVP		
	HOMO (eV)	LUMO (eV)	HOMO-LUMO gap (eV)	HOMO (eV)	LUMO (eV)	HOMO-LUMO gap (eV)
1 (quinone)	−4.9203	−3.4363	**1.484**	−4.4962	−3.2543	**1.2419**
1 (imine)	−4.912	−2.9941	**1.9179**	−4.8040	−2.8660	**1.938**
2	−5.8621	−3.6328	**2.2293**	−5.7602	−3.5483	**2.2119**

Figure 6.5. A Cryo-EM image of BTABQ and its FFT. The diffraction spots in b correspond to a *d* spacing of 3.15 Å, matching well with the interlayer distance of BTABQ 2D layers. The π–π stacking direction of BTABQ 2D layers is parallel to the long axis of this BTABQ rod, as indicated by the white arrow in **a**. Higher magnification images of the highlighted dashed square areas are shown in Figure 6.6.
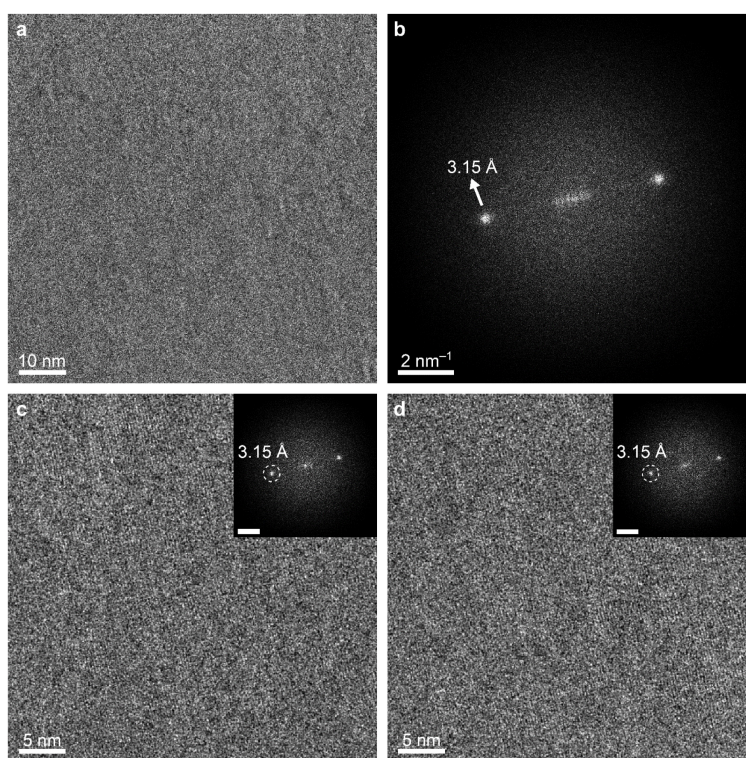

Figure 6.6. High magnification Cryo-EM images of BTABQ. **a,** the yellow dashed square area; **c,** green dashed square area; **d,** blue dashed square area. **b**, FFT of **a**. Scale bars of FFT, 2 nm^{-1}. The π–π stacking of BTABQ 2D layers can be directly seen and confirmed by FFT.
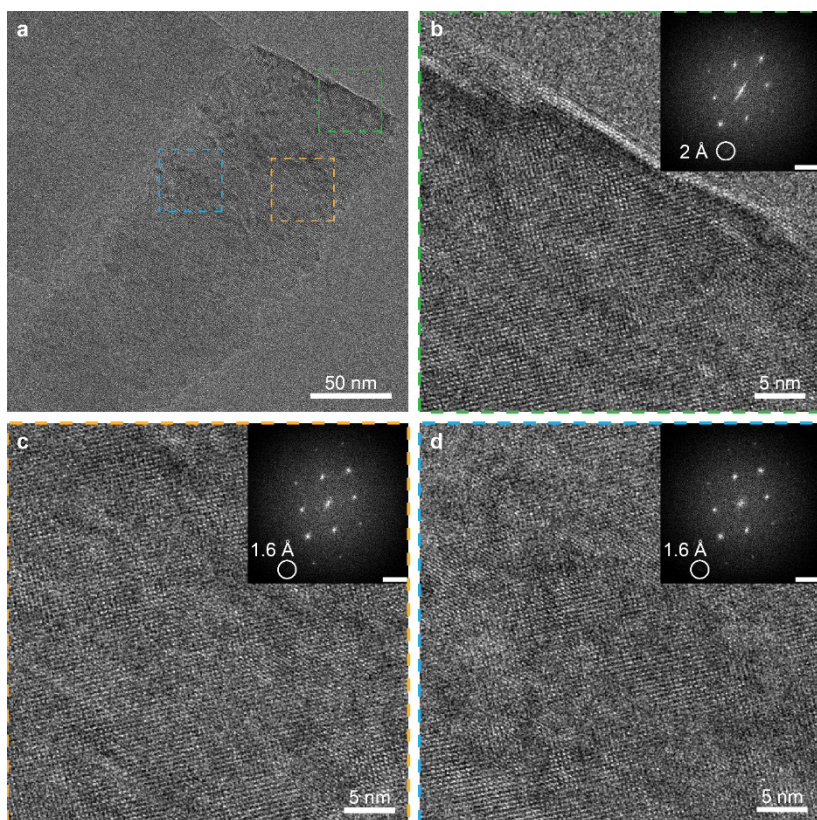
Figure 6.7. Cryo-EM images of BTABQ. **a**, A Cryo-EM image of a single crystal of BTABQ. **b**, A high magnification micrograph of the green dashed square area and its FFT. **c**, A high magnification micrograph of the yellow dashed square area and its FFT. **d**, A high magnification micrograph of the blue dashed square area and its FFT. The short white dashes in **b**, **c**, and **d** are individual BTABQ molecules. The highly ordered intermolecular solid-state packing is revealed by the FFT. The highest resolution is 1.6 Å. Scale bars of FFT, 2 nm^{-1}.
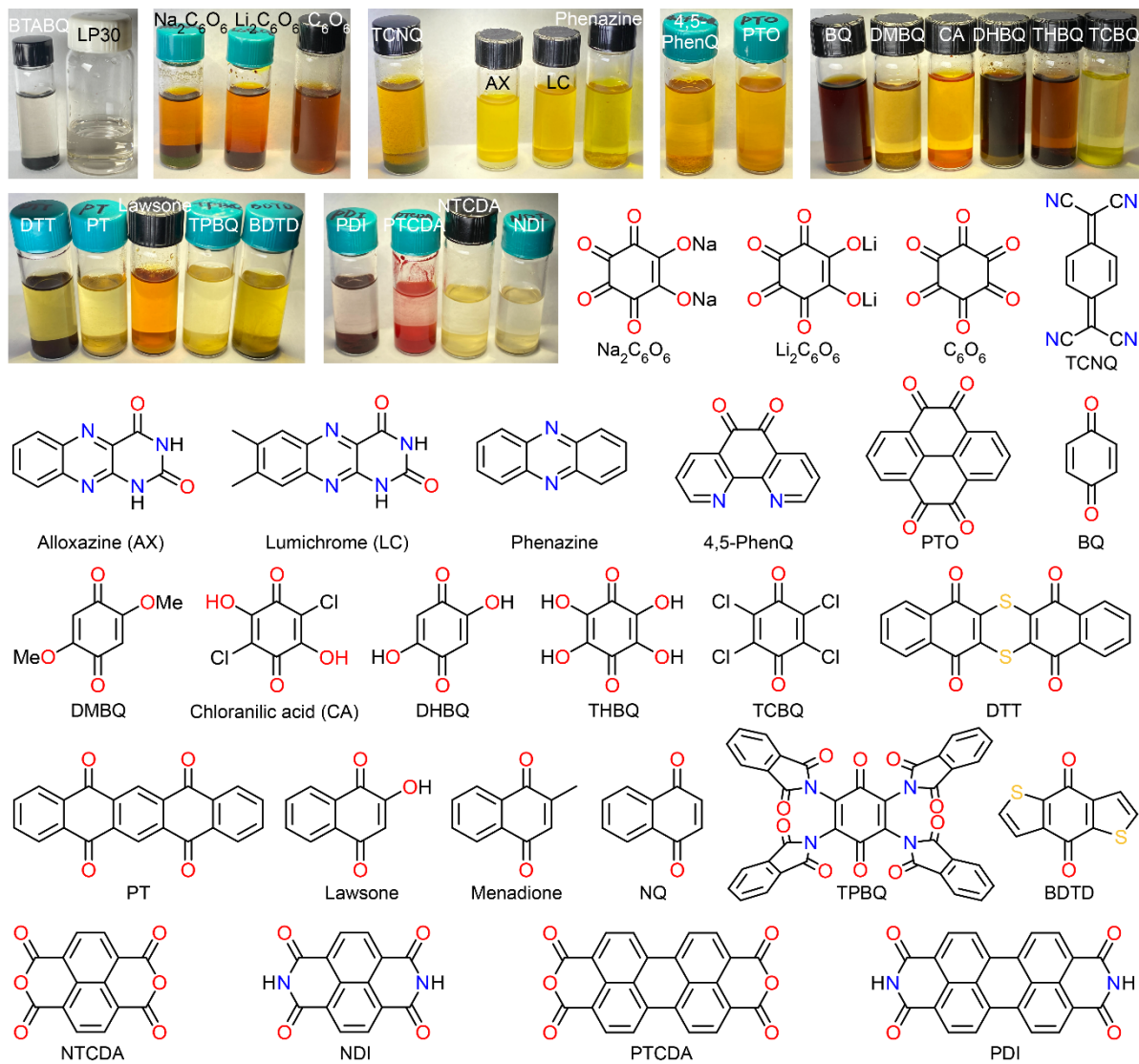
Figure 6.8. Solubility tests of BTABQ and common molecular OEMs in LP30 electrolyte. The photos were taken after three-day soaking. While BTABQ shows no dissolution into LP30 electrolyte, most of the exanimated molecular OEMs undergo various degrees of dissolution into LP30 electrolyte.
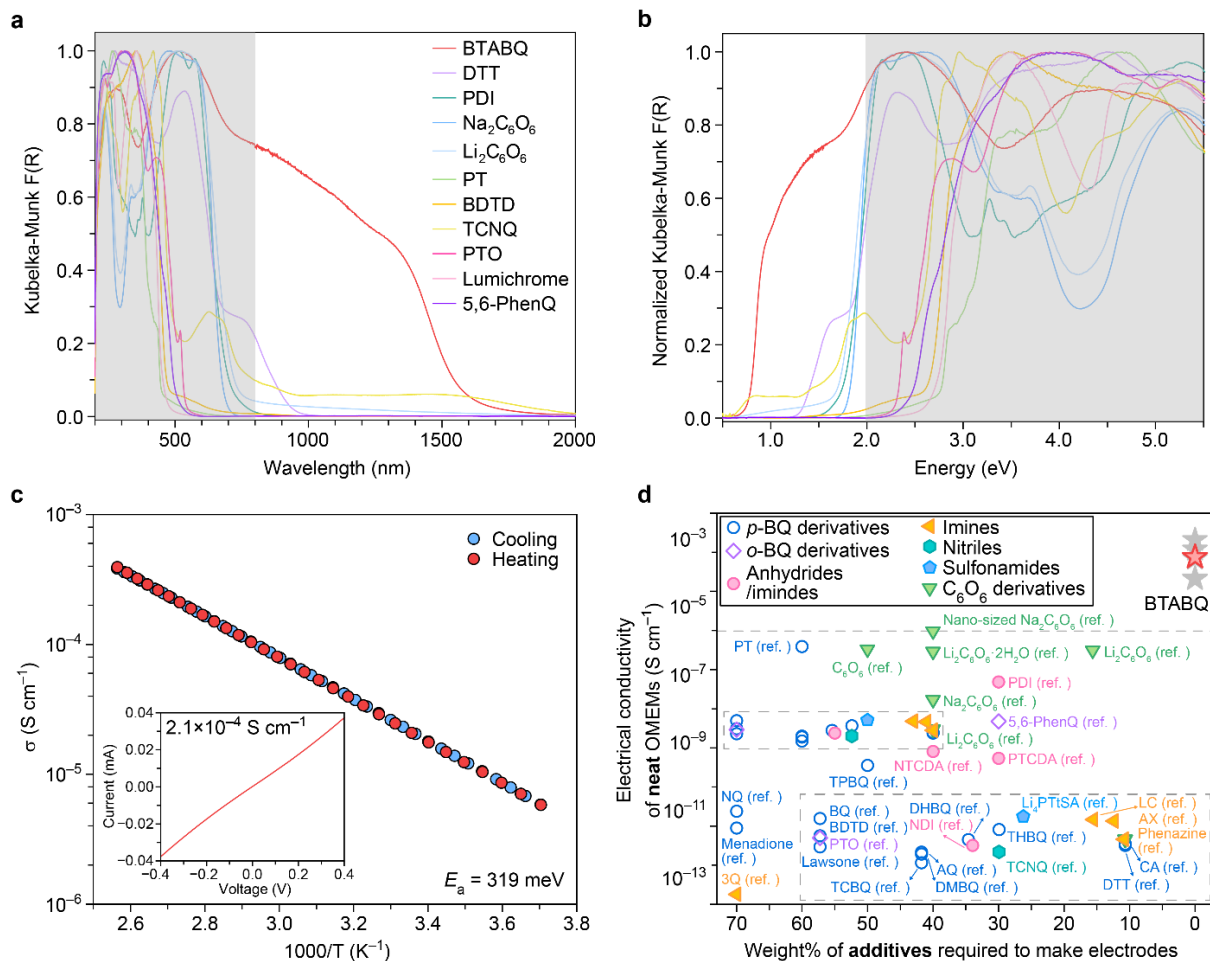
Figure 6.9. Electronic properties of BTABQ and common molecular OEMs. **a,** DRUV-Vis spectra of BTABQ and common molecular OEMs. **b,** DRUV-Vis spectra plotted in the energy scale, highlighting that only BTABQ exhibits significant low-energy absorption. **c,** Temperature dependence of the electrical conductivity of BTABQ, revealing the thermally-activated carrier transport behavior. The fitting of data using Arrhenius equation gives an activation energy E_a of 319 meV. Inset shows an *I-V* curve of BTABQ pellet at room temperature. **d,** Electrical conductivity values of different classes of molecular OEMs and BTABQ versus typical amounts of additives required for electrode fabrication.
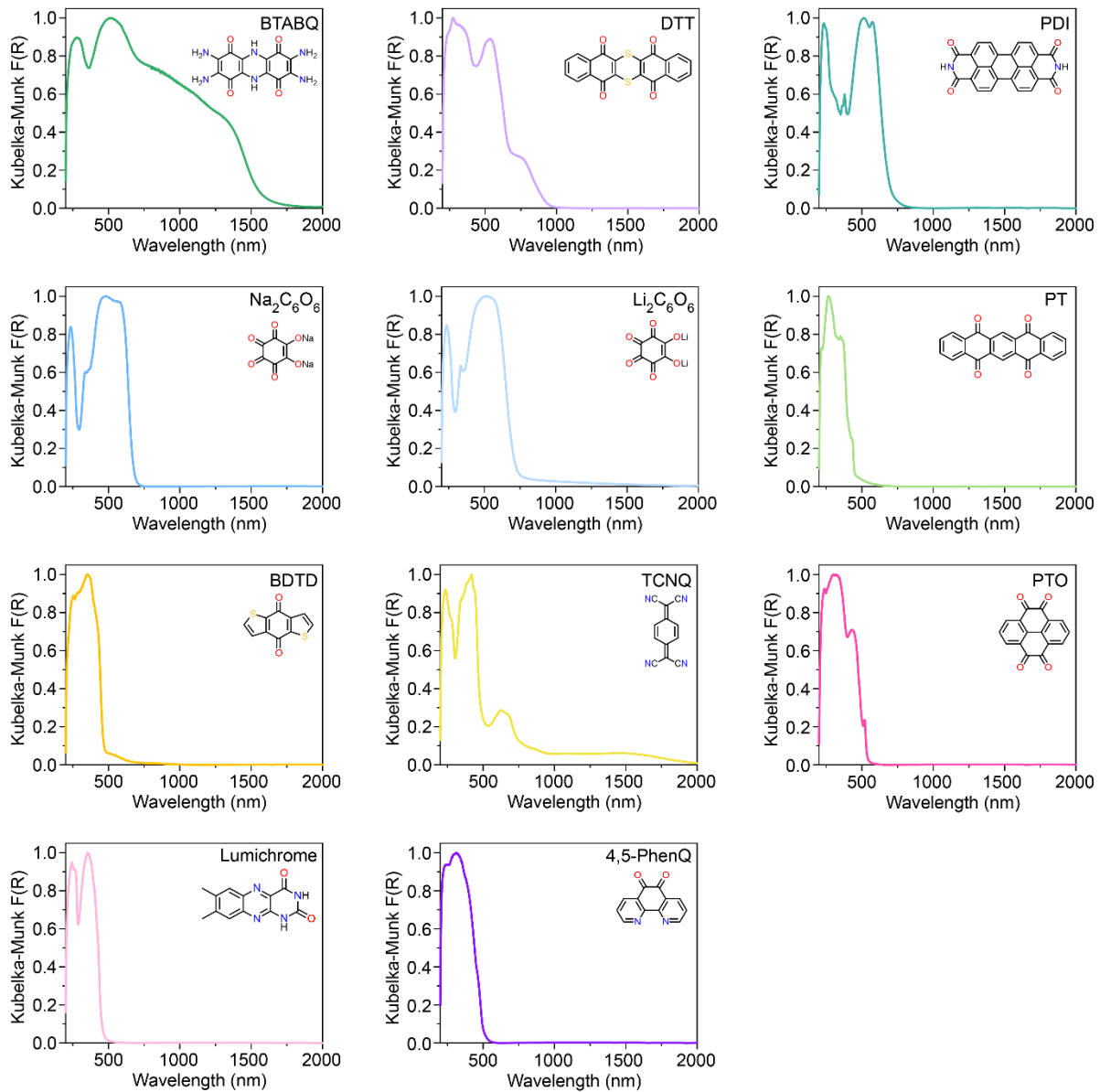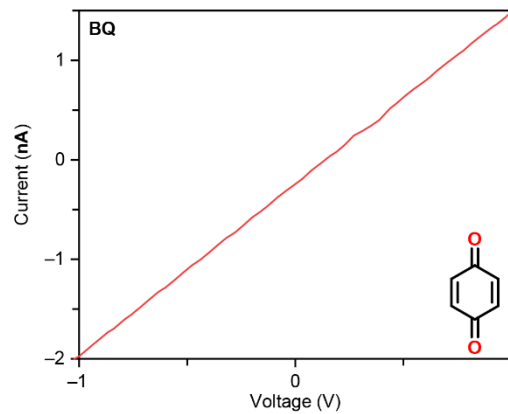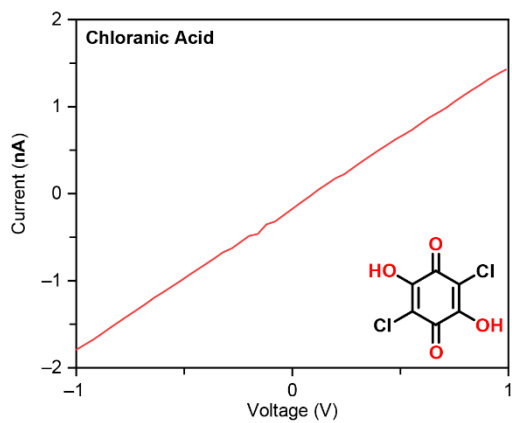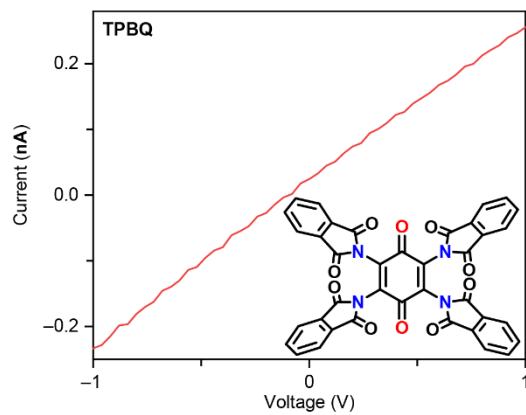
Figure 6.10. DRUV-Vis-NIR spectra of BTABQ and selected molecular OEMs.
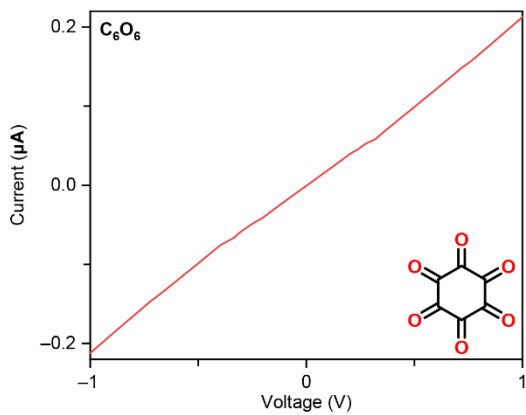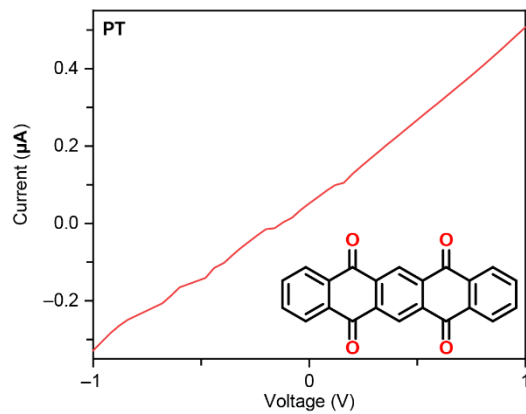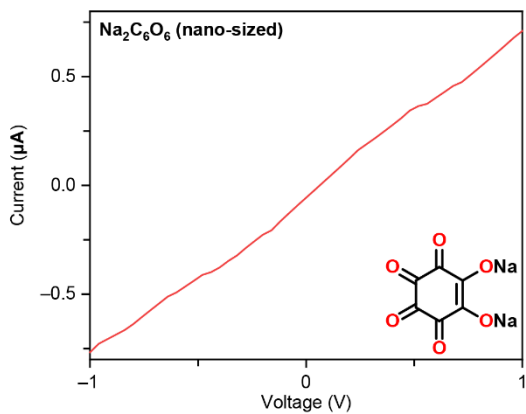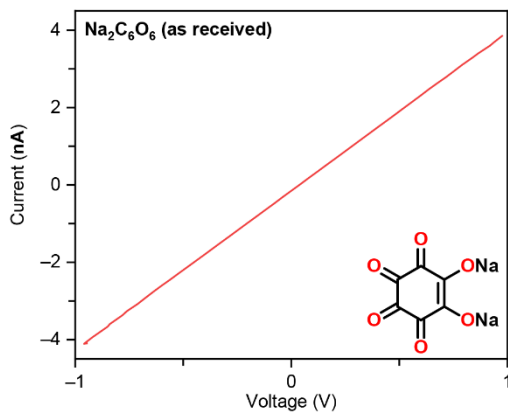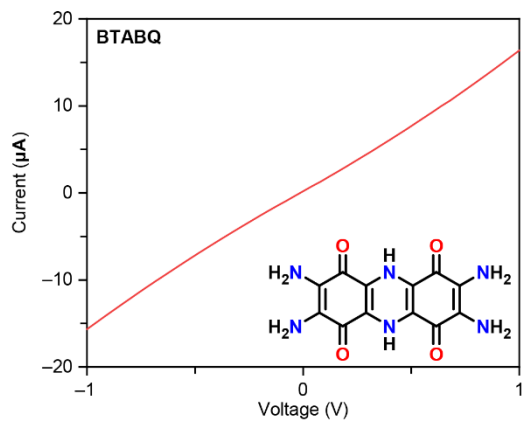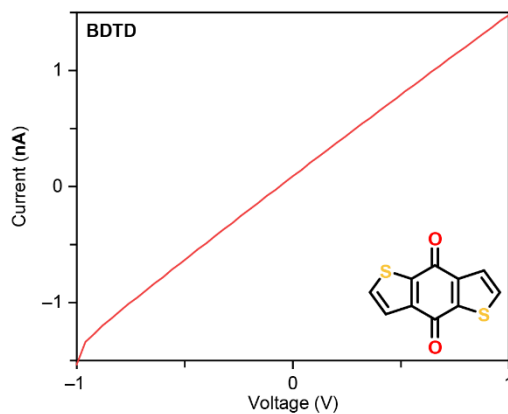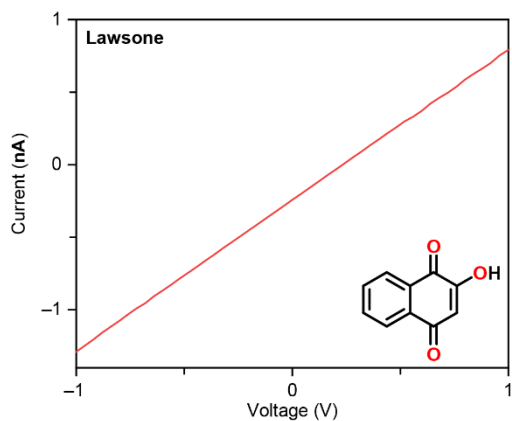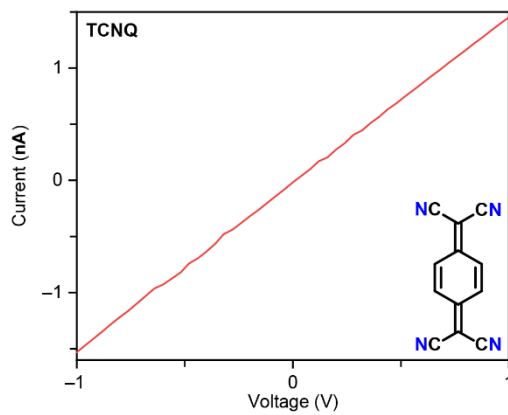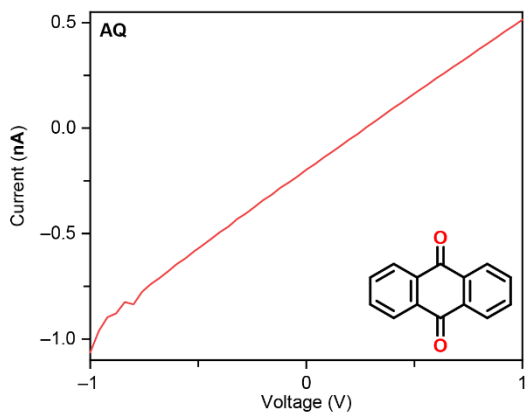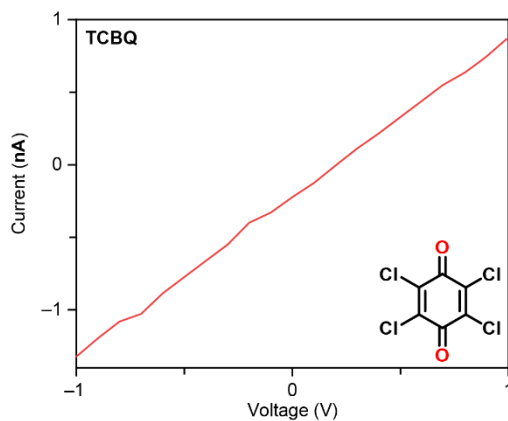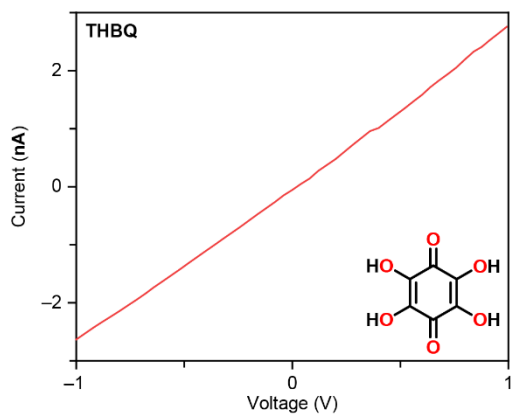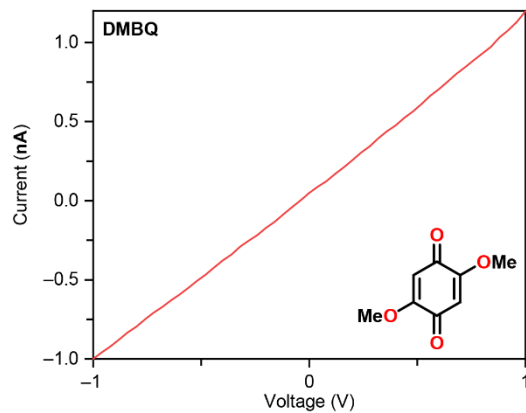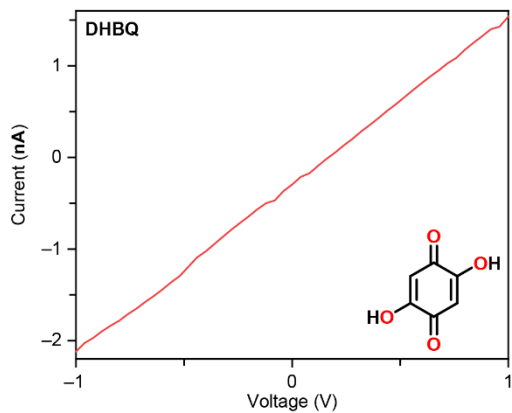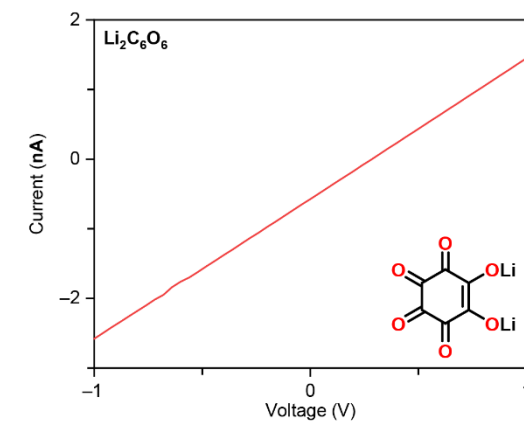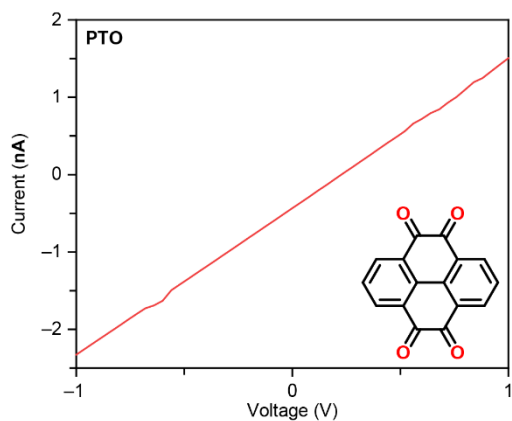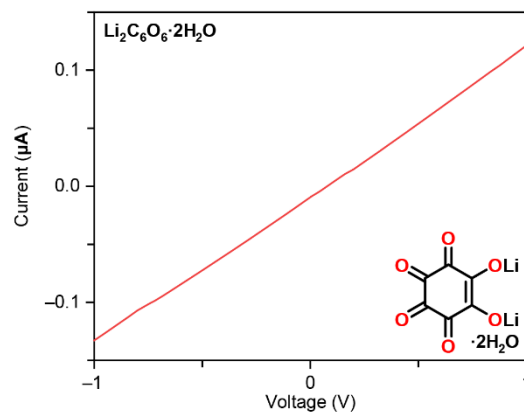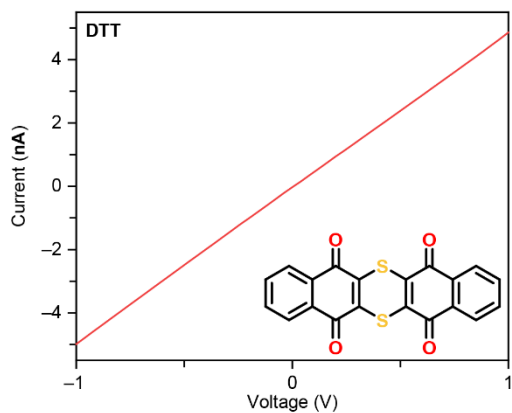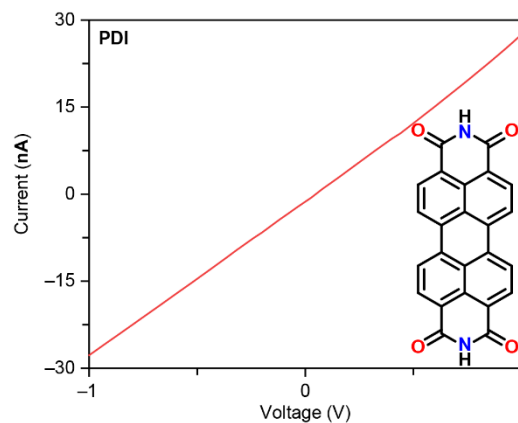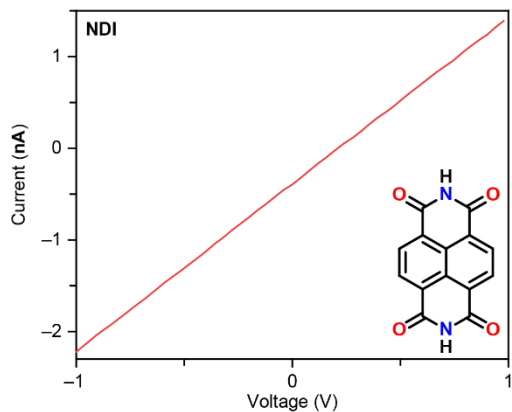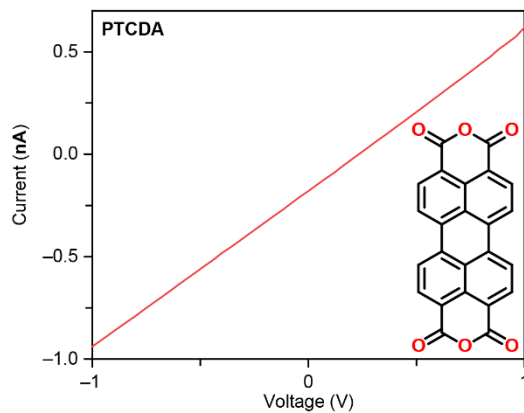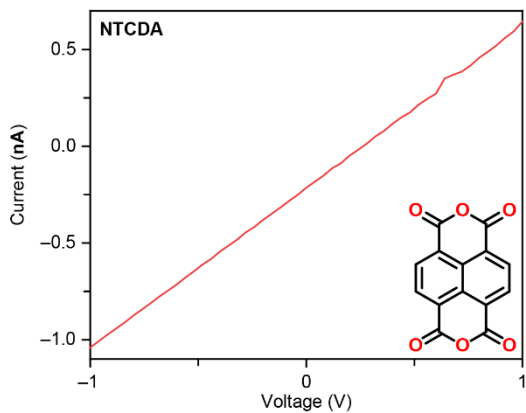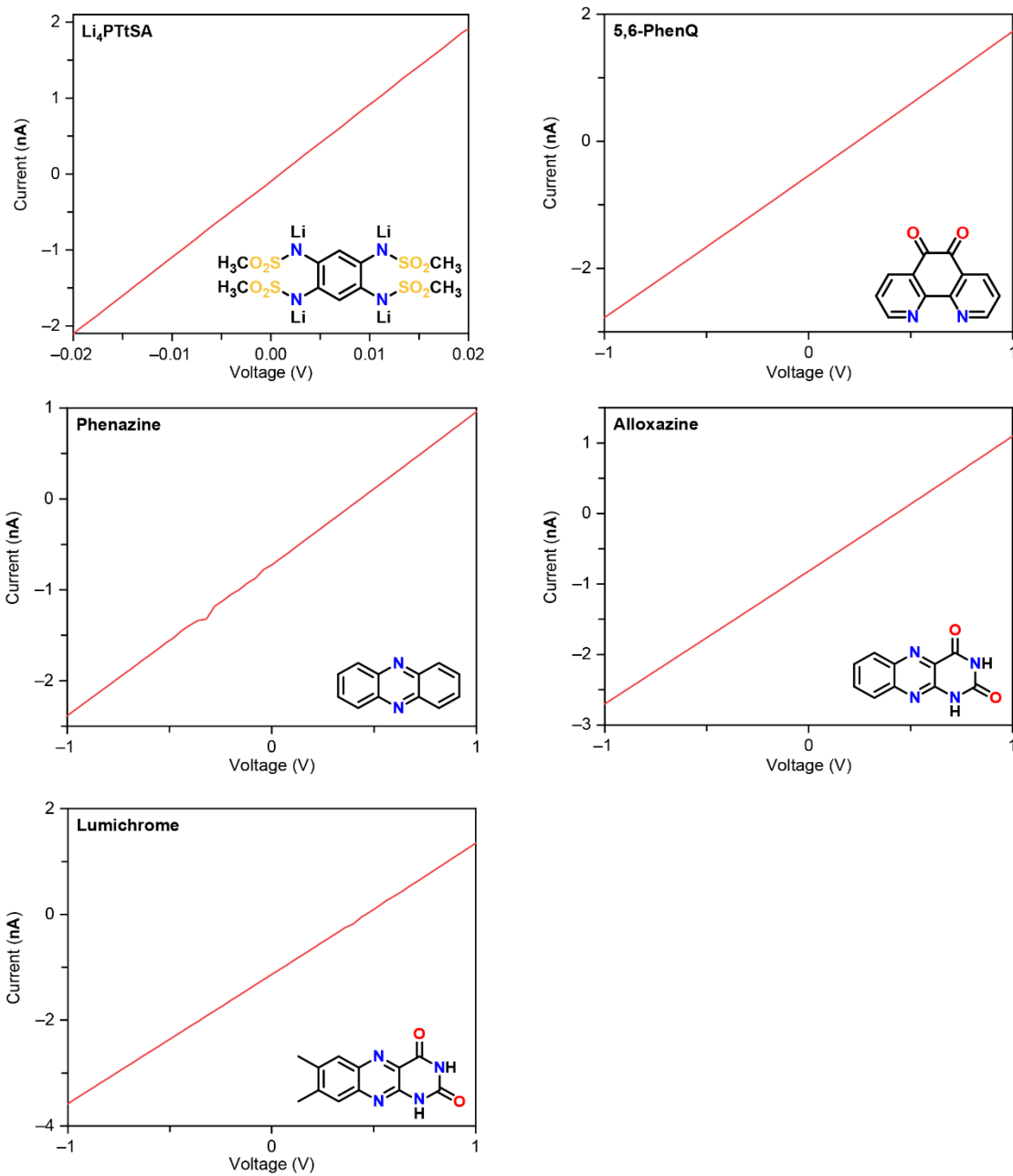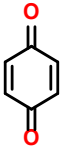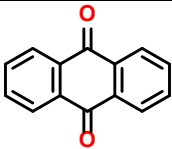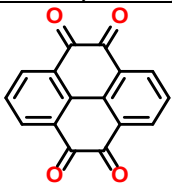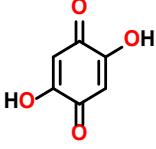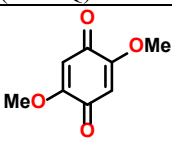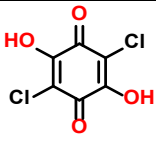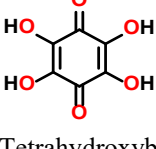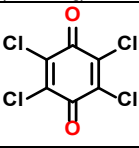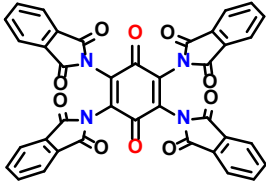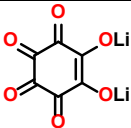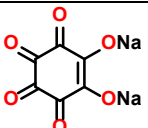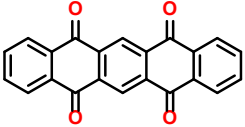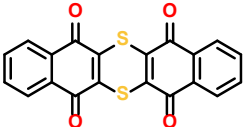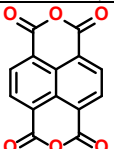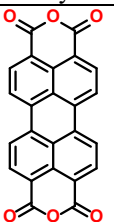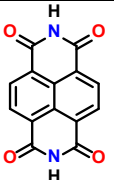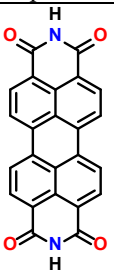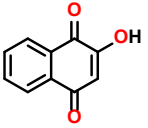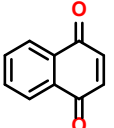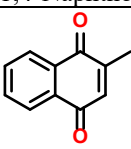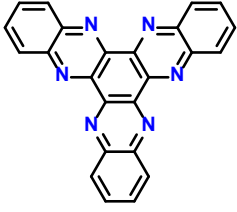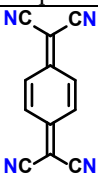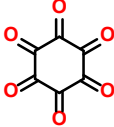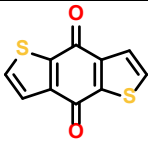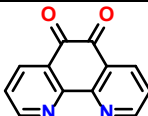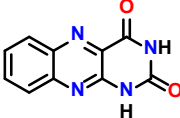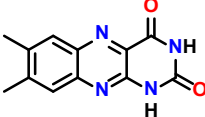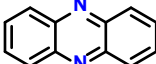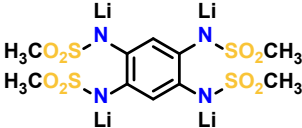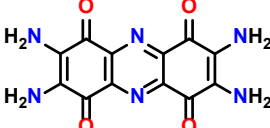
Figure 6.11. *I-V* curves of two-probe devices of BTABQ and common molecular OEMs with nominal voltage ≥ 2.0 V.

Table 6.2. Summary of electrical conductivity of common molecular OEMs with nominal voltage ≥ 2.0 V and the corresponding active material content when they are used to make electrodes.

Chemical structure of OEMs	Active Material Content (%)	Electrical Conductivity (S/cm)	References
Benzoquinone (BQ)	30	5.0×10^{-9}	*Adv. Sci.* **2015**, *2*, 1500124.
Anthraquinone (AQ)	40	2.0×10^{-9}	*Chem. Commun.* **2009**, 448–450.
Pyrene-4,5,9,10-Tetraone (PTO)	30	2.9×10^{-9}	*Chem. Sci.* **2013**, *4*, 1330–1337.
2,5-Dihydroxy-1,4-benzoquinone (DHBQ)	44.6	2.8×10^{-9}	*J. Power Sources* **2013**, *221*, 186–190.
2,5-Dimethoxy-1,4-benzoquinone (DMBQ)	40	1.9×10^{-9}	*J. Power Sources* **2010**, *195*, 8336–8340.
Chloranilic acid (CA)	60	2.4×10^{-9}	*Energy Environ. Sci.* **2014**, *7*, 4077–4086.
Tetrahydroxybenzoquinone (THBQ)	47.6	3.7×10^{-9}	*J. Power Sources* **2013**, *221*, 186–190.
	a) 50 b) 40	1.5×10^{-9}	a) *Angew. Chem. Int. Ed.* **2017**, *56*, 12561−12565. b) *Chem. Mater.* **2015**, *27*, 7258–7264.

Tetrachlorobenzoquinone (TCBQ)

Compound			
 Tetraphthalimide benzoquinone (TPBQ)	50	3.6×10^{-10}	*Angew. Chem. Int. Ed.* **2017**, *56*, 12561−12565.
 $Li_2C_6O_6$	(a) 60 (b) 85 [a]	2.3×10^{-7}	(a) *J. Phys. Chem. Lett.* **2014**, *5*, 3086–3092. (b) *ChemSusChem* **2008**, *1*, 348–355.
 $Na_2C_6O_6$	60	1.7×10^{-8} (as received); 9.3×10^{-7} (nano-sized)	*Nat. Energy* **2017**, *2*, 861–868.
 5,7,12,14-Pentacenetetrone (PT)	40	3.9×10^{-7}	*Int. J. Electrochem. Sci.* **2011**, *6*, 2905–2911.
 Dibenzo[*b,i*]thianthrene-5,7,12,14-tetraone (DTT)	60	2.5×10^{-9}	*Angew. Chem. Int. Ed.* **2016**, *55*, 6428–6432.
 Naphthalenetetracarboxylic dianhydride (NTCDA)	a) 80 [b] b) 60	8.1×10^{-10}	a) *Adv. Mater.* **2007**, *19*, 1616–1621. b) *Nanoscale Adv.* **2021**, *3*, 3199–3215.
 Perylenetetracarboxylic dianhydride (PTCDA)	a) 80 [a] b) 70	5.4×10^{-10}	a) *Adv. Mater.* **2007**, *19*, 1616–1621. b) *Adv. Energy Mater.* **2014**, *4*, 1400554.
	45	2.4×10^{-9}	*Chem. Mater.* **2014**, *26*, 7151–7157.

Structure			
Naphthalenediimide (NDI)			
Perylenediimide (PDI)	70	4.9×10^{-8}	*ACS Appl. Mater. Interfaces* **2015**, *7*, 21095−21099.
Lawsone	Loaded onto porous gas-diffusion layer (GDL) current collector	1.0×10^{-10} (Literature value); 2.3×10^{-9} (Measured value).	*Adv. Energy Mater.* **2017**, *7*, 1602279.
1,4-Naphthoquinone (NQ)	Loaded onto porous GDL current collector	2.4×10^{-11} (Literature value)	*Adv. Energy Mater.* **2017**, *7*, 1602279.
Menadione	Loaded onto porous GDL current collector	9.0×10^{-12} (Literature value)	*Adv. Energy Mater.* **2017**, *7*, 1602279.
Triquinoxalinylene (3Q)	30	1.8×10^{-13} (Literature value)	*Nat. Energy* **2017**, *2*, 17074.
Tetracyanoquinodimethane (TCNQ)	47.6	2.0×10^{-9}	*Sci. Rep.* **2012**, *2*, 453.
Hexaketocyclohexane (C_6O_6) [c]	50	3.3×10^{-7}	*Angew. Chem. Int. Ed.* **2019**, *58*, 7020 −7024.
	30	3.1×10^{-9}	*Adv. Energy Mater.* **2013**, *3*, 600– 605.

Benzo[1,2-b:4,5-b′]dithiophene-4,8-dione (BDTD)			
1,10-Phenanthroline-5,6-dione (5,6-PhenQ)	30	4.7×10^{-9}	Chem. Sci. 2013, 4, 1330–1337.
Alloxazine (AX)	41	4.6×10^{-9}	Nat. Commun. 2014, 5, 5335.
Lumichrome (LC)	43	4.8×10^{-9}	Nat. Commun. 2014, 5, 5335.
Phenazine	40	2.8×10^{-9}	Energy Stor. Mater. 2019, 20, 462–469.
Li$_4$PTtSA	50	5.1×10^{-9}	Nat. Mater. 2021, 20, 665–673.
Tetraamino-phenazine-1,4,6,9-tetrone (TAPT)	60	1.16×10^{-8}	Angew. Chem. Int. Ed. 2022, 61, e202207221.

[a] Rapid capacity decays. [b] The cell is not rechargeable after the second cycle due to electrode dissolution. [c] The nominal voltage is 1.7 V.

6.3.2 Neat BTABQ as cathodes for organic batteries

Due to its high conductivity and poor solubility, neat BTABQ can be directly used as electrodes (see 6.4.3) in Li-ion half cells using lithium anode and commercial LP30 electrolyte (1.0 M LiPF$_6$ in 1:1 ethylene carbonate (EC)/dimethyl carbonate (DMC)). Galvanostatic charge-discharge (GCD) voltage profiles (Figure 6.12a) recorded at 25 mA g^{-1} (0.125 C) between 1.6–3.2 V (versus Li$^+$/Li except for other notice) exhibit initial discharge and charge capacities of 297 mAh g^{-1} and 258 mAh g^{-1} based on the cathode mass, respectively, offering a first-cycle Coulombic efficiency (CE$_{first}$) of 87%, which is comparable to the values (80–86%) of commercial NMC cathodes[30]. While three broad plateaus centered around 2.3 V, 2.7 V and 3.0 V were observed during charging, two distinct plateaus between 2.9–2.6 V and 2.3–2.0 V were observed during discharge, which store approximately equal amount of charge, ~130

mAh g^{-1}, resulting in a nominal discharge voltage of 2.5 V. Similar voltage profile and capacity were also noted using electrochemically pre-lithiated graphite anodes (GrLi, see 6.4.3; Figure 6.13a). Increasing areal mass loadings to 10 mg cm^{-2}, which has rarely been realized in organic cathodes even with more than 50 wt.% of carbon, only slightly decreased the reversible discharge capacity to 181 mAh g^{-1} relative to 205 mAh g^{-1} observed for 2.5 mg cm^{-2} (Figure 6.12a).
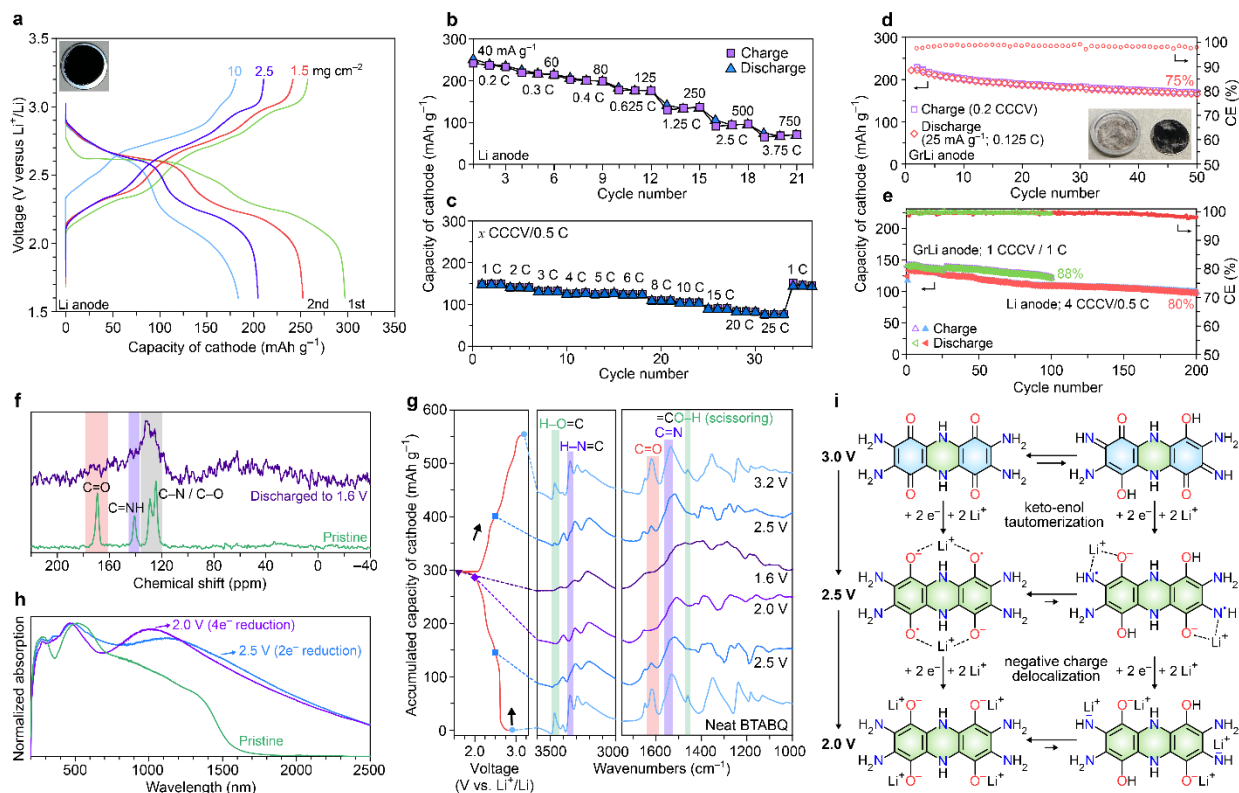
Figure 6.12. Characterization of neat BTABQ electrodes. **a,** GCD voltage profiles of three neat BTABQ electrodes obtained in a half-cell configuration at 25 mA g^{-1} except for the red trace which is recorded at 40 mA g^{-1}. Increasing the electrode mass loadings from 1.5 to 10 mg cm^{-2} led to a 70% retention of reversible capacity. **b,** Power capability of neat BTABQ electrodes recorded from 40 mA g^{-1} (0.2 C) to 750 mA g^{-1} (3.75 C). **c,** Power capability recorded at various CCCV charging rates and a discharge rate of 0.5 C. **d,** Slow cycling of a BTABQ/GrLi half cell. Inset shows the photo of a disassembled coin cell after cycling. **e,** Cycling studies of neat BTABQ half cells at higher rates of 1 CCCV/1 C and 4 CCCV/0.5 C. **f,** Ex-situ ^{13}C ssNMR spectrum of neat BTABQ electrode discharged to 1.6 V shows disappearance of both C=N (purple) and C=O (red) signals. **g,** Ex-situ FTIR spectra of neat BTABQ electrodes at various stages of a discharge-charge cycle show reversible changes in chemical signatures. **h,** Ex-situ DRUV-Vis spectra of BTABQ at various states of discharge. **i,** Schematic representation of the redox mechanism of both quinone- and imine-form of BTABQ.

Faster charging rates of 0.4 C and 2.5 C deliver discharge capacities of 207 and 106 mAh g^{-1} (Figure 6.12b), respectively. Using carbon-coated copper current collectors that commonly used for commercial anodes further improved the fast-charging capability, delivering discharge capacity of 125 and 105 mAh g^{-1} upon 10-minute and 6-minute CCCV (constant current constant voltage) charging, respectively (Figure 6.12c). Diffusion coefficients of Li$^+$ in neat BTABQ electrodes obtained using Galvanostatic intermittent titration techniques (GITT) revealed values of ~10^{-10} cm^2 s^{-1} throughout the discharge/charge processes

287

(Figure 6.13b). The diffusion coefficients are similar to that of state-of-the-art inorganic cathodes[28], demonstrating facile Li^{+} diffusion amid BTABQ crystals and more significantly, within each BTABQ crystal likely due to its layered structures and hydrogen-bonding networks.
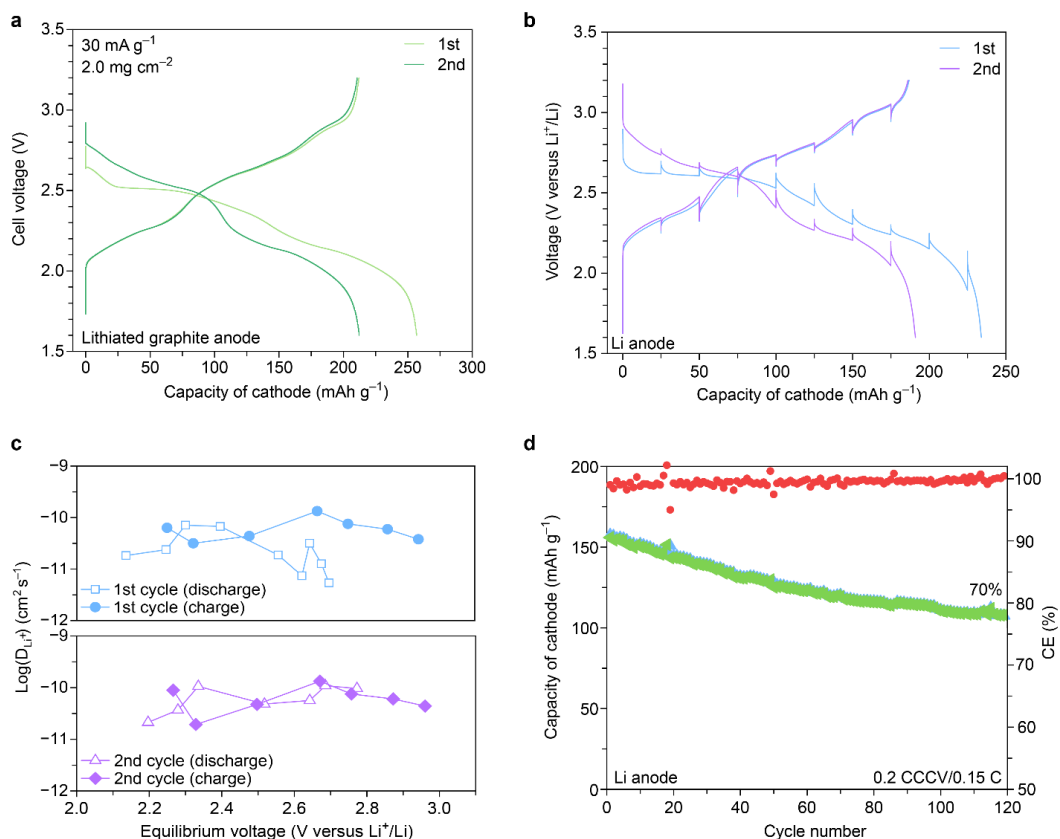
Figure 6.13. Battery performances of neat BTABQ-based half-cells using LP30 electrolyte. **a,** Typical GCD voltage profiles of neat BTABQ/GrLi half cells. **b,** GITT voltage profiles of a neat BTABQ/Li half-cell recorded at 0.1 C. **c,** Diffusion coefficients calculated based on GITT data. **d,** Slow cycling study of neat BTABQ/Li half-cell.

Cycling studies at low charging/discharging rates are generally employed to evaluate the ability of OEMs against dissolution into electrolyte. Neat BTABQ electrodes can at least stably cycle 50 cycles at 0.2 CCCV /0.125 C and 100% depth of discharge (DOD) with a capacity retention of 75% and an average CE of over 98% (Figures 6.12d, 6.13d). Remarkably, no electrode dissolution was observed after cycling, but BTABQ rods instead fractured into flakes along the cross-section, as verified by ex-situ SEM images (Figure 6.14). Cycling at higher rates of 1 CCCV/1 C and 4 CCCV/0.5 C exhibited near 100% CE and better retention of 88% and 80% over 100 cycles and 200 cycles, respectively (Figure 6.12e). Such cycling performance of neat OEM electrodes is unprecedented and serves as a testament for facile ion diffusion and electron transport capability, and virtual insolubility of BTABQ in battery electrolytes.
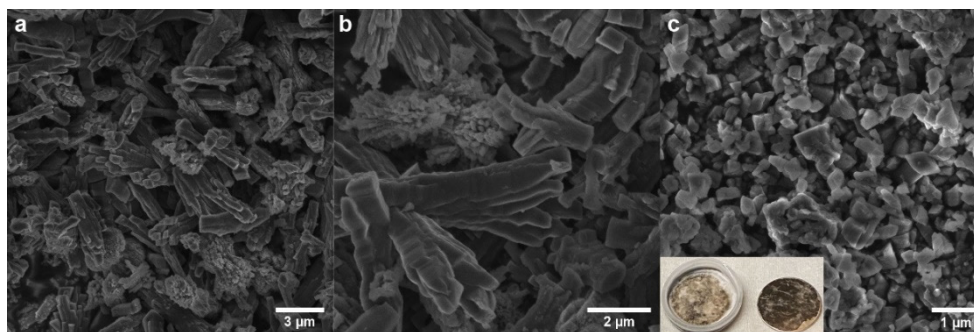
Figure 6.14. SEM images of pristine and cycled BTABQ electrodes. **a, b,** Pristine BTABQ electrode. **c,** BTABQ electrode after 80 cycles at 0.2 CCCV/0.1 C. Inset shows the photo of the corresponding cycled electrode and separator, confirming little electrode dissolution has happened.

Employing neat BTABQ as the cathode also enabled a direct spectroscopic analysis of the redox processes without any possible influences from electrode additives. *Ex-situ* ^{13}C ssNMR spectrum of BTABQ that is discharged to 1.6 V (Figure 6.12f) reveals the disappearance of both C=N (140.8 ppm) and C=O (169.2 ppm) signals, indicating that both functional groups are reduced during discharge. Ex-situ FTIR spectra of BTABQ measured at different potentials (Figure 6.12g) also exhibit a gradual decrease and recovery of the intensities of C=O and C=N stretching peaks at 1618 cm^{-1} and 1531 cm^{-1}, respectively, during discharge and the subsequent recharge process. Interestingly, the O–H (3464 cm^{-1}) and imine N–H (3346 cm^{-1}) stretching peak, and O–H scissoring peak coupled with the center dihydropyrazine ring modes (1460 cm^{-1}), which stem from the imine tautomer (Figure 6.15a), almost completely disappear when BTABQ is discharged to the first plateau at ~2.5 V, indicating that the reduced imine form readily transforms to the more stable reduced quinone form, likely through the hydrogen bonding network (Figure 6.12i). Given that the quinone form has a lower LUMO energy (Figure 6.1a) and thus in theory, a higher reduction potential relative to the imine form, the quinone form is likely to be reduced first during discharge process and the imine form tautomerizes to the quinone form simultaneously. The reduced BTABQ at 2.5 V is proposed to contain diradicals, which is supported by its DRUV-Vis spectrum revealing a significant polaronic band centered around 1200 nm (Figure 6.12h). Subsequent two-electron reduction gives the fully reduced BTABQ, corresponding to the second plateau centered around 2.2 V. *Ex-situ* DRUV-Vis spectra of BTABQ discharged to both 2.5 V and 2.0 V (Figure 6.15b) also reveal less intramolecular electronic delocalization relative to pristine BTABQ due to the lack of tautomerization (Figure 6.12h), as verified by the blue-shifted absorption at 2.67 eV (2.0 V) and 2.56 eV (2.5 V) relative to 2.41 eV of pristine BTABQ. Surprisingly, the intermolecular electronic delocalization is promoted upon discharge, indicated by the significantly enhanced polaronic absorption in the near-infrared region (Figure 6.12h). Therefore, the electrical conductivity of BTABQ discharged to 2.0 V remains essentially unchanged compared to its pristine state (Figure 6.15c). The redox process of BTABQ is fully reversible and the molecular structure of BTABQ remains robust upon cycling, supported by the retention of its FTIR

spectrum after long cycling (Figure 6.15d). Overall, these features together rationalize the redox behavior of BTABQ as a two-step, 4-electron reduction process with a high theoretical capacity of 356 mAh g^{-1}.
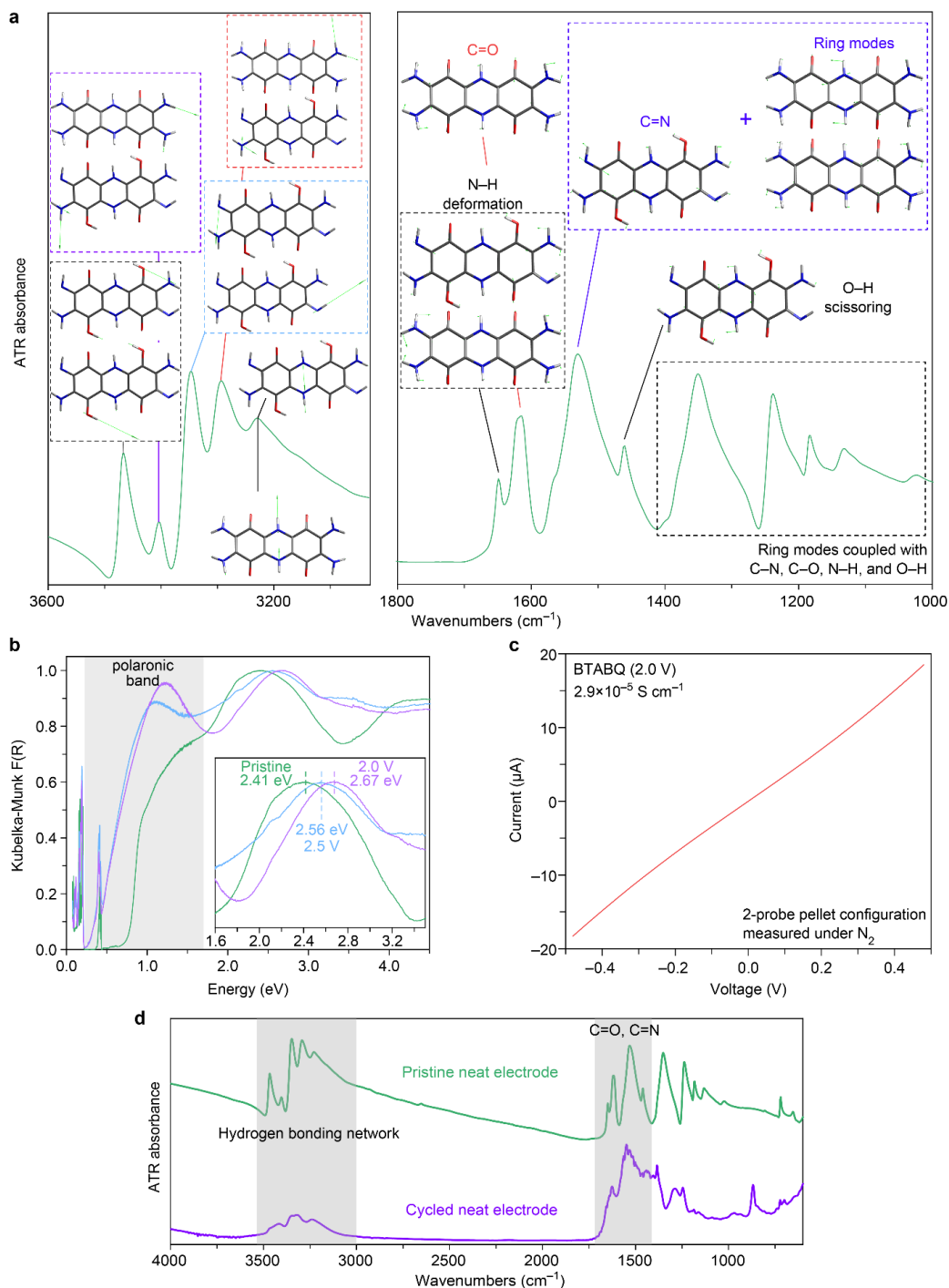
Figure 6.15. Mechanism studies of the charge storage process of neat BTABQ electrodes. **a,** ATR-FTIR spectrum of BTABQ and the corresponding calculated vibrational modes. **b,** DRUV-Vis spectra of neat BTABQ electrodes in the pristine state, discharged to 2.5 V, and 2.0 V (versus Li$^+$/Li). **c,** The *I-V* curve and corresponding electrical conductivity of BTABQ discharged to 2.0 V. The obtained electrical conductivity value is on par with the average value of pristine BTABQ. **d,** ATR-FTIR spectra of neat BTABQ electrodes in the pristine state and after slow cycling at 0.2 CCCV/0.15 C for 120 cycles.

6.3.3 BTABQ cathodes with practical level active material content

To approach the theoretical capacity of BTABQ while not scarifying the electrode-level capacity due to the use of significant amount of conductive additives and binders, BTABQ composite electrodes with at least 90 wt.% active material content were studied for practical purposes. 5 wt.% of carbon black served as the conducting additive, while 5 wt.% of carboxymethyl cellulose (CMC) and/or styrene butadiene rubber (SBR) were chosen as binders. The use of CMC/SBR enables environmentally friendly water-based electrode slurry preparation process, eliminating the use of toxic N-methyl-2-pyrrolidone.[32] Studies on composite electrodes were conducted in both commercial carbonate electrolytes, and ether-based electrolytes that are extensively used in upcoming organic[36], lithium-metal and sulfur-based batteries[37].
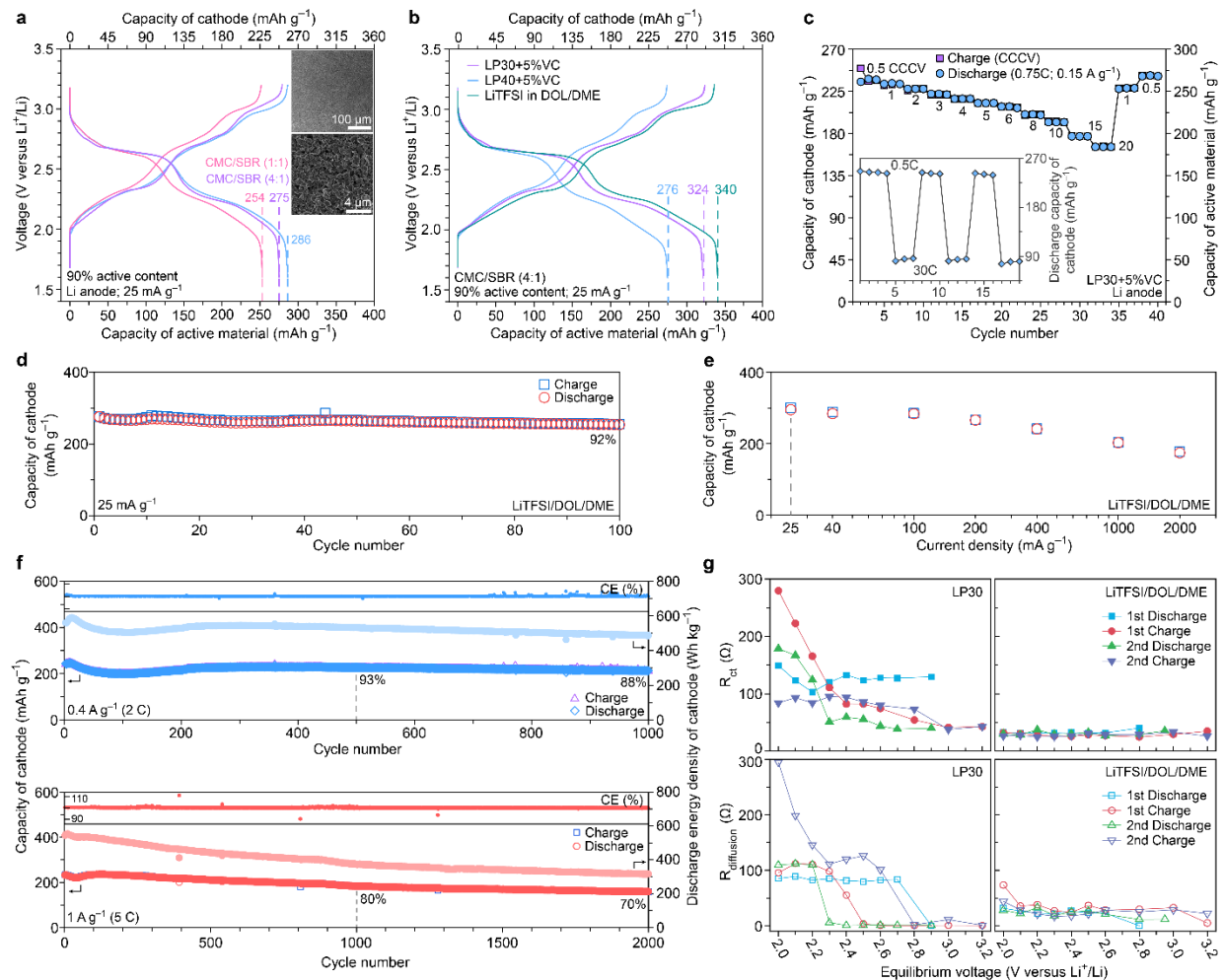
Figure 6.16. Performance Characterizations of composite BTABQ electrodes with 90 wt.% active material. **a,** GCD voltage profiles of BTABQ composite electrodes with various binder compositions at using LP30 electrolyte. Insets are the SEM images of BTABQ composite electrodes using CMC/SBR (4:1) as the binder. **b,** GCD voltage profiles of the optimized BTABQ composite electrodes in different electrolytes. **c,** Power capability studies of BTABQ performed at a constant current discharge rate of 0.75 C and CCCV charge rates from 0.5 to 20 C. Inset shows the cycling study at 0.5 C charge and 30 C discharge. **d,** Cycling study of BTABQ at 25 mA g^{-1} in LiTFSI/DOL/DME electrolyte. **e,** Average capacity of cathodes over 600 hour-cycling at current densities ranging from 25 to 2000 mA

g^{-1}. **f,** Cycling studies of BTABQ at 0.4 A g^{-1} (2 C) and 1 A g^{-1} (5 C) in LiTFSI/DOL/DME electrolyte. **g,** R$_{ct}$ and R$_{diffusion}$ of BTABQ-Li cells in LP30 and LiTFSI/DOL/DME electrolytes.
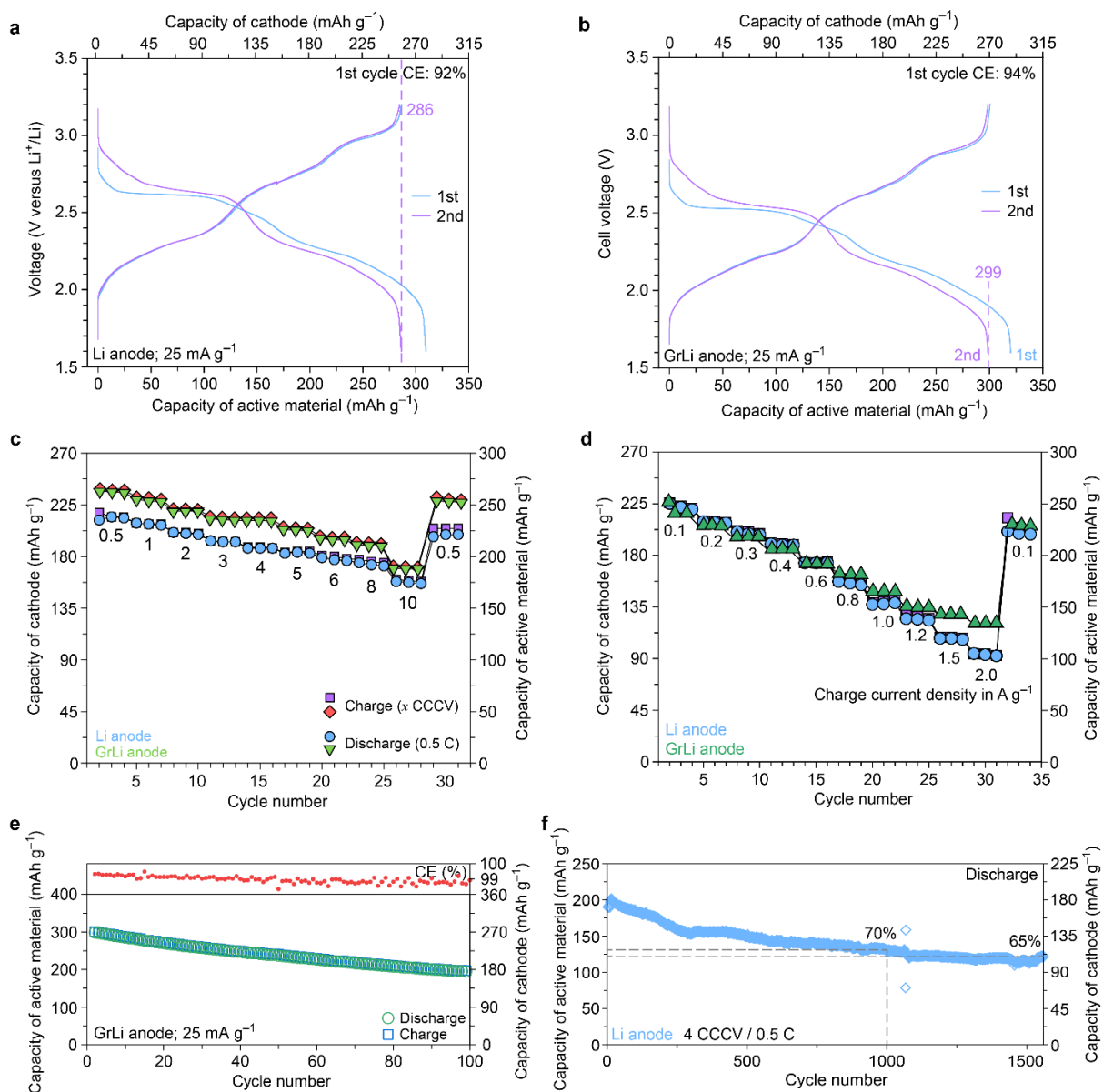
Figure 6.17. Battery performances of half cells based on BTABQ/CMC/CB composite electrodes with 90% active content. **a,** The first- and second-cycle voltage profiles of a BTABQ-Li half cell at 25 mA g^{-1} in LP30. **b,** The first- and second-cycle voltage profiles of a BTABQ-GrLi half cell. **c,** Power capability studies of BTABQ half cells using Li and GrLi anodes. Constant current discharge rate of 0.5 C and increasingly faster CCCV charging rates from 0.5 to 10 C are analyzed. **d,** Power capability of a BTABQ/Li half-cell and a BTABQ/GrLi half-cell recorded up to 2000 mA g^{-1}. **e,** Voltage profiles of the cell in **d** under various current densities. **f,** Power capability studies of the cell in **d** using both CCCV and constant-current protocols.
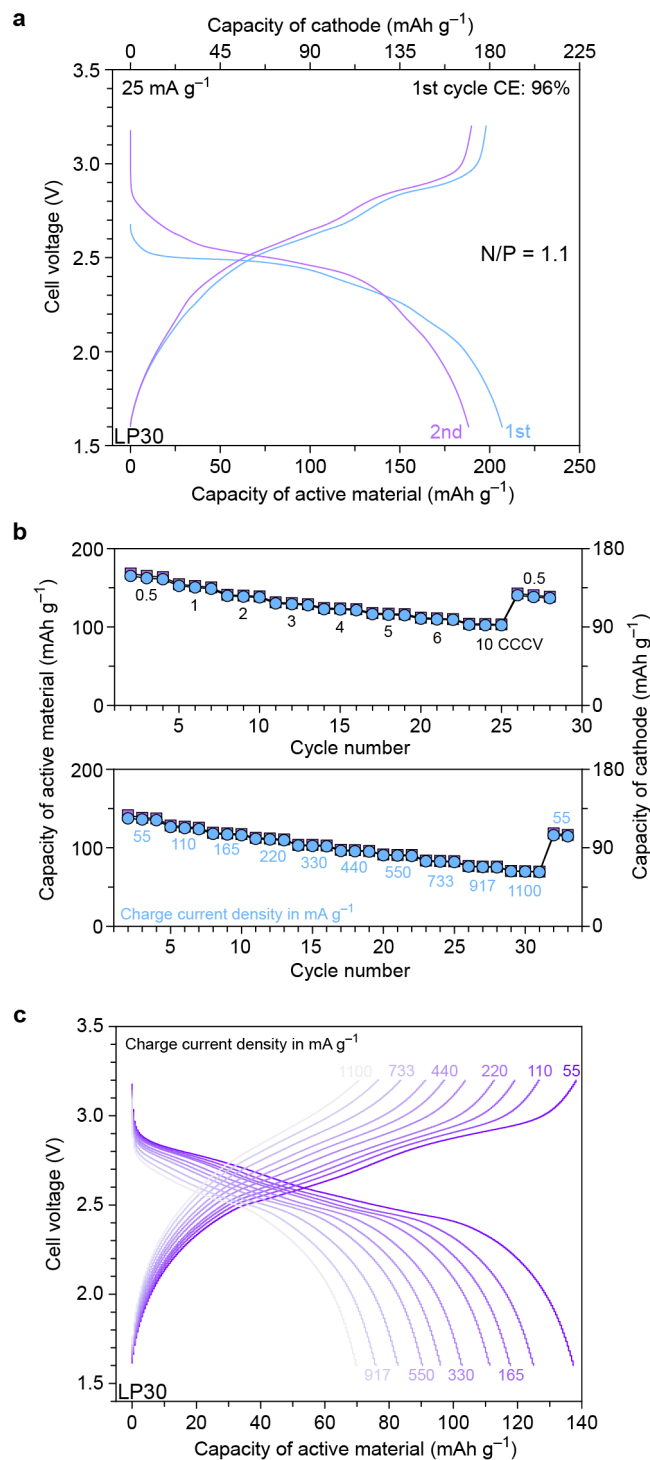
Figure 6.18. Constant-current charge-discharge studies at 25 mA g⁻¹ of BTABQ composite electrodes in LP30VC and LP40VC electrolytes. **a,** The first- and second-cycle voltage profiles of a BTABQ-GrLi cell with a N/P mass ratio of 1.1. **b,** Power capability studies of the cell in **a** using both CCCV (upper) and constant-current (lower) protocols. **c,** Voltage profiles of the cell in **a** under various current densities.

Compared to neat electrodes, CMC-only BTABQ composite electrodes delivered greater reversible capacity of 286 mAh g⁻¹$_{\text{BTABQ}}$ (Li anode) or 299 mAh g⁻¹$_{\text{BTABQ}}$ (GrLi anode) at 25 mA g⁻¹ in LP30 with

enhanced CE_{first} of 92%~94% (Figure 6.16a, 6.17a,b), exhibited significantly improved rate capability and cycling stability over neat BTABQ electrodes (vide supra, Figure 6.17c-f). A proof-of-concept BTABQ-GrLi full-cells with a N/P mass ratio of 1.1 also exhibited cathode capacity reaching 180 mAh g^{-1} (Figure 6.18). However, CMC-only BTABQ composite electrodes suffer from poor adhesion to current collectors. Although BTABQ composite electrodes exhibited decreasing capacity with increasing SBR content (Figure 16a), the use of SBR in addition to CMC, as in commercial graphite anodes, substantially enhanced mechanical integrity and adhesion of BTABQ to the current collector (Figure 6.19). Therefore, CMC-to-SBR ratio of 4:1 was chosen to balance the capacity and mechanical properties, leading to optimized electrodes with uniform and robust coating (Figure 6.16a insets), and a reversible capacity of 275 mAh g^{-1}_{BTABQ}. Due to the intrinsic insolubility of BTABQ and the use of CMC/SBR, such electrodes show no or very limited dissolution in LP30 at either 80 °C or 100 °C after 24 hours (Figure 6.20).
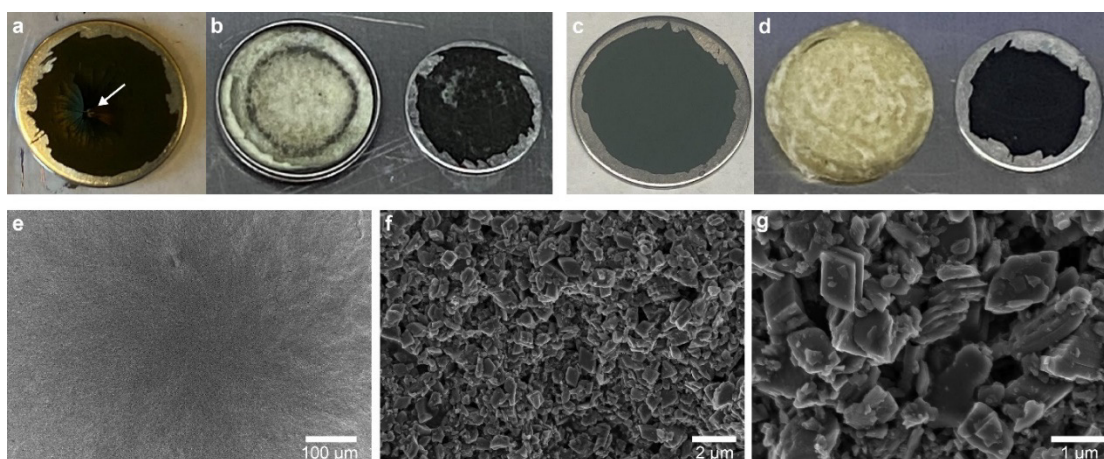
Figure 6.19. Characterization of BTABQ composite electrodes using either only CMC or both CMC and SBR as the binder. **a,** A BTABQ composite electrode using only CMC as the binder. **b,** A BTABQ composite electrode using only CMC as the binder and the separator after cycling. **c,** A BTABQ composite electrode using both CMC and SBR as the binder. **d,** A BTABQ composite electrode using both CMC and SBR as the binder and the separator after cycling. **e-g,** SEM images of BTABQ composite electrode using both CMC and SBR as the binder.

As a widely used strategy in commercial LIBs to improve performance and stability, the addition of 5% vinylene carbonate (VC) to LP30 electrolyte (LP30VC)[34,35] lead to an initial discharge capacity of 356 mAh g^{-1}_{BTABQ} for BTABQ that matches its theoretical capacity, and an improved reversible capacity of 324 mAh g^{-1}_{BTABQ} (Figure 6.16b). Rate capability studies performed upon increasing CCCV charging rate in LP30VC revealed cathode capacity of 192 and 166 mAh g^{-1} at 10 and 20 CCCV (Figure 6.16c), which correspond to total charging times of 6 and 3 minutes, and capacity retention of 80% and 70%, respectively, relative to 240 mAh g^{-1} at 0.5 CCCV (i.e., a total charging time of 2 hours). Additionally, stable fast-switching between 239 mAh g^{-1} at 0.5 C and 90 mAh g^{-1} at 30 C further highlights the remarkable power capability of BTABQ (Figure 6.16c inset). Replacing LP30VC with LP40VC (1.0 M LiPF$_6$ in 1:1 EC/diethyl carbonate (DEC) with 5% VC) enhanced the cycling stability (Figure 6.21) and the performance when using GrLi anodes (Figure 6.22).
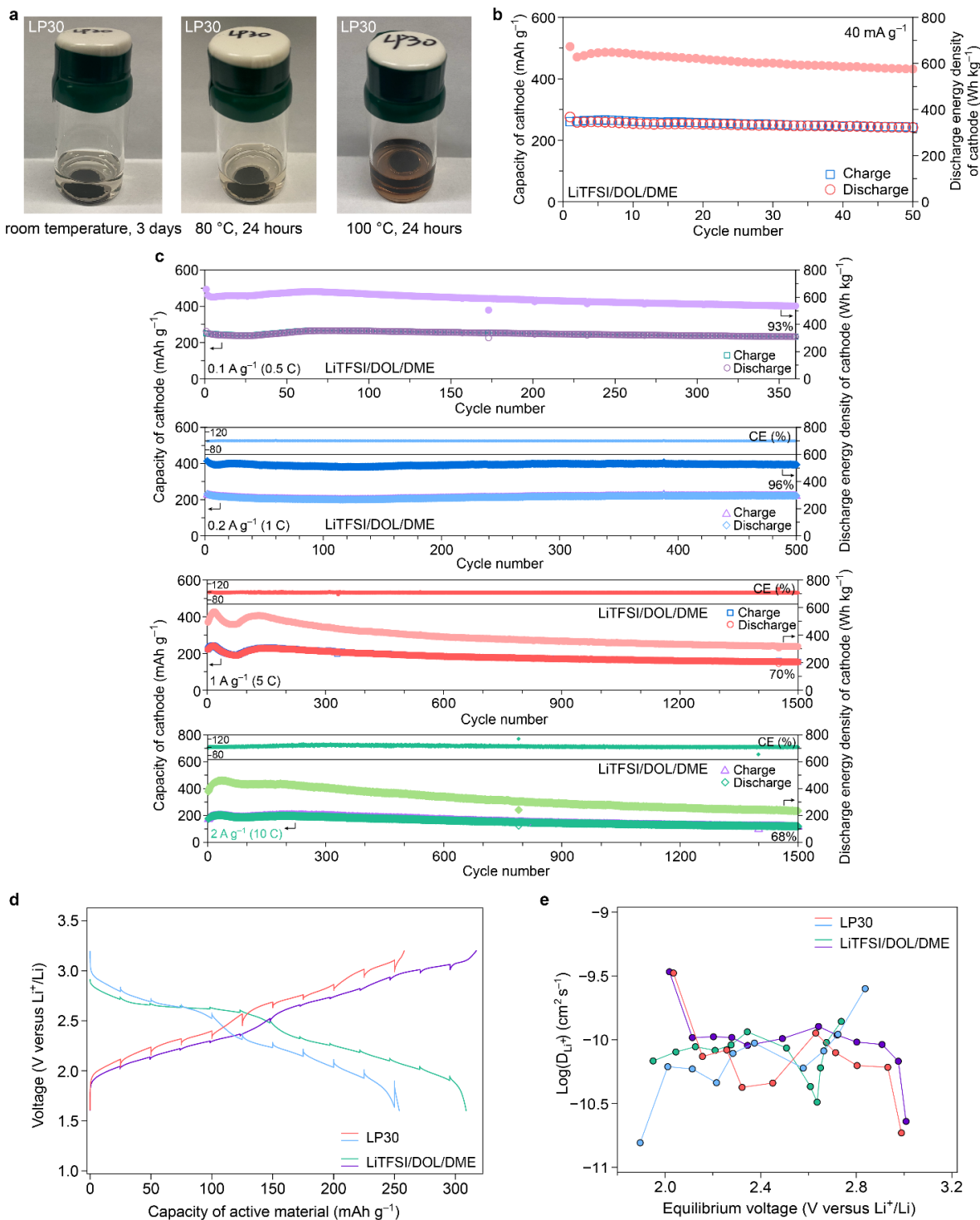
Figure 6.20. Battery performances of half cells based on BTABQ/CMC/SBR/CB composite electrodes with 90% active content and an optimized CMC:SBR ratio of 4:1. **a,** Soaking studies of BTABQ composite electrodes in LP30 electrolyte at room temperature, 80 °C, and 100 °C. **b,** Cycling study of a BTABQ-Li cell at 40 mA g^{-1}. Cathode capacities of 260 mAh g^{-1} and 242 mAh g^{-1} were observed for the second and 50th cycle, respectively, corresponding to a capacity retention of 93%. **c,** Cycling study of BTABQ-Li cells at 0.1, 0.2, 1, and 2 A g^{-1}. Corresponding cathode capacities of 232, 222, 153, and 120 mAh g^{-1} were observed after 360, 500, 1500, and 1500 cycles, respectively. **d, e,** GITT data of BTABQ-Li cells in either LP30 or LiTFSI/DOL/DME electrolytes.

295
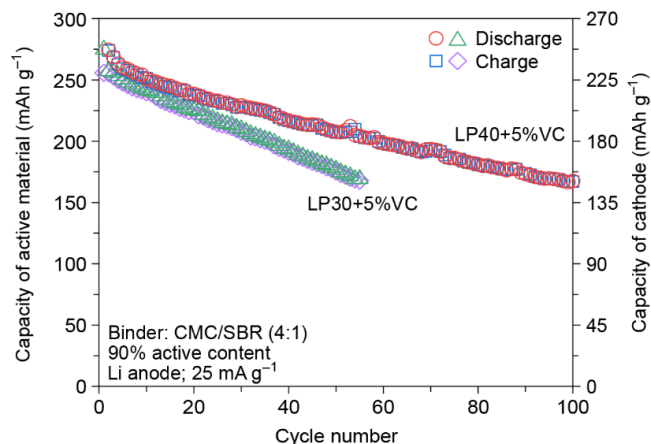
Figure 6.21. Constant-current charge-discharge studies at 25 mA g^{-1} of BTABQ-Li half cells in LP30VC and LP40VC electrolytes.
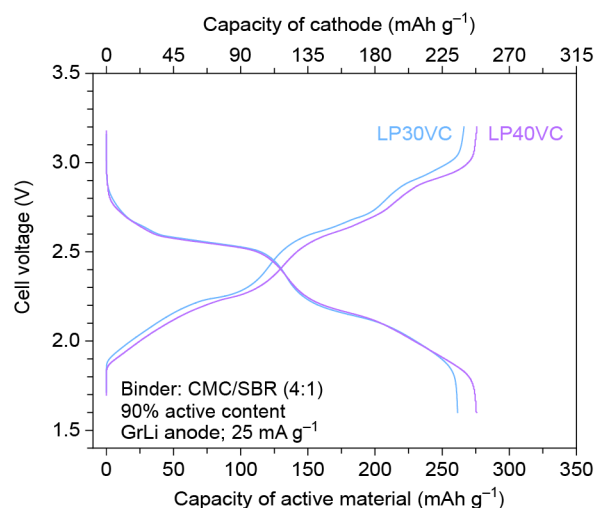
Figure 6.22. Voltage profiles of BTABQ-GrLi half cells in LP30VC and LP40VC electrolytes at 25 mA g^{-1}.

Compared with carbonate electrolytes, ether-based electrolytes such as 1.0 M lithium bis(trifluoromethanesulfonyl)imide in 1:1 1,3-dioxolane/dimethoxyethane (LiTFSI/DOL/DME) are known to deliver better CE versus lithium anodes. BTABQ composite electrodes delivered reversible capacities up to 340 mAh g$^{-1}_{BTABQ}$ (Figure 6.16b) with enhanced CE$_{first}$ of 95%~100% based on five cells (Figure 6.23), and stable cycling at 25 mA g^{-1} and 100% DOD in LiTFSI/DOL/DME, exhibiting cathode capacity of 254 mAh g^{-1} after 100 cycles (Figure 6.16d). Such capacity retention (92%) outperforms the slow cycling in carbonate electrolytes (Figure 6.21). Cycling studies at higher current densities (Figure 6.20b,c) ranging from 40 mA g^{-1} (0.2 C) to 2000 mA g^{-1} (10 C) revealed limited drop of the average capacity over 600-hour cycling from 256 to 157 mAh g^{-1} (Figure 6.16e), suggesting an outstanding power performance. More specifically, cycling studies at 0.4 A g^{-1} (2 C) and 1 A g^{-1} (5 C) revealed cathode capacity of 213 mAh g^{-1} and 159 mAh g^{-1} after 1000 cycles and 2000 cycles (Figure 6.16f), corresponding

to capacity retention of 88% and 70%, respectively. GITT studies revealed slightly higher diffusion coefficients of Li$^+$ in LiTFSI/DOL/DME relative to LP30 (Figure 6.20d,e). Remarkably, significantly lower charge transfer resistances (R$_{ct}$), ranging from 20 to 40 Ω during the whole charge/discharge process, were observed in LiTFSI/DOL/DME relative to LP30 (Figure 6.16g). Interestingly, ion diffusion resistances (R$_{diffusion}$) remained below 40 Ω from 2.1 V to 3.2 V in LiTFSI/DOL/DME, which is drastically different from the step-like increase of R$_{diffusion}$ at higher degree of discharge in LP30. Nevertheless, the R$_{ct}$ and R$_{diffusion}$ values observed in both electrolytes are among the lowest values observed for any cathode materials at similar active content levels, and even lower than most organic cathodes with significant amount of conducting additives. Overall, these performances indicate the ability of BTABQ to intercalate Li ions rapidly and reversibly and function as a cathode against lithium or GrLi anodes, highlighting its potential for application in lithium metal batteries and LIBs, respectively.
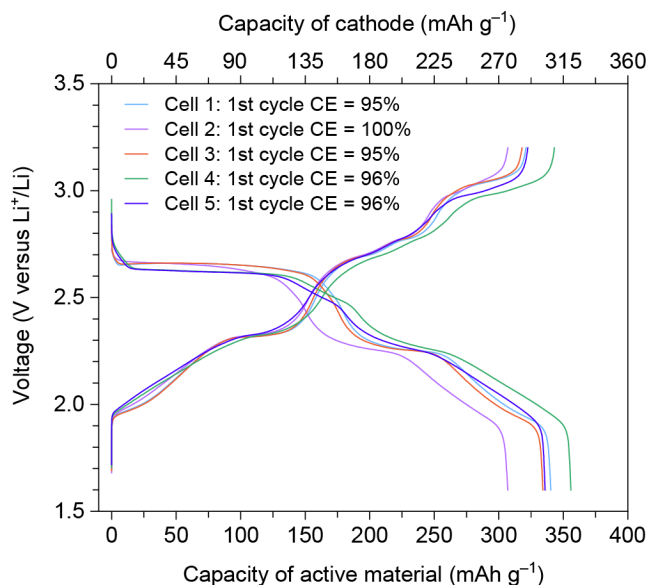
Figure 6.23. Voltage profiles of five BTABQ-Li half cells in LiTFSI DOL/DME measured at 25 mA g^{-1}. The typical first-cycle Coulombic efficiency (CE) is equal to or higher than 95%.

6.3.4 Structural and morphological evolution

Structural and morphological evolution of BTABQ during its electrochemical operation were probed using in-situ and ex-situ PXRD, SEM and cryo-EM analyses, affording critical insights of changes in the interlayer spacing and in-plane ordering of BTABQ molecules as a function of applied potentials. In-situ PXRD patterns (Figure 6.24a) recorded in a custom-made coin cell using a CCCV protocol (see 6.4.3 and Figure 6.25) identify notable and systematic changes in the (102) reflection (Figure 6.1b) of BTABQ. From its pristine inter-layer spacing of 3.14 Å, reduction of BTABQ to its half-discharged state at 2.4 V via a two-electron reduction led to a gradual and complete expansion of inter-layer spacing to 3.33 Å.

Successive two-electron reduction of BTABQ to its fully-discharged state at 1.7 V and the subsequent two-electron oxidation back to its half-charged state at 2.4 V did not reveal notable structural changes. The following re-charging from 2.4 V to its fully-charged state at 3.1 V led to a gradual decrease in interlayer spacing to 3.18 Å, which is 0.04 Å larger than its pristine state. Although the variation of the in-plane arrangement of BTABQ molecules were also noted according to the evolution of (110), (111), (1$\bar{4}$1), and (051) reflections, they were too convoluted to clearly elucidate the in-plane structural changes. Instead, ex-situ Cryo-EM images of BTABQ microcrystals at various states of charge confirmed the variation of inter-layer spacing while providing insights into the changes of in-plane ordering. While the interlayer spacing of BTABQ slightly increased from 3.14 Å to 3.18 Å (Figures 6.24b-c, 6.26a-c) after the first discharge-charge cycle, the in-plane ordering due to hydrogen bonding interactions is strongly affected, as verified by the variation of the d spacing corresponding to (011) reflection from ~7.3 Å to ~9.1 Å (Figure 6.24c). We attribute such disordering to the interruption of intermolecular hydrogen bonding interaction during lithium insertion/de-insertion. The interlayer spacing remained unchanged at 3.18 Å after 1000 cycles (Figure 6.26d-f) and the in-plane ordering is restored with a 7% expansion in unit cell volume, as solved by indexing FFT patterns (see 6.4.3). Upon discharge, reduced BTABQ molecules show substantially augmented electrostatic repulsion which, along with Li$^+$ insertion, leads to the increased intermolecular separation. Although the inter-layer spacing increases to 3.33 Å, the expansion preferentially happens along the in-plane direction (Figures 6.24d-e, 6.27a-f). The volumetric expansion of BTABQ upon discharge does not break the particles, nevertheless, the induced in-plane disordering roughens the surface of BTABQ crystals, which is clearly seen in their ex-situ SEM images (Figure 6.27g). The disorder-induced inhomogeneity of BTABQ crystal surface retained while charging back to 2.4 V, and largely but not completely disappear upon fully re-charge (Figure 6.28). Although BTABQ electrode retains its chemical state after prolonged cycling, as supported by corresponding FTIR spectra of cycled electrodes (Figure 6.26g-j), the disorder-induced morphological change accumulated upon cycling, as seen by the ex-situ SEM images (Figure 6.24g).
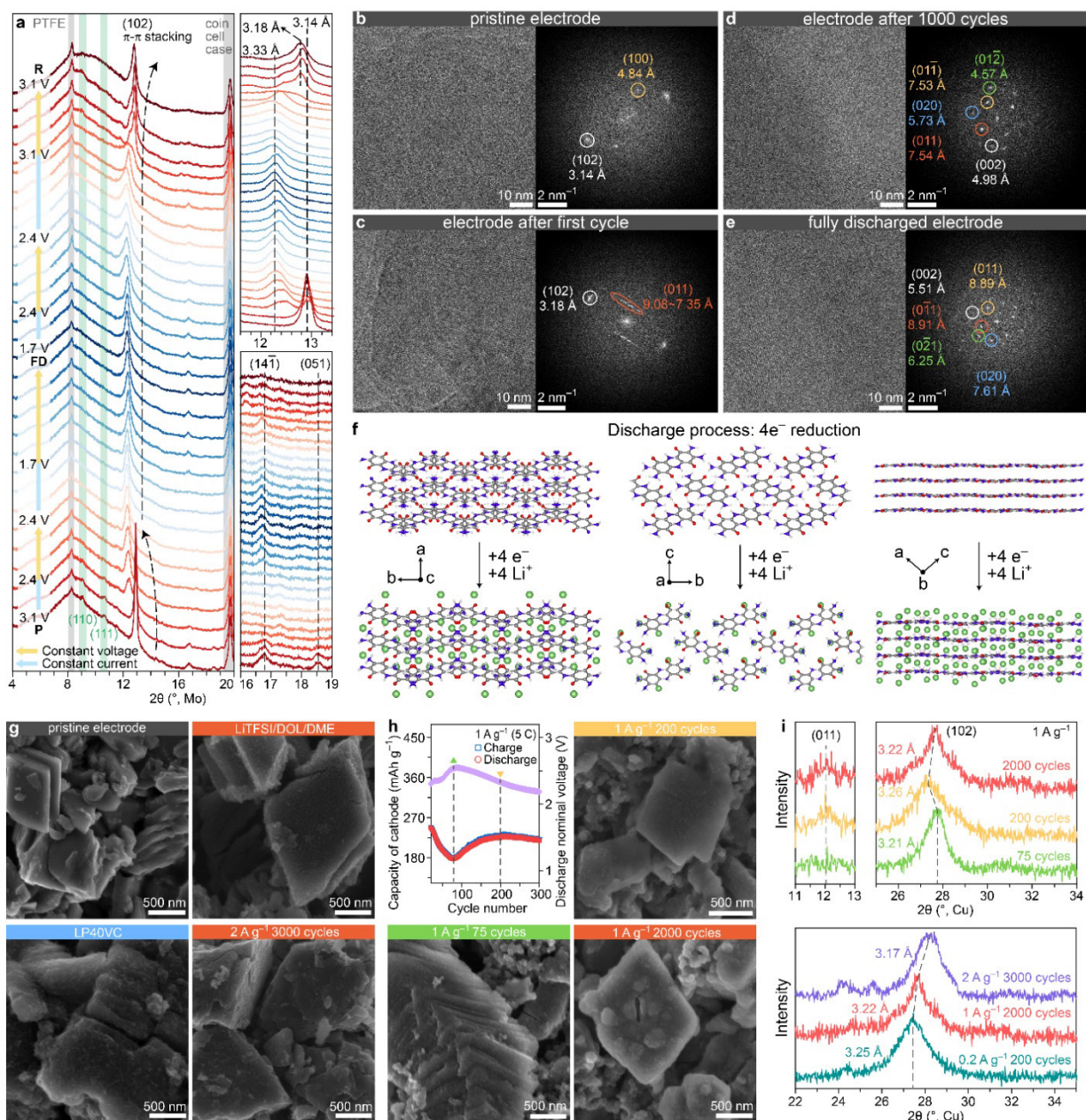
Figure 6.24. Structural and morphological evolution of BTABQ during discharge and charge. **a,** In-situ PXRD patterns of BTABQ recorded at various stages of the first charge/discharge cycle. CCCV protocols were used for both charge and discharge processes to ensure complete chemical transformations at various stages of the cycle. Reversible changes were observed in the out-of-plane (interlayer) and in-plane packing of BTABQ molecules. **b–e,** Ex-situ Cryo-EM images and corresponding FFT of pristine BTABQ, after first cycle, after 1000 cycles and fully discharged electrode. **f**, Crystal structure changes of BTABQ upon discharging shown along *a*, *b*, and *c* crystallographic directions. **g,** Ex-situ SEM images of pristine and cycled electrodes in different electrolytes. **h,** Cycling data of BTABQ at 1 A g^{-1} in LiTFSI/DOL/DME, and the ex-situ SEM images of electrodes after 75, 200, and 2000 cycles. **i,** PXRD patterns of cycled BTABQ electrodes under various current densities.

299
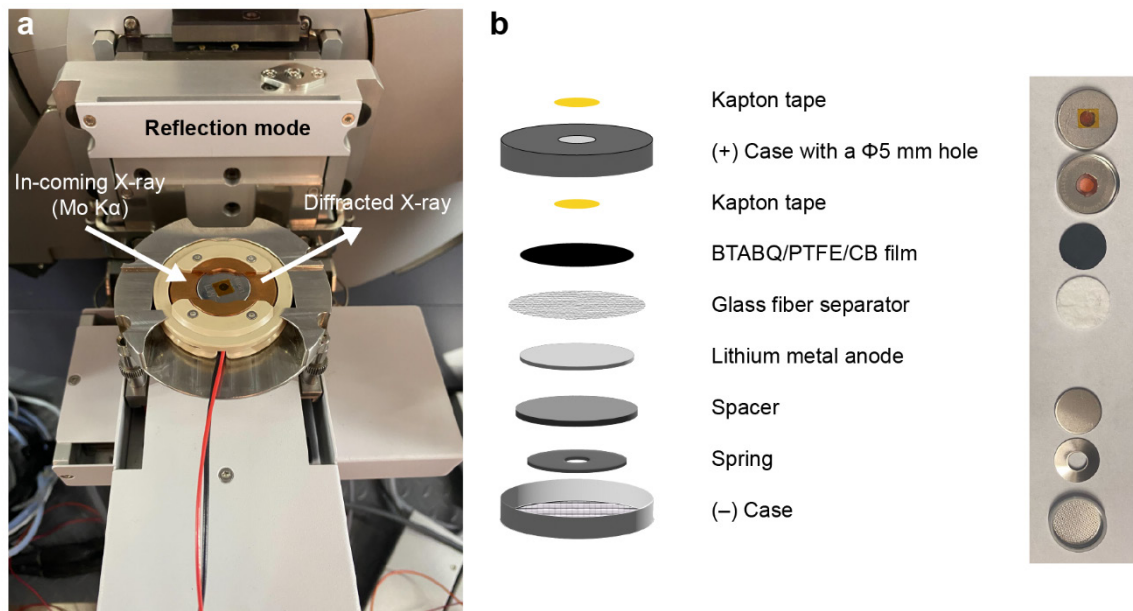
Figure 6.25. Instrument set-up and custom-made coin cell for in-situ PXRD measurements. **a,** In-situ battery holder for coin cell and the Bragg-Brentano configuration of in-situ PXRD measurements. **b,** Schematic illustration, and the photo of custom-made coin for in-situ PXRD measurements.

A more complicated structural and morphological evolution of BTABQ during cycling was observed using LiTFSI/DOL/DME, which is likely the cause of its unique cycling behavior (Figure 6.24h). During the initial drop of capacity to the valley point (~75 cycles), the in-plane arrangement of BTABQ molecules were substantially disturbed, as indicated by the disappearance of (011) reflection in its ex-situ PXRD pattern (Figure 6.24i), which led to significant inhomogeneity of crystallite surface, as verified by the corresponding SEM image (Figure 6.24h). The subsequent cycling revealed an increase of capacity to a maximum after ~200 cycles, during which the in-plane ordering gradually restored and interlayer spacing became notably larger from 3.21 Å to 3.26 Å, as supported by the *ex-situ* PXRD pattern. Consequently, ex-situ SEM image revealed that the inhomogeneity also largely diminished accompanying the restoring of in-plane ordering (Figure 6.24h). Similar to the cases using carbonate electrolytes, the disorder-induced morphological change gradually accumulated during the remaining cycling. Interestingly, the increasing of interlayer spacing is highly dependent on the charging/discharging rate, where slower rates led to more significant expansion (Figure 6.24i), highlighting the importance of layered structures of BTABQ. Overall, the above structural analyses complement the mechanistic understanding of the redox processes (vide supra) and provide a thorough understanding of Li^+ ion intercalation in BTABQ.
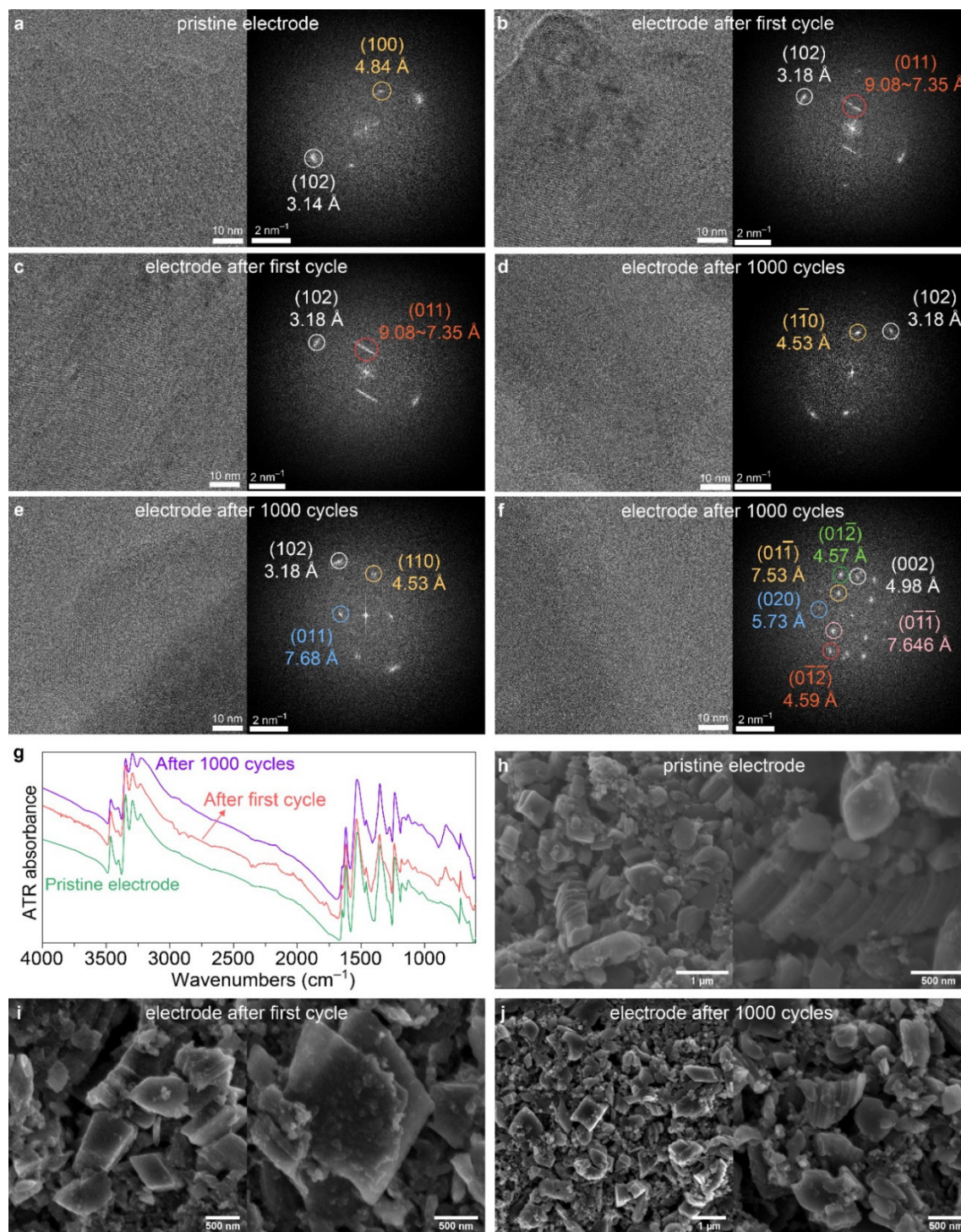
Figure 6.26. *Ex-situ* Cryo-EM, spectroscopic and SEM studies of pristine and cycled BTABQ electrodes. **a,** Cryo-EM images and the corresponding FFT of pristine BTABQ electrodes. **b-c,** Cryo-EM images and the corresponding FFT of BTABQ electrodes after the first discharge-charge cycle. **d-f,** Cryo-EM images and the corresponding FFT of BTABQ after 1000 cycles. **g,** ATR-FTIR spectra of BTABQ electrodes in the pristine state, after the first discharge-charge cycle, and after 1000 cycles. The three essentially identical spectra reveal that the chemical and molecular structure of BTABQ is resilient upon prolonged cycling. **h,** SEM images of pristine BTABQ electrodes. **i,** SEM images of BTABQ electrodes after the first discharge-charge cycle. **j,** SEM images of BTABQ after 1000 cycles.
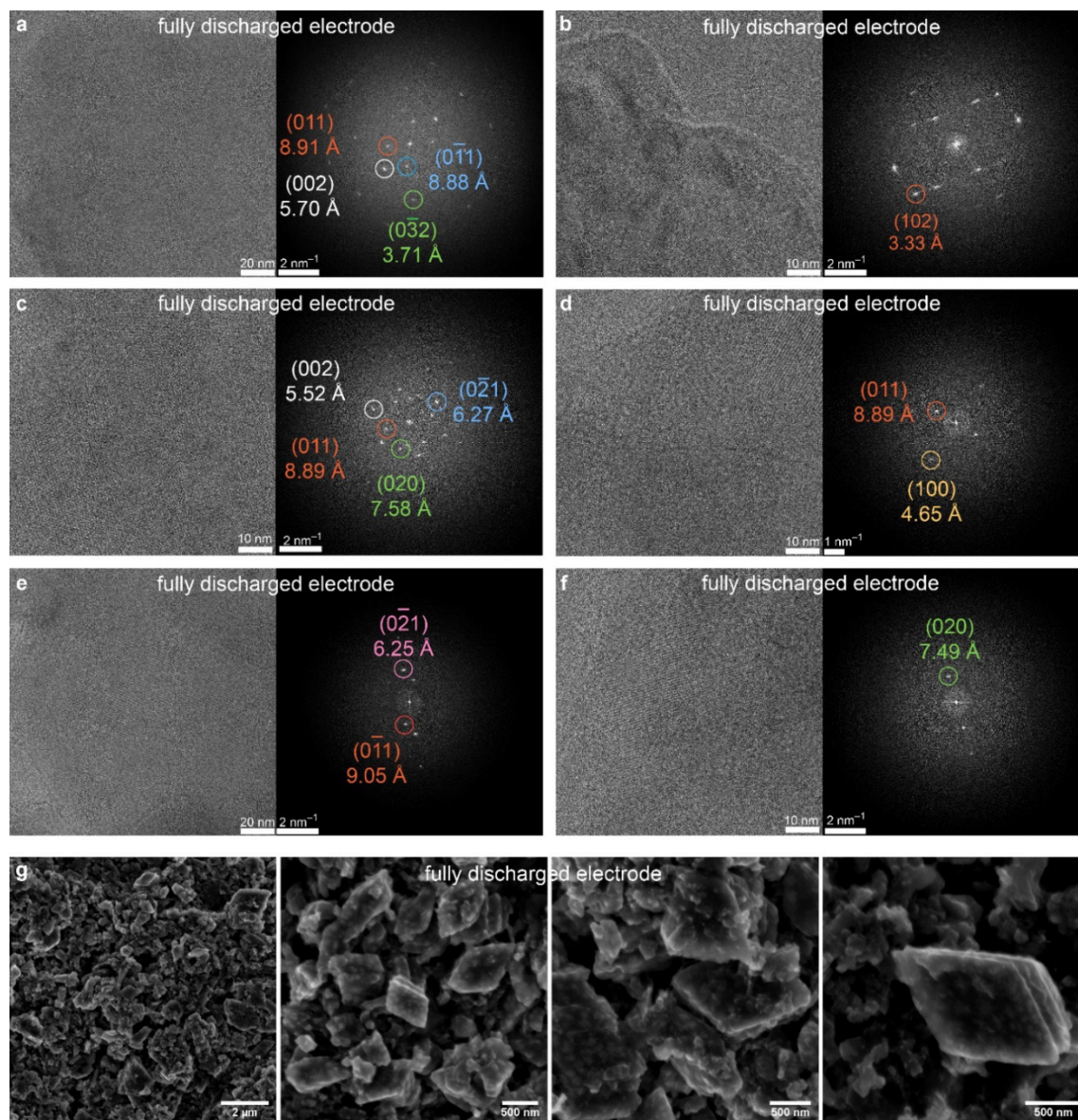
Figure 6.27. *Ex-situ* Cryo-EM and SEM images of discharged BTABQ electrodes. **a-f,** Cryo-EM images and the corresponding FFT of fully discharged BTABQ electrodes. **g,** SEM images of fully discharged BTABQ.
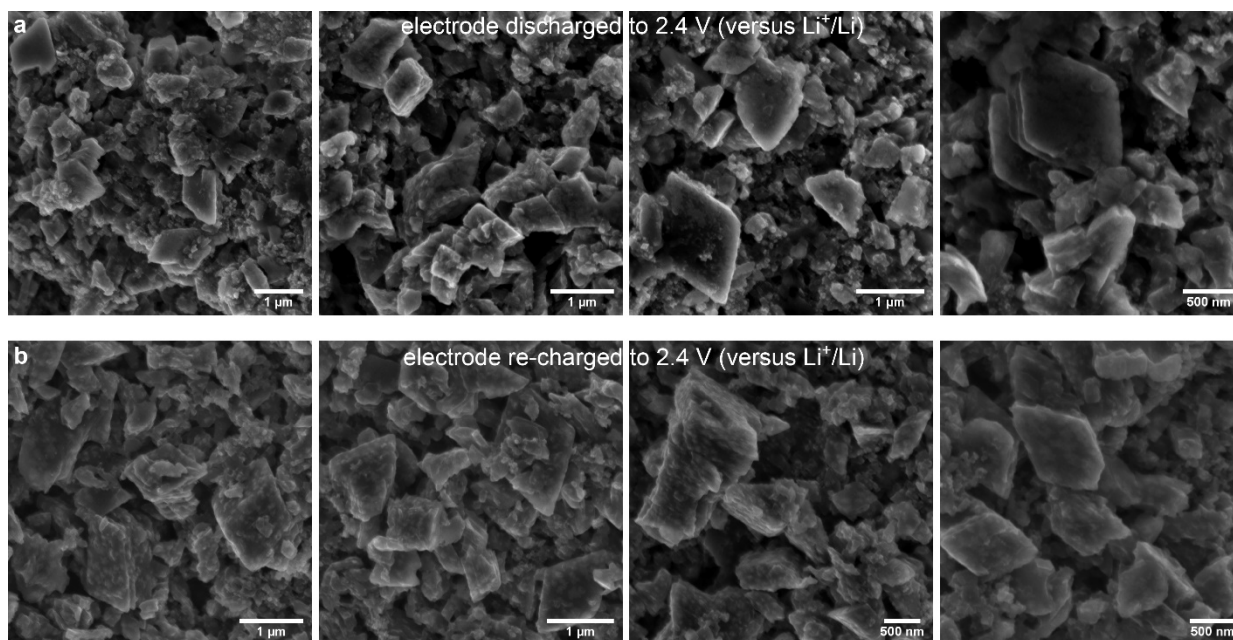
Figure 6.28. *Ex-situ* SEM images of BTABQ composite electrodes. **a,** Electrodes discharged to 2.4 V in the first discharging process. **b,** Electrodes re-charged to 2.4 V in the first charging process.

6.3.5 Towards practical organic rechargeable LIBs

One of the most urgent challenges for OEMs is the difficulty of achieving high areal mass loadings for active materials[31]. Lower material densities of typical OEMs necessitate fabrication of thicker electrodes to achieve similar areal mass loadings relative to inorganic cathodes. However, intrinsically insulating common OEMs render discouragingly high ohmic resistances for electrodes with practical-level mass loadings. Electrically conductive and highly insoluble BTABQ with a crystallographic density of 1.9 g cm^{-3} stands to enable high active-material mass loadings and areal capacities. Indeed, BTABQ-Li cells with mass loadings up to 15 mg cm^{-2} deliver cathode capacities ~230 mAh g^{-1} in LP40VC or LiTFSI/DOL/DME electrolytes (Figures 6.29a, 6.30a). Cycling electrodes with a mass loading of 12 mg cm^{-2} at a current density of 0.1 A g^{-1} and 100% DOD delivered a cathode capacity of 166 mAh g^{-1} after 150 cycles, corresponding to an 87% capacity retention (Figure 6.29b). Moreover, increasing currents from 25 to 125 mA g^{-1} delivered a consistent average discharge voltage of 2.5 V and a 75% capacity retention, indicating good rate capability (Figures 6.29b inset, 6.30b). Furthermore, BTABQ-GrLi full-cells using LP40VC with BTABQ mass loadings as high as 16 mg cm^{-2} and N/P mass ratios as low as 1.1 in LP40VC stored areal cathode capacities reaching 3 mAh cm^{-2} at 25 mA g^{-1} (Figures 6.29a, 6.30c-d).
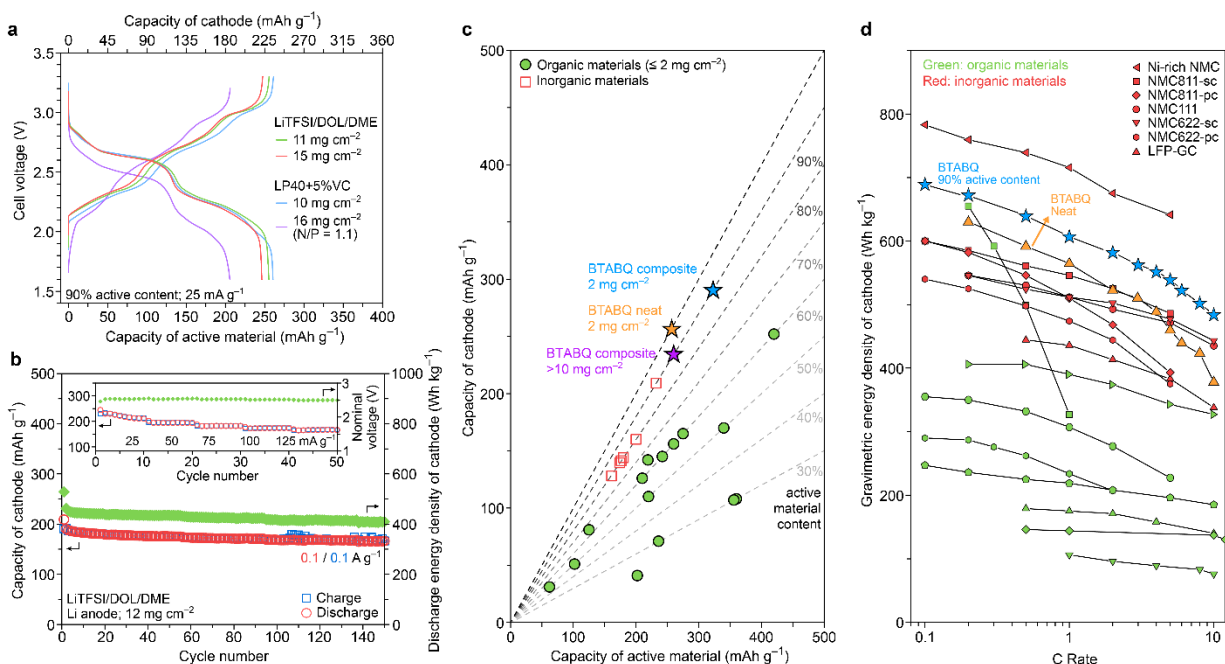
Figure 6.29. Practical-relevant examinations and performance comparisons. **a,** GCD voltage profiles of BTABQ composite electrodes at mass loadings over 10 mg cm^{-2}. Li anodes were used except the purple trace which used GrLi anode. **b,** Cycling study of a BTABQ composite electrode with a mass loading of 12 mg cm^{-2} at 0.1 A g. Inset shows the rate capability study of a BTABQ composite electrode with a mass loading of 11 mg cm^{-2}. **c,** A comparison of active material-based and electrode-based gravimetric specific capacities for various reported OEMs, BTABQ and inorganic cathodes. **d,** A comparison of electrode-based gravimetric energy densities of various cathode materials reported for LIBs. Materials chosen in this comparison have an average discharge voltage greater than 2 V versus Li$^+$/Li. For inorganic cathodes, reports with the highest level of material optimization, i.e., either through electrode coatings, doping or a control on the crystalline domain sizes, are chosen here[38–41]. For organics cathodes, best performing materials are mainly chosen from prominent, recent reviews[5–7].

A comparison of electrode-level specific capacities and energies of BTABQ with state-of-the-art inorganic and organic cathode materials is shown in Figure 6.29c and 6.29d (Tables 6.3, 6.4). Because of the insulating nature and the propensity for dissolution of OEMs, reports on organic electrodes typically require large amounts (30~70 wt.%) of conducting additives and binder, substantially greater than the commercial standard of 5~10 wt.%. However, this important factor is rarely discussed in reports of OEMs that show high material-level metrics, which are commonly achieved at the cost of low electrode-level metrics. In our case, with an active material loading of 90%, BTABQ stores up to 306 and 240 mAh g^{-1} at the electrode-level for mass loadings of 2 and >10 mg cm^{-2}, respectively (Figure 6.29c). Correspondingly, electrode-level specific energies of BTABQ over a range of C rates outperform most well-optimized and best-performing inorganic materials (Figure 6.29d). For instance, BTABQ delivers more electrode-level energy density than single-crystalline NMC811 (NMC811-sc) at charging rates from 0.1 to 10 C. Notably, BTABQ also delivers higher energies than graphite-coated LiFePO$_4$ (LFP-GC), a relatively cheaper material among inorganic cathodes, at charging rates that are at least 10 times faster. Remarkably, BTABQ, being an OEM, also offers broader advantages in terms of resource abundance and ease of synthesis,

projecting savings up to three-fourths of the costs and CO_2 emissions from current technologies per kWh of storage capacity. Detailed in Supplementary Information, we showed that BTABQ can not only be synthesized in large scale using dimethylformamide, but also using environmentally friendly solvents like ethanol and methanol (Figures 6.31-33), which could further contribute to sustainability. Additionally, conventional knowledge on the role of material and cell-level characteristics such as the particle size, electrode coatings and electrolyte additives suggest plenty of room for industry-level optimization of energy storage performance of BTABQ. Similarly, adoption of standard engineering methods, such as calendaring, can further enhance power capability and cycle life. These strategies can draw confidence from the high theoretical energy density of BTABQ (890 Wh kg^{-1}) and compete with the next-generation high-Nickel transition metal layered oxide cathodes. Overall, the demonstration of an organic molecule as a competent and viable alternative for Co-containing inorganic cathodes provides important blueprints toward design and use of sustainable electrode materials in LIBs.
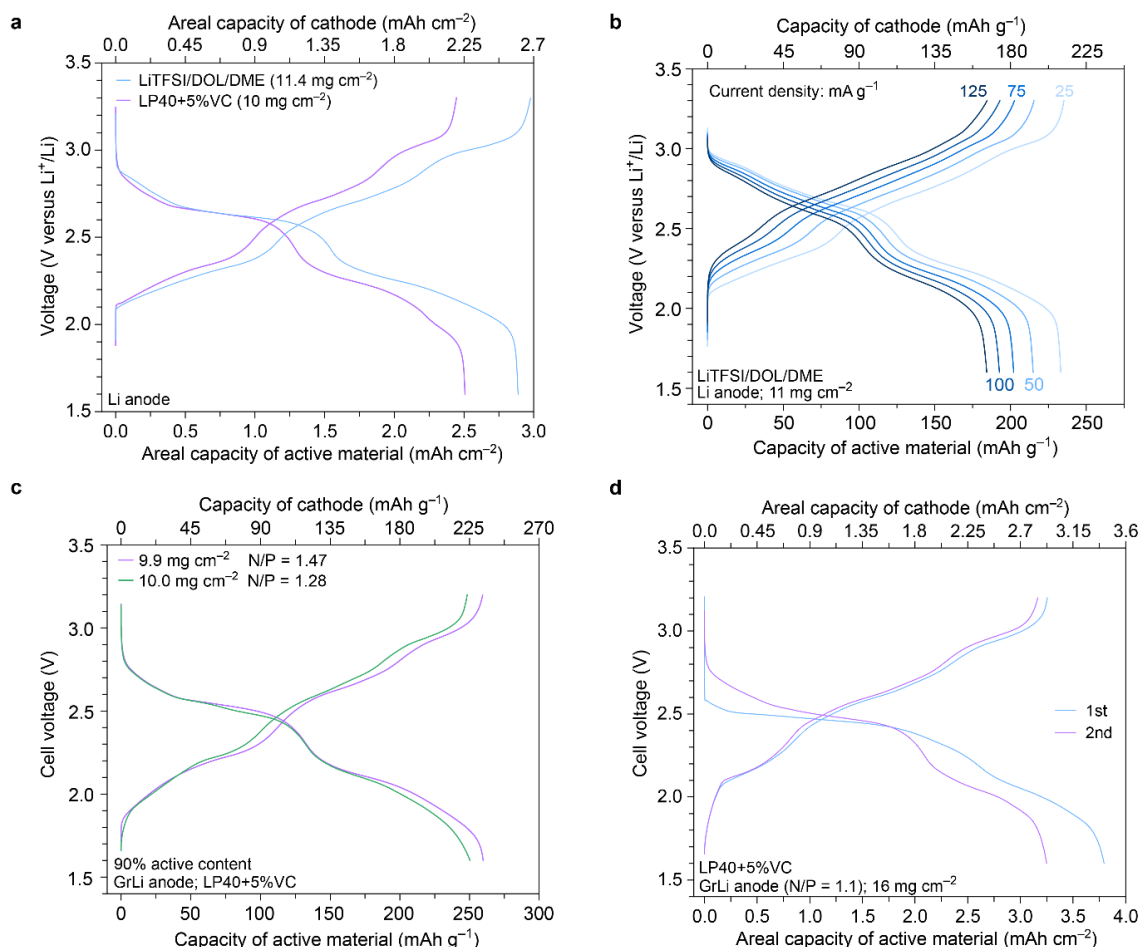
Figure 6.30. Battery performances of half and full cells based on BTABQ composite electrodes with 90% active content and an optimized CMC:SBR ratio of 4:1. **a,** GCD voltage profiles of BTABQ-Li half cells with high active-material mass loadings (> 10 mg cm^{-2}) in LP40VC and LiTFSI/DOL/DME electrolytes. **b,** Voltage profiles of a BTABQ-Li half cell at current densities from 25 to 125 mA g^{-1}. **c, d,** Voltage profiles of BTABQ-GrLi full cells in LP40VC.

Table 6.3. Electrochemical performance of BTABQ versus reported organic cathode materials.

Active Material	Electrode composition (Active material: Conductive Carbon: Binder)	Highest specific capacity of active material (mAh/g)	Highest specific capacity of the electrode (mAh/g)	Average discharge voltage (V vs. Li$^+$/Li)	Electrode based energy density (Wh/kg)
Used in Figure 5c:					
LiDHAQS	50:40:10	340	**170**	2.5	425 at 0.1 C
Lawsone-Li	60:30:10	275	**165**	2.25	371 at 0.2 C
PDHBQ	60:30:10	242	**145**	2.0	291 at 0.2 C
PTO	30:60:10	360	**108**	2.74	295 at 0.1 C
PI5	60:30:10	210	**126**	2.4	303 at 1 C
PDB	30:60:10	236	**71**	2.5	177 at 0.1 C
N-heteroaromatic (3Q)	30:60:10	356	**108**	1.7	182 at 1 C
TEMPO	65:30:5	125	**81**	3.4	275 at 0.5 C
Used in Figure 5c and 5d:					
Li$_4$DHTPA	65:30:5	219	**142**	2.5	355 at 0.1 C 227 at 5 C
Calix[4]quinone	60:30:10	420	**252**	2.6	655 at 0.2 C 327 at 1 C
TPBQ	50:40:10	220	**110**	2.25	247 at 0.1 C 196 at 5 C
AQC	60:30:10	210	**126**	2.3	290 at 0.1 C 234 at 1 C
PBQS	60:30:10	260	**156**	2.6	406 at 0.1 C 343 at 5 C
Pentakis-fused tetrathiafulvalene	20:70:10	202	**41**	3.6	144 at 1 C 137 at 10 C
PVMPT	50:40:10	62	**31**	3.45	106 at 1 C 76 at 10 C
PTMA	50:40:10	110	**55**	3.5	192 at 0.1 C 158 at 5 C
TAPT	60:30:10	353	**212**	2.5	529 at 0.3 C 432 at 5.6 C
BTABQ	**90:5:5**	**340**	**306**	**2.5**	**765 at 0.125C**

Table 6.4. Electrochemical performance of BTABQ versus reported inorganic cathode materials.

Active Material	Electrode composition (Active material: Conductive Carbon: Binder)	Highest specific capacity of active material (mAh/g)	Highest specific capacity of the electrode (mAh/g)	Average discharge voltage (V vs. Li^+/Li)	Electrode based energy density (Wh/kg)
NMC622-SC	80:10:10	180	144	3.75	540 at 0.1 C 375 at 5 C
NMC622-PC	80:10:10	180	144	3.75	540 at 0.1 C 393 at 5 C
NMC811-SC	80:10:10	200	160	3.75	600 at 0.1 C 486 at 5 C
NMC811-PC	80:10:10	200	160	3.75	600 at 01 C 393 at 5 C
H-NMC111	80:10:10	175	140	3.9	546 at 0.1 C 471 at 5 C
LFP-GC	80:10:10	161	129	3.45	555 at 0.5 C 422 at 10 C
LCMO-LCO	80:10:10	175	140	3.9	546 at 0.1 C 477 at 5 C
Ni-Rich	90:5:5	232	208	3.75	870 at 0.1 C 712 at 5 C
BTABQ	**90:5:5**	**340**	**306**	**2.5**	**765 at 0.125 C** **540 at 5 C**
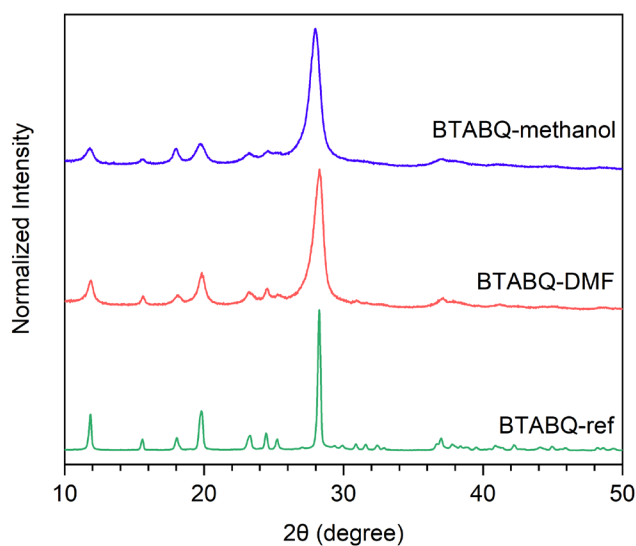
Figure 6.31. PXRD patterns of BTABQ synthesized using different methods. BTABQ-ref is synthesized using the procedures described in the 6.4.2; BTABQ-DMF is synthesized in DMF without the use of tetrabutylammonium salts; BTABQ-methanol is synthesized in methanol.
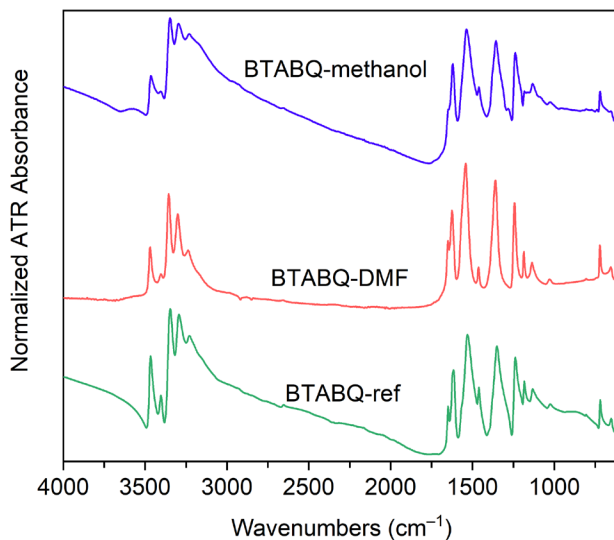
Figure 6.32. ATR-FTIR spectra of BTABQ synthesized using different methods. BTABQ-ref is synthesized using the procedures described in the Method part; BTABQ-DMF is synthesized in DMF without the use of tetrabutylammonium salts; BTABQ-methanol is synthesized in methanol.
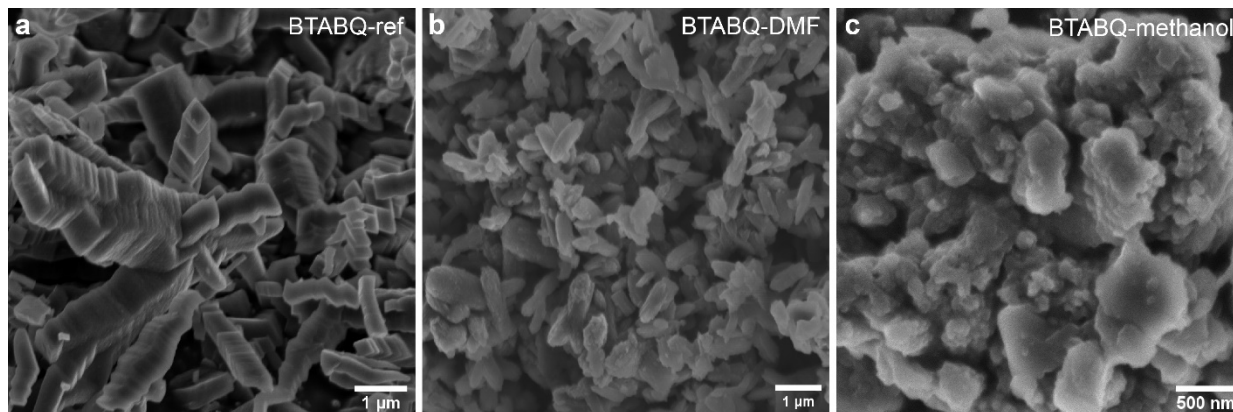
Figure 6.33. SEM images of BTABQ synthesized using different methods. **a,** BTABQ synthesized using the procedures described in the Method part. **b,** BTABQ synthesized in DMF without the use of tetrabutylammonium salts. **c,** BTABQ synthesized in methanol.

6.4 Materials and Methods

6.4.1 Materials

All commercially available chemicals were used without further purification unless otherwise noted. Potassium phthalimide (98%, Sigma-Aldrich), acetonitrile (HPLC grade, Sigma-Aldrich), dimethylformamide (HPLC grade, VWR Chemicals BDH), hydrazine hydrate (Sigma- Aldrich), tetrabutylammonium chloride (99%, Alfa-Aesar), tetrabutylammonium bromide (98%, Sigma-Aldrich), methanol (VWR Chemicals BDH), ethanol (KOPTEC 200 proof), LP30 (GOTION), LP40 (GOTION), LiTFSI (Battery grade, DoDoChem), DOL (Battery grade, DoDoChem), DME (Battery grade,

DoDoChem), vinylene carbonate (Battery grade, Sigma-Aldrich). All yields refer to isolated yields. House DI water and house nitrogen were used during the synthesis. NMR solvents were purchased from Cambridge Isotope Laboratory.

6.4.2 Synthetic Methods

BTABQ is synthesized using a solvothermal method in dimethylformamide. Precursor tetraamino-*p*-benzoquinone (TABQ) is synthesized using the procedure described in 3.5.2. To a 250 mL pressure tube with a PTFE cap was added 1.07 g of TABQ, 6.8 g of tetrabutylammonium chloride (99%, Alfa Aesar), and 60 mL of dimethylformamide. The tube was capped under ambient conditions, sonicated for 1 min, and heated in an isothermal oven at 120 °C for 12 hours, after which it was cooled down to room temperature. Then the reaction mixture was filtered and washed with DMF until the filtrate coming out became colorless. The resulting dark-greenish black solid was further washed with methanol and dried under air yielding 0.32 g of BTABQ (33% yield). BTABQ is poorly soluble in common NMR solvents. Solid-state NMR of BTABQ: 169.3 ppm (*C*=O), 140.8 ppm (*C*=N), 129.1 ppm/124.5 ppm (*C*–N/*C*–O). Elemental analysis: $C_{12}H_{10}O_4N_6$, found: C, 47.45%; H, 3.25%; N, 27.08%; calculated: C, 47.69%; H, 3.33%; N, 27.81%. MALDI-TOF: $[M+H]^+$: found, 302.808; calculated: 303.1; within the ±1 Da error of the instrument. FTIR (cm^{-1}): 3470, 3404, 3356, 3298, 3235, 1651, 1626, 1614, 1568, 1543, 1462, 1364, 1244, 1186, 1136, 721, 654. The crystal structure and phase purity of BTABQ were characterized by the WAXS pattern.

6.4.3 Electrochemical Measurements

Electrochemical performances of BTABQ were tested in half-cell and full-cell configurations using CR2032 coin cells. All electrode preparations were carried out under ambient conditions. Neat BTABQ electrodes (i.e., 100% active material content) were made by coating well-mixed (upon sonication) slurry of BTABQ in ethanol on stainless steel disks. BTABQ composite electrodes contain 90 wt% of BTABQ, 5 wt% of carbon black (CB) and 5 wt% of mixtures of carboxymethyl cellulose (CMC) and styrene butadiene rubber (SBR) with various ratios. CMC and SBR were well dissolved/suspended in small amount of water (50~100 μL/mg) upon heating at 85 °C and vigorous stirring for an hour. Well-mixed BTABQ and CB powders were transferred into the CMC/SBR aqueous mixture, and the resulting suspension was vigorously stirred at 85 °C for an hour to produce the electrode slurry, which was then coated on stainless steel disks. All electrodes were dried under ambient condition before drying overnight in a vacuum oven at 100 °C. Areal mass loadings of the dried electrodes are 1.5 – 3.0 mg cm^{-2} for studies using low mass loadings, and 10 – 16 mg cm^{-2} for practical-relevant studies. Resulting areal specific capacities ranged from 0.5 to 3.2 mAh cm^{-2}. Half-cell tests were performed in coin cells assembled in an Argon-filled glove box using a Lithium chip or pre-lithiated graphite as the counter electrode and a piece

of Celgrad-2025 as the separator. For this, large pieces of commercial graphite (MTI Corporation) (> 14 mg) were first electrochemically pre-lithiated in Li-half-cells in two full cycles of charge and discharge at a slow current rate of 0.05 C. Similarly, full cells were assembled using BTABQ cathode and pre-lithiated graphite anodes in N(negative)/P(positive) mass ratios ranging from 1 – 1.5. Slurries of commercial graphite powders (<20 µm, Sigma Aldrich) were prepared by mixing 90 wt% graphite with 5 wt% carbon black (CB), 2.5 wt% Carboxymethyl cellulose (CMC) and 2.5 wt% Styrene Butadiene Rubber (SBR) using water and coating on copper foils. Commercial electrolyte composition containing 1 M $LiPF_6$ dissolved in ethylene carbonate: dimethyl carbonate = 1:1 solvent (LP 30) was used for most tests whereas, specialized composition of LP 40 (ethylene carbonate: diethyl carbonate = 1:1 solvent) and 5 wt% vinylene carbonate as an additive, were used for data in Figure 4. All electrochemical tests were performed within a potential range of 1.6 – 3.2 V versus Li^+/Li. Charge-discharge electrochemical tests were conducted using Landt Instruments at room temperature (25 °C). Galvanostatic Intermittent Titration Technique (GITT) and Cyclic voltammetry tests were performed using a BioLogic VMP-3 workstation. GITT measurements are carried out using a typical step profile at a current density of 25 mA g^{-1}, where each step consists of a 1-hour constant current charge or discharge and a subsequent 2-hour rest. During the GITT measurement, the electrode is completely wetted, so that the capacitive current measured arises entirely from the voltage sweep:

$$A \approx \frac{i}{C_m}\left(\frac{dE}{dt}\right)^{-1}$$

Where A is the real electrode electrolyte wetting area, C_m is the specific capacitance (18 µF cm^{-2}), E is the voltage. The real electrode electrolyte wetting area is calculated to be A = 2.37 cm^2.

The effective chemical lithium diffusion coefficient in the active material can be derived from the GITT potential response by following the method by Weppner and Huggins.[ref] The chemical diffusion coefficient can be calculated at each step, with the following formula:

$$D = \frac{4}{\pi}\left(\frac{iV_m}{Z_A FS}\right)^2\left[\left(\frac{dE}{d\delta}\right)\Big/\left(\frac{dE}{d\sqrt{t}}\right)\right]^2$$

Here, i is the current (A); V_m is the molar volume of the electrode (cm^3 mol^{-1}); Z_A is the charge number; F is the Faraday's constant (96485 C mol^{-1}); S is the electrode-electrolyte contact area (cm^2); $dE/d\delta$ is the slope of the coulometric titration curve, found by plotting the steady state voltages E (V) measured after each titration step δ; $dE/d\sqrt{t}$ is the slope of the linearized plot of the potential E (V) during the current pulse of duration t (s).

If sufficient small currents are applied for short time intervals, so that $dE/d\sqrt{t}$ can be considered linear and the coulometric titration curve can be also considered linear over the composition range involved in that step, we can get:

$$D = \frac{4}{\pi\tau}\left(\frac{n_m V_m}{S}\right)^2 \left[\frac{\Delta E_s}{\Delta E_t}\right]^2 \quad \left(\tau \ll {L^2}/{D}\right)$$

Here, τ is the duration of the current pulse (s); n_m is the number of moles (mol) of the active material; V_m is the molar volume of the electrode (cm^3 mol^{-1}); S is the electrode-electrolyte contact area (cm^2); ΔE_s is the steady-state voltage change, due to the current pulse and ΔE_t is the voltage change during the constant current pulse, eliminating the iR drop. L is the film thickness. The figure below shows the examples for charge and discharge, where $\Delta E_s = E_4 - E_3$, $\Delta E_t = E_2 - E_1$.

The measured density of the electrode is 1.1 g cm^{-3}, giving $V_m = 274.6$ cm^3 mol^{-1}.
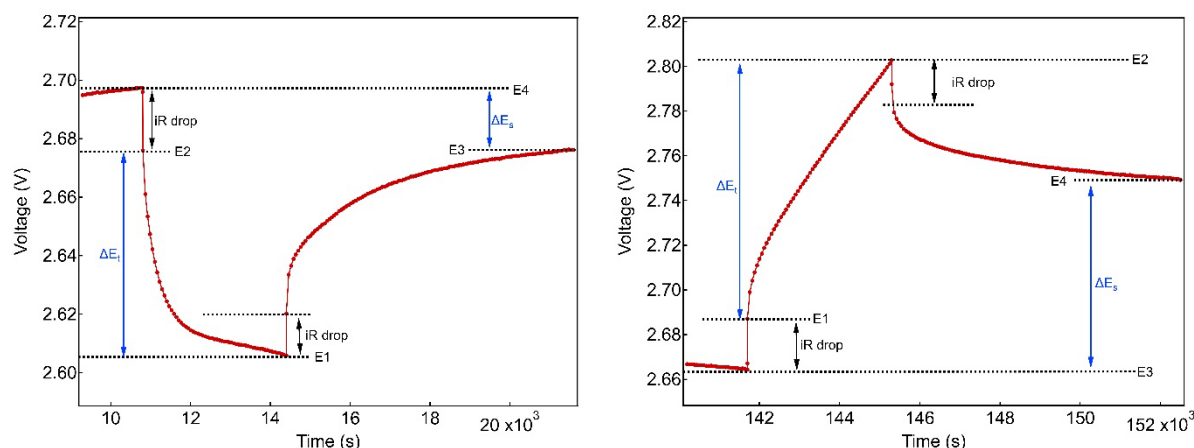
6.4.4 *In-situ* Powder X-Ray Diffraction

The *in-situ* PXRD measurements are performed using custom-made half-cells (Figure 6.25) on a Panalytical Empyrean diffractometer equipped with a Mo X-ray source, focusing mirror and Galipix 3D detector. The corresponding electrodes are prepared as thin films by repeated kneading and rolling of a slurry of activated carbon, acetylene black and a PTFE solution mixture (8:1:1) with ethanol. The prepared films are dried at 100 °C overnight prior to use. The PXRD patterns are recorded in the Bragg-Brentano θ/2θ geometry using an in-operando coin cell battery holder from 4° to 20°. The coin cell undergoes the first constant-current discharge at 0.1 C to 2.4 V and a subsequent constant-voltage step at 2.4 V for 5 hours. Then the coin cell undergoes the second constant-current discharge at 0.1 C to 1.7 V and a subsequent constant-voltage step at 1.7 V for 5 hours. For the re-charging process, two constant-voltage steps are at 2.4 V and 3.1 V, respectively.

6.4.5 Cryo-EM analyses

High-resolution Cryo-EM images were obtained at the Automated Cryogenic Electron Microscopy Facility in MIT.nano on a Talos Arctica G2 microscope operated at an accelerating voltage of 200 kV with a Falcon3EC direct electron detector. Pristine samples were prepared by sonicating BTABQ powders in isopropanol for 5 to 10 seconds. Discharged and recharged electrode samples were washed with dry THF in Ar box after dissembling coin cells, and the washed electrodes were dried under vacuum. The dried samples were dispersed in dry THF and sonicated for 30 to 60 seconds. Specimens were prepared by drop-casting sonicated samples onto C-flat^{TM} Cu grids with holey carbon for Cryo-EM in the glovebox. The TEM measurement conditions were adapted from previous report. All image acquisition was done using EPU at an exposure time of 5 s, with focusing done adjacent to the region imaged to minimize beam exposure prior to image acquisition (standard low dose imaging protocols). Analysis of the raw HRTEM data was done using Digital Micrograph (Gatan Microscopy Suite software).

According to the Cryo-EM images of the electrode after 1000 cycles and their FFT patterns, the d spacings of (020), (002), (102), and ($1\bar{1}0$) planes are found to be 5.73 Å, 4.98 Å, 3.18 Å, and 4.53 Å, respectively. Therefore, referring to the equation for calculating the d spacing of (hkl) planes in Monoclinic crystal systems,

$$\frac{1}{d_{hkl}^2} = \frac{1}{\sin^2 \beta} \left(\frac{h^2}{a^2} + \frac{k^2 \sin^2 \beta}{b^2} + \frac{l^2}{c^2} - \frac{2hl \cos \beta}{ac} \right)$$

we can obtain:

$$\begin{cases} a = 5.05 \text{ Å} \\ b = 11.46 \text{ Å} \\ c = 10.20 \text{ Å} \\ \beta = 102.35° \end{cases}$$

Similarly, based on the Cryo-EM images of fully discharged electrodes and their Fast Fourier-Transform (FFT) patterns, the d spacings of (020), (021), (102), (011), and (100) planes are found to be 7.61 Å, 6.25 Å, 3.33 Å, 8.89 Å, and 4.65 Å, respectively. Therefore, we can obtain:

$$\begin{cases} a = 4.69 \text{ Å} \\ b = 15.22 \text{ Å} \\ c = 11.06 \text{ Å} \\ \beta = 97.79° \end{cases}$$

6.4.6 Other Characterization Methods

Powder X-ray diffraction (PXRD)

Laboratory PXRD patterns were recorded using a Bruker Advance II diffractometer equipped with a θ/2θ reflection geometry and Ni-filtered Cu Kα radiation (Kα$_1$ = 1.5406 Å, Kα$_2$ = 1.5444 Å, Kα$_2$/ Kα$_1$ = 0.5). The tube voltage and current were 40 kV and 40 mA, respectively. Samples for PXRD were prepared by placing a thin layer of the appropriate material on a zero-background silicon crystal plate. For *ex-situ*

measurements, the washed and dried electrodes were placed onto the zero-background silicon crystal plate together with the stainless-steel current collector.

Wide-angle X-ray scattering (WAXS) measurements

WAXS measurements were conducted at the Soft Matter Interfaces beamline (12-ID) of the National Synchrotron Light Source II (NSLS-II) at Brookhaven National Laboratory with a beam energy of 16.1 keV and beam size of 200×20 μm. The Scattered data were collected in vacuum with a PILATUS3 300 kW detector (Dectris, Switzerland), consisting of 0.172 mm square pixels in a 1475×195 array. To obtain a wide range of wave vector transfer (q), a series of 2D diffraction patterns were collected by rotating the detector on an arc with the sample-to-detector distance being 275 mm. Scattering patterns from each detector angle were stitched together using custom software and then reduced to 1D scattering intensity versus q curve by circular average.

Elemental analyses (EA)

EA were performed by Robertson Microlit Laboratories, Ledgewood, New Jersey.

Scanning electron microscopy (SEM)

SEM images were collected at MIT MRSEC (formerly the Center for Materials Science and Engineering, or CMSE) on a Zeiss Merlin high-resolution scanning electron microscope with an InLens detector at an operating voltage of 3 or 4 kV.

Diffuse reflectance infrared Fourier transform spectroscopy (DRIFTS)

DRIFTS measurements were performed on a Bruker Tensor 37 (MIR source and KBr beam splitter) with a mercury cadmium telluride (MCT, cooled with LN_2) detector utilizing the DiffusIR™ accessory (Pike Technologies). To ensure air-free measurement, a sealable environmental chamber equipped with ZnSe window (Pike Technologies) was used. Samples were ground in air (or under Ar for ex-situ measurements) with dry KBr in a mortar and pestle (99.9%, Pike technologies) to produce solid mixtures (0.5-1% wt.). The data was averaged over 128 scans between $4000 - 600$ cm^{-1} with the resolution of 4 cm^{-1}. Each of the Kubelka-Munk function (F(R)) transformed DRIFTS spectra were normalized with respect to the DRUV–vis–NIR data by matching the F(R) values at 4000 cm^{-1}.

Diffuse reflectance UV-vis-NIR spectroscopy (DRUV–vis–NIR)

DRUV-Vis-NIR spectra were collected on a Cary 5000i spectrophotometer fitted with the UV-Vis DiffusIR accessory (Pike Technologies) between 200 and 2500 nm, at the scan rate of 600 nm/min under ambient conditions. A KBr baseline and a zero-background correction were collected prior to the sample measurements. Samples were prepared as described above for the DRIFTS measurements.

Room temperature electrical conductivity measurements

Electrical conductivities were measured at 296 K in ambient atmosphere on pressed pellets using a 2-probe or 4-probe setup described previously (Scheme 6.1). At least three pellets from different batches of

each sample were measured. The thickness of the pellets is between 0.3 mm and 1 mm. For each sample, the conductivity values were averaged to give the average conductivity value.

Variable temperature electrical conductivity measurements

Temperature-dependent electrical conductivities were collected from 270 K to 390 K using a Quantum Design PPMS DynaCool instrument equipped with the Electrical Transport Option. A four-contact probe cell was fabricated for the measurements as described previously. The temperature was varied at 5 K/min, and the resistance value was collected in AC mode for every 1 K. At least two heating-cooling cycles were performed. The phase angle remained within 1° throughout the entire temperature range of interest, which means that the difference of AC and DC resistance is below 1%.

Two-probe:

$$\sigma = \frac{L}{RA}$$

Four-probe:

$$\sigma = \frac{I}{V} \times \frac{L}{wt}$$
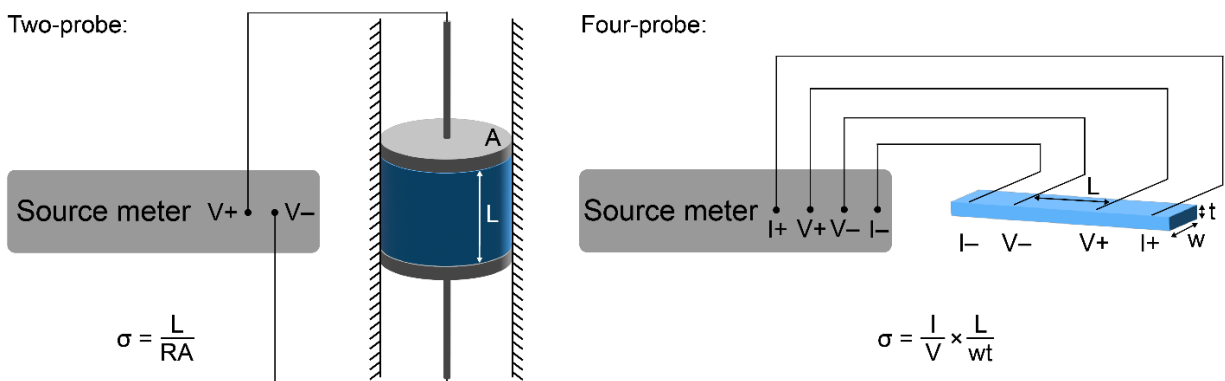
Scheme 6.1. Two-probe and four-probe setups for electrical conductivity measurements.

Computation

The calculations of both keto- and enol-form of BTABQ, including HOMO/LUMO energies and vibrational spectroscopy, were conducted at B3LYP/ma-def2-QZVP or B3LYP/def2-TZVP level using ORCA. Calculations of discharged BTABQ were conducted using the CASTEP software. Structures were equilibrated using the non-spin polarized GGA-PBEsol exchange-correlation function with a 489.8 eV plane-wave cut-off. Electronic convergence criteria were set to 2×10^{-6} eV/atom. The unit cell dimensions were taken from experimental results with no further optimization. Dispersion corrections were added by using the Tkatchenko-Scheffler method. OTFG ultrasoft pseudopotentials were used. The k-point set was $4\times1\times2$. The single-point calculations for the band structures were calculated using the same method, except with a 571.4 eV cut-off, a $5\times2\times3$ k-point set, and 1×10^{-6} eV/atom convergence criteria.

6.5 References

(1) Tarascon, J.-M., Key challenges in future Li-battery research. *Philos. Trans. R. Soc. A* **368**, 3227–3241 (2010).

(2) Sovacool, B. K., The precarious political economy of cobalt: Balancing prosperity, poverty, and brutality in artisanal and industrial mining in the Democratic Republic of the Congo. *Extr. Ind. Soc.* **6**, 915–939 (2019).

(3) Turcheniuk, K., Bondarev, D., Singhal, V., and Yushin, G. Ten years left to redesign lithium-ion batteries. *Nature* **559**, 467–470 (2018).

(4) Larcher, D., and Tarascon, J.-M. Towards greener and more sustainable batteries for electrical energy storage. *Nat. Chem.* **7**, 19–29 (2015).

(5) Poizot, P., Gaubicjer, J., Renault, S., Dubois, L., Liang, Y., and Yao, Y., Opportunities and Challenges for Organic Electrodes in Electrochemical Energy Storage. *Chem. Rev.* **120**, 6490–6557 (2020).

(6) Lu, Y., and Chen, J. Prospects of organic electrode materials for practical lithium batteries. *Nat. Rev. Chem.* **4**, 127–142 (2020).

(7) Kim, J., Kim, Y. Yoo, J., Kwon, G., Ko, Y., and Kang, K., Organic batteries for a greener rechargeable world. *Nat. Rev. Mater.* **8**, 54–70 (2023).

(8) Gent, W. E., Busse, G. M., and House, K. Z. The predicted persistence of cobalt in lithium-ion batteries. *Nat. Energy* **7**, 1132–1143 (2022).

(9) Mizushima, K., Jones, P. C., Wiseman, P. J., and Goodenough, J. B. Li_xCoO_2 ($0 < x < -1$): A new cathode material for batteries of high energy density. *Mater. Res. Bull.* **15**, 783–789 (1980).

(10) Gummow, R. J., and Thackeray, M. M. Lithium-cobalt-nickel-oxide cathode materials prepared at 400°C for rechargeable lithium batteries. *Solid State Ion.* **53–56**, 681–687 (1992).

(11) Shaju, K. M., Subba Rao, G. V., and Chowdari, B. V. R. Performance of layered $Li(Ni_{1/3}Co_{1/3}Mn_{1/3})O_2$ as cathode for Li-ion batteries. *Electrochim. Acta* **48**, 145–151 (2002).

(12) Patoux, S., and Doeff, M. M. Direct synthesis of LiNi1/3Co1/3Mn1/3O2 from nitrate precursors. *Electrochem. Commun.* **6**, 767–772 (2004).

(13) Padhi, A. K., Nanjundaswamy, K. S., and Goodenough, J. B. Phospho-olivines as Positive-Electrode Materials for Rechargeable Lithium Batteries. *J. Electrochem. Soc.* **144**, 1188 (1997).

(14) Padhi, A. K., Nanjundaswamy, K. S., Masquelier, C., Okada, S., and Goodenough, J. B. Effect of Structure on the Fe^{3+}/Fe^{2+} Redox Couple in Iron Phosphates. *J. Electrochem. Soc.* **144**, 1609 (1997).

(15) Rozier, P., and Tarascon, J. M. Review—Li-Rich Layered Oxide Cathodes for Next-Generation Li-Ion Batteries: Chances and Challenges. *J. Electrochem. Soc.* **162**, A2490 (2015).

(16) Li, W., Erickson, E. M., and Manthiram, A. High-nickel layered oxide cathodes for lithium-based automotive batteries. *Nat. Energy* **5**, 26–34 (2020).

(17) Schmuch, R., Wagner, R., Hörpel, G., Placke, T., and Winter, M. Performance and cost of materials for lithium-based rechargeable automotive batteries. *Nat. Energy* **3**, 267–278 (2018).

(18) Wang, S., Wang, L., Zhang, K., Zhu, Z., Tao, Z., and Chen. J., Organic $Li_4C_8H_2O_6$ Nanosheets for Lithium-Ion Batteries. *Nano Lett.* **13**, 4404–4409 (2013).

(19) Kolek, M., Otteny, F., Schmidt, P., Mück-Lichtenfeld. C., Einholz, C., Becking, J., Schleicher, E., Winter, M., Bieker, P., and Esser, B., Ultra-high cycling stability of poly(vinylphenothiazine) as a battery cathode material resulting from π–π interactions. *Energy Environ. Sci.* **10**, 2334–2341 (2017).

(20) Song, Z. Qian, Y., Liu, X., Zhang, T., Zhu, Y., Yu, H., Otani, M., and Zhou, H., A quinone-based oligomeric lithium salt for superior Li–organic batteries. *Energy Environ. Sci.* **7**, 4077–4086 (2014).

(21) Luo, Z., Liu, L., Zhao, Q., Li, F., and Chen, J. An Insoluble Benzoquinone-Based Organic Cathode for Use in Rechargeable Lithium-Ion Batteries. *Angew. Chem., Int. Ed.* **56**, 12561–12565 (2017).

(22) Peng, C. Ning, G.-H., Su, J., Zhong, G., Tang, W., Tian, B., Su, C., Yu, D., Zu, L., Yang, J., Ng, M.-F., Hu, Y.-S., Yang, Y., Armand, M., and Loh, K. P., Reversible multi-electron redox chemistry of π-conjugated N-containing heteroaromatic molecule-based organic cathodes. *Nat. Energy* **2**, 1–9 (2017).

(23) Liang, Y., Zhang, P., and Chen, J. Function-oriented design of conjugated carbonyl compound electrodes for high energy lithium batteries. *Chem. Sci.* **4**, 1330–1337 (2013).

(24) Lee, J., and Park, M. J. Tattooing Dye as a Green Electrode Material for Lithium Batteries. *Adv. Energy Mater.* **7**, 1602279 (2017).

(25) Huang, W., Zhu, Z., Wang, L., Wang, S., Li, H., Tao, Z., Shi, J., Guan, L., Chen, J., Quasi-Solid-State Rechargeable Lithium-Ion Batteries with a Calix[4]quinone Cathode and Gel Polymer Electrolyte. *Angew. Chem., Int. Ed.* **52**, 9162–9166 (2013).

(26) Chen, T., Banda, H., Yang, L., Zhang, Y., Parenti, R., and Dincă, M., High-rate, high-capacity electrochemical energy storage in hydrogen-bonded fused aromatics. *Joule* **2023**, in press.

(27) Tukamoto, H., and West, A. R. Electronic Conductivity of LiCoO2 and Its Enhancement by Magnesium Doping. *J. Electrochem. Soc.* **144**, 3164 (1997).

(28) Amin, R., and Chiang, Y.-M. Characterization of Electronic and Ionic Transport in $Li_{1-x}Ni_{0.33}Mn_{0.33}Co_{0.33}O_2$ (NMC333) and $Li_{1-x}Ni_{0.50}Mn_{0.20}Co_{0.30}O_2$ (NMC523) as a Function of Li Content. *J. Electrochem. Soc.* **163**, A1512 (2016).

(29) Xu, Y.-N., Chung, S.-Y., Bloking, J. T., Chiang, Y.-M., and Ching, W. Y. Electronic Structure and Electrical Conductivity of Undoped LiFePO4. *Electrochem. Solid-State Lett.* **7**, A131 (2004).

(30) Kasnatscheew, J., Evertz, M., Streipert, B., Wagner, R., Klöpsch, R., Vortmann, B., Hahn, H., Nowak, S., Amereller, M., Gentschev, A.-C., Lamp, P., Winter, M., The truth about the 1st cycle Coulombic efficiency of $LiNi_{1/3}Co_{1/3}Mn_{1/3}O_2$ (NCM) cathodes. *Phys. Chem. Chem. Phys.* **18**, 3956–3965 (2016).

(31) Ue, M., Sakaushi, K., and Uosaki, K. Basic knowledge in battery research bridging the gap between academia and industry. *Mater. Horiz.* **7**, 1937–1954 (2020).

(32) Drofenik, J., Gaberscek, M., Dominko, R., Poulsen, F. W., Mogensen, M., Pejovnik, S., Jamnik, J., Cellulose as a binding material in graphitic anodes for Li ion batteries: a performance and degradation study. *Electrochim. Acta* **48**, 883–889 (2003).

(33) Lee, J.-H., Lee, S., Paik, U., and Choi, Y.-M. Aqueous processing of natural graphite particulates for lithium-ion battery anodes and their electrochemical performance. *J. Power Sources* **147**, 249–255 (2005).

(34) Aurbach, D., Gamolsky, K., Markovsky, B., Gofer, Y., Schmidt, M., Heider, U., On the use of vinylene carbonate (VC) as an additive to electrolyte solutions for Li-ion batteries. *Electrochim. Acta* **47**, 1423–1439 (2002).

(35) Burns, J. C., Sinha, N. N., Coyle, D. J., Jain, G., VanElzen, C. M., Lamanna, W. M., Xiao, A., Scott, E., Gardner, J. P., and Dahn, J. R., The Impact of Varying the Concentration of Vinylene Carbonate Electrolyte Additive in Wound Li-Ion Cells. *J. Electrochem. Soc.* **159**, A85 (2011).

(36) Zhang, K., Guo, C., Zhao, Q., Niu, Z., and Chen, J. High-Performance Organic Lithium Batteries with an Ether-Based Electrolyte and 9,10-Anthraquinone (AQ)/CMK-3 Cathode. *Adv. Sci.* **2**, 1500018 (2015).

(37) Barchasz, C., Leprêtre, J.-C., Patoux, S., and Alloin, F. Electrochemical properties of ether-based electrolytes for lithium/sulfur rechargeable batteries. *Electrochim. Acta* **89**, 737–743 (2013).

(38) Song, J., Sun, B., Liu, H., Ma, Z., Chen, Z., Shao, G., Wang, G., Enhancement of the Rate Capability of $LiFePO_4$ by a New Highly Graphitic Carbon-Coating Method. *ACS Appl. Mater. Interfaces* **8**, 15225–15231 (2016).

(39) Moiseev, I. A., Savina, A. A., Pavlova, A. D., Abakumova, T. A., Gorshkov, V. S., Pazhetnov, E. M., and Abakumov, A. M., Single crystal Ni-rich NMC cathode materials for lithium-ion batteries with ultra-high volumetric energy density. *Energy Adv.* **1**, 677–681 (2022).

(40) Park, G.-T., Namkoong, B., Kim, S.-B., Liu, J., Yoon, C. S., and Sun, Y.-K., Introducing high-valence elements into cobalt-free layered cathodes for practical lithium-ion batteries. *Nat. Energy* **7**, 946–954 (2022).

(41) Ren, D., Padgett, E., Yang, Y., Shen, Y., Levin, B. D. A., Yu, Y., DiSalvo, F. J., Muller, D. A., and Abruña, H. D., Ultrahigh Rate Performance of a Robust Lithium Nickel Manganese Cobalt Oxide Cathode with Preferentially Orientated Li-Diffusing Channels. *ACS Appl. Mater. Interfaces* **11**, 41178–41187 (2019).

Acknowledgements

I wish to dedicate this last part of my Ph.D. thesis to my advisor, committee members, labmates, collaborators, families, and friends, without whom I cannot enjoy and complete my six-year graduate life. Words cannot really express all my appreciation to you, but I hope that you can feel the depth of my gratitude embedded in the following words.

I would like to first express my deepest appreciation to my advisor, Prof. Mircea Dincă, for his constant support, invaluable patience, constructive guidance, and expertise in chemical research. I have been benefiting tremendously from his scientific philosophy of always focusing on the key problems of the research fields of interest, which shaped my graduate research. His consistent belief and generous support in curiosity-guided research has encouraged me to explore a variety of different research topics with a significant degree of freedom. I'm particularly grateful to his continuous efforts to build and maintain a friendly, inclusive, and diverse ambiance in the group, which to me is one of the most important aspects that contribute to my great time here at MIT. Mircea, I cannot thank you enough for being my advisor.

I would like to extend my sincere gratitude to my thesis committee chair, Prof. Dan Suess, and committee member, Prof. Yogi Surendranath, for their support of my science endeavor. Their knowledge and expertise in chemical research, constructive advice and suggestions for my research projects, and support for my future academic career have helped me a lot during my Ph.D. time.

I could not have undertaken this journey without the mentorship from Dr. Jin-Hu Dou. Jin-Hu taught me about every aspects of research at the beginning of my graduate life, and helped me significantly with my research projects. I still remember vividly the times when we drove together to the Brookhaven National Laboratory and spent weeks there for experiments. He is also my close friend who has been giving me a lot of support and suggestions, especially for my future academic career. I would also like to express my great gratitude to Dr. Harish Banda for him being an excellent collaborator and a close friend. We have been in the Team Lamborghini and collaborating on various research projects during the time when you were in the group. I have learnt a lot of knowledge, skills, and techniques broadly related to electrochemical energy storage from your expertise in these areas. I am also thankful to Dr. Luming Yang and Dr. Chenyue Sun for providing constant support and encouragement, and being great friends and fans of anime, which brightened my days during my six-year PhD. I would like to thank my peers, Dr. Yi Qu and Dr. Mike Payne, for their support of graduate courses and research. I would like to thank Jules Oppenheim for his help with computational studies and really inspiring discussions about both of our research projects. I am also grateful to Dr. Eric Metzger, Dr. Maciej Korzyński, Dr. Elise Miner, Dr. Adam Rieth, Dr. Hoyoung Park, Dr. Amanda Stubbs, Dr. Grigorii Skorupskii, Dr. Lilia Xie, Dr. Ruomeng Wan, Dr. Maxx Arguilla, Dr. Robert Day, Dr. Dong-Gwang Ha, Dr. Ruperto (Rain) Mariano, Dr. Ivo Stassen,

Dr. Michal Borysiewicz, Dr. James Bour, Dr. Robert Comito, Dr. Xin He, Dr. Constanze Neumann, Dr. Ashley Wright, Garrett Hegel, Bhavish Dinakar, Nathan Gin, Andrei Iliescu, Junyong Mo, Alice Su, Bowen Tan, Zhentao Yang, Eric You, Kim Zhang, Dr. Justin Andrews, Dr. Won Ho Choi, Dr. Ai He, Dr. Val Hosseininasab, Dr. Young-Moo Jo, Dr. Stavroula (Alina) Kampouri, Dr. Dong-Ha Kim, Dr. Patrick Sarver, Dr. Jiande Wang for being great labmates.

Thanks should also go to all my collaborators. I would like to express my special thanks to my collaborators in University Fribourg, Switzerland, including Prof. Ali Coskun and his students, Patrick Fritz and Timur Ashirov. I'm always impressed by their magic to synthesize complex organic linkers for me to build innovative conductive metal-organic frameworks. I also enjoyed my time in characterizing the intriguing properties of porous organic polymers they made. A lot of my research works would not have been successful without the help from Dr. Jian Li with his expertise in using electron diffraction to solve the crystal structures of microcrystalline materials. I am also grateful for the help from my collaborators from the Brookhaven National Laboratory, including but not limited to Dr. Ashley Head for her assistance with ambient pressure X-ray photoelectron spectroscopy, and Dr. Yugang Zhang for his assistance with small-angle/wide-angle X-ray scattering measurements.

I also hope to express my sincere gratitude to all my friends for their encouragements and support, no matter where their physical locations are. I hope to express my special thanks to Prof. Mingjiang Zhong and his wife Dr. Hui Zhi for being close friends to both my wife and me. Their constant support to us has brightened our life, especially the time since pandemic.

Lastly, I hope to thank my wife, Mengxue Cao, and my parents, Jinzhu Lin and Tongpeng Chen, for their unconditioned love and unbudging support. The weekends I spent with my wife in New Haven and occasionally in Boston were the happiest times during my Ph.D. years. I hope you all will feel proud of me. I would also be remiss in not mentioning my cat, Da Bing (means "big pancake"), for all the entertainment and emotional support.